

ZEROth-ORDER DESIGN REPORT

for the

NEXT LINEAR COLLIDER



This document, and the material and data contained therein, was developed under sponsorship of the United States Government. Neither the United States nor the Department of Energy, nor the Leland Stanford Junior University, nor their employees, nor their respective contractors, subcontractors, or their employees, makes any warranty, express or implied, or assumes any liability of responsibility for accuracy, completeness or usefulness of any information, apparatus, product or process disclosed, or represents that its use will not infringe privately-owned rights. Mention of any product, its manufacturer, or suppliers shall not, nor is it intended to, imply approval, disapproval, or fitness for any particular use. A royalty-free, nonexclusive right to use and disseminate same for any purpose whatsoever, is expressly reserved to the United States and the University.

DISCLAIMER

Portions of this document may be illegible in electronic image products. Images are produced from the best available original document.

PUB
~~EBNL-5424~~
SLAC-474-*Vol.1*
UCRL-ID-124161
UC-414

Zeroth-Order Design Report for the Next Linear Collider

Volume I

The NLC Design Group

May, 1996

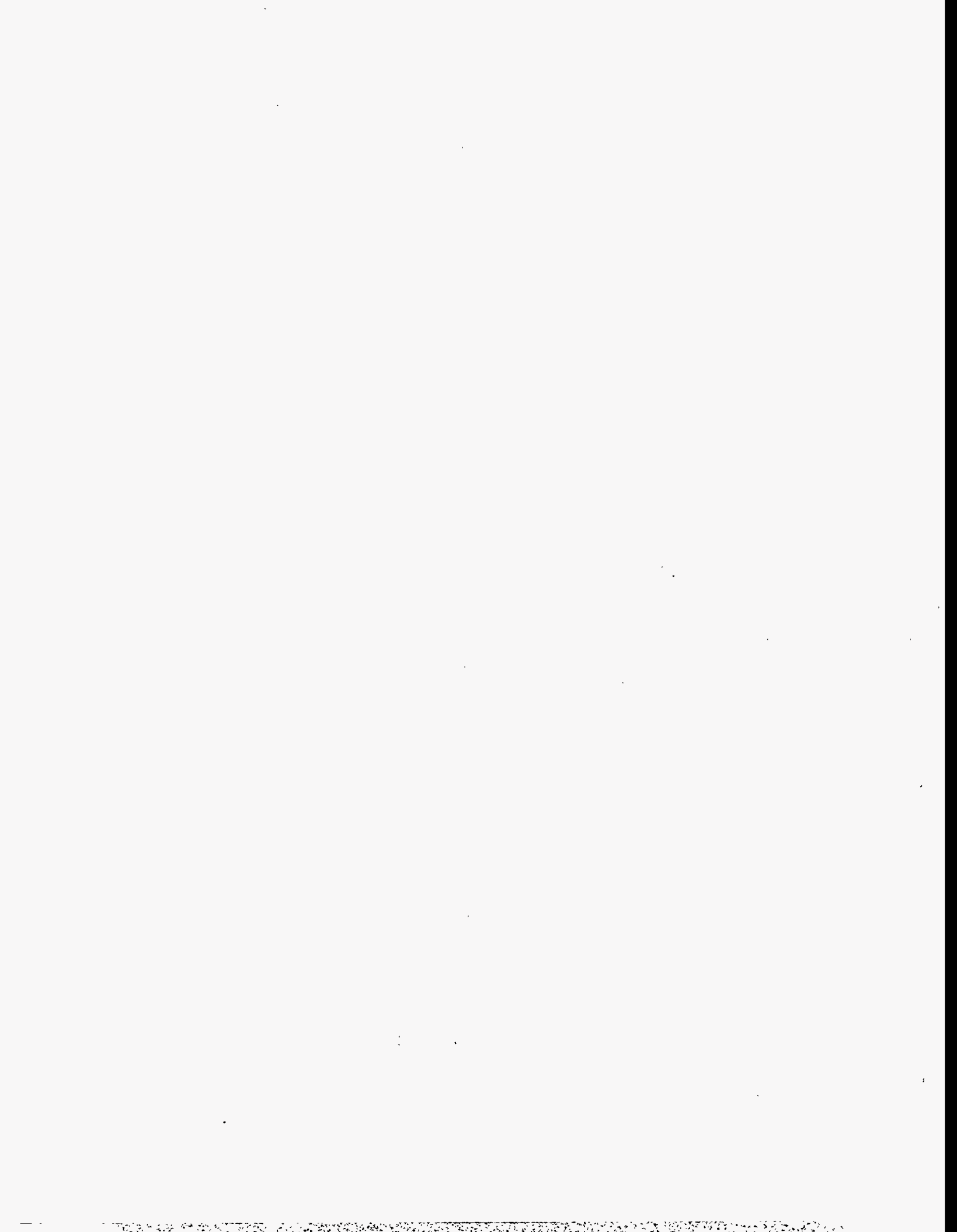
Prepared for the Department of Energy under contract number DE-AC03-76SF00515 by Stanford Linear Accelerator Center, Stanford University, Stanford, California. Printed in the United States of America. Available from National Technical Information Service, US Department of Commerce, 5285 Port Royal Road, Springfield, Virginia 22161.

This document is available on the World Wide Web at <http://www.slac.stanford.edu/>.

MASTER

DISTRIBUTION OF THIS DOCUMENT IS UNLIMITED

DLC



The NLC Design Group

C. Adolphsen, R. Aiello, R. Alley, R. Assmann, K.L. Bane, T. Barklow, V. Bharadwaj, J. Bogart, G.B. Bowden, M. Breidenbach, K.L. Brown, D.L. Burke, Y. Cai, G. Caryotakis, R.L. Cassel, P. Chen, S.L. Clark, J.E. Clendenin, C. Corvin, F.-J. Decker, A. Donaldson, R.A. Early, K.R. Eppley, S. Ecklund, J. Eichner, P. Emma, L. Eriksson, Z.D. Farkas, A.S. Fisher, C. Foundoulis, W.R. Fowkes, J. Frisch, R.W. Fuller, L. Genova, S. Gold, G. Gross, S. Hanna, S. Hartman, S.A. Heifets, L. Hendrickson, R.H. Helm, H.A. Hoag, J. Hodgson, J. Humphrey, R. Humphrey, J. Irwin, R.K. Jobe, R.M. Jones, L.P. Keller, K. Ko, R.F. Koontz, E. Kraft, P. Krejcik, A. Kulikov, T.L. Lavine, Z. Li, W. Linebarger, G.A. Loew, R.J. Loewen, T.W. Markiewicz, T. Maruyama, T.S. Mattison, B. McKee, R. Messner, R.H. Miller, M.G. Minty, W. Moshhammer, M. Munro, C.D. Nantista, E.M. Nelson, W.R. Nelson, C.K. Ng, Y. Nosochkov, D. Palmer, R.B. Palmer, J.M. Paterson, C. Pearson, R.M. Phillips, N. Phinney, R. Pope, T.O. Raubenheimer,¹ J. Rifkin, S.H. Rokni, M.C. Ross, R.E. Ruland, R.D. Ruth, A. Saab, H. Schwarz, B. Scott, J.C. Sheppard, H. Shoaee, S. Smith, W.L. Spence, C.M. Spencer, J.E. Spencer, D. Sprehn, G. Stupakov, H. Tang, S.G. Tantawi, P. Tenenbaum, F. Tian, K.A. Thompson, J. Turner, T. Usher, A.E. Vlieks, D.R. Walz, J.W. Wang, A.W. Weidemann, D.H. Whittum, P.B. Wilson, Z. Wilson, M. Woodley, M. Woods, Y.T. Yan, A.D. Yeremian, F. Zimmermann; *Stanford Linear Accelerator Center, Stanford, California, USA*

A. Jackson, W.A. Barletta, J.M. Byrd, S. Chattopadhyay, J.N. Corlett, W.M. Fawley, M. Furman, E. Henestroza, R.A. Jacobsen, K.-J. Kim, H. Li, H. Murayama, L. Reginato, R.A. Rimmer, D. Robin, M. Ronan, A.M. Sessler, D. Vanecek, J.S. Wurtele, M. Xie, S.S. Yu, A.A. Zholents; *Lawrence Berkeley National Laboratory, Berkeley, California, USA*

L. Bertolini, K. Van Bibber, D. Clem, F. Deadrick, T. Houck, M. Perry, G.A. Westenskow; *Lawrence Livermore National Laboratory, Livermore, California, USA*

M. Akemoto, T. Higo, K. Higashi, K. Kubo, K. Oide, K. Yokoya; *KEK National Laboratory, Tsukuba, Japan*
L. Rinolfi; *CERN, Geneva, Switzerland*

J.A. Holt; *Fermilab National Laboratory, Batavia, Illinois, USA*

V. Telnov; *Budker Institute for Nuclear Physics, Novosibirsk, Russia*

T. Takahashi, T. Ohgaki; *Hiroshima University, Hiroshima, Japan*

J. Rosenzweig; *University of California, Los Angeles, Los Angeles, California, USA*

S. Lidia; *University of California, Davis, Davis, California, USA*

N.M. Kroll; *University of California, San Diego, San Diego, California, USA*

A.J. Dragt, R.L. Gluckstern; *University of Maryland, College Park, Maryland, USA*

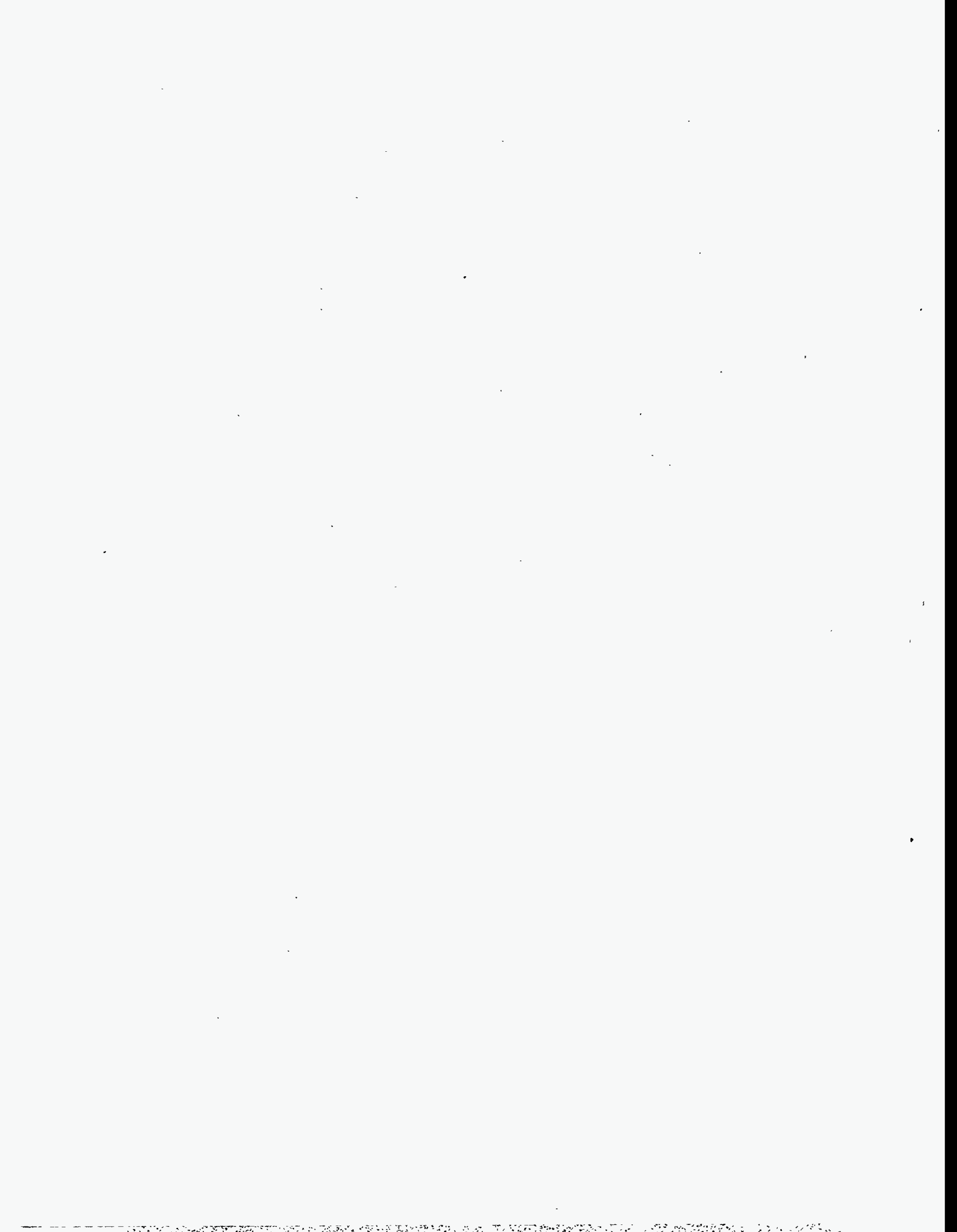
S.R. Hertzbach; *University of Massachusetts, Amherst, Massachusetts, USA*

G. Giordano; *University of Milano, Milan, Italy*

R.E. Frey; *University of Oregon, Eugene, Oregon, USA*

D.D. Meyerhofer; *University of Rochester, Rochester, New York, USA*

¹Editor-in-chief.

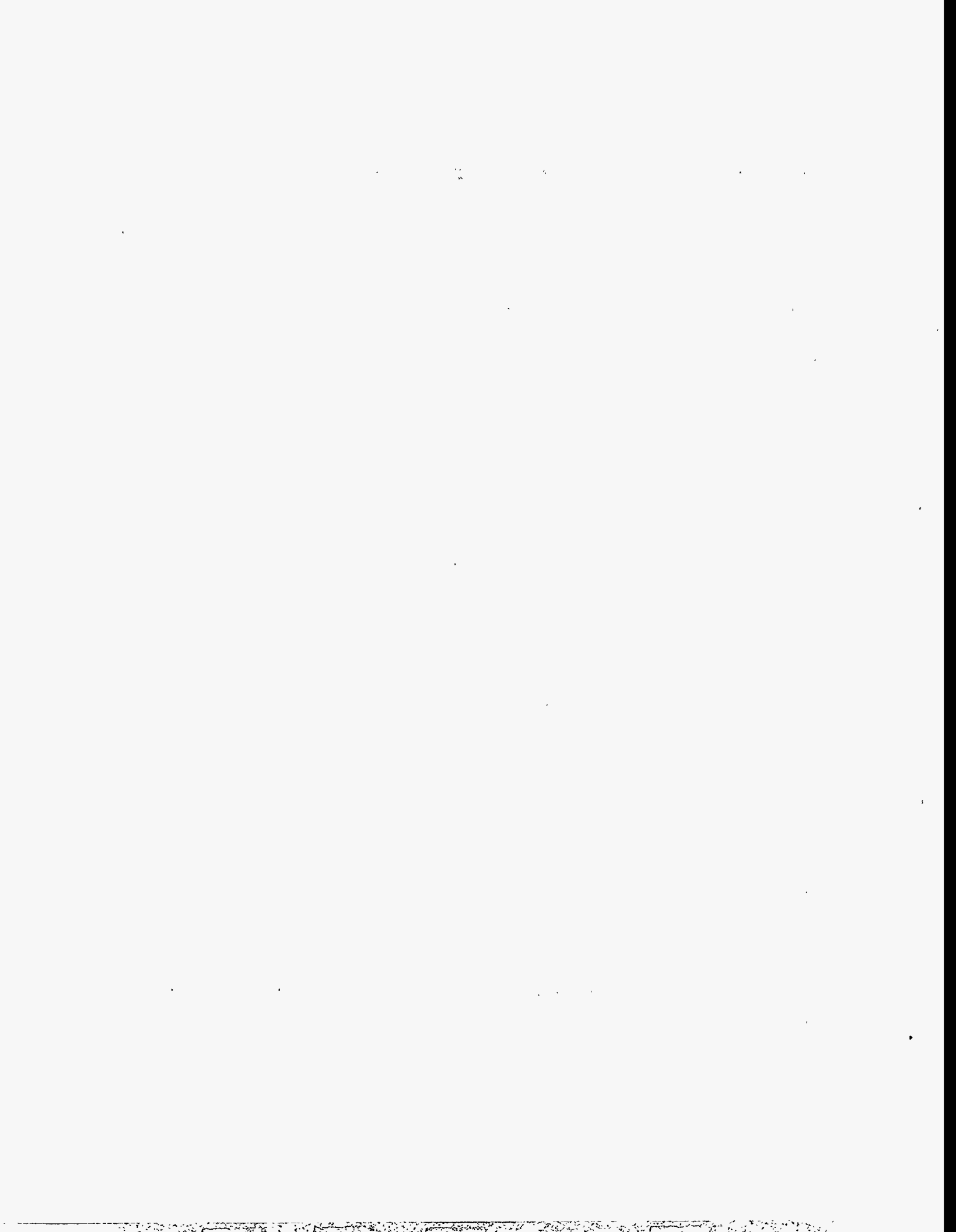


Acknowledgments

This design for the Next Linear Collider (NLC) relies heavily on the first linear collider—the Stanford Linear Collider (SLC)—and on all the people who proposed, designed, and commissioned this pioneering accelerator. Without their work, none of this would have been possible (or necessary). In addition, the design owes much to the extensive international research effort that is investigating the different technological paths to a future linear collider. Finally, the NLC Design Group is a list of people, authors and non-authors, who have contributed significantly to this design; our apology in advance to anyone whose name may have inadvertently been omitted.

In the process of completing this “Zeroth-Order Design” for the NLC, we have held two internal reviews and, more recently, an international external review. All of these have been very important to the design and we thank all of those who assisted. In particular, we thank the members of the external review panel which consisted of: Gerry Dugan, Helen Edwards, Hans Frischholz, David Gurd, Tom Himel, Steve Holmes, Norbert Holtkamp, John Ives, Robert Jameson, Katsunobu Oide, Satoshi Ozaki, John Rees, Nobu Toge. A number of useful comments were made, some of which already have been incorporated into the design. Most members of the internal review committees are listed in the contributors list; additional useful suggestions were given by H. DeStaebler, J.T. Seeman, R.H. Siemann, U. Wienands, and M. Zisman, along with many other members of the LBL, LLNL, and SLAC communities.

Finally, we would like to thank Angie Seymour, Marge Bangali, and Mary Litynski for administrative support, Terry Anderson, Sylvia MacBride, and Jim Wahl for creating the illustrations, and Jamie Walker and Laurie Gennari for producing this document.



Contents

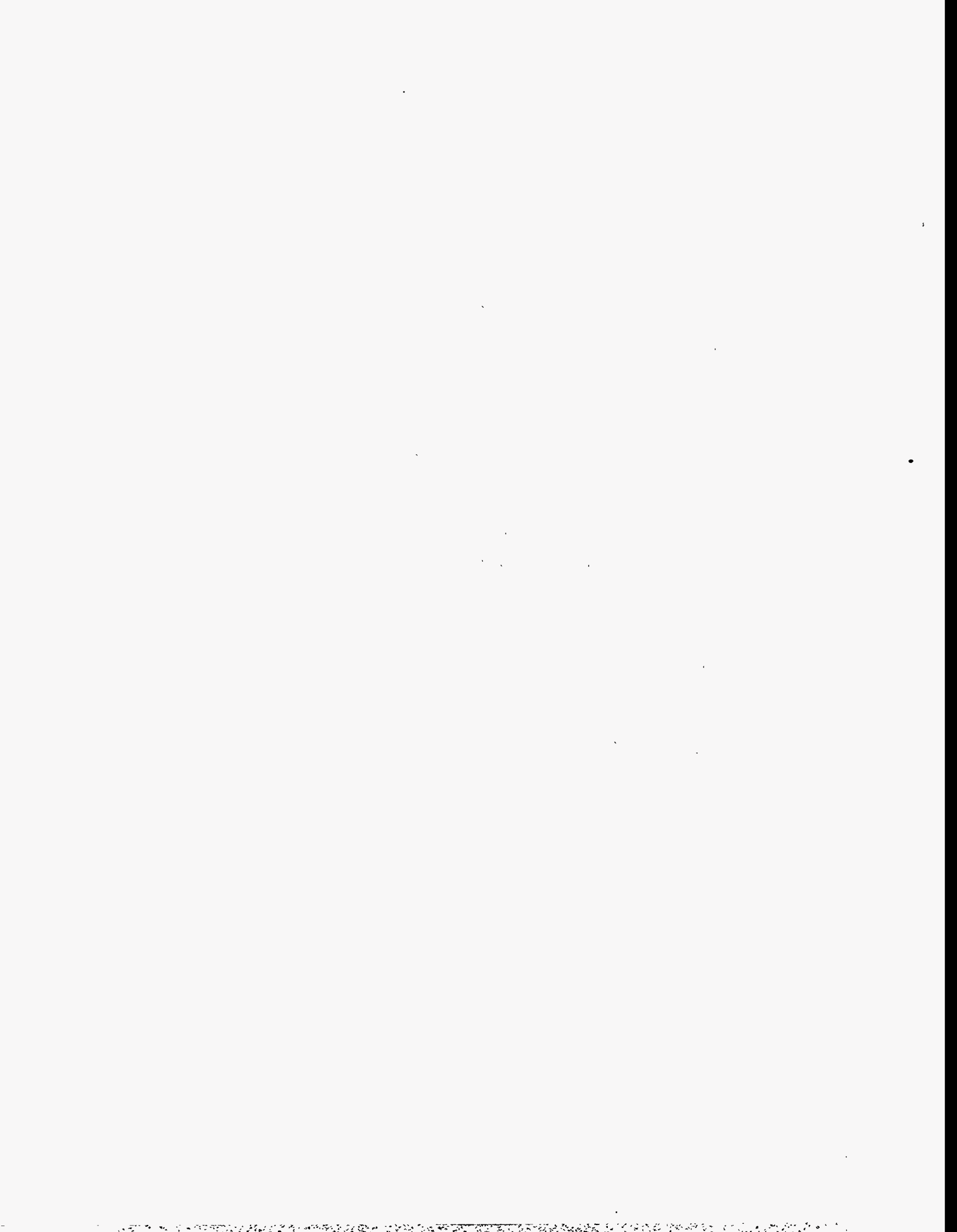
Preface	xi
Volume I	1
1 Introduction	1
1.1 Goals for the Next Linear Collider	1
1.2 Accelerator Design Choices	3
1.3 The Next Linear Collider	8
1.4 Outlook for the Next Linear Collider	15
1.5 NLC Systems Overview	15
2 Electron Source	25
2.1 Introduction	27
2.2 Polarized Electron Gun	30
2.3 NLC Laser System	37
2.4 NLC Electron Injector Beam Dynamics	41
2.5 Buncher Cavities	51
2.6 Positron Drive Linac	51
2.7 Diagnostics	53
2.8 Operation	56
2.9 Conclusion	57
2.A Polarized e^- Beam Photocathode RF Gun Development for the NLC	58
2.B Charge Limit and its Implications on High-Polarization Long-Pulse Charge	74
3 Positron Source	83
3.1 Introduction	85
3.2 Positron Yield Simulation	90
3.3 Drive Electron Accelerator	92
3.4 Positron Production Target	92
3.5 Positron Collection System	97
3.6 Beam Dynamics and Transport	99
3.7 Positron Linac	101
3.8 Radiation Control Issues	103
3.9 Magnets	105
3.10 Diagnostics and Instrumentation	106
3.11 Feedback and Stability	108
3.12 Operations and Tuning Procedures	109
3.13 Control System Needs	110
3.14 Other Considerations	110
3.15 Summary	111

4	NLC Damping Rings	115
4.1	Introduction	117
4.2	System Overview and Parameter Determination	118
4.3	Lattice Design	133
4.4	Collective Limitations	166
4.5	RF Systems	195
4.6	Vacuum Systems	211
4.7	Feedback and Feedforward Systems	217
4.8	Vibration and Stability	223
4.9	Alignment and Supports	226
4.10	Magnet Design and Power Supplies	229
4.11	Instrumentation for the Main Damping Rings	246
4.12	Conclusions and Comments	249
5	Bunch Compressors and Prelinac	257
5.1	Introduction	258
5.2	Requirements and Design Options	260
5.3	System Design	265
5.4	Longitudinal Dynamics	281
5.5	Transverse Dynamics	298
5.6	Tolerances	310
5.7	Conclusions and Comments	314
6	Low-Frequency Linacs and Compressors	319
6.1	Introduction	320
6.2	Beam-Loading Compensation	320
6.3	Numerical simulation of beam-loading compensation	324
6.4	Klystrons	333
6.5	Dipole Wakefields	335
7	Main Linacs: Design and Dynamics	343
7.1	Introduction	345
7.2	Parameters and Specifications	346
7.3	System Design	349
7.4	Emittance Dynamics	366
7.5	Alignment, Stability, and Feedback	392
7.6	Simulation Studies	406
7.7	Tolerances	429
7.8	Operations and Machine Protection System	431
7.9	Linac Components	432
7.10	Instrumentation	440
7.11	Discussion	449
8	RF System for the Main Linacs	455
8.1	Introduction	457
8.2	Accelerator Structure	466
8.3	RF Pulse Compression and Power Transmission	493
8.4	High-Power Klystrons	502
8.5	Klystron Pulse Modulator	517
8.6	RF Drive and Phasing Systems	530
8.7	RF Protection and Monitoring Systems	546

Volume II	555
9 Collimation Systems	555
9.1 Introduction to Beam Delivery Systems	556
9.2 Post-Linac Collimation	560
9.3 Pre-Linac Collimation	631
9.4 Bunch Length Collimation	634
10 IP switch and big bend	643
10.1 Introduction	644
10.2 The IP Switch	644
10.3 The Big Bend	648
11 Final Focus	659
11.1 Introduction	661
11.2 Parameters and Specifications	662
11.3 Skew Correction and Diagnostic Section	665
11.4 Beta-Matching Section	669
11.5 Chromatic Correction and Final Transformer	676
11.6 The Final Doublet	743
11.7 Crossing Angle, Crab Cavity, and Solenoid	767
11.8 The Beam Extraction and Diagnostic System (The Dump Line)	774
11.9 Conclusions and Comments	800
11.A The Beam Dumps	802
12 The Interaction Region	815
12.1 Introduction	816
12.2 The Luminosity Spectrum	817
12.3 Detector Background Sources	823
12.4 Detector Issues	836
12.5 Conclusions	851
13 Multiple Bunch Issues	855
13.1 Introduction	856
13.2 Major Impacts of Multibunching	857
13.3 Machine Protection and Operations	864
13.4 Instrumentation Specifications	865
13.5 Experimental tests related to multibunch issues	865
13.6 Summary and Conclusions	865
14 Control System	869
14.1 Introduction	870
14.2 NLC Requirements	870
14.3 Architectural implications	875
14.4 The Control System Model	876
15 Instrumentation	887
16 Machine Protection Systems	889
16.1 Introduction	890
16.2 Single Pulse Induced Failure	890

17 NLC Reliability Considerations	903
17.1 Goals	904
17.2 Reliability and Availability	904
17.3 Target NLC Availability	905
17.4 NLC Machine Availability and System Reliability	906
17.5 A Formal Solution	908
17.6 Three Examples: Klystrons, Power Supplies, and Motors	911
17.7 Summary	911
18 NLC Conventional Facilities	915
18.1 Introduction	916
18.2 Site	916
18.3 Campus	917
18.4 Injectors	917
18.5 Linac	917
18.6 Detectors	918
A An RF Power Source Upgrade to the NLC Based on the Relativistic-Klystron ...	925
A.1 Introduction	926
A.2 A Design for an RK-TBA-Based rf Power Source	927
A.3 TBNLC Physics Studies	937
A.4 TBNLC Engineering Design	947
A.5 RTA Test Facility	956
A.6 Conclusions	964
B A Second Interaction Region For Gamma-Gamma, Gamma-Electron and ...	971
B.1 Introduction	973
B.2 Physics Opportunities at $\gamma\gamma$ Collider: The Higgs Sector and Other New Physics	974
B.3 Major Parameters	978
B.4 CP Issues	980
B.5 IP Issues	987
B.6 Luminosity Calculations	989
B.7 Backgrounds and Other Detector Considerations	999
B.8 Laser Optical Path in IR	1006
B.9 Gamma-Gamma Final Focus System	1015
B.10 Extraction and Diagnostic Line	1019
B.11 Laser Technology I: Solid State Lasers	1020
B.12 Free-Electron Lasers	1030
C Ground Motion: Theory and Measurement	1043
C.1 Introduction	1044
C.2 Theory	1044
C.3 Ground Motion Measurement Devices	1057
C.4 SLAC Ground Motion Measurements and Analysis	1063
D Beam-based Feedback: Theory and Implementation	1075
D.1 Introduction	1076
D.2 Planned NLC Feedbacks	1076
D.3 Feedback System Design	1077
D.4 Performance Questions	1077

D.5	Adaptive Cascade	1078
D.6	Rate Considerations and Corrector Speeds	1078
D.7	Calibrations and Modeling	1079
D.8	Global Performance Characterization	1079
D.9	Summary	1080



Preface

This “Zeroth-Order Design Report” (ZDR) for the Next Linear Collider (NLC) is being created at a time of both great opportunity and uncertainty in the future directions that will be taken by the world-wide community of high-energy physics. There is exciting news that the Large Hadron Collider project has been approved for construction at CERN, and the planned involvement by physicists and engineers from countries around the globe will make this the first accelerator to be designed and built by a truly world-wide collaboration. By contrast, the cancellation of the SSC has demonstrated the necessity of international collaboration on such large scientific projects. The community of scientists and engineers at work on the accelerator physics and technologies of high-energy electron-positron colliders has recognized this need, and has made concerted effort to coordinate research activities to optimize our combined understanding and knowledge. This ZDR is one further step in this process.

The first electron-positron linear collider, the Stanford Linear Collider (SLC), began operation in 1989 with the dual purpose to explore the particle physics of the Z^0 boson and to develop the accelerator physics needed for a future TeV-scale linear collider. The SLC program has proven to be quite successful on both counts. Experiences gained and lessons learned from this prototype collider are a firm foundation for the design and implementation of a next generation machine. Developments at laboratories around the world have led to several choices of technologies to efficiently accelerate beams of electrons and positrons to high energy, and major test facilities presently nearing completion will soon allow evaluation of complete systems of these acceleration techniques. Additional test facilities already, or soon will, provide demonstrations and experience with techniques to create and control the delicate beams required to achieve the high luminosities needed for particle physics at the TeV-scale.

This NLC ZDR has been completed in the above context as a feasibility study for a TeV-scale linear collider that incorporates a room-temperature accelerator powered by rf microwaves at 11.424 GHz—similar to that presently used in the SLC, but at four times the rf frequency. The purpose of this study is to examine the complete systems of such a collider, to understand how the parts fit together, and to make certain that every required piece has been included. The “design” presented here is not fully engineered in any sense, but to be assured that the NLC can be built, attention has been given to a number of critical components and issues that present special challenges. More engineering and development of a number of mechanical and electrical systems remain to be done, but the conclusion of this study is that indeed the NLC is technically feasible and can be expected to reach the performance levels required to perform research at the TeV energy scale.

It is important to recognize that the contents of this ZDR include the work of many people not acknowledged as authors in the subsections of the report. This ZDR is the result of many years of discussion and investigation with scientists and engineers from around the world. References have been given in the text, but it is not always possible to accurately identify the true source of many of the notions and ideas included in a work of this type. The authors of this report apologize in advance for omissions. Effort has been made to use technical definitions in this ZDR that conform as widely as possible to those used in the recently completed International Linear Collider Technical Review Committee Report (The TRC Report, edited by G. Loew, SLAC Report-471, 1996). The ideas and parameters that appear in this ZDR have evolved from those given in the TRC report. Even so, the TRC report is a valuable companion to this document.

Introduction

1.1 Goals for the Next Linear Collider

For the past 25 years accelerator facilities with colliding beams have been the forefront instruments used to study elementary particle physics at high energies (Figure 1-1). Both hadron-hadron and electron-positron colliders have been used to make important observations and discoveries. Direct observations of the W^\pm and Z^0 bosons at CERN and investigations of the top quark at Fermilab are examples of physics done at hadron colliders. Electron-positron colliders provide well-controlled and well-understood experimental environments in which new phenomena stand out and precise measurements can be made. The discoveries of the charm quark and τ lepton at SPEAR, discovery of the gluon and establishment of QCD at PETRA and PEP, and precision exploration of electroweak phenomena at the SLC and LEP are highlights of the results produced by experiments at electron-positron colliders.

The ability to study nature with these two different kinds of instruments has proven essential to the advancement of our understanding of particle physics. This will remain true as we seek answers to questions posed at the TeV energy scale:

- What is the top quark, and what are its interactions?
- Why is the symmetry of the electroweak interaction broken, and what is the origin of mass?
- Do Higgs particles exist? If so, how many, and what are their structures and interactions?
- Is the world supersymmetric, and if so, what is its structure, and is it part of a larger unification of nature?
- Are quarks, leptons, and gauge bosons fundamental particles, or are they more complex?
- Are there other new particles or interactions, and what might nature contain that we have not yet imagined?

The Large Hadron Collider (LHC) in Europe offers an entry into the TeV energy regime with significant opportunity for discovery of new phenomena. The planned participation in the design, construction, and utilization of this collider by nations around the world will make the LHC the first truly global facility for the study of particle physics. This will be an exciting and important step in the continuing evolution of our science.

The companion electron-positron collider at this next step in energy, a Next Linear Collider (NLC), will provide a complementary program of experiments with unique opportunities for both discovery and precision measurement. To understand the nature of physics at the TeV scale, to see how the new phenomena we expect to find there fit together with the known particles and interactions into a grander picture, both the LHC and an NLC will be required.

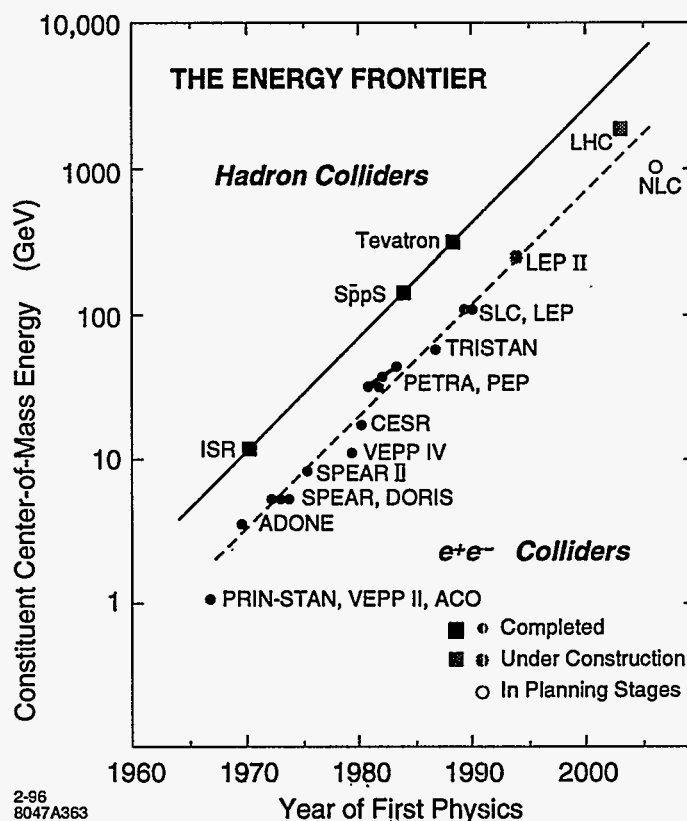


Figure 1-1. The energy frontier of particle physics. The effective constituent energy of existing and planned colliders and the time of first physics results from each.

Studies of physics goals and requirements for the next-generation electron-positron collider began in 1987-88 in the United States [Ahn 1988, Snowmass 1988, Snowmass 1990], Europe [LaThuile 1987, DESY 1990], and Japan [JLCI 1989, JLCII 1990]. These regional studies have evolved into a series of internationally sponsored and organized workshops [Finland 1991, Hawaii 1993, Japan 1995] that continue to build an important consensus on the goals and specifications of a Next Linear Collider. More recently, a series of workshops were held over the past year at locations throughout the United States. Working groups were established at a first meeting in Estes Park, Colorado to provide a framework for people to participate in the discussions of various topics in physics and experimentation at linear colliders. These groups continued to meet at subsequent workshops held at Fermilab, SLAC, and Brookhaven Laboratories. The results of those meetings is presented in a companion document "Physics and Technology of the Next Linear Collider" [NLC Physics] which also provides a summary of the NLC design.

A picture has emerged of a high-performance collider able to explore a broad range of center of mass energies from a few hundred GeV to a TeV and beyond (Figure 1-2). The goals of particle physics at TeV energies require luminosities $\sim 10^{34} \text{cm}^{-2} \text{sec}^{-1}$ and reliable technologies that can provide large integrated data samples. It is important that the beam energy spread remain well controlled and that backgrounds created by lost particles and radiation from the beams be maintained at low levels. This will assure that the clean experimental environment, historically offered by electron-positron colliders, remains intact. Beam polarization, an additional tool available at a linear collider that provides new and revealing views of particle physics, is also a requirement for any future collider.

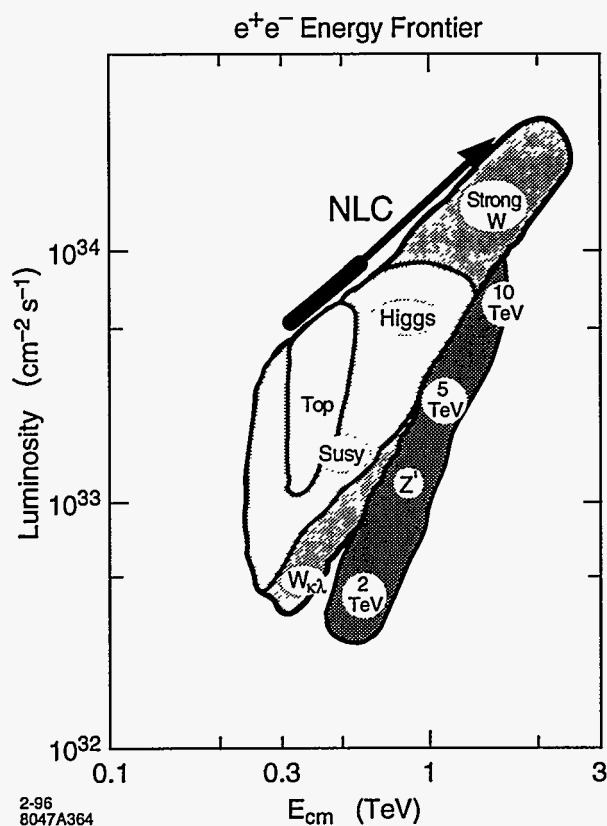


Figure 1-2. Physics goals for a TeV-scale e^+e^- collider.

In this first chapter, we introduce the accelerator physics and technologies of the Next Linear Collider, discuss its design choices and philosophies, and provide a brief status report on the R&D program that is being carried out in support of the NLC design effort. The last section of this chapter will provide an overview of the NLC design and then the design is presented in the following seventeen chapters. This is supplemented with four appendices that describe an alternate power source that might be used for the 1.5 TeV upgrade, a possible second interaction region, ground motion studies, and a description of beam-based feedback which is utilized throughout the collider design. As stated, there is also a companion document “Physics and Technology of the Next Linear Collider”, that contains results from a series of workshops studying the physics and experimental issues in the NLC as well as a shorter summary of the collider design.

1.2 Accelerator Design Choices

1.2.1 The Stanford Linear Collider

The Stanford Linear Collider (Figure 1-3) was conceived and built to accomplish two goals: to study particle physics at the 100-GeV energy scale and to develop the accelerator physics and technology necessary for the

realization of future high-energy colliders. The SLC was completed in 1987 and provided a first look at the physics of the Z^0 in 1989. In time, the luminosity provided by this machine has grown steadily (Figure 1-4), and has allowed particle physicists to make unique and important studies of the Z^0 and its decays.

The design of the Next Linear Collider (NLC) presented in this document is intimately connected with experiences gained at the SLC. Our choices of technologies and philosophies of design have direct links to these experiences and considerable overlap with them. Lessons have been learned and techniques developed at the SLC that are relevant to the design and implementation of every part and system of the NLC:

- Injectors
 - Stabilized high-power electron sources
 - Polarized electrons
 - High-power targets and positron capture
- Damping Rings
 - Stabilized fast (50 ns) injection and extraction systems
 - Sub-ps phase synchronization with linac rf systems
- Linear Acceleration
 - Management of large rf systems
 - rf phase control
 - “Time-slot” compensation
 - Short-range longitudinal wake compensation
 - Multibunch beam loading compensation
- Linac Emittance Preservation
 - Beam-based alignment
 - LEM—energy/lattice matching
 - BNS damping
 - Coherent wakefield cancelation
 - Dispersion-free steering
- Final Focus Systems
 - Second-order chromatic optics and tuning
 - Precision diagnostics
 - Beam-beam control and tuning
- Experimentation
 - Theory and modeling of backgrounds
 - Vulnerability of detector technologies
 - Collimation—theory and implementation
- Systems Performance and Operation

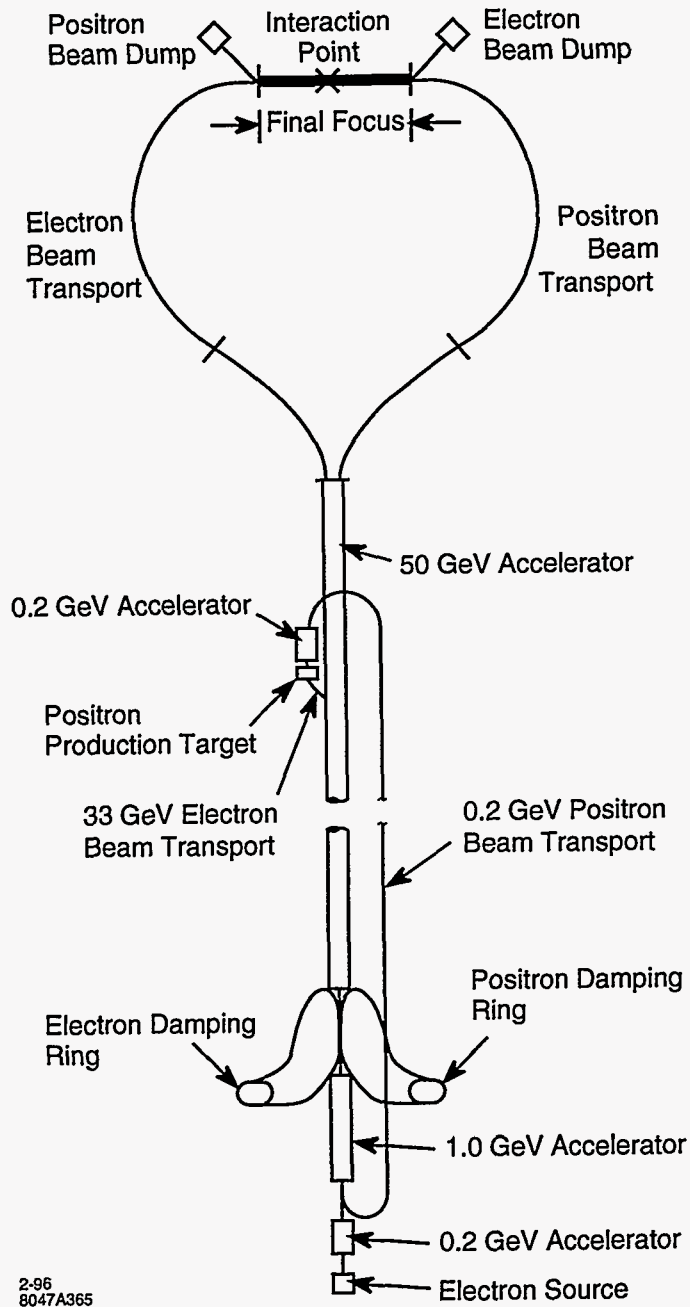


Figure 1-3. The Stanford Linear Collider (SLC).

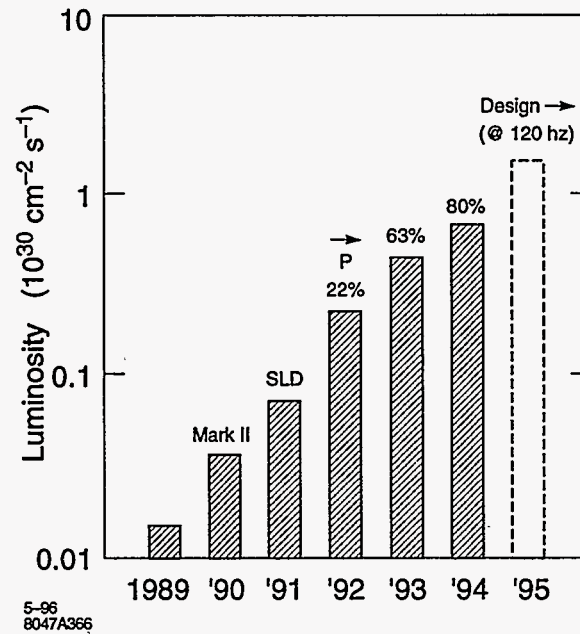


Figure 1-4. Performance of the SLC from early commissioning. Polarization of the electron beam is also shown.

- Precision instrumentation—BPMs and wire scanners
- Feedback theory and implementation
- Importance of on-line modeling and analysis
- Automated diagnostics and tuning
- Mechanical stabilization of supports and components
- Thermal stabilization of supports and components
- Reliability
- History monitoring (from seconds to years)

1.2.2 Future Linear Colliders

The basic components of any linear collider are those already incorporated into the SLC. The energy of such a future collider must be five to ten times that of the SLC, and a TeV-scale collider must be able to deliver luminosities that are several orders of magnitude greater than those achieved at the SLC. A generic collider complex is diagrammed in Figure 1-5. Trains of bunches of electrons and positrons are created, condensed in damping rings, accelerated to high energy, focused to small spots, and collided to produce a brightness given by

$$L = \frac{nN^2 H f}{4\pi\sigma_x^* \sigma_y^*}, \quad (1.1)$$

where

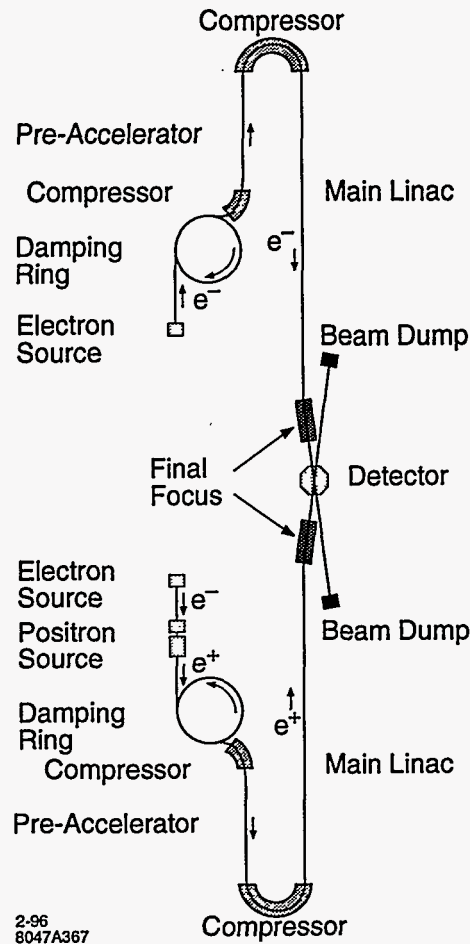


Figure 1-5. Layout of a TeV-scale linear collider (not to scale).

- n = number of bunches per train,
- N = number of particles per bunch,
- H = Length enhancement,
- f = machine repetition rate,

and σ_x^* and σ_y^* are the horizontal and vertical beam dimensions at the collision point. Equation 1.1 can be written as

$$L = \frac{1}{4\pi E} \frac{NH P}{\sigma_x^* \sigma_y^*}, \quad (1.2)$$

where P is the average power in each beam. The factor N/σ_x^* determines the number of beamstrahlung photons emitted during the beam-beam interaction, and since these photons can create backgrounds in experimental detectors, this factor is highly constrained. It is mainly the last ratio that can be addressed by accelerator technology; high luminosity corresponds to high beam power and/or small beam spots. These two parameters pose different, and in many cases contrary, challenges to the accelerator physicist, and several technologies that represent differing degrees of compromise between beam power and spot size are being developed. Table 1-1 summarizes the initial stage of the mainstream design choices.

	Rf Freq (GHz)	Rf Grad (MV/m)	Total Length (km)	Beam Power (MW)	σ_y (nm)	Luminosity ($10^{33} \text{ cm}^{-2} \text{ s}^{-1}$)
SuperC	1.3	25	30	8.2	19	6
S-Band	3.0	21	30	7.3	15	5
X-Band	11.4	50	16	4.8	5.5	6
2-Beam	30.0	80	9	2.7	7.5	5

Table 1-1. Linear collider design parameters ($E_{cm} = 500 \text{ GeV}$).

Facility	Location	Goal	Operations
SLC	SLAC	Prototype Collider	1988-1998
ATF	KEK	Injector	1995
		Damping Ring	1996
TTF	DESY	SuperC Linac	1997
SBTF	DESY	S-band Linac	1996
NLCTA	SLAC	X-band Linac	1996
CTF	CERN	2-Beam Linac	1996
FFTB	SLAC	Final Focus Interaction Region	1994

Table 1-2. Linear collider test facilities around the world.

Each of the technologies in Table 1-1 is being pursued by physicists and engineers at laboratories around the globe. This strong international effort is remarkably well coordinated through collaborations that combine to provide a set of test facilities to address each of the important aspects of the collider design and implementation. A summary of the facilities presently in operation or under construction is given in Table 1-2.

1.3 The Next Linear Collider

1.3.1 Technology Choice and Design Philosophy

The goal to reach 1 to 1.5-TeV center-of-mass energy with luminosities of $10^{34} \text{ cm}^{-2} \text{ s}^{-1}$ or better and our experiences with the SLC guide our choice of technologies for the NLC. We believe that the most natural match to these design goals is made with normal-conducting X-band (11.424 GHz) microwave components patterned after the S-band technology used in the SLC. A schematic of a section of the rf system for the NLC is shown in Figure 1-6. Our choice of technology has required the development of new rf klystrons and advanced pulse compression systems, but provides confidence that accelerating gradients of 50-100 MV/m can be achieved and used in the implementation of the collider. The technical risk of building a collider with new X-band technologies is perhaps greater than simply building a larger SLC at S-Band, but the goal to reach 1-1.5 TeV is substantially more assured, and capital costs to reach these energies will be lower.

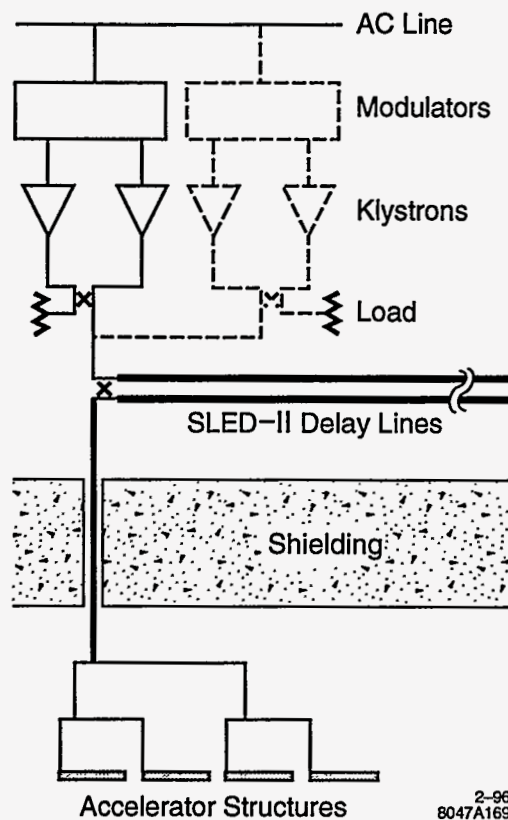


Figure 1-6. Normal-conducting microwave rf system for the NLC.

The NLC is designed with a nominal center-of-mass energy of 1 TeV. It is envisaged to be built with an initial rf system able to drive the beams to 0.5-TeV center-of-mass energy, but with all the infrastructure and beam lines able to support 1 TeV. The rf system design incorporates the ability to replace and add modulators and klystrons without access to the accelerator beam line (dashed lines in Figure 1-6), so an unobtrusive, smooth, and adiabatic transition from 0.5 TeV to 1 TeV center-of-mass energy can be made with modest and expected improvements in X-band technology. This allows the collider to begin operation with the greatest of margins in cost and performance, and provides an excellent match to the anticipated physics goals at the energy frontier (Figure 1-2). Our philosophy is akin to that taken previously in the construction of the SLAC linac which provided a 17-GeV electron beam at its inauguration, was improved to 35 GeV, and with continued advances in S-band technology, now provides 50-GeV electrons and positrons for the SLC.

The NLC design also incorporates multiple paths to further upgrade the center-of-mass energy to 1.5 TeV. The "trombone" shape of the collider layout would easily accommodate a straightforward albeit expensive increase in the length of the main accelerators without requiring extensive modification of the remainder of the complex. This final energy might also be accomplished by development of new, more efficient, X-band technologies; for example, gridded klystrons, cluster klystrons, or relativistic two-beam klystrons.

The highest level parameters of the NLC are listed in Table 1-3. At each of the nominal 0.5 and 1.0-TeV cms energies, three sets of parameters define the operating plane of the collider. The expected luminosity is constant over the operating plane, but is achieved with differing combinations of beam current and spot size.

	NLC-Ia	NLC-Ib	NLC-Ic	NLC-IIa	NLC-IIb	NLC-IIc
Nominal CMS Energy (TeV)		0.5			1.0	
Luminosity w/ IP dilutions (10^{33})	5.8	5.5	6.0	10.2	11.0	10.6
Repetition Rate (Hz)		180			120	
Bunch Charge (10^{10})	0.65	0.75	0.85	0.95	1.10	1.25
Bunches/RF Pulse		90			90	
Bunch Separation (ns)		1.4			1.4	
$\gamma\epsilon_x$ at IP (10^{-8} m-rad)		400			400	
$\gamma\epsilon_y$ at IP (10^{-8} m-rad)	7	9	11	9	11	13
β_x/β_y at IP (mm)	8/0.125	10/0.150	10/0.200	10/0.125	12/0.150	16/0.200
σ_x/σ_y at IP (nm)	264/5.1	294/6.3	294/7.8	231/4.4	250/5.1	284/6.5
σ_z at IP (μ m)	100	125	150	125	150	150
Υ (Beamstrahlung Param.)	0.10	0.09	0.09	0.33	0.29	0.29
Pinch Enhancement	1.4	1.4	1.5	1.4	1.4	1.5
Beamstrahlung δ_B (%)	3.5	3.2	3.5	12.6	12.6	12.1
# Photons per e^-/e^+	0.97	1.02	1.16	1.65	1.77	1.74
Unloaded Gradient (MV/m)		50			85	
Effective Gradient (MV/m)	31.5	29.4	27.2	58.3	55.1	51.4
Active Linac Length (km)		8.15			8.90	
Min. Total Site Length (km)		23.8			30.5	
Max. Beam Energy (GeV)	267	250	232	529	500	468
Power/Beam (MW)	4.2	4.8	5.5	6.8	7.9	9.0
# of Klystrons		4528			9816	
Klystron Peak Pwr. (MV)		50			72	
Pulse Comp. Gain		3.6			3.6	
RF System Efficiency (%)		28			37	
Total AC Power (MW)		121			193	

Table 1-3. Present IP and linac parameters of NLC designs.

This provides a region in parameter space where the collider can be operated. Construction and operational tolerances for the various subsystems of the collider are set by the portion of the operating plane that is most difficult. For example, the more difficult parameters for the final focus are those of case (a), in which the beam divergences are large. In contrast, preserving the emittance of the beam in the linac is more difficult in case (c), in which the beam charge is highest and the bunch length longest. This design philosophy builds significant margin into the underlying parameters of the collider.

An important element in the design strategy of the NLC is the use of the beam to measure and correct errors in electrical and mechanical parameters of the accelerator. These techniques, many in extensive use at the SLC and FFTB, are able to achieve far greater accuracy than is possible during fabrication and installation of components. For example, the use of optical matching and beam-based alignment algorithms considerably loosen tolerances required on magnet strengths and positioning. These procedures require accurate measurement of the properties of the beam and extensive online modeling and software. The existence of instrumentation suitable for these purposes is an important aspect of the readiness of technologies for the collider.

Additional performance overhead has been included in the designs of most subsystems of the NLC and errors that we anticipate occurring during machine tuning and operations have been taken into account. For example, the injector systems, *i.e.*, the particle sources, damping rings, and bunch compressors, are designed to provide 20% more charge than is indicated in Table 1-3 providing a substantial margin over the required performance. Similarly, fabrication and alignment tolerances for the main linac structures are specified without assuming benefit from certain global tuning methods such as coherent wakefield cancelation. These are powerful techniques in routine practice at the SLC, but our philosophy is to use them only to provide operational margin. We also recognize that the beam-based tuning cannot be done with perfect accuracy. For example, we have analyzed the tuning procedure for the final focus and estimated a 30% increase in the spot size at the IP due to errors that we anticipate will occur in measuring and correcting aberrations inherent in the optics. (This is included in Table 1-3.) This layered approach to specification of collider performance is an important part of our design philosophy.

1.3.2 Status Report on Technologies for the NLC

Progress in development of X-band rf components has been impressive in recent years. Prototype klystrons now produce 50 MW, 1.5 μ s-long pulses with performance characteristics that are correctly modeled by computer codes. This exceeds the requirements of the initial 0.5-TeV stage of the NLC. In addition, the most recent prototype produces 75 MW, 1.1 μ s-long pulses, as required for upgrading the NLC to 1-TeV center-of-mass energy. Tests of pulse-compression transformers have exceeded most goals of the NLC, and high-power rf windows and mode converters that allow high-efficiency transfer of power between components have been successfully tested. Examples of these results are shown in Figure 1-7.

The voltage gradient that can be used in a particle accelerator can be limited by the dark current created when electrons are drawn from the surfaces of the accelerator structures and captured on the accelerating rf wave. For a given rf frequency, there is a well-defined gradient beyond which some electrons emitted at rest will be captured and accelerated to relativistic velocities. The capture gradient at S-band is about 16 MV/m, and scales to 64 MV/m at X-band. These are not actual limits to gradients that can be utilized in an accelerator since much of the charge is swept aside by the focusing quadrupoles of the machine lattice, but the dark current will grow rapidly above these values, and may adversely affect the primary beam or interfere with instrumentation needed for tuning. Gradients somewhat above the capture field are likely to be useful in practice, but the operational limits are not well known since no large-scale high-performance

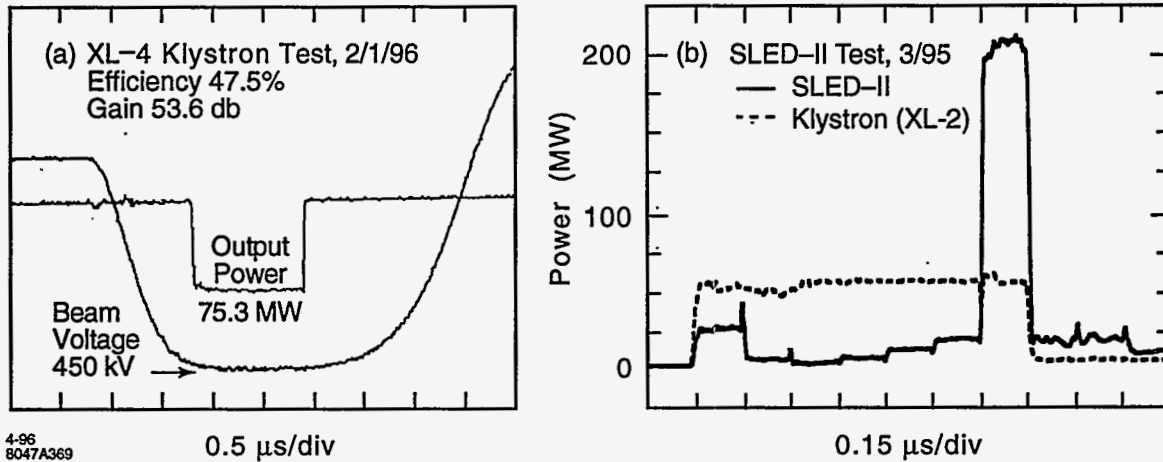


Figure 1-7. Results of tests of X-band components: (a) high-power klystrons, and (b) rf pulse compression systems.

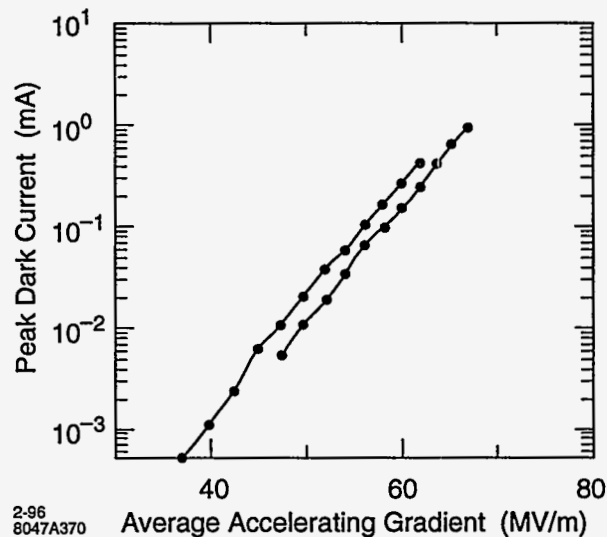


Figure 1-8. Processing of X-band accelerator structures to high gradient.

facility has been operated significantly above capture gradient. Expected thresholds of dark currents in S-band and X-band structures have been confirmed and it has been shown that (unloaded) gradients as high as 70 MV/m can be attained at X-band (Figure 1-8).

The electro-mechanical design of the main linac accelerator structures must not only produce the desired gradient, but must also minimize wakefields excited by the passage of the beam. The retarded electromagnetic fields left by each particle can disrupt the trajectories of particles that follow it through the accelerator. Many techniques to control the effects of the short distance intrabunch wakefields have been developed, tested, and put into use at the SLC. It will be necessary to also control long-range wakefields at the NLC in order to allow trains of closely spaced bunches to be accelerated on each rf pulse.

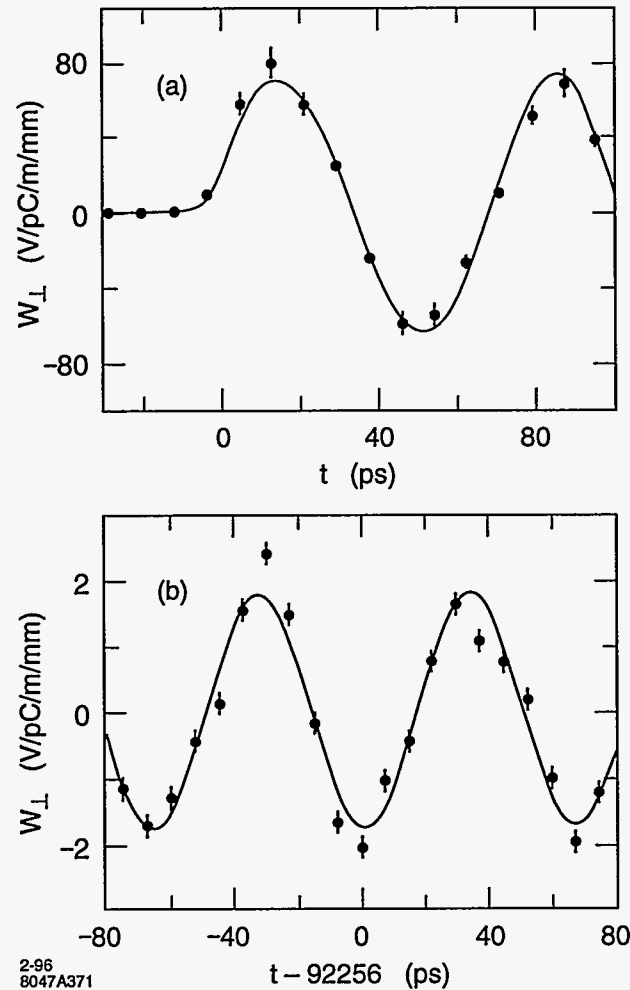


Figure 1-9. Measured (circles) and predicted (line) transverse dipole wakefields in a 1.8-m-long X-band accelerator structure where (a) shows the wakefield immediately following a bunch and (b) shows the wakefield 92 ns later; note the large decrease in amplitude.

Structures that suppress wakefields by careful tuning of their response to the passage of the beam have been developed, and tests have been performed at a facility (ASSET) installed in the SLAC linac (Figure 1-9). Agreement with theoretical expectations is excellent and lends confidence to the design and manufacture of these structures. A more advanced design that further mitigates the long-range wakefields by coupling non-accelerating rf modes to external energy-absorbing materials has been completed, and a prototype of this new structure is being readied for testing in ASSET as well.

Work remains to be done on X-band rf technologies, but with prototype components now in hand, tests of completely integrated systems have begun. A fully engineered accelerator is under construction at SLAC that will allow optimization of rf systems and provide experience with beam operations at X-band frequencies. This test accelerator will be a 40-m-long section of six, 1.8 m X-band structures powered by 50-75 MW klystrons to an accelerating gradient of 50-85 MV/m. Commissioning of this facility has begun, and operations are expected to be under way by the end of this year (Table 1-2).

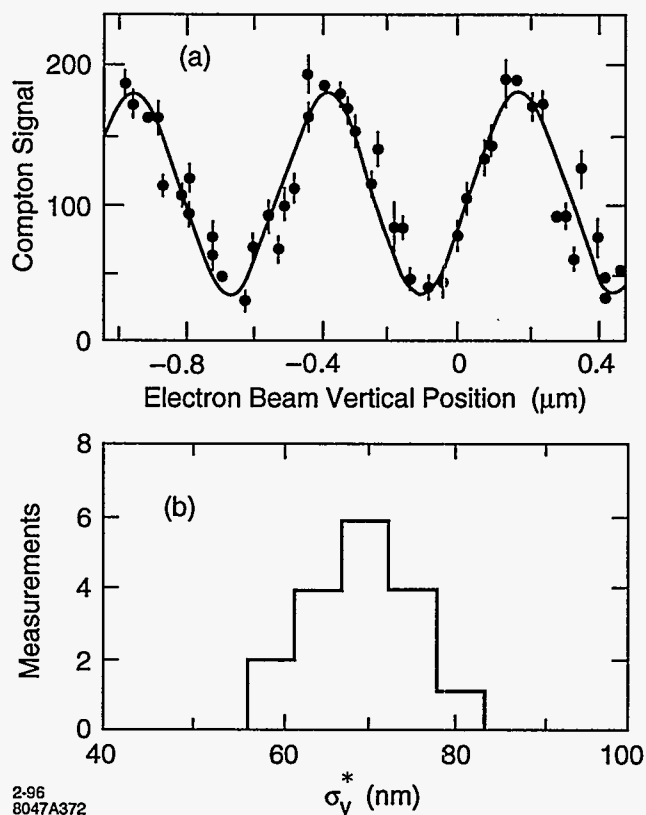


Figure 1-10. Measurement of 70-nm beam spots with a laser-Compton beam size monitor in the FFTB. (a) The rate of Compton scatters from a laser interference pattern used to determine the beam size, in this case 73 nm. (b) Repeatability of spot measurement over periods of several hours.

The spot sizes that must be produced at the interaction point of the NLC represent significant extrapolations from those achieved at the SLC. It is important to demonstrate that it is possible to demagnify a beam by the large factor needed in the NLC. An experiment has been performed by the Final Focus Test Beam Collaboration to show that such large demagnifications can be achieved. The Final Focus Test Beam (FFTB) is a prototype beam line installed in a channel located at the end of the SLAC linac at zero degrees extraction angle. The FFTB lattice is designed to produce a focal point at which the beam height can be demagnified by a factor of 380 to reduce the SLC beam ($\gamma\epsilon_y = 2 \times 10^{-6}$ m-rad) to a size smaller than 100 nm. The demagnification factor of the FFTB beam line is well in excess of that needed for the NLC.

The FFTB optics are chromatically corrected to third-order in the beam energy spread. (The SLC is corrected to second order.) All magnetic elements are mounted on precision stages that can be remotely positioned with step size of ≈ 0.3 micron, and beam-based alignment procedures were developed that successfully place these elements to within 5–15 microns of an ideal smooth trajectory. New state-of-the-art instruments were developed and used to measure the FFTB beam positions and spot sizes. Following a brief shake-down run in August of 1993, data were taken with the FFTB during a three-week period in April and May of 1994. Beam demagnifications of 320 and spot sizes of 70 nm were controllably produced during this period. Measurement of these beams is shown in Figure 1-10. The design of the NLC final focus follows that of the FFTB, and the experiences gained from the FFTB are incorporated into the tuning strategies of the NLC.

Important advances have also been made in instrumentation required to measure and control properties of the beam. The SLC control system has evolved dramatically over the past years to include extensive online modeling and automation of data analysis and tuning procedures. Scheduled procedures use sets of wire scanners to make complete measurements of the beam phase space, and provide recorded histories of machine performance. Online data analysis packages are able to reconstruct fully coupled non-linear optical systems. Beam-based feedback and feedforward are in routine operation in the SLC with over 100 loops providing control of beam trajectories and energies. Beam position monitors have been developed for the FFTB that achieve pulse-to-pulse resolutions of 1 micron, and new position monitors have recently been installed that are able to measure beam motions of 100 nm. The FFTB focal point spot monitors have demonstrated techniques to measure beam sizes of 30–40 nm, and extrapolation of these techniques to sizes as small as 10 nm can be expected to be successful.

1.4 Outlook for the Next Linear Collider

As the SLC has systematically increased its luminosity, the accelerator physics and technologies of linear colliders has matured. Experiences and lessons learned from the task of making this first collider perform as an instrument for particle physics studies make a firm foundation on which to base the design and technology choices for the next linear collider. At the same time, the essential demonstrations of new collider technologies have either taken place or soon will be underway. The experimental program with the FFTB is providing the experience needed to evaluate limitations to designs of final focus and interaction regions. The ability to demagnify beams by the amount required for the NLC has already been achieved. Microwave rf power sources have exceeded requirements for the initial stage of the NLC and critical tests assure us that this technology can be expected to drive beams to center-of-mass energies of a TeV or more. Fully integrated test accelerators are presently under construction at CERN, DESY, KEK, and SLAC that will soon provide answers to questions of technical optimization and costs of the major components of a TeV-scale collider.

Given the great international interest and commitment to the goals of a TeV-scale high-performance e^+e^- collider, it is certain that its final design, construction, and utilization will be a global effort. It is important that the scientific community put into place foundations for such a collaboration. The international character of the linear collider project is already reflected in the collaborations at work on the accelerator physics and technology of linear colliders and in the process of international discussion and review of progress in the field [Loew 1995]. It is essential that we continue to build on this base of understanding and cooperation and make certain that all involved in this enterprise are full party to its final realization.

1.5 NLC Systems Overview

The Next Linear Collider consists of a set of subsystems—injectors, linacs, beam delivery, and interaction regions. These are responsible for creating intense and highly condensed beams of positrons and polarized electrons, accelerating them to high energy, focusing them to small spots, and colliding them in an environment that allows sensitive particle detectors to operate for physics. In this section, we introduce these various parts of the collider while pointing to the more detailed discussions in the following text. We will also describe the energy upgrade and other more global issues.

A schematic of the NLC is shown in Figure 1-11. The physical footprint of the collider complex is approximately 30 km in length and less than 1 km wide. This includes all beam transport lines in the injectors

and linacs necessary to obtain 1 TeV center-of-mass energy, and all space need in the beam delivery sections to accommodate 1.5 TeV center-of-mass energy. To reach 1.5 TeV, however, it may be necessary to extend the “trombone” layout of the collider to provide additional length for the linac. This can be done without moving the injectors or damping rings.

Injectors

The injector systems prepare the beams for injection into the main linacs at a beam energy of 10 GeV. The injectors consist of the polarized electron and positron sources, the damping rings, which reduce the transverse emittances of the beams, and the bunch compressors, which reduce the bunch lengths. Because they must provide a stable and reliable platform for the rest of the linear collider, we have been careful to design the systems with substantial operating margin.

The polarized electron source (Chapter 2) for the NLC is copied from the present SLC system which generates beams with $> 75\%$ polarization and operates very reliably. The NLC source includes a polarized laser, a photocathode electron gun, and a non-relativistic subharmonic bunching system. The new challenge for the NLC source is that it must produce trains of 90 bunches spaced by 1.4 ns at the machine repetition rate of 120–180 Hz. This is done by modulating a 126-ns laser pulse with a series of resonant rf Pockels cells. To get a relatively rectangular intensity profile, the modulation is performed using the first and third harmonic of the bunch spacing.

The bunched beam from the electron source is accelerated in an S-band (2.856 GHz) booster linac to 2 GeV and then injected into a damping ring (Chapter 4). The damping ring stores four trains of 90 bunches at once, extracting the oldest train as a new one is injected. It is designed to damp the transverse phase space of the beam from the incoming normalized emittances of $\gamma\epsilon_{x,y} = 1 \times 10^{-4}$ m-rad to $\gamma\epsilon_x = 3 \times 10^{-6}$ m-rad and $\gamma\epsilon_y = 3 \times 10^{-8}$ m-rad. These damped horizontal and vertical emittances are much smaller than those achieved in the SLC damping rings, and are comparable to those in the present generation of synchrotron light sources such as the Advanced Light Source at Lawrence Berkeley National Laboratory. To attain the small emittances, the ring is designed with a strong focusing lattice and uses beam-based techniques to achieve the required alignment of the ring magnets. The damping ring design incorporates lessons and techniques learned from operation of the SLC as well as experiences from the more modern synchrotron light sources. Finally, many of the components required in the rings have already been or soon will be designed and tested in other storage rings. This includes the wiggler magnets, which are included in the NLC design to reduce damping times, multibunch feedback and rf systems, and the vacuum system.

The technique for production of positrons that is planned for the NLC (Chapter 3) is also largely copied from that used at the SLC. Here, positrons are created in electromagnetic showers produced by targeting a 3–6 GeV electron bunch train onto a rotating $W_{75}Re_{25}$ target; the 3–6 GeV electron beam is produced with a conventional thermionic electron source and accelerated in a separate S-band linac. The large emittance positron beam is captured and accelerated to 2 GeV in a large-aperture L-band (1.428 GHz) linac. This lower frequency rf system has a smaller beam loading and leads to a good capture efficiency because of the increased longitudinal and transverse apertures.

At the 2-GeV point, the positron beam, with transverse emittances of 0.06 m-rad, is cycled through a large-aperture pre-damping ring (Chapter 4). The pre-damping ring damps the incoming positron emittances to $\gamma\epsilon_{x,y} = 1 \times 10^{-4}$ m-rad prior to injection into a main ring which is identical to that used for the polarized electron beam. Finally, the overall layout also includes transport lines that will allow the drive electron beam to bypass the positron production target and pre-damping ring to allow the study of e^-e^- or $\gamma\gamma$ collisions (with both electron or photon beams polarized).

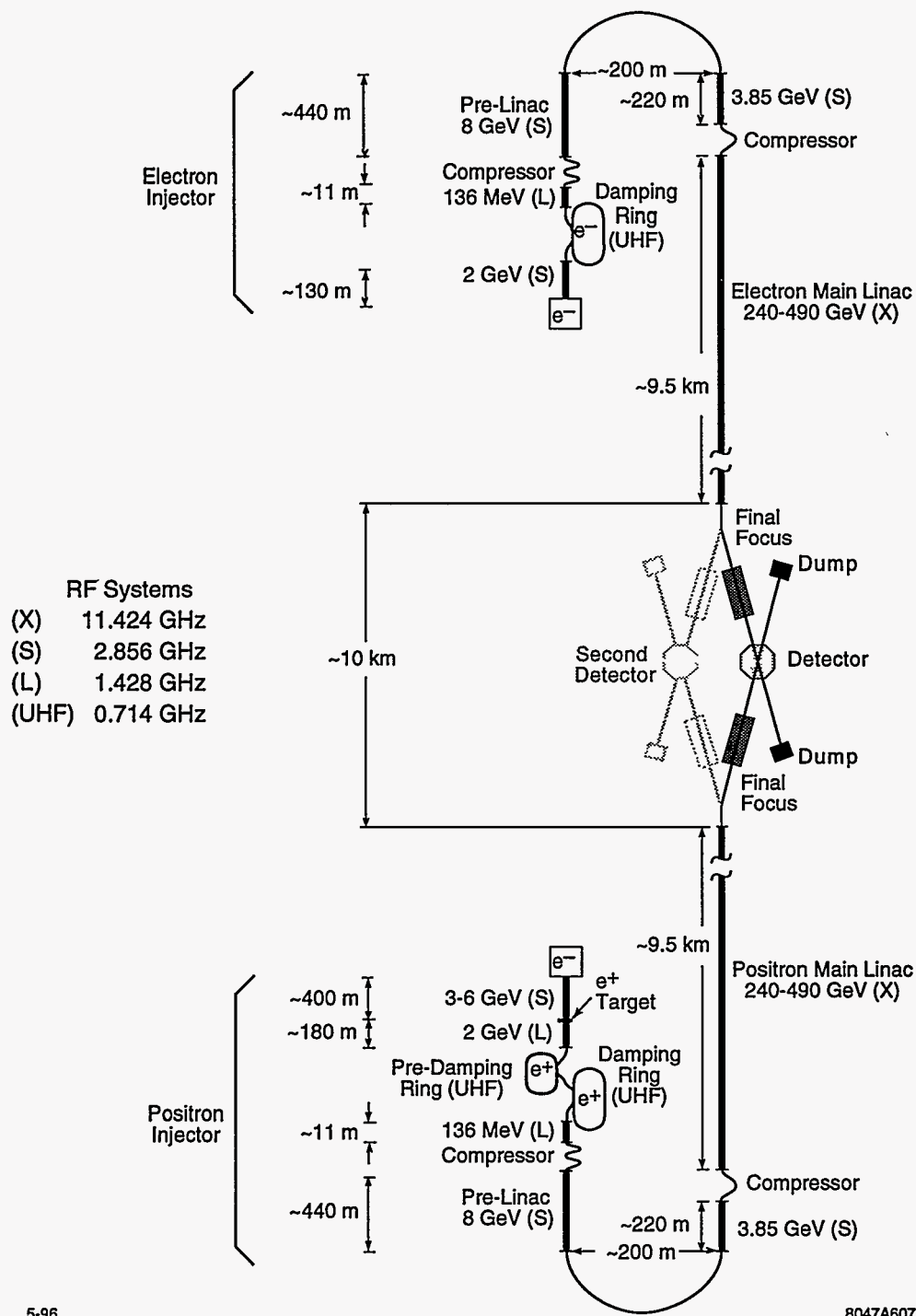


Figure 1-11. Schematic layout of NLC systems (not to scale).

Next, the lengths of the electron and positron bunches become too great in the damping rings for the beams to be successfully accelerated in the main X-band linacs, so they must be reduced (Chapter 5). This is done in two stages. A first bunch compressor, located immediately after the damping rings, reduces the bunch length from 4 mm to 500 μm to optimize injection into an S-band linac that accelerates the beams to 10 GeV. The bunch lengths are then further compressed to 100–150 μm in a compressor that rotates the longitudinal phase space by 360° and reverses the direction of travel; this arc allows for future upgrades of the main linac length and permits feedforward of the bunch charge and trajectory made in the damping rings and compressors.

Finally, the rf acceleration throughout the injector systems, *i.e.*, the bunch compressor rf, the 8-GeV prelinacs, and the 2-GeV booster linacs, is performed with relatively low frequency rf. In particular, the positron booster linac and the first bunch compressors operate at L-band (1.4 GHz) and the electron booster linac, the prelinacs, and the second bunch compressor operate at S-band (2.8 GHz). Although these systems are, in general, longer and more expensive than higher frequency accelerator systems, we feel that they are needed at the lower beam energy. In particular, we have designed the systems so that they have small beam loading and relatively loose alignment tolerances. This is important to provide the reliability and stability that is desired in the injector systems. Of course, such lightly-loaded systems are inefficient and could not be used to accelerate the beams to very high energy.

To minimize the long-range transverse wakefields, all of the accelerator structures are damped and detuned structures, similar to those developed for the X-band main linacs. In addition, the beam loading is primarily compensated using the ΔT (early injection) method which is discussed in Chapter 6. This has the advantage of canceling the bunch-to-bunch energy deviations locally within an accelerator structure thereby minimizing the transverse emittance growth due to dispersive and chromatic effects. Details of the multibunch beam loading compensation in the injector linacs as well as the low frequency accelerator structures and power sources is presented in Chapter 6.

Main Linacs

The main linacs of the NLC use normal-conducting traveling-wave copper structures operating at X-band (11.424 GHz). The choice of such a high frequency, relative to existing high-energy linacs, allows higher accelerating gradient, shorter linac length, and lower AC power consumption for a given beam energy. Considering the size, weight, cost, and availability of standard microwave components, we have chosen a frequency in the X-band for a design that is upgradeable from an initial 500-GeV center-of-mass energy to 1 TeV or more.

In the 500-GeV center-of-mass design, the required rf power is generated by 50 MW klystrons in 1.2 μs pulses which is then compressed to 0.24 μs , with higher peak power, by a passive rf transformer (SLED-II); this provides an unloaded acceleration gradient of 50 MeV/m. The upgrade to 1-TeV center-of-mass energy is accomplished by doubling the number of modulators and by replacing each 50-MW klystron with a pair of 75-MW klystrons. This attains an unloaded gradient of 85 MV/m. To achieve the full 1-TeV center-of-mass design, the total active length of linac must be increased slightly from 16,300m to 17,700m. This would be done by replacing spool pieces at the ends of the linac beam lines with accelerator structures. In addition, the planned upgrade includes improvements in the modulator and pulse compression systems to increase the rf system efficiency. The rf system for both the 500-GeV design and the 1-TeV upgrade is described in Chapter 8.

The rf system operates with a repetition frequency of 120–180 Hz. On each rf pulse, a train of 90 bunches is accelerated in each linac. While the number of particles in each of these bunches is small compared to that in the SLC, the total charge accelerated by each rf pulse is more than an order of magnitude greater. This

multibunch design and the correspondingly larger fraction of energy transferred from the power sources to the beam is one of the important differences between the SLC and the NLC.

Extensive effort has been made on the design of an accelerator structure and rf system to ensure that both the beam loading can be compensated to the level required and the long-range transverse wakefield does not significantly increase the transverse emittances. The beam loading is compensated by optimizing the temporal profile of the rf pulse by shifting the phase of the rf from the klystrons. The long-range transverse wakefields have been reduced by tailoring the cell-to-cell dipole mode frequency to yield a Gaussian-like decay of the wakefield and by coupling each of the cells to four damping manifolds; this accelerator structure is referred to as a Damped-Detuned Structure (DDS). The technical designs of these rf components are described in Chapter 8 while many of the issues associated with the multibunch operation are summarized in Chapter 13.

The design and layouts of the linacs and the beam dynamics studies are presented in Chapter 7. The focusing lattice of the linac is designed to allow the center-of-mass energy to vary from 300 GeV to 1 TeV. Thus it does not have to be modified for the 1-TeV upgrade; the upgrade to 1.5-TeV will require changes. To verify the state of the beam, five diagnostic stations, located along each of the two main linacs, will include laser wire scanners to measure the transverse phase space, beam-based feedbacks to correct for centroid shifts of the bunch train, multibunch BPMs and high-frequency kickers to measure and correct bunch-to-bunch position errors, and magnetic chicanes to provide non-invasive energy and energy spread measurements.

The components in the linacs will have to be aligned to a few microns of a tuned reference orbit to prevent excessive emittance growth. This will be done using beam-based alignment techniques and high resolution beam position monitors. Studies of vibration and stability, based on measurements of the ground motion made at SLAC and described in Appendix C, show that the linac is not extremely sensitive to the motion. Fast feedback systems, similar to those used at the SLC and described in Appendix D, are required to stabilize the beam and the trajectories will need to be re-steered every 30 minutes; neither of these presents an operational limitation.

The Beam Delivery System

The beam delivery system consists of a collimation section, a switchyard, the final focus, the interaction region, and the beam extraction and dump. These are shown schematically in Figure 1-12. The overall lengths of the beam lines have been designed to allow for a final beam energy of 750 GeV.

After acceleration in the main linacs, the beams enter the collimation sections, described in Chapter 9, where particles at the extremities of the energy and transverse phase space are eliminated. The collimation is performed in both the horizontal and vertical planes at two betatron phases that differ by 90° to effectively cut the beam in both position and angle. This primary collimation is then followed by a secondary collimation in both planes and both phases to remove particles that are scattered by the edges of the primary collimators. The collimation regions have been designed to absorb 1% of the nominal beam power while surviving the impact of a full bunch train. The system consists of a series of spoilers and absorbers which have been optimized to reduce the transverse geometric and resistive-wall wakefields. Although the collimation sections are rather extensive, our experiences at the SLC and Final Focus Test Beam (FFTB) have proved the need to perform this function very carefully.

The collimation regions are followed by passive switching sections (Chapter 10) which are used to direct the beams to one of two possible interaction points (IPs). The beams are each deflected in the switchyard by 10 mrad to produce a net 20-mrad crossing angle at the IPs. This deflection introduces only little emittance growth,

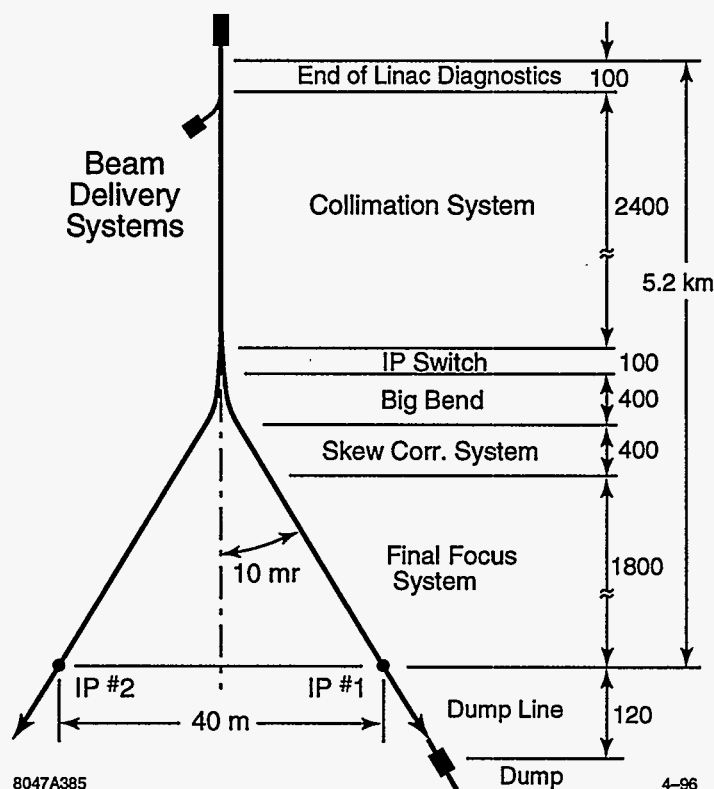


Figure 1-12. Schematic layout of the beam delivery system.

but greatly reduces detector backgrounds and provides the IP crossing angle required to collide the closely spaced bunches in each train.

The NLC final focus is described in Chapter 11. It follows the design of the FFTB at SLAC. The optics consist of a matching section with appropriate instrumentation to measure the incoming beam phase space, horizontal and vertical chromatic correction sections, a final transformer, a final doublet, and a diagnostic dump line for the exiting beam. The final focus system is chromatically corrected to third order. It demagnifies the transverse beam sizes by a factor of 80 horizontally and 300 vertically. A dedicated geometry adjustment section is included to facilitate the adiabatic upgrade from 350 GeV to 1.5 TeV center-of-mass without changing the IP position and requiring only minor transverse realignment of the beam line.

Although there is less demagnification than in the FFTB, the vertical spot size at the IP is roughly 15 times smaller than that attained in the FFTB. This imposes stringent tolerances which are achieved using beam-based tuning techniques and feedback systems. Measurement of the final spot size is a particular challenge, but can be performed with an advanced laser fringe monitor similar to that used in the FFTB and in-situ tuning of the spot sizes and luminosity can be done using measurements of the beam-beam deflections and techniques developed at the SLC. An extensive accounting of all the aberrations and the limitations of the tuning methods, including the different time scales required and the measurement accuracy, has been included in the luminosity calculations; these amount to a reduction in luminosity of 30-40%.

Interaction Region

Two interaction regions (IRs) are included in the layout of the NLC. The two important issues for the NLC IRs are the backgrounds and masking and the vibration stabilization of the final doublet; these are discussed in Chapter 12. The two IRs, of course, must share the available luminosity, but it will be possible to install two complementary experiments. As with all colliders, the interaction region will be a very crowded location. The final quadrupole magnets of the machine optics must be positioned as closely as possible to the collision point, and high-Z masking must be installed to protect elements of the experimental detector. The detector itself will require clear access to as much of the volume around the interaction point as possible. The design presented in this document includes quadrupoles two meters from the interaction point, and complete access for detector elements at polar angles greater than 150 mr. Calorimetric measurement of Bhabha scatters at smaller polar angles should also be possible, and are expected to provide precise determination of the luminosity-weighted center-of-mass energy spectrum.

The NLC is designed to collide electrons and positrons beams at a small (20 mr) crossing angle. This prevents the tightly spaced bunches of one beam from being disturbed as they approach the interaction point by bunches in the opposing beam that are leaving the interaction point. To avoid loss of luminosity due to this crossing angle, it is necessary to use a pair of small deflecting-mode rf cavities to "crab" the beams so that the bunches collide head-on. This is a new task not encountered at the SLC, but a system with reasonable specifications has been designed.

Global Considerations

Finally, the last five chapters discuss more global issues in the collider. As mentioned, the NLC will operate with long trains of bunches. Multibunch operation is one of the major differences between the NLC and the SLC. The issues associated with the multibunch operation are covered throughout the text but, because it is an important topic, we summarize these issues in Chapter 13.

Next, the control system and the instrumentation issues are outlined in Chapters 14 and 15. With the heavy utilization of beam-based alignment and tuning, the control system and the instrumentation design are very important for the NLC. The control system design uses many lessons learned from the SLC control system which has evolved substantially to meet the SLC requirements. Similarly, much of the required instrumentation is based on designs that have already been demonstrated. In the future, we will organize the description of the instrumentation into a unifying chapter but, at this time, the design and requirements are described throughout the text. Chapter 15 provides a short introduction to the philosophy of the instrumentation design and utilization.

The Machine Protection System (MPS) is described in the next chapter, Chapter 16. Because of the very high beam density and large beam power, the MPS is a difficult system and imposes significant constraints on the operation of the collider.

Finally, the NLC is a large and complex instrument and reliability is very important consideration. The SLC operates with an overall accelerator availability of roughly 80% and the NLC will be roughly ten times larger. Simple scaling of the SLC fault rates would suggest that the NLC would be effectively inoperable. Reliability considerations need to be addressed in the design from the onset and they are discussed in Chapter 17.

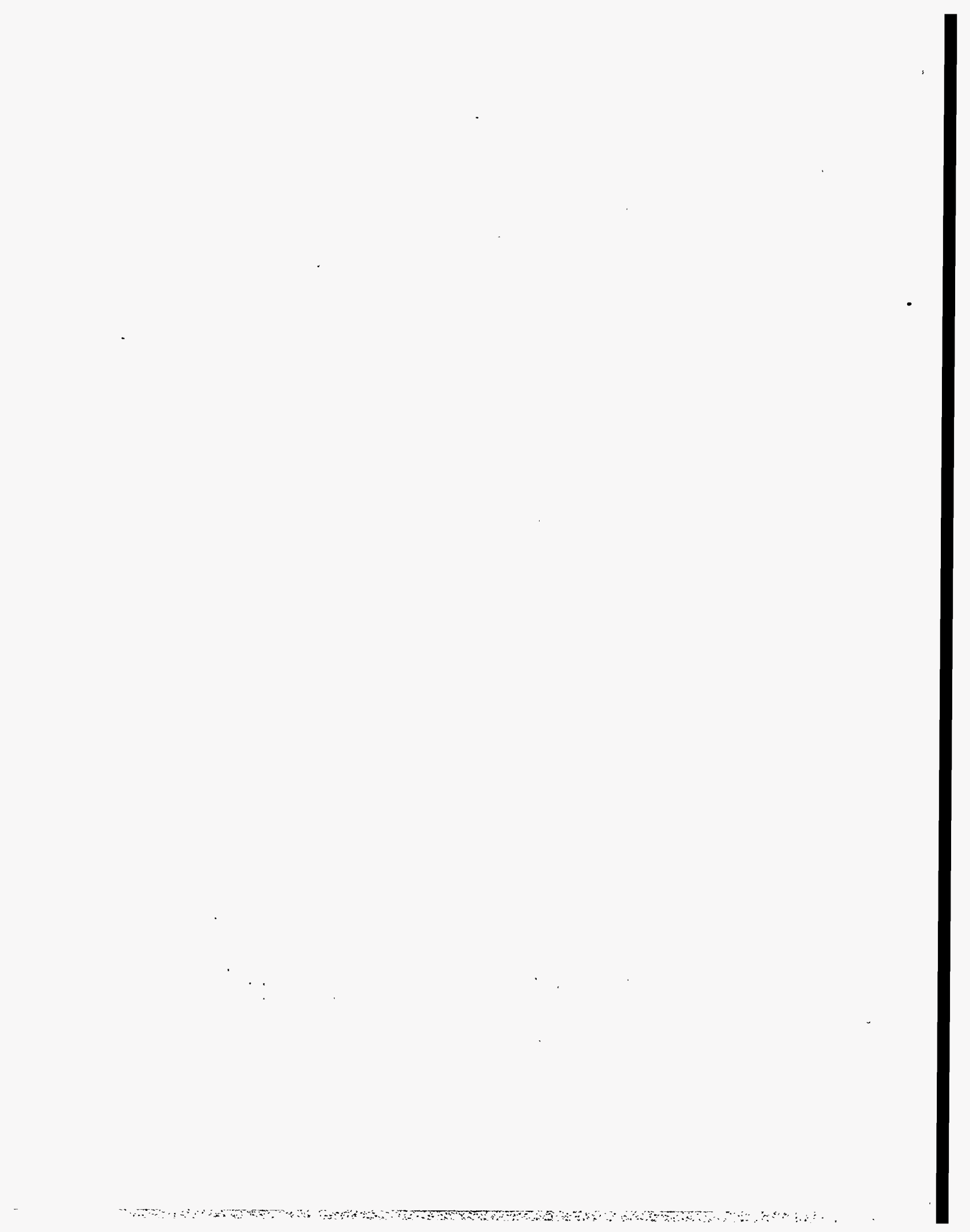
Lastly, the facilities and conventional systems for the NLC are described in Chapter 18. This includes the power and cooling distribution, the accelerator housing and the klystron gallery, as well as the campus and support facilities.

Appendices

In addition to the main body of the text, four appendices are included in this document. Appendices A and B present a possible rf system for a 1.5-TeV center-of-mass upgrade which is based on a Two-Beam Accelerator and a design for an interaction region to produce and study $\gamma\gamma$ collisions. These are followed by Appendices C and D which discuss ground motion theory and measurements and the implementation and limitations of beam-based feedback.

References

- [Ahn 1988] C. Ahn, *et al.*, SLAC-Report-329, 1988.
- [CERN 1987] Proceedings of the Workshop on Physics at Future Accelerators (La Thuile), CERN, Geneva, 1987.
- [Snowmass 1988] Proceedings of the 1988 DPF Summer Study: Snowmass '88, High Energy Physics in the 1990s, E.L. Berger, ed., Snowmass, CO, 1988.
- [JLCI 1989] Proceedings of the First Workshop on Japan Linear Collider (JLC I), S.Kawabata, ed., KEK, 1989.
- [Snowmass 1990] Proceedings of the 1990 DPF Summer Study on High Energy Physics: Research Directions for the Decade, F. Gilman, ed., (Snowmass, CO, 1990).
- [JLCII 1990] Proceedings of the Second Workshop on Japan Linear Collider (JLC II), (KEK, 1990).
- [DESY 1990] Workshop on Electron-Positron Collisions at 500 GeV: The Physics Potential, (DESY, 1990).
- [Finland 1991] Proceedings of the First International Workshop on Physics and Experiments with Linear Colliders, R. Orava, ed., (Saariselka, Finland, 1991).
- [Hawaii 1993] Proceedings of the Second International Workshop on Physics and Experiments with Linear Colliders, F. Harris, et al., eds., (Waikoloa, Hawaii, 1993).
- [Japan 1995] Proceedings of the Third International Workshop on Physics and Experiments with Linear Colliders, (Iwate, Japan, 1995).
- [LaThuile 1987] Proceedings of the 1987 LaThuile Meeting: Results and Perspectives in Particle Physics, M. Greco, ed., (Gif-sur-Yvette, France, 1987).
- [NLC Physics] "Physics and Technology of the Next Linear Collider: A Report Submitted to Snowmass 1996", SLAC Report-485; BNL-52-502; Fermilab-Pub-96/112; LBNL-Pub-5425; UCRL-ID-124160.
- [Loew 1995] G. Loew, et al., International Linear Collider Technical Review Committee Report, SLAC Report-471 (1996).



Electron Source

Contents

2.1	Introduction	27
2.2	Polarized Electron Gun	30
2.2.1	Specifications	30
2.2.2	Design Philosophy	32
2.2.3	Photocathode	32
2.2.4	Polarization	34
2.2.5	Vacuum and Mechanical Design	35
2.2.6	Loadlock and Cathode Preparation Chamber	35
2.2.7	Inverted Geometry Gun Tests	36
2.2.8	Reliability	36
2.2.9	Operation	36
2.3	NLC Laser System	37
2.3.1	Pump Lasers	37
2.3.2	Ti:Sapphire Oscillator	39
2.3.3	Pulse Shaping	39
2.3.4	RF Laser Modulator	39
2.3.5	Ti:Sapphire Power Amplifier	40
2.3.6	Pulse Train Length, Intensity, Spot Size, and Steering Control	41
2.3.7	Overall Technical Risks	41
2.4	NLC Electron Injector Beam Dynamics	41
2.4.1	NLC Injector Baseline Design	41
2.4.2	Electron Gun Optics	41
2.4.3	Intensity Jitter Limiting Aperture	42
2.4.4	Bunching System	43
2.4.5	Injector Linac	47
2.5	Buncher Cavities	51
2.6	Positron Drive Linac	51
2.7	Diagnostics	53
2.8	Operation	56
2.8.1	Initial Set-up and Beam Maintenance	56
2.8.2	Troubleshooting	57
2.9	Conclusion	57
2.A	Polarized e^- Beam Photocathode RF Gun Development for the NLC	58
2.A.1	Introduction	58
2.A.2	Beam Dynamics	59
2.A.3	Material and RF Considerations	64
2.A.4	Laser System	68

2.A.5	Integrated System	73
2.A.6	Conclusions	73
2.B	Charge Limit and its Implications on High-Polarization Long-Pulse Charge	74
2.B.1	Introduction	74
2.B.2	Generalization of CL Effect to Long-Pulse Operation	74
2.B.3	Where We Are	76
2.B.4	Cathode Improvements and Outlook	77

2.1 Introduction

The electron injector for the Next Linear Collider (NLC) is based on the design of the injector for the SLC because many of the performance requirements for the NLC are similar to the SLC. The main difference is that the NLC injector has to deliver a train of bunches, therefore multibunch issues must be addressed.

The SLC polarized source which has operated so successfully since 1992, can be duplicated for the NLC with almost no changes to the polarized gun. We expect that the polarized source system will operate at better than 99% uptime efficiency based on the SLC experience. With ultra-high vacuum achieved in the SLC gun, the cathode lifetime has improved such that now it is greater than thousands of hours. Similar to the SLC, greater than 80% electron polarization will be achieved in the NLC. Some integrated experiments need to be performed to demonstrate that the polarized cathodes and cathode handling techniques available today can be applied to the cathode for the NLC polarized gun to achieve the required current for the NLC at greater than 80% polarization (Appendix 2.B).

There will be two electron injectors on the NLC: one for the collision and another for the positron-production electrons. The collision electron injector will have a polarized electron gun while the electron injector for positron production will have a thermionic gun. The injector for the collision electrons goes up to 2 GeV and has a lattice to match the beam into the linac-to-ring transition. The drive linac for the positron source goes up to 3.11 GeV in the first phase and 6.22 GeV in the second phase, and has the necessary optics to transport the beam to one of the two parallel beam lines for the positron production systems.

The low-energy transport portion of both electron injectors will be identical to provide operational flexibility and the flexibility of exchanging the thermionic electron gun for a polarized gun for future upgrades where two polarized electron sources are needed for $\gamma - \gamma$ collisions.

Figure 2-1 shows the injector for the collision electrons from the gun up to the linac to ring transition point. The bulk of this chapter addresses the collision electron injector beam line but Section 2.6 addresses the positron drive injector in as far as it is different from the collision electron injector.

The baseline approach for the NLC injector will be a conventional system with a DC polarized gun and bunching system. The conventional subharmonically bunching injector approach [James 1981] is a proven, mature technology, used on injectors around the world, including on the SLC. The polarized electron gun and laser system are similar to the one which has been very successfully and reliably used on the SLC.

Some differences in this system are necessary to provide for the long bunch train. The laser system will produce a 126-ns-long train of bunches which are nearly rectangular in shape with a full-width-half-maximum value of 700 ps, and 1.4-ns apart. The beam intensity at 80 MeV needs to be about $1.9 \times 10^{10} e^-$ in 22 ps for each bunch, an average pulse train current of 1 A. The rms intensity jitter needs to be within 0.5% integrated over the entire train.

The polarized source rf gun injector approach should be studied in parallel (Appendix 2.A) to take advantage of the extremely low emittances achievable with rf guns, but at this point the technology of producing polarized electrons with rf guns has yet to be developed and is not the baseline approach for NLC.

The injector described in this section is shown in Figure 2-1. Our goal is to design an injector beam line such that it can produce the required beam parameters for both NLC-I and NLC-II as shown in Table 2-1. It has a 120-kV DC polarized electron gun which needs to produce $2.8 \times 10^{10} e^-$ in each bunch for NLC-II. The gun will house a 3-cm² cathode. All the current SLC polarized guns have a 3-cm² cathode, though the original gun with a 2-cm² cathode has been used for SLC operation.

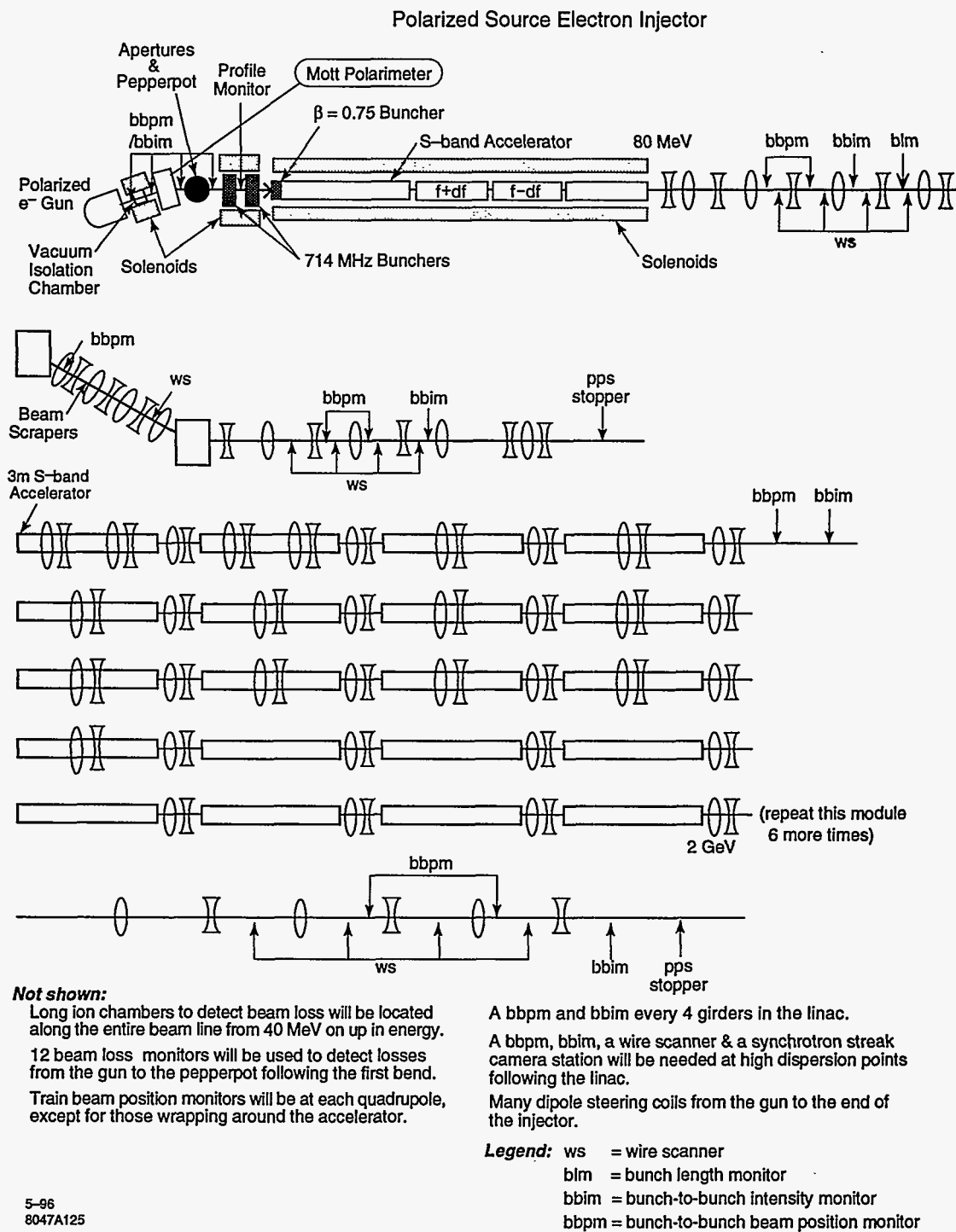


Figure 2-1. 2-GeV polarized electron source injector.

A vacuum isolation chamber and a 20° bend protect the polarized electron gun from the downstream environment. The 20° bend also allows us to switch the beam into a Mott polarimeter station for occasional source polarization measurements. The train-to-train intensity jitter of the beam at the gun may be close to the allowed threshold of 0.5% due to the incoming laser intensity jitter on the photocathode. This will limit energy jitter in the linac to 0.25% as described in Chapter 1. An aperture 24-cm downstream of the 20° bend will be used to further reduce the electron beam intensity jitter of the bunched beam. Two 714-MHz standing-wave subharmonic bunchers and an S-band buncher-accelerator section compress the beam from the gun such that 83% of the charge is captured in 18° of S-band or 17.5 ps. PARMELA simulations were conducted from the gun through the second accelerator section, where the beam reaches $80 \text{ MeV} \pm 0.6\%$ in energy. This energy spread is for a single bunch not including the beam-loading effect due to the long bunch train.

Beam-loading effects in the subharmonic bunchers are mitigated by using cavities with low R/Q to minimize the beam loading and inject the beam during the fill time of the cavity. Axial magnetic field focusing will be used on the first two accelerator sections (up to 80 MeV) where the beam is expected to have a larger energy spread than in the rest of the injector linac. At 80 MeV, there will be an isochronous and achromatic bend to connect the low-energy beam line to the main injector beam line. This bend allows us to construct another low-energy injector line in the future which may be needed either for more reliability in the polarized source or possibly for the first polarized source rf gun injector for the NLC. There is a set of wire scanners on both sides of the achromatic bend to measure emittance of the beam from the low-energy beam line and the emittance going into the injector linac after the bend. In addition, the chicane will have a set of scrapers at the high-dispersion point to clip away tails which are not in the main bunch and a wire scanner following the scrapers to measure the energy spread. From 80 MeV up to 2 GeV, the linac will use 3-m accelerator sections and Δt method for beam-loading compensation. Each module will consist of four 3-m accelerator sections powered by 2 S-band Klystrons similar to the SLAC 5045 klystrons except for the slightly longer $4\text{-}\mu\text{s}$ pulse width. Quadrupole doublets between each section and some wrapped around the first few sections will be used to control the transverse dimension of the beam.

There are only a couple of technological-breakthrough issues associated with the baseline injector chosen for the NLC. We need to demonstrate in an R&D program that we are able to produce cathodes with the 80% polarization and the up to 3.2-A average current needed for NLC-II. Currently available photocathodes with 80% polarization and 3-cm^2 emitting area are capable of producing only one fourth as much charge as is required for NLC-I with the (Appendix 2.B). It would be important to develop an 80% polarization cathode that will produce at least the required charge for NLC-1. If such a cathode is not developed in time then it is possible to increase the charge by doubling the area of the cathode with some compromise to the beam emittance at the gun to produce at least half the required charge for NLC-1. Other options for increasing the charge from the cathode could include development of the gun technology such that higher electric field would be tolerable at the cathode.

The beam-loading compensation both in the subharmonic bunchers and in the injector accelerator need to be simulated in detail, and physically realizable cavities need to be designed for the bunchers and the accelerators. These technologies will be demonstrated in the Next Linear Collider Test Accelerator (NLCTA) injector upgrade.

The development of a reliable and stable polarized-source-rf-gun injector deserves a concentrated parallel effort in the laboratory. If it could be demonstrated that the polarized-source rf gun system with the much lower beam emittance can be reliably and stably operated, then it will simplify the damping ring design or at least make it easier to operate. If the demonstration programs prove successful, the polarized-source rf gun could become the baseline injector for the NLC in which case we might also use an rf gun for the positron drive injector to make it similar in operation to the collision electron beam line.

Parameters	NLC-I			NLC-II			Overhead 20%	SLC achieved
	A	B	C	A	B	C		
N/bunch at IP (10^{10})	0.65	0.75	0.85	0.95	1.1	1.25	1.5	8.8
N/bunch at Gun (10^{10})	1.2	1.4	1.6	1.75	2.0	2.3	2.8	
Iave at gun (A)	1.4	1.7	1.9	2.0	2.4	2.7	3.2	
N/bunch at intensity jitter aperture (10^{10})	0.95	1.15	1.3	1.4	1.63	1.85	2.2	
N/bunch at 80 MeV (10^{10}) in 18ps	0.83	0.97	1.1	1.2	1.4	1.6	1.96	
Iave at 80 MeV (A)	0.95	1.11	1.26	1.37	1.58	1.8	2.2	
N/bunch at damping ring (10^{10})	0.75	0.88	1.0	1.1	1.28	1.45	1.7	

Parameters	NLC Required	Simulation	SLC no train
Bunch train durations (ns)	126	126	
Bunch separation (ns)	1.4	1.4	
PW at the gun FWHM (ps)	700	700	2000
PWedge after bunching (ps)	18	18	18
$\epsilon_{n,rms}$ at 40 MeV (10^{-4} m-rad)	1.0	0.5	1 to 1.3
$\Delta E/E_{edge}$ at entr. to DR. (%)	± 0.6	± 0.6	± 0.6 to 0.8
Train-to-train intensity jitter (%)	<0.5%	negligible w/ intensity jitter limiting aperture	0.8 at gun 0.5 after bunching

Table 2-1. NLC polarized electron source parameters up to the damping ring.

2.2 Polarized Electron Gun

2.2.1 Specifications

The principal requirements of the polarized electron gun are given in Table 2-2. To achieve 1.5×10^{10} e^- /bunch at the interaction point (IP), about 2.8×10^{10} e^- /bunch or a peak current of 4.5 A must be extracted from the cathode. The maximum current that can be extracted is established by the space-charge limit of the gun. The gun will be designed for a space charge limit of 13 A at the operating voltage. Assuming adequate laser energy, the ability to extract high peak currents at a given voltage depends on the internal charge limit of the cathode, which in turn depends primarily on the success in achieving a negative electron affinity surface. Achieving a successful negative electron affinity surface requires an ultrahigh vacuum system with total system pressure $\leq 10^{-12}$ Torr (excluding H_2).

Field emission associated with a DC-biased cathode can be destructive to a negative electron affinity surface. Thus the average dark current should be 25 nA or less. To achieve this goal, the electric field on the cathode electrode surface should be kept below 7 MeV/m at the operating voltage.

The intensity variations in the extracted electron pulse, including the jitter, are dominated by the properties of the laser pulse. On the other hand, the energy variations depend on the space-charge forces and the

Gun vacuum	$\leq 10^{-12}$ Torr (excluding H ₂)
Operating voltage	120 kV
Cathode area	3 cm ²
Extraction field	2.0 MV/m
Maximum field on cathode electrode	<7 MV/m
Space charge limit	13 A
Peak current at gun NLC I	2.5 A or $1.6 \times 10^{10} e^-$ /bunch
NLC II	4.5 A or $2.8 \times 10^{10} e^-$ /bunch
Number of bunches NLC I	90
NLC II	90
Bunch width at gun	700 ps FWHM
Bunch spacing	1.4 ns
Macropulse repetition rate NLC I	180 pps
NLC II	120 pps
Dark current	<25 nA DC
Intrapulse energy variation	$\leq 1\%$
Gun normalized rms emittance	$< 5 \times 10^{-6}$ m-rad
Beam loss before bend	<0.1%
Cathode lifetime	≤ 200 h
Operating efficiency in any 1-week period	$\sim 98\%$
Polarization	$\leq 80\%$

Table 2-2. Gun specifications.

properties of the high-voltage power supply system for biasing the cathode. The energy variation within the electron pulse should be $\leq 1\%$, and the intensity variation $\leq 0.5\%$ at the gun.

As with the SLC source, it is assumed that if the normalized emittance of the electron beam at the gun is a factor of 10 less than that of the bunched beam, the bunched beam will not be affected by small changes in the gun emittance.

The $1/e$ decay rate of the quantum efficiency of the cathode should be ≥ 200 h to ensure a high-operating efficiency. The lifetimes may be a moot question if it is determined that the cathodes can be cesiated at the operating high voltage without damaging the surface of the semiconductor crystal. The cathode in the SLC gun has a lifetime >1000 hrs.

The electron beam should have the highest possible polarization, preferably $>80\%$, while still meeting all other NLC specifications, in particular the intensity requirements. While the present-generation strained GaAs photocathodes used for the SLC have satisfactory polarization performance, they are incapable of generating the long, high-intensity bunch train required by the NLC owing to an inherent cathode charge limit phenomenon [Alley 1995]. A detailed description of the charge limit phenomenon, its implications on long pulse charge production, and the steps to be taken towards meeting the polarization and charge requirements of the NLC source are given in Appendix 2.B. The insufficient charge performance may be remedied by substantially increasing the doping density in the strained GaAs. Unfortunately, the increased doping density also degrades the beam polarization. Research is underway to develop a strained GaAs cathode capable of both $>80\%$ polarization and NLC charge production with reasonably sized cathodes.

2.2.2 Design Philosophy

Except for the issues associated with long pulse (on the order of 100 ns) operation, the SLC polarized electron source has been shown to meet the gun specifications given above. Thus it is planned to use much of the SLC-source design features for the NLC source. The features include an extremely good vacuum system to ensure long cathode lifetimes, use of a loadlock for installing and removing cathodes in the gun, and provision for testing backup cathodes and guns.

The SLC polarized electron gun with a loadlock will be the baseline design for the NLC source. Its performance and reliability have been well established with three years of smooth and nearly maintenance-free operation on the SLC. The "inverted-geometry" gun, which has a grounded body, will be considered as a logical upgrade if it is proven to be as reliable as the SLC gun. This gun has the advantage of being more compact with a simplified high-voltage operation, but it requires more testing in an accelerator environment. The cross sections of the SLC gun and the inverted-geometry gun are shown in Figures 2-2 and 2-3. The beam characteristics for the two guns are essentially identical because of similar focusing electrode design and the use of identical beam optics components. Both types of guns are configured to use the same gun support bench and will mate the downstream beam line in an identical manner. Therefore, switching between the two types of guns is as easy as switching between two guns of the same type, which should take about one day.

The preparation of photocathodes for polarized guns is a highly sophisticated operation that is not compatible with the accelerator environment. Thus it is necessary to have a cathode preparation laboratory that is separate from the accelerator. The preparation laboratory will be equipped with an ultrahigh vacuum (UHV) cathode test system capable of measuring the polarization as well as the quantum efficiency of a cathode sample at low voltage. Cathodes prepared in this laboratory for either the NLC operating source or the spare will be transported under vacuum.

Additional facilities, including certified clean rooms, will be necessary for the assembly and repair of guns.

2.2.3 Photocathode

Due to their superior polarization performance, photocathodes of strained GaAs epitaxially grown on GaAsP will be the primary candidates for use on the NLC. As is discussed in Appendix 2.B, the intrinsic charge limit effect inherent in p-type negative electron affinity semiconductor photocathodes may lead to inadequate charge performance for the NLC bunch train, from SLC-type uniformly doped strained GaAs cathodes with >80% polarization. However, there is room for significant improvement on the photoemission characteristics for such cathodes. More cathode research and development is expected to yield high-polarization, high-intensity cathodes that will meet the NLC requirement.

Conventional cathode preparation requires heat cleaning at 600°C for 1 hour. This high temperature results in some unwanted reconstruction at the surface. In addition, providing the high temperature in an UHV system places a definite limit on the reliability of the system due to the possibility of cathode contamination during the accompanying high pressures, and also because of the high potential to open a vacuum leak. Several techniques for low-temperature cathode preparation are being explored, including capping (following fabrication of the cathode) with a low-temperature protective layer, and cleaning at low temperature in a cathode preparation chamber using an atomic hydrogen (H*) beam.

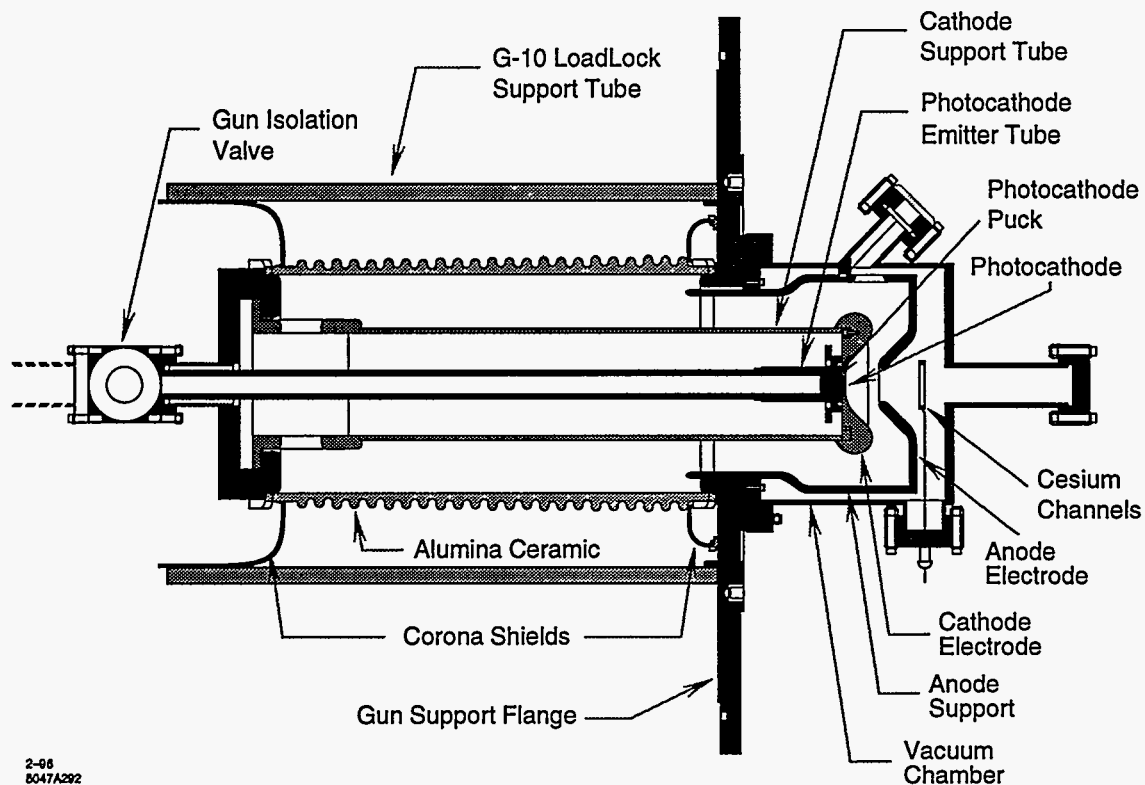


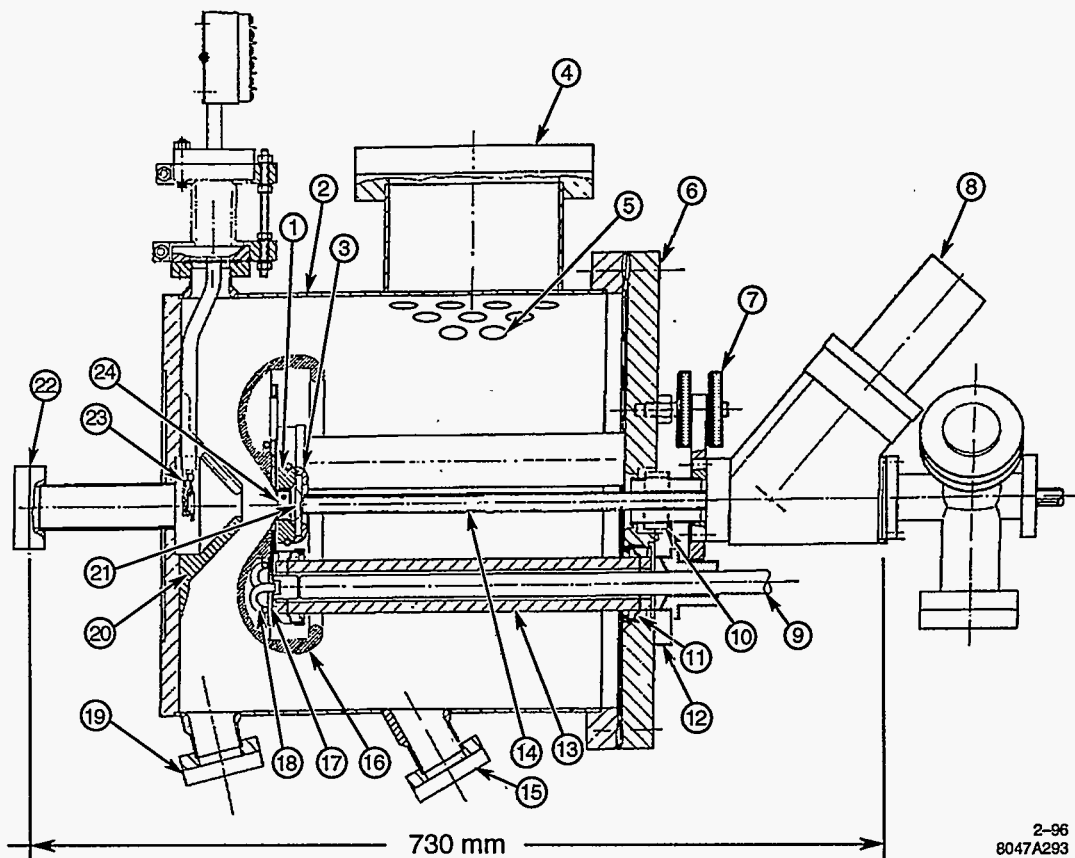
Figure 2-2. Cross section of the SLC polarized electron gun (loadlock not shown).

Reducing the dark current in the SLC source to <50 nA has usually been difficult to achieve. Ultrahigh-purity water cleaning techniques now under investigation may make it easier to achieve the low levels of dark current desired for the NLC. It is possible to use a pulsed high-voltage cathode bias if necessary.

As described in Appendix 2.B, a successful low-temperature heat-cleaning technique will allow operation with a cathode having high-dopant density at the surface. Such a cathode may greatly increase not only the cathode charge limit, but also the quantum efficiency (QE) achievable when cesiating. With high initial QE achieved with the high dopant density, and long lifetimes achieved by having a clean UHV system and low dark current, it should be possible to operate the NLC source for many days without recesiating. The SLC has already demonstrated that such sources can operate continuously for many months without cathode maintenance other than recesiation. A recesiation, which takes 15 to 30 minutes, can be done by machine operators through the computer control system. The interval between cesiations on the SLC is about one week and it gets longer as the gun remains under vacuum.

The quantum efficiency decay rate, that is, the cathode lifetime is an important operating parameter. Lifetimes of over 1000 hours have been achieved with the SLC. A lifetime of 200 hours corresponds roughly to a drop of 10%/day in the value of the QE.

Other types of photocathodes are being investigated in various laboratories around the world including SLAC. The gun can accommodate any of these if they should prove superior to the SLC cathodes. A fundamental requirement for choosing a new type of photocathode material is that the polarization of the electron beam should be at least as high as the highest achieved in SLC with the GaAs-GaAsP strained



2-96
8047A293

Figure 2-3. Cross section of inverted gun: (1) docking mechanism and puck holder, (2) gun body, (3) shielding rings, (4) ion pump port, (5) pumping holes, (6) end flange, (7) jacks, (8) access valve, (9) high-voltage cable, (10) bellows, (11) Kovar weld ring, (12) gas seal flange, (13) ceramic insulator, (14) transporter rod (only in place while changing cathode), (15) Viewing port, (16) cathode electrode, (17) support plate, (18) gas tubes, (19) illumination window, (20) anode electrode, (21) puck, (22) exit port to beam line, (23) cesiator, (24) photocathode.

lattice cathodes, and the charge limit associated with the cathode must not prohibit achievement of the desired electron intensities. In addition, there must be a source laser capable of producing the required energy at the wavelength that provides the highest polarization.

2.2.4 Polarization

The polarization of the electrons extracted into vacuum from the 100-nm SLC strained-lattice photocathodes is about 80% for the high peak intensity SLC pulses, and about 85% for very low intensity pulses for which the cathode QE can be very low. The effort to improve the GaAs-GaAsP cathodes is aimed at producing cathodes with greater than 80% polarization at NLC beam intensities with moderate-sized (3 to 9-cm²) cathodes.

The polarization of the NLC cathodes during full current extraction must be tested for each cathode crystal before it is installed at the injector. To perform such tests, a Mott polarimeter and spin rotator, optimized for the operating energy of the NLC source, will be an integral part of the source. The Mott polarimeter will be calibrated against a polarimeter known to have an absolute accuracy of 1% or better.

There are conditions at the source that can change the polarization of the electron beam slightly. Thus, as a diagnostic the operating source as well as the development system will be equipped with a Mott polarimeter as shown in Figure 2-1.

2.2.5 Vacuum and Mechanical Design

To achieve the desired high-voltage performance, it is critical to minimize field emission from the surface regions that see high electric fields. Extremely careful attention will be given to the fabrication of the cathode and anode electrodes and the cleanliness of all surfaces exposed to the gun vacuum. The electrodes will be fabricated using stainless steel with low carbon content and low inclusion density. The machined electrodes will be polished with diamond paste to a 1-mm finish with zero tolerance on visible pits and scratches. All components that operate at high voltage will be flushed with high-purity water before final vacuum firing. The assembly and alignment of the gun vacuum components will be done in a Class 100 clean room to avoid air-borne contamination.

Both ion pumps and nonevaporable getter (NEG) pumps will provide the pumping power for all gas species with the exception of inert gases. A high-sensitivity residual gas analyzer (RGA) will be used to monitor the gun vacuum. Following assembly, the gun is to be baked until the room temperature vacuum is $\sim 10^{-12}$ Torr excluding H_2 .

The conductance between the gun chamber and the injector where the vacuum is significantly poorer will be minimized by a vacuum isolation chamber characterized by limited aperture conductance and extremely high pumping speed. A modest bend of 20° after the vacuum isolation chamber will further isolate the gun vacuum system and prevent back-reflected electrons from hitting the cathode or induce gas desorption near the cathode.

To attain the desired high-voltage performance, the gun must be high-voltage processed following the vacuum bake to eliminate field emission spots on the cathode electrode surfaces. This process involves gradually increasing the voltage in the presence of a low pressure of N_2 if necessary—until the dark current at the operating voltage is well below 25 nA.

2.2.6 Loadlock and Cathode Preparation Chamber

While the gun provides a vehicle for extracting high-intensity electron beams from a photocathode and at the same time providing the necessary UHV conditions required for reliably operating a negative electron affinity photocathode, its functionality is fully realized only with the help of a loadlock and a cathode preparation chamber. The preparation chamber is a UHV system in which a cathode is prepared to have a negative electron affinity surface, while the loadlock allows the cathode to be installed in and removed from the preparation chamber and installed in the gun itself without breaking vacuum in either system.

Since the cathode preparation is time consuming, taking about 8 hours and even longer when using a loadlock, it is best done in a chamber separate from the gun. The necessary cleaning techniques and the recipe for applying Cs_2 and an oxide are well established.

2.2.7 Inverted Geometry Gun Tests

The prototype inverted structure gun at SLAC will be extensively tested to ensure it can match the SLC photocathode gun for good cathode performance. Based on the results of these tests, the details of the NLC gun upgrade design will be determined.

2.2.8 Reliability

Based on the SLC experience, it is believed that achieving near 100% operating reliability over a period of several years of continuous operation is possible. The provisions to be incorporated into the NLC source to ensure this result are:

- Use of a loadlock system to insert and remove cathodes into the gun without breaking the gun vacuum.
- Possibly using a double-gate valve for connecting the gun to the loadlock to reduce the chance of vacuum contamination of the gun should one gate valve fail.
- A vacuum isolation/differential pumping section downstream of the gun to protect it from the poorer vacuum system of the injector.
- Provision for a spare polarized electron source for completely testing cathodes for intensity, lifetime, and polarization.
- Provision of a transfer system for moving cathodes under vacuum between the NLC source, the spare source, and the cathode activation chamber.
- Provision of spare guns and spare cathode activation chambers.

2.2.9 Operation

Following the SLC experience, it is possible for the accelerator operators to remotely monitor and perform routine maintenance on the polarized electron source through a computer control system. For this purpose, the following displays will be available to the operators:

- The full residual gas spectrum of the gun and downstream vacuum systems.
- The transverse and longitudinal shape of the electron pulse at the gun.

A complete set of analog and digital signals will be available to the operators. These signals will also be history-buffered. The analog data will be collected locally for each pulse over the last few-minute period.

A representative value of the data will be history-buffered unless the system indicates a problem, such as a vacuum burst, in which case data will be recorded for every pulse. The principle operational task for the operator is to periodically cesiate the cathode. As the SLC has thoroughly demonstrated, this process can be fully automated (but initiated by operator command).

2.3 NLC Laser System

The NLC laser requirements are driven by the requirements on the electron beam from the polarized source photocathode [Alley 1994]. The most important of these requirements are the polarization and the charge limit properties of the GaAs cathodes. The laser wavelength needed varies with different cathode types and is chosen to maximize these parameters. Thus a range of wavelengths from 760 to 890 nm is needed. A quantum efficiency of 0.1% is assumed for the cathode based on the SLC experience. Electron beam optics considerations determine the other properties of the laser system such as longitudinal and transverse shape, stability, and so on.

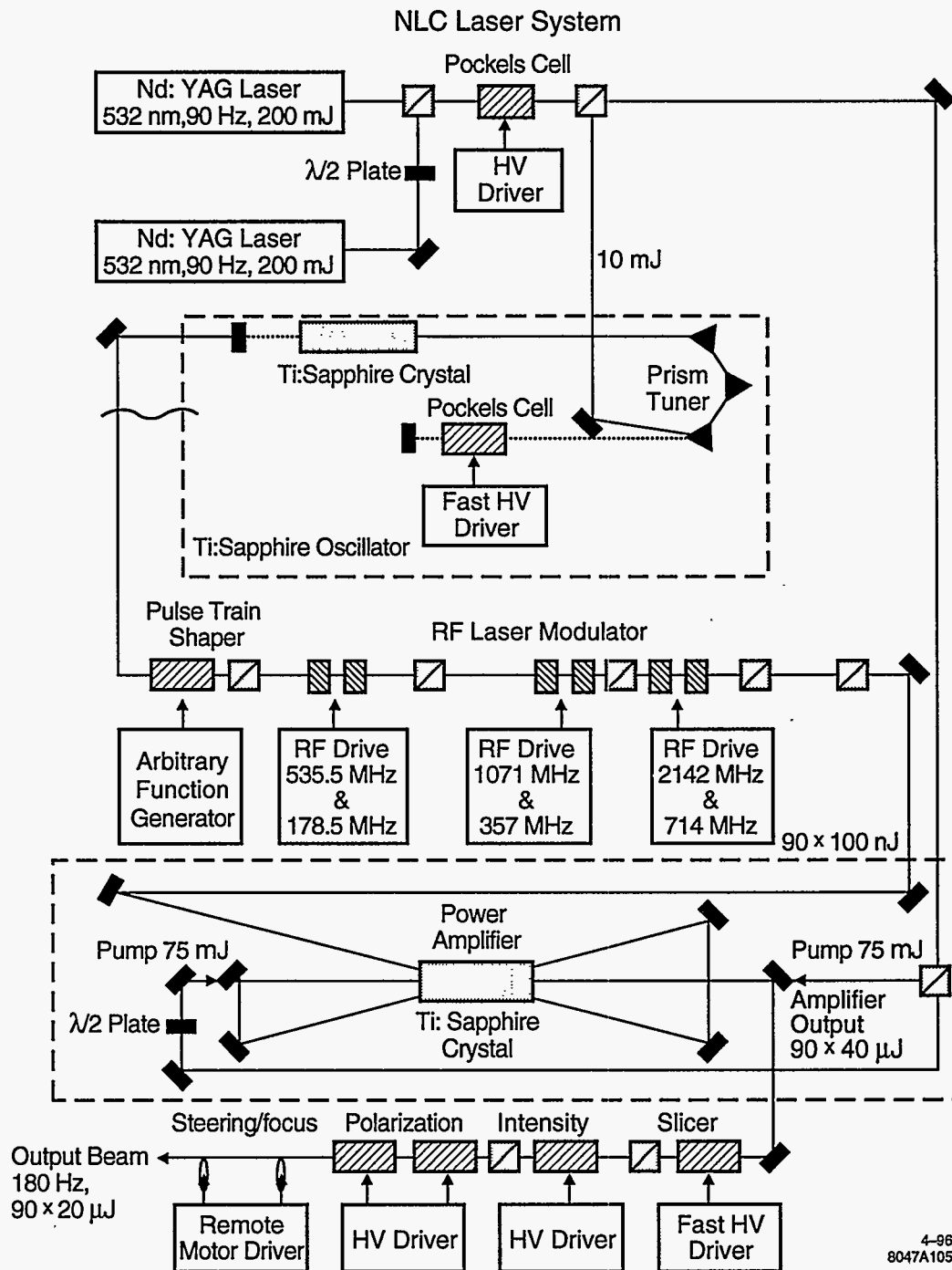
The proposed NLC laser system uses Titanium-doped sapphire (Ti:Sapphire) as the primary laser material. Pumping of the Ti:Sapphire is provided by a pair of commercial Nd:YAG lasers. Overall macropulse optical shaping is performed with an electronic feedback driving a Pockels cell attenuator. Micropulse shaping and selecting is done with a series of resonant Pockels cells. All of the technology used is fairly conventional, although the resulting system is somewhat complex. A schematic of the laser system is shown in Figure 2-4. The laser system is expected to meet the following specifications:

Wavelength	760 to 890 nm
Polarization	> 99.7%
Bunch train length	Up to 150 ns
Bunch spacing	714 MHz, 357 MHz or 178.5 MHz
Bunch width	< 1 ns as close to rectangular as possible.
Pulse contrast	< 5:1000 for the 714 MHz spacing, more is tolerable for the 357 and 178.5-MHz spacing.
Spot size on the cathode	Variable from 10 to 20-mm in diameter.
Transverse uniformity	As close to rectangular as possible.
Bunch energy	20 mJ
Bunch train energy stability	0.5% rms
Repetition rate	180 Hz

2.3.1 Pump Lasers

The pump laser system is required to produce a total of 150 mJ, 180 Hz, at approximately 500-nm wavelength. This can be done using two commercial *Q*-switched frequency-doubled Nd:YAG lasers. We have chosen to use two Coherent Infinity YAG lasers. These lasers use a seed laser and a phase conjugate amplifier configuration to obtain good transverse mode quality at high repetition rates. The two pump lasers are each operated at 90 Hz, and interleaved to obtain the required 180-Hz output.

Beam interleaving is achieved by rotating the polarization of one of the pump lasers and then combining them with a polarizing splitter/combiner. A pulsed Pockels cell is used to control the polarization of the



4-96
8047A105

Figure 2-4. Schematic diagram of the NLC polarized source laser system.

combined pump beam. A waveplate is used to adjust the splitting ration between the oscillator and amplifier. A second waveplate and polarizer is used to adjust the pump energy to each end of the amplifier.

2.3.2 Ti:Sapphire Oscillator

The oscillator produces a long (~ 150 ns) optical pulse with approximately 1 mJ of energy. Wavelength tuning is accomplished with a series of Brewster angle prisms (birefringent tuners would also work). A Pockels cell and the S-polarization loss of the prisms are used to Q-switch the cavity. The resulting output pulse is later chopped to produce the required pulse structure.

The primary source of output fluctuation in this system are changes in pump laser energy changing the output pulse energy and timing (due to changes in gain). The timing changes, coupled with the pulse chopping, produce additional intensity fluctuations. We plan to use a feedforward system which, on each pulse, adjusts the Q-switch time for the Ti:Sapphire laser to compensate for changes in the pump energy. If the system detects a high energy pump pulse, it delays the Q-switch time to compensate for the decreased build-up time (due to higher gain). The system is adjusted to slightly under-compensate for the gain change, the resulting slight timing shift (of the Q-switched pulse, not the output) compensates for the changes in Q-switched pulse energy.

A system of this type is used on the SLC source laser to provide an output with intensity fluctuations of $<1\%$ rms (0.6% has been demonstrated) with pump fluctuations of $>3\%$ rms. The limiting factor here is the stability of the pump laser intensity. We believe this technology can be improved to reduce output fluctuations to $<0.5\%$ rms (with expected pump fluctuations of $<2\%$ rms) and to improve the feedforward system.

All the oscillator components are commercially available. With the exception of the intensity stability, the required output parameters should be obtainable using conventional technology. The intensity stability should be obtainable with a modest extension of the feedforward technology used at SLAC.

2.3.3 Pulse Shaping

The pulse shaper uses an arbitrary function generator and a fast (10 ns) high-voltage (5 kV) amplifier driving a Pockels cell to shape the output pulse. The final electron beam pulse train shape will be measured and a software feedback will be used to control the function generator. The Pockels Cell are commercially available. The high-voltage driver is similar to units developed at SLAC for other laser projects.

2.3.4 RF Laser Modulator

The NLC requires a train of bunches about 1-ns wide, nearly square in shape, and 1.4-ns apart. In addition, the option of running with a 2.8 or 5.6-ns bunch separation is also desired. The laser system will use a series of rf-driven resonant Pockels cells to produce the required pulse shape. Two rf-driven Pockels cells at $f_1 = 714$ MHz and $f_2 = 2142$ MHz in series and a polarizer will produce an optical train according to the equation $OT_{1,4} = A \sin^2[\sin(\omega_1 t - \pi/4) + 0.2 \sin(\omega_2 t - 3\pi/4) + \pi/4]$ which is a train of nearly square pulses 1.4-ns apart and 1-ns wide as illustrated in Figure 2-5. To produce the 2.8-ns pulse separation, this system

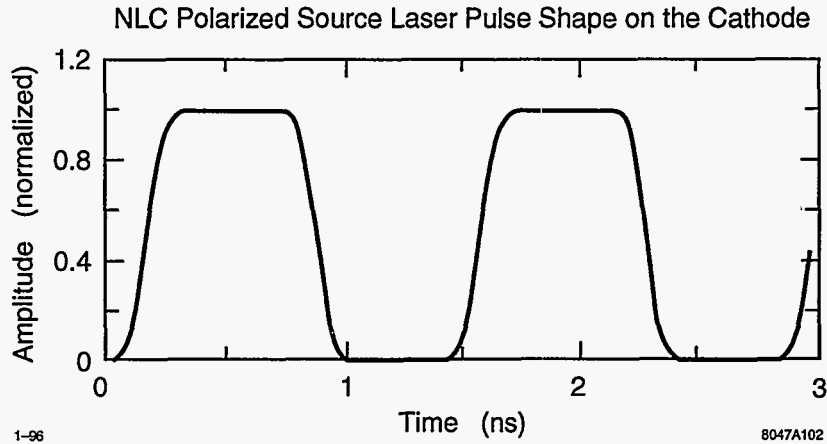


Figure 2-5. NLC polarized source laser pulse shape at the cathode.

of Pockels cells and polarizer is used in series by two other Pockels cells at $f_3 = 357$ MHz and $f_4 = 1071$ MHz and a polarizer, and for the 5.6-ns bunch separation, an additional pair of Pockels cells at $f_5 = 178.5$ and $f_6 = 535.5$ MHz and a polarizer is used. Thus, the equation for the train of bunches separated by 5.6 ns is the product of the output of each of the pair of Pockels cells and polarizer systems:

$$\begin{aligned}
 OT_{5.6} = & A \sin^2[\sin(\omega_5 t + \pi/16) + 0.2 \sin(\omega_6 t + 3\pi/4) + \pi/16]^* \\
 & * \sin^2[\sin(\omega_3 t + \pi/8) + 0.2 \sin(\omega_4 t + 3\pi/8) + \pi/4]^* \\
 & * \sin^2[\sin(\omega_1 t - \pi/4) + 0.2 \sin(\omega_2 t - 3\pi/4) + \pi/4]
 \end{aligned} \quad (2.1)$$

The laser intensity between the main pulses is almost completely quenched and the area of the residual pulse between the main pulses is 0.2, 0.5, and 1.4% of the main pulse for the 1.4, 2.8 and 5.6-ns separation cases, respectively. It is expected that most of this charge produced between the main pulses will be lost early in the injector beam line due to its poor bunching and matching into the lattice, as compared to the main bunch.

If standard KDP Pockels cells are used, a peak rf voltage of approximately 5 kV is required. With a resonant circuit $Q=100$, the required drive power is approximately 3 kW peak (<1 W average).

2.3.5 Ti:Sapphire Power Amplifier

The power amplifier operates in a 3-pass "bow tie" configuration with a gain of 10 each pass. A fairly conservative amplifier efficiency of 5% is assumed. Both ends of the laser rod are pumped to reduce the possibility of damage from the pump laser energy density. The required pump energy density of approximately 2 J/cm^2 is within the limits for continuous operation. The average pump power to the crystal is approximately 30 W, well within the thermal fracture limit for Ti:Sapphire. The Ti:Sapphire thermal fracture limit is 5 times more than for the YAG [Wanant 1994], the YAG limit is 30 W/cm^2 , [Koechner 1992], and the spot size on the cathode is 2 to 3 cm^2 .

The feedforward system used in the oscillator can also compensate for changes in the gain of the amplifier. This should permit operation at the required 0.5%-rms output stability.

2.3.6 Pulse Train Length, Intensity, Spot Size, and Steering Control

The train of pulses from the amplifier is sliced to the desired overall length with a fast, high-voltage driver and a Pockels Cell. This system will probably have rise and fall times of approximately 5 ns. Faster pulses may be possible, but some high-voltage driver development would be required. The output intensity is controlled by a high-voltage amplifier driving a Pockels cell.

The output polarization is switched using two Pockels cells and high-voltage driver. Laser circular polarizations >99.7% are easily obtainable. Electron polarization measurements can be used to optimize the drive voltage on the Pockels cells to eliminate any birefringence in the transport line to the photocathode.

The beam spot size and position on the photocathode can be controlled with a remotely actuated telescope.

The propagation path and optics of the laser will be determined by the geometry of the physical layout of the injector with respect to the laser and is straightforward.

2.3.7 Overall Technical Risks

The most challenging requirement for the laser system is the output intensity stability. It is believed that this can be met with the use of feedforward system. The rf laser modulation is in principle straightforward, but some development may be required to obtain the required electrical Q s for the Pockels cells. The transverse mode structure from the output of the amplifier is difficult to predict. With the addition of spatial filtering, it should be possible to produce a good transverse-mode beam. In general, development of this laser system is anticipated to require approximately three man years.

2.4 NLC Electron Injector Beam Dynamics

2.4.1 NLC Injector Baseline Design

As shown in Figure 2-1 and discussed in Section 2.1, the NLC injector is like the conventional injector used on the SLC with a DC high-voltage gun and subharmonic bunching system. In this section we describe the beam dynamics from the gun through the injector linac.

2.4.2 Electron Gun Optics

The plan is to use a modulated laser to extract an electron bunch train from the photocathode. The electron beam energy from the gun will be 120 keV, a comfortable operating point for the polarized electron source. The proposed gun for the NLC polarized electrons has a large, 3-cm² cathode. The electrodes are shaped to minimize emittance for operating bunch currents and reduce the electric field gradients near the cathode to avoid arcing in this region. We used EGUN to simulate the beam from the gun. Figure 2-6 shows the ray-trace of the beam from the cathode to 12-cm downstream. The normalized edge emittance is 5.6×10^{-6} m-rad and the beam envelope radius is 1.2 cm at the tip of the anode.

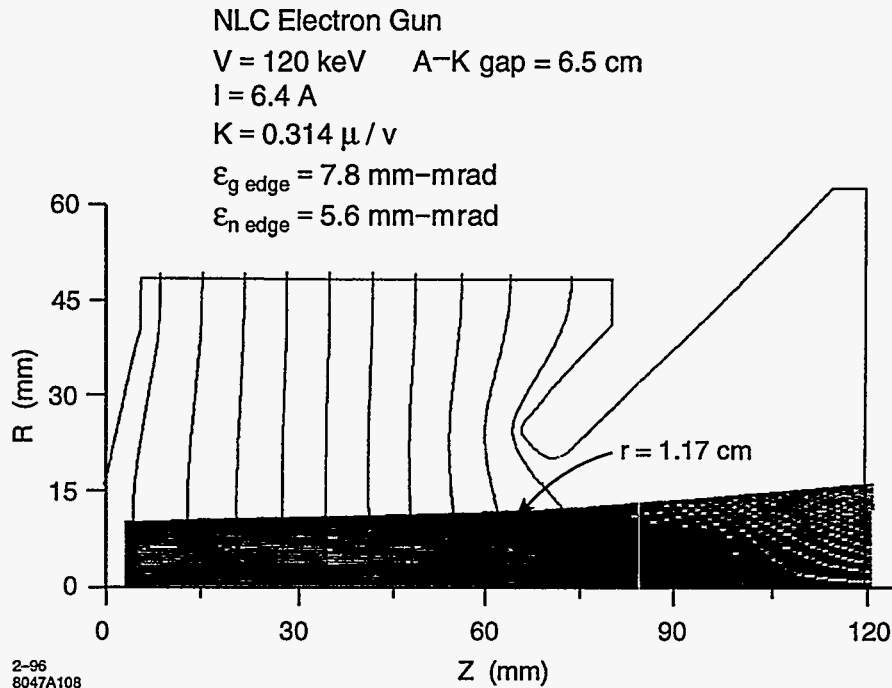


Figure 2-6. Ray trace of the NLC electron beam from the gun.

2.4.3 Intensity Jitter Limiting Aperture

A scenario for reducing the electron intensity jitter is to locate a fixed aperture in the 120-keV beam line at a location where the beam size is proportional to space charge. With this method, we hope to reduce the intensity jitter by scraping more charge when more charge is produced at the gun and less charge when less charge is produced at the gun. For the proposed NLC injector design, such a location exists 24-cm downstream of the 20° bend. Using a 1.25-cm aperture, we can reduce a 2% intensity jitter at the gun to be immeasurable in the bunched beam, while losing 17% of the charge in the aperture. Since this loss occurs after the gun vacuum isolation chamber and the 20° bend, it should not cause any damage to the photocathode based on various gun test experiences on the SLC polarized source. Figure 2-7 shows the correlation of charge per bunch in the downstream part of the injector with the charge produced at the gun. Figure 2-8 shows the charge in 18 ps at 80 MeV with and without the aperture. Notice that without the aperture the correlation has about a 45° slope, while with the appropriate aperture the slope is greatly reduced for the bunched beam intensity.

Studies were conducted to see how sensitive this scheme is to the location of the aperture along the beam line and to various nominal charge intensity scenarios. To study the effect of the criticality of the location of the aperture it was moved in simulations by $\pm 2 \text{ cm}$ from the nominal location and no observable difference in the performance of the aperture was detected. Reducing the nominal operating intensity to 3/4 or 1/2 of the nominal charge has a measurable effect on the aperture size needed for reducing the intensity jitter. At 3/4 charge, an aperture 1.5-mm smaller in radius is needed and at 1/2 charge, another 1-mm smaller is needed. To accommodate the changes in the operating intensity from the gun, the aperture would have to be mechanically designed such that its size can vary in small increments of less than 1 mm.

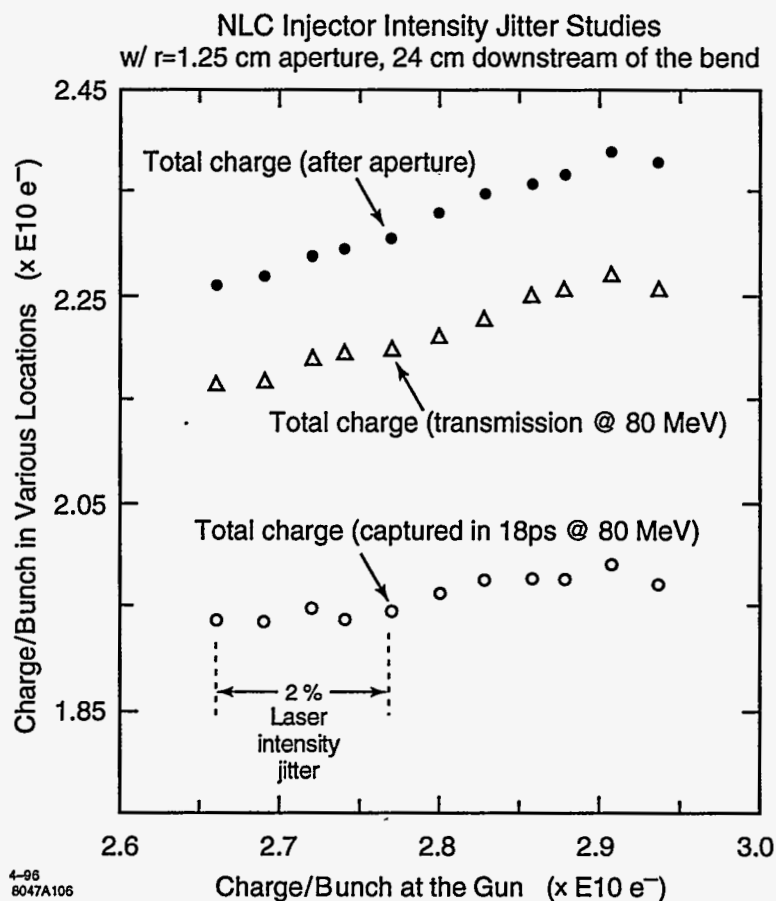


Figure 2-7. NLC injector intensity at various locations as a function of charge from the gun going through a fixed aperture after the 20° bend near the gun.

2.4.4 Bunching System

As shown in Figure 2-1, two 714-MHz standing wave subharmonic bunchers are located 74-cm apart downstream of the intensity jitter limiting aperture. The S-band buncher is a four-cavity, $\beta = 0.75$ traveling-wave section and is located 42-cm downstream of the second subharmonic buncher. Immediately following the S-band buncher is a $\beta = 1$, 3-m S-band accelerator section which acts as a further buncher in the first meter. This bunching system compresses the beam such that 83% of the in-coming charge is captured in 18° of S-band or 17.5 ps. Given that 17% of the beam is lost in the intensity limiting aperture, for $2.8 \times 10^{10} e^-$ per bunch at the gun we expect to have $1.96 \times 10^{10} e^-$ in 18 ps per bunch after bunching. PARMELA simulations were conducted from the gun to the end of the second accelerating section where the beam energy is $80 \text{ MeV} \pm 0.6\%$. Figure 2-9(a), (b), (c), and (d) show the single bunch charge distribution profile in time, transverse particle distribution, longitudinal particle distribution, and the energy spread profile, respectively, at the end of the second accelerator section.

At the end of the second accelerator section the beam-normalized rms emittance is 4.5×10^{-5} m-rad. Figure 2-10 shows the normalized rms emittance from the gun up to the end of the second accelerator section and Figure 2-11 shows the beam edge envelope.

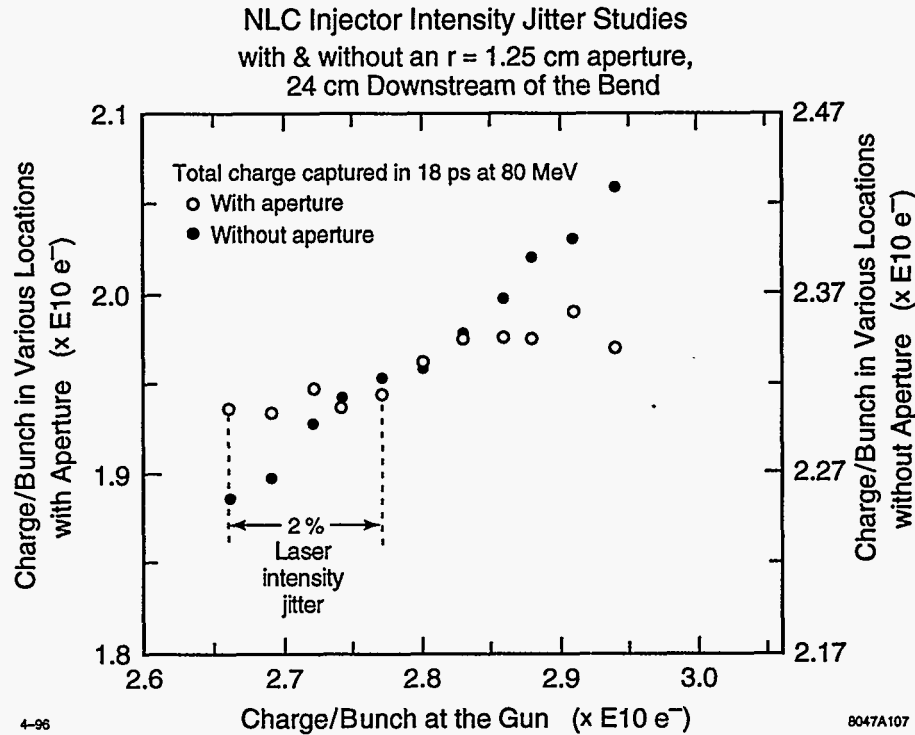


Figure 2-8. NLC injector intensity after bunching as a function of charge from the gun with and without an aperture after the bend.

Beam loading in the subharmonic bunchers is minimized by judiciously choosing a low $R/Q \sim 10\Omega$, a high $Q_0 \sim 10000$, and a coupling coefficient of $\beta = 1$, we can force a low beam-induced voltage and a long filling time of the cavity, thus minimizing the effects of beam loading in it. The fill time in this case will be $2.2 \mu\text{s}$, much greater than the 126-ns bunch train length.

Since 17% of the charge is intercepted by the intensity jitter limiting aperture for the highest charge operating scenario, with 4.5 nC from the gun there will be 3.7 nC at the first subharmonic buncher and with a 700-ps bunch length it will occupy 180° of the 714-MHz subharmonic buncher rf. The beam-induced voltage in the first subharmonic buncher by the time the ninetieth bunch goes through will be:

$$V_{b1} = [0.5q(R/Q)\omega/\pi] \times 90 \text{ bunches} = 3.7 \text{ nC} \times 10\omega \times 714 \text{ MHz} \times 90 = 2.4 \text{ kV} \quad (2.2)$$

For the second subharmonic buncher, the bunch length is more like a δ function and

$$V_{b2} = [0.5(R/Q)\omega] \times 90 \text{ bunches} = 3.7 \text{ nC} \times 10\omega \times \pi \times 714 \text{ MHz} \times 90 = 7.5 \text{ kV} \quad (2.3)$$

Bunching simulations indicate that we need 18 kV in the first subharmonic buncher and 34 kV in the second for optimum bunching for the highest charge scenario. Since the centroid of the bunch is at about 90° ahead of the crest, the induced phase change in the first subharmonic buncher will be $\arctan(2.4/18) \sim 8^\circ$ and in the second $\arctan(7.5/34) \sim 12^\circ$. This phase shift is not negligible and needs to be compensated. We plan to drive the cavity with as much power as would be needed to compensate for the voltage induced by the beam in the steady state plus the voltage needed for optimum bunching, and then inject the beam during the fill time of the cavity when the voltage in the cavity reaches the voltage needed for optimum bunching. At the time of beam injection, the phase of the generator power must be shifted by the amount that would be induced by the beam in the steady state.

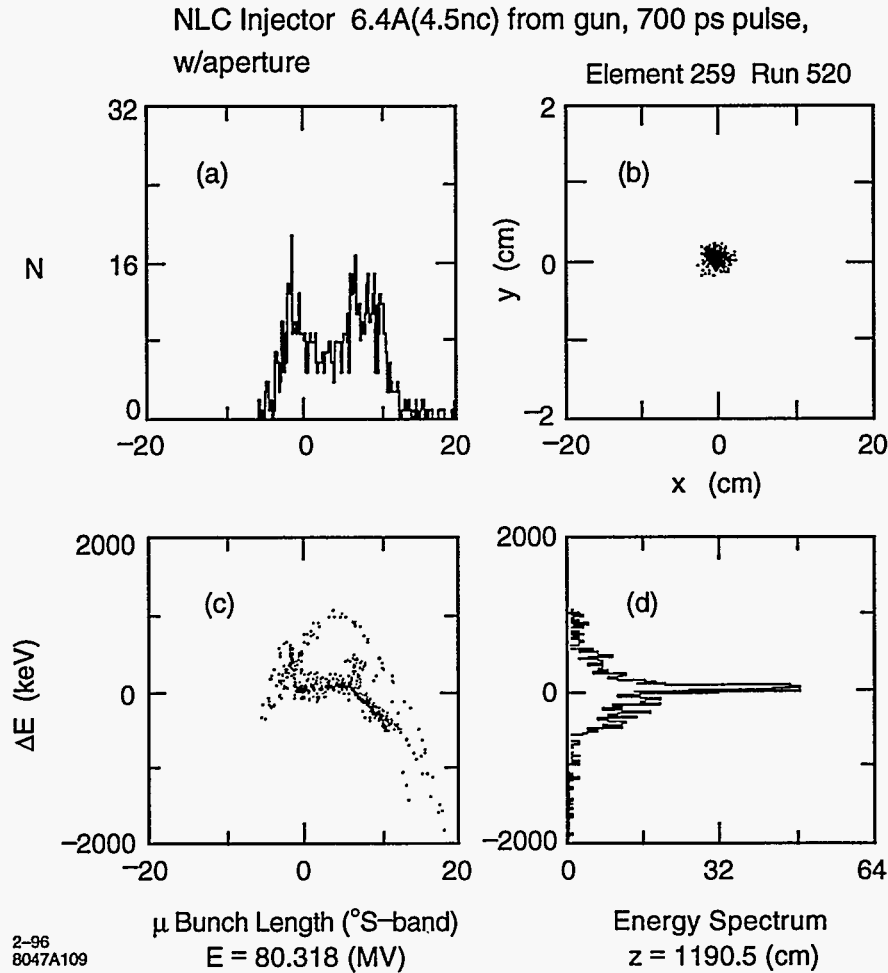


Figure 2-9. PARMELA results of beam longitudinal and transverse distribution at the end of the second accelerator section. (a) bunch shape, (b) transverse distribution, (c) longitudinal distribution, (d) energy spread.

The average current in the bunch train is $3.7 \text{ nC}/1.4 \text{ ns} = 2.6 \text{ A}$. The steady-state beam loading in the first subharmonic buncher where the beam occupies 180° of the rf, is $(1/2) \times I_b \times (R/Q) \times Q_0 / (1 + \beta) = 65 \text{ kV}$. The generator power needed for bunching and beam-loading compensation is 42.3 kW . For a beam which is at 90° ahead of the crest, the steady-state phase shift is $\arctan(V_{bs}/V_g) = \arctan[65/(18 + 65)] = 38^\circ$, where V_{bs} is the steady-state beam induced voltage, and V_g is the generator voltage. Thus, at the time of the beam injection, the generator power is shifted by 38° , which is felt by the cavity at the fill rate. By the time the entire bunch train goes through the cavity, the generator voltage felt by the cavity is only 2.3 kV with an 8° phase shift, exactly what is needed to compensate for the beam loading.

For the second subharmonic buncher where the bunch width is a δ function compared to 714 MHz , the steady-state beam loading is $I_b \times (R/Q) \times Q_0 / (1 + \beta) = 130 \text{ kV}$. The generator power needed to compensate for beam loading plus the bunching voltage is 167.8 kW . The phase shift induced by the steady-state beam loading is $\arctan[135/(34 + 135)] = 39^\circ$.

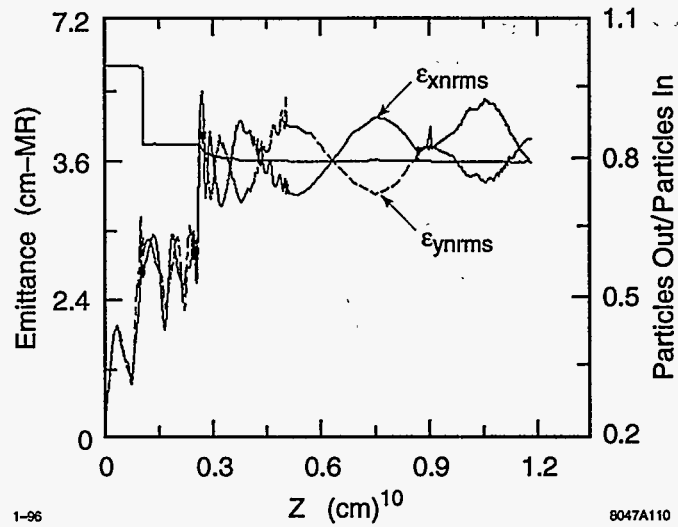


Figure 2-10. Beam emittance along the injector from gun to the end of the second accelerator section (80 MeV).

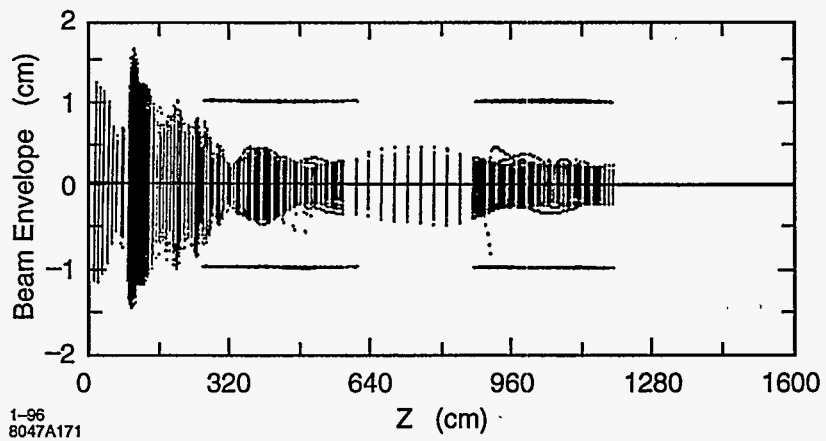


Figure 2-11. Electron beam edge envelope from gun to end of the second accelerator section (80 MeV).

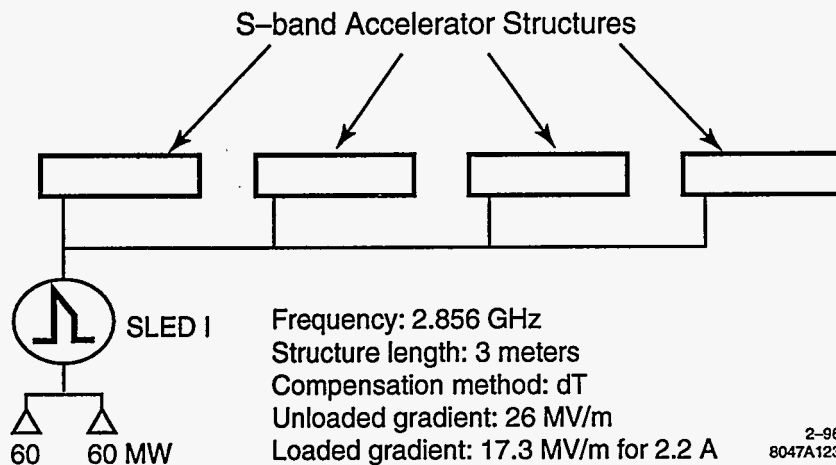


Figure 2-12. A single module configuration for the 2 GeV electron injector linac.

2.4.5 Injector Linac

The Linac for accelerating the bunched electrons from 80 MeV to 2 GeV consists of 3-m S-band structures. The nominal rf frequency for the accelerator structures is 2856 MHz. Two SLC model 5045 klystrons drive one SLED1 cavity and the power out of the SLED drives four accelerator sections on one module. Figure 2-12 shows the layout of one module, and the injector for the collision electrons will employ 11 such modules. The beam loading compensation method using the Δt technique for the S-band linac is described in detail in Chapter 6. For the highest charge operating scenario, the maximum current in the injector linac will be 2.2 A. For 2.2 A in the injector linac the maximum possible energy gain per module is 208 MeV with 60-MW usable klystron power in the accelerating structures. The central energy variation from bunch 1 to bunch 90 is about 0.005% at the end of each accelerator section, and the single bunch energy spread due to the bunch width and assuming the beam is on the crest will be $\pm 0.6\%$ edge.

The lattice from 80 MeV to 2 GeV up to the linac-to-ring transition was designed using MAD. A 30° achromatic bend system at 80 MeV allows us to introduce a second injector line parallel to the first one up to 80 MeV. Two sets of emittance measurement stations are included, one on each side of the bend to measure emittance coming out of the bunching system and the other for measuring the emittance into the 2-GeV accelerator. The transport line from the end of the second accelerating section to the beginning of the first injector linac module has been designed. The lattice is shown in Figure 2-13. The bend is an achromatic and isochronous system consisting of two rectangular dipole magnets which bend the beam by 30° . A FODO lattice with seven identical quads separated by 70 cm from center to center are used. The beam envelope for $\pm 2\%$ energy spread is less than 1 cm in radius at its maximum and comfortably fits in a 1.5-in pipe. The bunch length expansion is only 0.08 ps per 1% energy spread. The total length of the achromatic bend is 4.9 m.

The accelerator lattice is designed to take the $\beta = 1.4$ m beam achieved at the end of the second accelerator with PARMELA simulation and increase it by a factor of the square root of the energy up to 2 GeV. As shown in Figure 2-1, wrap-around quadrupoles are used around the first part of the accelerator section to maintain the small β function at the low energy end where the wakefield effects are more significant. We assumed that each module contributes 192 MeV for the lattice design to allow for some energy overhead.

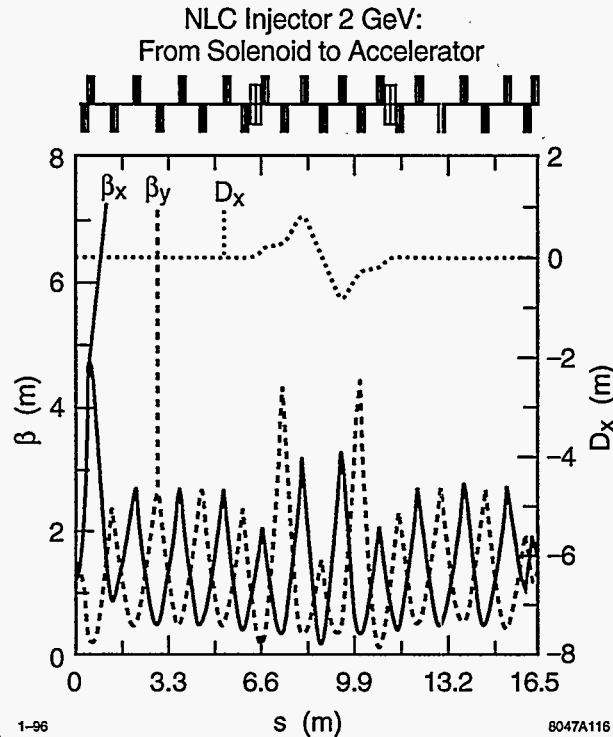


Figure 2-13. *Electron injector lattice to transport beam from the end of the solenoids to the injector accelerator.*

With this assumption, the beam reaches 2 GeV after 10 modules, thus there is an additional module for overhead. While the spare module will not accelerate the beam during normal operation it still needs at least one klystron to be operating for beam loading compensation in that module as described in more detail in Chapter 6. If a klystron fails in one of the accelerating modules then the spare module can be powered in the nominal way while the module with the problem klystron becomes the spare. Figure 2-14 shows the lattice for the accelerator and Figure 2-15 shows the lattice for the matching section from the end of the 2-GeV linac to the linac-to-ring transition. Another emittance measurement station is included in this portion of the injector. Figure 2-16 shows that the pole-tip field of all the quadrupoles in the 2-GeV injector is under 8 kGauss, which is a very comfortable operating range.

The energy spread from the beginning of the train to the end of the train due to beam loading is compensated for completely at the end of each accelerator section. Thus at the doublets between the acceleration sections, the energy spread is uniform from the first to the last bunch and is due only to the single-bunch width. However, at the wrap-around quads on the accelerator sections themselves, at the beginning of the accelerator there is energy variation in the energy of the individual bunches within the train. This is because the gradient at the quad location is different when the first bunch goes by versus when the last bunch goes by. We tracked the first, the middle and the last bunch of the train through the design lattice to see how this effects the emittance out of the injector for the various bunches. We assumed an input single-bunch energy profile which is similar to the energy profile at 80 MeV as calculated by PARMELA, and central energy variation at the wrap-around quads based on the beam loading compensation scheme. Tracking simulations show that at the end of the 2-GeV linac there is only 3% emittance growth in the x plane and none in the y plane. The bends in the 80-MeV achromat are in the x plane.

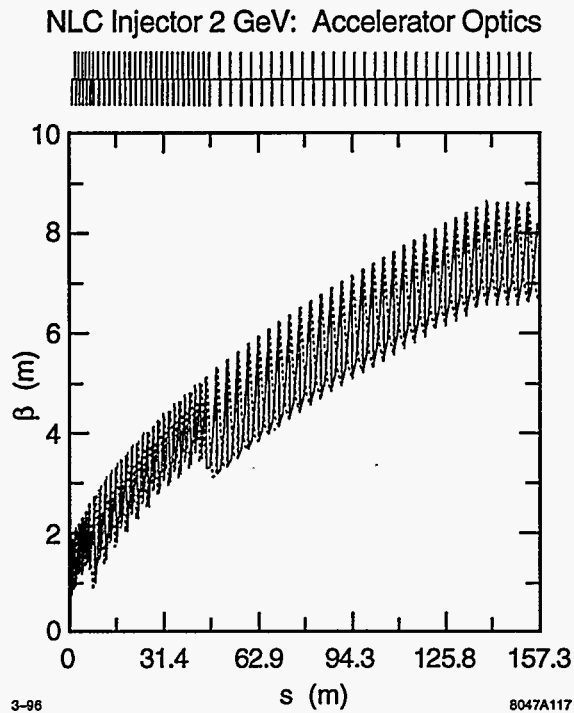


Figure 2-14. Electron injector lattice over the 2-GeV accelerator.

The effects of the wakefield on the emittance were estimated assuming that the beam is offset by one sigma from the accelerator centerline and that the β grows as the square root of the energy monotonically starting with 1.5m at 80 MeV. At 2 GeV the actual emittance of the beam increases by only 4% but the effective emittance growth, taking into account that the beam is not centered, is 44%. Even with this emittance growth the total emittance will be about 0.63×10^{-4} m-rad, well within the 1×10^{-4} m-rad threshold.

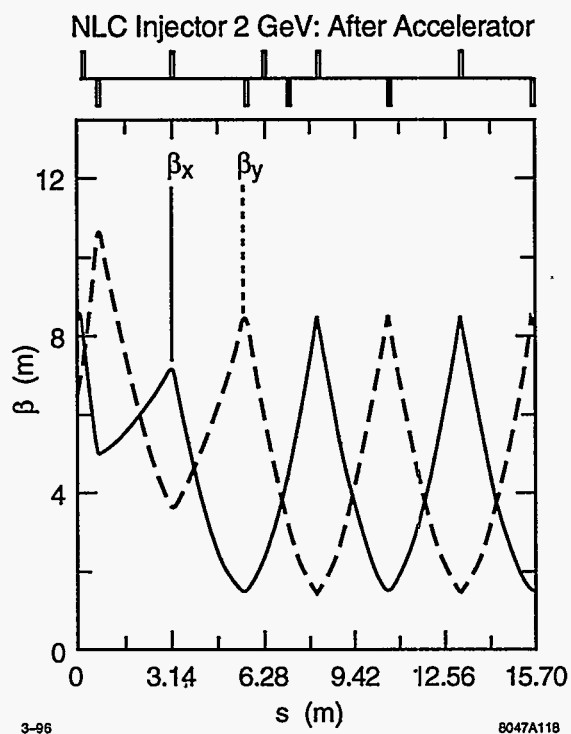


Figure 2-15. Electron injector lattice from the 2-GeV accelerator up to the damping ring.

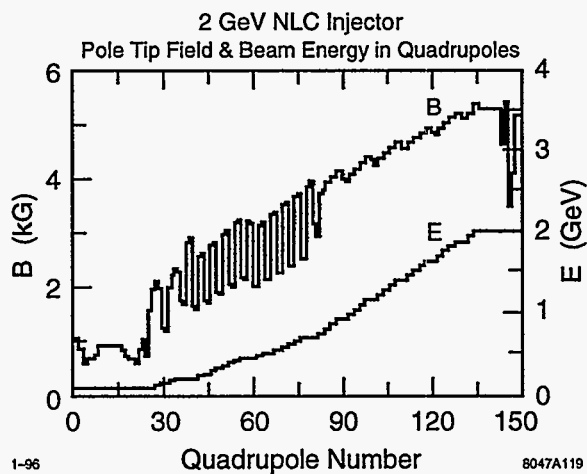


Figure 2-16. Electron injector quadrupole pole-tip fields and electron beam energy from the end of the solenoids up to the damping ring.

2.5 Buncher Cavities

There are two types of bunchers: Two standing wave 714-MHz subharmonic bunchers and an S-band traveling wave buncher with four cavities with a phase velocity of 0.75 c. The traveling wave buncher is similar to the one on the SLC and will be integrally brazed onto the first 3-m accelerator structure.

The subharmonic buncher will have the following parameters:

$$\begin{aligned} f &= 714 \text{ MHz} \\ R/Q &\sim 10 \text{ W} \\ Q &\sim 10000 \\ \beta &\sim 1 \end{aligned}$$

Subharmonic structures with similar parameters need to be constructed for the NLCTA injector upgrade project, thus much experience is expected to be gained in this area.

2.6 Positron Drive Linac

The linac for the positron drive beam is similar to the injector of the collision electron beam. Two differences are that the positron drive linac will use a thermionic gun and will extend to 3.11 GeV in NLC I and 6.22 GeV in NLC II with optics to transport the electron beam to one of the parallel positron production beam lines. Figure 2-17 shows the electron injector for the positron drive beam. Initially, accelerator sections will be installed to accommodate the 3.11-GeV injector with one module to spare, and room will be left to install accelerating sections to double the energy of the drive beam for NLC II.

The thermionic DC gun rather than a photocathode DC gun is chosen for the positron drive injector because thermionic guns are easier to construct and operate, and they do not have an expensive laser system associated with them. One major difference between the thermionic gun for the NLC and the thermionic gun which was used on the SLC is that the NLC requires a bunch train format right from the gun. The nominal bunch train consists of 90 bunches, each bunch 700 ps in full-width-half-maximum and 1.4-ns apart. In addition, we must be able to change the bunch separation to 2.8 and 5.6 ns. We believe it will be too difficult to achieve all three possible train structures with one pulser, but since the change in train format is not a routine operation and we would be willing to take the time to exchange pulsers, we feel that it would be possible to construct three different pulsers, one for each bunch separation scenario. The 1.4-ns bunch interval pulser can be a resonant pulser while the other two would have to be broad-band pulsers similar to the ones constructed for the KEK Advanced Test Facility thermionic gun [Naito 1994].

The positron drive injector beamline from the gun through 80 MeV is identical to the polarized e-beam injector. The lattice from 80 MeV to the spoiler in front of the positron target in either of the two parallel positron production lines has been designed. Figure 2-18 shows the β function from 80 MeV through the 3.11-GeV linac and the allocated space for additional accelerators for NLC II. Figure 2-19 shows the β function for the beam transport from the end of the accelerator to the spoiler including the 10° achromatic bend to switch the beam to either of the positron production lines. The beam size at the spoiler in front of the positron target is designed to be $\sigma = 0.5 \text{ mm}$, about 1/3 of the size required at the target after the spoiler. Figure 2-20 shows the quadrupole pole-tip strengths for the positron drive beam linac which are at very reasonable values at less than 8 kGauss.

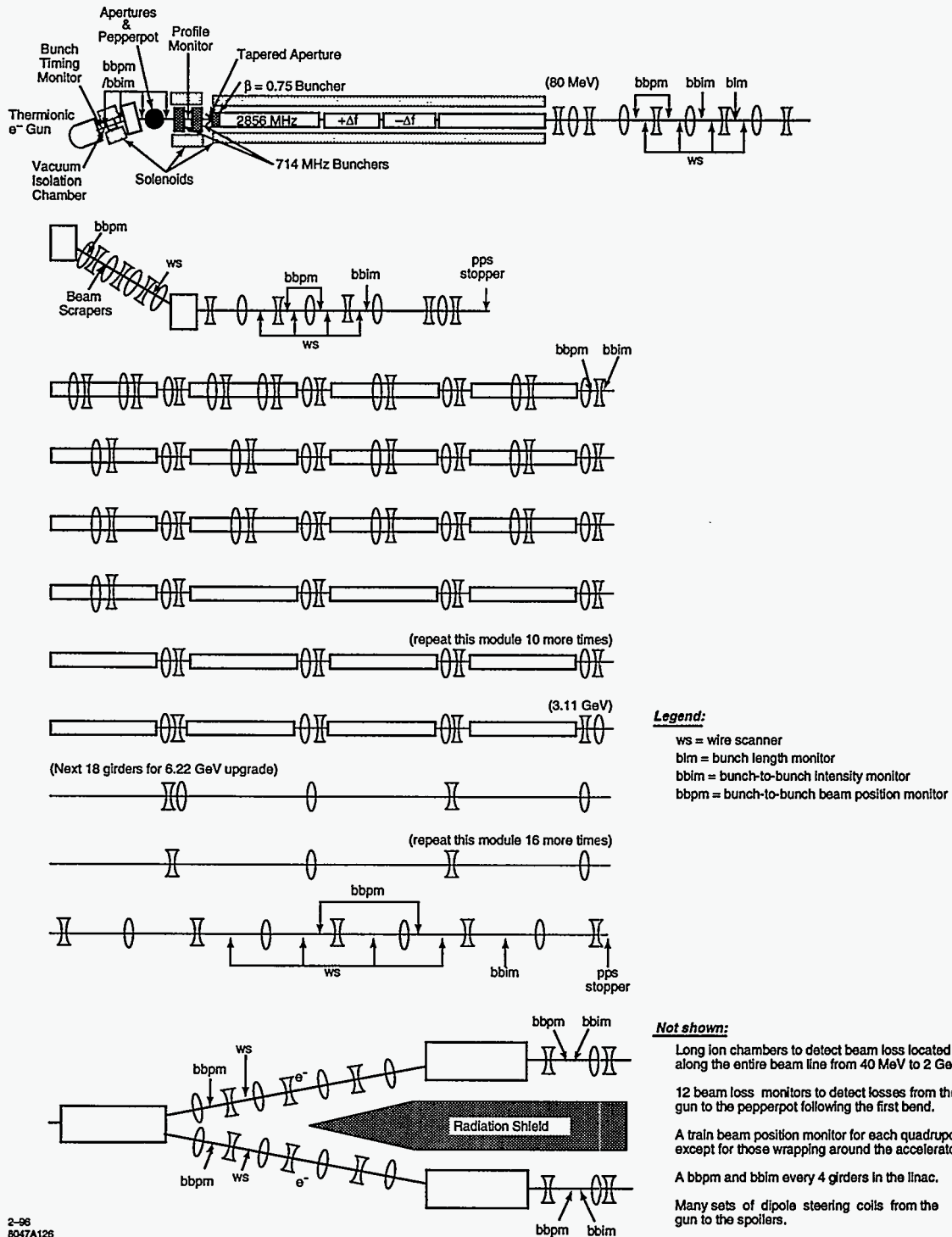


Figure 2-17. Electron linac for the positron drive beam.

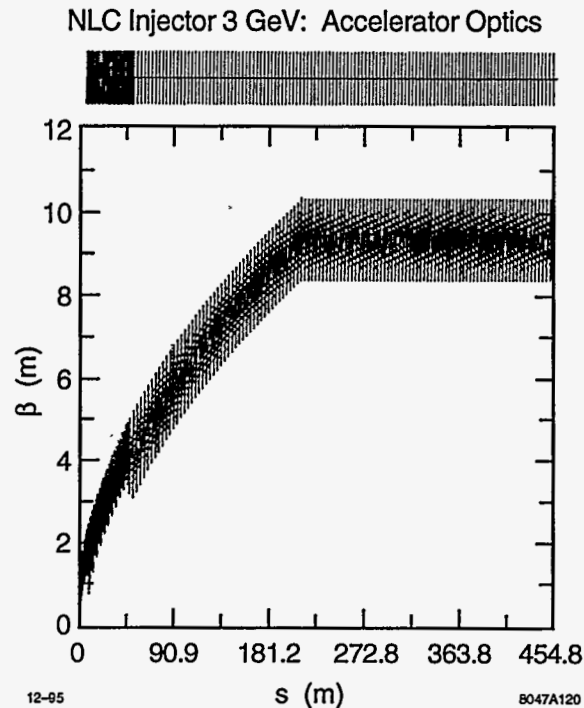


Figure 2-18. Positron drive linac lattice to transport the electron beam from the end of the solenoids to the bend at the end of the drive linac.

As mentioned before, the β function and the beam line up to 2 GeV is identical to the collision electron case but the β continues to grow as the square root of the energy up to 3.11 GeV in this lattice. Using these parameters, the wakefield contribution to emittance growth was estimated for the 3.11-GeV linac in a similar way as for the 2-GeV collision electron injector linac. The actual beam emittance of the last bunch increases by 11% at the end of the 3.11-GeV linac but the effective emittance increase due to the beam being offset by one sigma is 52%. This is still acceptable for the drive injector for positron production.

No special difficulties are expected with the positron drive injector which have not already been taken into consideration for the collision electrons.

2.7 Diagnostics

The purpose of the diagnostics system is several-fold: to aid in tuning the injector, to diagnose the beam parameters including jitter, and to be used for machine protection triggers. The diagnostics consist of charge monitors and beam position monitors some of which are capable of measuring the parameters for a small group of bunches in a portion of the train selected by the user, bunch-to-bunch timing monitor, aperture/pepperpot insert, beam profile monitors, bunch length monitor, emittance measurement and energy spread measurement stations after 80 MeV and 2 GeV. There is a rather high density of current monitors and position monitors in the beam line from the gun through 80 MeV. Every doublet in the injector linac has a beam position monitor in it. There will be microchannel-plate photomultiplier-tube beam loss monitors in the 120-keV region and a PLIC cable in the region from 40 MeV and beyond.

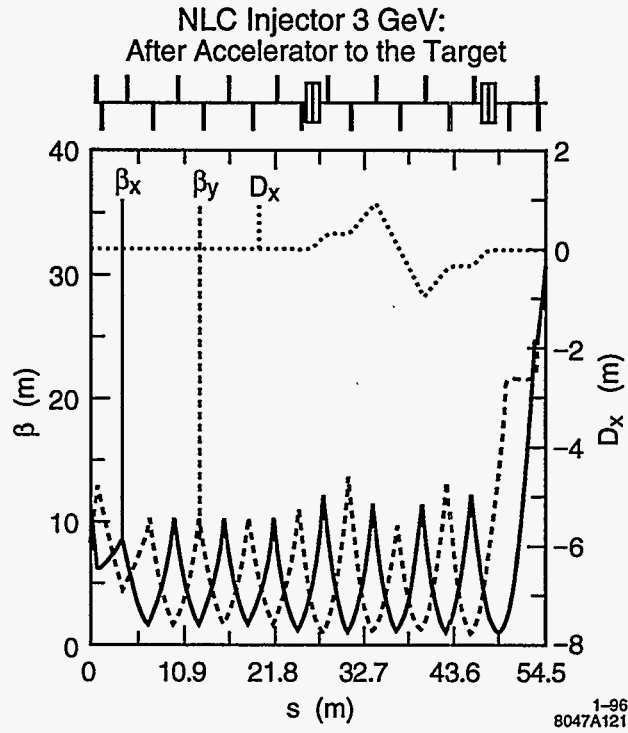


Figure 2-19. Positron drive beam lattice from the end of the diagnostics station after the drive linac up to the spoiler.

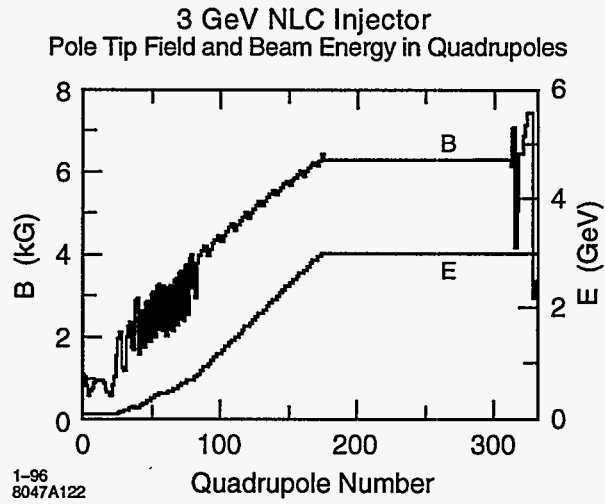


Figure 2-20. 3-GeV NLC injector. Pole-tip field and beam energy in quadrupoles.

Diagnostic	Total Bunch Train		Bunch bundle ^a	
	Range	Resolution	Range per bunch	Resolution per bunch
Toroid charge mon.	45-250 × 10 ¹⁰ e ⁻	±0.2%	0.5-3 × 10 ¹⁰ e ⁻	±1%
Gap current mon.	45-250 × 10 ¹⁰ e ⁻	±3%	0.5-3 × 10 ¹⁰ e ⁻	±3%
charge				
pulse width	1-150 ns	±1 ns	~200 ps	—
Streak Camera	1-150 ns	±1 ns	5-40 ps	1 ps
Beam loss mon.	0-10 ⁸ e ⁻	10 ⁷ e ⁻	—	—
Beam position mon.	0-1 cm	±20μ	0-1 cm	±20μ
Beam size mon.				
at the cathode ^b	R=0 - 1.5 cm edge	±1%	R=0 - 1.5 cm edge	±1%
at 120 keV	R=0 - 1.5 cm edge	±1%	R=0 - 1.5 cm edge	±1%
at 80 MeV	R=0.2 - 1 cm edge	±1%	R=0.2 - 1 cm edge	±1%
Energy	80 MeV	±0.2%	~80 MeV	±0.5%
Energy spread at 80 MeV	~4%	±0.2%	~4%	±0.2%
Pepper pot	Qualitative diagnostic			
Bunch length monitor	Qualitative measurement for tuning by maximizing signal			

^a Bunch bundle represents a group of bunches as close to a single bunch as possible. Some of the diagnostics may not be fast or sensitive enough to measure single bunch parameters but can measure a group of about five adjacent bunches and this would be sufficient. These diagnostics would require a timing gate width of about 3ns, with a 0.5-ns rise time and 10-ps timing stability. The details of how to construct such diagnostics will be covered in Chapter 15.

^b A profile of the laser at a screen located at the image point of the cathode.

Table 2-3. Injector diagnostics and their specifications.

Most of the monitors at the gun and at the end of the first accelerator section need to have the ability to measure variation from bunch-to-bunch within the same bunch train. Measuring the variation between a group of bunches in 5-ns intervals would be sufficient, that is, it is not necessary to measure the parameter of a single bunch.

Figure 2-1 shows the various kinds of monitors on the e⁻ injector beam line. The drive linac for the positrons will have these same diagnostics except the wire scanners for the linac emittance measurement will be located just upstream of the achromatic bends up to the two positron production lines. In addition there will be bunch-to-bunch beam position monitors, intensity monitors and wire scanners in the achromatic bends and just upstream of the spoilers as shown in Figure 2-17.

Table 2-3 shows the various diagnostics in the injector, and their specifications.

2.8 Operation

2.8.1 Initial Set-up and Beam Maintenance

Figure 2-1 shows a schematic of the injector beam line components from the gun anode up to 2 GeV. Each of the subharmonic bunchers, the S-band buncher and the S-band accelerator sections will have independent rf phase and amplitude control. There are beam steering coils at the gun and after the bend. Large steering coils are draped over the solenoids from the subharmonic bunchers through the second accelerator section. There is a set of steering coils on each module in the injector linac.

The procedure for operating the NLC injector has several aspects. First of all it is necessary to set the focusing, bunching, and accelerating parameters of the injector to the optimum values for beam transport and quality. Then it is necessary to maintain the optimized beam quality achieved during startup over a long period of time. Finally it is necessary to establish guidelines for troubleshooting problems when the beam quality deteriorates. Additionally, it is necessary to establish good, clean configuration records to aid in recovering from various faults or down times.

To set up the injector parameters initially, it is necessary first of all to have good calibration data on all the beam diagnostics, the various power supplies, and rf drivers including the losses in cables and processing electronics. It is necessary to characterize the subharmonic bunchers and buncher and accelerating sections so that one can actually convert the power measured at the test points into electric fields as the beam sees it. Having calibrated the various components such that one can determine the state of the injector and the beam in it, we can then start the tuning procedure.

At first and when turning on the beam after long down times, it is necessary to establish a good quality, single-bunch beam all the way to the end of the injector before going to long-pulse operation.

The first order of business is to establish beam from the gun by shaping and pointing the laser on the photocathode and adjusting its power for the desired charge from the gun. Next, the beam is transported around the 20° bend to the subharmonic buncher by using the magnetic lens and solenoid strengths designated by the simulations and by steering. Once the beam reaches the subharmonic bunchers, it is necessary to synchronize the beam with the rf of the Subharmonic bunchers, the accelerators, the current monitor, and beam position monitor sampling cycles. Next, we need to bunch the beam and steer it to achieve at least 80% of the gun charge captured in 18 ps at 80 MeV. It might also be necessary to adjust the strengths of the axial magnetic field coils to achieve the simulation beam size at the profile monitor. Next, we steer the beam in the injector linac while phasing the klystrons to maximize the energy using the energy spread wire scanners both in the chicane at 80 MeV and 2 GeV. Once the desired quality beam is achieved at the end of the injector, all configurations and beam parameters should be archived for future use.

Now it is time to lengthen the train gradually without losing beam on the monitors all the way to the end of the injector. The subharmonic buncher timing and the phase of the compensating klystrons is adjusted slowly to maximize the signal on the bunch length monitor and to minimize the energy spread on the energy spread wire scanners. Once the long bunch train configuration is set, we can then adjust the intensity jitter limiting aperture for the optimal size. This process also has to be done slowly, adjusting the timing of the subharmonic buncher and the power in the compensating klystrons at the same time. Next we can use the scrapers in the 80-MeV chicane to clip away the tails. More adjustment of the power in the compensating klystrons will be necessary.

Configuration files showing the orbit and charge transmission of the beam throughout the injector and all the device settings will be saved. In addition, the bunch length, the energy and energy spread, the emittance of the beam at 80 MeV, and at the entrance to the damping ring should be measured. This information is important for expediting the accelerator setup in the future and maintaining the beam quality in a consistent way.

To maintain the beam quality day-to-day, various steering and energy feedback systems will be used. RF and magnet parameters, as well as beam parameters, will be compared to the parameters in the best saved configuration files and flagged if they are off by more than the allowed tolerance.

2.8.2 Troubleshooting

Some of the typical things that can go wrong in the injector are that the energy spread of the beam downstream, for example, at the damping ring is too large. If this spread cannot be reduced to an acceptable size by phasing the accelerators, most likely the phases of the bunching components have drifted away from optimum. Check their phase and amplitude against the saved optimized configuration and make the necessary changes. It is important to simultaneously maximize the signal at the bunch length monitor

Another problem could be the increase in energy jitter. This usually stems from rf-amplitude jitter in the accelerator or bunching rf sources and should be fixed by the rf technicians.

Another problem could be the increase in intensity jitter. This could stem from a number of reasons. Check the intensity jitter of the laser as it will be running on the edge of available technology as far as intensity jitter is concerned. Another cause for intensity jitter is when the beam is large compared to the various apertures and is not centered, thus is being scraped. One can check this with the various screens and PLIC signals. The most effective knobs for solving this problem are the small lenses near the gun and after the bend and the second most effective are the steering coils.

It is impossible to enumerate all the possible problems which can occur in the injector area, but we have addressed the most common ones.

2.9 Conclusion

The NLC polarized source injector will be a conventional injector employing subharmonic bunching to achieve the required bunch intensity and structure. Simulation results show that it is possible to capture 83% of the charge into the subharmonic buncher system into 18-ps bunches when a train of bunches are produced from the gun which are 700-ps wide and 1.4-ns apart. The total energy spread at 2 GeV is expected to be $\pm 0.6\%$, well under the $\pm 1\%$ threshold. The emittance, including wakefield effects, is expected to be less than 0.6×10^{-4} m-rad, well within the about 1×10^{-4} m-rad threshold. The charge intensity jitter limiting aperture is able to reduce 2% incoming intensity jitter to an immeasurable amount at the cost of losing 17% of the charge from the gun. Using the Δt compensation technique in the injector linac, we can reduce the bunch train energy spread without any effect on the single-bunch energy spread at the end of the injector.

The injectors for both the collision and positron drive electron beams are almost identical up to 2 GeV with the exception that the positron drive injector will use a thermionic gun. This should allow us to reduce construction costs and operational complications.

The NLC injector scheme is similar to the current SLC injector with the added complication of working with a long bunch train instead of a single bunch. There are several issues regarding this added complication which deserve a hard look either in detailed simulations and or demonstrations in a laboratory environment. The R&D programs needed to ensure us of success with the NLC injector are: 1) The cathode charge limit as addressed in Appendix 2.B. 2) The beam-loading compensation in the bunching system. 3) Demonstrate the production of the 1.4-ns-separation bunch train in the thermionic gun. 4) Development of a reliable and stable polarized source rf gun to produce small emittance beams from the injector, thus simplifying the operation and maybe the design of the damping ring. Item 1) can be studied in the SLC polarized source laboratory. Item 2) and 3) will be demonstrated in the NLCTA upgrade. There are several options for demonstrating item 4). One of these options would be to use the rf gun test stand being constructed at SSRL.

Despite the differences between the SLC and NLC sources, experience with the SLC can be applied and extended for a reliable and stable operation of the NLC injector.

2.A Polarized e^- Beam Photocathode RF Gun Development for the NLC

2.A.1 Introduction

While the baseline injector design for the NLC polarized electron source is presently a conventional polarized DC gun with a subharmonic bunching system, the development of a low-emittance polarized electron beam rf gun in parallel, as a possible future upgrade, is important to simplify the damping ring design and/or operation.

Polarized e^- beam photocathode rf gun injectors are an attractive alternative to the conventional electron source for the NLC because of the possibility of achieving very low electron beam transverse emittance and thus making it possible to reduce the size of the damping ring or at least making it easier to operate. Simulation results show that it is possible to achieve normalized rms emittance of $\epsilon_{n,rms} = 1$ mm-mr for a 1 nC bunch, 10 to 20 ps in width [Gallardo 1993, Palmer 1995b, Sheffield 1993]. Some experiments have been conducted at LANL and BNL to achieve beams which are very similar in quality to these simulation results. The low emittances are achieved due in part to the emittance compensation technique discussed in reference [Carlsten 1989]. The NLC requirements for the beam from the rf gun are about 4 nC in a 10 to 20-ps bunch 1.4-ns apart in a train of 126 ns. The normalized, rms emittance requirements at the input of the current NLC damping ring design is $< 10^{-4}$ mm-mr rms at the damping ring. The emittance damping time in the ring depends on the emittance of the incoming beam. For each order of magnitude reduction in the input beam emittance, the number of bunch trains to be simultaneously stored in the ring can be reduced by 1, thus also reducing the size of the ring. Even a factor of 2 or 3 reduction in emittance would be helpful in improving the operation of the damping ring even if its design is not simplified.

Photocathode rf guns have shown themselves to be a stable and reliable source for the FEL community [Travier 1994]. In the NLC, Cylindrically Symmetric Emittance-Compensated Polarized RF Gun Development program, the work of the FEL community would be extended to the development of a polarized source, emittance-compensated, ultra-high-vacuum rf gun. This new gun design would address the issues associated with polarized rf guns some of which are discussed in reference [Clendenin]. The main technical issues to resolve for polarized rf guns which are more difficult than for the DC guns are: 1) A stable and reliable pulsed laser system to produce the electron bunch train, 2) the beam dynamics associated with producing a

low-emittance electron bunch train including the possible depolarization effects due to strong space charge and transverse magnetic fields near the cathode, 3) elimination of field asymmetries in the gun which will cause emittance growth, 4) the ultra-high-vacuum environment which is difficult to achieve in rf guns but is required by the GaAs cathodes for long lifetimes, 5) the effect of high-gradient fields on GaAs cathodes, 6) cathode issues such as promptness of the photoemission, cathode lifetimes and quantum efficiency, and 7) finally, the reliable and efficient operation as a injector system.

A development program for an asymmetric beam rf gun is also important, since the emittance required at the interaction point is two orders of magnitude smaller in the vertical plane than in the horizontal plane. An asymmetric beam could be produced at the cathode of the rf gun by the production of an asymmetric transverse laser pulse. This program would initially proceed with the unpolarized source, emittance-compensated rf gun, since the flat-beam emittance compensation has not yet been experimentally demonstrated.

2.A.2 Beam Dynamics

In this section we shall discuss two parallel R&D efforts that will elucidate two areas of accelerator physics and in the end allow the combining of these developments to produce a flat-beam polarized rf gun.

The study of negative electron affinity (NEA) GaAs in high-gradient fields, along with the development of a dedicated cylindrically symmetric, polarized-source rf gun facility is one of these development programs.

Intensive programs to study and demonstrate low-emittance, high-brightness beams from symmetric photocathode rf guns is ongoing at LANL, BNL, SLAC, UCLA and other laboratories abroad. The best available symmetric rf gun emerging from these studies should be used for studying the survivability of polarized e^- source cathodes in rf guns. This will allow for the study of vacuum conditions, field amplitudes, and cesiation processes that are necessary for the production of polarized electrons without the additional problems of flat-beam production.

In another development program for the flat electron beam production, the physics of emittance compensation of a flat-beam and rf field uniformity can be addressed without the added difficulty of polarized electron production.

Round Beam

PARMELA simulations of injectors for FELs show that it is possible to produce an electron beam with a transverse normalized emittance of $\epsilon_{n,rms} = 1$ mm-mr. The beam parameters from these simulations are listed in Table 2-4 and shown in Figure 2-21. Simulation studies of L- and C- band systems are ongoing using the S-band system as a baseline [Kirk 1995].

The emittance compensation scheme realigns different "slices" [Sheffield 1992] of an electron bunch. Depending on the cathode spot size, total charge per bunch, and peak field at the cathode, the precise position of the compensation solenoid [Palmer 1995a] is critical. Figure 2-22 shows this for the parameter set in Table 2-4. In the physical construction of the gun and solenoid magnet, the waveguide physically limits the position of the magnet with respect to the cathode of the gun. This problem has been corrected in the proposed L-band rf gun being designed for the TESLA X-ray FEL [TESLA FEL]. It uses a "door-knob" rf coupler downstream of the full cell, eliminating the physical constraint of the waveguide and maintaining cylindrical symmetry. As a result, this scheme eliminates the higher-order spatial harmonics that can also

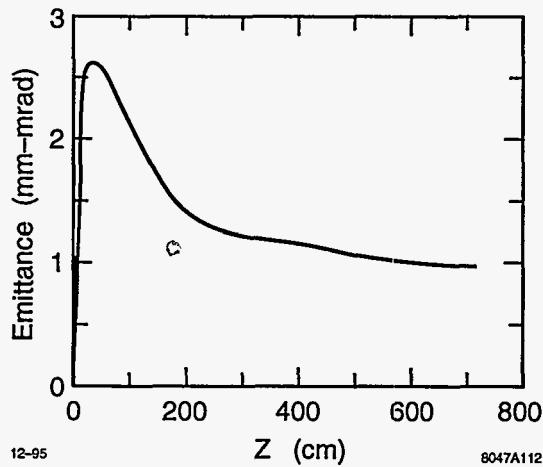


Figure 2-21. PARMELA simulations of emittance compensation for the BNL/SLAC/UCLA S-band rf gun

Total Charge	1 nC
Number of particles	10K
Cathode Spot Size	1 mm radius
Longitudinal Profile	Flat-top
Transverse Profile	Flat-top
Initial Cathode KE	.5 eV
Initial Thermal Emittance, ϵ_0	0 mm-mr
$E_{Full\ Cell}/E_{Half\ Cell}$	1.00
E_0 at Cathode	160 MV/m

Table 2-4. Electron bunch parameters used in PARMELA.

cause emittance growth, and allows for the precise positioning of the compensation magnet. The tuners and vacuum connections to the gun will also physically limit the magnet position, but these problems can be eliminated by longitudinal connections to the gun body versus radial coupling used in the previous gun designs.

Asymmetric Emittance RF Photocathode Electron Sources for the NLC

While the expected performance of cylindrically symmetric rf gun photo-injector systems is well understood from theoretical analysis and simulation, which have been benchmarked by experiment, an extension to a fully three-dimensional approach has not until recently been undertaken by investigators at UCLA and Fermilab. This effort has been motivated by the demands of the superconducting TESLA linear collider design, in which the normalized emittances are $\epsilon_{x,y}=20$, 1 mm-mr at $Q=8.3$ nC. In this machine, it is possible to have asymmetric emittances at the injection point of an electron linac which meet the constraints set by the interaction point. While the emittances may not be low enough to eliminate the need for an

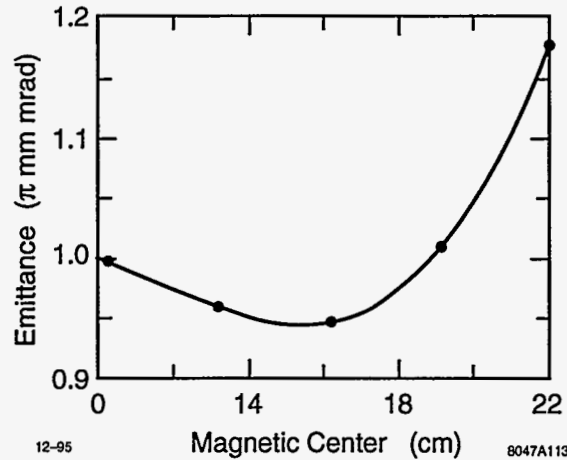


Figure 2-22. Optimized emittance versus magnetic center.

electron damping ring in the NLC designs under consideration here, benefits in designing and operating the damping ring may be derived from injection of lower, asymmetric-emittance electron beams.

To state simply, the approach to design an asymmetric rf photoinjector source [Rosenzweig 1993], one uses the fact that the temperature of the emitted beam particles from a photocathode is only a function of cathode material and laser photon energy. This allows the creation of asymmetric emittances $\epsilon_x \gg \epsilon_y$ by illuminating the photocathode with a ribbon laser pulse ($\sigma_x \gg \sigma_y$). Typically, the dominant emittance growth mechanism at relevant current densities is space-charge, and this is conveniently mitigated by the ribbon geometry of the electron beam pulse. One must also pay attention to the potential for rf-induced emittance growth, especially in the horizontal dimension where the beam is large. In the spirit of the problem for cylindrically symmetric systems performed by K.J. Kim [Kim 1989], we have examined the scaling of emittances with respect to beam dimensions, accelerating gradient and phase, and beam charge. The "thermal" contribution to the emittance given by the finite spread in transverse momenta of photo-emitted electrons is, assuming 0.1 eV emission temperature (typical of semiconductors),

$$\epsilon_{x,y}^{th} \cong \sqrt{\frac{kT_{\perp}}{m_e c^2}} \sigma_{x,y} \cong 0.25 \sigma_{x,y} \text{ (mm) mm-mr} \quad (2.4)$$

For TESLA, this implies beam sizes of $\sigma_x < 4$ cm, and $\sigma_y < 2$ mm, while for the NLC requirements we must have $\sigma_x < 0.4$ cm, and $\sigma_y < 0.2$ mm. This is a potential challenge for the NLC cases, because a $Q = 4$ nC beam of such a small cross-section implies an accelerating field needed at the cathode to overcome longitudinal space charge of $E > 72$ MV/m at injection. Under the assumptions of a cylindrically symmetric rf cavity structure, it is easy to derive the minimum rf contribution to the rms emittances, which can be written as

$$\epsilon_{x,y}^{rf} \cong \frac{eE_{rf}}{\sqrt{8}m_e c^2} \sigma_{x,y}^2 (\Delta\phi)^2 \quad (2.5)$$

where $\Delta\phi = \left(\frac{\omega}{c}\right) \sigma_z$ is the phase extent of the beam. Minimizing these quantities implies operation at low frequency, low accelerating gradient, and with small bunch sizes in all dimensions. For our case, we are considering a fairly large horizontal beam size as well as high gradient, and so this is an issue for the horizontal emittance.

There are a number of proposed ways to remove or minimize the emittance-diluting phase-dependent defocusing due to the transverse rf forces in the gun. Because of the use of emittance compensation to deal

with the space-charge contribution to the emittance, it is perhaps wisest to use a scheme which mitigates the transverse kick in the x direction. This can be accomplished by removing as best as possible the dependence of the rf fields on x . It should be noted in this regard that the defocusing kick induced at the end of a cylindrically symmetric cavity is approximately equal parts electric and magnetic. The electric component of the kick is mainly due to the fringing fields near the iris at the exit of the gun. The fringe field can be made mainly vertical simply by making the iris opening a slit, long in the horizontal dimension.

The magnetic component, however, cannot be so easily diminished, as it is not dependent on the iris, but on the accelerating field in the interior of the cavity. The only way to diminish the magnetic force in the horizontal direction is to break the symmetry of the cavity outer wall. The simplest asymmetric structure is a rectangular box cavity, but this only diminishes (does not eliminate) the horizontal rf forces, and produces a sinusoidal dependence of the accelerating field on the x dimension. A better choice is to use an "H-shaped" structure (as suggested by R. Miller), which has been investigated in the context of sheet-beam klystron development at SLAC. In this structure, the accelerating field in the "bar" region of the H-cavity has no dependence on x and therefore has acceleration independent of transverse position, as in a symmetric structure. It should be noted that the vertical forces (which are due mainly to the backward speed-of-light space harmonic in this p-mode structure), in this case in the bar region, are now entirely in the vertical dimension, and are twice as large as the equivalent symmetric cavity. The function of the side regions is to allow the longitudinal field to go to zero sinusoidally, to satisfy the boundary condition, and choose (along with the vertical dimension) the cavity resonant frequency.

An analysis of the space-charge contribution to the emittance gives the following scaling, derived from both approximate analysis and PARMELA simulation [Rosenzweig 1995]:

$$\epsilon_{x,y}^{sc} \approx \frac{2N_b r_e}{7\sigma_{x,y} W} e^{-3\sqrt{W}\sigma_y} \sqrt{\frac{\sigma_y}{\sigma_z}} \quad (2.6)$$

$$W = \frac{eE_{rf}}{2m_e c^2} \sin(\phi_o) \quad (2.7)$$

Here, $\epsilon_x^{sc} \approx \frac{\sigma_x}{\sigma_y} \epsilon_y^{sc}$ is approximately obeyed; this is a consequence of the fact that for an ellipsoidal charge distribution, the normal electric field at any bunch boundary is approximately the same as any other. It should be noted that minimizing the space-charge contributions to the emittances implies operation at high accelerating gradient. It should also be emphasized at this point that these emittances, induced by the space charge at low energy, are mainly due to the different orientations of each "z-slice" of the beam. A scheme is discussed below, emittance compensation, which can remove these correlations, effectively lowering the emittances of the bunch. Before taking up this discussion, it should also be pointed out that one cannot arbitrarily reduce σ_y , because of the limit on surface charge density emitted from the cathode before the retarding space-charge cuts off emission ($\sigma_x \sigma_y > 2 \frac{Q}{E_x}$).

This effect has been observed at UCLA. It is instructive to look at the product of the emittances, to see if there is some chance of achieving the desired emittances without the need for emittance compensation

$$\epsilon_x^{sc} \epsilon_y^{sc} \approx \left[\frac{2N_b r_e}{7W} \right]^2 \frac{e^{-6\sqrt{W}\sigma_y}}{\sigma_x \sigma_z} \quad (2.8)$$

The argument in the exponential in this expression is generally smaller than one for reasonable accelerating gradients, and so one can see that, in general, a beam large in the longitudinal and horizontal dimensions is needed to minimize the product of the space-charge emittances. Unfortunately, these are precisely the dimensions that the rf contributions are sensitive to, and thus one cannot consider making them arbitrarily large. As an example of a design where the rf contribution is not yet significant, we take $N_b = 5 \times 10^{10}$, $W=80$,

$\sigma_z = 2$ mm, $\sigma_x = 2$ cm, $\sigma_y = 1$ mm. In this case, we have $\epsilon_x^{sc} \epsilon_y^{sc} \approx 450$, as opposed to $\epsilon_x^{sc} \epsilon_y^{sc} \approx 20 \sim 50$ as needed by TESLA, and we miss the design goal by a minimum of three to four in both dimensions. For the NLC case, the degree to which the design goals will not be met without emittance correction is even larger.

It is apparent that further efforts must be made to achieve the emittances needed for linear collider designs; that is, one must employ an emittance compensation scheme for sheet beams accelerated in asymmetric rf structures. Emittance compensation is essentially a process by which the correlations (mainly as a function of the longitudinal position in the bunch) in the beam's transverse phase space that are induced by space-charge forces operating at low energy (in the photocathode gun), are removed by focusing the beam, reversing the direction of additional correlations. When the orientation of the transverse phase space ellipse of each "z-slice" has the same angle, the linear component of the emittance due to this effect is removed. Since the space-charge forces must still be large enough after the focusing lens to allow for compensation, this scheme tends to work better at lower accelerating gradients for convenient focusing geometries. This happy direction in the design of the system allows us to mitigate concerns about the rf contribution to the emittance, and about peak and average rf power (source and heat dissipation problems), in both the symmetric and asymmetric cases. In the asymmetric case, we must have the rf contribution to the transverse phase space trajectories be small, or else the space-charge compensation will suffer from interference. This condition is achieved by the choice of large aspect ratio (sheet) beam profile, and the asymmetric structure described above.

While the serious design calculations must be performed with simulation programs which include as many real experimental effects as possible, these are very time consuming. One needs to have a model with which to predict the approximate behavior of the system before proceeding to simulation. This has been developed; it is a program which integrates the envelope equations for a number of different "z-slices," at positions. The focusing can arise from conventional quadrupole focusing, or from the first order transient kicks. It is apparent that further efforts must be experienced by electrons at the exit and the entrance of the rf cavities, and the second order (alternating gradient focusing) in the interior of the rf cavities. Solenoidal focusing is not allowed in this device, because of a coupling of the x and y phase planes due to an $\vec{E} \times \vec{B}$ rotation which is, of course, dependent on longitudinal position in the beam. The emittance terms included in the envelope calculations are only the thermal components.

The results of a typical calculation are shown in Figure 2-23. In this case, the vertical emittance is well compensated, while there is essentially no improvement in the horizontal emittance. This is because the effective defocusing strength associated with the space charge is different in the two dimensions, as can be seen from the envelope equation

$$K_{x,y}^{sc} = \frac{4I(z_i)}{I_0 \gamma^3 (\sigma_x + \sigma_y) \sigma_{x,y}} \quad (2.9)$$

Because of this, the compensation process generally proceeds much faster in the small dimension, and thus it is difficult to design a system which simultaneously compensates in the vertical and horizontal dimensions.

The solution to this difficulty is straightforward: since the beam near the cathode is very much larger in x than in y or z , one can effectively remove the dynamics in the x direction (and the dependence on x of the y and z components of the space-charge forces), as is already done for the rf contributions, from consideration by making the beam distribution uniform in x . The effect of this is illuminated by Figure 2-24, which displays the x component of the force along the x axis of the bunch, and the y component of the force at one sigma in y , in the y - z plane, for two cases: (a) where the beam distribution is Gaussian in all three dimensions, and (b) where it is Gaussian in y and z , but uniform up to a hard boundary in x . It can be seen that for the tri-Gaussian beam that the horizontal forces rise approximately linearly to a large value at about one sigma in x . For the uniform distribution in x , however, there is very little horizontal field over about 85 to 90% of the beam, and the field rises steeply and nonlinearly near the beam boundary. As was noted before, the

maximum field is nearly the same, but the region of the beam which is affected is much smaller. Note that the vertical field is also nearly uniform over almost all of the beam, again degrading near the beam edge. In practice, one uses this final 10 to 15% of the beam as "guard charge" during the compensation to remove the horizontal field and homogenize the vertical field, then removes it by collimation after the linac section. In this way, one effectively removes the x dimension from the compensation problem, reducing the problem to two dimensions, as in the (by now well understood) cylindrically symmetric case. It should be noted in this regard that the multiple-envelope model for emittance compensation dynamics has been compared extensively to simulation as well as extended analytically by Serafini and Rosenzweig [Serafini 1995], and essentially validated for cylindrically symmetric beams. Benchmarking of the models in the asymmetric case awaits further refinements of three-dimensional computational tools.

The expected emittances in the case of a 2856-MHz, 1.5 or 4-nC can be scaled from the previously investigated 1300-MHz, 10-nC, 35-MV/m rf gun TESLA case, where the emittances are $\epsilon_{x,y} = 30, 2$ mm-mr. The beam dimensions, charge, electromagnetic fields, and emittances all scale linearly with rf wavelength, while scaling of charge at a given wavelength scales the emittances approximately linearly with the charge. Thus we expect that a 77-MV/m rf gun at 2856 MHz should produce emittances of approximately $\epsilon_{x,y} = 4.5, 0.3$ mm-mr at 1.5 nC and $\epsilon_{x,y} = 12, 0.8$ mm-mr at 4 nC.

2.A.3 Material and RF Considerations

Vacuum

It has been the SLC polarized-source experience that for successful and reliable operation, the vacuum in the vicinity of the cathode needs to be extremely low, on the order of 10^{-11} Torr and the partial pressure of some diatomic gases such as CO must be maintained in the mid 10^{-12} range [Schultz 1992]. The ultra-high-vacuum system is a critical part of making the polarized-electron rf gun work, not only because of the cathode but also to prevent any possible rf arcing in the gun, thus damaging the cathode. Some great progress has been made in Japan in selecting appropriate copper and treating it with pressurized ultrapure water to achieve vacuum levels of 2×10^{-10} Torr in an S-band standing-wave cavity. The cavity was excited with a 2856-MHz klystron, and surface gradients of 337 MV/m were achieved without arcing or any rise in the pressure in the presence of rf [Yoshioka 1994, Matsumoto 1994]. Demonstration of the survivability of the polarized cathode in the rf gun is needed.

It has been proposed that the new 1.6-cell rf gun designed by the BNL/SLAC/UCLA collaboration be constructed out of High Isostatic Pressure(HIP) processed Oxygen Free High Conductive (OFHC) Cu [Palmer priv] to minimize the vacuum problems associated with a high-gradient gun. This gun has been symmetrized to remove the dipole-like spatial harmonic of E_z . It has been proposed that future guns of the BNL/SLAC/UCLA collaboration have their quadrupole-type fields symmetrized thereby eliminating the next higher-order mode emittance growth factor. This would allow for more pumping on the gun and thereby reduce the ultimate vacuum limit.

Assuming that the out-gassing rate of copper is 10^{-12} Torr ℓ/s cm^2 , an estimate of the needed pumping speed can be calculated. The total surface area of a state-of-the-art, BNL-type, S-band rf gun is on the order of 420 cm^2 . Therefore this type of rf gun will need 42 ℓ/s of total pumping speed to maintain the gun vacuum on the order of 10^{-11} Torr. This amount of pumping does not take into account the conductance-limiting effects of the waveguide to full-cell coupling iris.

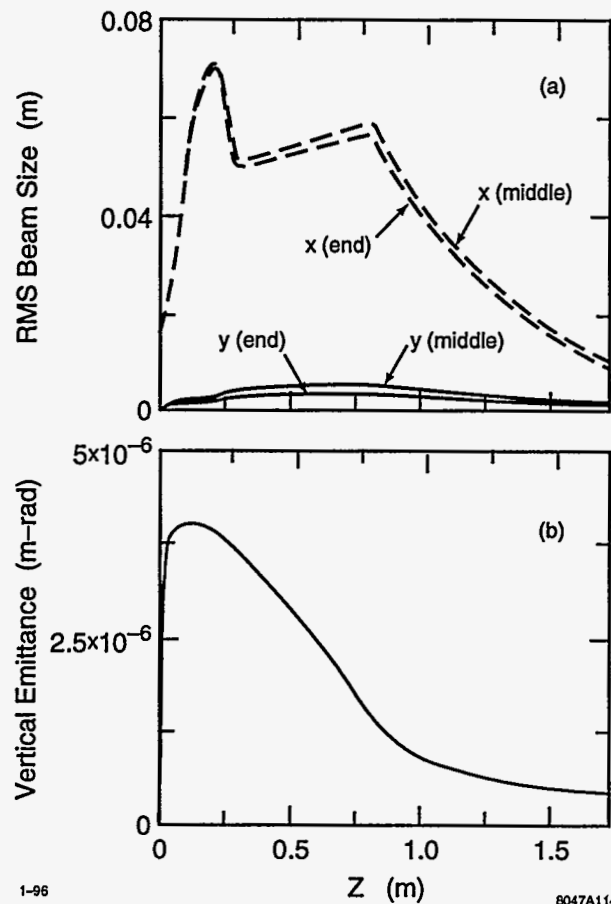


Figure 2-23. (a) Rms beam sizes for two beam slices in multiple-slice model calculation of emittance compensation for 10-nC beam. A vertically focusing quadrupole is placed symmetrically over the cathode plane, followed by a horizontally focusing quadrupole, another doublet, a drift, and a TESLA cavity linac. (b) Vertical emittance evolution in this case.

The polarized source cathode will need to be recesiated periodically and activated less occasionally. Both of these procedures are a threat to the required ultra-high-vacuum environment. A scheme involving a "loadlock" where the cathode can be retrieved and isolated from the gun vacuum environment to carry out these procedures needs to be incorporated into the gun design. Another possible option might be to mask the cathode with a "shroud" which is part of the cesiation or activation mechanism lowered directly into the gun. Further design studies to pin down the optimum way to carry out the cesiation and activation procedures is essential.

High-gradient Effects

The effects of high gradients in the vicinity of the GaAs cathode are best studied with a specially designed HIP copper rf gun whose design allows for a 42 ℓ/s pumping speed. This design should incorporate an rf feed that will eliminate the dipole-field asymmetry and allow for the mechanical positioning of the emittance compensation magnet in its optimal position. The properties of the various cathode materials will detune

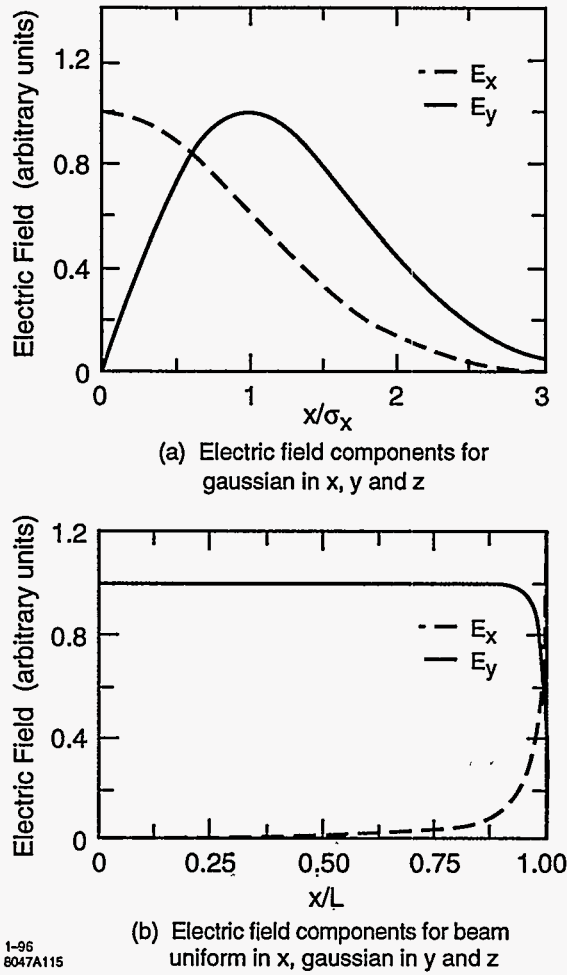


Figure 2-24. Electric field components for (a) uniform, as opposed to (b) horizontally-Gaussian density profile.

the half-cell resonant frequency and thereby effect the field balance of the gun. Symmetric tuners in both the full and half cell will be needed to maintain the $f_{\pi} = 2856$ MHz with the interchange of different cathode material under ultra-high-vacuum conditions. Also, the field levels in the full and half cell will need to be monitored during operation. The mechanical and rf design of these coupling probes should not induce dipole asymmetries in the cavities which would cause emittance growth in the beam.

To maintain the high gradient in the gun necessary for the emittance compensation at S-band, the mechanical design should take into account the scheme discussed in Section 2.A.3, "Vacuum", for the recession process of NEA photocathode materials.

There is a plan to install a GaAs cathode from SLAC in the rf gun at CERN and to study survivability in the presence of rf. The success of this test would be important in building confidence in the feasibility of polarized-source rf guns, but failure would not necessarily rule out the possibility of using a polarized rf gun for the NLC since the CERN Linear Collider Test Facility (CLIC) gun is not specifically designed for this test.

It is important to pursue a dedicated effort to carry out the full measure of high-gradient studies at SLAC. This would entail the design and construction of a new rf gun which includes the necessary upgrades discussed above to make the present BNL/SLAC/UCLA 1.6-cell S-band rf gun a polarized electron source.

Photocathode Response Time

In order for an S-band rf gun to produce a beam with a bunch length that meets the NLC injector requirement, *i.e.*, not to exceed 20 ps in full pulse length, the response time of the photocathode must be ≤ 10 ps. For a thin strained GaAs photocathode whose surface is treated to have negative electron affinity, the photoemission response time is determined by the thickness of the active layer, which is typically 100 nm, and by the electron diffusion coefficient. With a doping density in the mid- 10^{18} - cm^{-3} range, the diffusion coefficient in GaAs is about $35 \text{ cm}^2/\text{s}$ at room temperature [Sze 1981]. Thus, in the absence of multiple emission attempts, the response time for a 100-nm-thick cathode is estimated to be approximately 3 ps, which adequately meets the requirement for response time. However, this estimate ignores the likely scenario in which an excited electron may require several attempts to be emitted as it may fail to escape the first time or even the first few times it reaches the cathode surface and, as such, must be regarded as a lower limit on the response time. Electrons that are emitted after multiple escape attempts will ultimately lead to a longer response time and may prevent negative electron affinity photocathode from being incorporated into an S-band rf gun.

Measurements of the response time for GaAs photocathodes have been made only with bulk samples [Aleksandrov 1995, Hartmann 1995a]. Aleksandrov *et al.*, placed an upper limit of 40 ps on the response time, whereas Hartmann *et al.*, found it to be about 30 ps. However, both measurements were done under the condition that the cathodes' quantum efficiencies were more than an order of magnitude lower than that of an optimally activated bulk GaAs, implying that the essential property of negative electron affinity is or close to be lost. Therefore, the measured response time is actually that of a thin active emitting layer at the surface of the bulk GaAs cathode, whose thickness is probably on the order of 100 nm due to the lack of negative electron affinity, rather than that of the bulk GaAs cathode. In this sense, these two studies may represent an experimental approximation for measuring the response time of a 100 nm strained GaAs cathode. Of course, since the response time depends quadratically on the thickness of the active emitting layer and it is difficult to estimate its exact value given a bulk GaAs cathode with a low quantum efficiency, the measured response time should be regarded only as an order of magnitude estimate for a 100-nm strained GaAs cathode. Ultimately, the exact response time for such a cathode must be determined experimentally under a high quantum efficiency condition appropriate for high beam intensity operation. At present, it appears that the response time of such cathodes may marginally satisfy the requirement of an S-band rf gun.

Photocathode Charge Limit

For a thin strained GaAs photocathode to be used in an rf gun for NLC, it must be capable of producing up to 3 nC of charge for an approximately 20-ps-long bunch, which implies that the charge limit of the cathode for a 20 ps charge pulse needs to be ≥ 3 nC. Earlier charge limit studies at SLAC has shown that the cathode charge limit in a 2-ns pulse depends almost linearly on the cathode bias or equivalently the extraction electric field at the surface within a range from 0.15 to 1.8 MV/m [Tang 1994a]. In an rf gun, the extraction field at the cathode surface is on the order of 100 MV/m, which is about two orders of magnitude higher than that in an SLC polarized electron gun operated at 120 kV. If the linear scaling with respect to extraction field remains valid up to orders of magnitude higher fields, then, the charge limit of a similar cathode in an rf gun will be scaled higher by the same factor. The maximum observed charge limit for a 2-ns charge pulse from a 100-nm strained GaAs cathode with an 80% polarization in an SLC gun was about $9.5 \text{ nC}/\text{cm}^2$ at an extraction field of 1.8 MV/m. Scaling to 100 MV/m yields the charge limit for a 2-ns pulse in the rf gun

to be about 530 nC/cm^2 . Based on the fact that the typical size of the laser beam used to illuminate the cathode in an S-band rf gun is 1-mm in radius, the maximum extractable charge from such a cathode for a 2-ns pulse is estimated to be approximately 17 nC.

It remains to estimate the charge limit in the rf gun for a 20-ps pulse. Unfortunately, no systematic studies on the effect of the pulse length, especially in the picosecond regime, on the charge limit have been made. Observation made during earlier R&D experiments of the SLAC polarized electron source has shown that the charge limit does depend, albeit not strongly, on the pulse length. For example, the charge limit for a 200-ns pulse was observed to be more than five times greater than that of a 2-ns pulse in an SLC gun. Physics consideration suggests that from 2 ns to shorter time scales the charge limit should depend on the pulse length more weakly. Thus, given the estimated charge limit of 17 nC in an rf gun for a 2-ns pulse, the prospect of achieving $\geq 3 \text{ nC}$ in a 20-ps pulse appears reasonable. Plans have been made to systematically study this dependence for pulse lengths ranging from several nanoseconds to sub-nanosecond scales to further our understanding of this important issue. Finally, it is worth noting that the extremely high extraction field in an rf gun will greatly mitigate the multi-bunch effect of the charge limit phenomenon.

2.A.4 Laser System

Energy Requirements

The laser system for an rf gun for NLC, which is shown in Figure 2-25, must produce a train of 90 pulses separated by 1.4 ns, corresponding to a frequency of 714 MHz. This 126-ns pulse train (the macropulse) repeats at 180 Hz. Each of these 90 micropulses in the train must have a width adjustable between 5 and 20 ps, so that the emittance can be minimized. This optimization will also involve adjusting the temporal pulse shape (to be discussed below). Each pulse must be sufficiently intense to generate a charge of up to 4 nC (2.5×10^{10}) electrons. To obtain the high polarization (80%) now achieved with the SLC's DC cathode, a strained GaAs cathode would again be used, with an excitation wavelength near 850 nm. For this material and wavelength, a quantum efficiency of 0.1% has been measured in the DC gun. In an rf gun, the efficiency could be higher due to enhancement by the high rf electric field on the cathode, or lower if the rf causes degradation of the surface. Assuming $QE = 0.1\%$, the laser must produce a train of pulses on the cathode with at least six μJ /micropulse and 0.5 mJ for the macropulse. With a safety factor of eight to allow for losses in the optics and declines in quantum efficiency, the laser must be capable of delivering up to 4 mJ at the output of the laser pulse compressor over the 90-pulse train.

Stability Requirements

A high degree of stability in several laser parameters is essential for the NLC. Variations in the energy per pulse, both within one macropulse and from macropulse to macropulse, should be limited so that the charge per pulse is constant. Charge fluctuations vary the beam loading in the accelerator sections, and hence introduce additional energy spread in the beam. Allowable intensity jitter budgets are discussed in Chapter 1. The allowable macropulse charge intensity fluctuation needs to be less than 0.5% rms. Thus for the NLC, we require a variation of no more than 0.5% rms in the macropulse laser energy and in the overall flatness of the envelope of the micropulses in each macropulse. Fluctuations of 2% are tolerable from one micropulse to the next.

In an rf gun, the laser pulse must occupy a small fraction of the rf period, with typical widths of 10 to 15 ps. The laser's repetition frequency must be tightly locked to a subharmonic of the rf frequency. Pulse-to-pulse

Schematic of the Polarized Source RF Gun Laser System

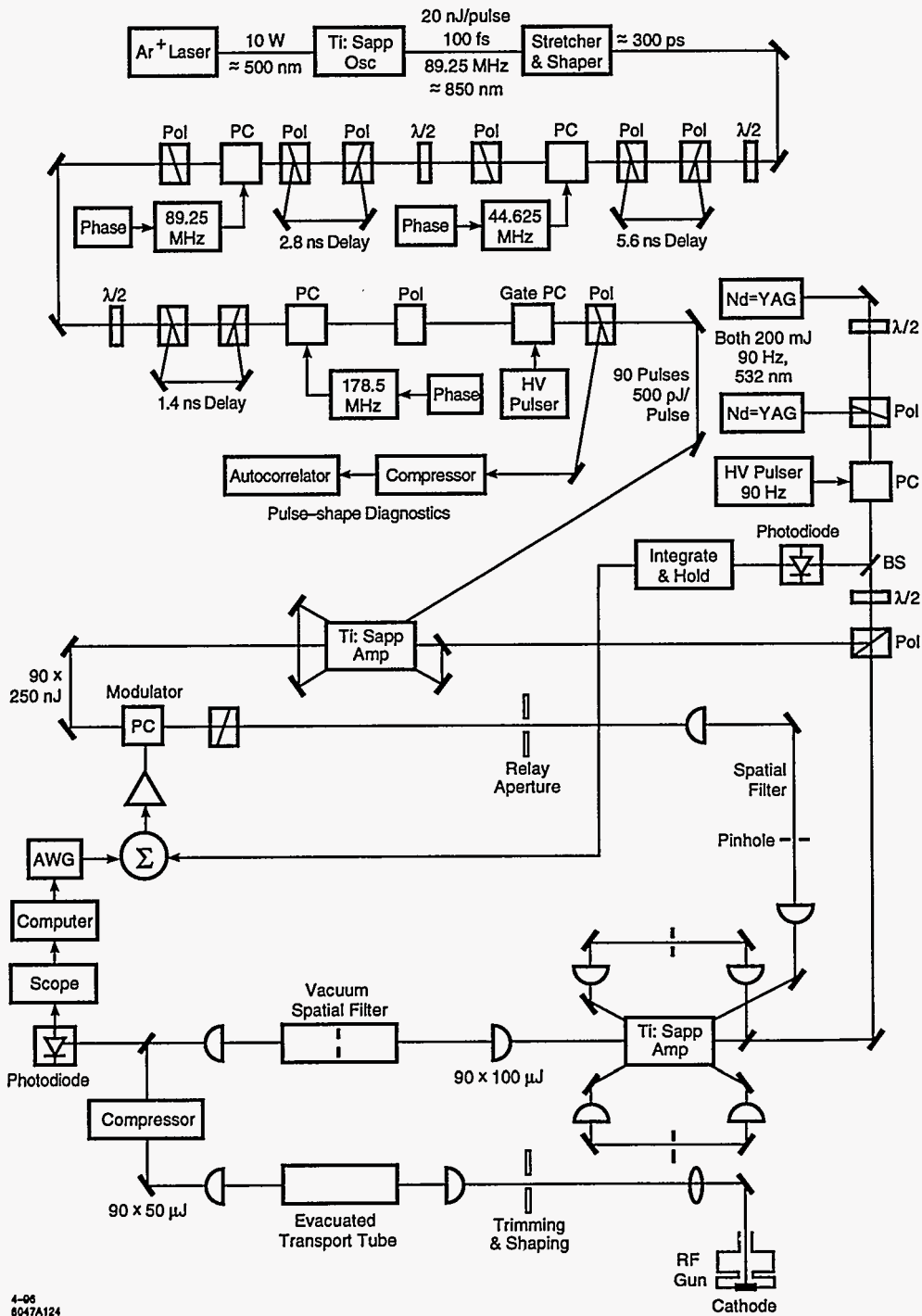


Figure 2-25. Schematic diagram of the polarized-source rf gun laser system.

timing jitter, with respect to the phase of the gun's rf, leads to energy changes and also affects the beam's transverse phase space. This jitter must be kept below 1 ps rms.

The goals also include 1% variations in the diameter of the laser spot on the photocathode, with a centroid location that varies by no more than 1% of the diameter. The micropulse duration should also fluctuate by no more than 1%. Techniques for achieving this stability will be discussed below.

Oscillator

A CW actively mode-locked oscillator is needed to obtain picosecond pulses synchronized with the rf. As with the DC gun's laser, titanium sapphire is a natural choice for this wavelength range. Commercial mode-locked Ti:sapphire oscillators are available with wide tunability (from 700 to 1060 nm), 1 to 2 W of output power, and, in some types, with pulse widths selectable from 0.1 to 60 ps. A 10-W CW argon-ion laser provides the pumping, and can be stabilized with feedback for both pump power and pointing. Compared to other oscillators (*e.g.*, Nd:YLF or Nd:YAG), it is difficult to lock Ti:sapphire oscillators to an external rf source, since they tend to self-mode-lock due to inherent nonlinearities, without any reference to an external drive. However, carefully timed feedback to adjust the cavity length can control both the mode-locking frequency and phase relative to the reference signal. The commercial products claim a timing jitter below 2-ps rms, but measurements of 1 ps have been made, approaching the best values obtained with Nd:YLF. However, these units support pulse trains at frequencies of about 80 to 100 MHz. A new design with an extremely short cavity would be needed to mode-lock at the 714 MHz required for the NLC.

It is possible to provide a higher pulse-train frequency while making use of a standard oscillator. Start with a linearly polarized laser operating in the commercial range, at 89.25 MHz, which is 1/8 of the desired frequency and corresponds to a pulse spacing of 11.2 ns. Split the beam in two with a half-wave plate and polarizer. Delay one beam by half the pulse spacing, 5.6 ns, which requires an additional path of 1.7 m. Recombine the beams with a second polarizer, then use a Pockels cell driven by rf at 44.6 MHz to restore all pulses in the train to the original polarization. By repeating this process two more times with delays of 2.8 and 1.4 ns, and with Pockels cells at 89.25 and 178.5 MHz, we can prepare a complete pulse train with the desired 1.4-ns spacing. At times, the NLC may be operated with micropulses spaced by 2.8 or 5.6 ns. The number of pulses would be reduced by the same factor, so that the macropulse duration remains fixed. These spacings are readily accomplished by rotating the waveplates at the third (and second, for the 5.6-ns case) splitting, so that no splitting takes place.

Efforts are also underway to develop a mode-locked Ti:sapphire oscillator with a pulse train repeating at a very high rate. Hartmann and colleagues [Hartmann 1995b] have built a 76.54-MHz Kerr-lens-mode-locked Ti:sapphire oscillator synchronized with an external rf source. They have presented preliminary results from a second oscillator with a repetition rate of 1.039 GHz; this frequency will next be raised to 1.225 GHz, and the eventual goal is 2.45 GHz. Even the demonstrated operating frequency is fast enough for the NLC, and such a laser would avoid the elaborate split-and-delay procedure of the previous paragraph.

Diode lasers may offer a promising alternative that can provide even lower jitter. Their small size makes them well suited for high repetition rates. They can be actively mode-locked with minimal jitter, since the laser gain can be directly modulated by applying an rf signal to the diode, without the need for an acousto-optic device to modulate the cavity Q . Diode lasers combining active and passive mode-locking have been developed [Delfyett 1992] at frequencies from 302 to 960 MHz, at wavelengths near 830 nm, and with bandwidths of 4–10 nm. When followed by another diode acting as an amplifier, and after removing the chirp, Fourier-transform-limited pulses of 0.46 ps with a jitter of 0.4 ps were obtained. These pulses can be dispersively stretched to any desired width while maintaining the low jitter. Filtering in the compressor removes unwanted spontaneous emission. However, compared to the Ti:sapphire oscillator, the output power

is low, typically 10 mW, and so more amplification would be needed. There is also considerably less tunability. This second drawback may not be too serious, since a diode laser could be prepared to operate at whatever wavelength proves best for the polarized rf gun. Wider micropulse spacings can be implemented by driving the diode laser directly at 357 or 178.5 MHz, so that the gain is high only at multiples of the fundamental cavity spacing. With further development, this source may be well suited to providing the high repetition rate and low jitter needed for NLC.

A4.4 Amplifier

With either oscillator, the amplifier is similar to that proposed for the laser system for the NLC's DC gun—a multiple-pass Ti:sapphire amplifier pumped by two *Infinity* Nd:YAG lasers from Coherent Inc., each providing 200 mJ at 532 nm in alternation at 90 Hz. However, the pulsed oscillator used with the DC gun produces 100 nJ in each micropulse, after allowing for the losses in the Pockels cells that shape its train of square, 1-ns-wide pulses. This is more energy than is produced by either type of CW mode-locked oscillator. Consequently, we need more amplifier gain, which can be obtained with two amplifier stages, with the pump light split between them. With the Ti:sapphire oscillator, the 3-pass bowtie configuration with a gain of 8 to 10 per pass, would be suitable for both stages. For the diode laser, where the energy extraction would be very low in the first pass, a 5-pass first stage and a 3-pass second stage would provide sufficient gain.

Fourier-Relay Optics

A technique known as Fourier relay optics can address the conflict between two important goals: better energy extraction by filling the rod more completely, while maintaining a clean transverse mode. Initially, the oscillator beam is trimmed in an aperture. The technique combines relay imaging, in which lenses relay an image of this aperture to each pass through an amplifier rod, and filtering of the beam's spatial Fourier transform. At each step, a lens of focal length f_1 is placed a distance f_1 after one of the image planes. The Fourier transform is formed at the focus, f_1 beyond the lens, where higher spatial harmonics are removed by a pinhole. A second lens with focal length f_2 then recollimates the beam (with expansion f_2/f_1) and forms the relay image at a distance $f_1 + f_2$ from the previous image plane. An image of the aperture is finally relayed to the photocathode, to define the area of photoemission.

Shaping the Beam in Space

We usually consider laser pulses that are Gaussian in time and space. However, it would be useful to investigate ways of making electron pulses that are more square, with steeper sides and flatter tops. Simulations of Brookhaven's rf electron gun have shown that electrons emitted during the temporal tails of a Gaussian laser pulse occupy a different region of phase space than those emitted near the middle. With a flatter laser pulse, the electrons are more tightly clustered, with a lower emittance over the full pulse (although the instantaneous "slice" emittance at times within the pulse is similar). Calculations also show that flattops in both space and time are best for emittance compensation using solenoidal focusing after the gun.

To shape the pulse in space, a position-dependent attenuation could be applied to the beam [Van Wouterghem 1993]. Relay imaging should be used after the flattening, to limit diffraction. Stability of the laser's position and diameter on the photocathode can be achieved by trimming the edge of the beam with an aperture on the final relay plane; this aperture is then imaged onto the photocathode. While a Gaussian beam could still have fluctuations in the position of the centroid within the aperture, with a flattop beam, pointing jitter does not cause any change in cathode illumination.

An rf gun that directly produces a spatially flat electron beam is under consideration. The flat-beam gun would have a vertical beam size and emittance substantially smaller than the horizontal, as ultimately required at the interaction point. The required flat laser pulse can readily be produced with a small modification of the final relay stage: a pair of cylindrical lenses could provide different magnifications in the two transverse directions to produce an ellipse on the cathode.

Stretching, Compressing, and Shaping the Micropulses in Time

In amplifiers for picosecond and especially subpicosecond pulses, the peak power must be limited to avoid optical damage and nonlinearities. The Ti:sapphire oscillator can produce a 0.1-ps pulse with a large bandwidth. The dispersion of a grating pair can then stretch the pulse to hundreds of picoseconds, so that the peak power is reduced before amplification. The stretching results from having different wavelengths in the pulse take different optical paths, and so correlating time, space, and wavelength. After amplification, the process can be reversed to compress the pulse to the original or any greater width. This technique is known as chirped-pulse amplification [Maine 1988].

During the stretching, temporal pulse shaping is readily accomplished in the dispersive region between the gratings, by using a spatially varying filter to selectively attenuate the wavelengths corresponding to different times [Skupsky 1993]. (Filtering could also be done in the compressor, but the power levels are higher.) More sophisticated shaping, including the production of square picosecond pulses, has been achieved using both amplitude and phase masks to manipulate the pulse's Fourier transform [Weiner 1988]. The rise time and flatness of the resulting pulse are limited by the bandwidth of the input pulse, determined by the oscillator's pulse width. Thus the shaped pulse cannot rise faster than the oscillator.

For lower-resolution shaping, an interesting possibility is the use of a linear array of liquid crystals to form a voltage-controlled, spatially varying, amplitude mask, allowing active control of the pulse shape. Guided by measurements of the amplified pulse shape, a computer could provide a feed forward, adaptive control system.

Pulse-width stability is important for the NLC's performance. If the bandwidth of the oscillator pulse is wider than that transmitted by the phase and amplitude masks, so that the masks are illuminated almost uniformly, then fluctuations in the oscillator width do not affect the final pulse width or shape, which is determined only by the masks and the pulse compressor following the amplifiers.

Feedback and Feed-Forward Corrections

A high-extinction (>1000), fast-rise, variable-width, Pockels-cell gate after the oscillator chops the pulse train to the desired length. Over the course of the macropulse, a substantial fraction of the energy stored in the amplifiers by the pump laser is extracted. To compensate for the resulting drop in gain for the later micropulses, a second Pockels cell after the oscillator or between the amplifiers modulates the macropulse, attenuating the early pulses to flatten the envelope of the pulse train. An arbitrary waveform generator drives the Pockels cell with a waveform that results in a flat pulse train after amplification. A computer controls the process in a feed-forward loop: the computer monitors the envelope with a photodiode and continually reprograms the arbitrary waveform generator for subsequent macropulses to maintain the desired envelope.

For modulation, it is convenient to use a cell that imposes a transverse field across a crystal such as Lithium Tantalate (LTA). Although the extinction is not as high as that of the more common, longitudinal-field, Deuterated Potassium Dihydrogen Phosphate (KD*P) cell used for the gate, the switching voltage is much lower—about 150 V rather than 8000 V for half-wave rotation. The difficulty of making a high-voltage,

high-speed, linear amplifier is avoided; instead, a transverse-field cell is available from Conoptics matched to a 120-MHz solid-state linear amplifier. The high bandwidth of the driver, and its 1-V input, allow for sophisticated control of the macropulse envelope.

Feed-forward should compensate well for droop and slow drifts in the laser's performance. Random, shot-to-shot fluctuations will also arise, largely due to fluctuations in the flash lamps of the pump laser. Feedback within each macropulse is needed to correct for shot-to-shot changes in the envelope. An error signal for feedback could be made by comparing the measured envelope to a square pulse. This difference could then be subtracted from the arbitrary waveform generator output. However, cable delays and the amplifier's internal propagation delay limit the feedback bandwidth to about 3 MHz. In principle, the amplified pulses could be measured, then delayed with several meters of optical path while the voltage on a Pockels cell is adjusted. Fast and precise electronics would be required to achieve the desired accuracy. Such a correction has been tried briefly on the SLC's gun laser, but noise in the electronics limited the correction to about 2%.

Other approaches are more practical. We could monitor the pump energy and derive a correction added to the arbitrary waveform generator output over the macropulse. Since the *Infinity* pump laser has a pulse duration of 3.5 ns and titanium-sapphire has an upper-state lifetime of 3 μ s, there is sufficient time between pumping and extracting to make this correction. Alternatively, we could widen the gate, then use the modulator Pockels cell to shape the pulses into two trains separated by about 1 μ s. After amplification, the earlier one, occurring after the rods are pumped but before the gun's rf starts, would be measured to sense the system gain. The later pulse could then be corrected and sent to the gun.

2.A.5 Integrated System

Once the various physics issues and technical difficulties have been resolved for the polarized source photocathode rf guns, an integrated system including the laser and accelerator beam line up to 80 MeV needs to be constructed and demonstrated to operate in a stable, reliable, and efficient way, for an extended period of time. When the system integration tests show that a polarized photocathode rf gun can operate with a 99% availability, it will become the most attractive option as an injector for the NLC.

2.A.6 Conclusions

The polarized source photocathode rf gun is a significant option for the NLC injector because of the potential of producing low emittance bunch trains from the injector region, thus simplifying the design of the damping ring or at least simplifying the operation of the damping ring. If the various physics issues concerning the beam dynamics and the technology issues of reliable operation of a polarized source rf gun are solved in the laboratory, it would become the most attractive option for the polarized electron source for the NLC.

2.B Charge Limit and its Implications on High-Polarization Long-Pulse Charge Production

2.B.1 Introduction

The charge limit (CL) phenomenon refers to the suppressed emission of excited electrons in the conduction band from a p-type negative electron affinity (NEA) or nearly NEA semiconductor cathode due to an increase in the surface work function caused by those electrons that fail to escape and eventually become trapped at the surface [Woods 1993]. This happens because among the largely thermalized conduction band electrons that reach the surface, only a fraction of them may successfully escape due to limited escape probability as determined by the surface NEA property. The electrons trapped at the surface are removed mainly by combining with holes that tunnel to the surface through the band-bending potential barrier at a rate critically dependent on the doping density [Tang 1994b]. Charge limit (CL), or suppressed emission, occurs only if the excitation laser intensity is sufficiently high such that the rate of electrons getting trapped at the surface considerably exceeds the rate of removal and, therefore, leads to an appreciable buildup of electrons at the surface within the laser pulse duration. CL is not a total charge limit, as was originally believed. In a long-pulse mode, CL will likely manifest itself as a current limit. CL depends on the extraction electric field, in this respect bearing a vague resemblance to the space-charge limit, as well as on the cathode's quantum efficiency (QE) [Tang 1993]. The significance of the CL effect with respect to high-current long-pulse charge production is well addressed in reference [Tang 1994c].

In the summer of 1993, a systematic experimental study on the CL phenomenon using a series of strained layer GaAs cathodes was conducted. The cathodes used in that study included 100-nm and 300-nm high- and medium-doping (2×10^{19} and $5 \times 10^{18} \text{ cm}^{-3}$, respectively) strained GaAs, etc.. It is fair to state that from this study most of the important properties of the CL phenomenon for 2-ns pulses were learned. These results may be used to project the CL behavior for long-pulse (~ 100 -ns) operations before actual long-pulse CL data become available. Reference [Tang 1994c] furnishes a quantitative analysis of the prospects of producing the required charge from a polarized electron photocathode for the NLC using the 300-nm medium- and high-doping strained GaAs cathodes used in the 1993 study. The conclusion was that charge production for the NLC appears possible only with the high-doping cathode. The fundamental deficiency associated with the medium-doping cathode was its long relaxation time of the bunch-bunch effect, which leads to a substantial increase in the surface work function and, therefore, strongly suppressed emission in the high-current long-pulse operation required by the NLC.

2.B.2 Generalization of CL Effect to Long-Pulse Operation

In the following, a similar long-pulse CL analysis as presented in reference [Tang 1994c] shall be given for a 100-nm high-doping strained GaAs cathode, also used in the 1993 study. When excited at the band-gap threshold, that is, at 866 nm, this cathode yielded a maximum polarization for emitted electrons of about 65%. The relevant experimental 2-ns CL data from this cathode are shown in Figures 2-26 and 2-27. For the sake of facilitating our quantitative analysis, it will be assumed that a 866-nm laser pulse with a sufficiently long, flat-top pulse length (>126 ns) is used to illuminate the cathode. Under the illumination of the long laser pulse, the cathode response will first undergo a transient period during which the photocurrent yield will vary (or more exactly, decrease) with time. The duration of the transient period will be determined by the relaxation time of the bunch-bunch effect and the instantaneous laser power within the pulse. A steady

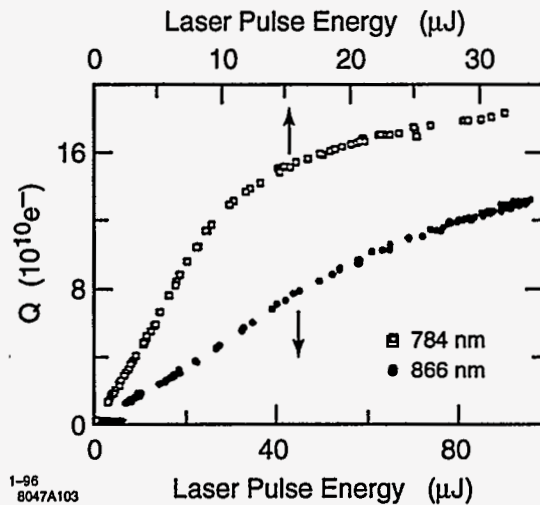


Figure 2-26. Change vs. laser pulse energy for a 100-nm high-doping strained GaAs cathode with $QE = 22\%$ measure at 833 nm. The cathode is biased at 120 kV. Note that charge saturation was not reached at 866 nm due to insufficient laser energy.

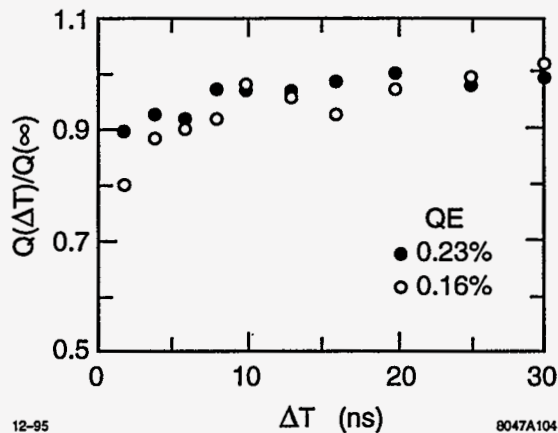


Figure 2-27. Bunch-bunch effect for a 100-nm $2 \times 10^{19} \text{ cm}^{-3}$ doped strained GaAs sample for two different QE conditions (measured at 833 nm). Bunch 2 is at peak polarization with a laser pulse energy of $95 \mu\text{J}$ at 866 nm. Laser pulse 1 is at 784 nm and has $32 \mu\text{J}$.

emission state will be realized following this initial transient period. It is this steady-state emission current that we will try to evaluate based on the available 2-ns charge pulse data.

Based on the earlier assumption that the beam from the gun is a long 126-ns square pulse, we need a steady-state emission of roughly 4 A from the cathode to meet the NLC Phase I requirement. We may view the long pulse as consisting of many back-to-back 2-ns pulses of 5×10^{10} electrons each. As shown in Figure 2-27, the bunch-bunch effect is almost completely diminished after 10 ns. Therefore, the emission of an arbitrary 2-ns pulse can be affected only by the five preceding 2-ns pulses. From Figure 2-26 we can see that a laser pulse of about $30 \mu\text{J}$ at 866 nm, or about $5 \mu\text{J}$ at 784 nm, is needed to produce a single stand-alone 2-ns pulse of 5×10^{10} electrons at $QE(833 \text{ nm}) = 0.22\%$ (slightly below the cathode's maximum QE of 0.23%). Neglecting the inter bunch effect, the total laser energy for five such pulses is $150 \mu\text{J}$ at 866 nm or $25 \mu\text{J}$ at

784 nm, which is less than the Bunch 1 laser energy used for taking the inter-bunch effect data shown in Figure 2-27. Here, the fact that Bunch 1 is at 786 nm hardly matters at all because the first bunch serves to pump a large number of electrons into the conduction band, thus saturating the cathode surface with electrons, and photoexcitation at 786 nm is about six times as efficient as at 866 nm for the cathode under study. Due to the accumulated electrons at the surface, the emission factor for the next pulse following these five pulses is reduced to about 0.9, corresponding to the first data point in Figure 2-27 for which Bunch 2 immediately follows Bunch 1 with a QE of 0.23%. This is a conservative estimate since it has been assumed that practically none of the electrons trapped at the surface during the five preceding pulses has been removed. Due to this interbunch CL effect, the actual laser energy required to produce a long pulse of intensity 5×10^{10} electrons per 2 ns needs to be about 10% higher. We can carry out the above sequence of analysis all over again with the upward-adjusted laser energy. Clearly, with a laser power of 15 kW (= $30 \mu\text{J}/2 \text{ ns}$) at 866 nm this cathode appears capable of producing the required 4-A-long pulse, with considerable headroom by noting that increasing the laser power would lead to an increased current up to a certain limit. Of course, overdriving the cathode with too much laser power would result in a decreased emission current due to overly suppressed emission. Even when the QE drops to 0.16%, this cathode still appears promising for generating the required 4-A steady-emission charge pulse.

In the NLC polarized electron source design, the long laser pulse that illuminates the cathode is actually modulated at a duty factor of 50% with a period of 1.4 ns. With such a modulated pulse, the charge buildup at the cathode surface that causes the charge limit effect will be reduced by a factor of two compared with a square pulse as assumed for the above analysis. This would allow us to double the instantaneous laser power in the modulated pulse while keeping the emission factor at a similar value and, therefore, lead to a factor of two increase in the instantaneous emission current in the steady emission state. Based on the above analysis, the 100-nm high-doping strained GaAs cathode appears capable of generating an 8-A instantaneous current in a 50% modulated pulse, which corresponds to a microbunch charge of 3.5×10^{10} electrons. Such charge performance should even be adequate for the 1.5 GeV NLC.

It must be stressed that the favorable conclusions obtained from this analysis and from reference [Tang 1994c] do not mean that high-doping cathodes are actually capable of generating NLC-type charge pulses. These analysis should be viewed as merely a logical and physically reasonable generalization of the CL effect from a nanosecond scale to a time scale of an order (or two orders) of magnitude greater. It is possible that new unknown CL properties may exist on such a long time scale which may adversely affect emission. Therefore, the ultimate proof must come from experiments.

2.B.3 Where We Are

Even if high-doping strained GaAs cathodes are indeed adequate with respect to charge production, they still suffer from the deficiency of lower polarization than their medium-doping counterparts. The highest polarization from a high-doping strained cathode is about 65% (with a 100-nm-thick active layer), which is substantially lower than the 80% polarization specified for the NLC. While medium-doping 100-nm strained GaAs cathodes, such as the ones used for E-143 and SLC94-95, meet the NLC polarization requirement, their long CL relaxation times severely limit their long-pulse charge production capability. Recent long-pulse charge tests using such a 100-nm strained GaAs cathode showed that these cathodes are capable of sustaining an emission current of about 0.7 A with an 80% polarization in an SLC gun. If, as proposed in the ZDR, a modulated laser pulse with a 1.4-ns period and a 50% duty factor within the pulse duration is used instead of the square laser pulse used in the test, the steady-state emission current within a microbunch should exceed 1 A, yielding a microbunch charge of $\geq 0.45 \times 10^{10}$ electrons. This leaves us about a factor of 4 (or 7) away

from realizing an NLC-I (or NLC-II) polarized electron source. While the difference is still substantial, an NLC source is certainly within reach.

2.B.4 Cathode Improvements and Outlook

The key to realizing an NLC source is improved cathode performance. Strained GaAs cathodes with a thickness on the order of 100 nm will be our primary choice because of their proven superiority in polarization performance. The 100-nm medium-doping strained GaAs currently used at SLAC may be improved via the following approaches:

1. Modulated cathode doping scheme: High doping ($2 \times 10^{19} \text{ cm}^{-3}$) in a thin, typically 10-nm, surface layer and low doping ($\leq 1 \times 10^{18} \text{ cm}^{-3}$) in the rest of the active layer. The high doping at the surface helps minimize the CL relaxation time, thereby enhancing the long-pulse current, whereas the low doping in the interior maximizes the electron polarization. The presently employed heat-cleaning method for NEA activation may not be compatible with such a cathode as it may destroy its modulated doping profile. Alternative cathode cleaning techniques, notably atomic hydrogen assisted low-temperature cleaning, will be investigated.
2. Cathode surface protection: As (Arsenic) capping. By growing an As cap layer of about 1- μm thick on strained GaAs before exposing to atmosphere, the active emission surface may be kept atomically clean. Such a clean surface may substantially improve the quality of an NEA activation. As a result, the cathode's quantum efficiency may be improved by about a factor of two. Such an improvement is expected to greatly suppress the CL effect, thereby maximizing the charge performance. As-capping is particularly desirable on modulated-doping cathodes since surface cleaning may be adequately performed at 400°C, which would leave the modulated doping profile intact, instead of at 600°C necessary for an uncapped cathode. The reduced heat cleaning temperature should also significantly improve the operational reliability of the loadlock system.

Other R&D areas on cathodes include tailoring the composition of both the substrate and the strained active layer to optimize the polarization and charge performances, and developing other types of cathode structures such as unstrained or strained superlattice cathodes.

At present, the Gun Test Lab and the Cathode Test Lab at SLAC are adequately equipped for polarization and 2-ns pulse charge tests. As new cathode materials arrive, such tests may be performed and the results may be used to project their long-pulse behavior. For actual NLC-type long-pulse tests, a high-powered long-pulse laser, such as the one discussed in Section 2.3 or a Q-switched flashlamp-pumped Ti:sapphire, must be developed.

In conclusion, the CL effect is the fundamental limiting factor for developing an NLC polarized electron source. The present SLC source is already within an order of magnitude in terms of charge performance from the ultimate NLC-III source. With the numerous possibilities of cathode improvements, however, the prospects for realizing an NLC source are very good. We should all be encouraged by the superb charge performance demonstrated by an As-capped KEK superlattice cathode [Kurihara 1995].

References

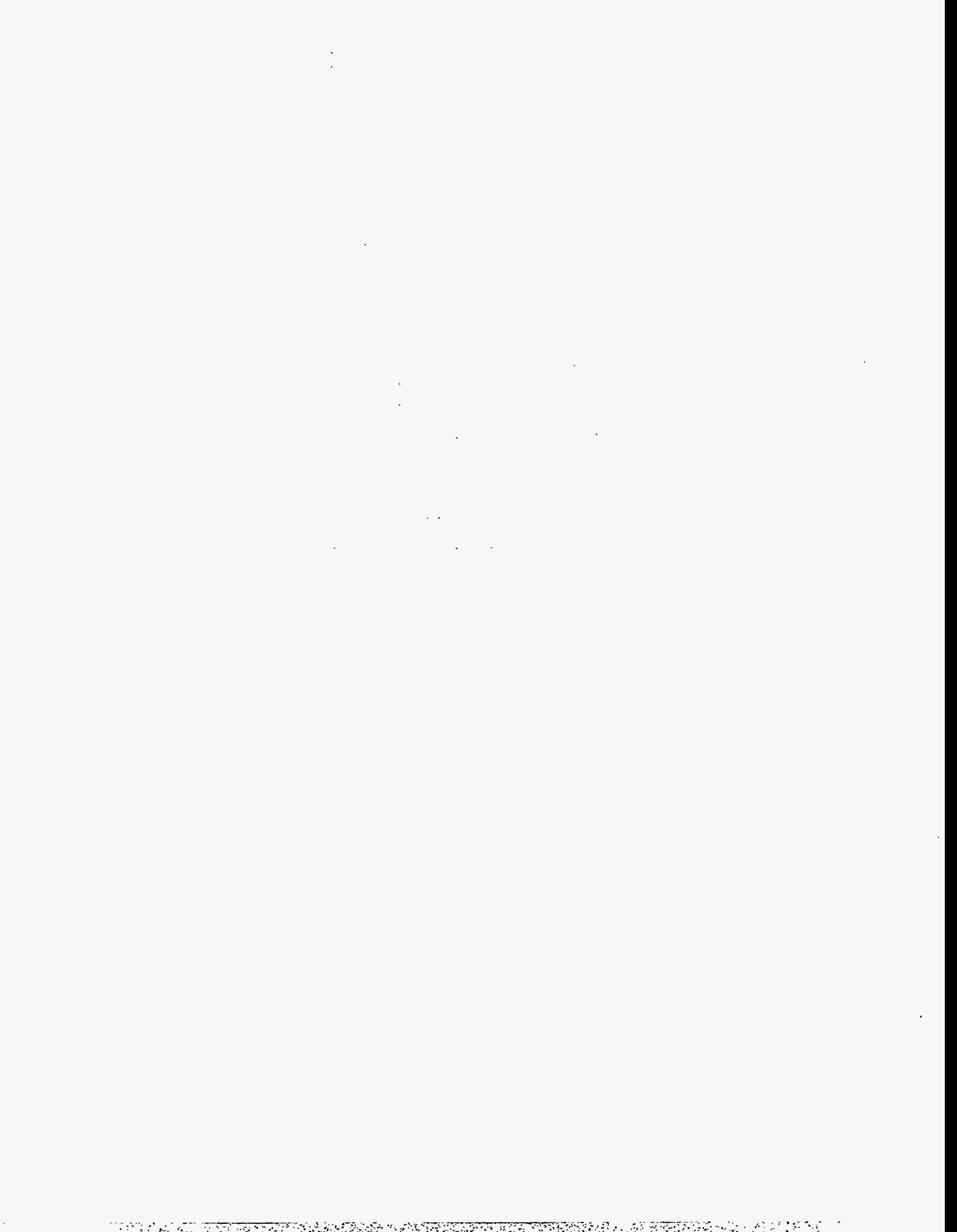
- [Aleksandrov 1995] A.V. Aleksandrov *et al.*, *Phys. Rev. E* **51**, 1449 (1995).
- [Alley 1994] R. Alley *et al.*, "The Stanford Accelerator Polarized Electron Source", SLAC-PUB-95-6489 (1994).
- [Alley 1995] R. Alley *et al.*, "The Stanford Linear Accelerator Polarized Electron Source", NIM in Physics Research, A365, 1-27 (1995).
- [Carlsten 1989] B.E. Carlsten, *Nucl. Instr. and Methods A* **285**, 313 (1989).
- [Clendenin] J. Clendenin *et al.*, "Prospects for Generating Polarized Electron Beams for a Linear Collider using an RF Gun", SLAC-PUB-6172.
- [Delfyett 1992] P.J. Delfyett *et al.*, *IEEE J. Quantum Electron.* **28**, 2203 (1992)
- [Gallardo 1993] J.C. Gallardo and H.Kirk, "An Injection Scheme for the Brookhaven ATF Utilizing Space-Charge Emittance Growth Compensation", *Proc. 1993 Part. Acc. Conf.*, 3615-3617 (1993).
- [Hartmann 1995a] P. Hartmann *et al.*, "Generation of short electron bunches from GaAs photocathodes", presented at the Workshop on Experiences with Polarized Electron Sources using GaAs Technology, Bonn, Germany (1995).
- [Hartmann 1995b] P. Hartmann *et al.*, "Experience with Polarized Electron Sources using GaAs Technology", poster presented at Univ. of Bonn, Germany (June 10, 1995).
- [Herrera-Gomez 1993] A. Herrera-Gomez, and W.E. Spicer, "Physics of high-intensity nanosecond electron source", *SPIE Proceeding Series*, **2022**, 51 (1993).
- [James 1981] M. B. James, R. H. Miller, "A High Current Injector for the Proposed SLAC Linear Collider", *IEEE Trans. Nucl. Sci.* NS-28, (3), 3461, (1981).
- [Kim 1989] K.J. Kim, *Nucl. Instr. and Methods A* **275**, 201-218 (1989).
- [Kirk 1995] H. Kirk *et al.*, *Proc. 1995 Part. Acc. Conf.*, 265 (1995).
- [Koechner 1992] Walter Koechner, *Solid State Laser Engineering*, Springer Series, NY, 1992.
- [Kurihara 1995] Y. Kurihara *et al.*, "A high polarization and high quantum efficiency photocathode using a GaAs-AlGaAs superlattice", *Jpn. J. Appl. Phys.*, **32**, 1837 (1995).
- [Maine 1988] P. Maine *et al.*, *IEEE J. Quantum Electron.* **QE-24**, 398 (1988).
- [Matsumoto 1994] H. Matsumoto *et al.*, "High Power test of a High Gradient S-band Accelerator Unit for the Accelerator Test Facility", *Proc. LINAC 94*, 302-304 (1994).
- [Naito 1994] T. Naito *et al.*, "Multi-Bunch Beam with Thermionic Gun for ATF", *Proc. LINAC 94*, 375 (1994).
- [Palmer priv] D.T. Palmer, private communication.
- [Palmer 1995a] D.T. Palmer *et al.*, TESLA FEL Group Meeting, August 1995.

- [Palmer 1995b] D.T. Palmer *et al.*, "Simulation of the BNL/SLAC/UCLA 1.6 Cell Emittance Compensated Photocathode RF Gun Low Energy Beam Line", *Proc. 1993 Part. Acc. Conf.* (1995).
- [Rosenzweig 1993] J.B. Rosenzweig and E. Colby, "Design of a High Duty Cycle, Asymmetric Emittance RF Photocathode Injector for Linear Collider Applications", *Proc. 1993 Part. Acc. Conf.*, 3021-3023 (1993).
- [Rosenzweig 1995] J.B. Rosenzweig and E. Colby, "Charge and Wavelength Scaling of RF Photo Injector Designs", *Advanced Accelerator Concepts (AIP Conf. Proc. 335) 724* (AIP, NY, 1995).
- [Sheffield 1992] R.L. Sheffield *et al.*, *Nucl. Instr. and Methods A318*, 282-289 (1992).
- [Sheffield 1993] R.L. Sheffield *et al.*, "Operation of the High Brightness LINAC for the Advanced Free-Electron Laser Initiative at Los Alamos", *Proc. 1993 Part. Acc. Conf.*, 2970-2972 (1993).
- [Schultz 1992] D. Schultz *et al.*, "The Polarized Electron Source Performance in 1992 for SLC-SLD", presented at the Tenth Int. Sym. on H.E. Spin Physics, Nagoya (Nov. 9-14, 1992).
- [Serafini 1995] L. Serafini and J.B. Rosenzweig, "Envelope Analysis of Intense Relativistic Quasi-laminar Beams in High Gradient Linacs", Submitted to *Phys. Rev. E* (1995).
- [Skupsky 1993] S. Skupsky *et al.*, *J. Appl. Phys.* **73**, 2678 (1993).
- [Sze 1981] S.M. Sze, *Physics of Semiconductor Devices*, 2nd edition (John Wiley & Sons, NY, 1981).
- [Tang 1993] H. Tang *et al.*, "Study of non-linear photoemission effects in III-V semiconductors", *Proc. 1993 Part. Acc. Conf.*, Washington DC, 3036 (1993).
- [Tang 1994a] H. Tang *et al.*, *Proc. Fourth European Part. Acc. Conf.*, 46 (1994).
- [Tang 1994b] H. Tang *et al.*, "Experimental studies of the charge limit phenomenon in NEA GaAs Photocathodes", *Proc. Fourth European Part. Acc. Conf.*, London, England, 46 (1994).
- [Tang 1994c] H. Tang *et al.*, "Prospects for a polarized electron source for next generation linear colliders based on a SLC-type gun", *Proc. of the 11th Intern. Symp. on High Energy Spin Phys.* (Bloomington, IN, 1994, in print).
- [TESLA FEL] TESLA FEL Collaboration, TESLA-FEL 95-03.
- [Travier 1994] C. Travier, "Review of Electron Guns", *Proc. EPAC94*, 317-321 (1994).
- [Van Wonterghem 1993] B.M. Van Wonterghem *et al.*, *Proc. Conf. Laser Coherence Control*, SPIE Vol. 1870, 64 (21-22 Jan. 1993).
- [Wanant 1994] R. Waynant, M. Ediger, *Electro-optics Handbook*, Optical and Electro-optical Engineering Series, 34 (McGraw-Hill, 1994).
- [Weiner 1988] A.M. Weiner *et al.*, *J. Opt. Soc. Am.* **B5**, 1563 (1988).

- [Woods 1993] M. Woods *et al.*, "Observation of a charge limit for semiconductor photocathodes", *J. Appl. Phys.* **73**, 8531 (1993).
- [Yoshioka 1994] M. Yoshioka *et al.*, "High Gradient Studies on UHV Room Temperature Cavities at S-Band for Linear Colliders", *Proc. LINAC 94*, 302-304 (1994).

Contributors

- Ray Alley
- David Burke
- Jym Clendenin
- David Farkas
- Allan Fisher
- Joseph Frisch
- Zhenghai Li
- Roger Miller
- Yuri Nosochkov
- Dennis Palmer
- Tor Raubenheimer
- Louis Rinolfi
- James Rosenzweig
- Huan Tang
- Kathy Thompson
- James Turner
- A. Dian Yeremian
- Dieter Walz
- Juwen Wang



Positron Source

Contents

3.1	Introduction	85
3.1.1	Overview	85
3.1.2	System Description	86
3.1.3	Parameters	86
3.2	Positron Yield Simulation	90
3.2.1	Target Yield	90
3.2.2	Ray Tracing through Capture Accelerator	90
3.3	Drive Electron Accelerator	92
3.3.1	Drive Electron Source	92
3.3.2	Drive Linac	92
3.4	Positron Production Target	92
3.4.1	Review of Target Test Data	92
3.4.2	Electron Beam Size	93
3.4.3	Beam Power and Target Size	93
3.4.4	Target Engineering Issues	94
3.4.5	Backup Power	96
3.4.6	Integration with Positron Collection System	97
3.5	Positron Collection System	97
3.5.1	Flux Concentrator	98
3.5.2	High Gradient L-Band Capture Accelerator	98
3.5.3	Tapered-Field and Uniform-Field Solenoids	98
3.5.4	Space Charge	98
3.6	Beam Dynamics and Transport	99
3.6.1	Control of Multibunch Beam Blow-up in Positron Linac	99
3.6.2	Aperture and Beam Optics System Parameter	99
3.6.3	Beam Position and Emittance Control	100
3.7	Positron Linac	101
3.8	Radiation Control Issues	103
3.8.1	Design Plan for Maintenance	103
3.8.2	Radiation Shielding	103
3.8.3	Radiation Hard Components	105
3.9	Magnets	105
3.9.1	Solenoids	105
3.9.2	Quadrupoles	105
3.9.3	Bending Dipoles	106
3.10	Diagnostics and Instrumentation	106
3.10.1	Specifications	106

3.10.2	Beam Intensity	106
3.10.3	Beam Position	107
3.10.4	Beam Size	107
3.10.5	Beam Bunch Length	108
3.10.6	Energy	108
3.10.7	Energy Spread	108
3.10.8	RF Phase and Amplitude Monitoring	108
3.11	Feedback and Stability	108
3.11.1	Intensity Uniformity Specifications	109
3.11.2	Transverse Orbit Stability	109
3.11.3	Energy Control	109
3.12	Operations and Tuning Procedures	109
3.13	Control System Needs	110
3.13.1	Specification	110
3.13.2	Special Requirements	110
3.14	Other Considerations	110
3.15	Summary	111

3.1 Introduction

3.1.1 Overview

The baseline positron source for the NLC is a conventional source based on an electromagnetic shower created by high-energy electrons impinging on a thick, high-Z target. Its design draws heavily on that of the SLC positron source, which has demonstrated excellent reliability over many years of operation. The source and its associated 2-GeV linac, initially built for the 500-GeV center-of-mass machine (NLC-I), must be upgradeable by simply doubling the energy of the incident electrons to produce the charge per pulse that meets the specification of the 1-TeV center-of-mass machine (NLC-II). In particular, NLC-II requires a train of 90 bunches with up to 1.25×10^{10} positrons/bunch in each accelerator pulse, at a pulse repetition rate of 120 Hz. This is a charge per pulse of about 23 times the design intensity of the SLC positron source. Target tests performed during the SLC R&D indicated a small (about 40%) margin of safety between the design and the destruction of the target from pulse heating. It appears wise to keep the pulse energy deposition density in the target below the SLC design value. Thus, the positron beam pulse intensity may be increased only by increasing the size of the drive electron beam to allow for increased pulse energy deposition in the target and by increasing the admittance of the positron capture system.

Therefore, the following strategy has been adopted in designing the positron source for NLC-II: (1) double the radius of the incident electron beam which allows the pulse energy deposition in the target, and hence the pulse positron production, to be quadrupled; (2) accelerate the positrons at an L-band frequency of 1428 MHz in a structure with an aperture slightly more than twice larger than the SLC source while maintaining the magnetic field of the uniform-field solenoid at the same value as in the SLC source. Doubling the beam radius on the target roughly quadruples the 4-D emittance of the outgoing positrons. However, the use of an L-band accelerator not only increases the 4-D transverse admittance by a factor of 16 but also doubles the longitudinal phase space admittance, though the benefit of the latter is not fully realized due to increased debunching caused by the more divergent particles. As a result, we find that the positron yield per electron per GeV is more than quadrupled in comparison with the SLC source. For NLC-I, a 50% increase in the radius of the incident electron beam is adequate. This leads to an improvement in the positron yield per electron per GeV by almost 40% over that of NLC-II. The net result of these scalings is that with incident electrons at 3.11 GeV and 6.22 GeV for NLC-I and NLC-II, respectively, the NLC source produces a positron beam with more than twice the intensity required at the interaction point. Such a safety margin is necessary for a conservatively designed positron source, as large beam losses may occur in transport through the booster linac and through the two damping rings. Assuming losses of 20% each in the booster linac and in the two damping rings and an additional 5% loss in the main linac and the final focus system, the source still boasts a 50% margin in beam intensity.

With the proposed scaling, the density of the energy deposited in the target for both machines is slightly below the SLC design, whereas the average deposited power is about a factor of 2.5 greater for both NLC-I and NLC-II. The higher average power is not a major problem, but it does exacerbate the problem of radioactivity which also has significant bearings on source maintainability. It will necessitate a larger-diameter rotating or trolley target and larger cooling water flow.

3.1.2 System Description

The proposed NLC positron source shares in design substantial similarity to its SLC counterpart. The conventional technique of producing positrons from e^\pm pair production by bombarding a conversion target with high-energy electrons will be used. Three subsystems comprise the NLC positron source: an accelerator for the drive electron beam, a positron production and collection system, and a positron booster linac. Figures 3-1 and 3-2 show a schematic layout of the NLC positron source. A brief description of each subsystem follows.

A DC electron gun, coupled to two subharmonic bunchers and an S-band buncher, produces an electron beam of the desired NLC multibunch structure, *i.e.*, with an inter-bunch spacing at 1.4 ns and a total of 90 bunches/pulse. The electron beam is then accelerated in an S-band linac to 3.11 GeV for the 500-GeV machine or 6.22 GeV for the 1-TeV upgrade before impinging on a positron production target. The drive beam intensity at the target is 1.5×10^{10} electrons/bunch.

The positrons emerging from the production target as a result of the electromagnetic shower cascade are captured by a 240-MeV L-band capture accelerator embedded in a uniform solenoidal field following an adiabatic phase-space matching device consisting of a flux concentrator and a tapered-field solenoid. The longitudinally varying magnetic field from the adiabatic matching device transforms the transverse phase space of the positron beam along the axis in such a way that

$$Br^2 = \text{const}, \quad (3.1)$$

and

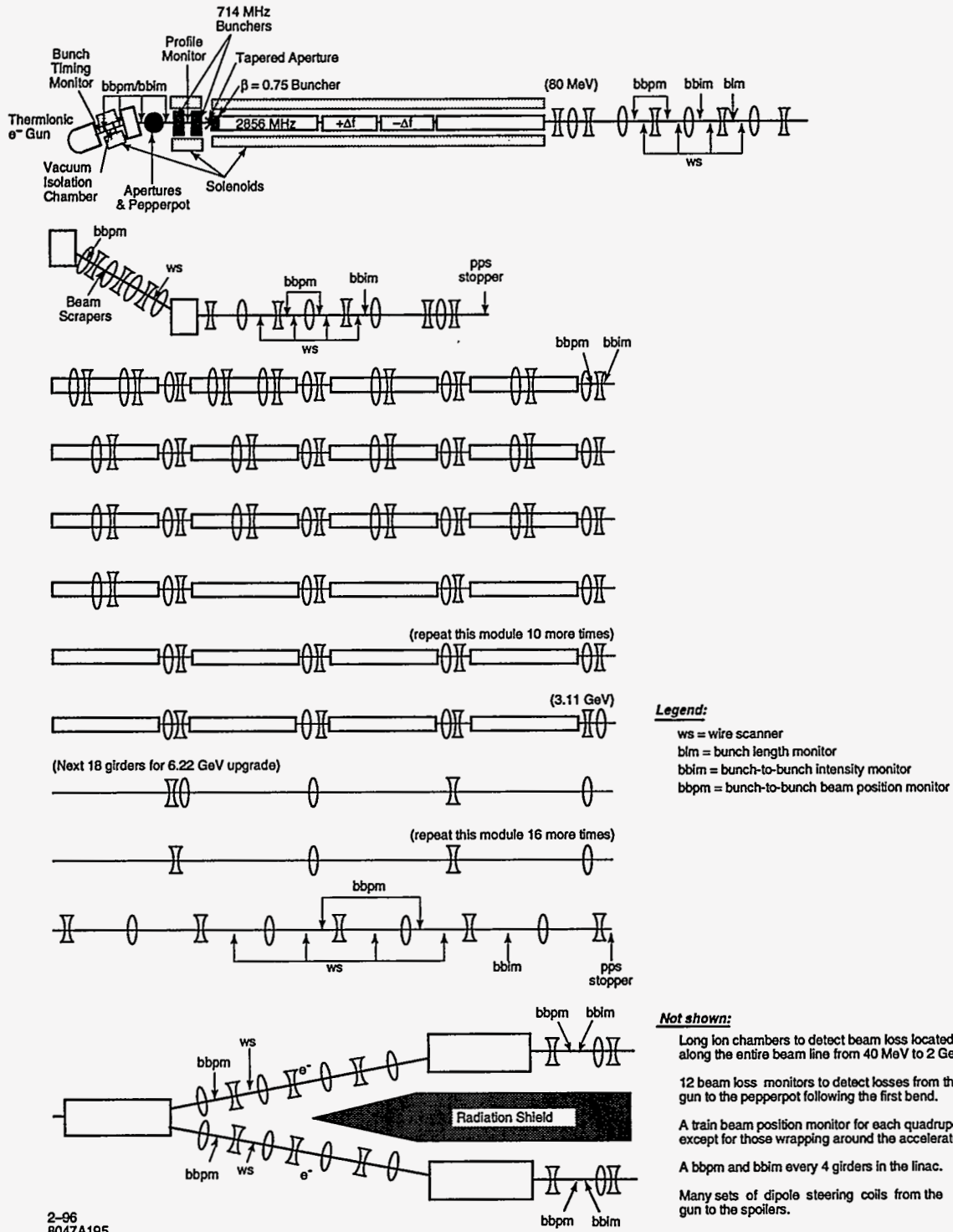
$$B/p_\perp^2 = \text{const}, \quad (3.2)$$

where B is the magnetic field, r is the radial displacement, and p_\perp is the transverse momentum. The choice for an L-band capture accelerator aims to boost mainly the 4-D transverse phase space acceptance by about a factor of 16 and the longitudinal phase space acceptance as well over a similarly designed S-band capture accelerator. The design employs a parallel dual source configuration for improved reliability. Electrons are dumped after the first bending magnet. Beam scrapers installed in between the bending doublet is used to collimate the positron beam in energy as well as in transverse phase space prior to its injection into the booster linac.

The collimated positron beam, with the same bunch structure as the electron drive beam, is accelerated in an L-band booster linac to 2 GeV for emittance damping in a pre-damping ring followed by a main damping ring. The optics for the positron booster linac is a FODO array with its beta function scaled as E , which must suppress multibunch beam blow-up due to wakefields and limit chromaticity induced emittance growth. A large number of large-aperture quadrupole magnets surrounding the L-band accelerating sections and smaller-aperture quadrupole magnets elsewhere are used to form the lattice.

3.1.3 Parameters

The important parameters of the NLC positron source for both the 500-GeV and the 1-TeV machines are summarized in Table 3-1. The positron beam intensities are obtained from numerical simulation after optimizing various design parameters. As a reference, the operating and design parameters of the SLC positron source are also included.



2-96
8047A195

Figure 3-1. Schematic layout of the NLC positron source (Part A): drive electron accelerator.

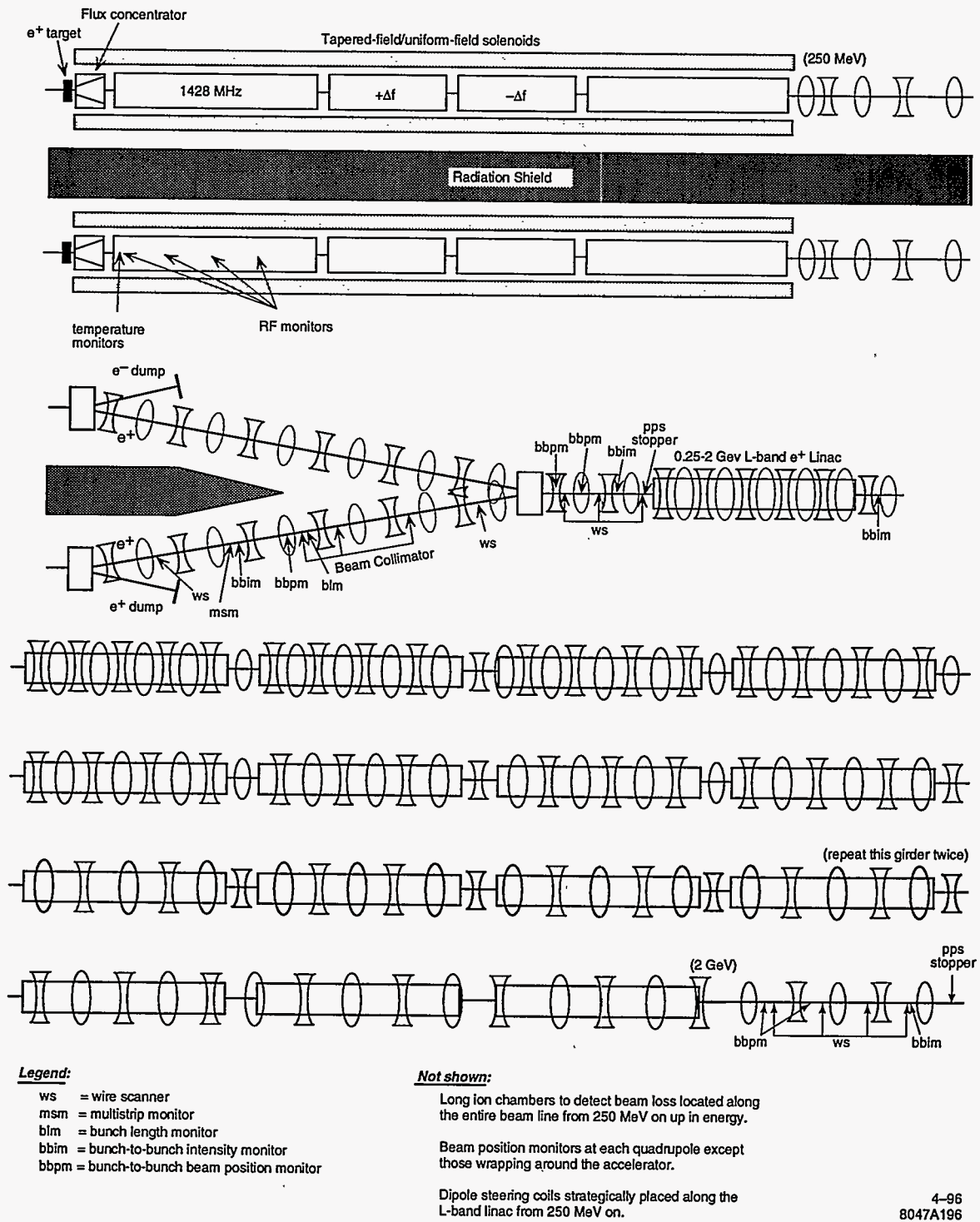


Figure 3-2. Schematic layout of the NLC positron source (part B): dual positron production/capture systems and 1.75-GeV booster linac.

Parameter	Unit	SLC 94	SLC max design	NLC-I (500 GeV)	NLC-II (1 TeV)
General Parameters:					
Ne ⁺ per pulse at IP	[10 ¹⁰]	3.5	5	76.5	112.5
# of bunches per pulse		1	1	90	90
Pulse duration	(ns)	0.003	0.003	126	126
Bunch spacing	(ns)	-	-	1.4	1.4
Repetition frequency	(hz)	120	180	180	120
Drive Electron Beam:					
Energy	(GeV)	30	30	3.11	6.22
Ne ⁻ per bunch	(10 ¹⁰)	3.5	5	1.5	1.5
Ne ⁻ per pulse	(10 ¹⁰)	3.5	5	135	135
Beam power	(kW)	20.2	47	121	161
RMS beam radius	(mm)	0.8	0.6	1.2	1.6
Beam energy density per pulse	(GeV/mm ²)	5.2×10^{11}	13.3×10^{11}	9.3×10^{11}	10.4×10^{11}
Positron Production Target:					
Material		W ₇₅ R ₂₅	W ₇₅ R ₂₅	W ₇₅ R ₂₅	W ₇₅ R ₂₅
Thickness	(R.L.)	6	6	4	4
Energy deposition per pulse	(J)	37	53	126	188
Power deposition	(kW)	4.4	9	23	23
Steady-state temperature	(°C)	100	200	400	400
Positron Collection:					
Accel. rf	(MHz)	2856	2856	1428	1428
Accel. gradient	(MV/m)	30	30	25	25
Minimum iris radius	(mm)	9	9	20	20
Edge emittance (allowing for 2 mm clearance)	(m-rad)	0.01	0.01	0.06	0.06
Positron yield per e ⁻		2.5 ^a	2.5 ^a	1.4	2.05
Ne ⁺ per bunch	(10 ¹⁰)	8.7	12.5	2.1	3.1
Ne ⁺ per pulse	(10 ¹⁰)	8.7	12.5	189	279

^a The actual yield immediately following the capture section is 4, but decreases to 2.5 after two 180° bends and a 2-km transport line.

Table 3-1. NLC Positron Source Parameters.

3.2 Positron Yield Simulation

Positron yield simulations have been performed for both drive beam energies, *i.e.*, 3.11 and 6.22 GeV for NLC-I and NLC-II, respectively. The results are already presented in Table 3-1. In this section we shall discuss in detail the simulation results using a 6.22-GeV drive beam.

3.2.1 Target Yield

The target yield for positrons has been calculated using the EGS program [Nelson 1985] for 6.22-GeV electrons impacting a $W_{75}Re_{25}$ target of thicknesses ranging from 4 to 6 radiation lengths. The optimal positron yield is obtained for a target thickness of about 5 radiation lengths. However, at this thickness about 23% of the beam energy is deposited in the target, as opposed to the 18% energy deposition in a 6-radiation-length-thick target in the SLC positron target. The increased volume density of energy deposition in the target is not desirable as it causes increased thermal stress which may lead to target failure. Therefore, a better choice would be to use a target of 4-radiation-lengths thick, for which the energy deposition is reduced significantly to about 14% while still retaining a respectable positron conversion yield. The total positron yield, defined as the number of positrons generated per incident drive electron, from such a target is about 12.5, whereas the total electron yield is about 15.8.

3.2.2 Ray Tracing through Capture Accelerator

The positron rays obtained from the EGS simulation have been traced through the flux concentrator and the capture accelerator up to the nominal 250-MeV point at the end of the capture region using the ETRANS program [Lynch 1989]. ETRANS is a ray tracing program developed at SLAC that integrates particle trajectories through static magnetic and rf fields while ignoring the effect of space charge and wakefields. The capture accelerator consists of two 5-m L-band (1428 MHz) accelerating sections with a loaded gradient of 25 MV/m and two off-frequency (1428 ± 1.4 MHz) 3-m sections for beam-loading compensation sandwiched in between the two accelerating sections. All four sections are embedded in a 0.5-T uniform solenoidal field. The rf phases of the accelerating fields in the capture region were varied to optimize the positron yield at the 250-MeV point. The best yield at the 250-MeV point, after applying energy and time cuts of ± 10 MeV and ± 30 ps, respectively, is found to be 2.05. With 1.5×10^{10} electrons/bunch in the drive beam, therefore, there will be approximately 3.1×10^{10} positrons/bunch in the L-band linac, which is a factor of 2.5 higher than the bunch intensity required at the interaction point. Figures 3-3 and 3-4 show the transverse and longitudinal phase space plots of the positron beam at the nominal 250-MeV point after the six-dimensional phase space cuts.

The electron rays emerging from the target were also traced through the capture accelerator. The electrons are approximately 65% more abundant than the positrons at the end of the capture system and have a most probable energy of about 230 MeV. These results are useful to evaluate the total beam loading in the capture accelerator and the power of the electron beam to be dumped after the first bending magnet.

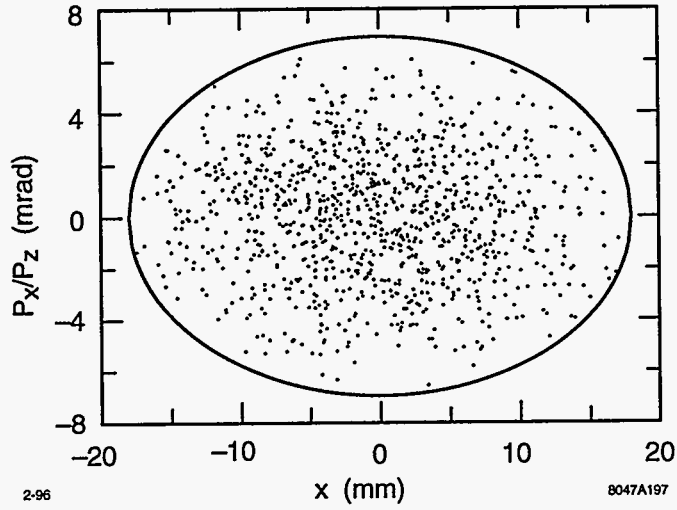


Figure 3-3. Transverse phase space plot of the positron beam at the the exit of the capture accelerator.

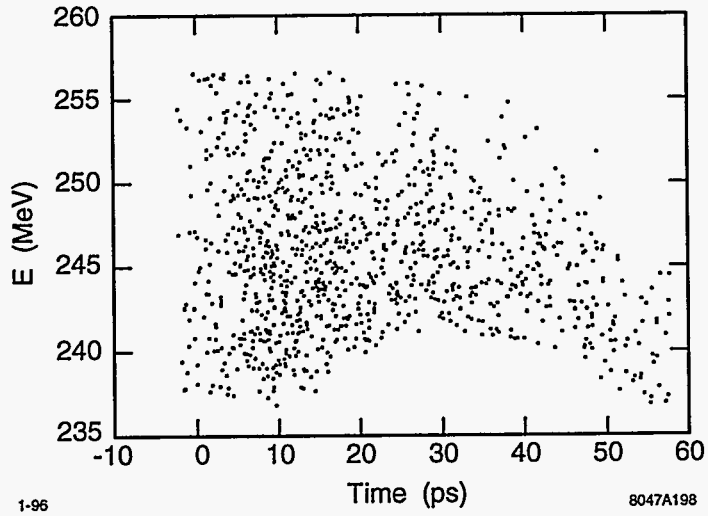


Figure 3-4. Longitudinal phase space plot of the positron beam at the exit of the capture accelerator.

3.3 Drive Electron Accelerator

3.3.1 Drive Electron Source

The baseline choice for the drive electron source is a DC thermionic cathode gun to be operated at 120 kV. A DC photocathode gun employing a bulk GaAs cathode and driven by a Ti:sapphire laser is considered as an option. The electron gun is required to deliver a very stable beam, with a pulse-to-pulse intensity jitter below 0.5% and a bunch-to-bunch intensity jitter below 2%. It is also required to have the capability to produce electron beams with variable bunch train structure to facilitate normal NLC operation as well as initial commissioning.

The injector design for the drive electron beam is identical to that of the NLC electron source (see Chapter 2). To summarize briefly, it consists of two 714-MHz standing wave subharmonic bunchers and a 2856-MHz traveling wave ($\beta = 0.75$) S-band buncher, followed immediately by an 80-MeV S-band accelerator.

3.3.2 Drive Linac

The drive linac is also identical to the electron linac used in the NLC electron source except that it will be longer to accelerate the electrons to the higher energies required for efficient positron production. For NLC-I, the linac will end at 3.11 GeV, followed by a long drift section which will later be replaced by more accelerating sections to boost the energy to 6.22 GeV for the 1-TeV upgrade. Beam loading compensation in the linac will be accomplished by using the Δt approach. See Chapters 6 and 2 for details on the rf and lattice design issues.

3.4 Positron Production Target

The design of the NLC positron production target is modified significantly from that of the SLC target to accommodate the significantly higher beam power delivered to the NLC target. In addition, the target motion mechanism is modified from that of trolling as used in the SLC source to that of rotating to eliminate intensity modulations in the positron beam as experienced in the SLC. The periodic trolling motion of the target and its drive mechanism in the intense magnetic field of the tapered-field solenoid induces Eddy current in the moving parts. The Eddy current in turn generates a periodically varying magnetic field, leading to a small intensity modulation in the captured positron beam with the same frequency as that of the trolling motion. With a rotating target, however, the induced Eddy current should remain roughly constant, thus eliminating the source of intensity modulation.

3.4.1 Review of Target Test Data

Thermal stress from short pulse (or single pulse) heating is the underlying mechanism that causes material failure when a target is bombarded by a high-intensity, high-energy electron beam. As in the SLC positron source, $W_{75}Re_{25}$ will be used as the target material for the NLC source because of its high-Z characteristic

and its excellent thermal and mechanical properties. Material failure tests were conducted at SLAC in the early 1980s for W-Re targets with the Re concentration ranging from 18.6% to 27.6% [Ecklund 1981]. For these tests, the energy of the drive beam was in the range of 20–25 GeV, and the target thickness varied from 5–7 radiation lengths. The material failure threshold in terms of the maximum allowable beam energy density on the target per beam pulse was found to be approximately

$$\rho_{\max} = \frac{N_- E_-}{\pi \sigma^2} = 2 \times 10^{12} \text{ GeV/mm}^2, \quad (3.3)$$

with about 20% of the beam energy deposited in the target. In the above expression, N_- is the number of electrons per pulse, E_- the electron beam energy, and σ the rms radius of the electron beam on the target.

In the above, the failure threshold is expressed in an area beam energy density per pulse. While this is a convenient quantity to characterize the drive beam, it must be emphasized that the most critical parameter for causing material failure is the volume density of energy deposition per pulse in the target. However, the volume energy deposition density depends strongly on the longitudinal position across the target thickness, and it is the maximum density that matters the most for target failure considerations. In practice, it is also useful to evaluate the average energy deposition density in the target. In terms of an average volume density, then, the failure threshold for $W_{75}Re_{25}$ is approximately 7×10^{10} GeV/mm² per radiation length per pulse.

3.4.2 Electron Beam Size

For NLC-II, the drive beam has an energy of 6.22 GeV with a pulse intensity of 1.35×10^{12} ($= 90 \times 1.5 \times 10^{10}$) electrons. In order to avoid damaging the target, *i.e.*, to keep the energy density per beam pulse on the target comfortably below the threshold of 2×10^{12} GeV/mm², the rms beam size of the incident electrons must be increased to 1.6 mm, twice the SLC drive beam size or four times the area. This yields a pulse beam energy density of 1.04×10^{12} GeV/mm² on the target. For NLC-I, the beam radius may be reduced to 1.2 mm, yielding a pulse beam energy density on the target of about 0.93×10^{12} GeV/mm². Since the electron beam size at the end of the 3.11-GeV or 6.22-GeV drive linac is typically much smaller than 1 mm (the normalized transverse emittance is less than 1×10^{-4} m-rad), a thin low-Z scatterer serving as an emittance spoiler must be used a few meters upstream of the target to blow up the beam size. For NLC-I and NLC-II, with 19% and 14% of the beam energy deposited in the 4-radiation-length thick target, the average volume density of energy deposition in the target is about 40% and 50% below the failure threshold, respectively.

3.4.3 Beam Power and Target Size

The average beam power deposited in the target amounts to approximately 23 kW for both NLC-I and NLC-II (Table 3-1). This power is about a factor of 2.5 and 5 larger than the SLC design and operating parameters, respectively. As the SLC positron production system has demonstrated good reliability, it is desirable to maintain a similar target size to beam power ratio for the NLC. Thus, by simply scaling the SLC target up a factor of 4, we find that the NLC target needs to have a diameter of about 20 cm. The target rotation frequency needs to be sufficiently high so that the areas of beam pulse impacts for two successive pulses do not overlap. Taking into account the increased beam size and the increased repetition rate (for NLC-I), the rotation frequency is chosen to be around 2 Hz.

3.4.4 Target Engineering Issues

By adopting a rotating target design, realizing a $\leq 1 \times 10^{-7}$ -Torr vacuum in the target chamber in an environment of very high radiation levels becomes a challenging issue due to the lack of suitable materials for use as a leak-free seal around the rotating target shaft. Instead of pursuing a perfect vacuum seal, the present design seeks to achieve the vacuum goal by using a combination of conductance limiting seals and several stages of differential vacuum pumping.

Target Motion Mechanism, Monitoring and Control

The target wheel will be connected by way of a drive shaft and driven by an inline electric motor (Figure 3-5). The shaft will have two sets of outboard bearings such that the shaft is cantilevered into the target vacuum chamber. Similar to the SLC system, a stepping motor will be used to drive the target shaft, and an angular position sensor will be used for shaft angle and speed monitoring.

Vacuum

The drive shaft will pass into the target vacuum chamber using a combination of radiation resistant seals and several stages of differential vacuum pumping along the length of the drive shaft (Figure 3-5). These seals involve a carbon and/or silver impregnated carbon element which rubs against a hard facing material such as tungsten carbide. These seals generally have tight clearances ($< 15 \mu\text{m}$). Seal designs would be selected with leak path lengths of 25 mm or more. The leak rate goal for the first stage seal is on the order of 1 Torr- ℓ /s or less. Seals reviewed in the study included axial face seals, radial face seals, radial labyrinth seals, axial labyrinth seals, and magnetic face seals.

At least three stages and possibly four stages of differential vacuum pumping will be used along the drive shaft to isolate the rotating wheel target in the 1×10^{-7} -Torr vacuum from atmosphere. The first stage and possibly the second stage could use a dry scroll pump such as the Varian 600DS. This pump is completely oil free and has a base pressure in the 1×10^{-3} -Torr range. Differential pumping stages #2 and #3 or #3 and #4 (depending on the total number of stages used in the pumping system) could each use a turbomolecular pump such as the Varian Turbo-V70D. The Varian Turbo-V70D is a completely sealed, maintenance-free unit and is available in radiation-hardened configurations. The base pressure on these turbo pumps is 8×10^{-10} Torr. Each turbo pump will be backed with an oil free dry scroll pump. The vacuum objectives for the stages of differential pumping system in a three-stage system are: stage #1, $1-3 \times 10^{-1}$ Torr; stage #2, $1-3 \times 10^{-4}$ Torr; stage #3, $1-3 \times 10^{-7}$ Torr. Vacuum in the target chamber will be about 1×10^{-7} Torr and provided by 30 ℓ /s or 60 ℓ /s ion pumps.

Figure 3-6 is a concept drawing showing a three-stage differential vacuum pumping system and support structure around the target drive shaft. This concept utilizes sets of radial labyrinth seals between vacuum pumping stages #1 and #2, stages #2 and #3, and again after stage #3. A bellows face seal with carbon contacting ring is used as the seal between atmosphere and stage #1.

A model two-stage differential pumping system with a rotating shaft will be built and experimented to prove the principle of this design and also to select the best seal materials.

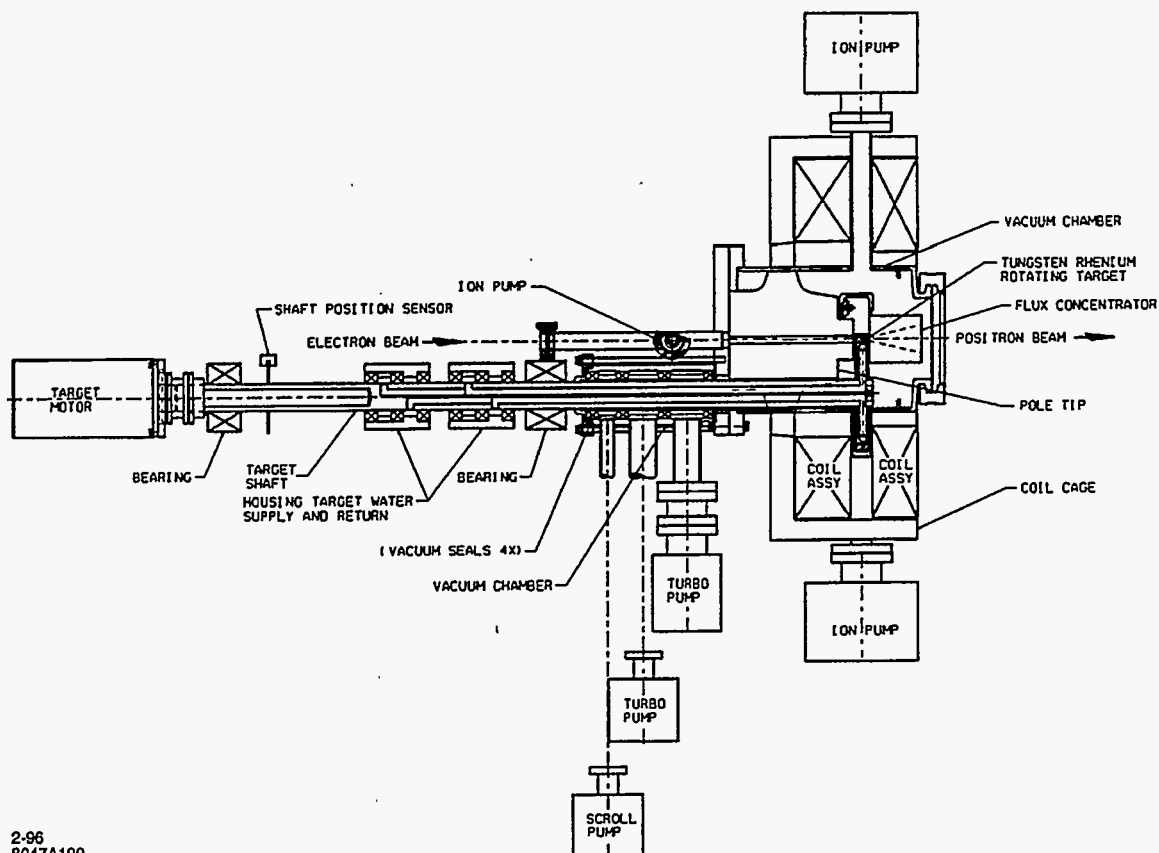


Figure 3-5. Schematic of the NLC positron target system.

Target Cooling

Figure 3-7 depicts a schematic cross-section view of the target wheel and drive shaft. Water supply and return lines will enter the shaft outside the vacuum space and pass through the center of the shaft to the target wheel assembly. The anticipated heat load on the wheel is about 23 kW for both NLC-I and NLC-II. The $W_{75}Re_{25}$ target element at the periphery of the wheel will be approximately 1.4-cm thick along the axial direction, and 1-cm thick in the radial direction. Cooling tubes will be located in a silver or copper casting adjacent to the $W_{75}Re_{25}$ target material to maximize the rates of heat conduction from the target to the cooling tube walls.

A high water velocity will be maintained in the cooling tubes (9–10 m/s) in order to yield a water side heat transfer film coefficient in the range of 17–20 kW/m²-°C. In order to produce the high cooling water velocity in the tubes, a water supply pressure of 200 psi (gauge) and return pressure of 75 psi (gauge) is assumed. Cooling water flow rate will be in a range of 80–120 l/min by using cooling tubes with a 3/8-in or 5/16-in outer diameter.

For both NLC-I and NLC-II, temperature drops across the various components from the center of the beam impact point on the target to the cooling water are estimated to be as follows: ~40°C across the water film inside the cooling tubes; ~30°C across the stainless steel tubing wall; ~50°C through the silver or

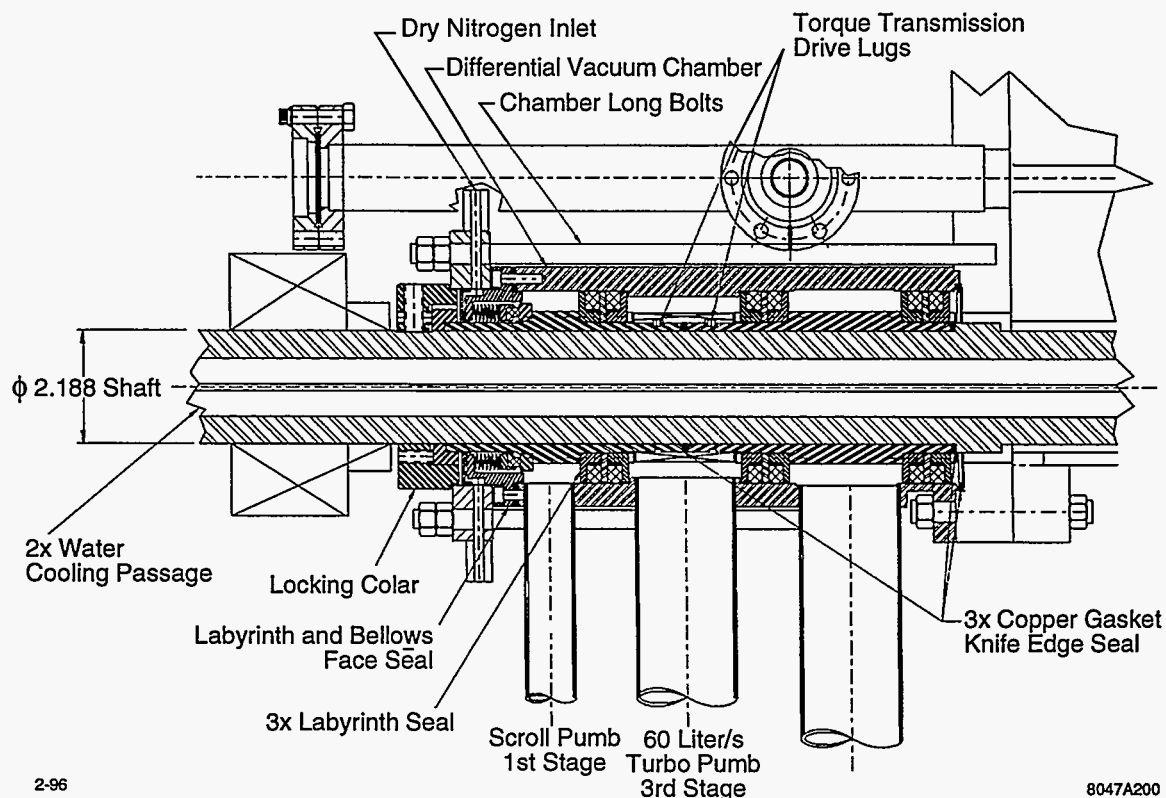


Figure 3-6. NLC rotating target differential vacuum vacuum chamber and seals concept.

copper casting around the cooling tubes from the $W_{75}Re_{25}$ target interface; and $\sim 220^{\circ}C$ from the center of the beam impact point through the $W_{75}Re_{25}$ to the silver or copper interface. Thus, during operation, the maximum steady-state temperature in the target will be about $400^{\circ}C$ which is quite comfortable for $W_{75}Re_{25}$. The steady-state temperature may be lowered substantially by modifications to the target design, such as reducing the radial thickness of the target to improve heat conductance.

The water supply and return lines to the target drive shaft will use radiation-hardened seals probably made from carbon and/or silver-filled carbon or metal composite.

3.4.5 Backup Power

The lack of a true vacuum seal in the positron target chamber means that, in the event of a power outage, the target chamber along with the capture accelerator will be vented due to lost pumping in the various stages. This will result in extended machine downtime as processing the accelerating sections following an air vent may take a long time. Therefore, it is essential to have a reliable emergency backup power system. The backup system may include an uninterruptible power source as well as a power generator, both commercially available. In addition, the atmosphere side of the first stage seal will be flooded with dry N_2 gas. This is designed to provide further insurance that even in the event of a vent through the multi-stage seals the target chamber and the capture accelerator will be filled with dry N_2 , which is relatively easy to pump out

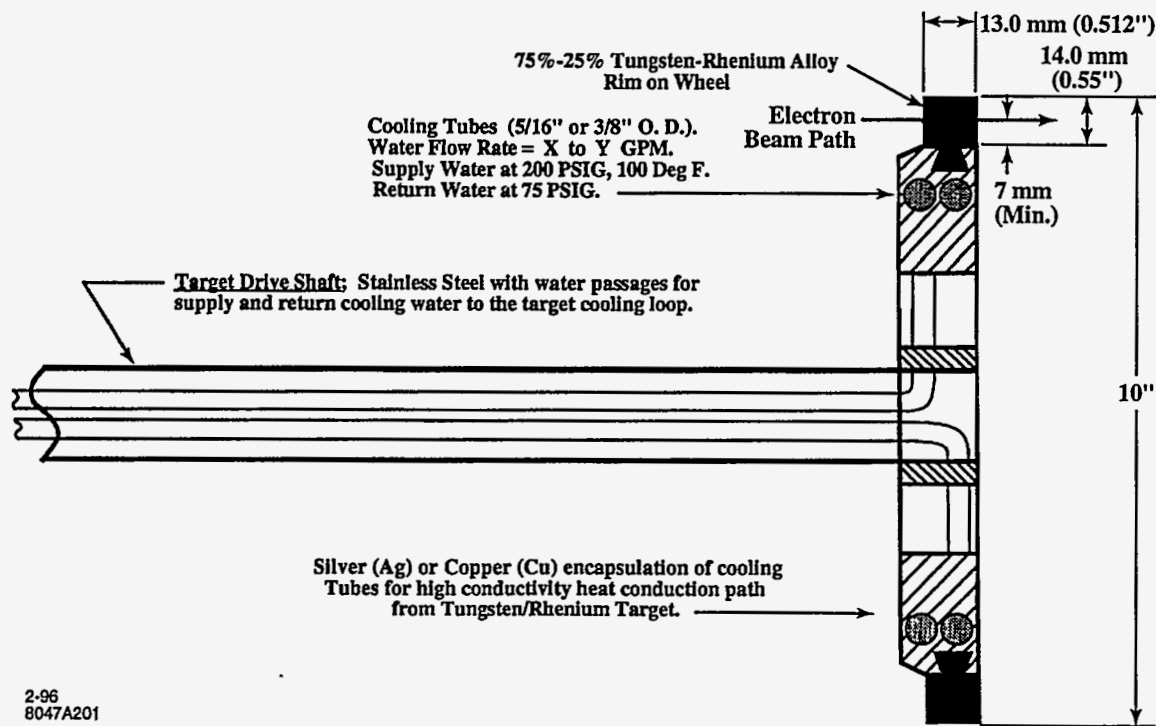


Figure 3-7. NLC positron source target wheel schematic section.

and processing the accelerator after venting to dry N_2 should be relatively quick. In addition, the use of a N_2 buffer gas also minimizes the amount of undesirable air gas species, such as H_2O , in the various differential pumping stages and the target chamber during normal operation.

3.4.6 Integration with Positron Collection System

The positron target system including its vacuum chamber must be closely mated to the flux concentrator and the subsequent capture accelerator to allow for efficient capture of positrons. As shown in Figure 3-5, the flux concentrator shares the same vacuum chamber as the target and is positioned close to it. The spacing between the flux concentrator and the first capture accelerating section must be kept at a minimum. Again, the SLC positron source serves as a design basis for these components and their integration.

3.5 Positron Collection System

The positrons emerging from the target have small spatial and temporal but large angular and energy distributions. Therefore, the use of a large-bandwidth phase-space transformer is essential to yield good capture efficiency of the positron beam into the capture accelerator which is embedded in a long solenoid magnet. As in the SLC positron source, a pulsed flux concentrator and a DC tapered-field solenoid

[SLC 1984] will be used immediately following the conversion target to provide the adiabatically-varying longitudinal magnetic field which is essential for realizing the phase-space transformation [Helm 1962].

3.5.1 Flux Concentrator

The design and fabrication of the flux concentrator will follow exactly the SLC version [Kulikov 1991]. It is designed to produce a 5.8-T peak field along its axis. The minimum radius of the internal cone of the flux concentrator needs to be increased from 3.5 mm in the SLC version to 4.5 mm for the NLC to accommodate the increased radial extent of the emerging positron beam as a result of the increased incident electron beam size. The flux concentrator will be machined from a single block of Cu. The details of the fabrication process are described in the paper by Kulikov *et al.*, [Kulikov 1991]. The main advantage of using a flux concentrator is that it boosts the positron capture efficiency by a factor of 2–3 compared to a capture system utilizing a 1.2-T tapered field solenoid only.

3.5.2 High Gradient L-Band Capture Accelerator

For high capture efficiency, the positrons entering the capture accelerator must be accelerated to relativistic energies as quickly as possible to minimize bunch lengthening. Thus, the accelerating gradient needs to be as high as practically possible. The present design calls for the maximum unloaded gradient in the L-band capture accelerator, consisting of two 5-m accelerating sections and two 3-m beam loading compensation sections, to be 28 mV/m. To achieve the desired gradient and also to facilitate beam loading compensation, each section will be powered by two 75-MW klystrons with SLED-I pulse compression. As the total beam loading current in the bunch train, including contributions from electrons as well as positrons both within and outside of the six-dimensional phase space acceptance window, can be up to 14 A for NLC-II, satisfactory beam loading compensation is realized only through the combined use of both Δt and Δf schemes. The positron beam energy at the end of the capture accelerator will be about 250 MeV, with a full energy spread of about $\pm 6\%$. The minimum iris radius of the disks will be 20 mm, and the outer radius of the disc-loaded waveguide will be about 11 cm. Chapter 6 contains more details on the rf design of the capture accelerator.

3.5.3 Tapered-Field and Uniform-Field Solenoids

A DC tapered-field solenoid producing a peak field of 1.2 T will be used in combination with the pulsed flux concentrator to serve as the phase space transformer, in which the magnetic field varies adiabatically from 7 T to 0.5 T. A 0.5-T uniform-field solenoid that encloses all four L-band accelerating sections will be used to provide transverse focusing in the capture accelerator. The design for the two solenoids is straightforward, as both have identical field specifications as those in the SLC positron source.

3.5.4 Space Charge

In this design, both the positrons and the electrons produced from the target will be collected and accelerated to about 250 and 230 MeV, respectively. The electrons will then be separated from the positrons after a

bending magnet and dumped. In the region between the target and the accelerator, the electron bunch and the positron bunch overlap in space. Thus, wakefield and space charge forces will likely be insignificant. Once entering the capture accelerator, however, the positrons and the electrons will be quickly separated longitudinally, and space charge and wakefield forces may become important. However, experience from operating the SLC positron source suggests that the ETRANS simulation without taking into account space charge and wakefield forces is adequate.

3.6 Beam Dynamics and Transport

3.6.1 Control of Multibunch Beam Blow-up in Positron Linac

The normalized emittance of the bunches coming into the L-band linac just upstream of the positron pre-damping ring is $\gamma\epsilon = 0.06$ m-rad. The initial energy is 250 MeV and the final energy is that of the damping ring, 2 GeV. Other parameters of this linac assumed for the present simulations are shown in Table 3-2.

Calculations were performed using the program LINACBBU [Thompson 1990] which assumes smooth focusing scaling as an arbitrary power of energy. The effect of the focusing lattice was approximated by fitting an average beta function scaling as a power of energy. We obtained a beta function of 1.93 m at the beginning of the linac, and scaled it along the linac as $\beta = (E/E_i)\beta_i$. The resulting beam radius at the beginning of the linac is 1.8 cm. It will probably be desirable to strengthen the focusing at the beginning even more, to keep the beam size significantly smaller than the iris size.

The wake function was scaled from the SLC S-band linac, keeping the lowest 50 transverse dipole modes and assuming an uncoupled model. We examined the cases of: (1) a linear detuning with 4% total frequency spread; and (2) a Gaussian detuning of 10% total spread, where the truncation of the Gaussian distribution frequencies is at ± 2 sigma. There is about a maximum of 60% growth in the transverse offsets, for the case of a 4% linear spread. There is essentially no growth (approximately 4% maximum) in the transverse offsets, for the case of a 10% Gaussian detuning. In neither case did we include any damping beyond that of copper (we took the Q s of the modes to be 18400).

Effects of misalignments and frequency errors were not included in the results reported here, but we do not expect them to change our conclusion that the 10% Gaussian detuning should be fully adequate to control the multibunch emittance growth.

3.6.2 Aperture and Beam Optics System Parameter

The aperture of the positron linac is determined by the minimum aperture of the disk-loaded L-band accelerating structure, which will be 20 mm in radius. To allow for inevitable alignment and steering errors, the realistic transverse aperture for the beam is conservatively chosen to be 18 mm. This aperture, along with the 0.5-T longitudinal field for transverse focusing in the 240-MeV capture accelerator, defines the normalized edge emittance of the captured positron beam to be about 0.06 m-rad.

A preliminary beam optics design for transporting the 0.06-m-edge emittance positron beam through the two magnetic bends and in the common L-band linac to the positron pre-damping ring is shown in Figures 3-8 and 3-9. The design uses a scaled FODO lattice consisting of a dense array of quadrupole magnets. The

Parameters	Values
Accelerating frequency	1428 MHz
Linac length	140 m
Initial energy	250 MeV
Final energy	2 GeV
Ne ⁺ per bunch	2.5×10^{10}
Bunch spacing	1.4 ns (2 rf buckets)
Initial beta function β_i (scales as E)	1.93 m
# bunches per train	90
Normalized emittance $\gamma\epsilon$	6×10^{-2} m-rad

Table 3-2. Parameters of positron booster linac.

quadrupole spacing is kept constant on the first accelerating section, and scaled as \sqrt{E} on the remaining 23 sections. The quadrupole strengths are all kept nearly the same. The phase advance is 60° at the beginning of the lattice and gradually decreases along the linac. This design leads to a quasi-linear E scaling of the maximum beta function. The choice of relatively small phase advances is necessary to minimize the chromaticity-induced emittance growth, which has an initial full energy spread of $\pm 6\%$ at the 250-MeV point and decreases to about $\pm 2\%$ at the end of the L-band linac.

As shown in Figure 3-9, the full beam radius has shrunk to < 16 mm in the first 5-m section. From there on, the beam size is further reduced by the strong-focusing lattice to a final value of about 13 mm at the 2-GeV point. These results, obtained from first-order TRANSPORT runs, illustrate that the positron beam size can be controlled satisfactorily in the L-band linac. However, second-order TRANSPORT calculation shows that beam size control in the L-band linac is not as easy as the first order calculation indicates, mainly due to the inherent single-bunch energy spread of the positron beam. This difficulty becomes more pronounced if the Δf beam-loading compensation scheme is used, which introduces large single-bunch energy spread along the linac. This is the main reason that the Δt scheme is chosen over the Δf scheme for beam loading compensation in the L-band positron linac.

3.6.3 Beam Position and Emittance Control

Due to the large transverse size of the positron beam and the limited aperture of the accelerating structure, reasonably good control (to within 0.2 mm) on the beam position is required throughout the 1.75-GeV L-band linac. A set of beam position monitors and X/Y steering correctors will be used to launch the positron beam into the linac. A beam position monitor and a pair of X/Y correctors will be installed in every gap between successive 5-m sections to maintain an optimal orbit in the L-band linac. It is also being considered to build beam position monitoring capabilities into the 5-m L-band structures by using the dipole signal so that the beam orbit in each 5-m section can be maintained at an optimum.

Efficient injection into the pre-damping ring depends critically on the preservation of the beam emittance in the L-band linac. Emittance growth due to chromaticity, wakefields, beam line and magnets misalignment, etc., must be minimized.

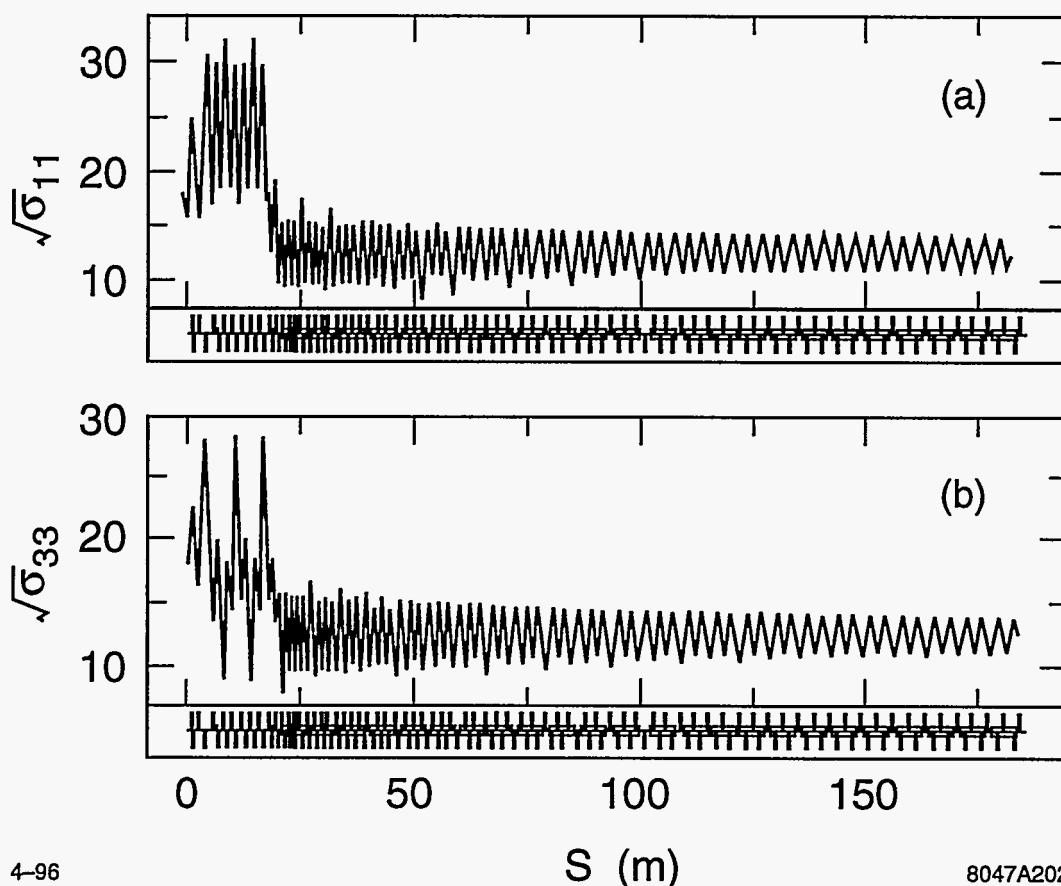


Figure 3-8. Transverse size (edge radius) of the positron beam from the exit of the capture accelerator to the end of the L-band booster linac.

3.7 Positron Linac

The L-band positron linac will consist of 12 accelerating modules. Each module contains two 5-m accelerating sections, which will be powered by two 75-MW L-band klystrons feeding a single SLED-I cavity. Beam loading compensation will be accomplished by using the Δt method, which offers the advantage of complete beam loading compensation at the end of each section without introducing single-bunch energy spread. The maximum attainable loaded energy gain for each module, assuming a beam current of 2.75 A across the bunch train, will be about 173 MeV. With an input beam energy of 250 MeV, the 12-module booster linac provides a large energy headroom—about 17% over the 2-GeV energy target.

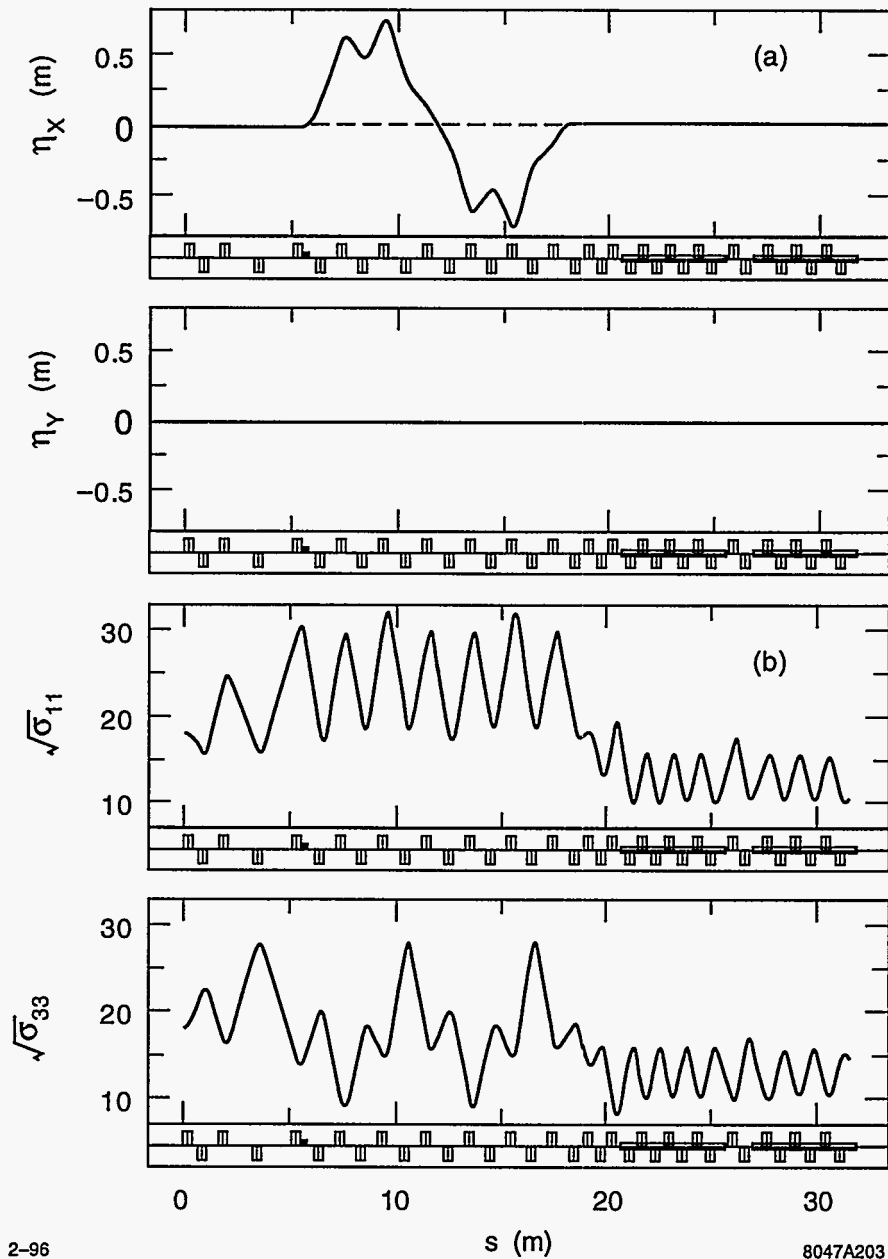


Figure 3-9. Dispersion function and transverse beam size through the the double-bend achromat and in the first two 5-m L-band sections.

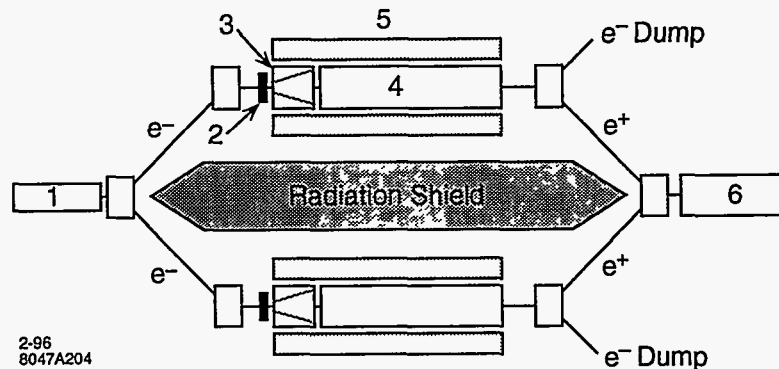


Figure 3-10. An artist's view of the NLC positron source with two side-by-side positron production and capture systems: 1 – drive electron accelerator, 2 – positron target, 3 – flux concentrator, 4 – L-band capture accelerator, 5 – tapered-field and uniform-field solenoids, 6 – positron booster linac.

3.8 Radiation Control Issues

3.8.1 Design Plan for Maintenance

Due to the high radiation activity in the areas around the target and the nominally 10-kW low-energy electron beam dump, access to these radiation-hot areas during a high-energy physics run must be delayed until the radiation activity drops to an acceptable level. As such cooling periods can be as long as several months, any maintenance work in these areas means extended downtime for the machine. A logical approach to improve the efficiency of the positron source is to add redundancy. In the present design, the positron source will have two identical positron vaults containing the positron production and collection systems, *i.e.*, from the target to the nominal 250-MeV point, adequately shielded from each other such that access to one vault is permitted while the other is in operation (Figure 3-10). The input electron beam can be directed to either system via a pair of bending dipoles which form an achromatic and isochronous beam line section. Likewise, the 250-MeV positron beam after the capture accelerator from either system can be directed into the 1.75-GeV L-band booster linac. If one system in use develops a problem during a run, we may quickly switch to the other system and continue the physics run. In the meantime, we can wait for the radiation level in the first positron vault to drop and then make an entry to repair or replace the broken components.

In addition to the dual positron vault design, efforts will be made to make the system components for positron production and collection as modular as possible to facilitate quick maintenance work. Use of materials that have long radiation decay times will be avoided.

3.8.2 Radiation Shielding

Primary Beam at Target

Figure 3-11 gives the calculated dose rate at 90° to a target-dump for various thicknesses of concrete shielding assuming a 150-kW beam of 6-GeV electrons impacting, conservatively chosen, a 30-cm-long and 10-cm-

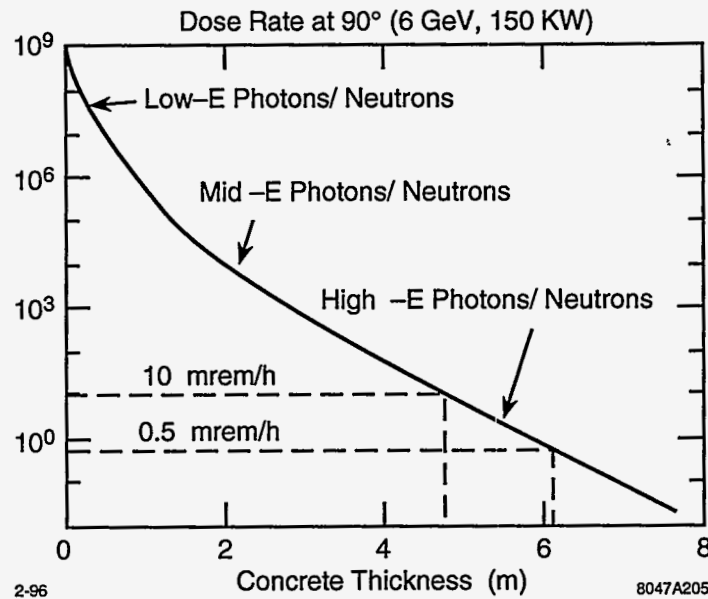
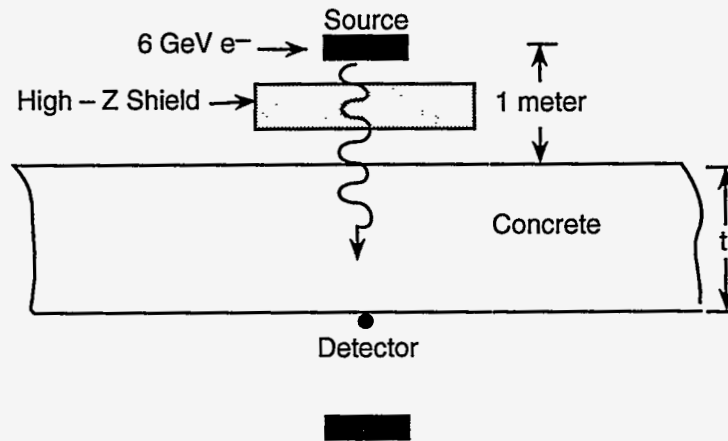


Figure 3-11. Calculated radiation dose rate versus thickness of concrete shielding.

diameter iron target. The distance from the target to the shield is fixed at 1 m and the dose rate is determined at the outside surface of the shield. High-energy neutrons are the dominant component after about 2 m.

The integrated shield design limit is normally 500 mrem per year, which corresponds to 0.5 mrem/h for 1000 hours of operation in a year. This level, and the concrete thickness required to attain it (6 m), are indicated by the dotted lines in the figure. However, there is no need to require the radiation level to be as low as 0.5 mrem/h since the induced activity from the target and other beam components will most likely limit the occupancy time and will likely be at the level around 5 mrem/h. Thus, a 5-m concrete wall would be adequate for shielding purpose. High-Z shielding can also be used near the target to reduce the amount of concrete. For example, Fe is roughly twice as effective for shielding high energy neutrons as concrete.

Low Energy Electron Dump

After the first bending magnet, the electrons that are captured and accelerated to about 230 MeV in the capture accelerator will be bent away from the positron beam trajectory and dumped. The average power of this electron beam is on the order of 10 kW, which necessitates a water-cooled beam dump. Two such dumps, made of a material such as copper, will be built on each side.

3.8.3 Radiation Hard Components

All components in the areas of high-radiation levels, particularly near the target and the low-energy electron dump, must be made of materials highly resistant to radiation. Particular consideration must be given to the target chamber including vacuum and cooling water seals, the tapered-field and uniform-field solenoids, all electrical cabling, various magnets, and other diagnostic instrumentation immediately downstream of the first bending dipole.

3.9 Magnets

3.9.1 Solenoids

The tapered-field solenoid and the uniform-field solenoid are scaled-up versions of the SLC solenoids. Their inner radii need to be increased to approximately 11 cm and the total length to about 17 m to accommodate the four L-band accelerating sections. Their outer radii will also need to be increased accordingly to produce the required 1.2-T field at the front end which, over about 15–20 cm, tapers down to a field of 0.5 T and remains constant for the length of the uniform-field solenoid. The total power consumption of this solenoid will be on the order of 1.5 MW.

3.9.2 Quadrupoles

Two types of quadrupole magnets, one large aperture type that wraps around the L-band accelerating structures and the other regular type that wraps around regular beam pipes, will be used to construct the lattice for the 1.75-GeV L-band linac. Over 100 large-aperture quadrupoles are needed. They will have a pole-tip radius of approximately 11 cm, a length of 38 cm, and a pole-tip field of about 6 kg. Their power consumption is on the order of 15 kW each.

Another 50 or so smaller aperture quadrupoles will be used throughout the entire L-band linac, including approximately 20 for matching the positron beam from the solenoid-field region into the common L-band booster linac while maintaining an achromatic nature for this beam line section, and approximately another 20 for use in between accelerating sections and in the instrumentation section following the booster linac. This type of quadrupoles will have a pole-tip radius of 6.8 cm and a length of 36 cm, with a pole-tip field of about 6 kg.

3.9.3 Bending Dipoles

Six bending magnets, three before and three after the positron production and capture systems (Figure 3-10), are needed for directing the drive beam into either positron vault and directing the captured positron beam into the L-band booster linac. The latter three dipoles will bend the positron beam by 16° , and will have a 5.175-kg field, a 13.6-cm gap, and a length of 36 cm. The former three need to bend the 6.22-GeV electron beam by 10° each.

3.10 Diagnostics and Instrumentation

The bulk of instrumentation for the positron source, including the drive electron beam accelerator, is for routine optimization and diagnosis. While most of the instrumentation will be similar to what is used in the SLC, new instrumentation will be developed to diagnose the multibunch NLC beam. To maintain the beam quality, energy, energy spread, and bunch length will require continuous real-time monitoring before and after the target.

Many of these diagnostics and instrumentation will be used to address intensity jitter requirements. Measurements of intensity, energy, and position across the bunches of a train will need to be done to diagnose pulse-to-pulse variations in intensity out of the pre-damping ring. This is particularly important with beam intensity and energy since changes in these two attributes will lead directly to intensity fluctuations in the pre-damping ring.

3.10.1 Specifications

Beam diagnostic devices and their specifications for the drive electron beam have already been discussed in Chapter 2. Most of these diagnostics will also be used for the positron beam, but their specifications need to be modified slightly. Table 3-3 shows a list of the positron beam diagnostics and their specifications.

3.10.2 Beam Intensity

Bunch-to-bunch and pulse-to-pulse intensity stability will be measured after the drive beam electron gun, after bunching, and just upstream of the target. see Chapter 2 for more details.

The positron beam intensities will be measured immediately after the bending magnet which separates the electrons from the positrons, after the first L-band section in the booster linac, and at the end of the booster linac.

Bunch intensities will be sampled for beam-loading compensation feedback.. High-bandwidth gap monitors appear feasible and development is in progress.

Diagnostic	Bunch Train		Bunch Bundle	
	Range	Resolution	Range (per bunch)	Resolution (per bunch)
Toroid charge mon.	$50\text{--}300 \times 10^{10} e^+$	$\pm 0.2\%$	$0.5\text{--}3.5 \times 10^{10} e^+$	$\pm 1\%$
Beam position mon.	0–2 cm	$\pm 20 \mu$	0–2 cm	$\pm 20 \mu$
Beam size mon.	$R = 0.5\text{--}2$ cm (edge)	$\pm 1\%$	$R = 0.5\text{--}2$ cm (edge)	$\pm 1\%$
Bunch length mon.	1–150 ns	± 1 ns	10–100 ps	2 ps
Energy	250 MeV	$\pm 0.2\%$	250 MeV	$\pm 0.5\%$
ΔE at 250 MeV	$\sim 12\%$	$\pm 0.5\%$	$\sim 12\%$	$\pm 0.2\%$
Multi-strip mon.	Qualitative diagnostic for beam tuning			

Table 3-3. Positron beam diagnostics and their specifications.

3.10.3 Beam Position

Position monitors, which measure the average bunch offset in a pulse train, will be placed in between every accelerator section near to or captured in any quadrupole magnet located there to monitor and, along with X/Y steering coils, correct and stabilize orbits via feedback loops. The centroid position of the bunches will also be important. High-bandwidth beam position monitors are feasible and development is being pursued but is expected to be expensive (see Chapter 15 for details). Placement of these monitors is lattice-dependent and in general will be used to diagnose and correct for wakefield and beam-loading problems. For the drive beam electrons, a set of these monitors to measure X, X', Y, Y' will be placed after the gun, after bunching, at the end of the S-band linac, and at two high-dispersion regions at 80 MeV and at the end of the linac (3.11 GeV for NLC-I and 6.22 GeV for NLC-II) for energy measurement. For the positron beam, two sets will be used, one after the first bending magnet (after the electrons are separated), and the other between the L-band linac and the pre-damping ring.

3.10.4 Beam Size

The size of a small group of bunches, or perhaps of each bunch, will be determined with standard SLC-type wire scanners using high-bandwidth detectors (such as those under development in Japan). This will facilitate optical matching and emittance control tuning needed to minimize intensity jitter due to tails in the transverse distributions. For the drive beam electrons, a set to measure transverse phase space distribution will be located at the 80-MeV point, and another set at the end of the S-band linac before the double-bend achromats leading to the two positron production/capture systems. See Chapter 2 for more details. For the positron beam, two full sets will be installed, one after the first bending magnet, and the other at the end of the L-band linac before the pre-damping ring.

3.10.5 Beam Bunch Length

For the drive beam electrons, a bunch length monitor will be installed at the 80 MeV point after the beam is bunched (see Chapter 2). For positrons, three monitors will be used, one in each of the two double-bend achromats following the capture accelerators, and a third at the end of the L-band linac.

3.10.6 Energy

The energy of the drive electron beam will be monitored before the positron target, not only to facilitate its stabilization through feedback, but also to measure the effects of tuning methods and schemes for machine protection recovery. This can be done through high-bandwidth beam position monitors as described earlier.

The positron beam energy will be monitored at each available point to ensure the beam is centered in the aperture and to measure the effects of tuning methods and schemes for machine protection recovery. Monitors will be placed after the first few sections, and between the end of the linac and the pre-damping ring. The energy of the individual bunches will also be monitored at these locations. This should be done with high-bandwidth beam position monitors as previously mentioned. Wires could be used and they have the advantage of measuring energy spread as well, but are too slow for other uses.

3.10.7 Energy Spread

The energy spread of the drive electron beam will be monitored and maintained at a minimum just before the positron target. Wires with high-bandwidth detectors can be used for reliable quantitative measurements as in SLC.

The energy spread of the positron beam will be measured using multi-strip beam size monitors and wires with high-bandwidth detectors and maintained at a minimum. Measurements will be done at two dispersion locations, *i.e.*, in the double-bend achromat using foils as in the SLC, and in the linac to pre-damping ring transfer line.

3.10.8 RF Phase and Amplitude Monitoring

The shape of rf pulses will be sampled at frequent intervals to ensure phase and amplitude stability. Slow drifts due to diurnal effects, etc., will be compensated with feedback loops. Pulse-to-pulse sampling and correlation with beam changes can be used to determine severity. The SLC prototype has these features.

3.11 Feedback and Stability

Software-driven feedbacks with high-speed data acquisition, calculation, and device control were integral to the success of the SLC prototype (see Appendix D), and will be used in the NLC positron source to control orbit, energy, and beam-loading compensation.

A significant fraction of the drive beam power will be deposited into the first L-band section in the positron capture accelerator. The amount of power deposition in the first section depends on the machine repetition rate and on the bunch structure (*i.e.*, number of bunches per pulse) as well. In order to maintain rf phase and amplitude stability in the first section during periods of machine rate and bunch structure changes, the temperature of the structure must be stabilized by appropriately adjusting the cooling water temperature with special hardware and control software. Of course, thermal stability is equally important for the remaining three sections in the capture accelerator. Depending on the amount of power deposition into these sections, similar temperature control hardware and software may also be necessary for them.

An intensity feedback using the gun pulsar with the capability of changing individual pulses is desirable for long-term stability. A beam-loading compensation feedback will be needed to keep bunch intensity variations minimized as pulse train intensity may change.

3.11.1 Intensity Uniformity Specifications

The specifications on the pulse-to-pulse, or train-to-train, and bunch-to-bunch intensity jitters for the positron beam are 0.5% and 2%, respectively. Assuming there is no intensity jitter amplification (or growth) from the drive electron beam to the positron beam, these jitter specifications should also apply to the drive electron beam. A stable DC electron gun coupled with a jitter limiting aperture downstream is expected to provide an electron beam meeting these jitter specifications. Beam intensity diagnostics will have a .2% resolution for pulse intensity measurements and a 1% resolution for bunch or bunchlet intensity measurements.

3.11.2 Transverse Orbit Stability

Feedbacks for maintaining transverse orbit will be used throughout the entire system, but will be particularly important at critical points such as at the positron target or at the entrance to the pre-damping ring. The SLC prototype feedback is adequate and beam position monitors that measure the average bunch offset in a pulse train will be used.

3.11.3 Energy Control

Energy feedback loops will be needed in three places: before the target to control the energy of drive beam electrons; after the capture accelerator to control the energy of positrons to be launched into the linac; and in the linac-to-ring line before the entrance to the pre-damping ring.

3.12 Operations and Tuning Procedures

Operations and tuning procedures will be designed to grow toward higher levels of automation as in the SLC prototype. Initial procedures for commissioning and optimizing the positron source will lead to the development of algorithms and feedbacks for maintaining the positron source.

The systems in the NLC positron source are very similar to the SLC prototype and many SLC procedures will be transferable for use on the NLC. However, modifications and additions will be made to address issues involving the significantly higher beam power, multibunch operation, and machine protection schemes.

3.13 Control System Needs

3.13.1 Specification

The control system needs to monitor and control some of the devices on the time scale of the repetition rate of the machine, *i.e.*, 180 Hz for NLC-I or 120 Hz for NLC-II. This will require effective software-based feedbacks such as are used in the SLC prototype. On a slower time scale, the system must monitor and control a variety of devices to include rf amplitude and phase, magnet fields, and beam monitors of all types. These are just a few of the generic tools necessary for successful NLC operation.

3.13.2 Special Requirements

The positron source has two special requirements on the control system. (i) For the L-band capture accelerator, especially the first section, rf phase control for maintaining a constant positron yield will require thermal stability of the accelerating structures. During rate recovery from a machine protection rate change, thermal stabilization in these sections will require a pre-established feedforward control that promptly adjusts the temperature of the structure cooling water. (ii) The backup power system needs to be controlled in such a way that uninterrupted power is delivered to the various vacuum pumps of the positron target chamber in the event of a power outage.

3.14 Other Considerations

While the SLC positron source has met its design goal in terms of beam intensity and demonstrated good reliability over many years of operation, its success has been marred by the extensive and constant tuning effort required for operating the source and by excessive beam intensity jitter often experienced. The difficulty in operating the SLC source is known to be caused mainly by the lack of dedicated accelerators for both the drive beam and the positron beam which greatly limits the tuning flexibility. The excessive intensity jitter appears attributable to successively smaller apertures in the positron system starting from the capture accelerator to the damping ring. Accompanying a loss of beam intensity at each aperture, there is generally a concurrent growth in the intensity jitter. The accumulative effect leads to an increase in the positron intensity jitter, after being extracted out of the damping ring, by $\geq 75\%$ over that of the drive beam.

Since the NLC positron source will have dedicated accelerators for the drive beam and the positron beam, its operational characteristics are expected to be improved significantly over its SLC counterpart. Also, since the smallest aperture in the NLC positron system by design is given by the capture accelerator immediately following the production target, minimal intensity losses are expected for the positron beam in the rest of the machine, including the L-band linac, the pre-damping, and the main damping ring. Judging from the SLC experience, one may expect that intensity jitter growth from the drive beam to the positron beam in

NLC may be insignificant. Thus, producing a sufficiently stable drive beam may be the only critical task. This is, however, not to say that beam intensity jitter in the NLC positron source is a trivial issue. On the contrary, since intensity stability is such a critical issue to the success of the NLC, intensity jitter in the NLC positron source warrants critical design considerations.

3.15 Summary

The NLC positron source has a conventional design based on the SLC positron source and will be built with existing technology only. The significantly higher beam intensity for NLC is realized by the combined use of a larger drive electron beam on the target and an L-band positron accelerator. The former permits a quadratic increase in the pulse energy of the drive beam, while the latter permits the accelerating structure to have a minimum iris radius slightly more than twice as large as that of the SLC S-band structure, which translates into a >16-fold increase in the four-dimensional transverse phase space admittance. The source upgrade from NLC-I to NLC-II is straightforward, simply requiring an 80% increase in the drive beam size (area) and a doubling of the drive beam energy (from 3.11 GeV to 6.22 GeV). Both the NLC-I and NLC-II sources are conservatively designed to have large intensity safety margins—about a factor of 2.5 higher than the highest conceivable operating intensity at the interaction point—to insure against possible unforeseen beam losses.

The design employs a rotating positron target, intended for eliminating beam intensity modulations induced by target motion, with multi-stage differential vacuum pumping along the target drive shaft. Two identical, inter-switchable, positron production and capture systems will be built side by side to improve the source efficiency.

References

- [Ecklund 1981] S. Ecklund, "Positron Target Material Tests", SLAC-CN-128 (1981).
- [Helm 1962] R.H. Helm, 1962, "Adiabatic Approximation for Dynamics of a Particle in the Field of a Tapered Solenoid", SLAC-4 (1962).
- [Kulikov 1991] A.V. Kulikov, S.D. Ecklund, and E.M. Reuter, 1991, "SLC Positron Source Pulsed Flux Concentrator", SLAC-PUB-5473 (1991), in Conference Record of the 1991 IEEE Particle Accelerator Conference, San Francisco, CA, 2005 (1991).
- [Lynch 1989] H.L. Lynch, 1989, "ETTRANS", SLAC Memorandum (1989).
- [Nelson 1985] W. Nelson, H. Hirayama and D. Rogers, 1984, "The EGS4 Code System", SLAC-Report-265 (1985).
- [SLC 1984] SLC, *SLC Design Handbook*, SLAC (1984).
- [Thompson 1990] K.A. Thompson, and R.D. Ruth, 1990, "Controlling transverse multibunch instabilities in linacs of high energy linear colliders", SLAC-PUB-4801, in *Phys. Rev. D* **41**, 964 (1990).

Contributors

- S. Ecklund
- P. Emma
- G. Gross
- A. Kulikov
- R. Miller
- W. Nelson
- L. Rinolfi
- H. Tang
- K. Thompson
- J. Turner
- T. Umemoto
- V. Vylet
- D. Yermian
- Z. Li

NLC Damping Rings

Contents

4.1	Introduction	117
4.2	System Overview and Parameter Determination	118
4.2.1	Overview	118
4.2.2	Damping Ring Complex Layout	121
4.2.3	Requirements	121
4.2.4	Parameters: Damping Times and Equilibrium Emittances	123
4.2.5	Scaling Relations	126
4.2.6	Ring Energy	127
4.2.7	Wigglers vs. Arcs	128
4.2.8	Lattice Specification	129
4.2.9	RF Parameters	132
4.3	Lattice Design	133
4.3.1	Main Damping Rings	133
4.3.2	Pre-Damping Ring	143
4.3.3	Injection Line	148
4.3.4	Extraction Line	152
4.3.5	PPDR-to-PDR Transfer Line	153
4.3.6	Bypass Lines	154
4.3.7	Trajectory Correction	154
4.3.8	Emittance Control and Matching	157
4.3.9	Dynamic Aperture	160
4.3.10	Polarization	165
4.4	Collective Limitations	166
4.4.1	Main Damping Ring: Impedance Model	167
4.4.2	Single-Bunch Potential Well Distortion and Longitudinal Microwave Instability	175
4.4.3	Single-Bunch Transverse Mode Coupling	180
4.4.4	Bunch-to-Bunch Synchronous Phase Variation	181
4.4.5	Coupled Bunch Instabilities	185
4.4.6	Ion Trapping	188
4.4.7	Positron-Electron Instability	190
4.4.8	Intrabeam Scattering	192
4.4.9	Beam-Gas Scattering	193
4.4.10	Lifetime Limitations	194
4.4.11	PPDR Collective Limitations	194
4.5	RF Systems	195
4.5.1	Main Damping Rings RF Systems	195

4.5.2	Pre-Damping Ring RF Systems	201
4.5.3	Low-Level RF Systems	203
4.5.4	Energy Compressors	211
4.6	Vacuum Systems	211
4.6.1	Main Damping Ring	211
4.6.2	Pre-Damping Ring	217
4.6.3	Transport Lines	217
4.7	Feedback and Feedforward Systems	217
4.7.1	Coupled Bunch Transverse Feedbacks	217
4.7.2	Stored Orbit Feedbacks	222
4.7.3	Injection Feedbacks	222
4.7.4	Extraction Feedbacks	222
4.8	Vibration and Stability	223
4.8.1	Vibration	223
4.8.2	Stability	226
4.9	Alignment and Supports	226
4.9.1	Girders and Supports	227
4.9.2	Mechanical Alignment	227
4.9.3	Beam-based Alignment	227
4.10	Magnet Design and Power Supplies	229
4.10.1	Main Damping Rings	229
4.10.2	Pre-Damping Ring	239
4.10.3	Injection and Extraction Kickers	242
4.10.4	Transport Lines	246
4.11	Instrumentation for the Main Damping Rings	246
4.11.1	Beam Position Monitors	247
4.11.2	Beam Size Monitors	248
4.11.3	Bunch Length Measurement	248
4.11.4	Polarization Measurement	248
4.11.5	RF Diagnostics	248
4.11.6	Ion Measurements	249
4.11.7	Conventional Diagnostics	249
4.12	Conclusions and Comments	249

4.1 Introduction

The NLC damping rings are designed to damp the incoming electron and positron beams to the very small emittances needed for collisions. The rings have three purposes: (1) damp the incoming emittances in all three planes, (2) damp incoming transients and provide a stable platform for the downstream portion of the accelerator, and (3) delay the bunches so that feedforward systems can be used to compensate for charge fluctuations.

To meet these goals, we have designed three damping rings: two identical main damping rings, one for the electrons (EDR) and one for the positrons (PDR), and a pre-damping ring for the positrons (PPDR). The pre-damping ring is needed because the incoming positron emittance is much larger than that of the electron beam. Each damping ring will store multiple trains of bunches at once. At every machine cycle, a single fully damped bunch train is extracted from the ring while a new bunch train is injected. In this manner, each bunch train can be damped for many machine cycles.

The parameters of the two main damping rings (MDR) are similar to the present generation of synchrotron light sources and the B-factory colliders that are being constructed in that they must store high-current beams (~ 1 A) while attaining small normalized emittances. Table 4-1 compares the NLC ring parameters with those of the SLAC B-factory Low Energy Ring (PEP-II LER), the Advanced Light Source (ALS) at Lawrence Berkeley National Laboratory (LBNL), and the Accelerator Test Facility (ATF) damping ring being constructed at KEK in Japan to verify many of the damping ring design concepts. In particular, the stored beam currents are less than half of what the PEP-II LER has been designed to store while the emittance, energy, and size of the rings are similar to those of the ALS and the ATF.

Thus, these other rings will be able to test and verify many of the accelerator physics issues that will arise in the NLC damping rings. In particular, strong coupled-bunch instabilities will be studied in the high current B-factories while issues associated with the very small beam emittances, such as intra-beam scattering and ion trapping, will be studied in the ALS and the KEK ATF damping ring. In addition, the PEP-II LER and the Advanced Photon Source (APS) at Argonne National Laboratory will be able to study the photoelectron-positron instability that is thought to arise in positron storage rings.

These similarities with other rings have also simplified the design process and we have been able to and will continue to benefit from the experience of these other accelerators. For example, the damping ring rf system is based on those developed for the SLAC B-factory and the ATF damping ring, the multibunch feedback systems are based upon the feedback systems which were designed for the SLAC B-factory and successfully verified on the ALS, and the vacuum system is similar to that used by the ALS. Furthermore, the design uses "C" quadrupole and sextupole magnets similar to those designed at the ALS and the APS at Argonne, a high-field permanent magnet wiggler very similar to a design developed and installed at Stanford Synchrotron Radiation Laboratory (SSRL), and a double kicker system for extraction similar to one to be tested in the KEK ATF.

Because the damping rings must form a stable and reliable platform for the rest of the linear collider, we have designed the rings conservatively. Whenever possible we have used concepts and designs that have been experimentally verified or will be verified in the near future and have not adopted some of the more exotic, although attractive, concepts that have been suggested. The one possible exception from this rule is the use of the TME lattice for the main damping rings instead of a standard TBA or Chasman-Green lattice. We felt that the advantages of the TME lattice—simpler and fewer bending magnets—justify this choice.

The damping ring complex consists of the injector lines for the damping rings, the positron pre-damping ring, the two main damping rings, and the transfer line between the pre-damping ring and the main

	NLC MDR	PEP-II LER	LBNL ALS	KEK ATF
Energy (GeV)	2.0	3.1	1.5	1.5
Circ. (m)	220	2200	200	140
Current (A)	1.2	3	0.6	0.6
$\gamma\epsilon_x$ (10^{-6} m-rad)	3	400	10	4
$\gamma\epsilon_y$ (10^{-6} m-rad)	0.02	16	0.2	0.04

Table 4-1. Comparison of NLC main damping rings with parameters of other rings.

positron damping ring. Section 4.2 gives an overview of the damping ring complex and defines the system requirements. Next, the determination of the parameters, various scaling relations, and some of the design tradeoffs that were made are discussed. The goal of this sections is to document our parameter choices so others may then explore alternate methods of optimization.

Section 4.3 presents the parameters and the optical designs of the main damping rings, pre-damping ring, injection and extraction lines, and PPDR-to-PDR transfer line. It also contains a description of the trajectory correction, emittance control and matching requirements, dynamic apertures, and the transport of the polarization through the damping ring complex.

The collective limitations are discussed in Section 4.4 and then, the rf and vacuum systems are described in Sections 4.5 and 4.6. This is followed by specifications of the feedback systems, supports and alignment techniques, magnet design and instrumentation. Finally, we discuss the ground vibration effects and some stability issues.

4.2 System Overview and Parameter Determination

In this section, we will first provide a brief overview of the damping ring complex and then we will enter a more detailed discussion of the requirements and parameter determination.

4.2.1 Overview

The damping ring complex consists of one damping ring for the electrons and both a pre-damping ring and a main damping ring for the positrons; as will be discussed, two positron rings are needed because the incoming positron emittance is very large. It also includes the transport line between the positron pre-damping ring and the main damping ring as well as elements in the extraction lines that complete the extraction system for the main damping rings. Finally, the damping ring complex includes the injection matching sections upstream of the rings which provide matching for the transverse phase space as well as the energy compressors to match the longitudinal phase space and spin rotators to orient the particle spin in the vertical direction for injection into the damping ring complex.

At present, most of the studies have concentrated on the main damping rings. Although relatively little of the detailed engineering has been performed, we have a good outline of the design and the problems we may encounter. In particular, we have identified and described solutions for the most difficult issues: these are the dynamic aperture, the vertical emittance, the impedance and instabilities, and the stability and jitter in

both longitudinal and transverse phase space. As stated, much of the design rests on work being performed for the B-factories presently being constructed and the KEK ATF damping ring.

One area which has not been studied sufficiently is the design of the bending magnets. Although we have confidence that the magnets could be constructed, they are high-field combined-function magnets that need additional research to fully verify their feasibility. We feel that it is justified to push their design since, if a design can be found, they are static devices that will not cause further trouble. If, instead, a reasonable design cannot be found, it is straightforward to scale the energy of the ring complex and reduce the requirements, although one also loses some of the tuning range in the present design and likely increases the cost.

In most aspects, the pre-damping ring has relatively loose requirements. The emittance and damping time requirements are not severe. The required beam stability is not very significant. The two difficult items are attaining the dynamic aperture and the injection/extraction kicker systems. At this time, the design is still in a preliminary stage but we have addressed the two issues just mentioned.

Main-Damping Rings

The Electron and Positron Damping Rings (EDR and PDR) are designed to damp beams with an injected emittance of $\gamma\epsilon_{x,y} = 1 \times 10^{-4}$ m-rad to an emittance of $\gamma\epsilon_x = 3 \times 10^{-6}$ m-rad and $\gamma\epsilon_y = 3 \times 10^{-8}$ m-rad. The rings will operate at 180 Hz and must provide sufficient damping to decrease an injected emittance by over four orders of magnitude.

The lattice is based on detuned Theoretical Minimum Emittance (TME) cells which were chosen because of eased requirements on the combined-function bending magnets. The damping is performed using both high-field bending magnets and ten 2.5-m sections of damping wiggler.

The rings operate with four trains of 90 bunches. The bunch trains are injected onto and extracted from the closed orbit using pulsed kickers and DC septa. To avoid coupled-bunch instabilities the rf cavities are based on those of the PEP-II B-factory and a transverse bunch-by-bunch feedback system is used. The rings are designed to operate with maximum bunch charges of 1.57×10^{10} particles; this is roughly 20% more than the maximum needed at the IP. In addition, the electron source has been designed to provide additional charge to allow for at least 10% losses during injection into the electron damping ring. Similarly, the positron source has been designed to produce at least 20% additional charge to provide for losses during injection into the pre-damping ring.

Finally, because the rings must generate extremely small beam emittances, there are tight jitter and alignment tolerances. Extensive effort has been made to include cancelations and tuning procedures in the design that will ease the tolerances to reasonable levels. In particular, all of the quadrupoles and all of the sextupoles will have independent power supplies. This will facilitate beam-based alignment as well as matching of the lattice functions.

Pre-Damping Ring

The Positron Pre-Damping Ring (PPDR) is designed to damp the large emittance positron beam from the positron source to an emittance of roughly $\gamma\epsilon_{x,y} = 1 \times 10^{-4}$ m-rad. At this point, the positrons are injected into the positron main damping ring (PDR) where they are damped to the desired final emittances. The pre-damping ring allows us to decouple the large aperture requirements for the incoming positron beams from the final emittance requirements of the linear collider.

The pre-damping-ring does not need to produce flat beams. Thus, to maximize the damping of the transverse phase space, the ring has a damping partition number $J_x \approx 1.4$ and operates on the coupling difference resonance. This increases the damping in both the horizontal and vertical planes. Furthermore, like the main damping ring, the ring damps multiple trains of bunches at once, the number of which is determined by the ring circumference. The initial design was only 114m in circumference and stored only two trains. The present design is roughly 50% larger and stores three bunch trains. Although this increase in circumference will certainly increase the cost of the ring, the previous design was very tightly packed making the component design and maintenance substantially more difficult; experience with the SLC damping rings strongly suggests that the increase in circumference is cost-effective.

The magnets and vacuum system are being designed to provide sufficient aperture to accept a 2-GeV beam with an edge emittance of $\gamma\epsilon_{x,y} = 0.09$ m-rad and $|\delta p/p| \leq 1.5\%$ plus 2-mm clearance for misalignments and mis-steering. Given the nominal injected edge emittance of $\gamma\epsilon_{x,y} = 0.06$ m-rad, this provides a substantial margin for injection and internal mismatches. In addition, the injectors specifications assume that roughly 20% of the delivered charge is lost at injection into the pre-damping rings while the pre-damping rings are designed to operate with a maximum bunch charge that is roughly 20% greater than the maximum required at the IP.

Like the main damping rings, all of the quadrupoles and all of the sextupoles will have independent power supplies. This will facilitate beam-based alignment as well as matching of the lattice functions which is especially important in the pre-damping ring because of the limited aperture.

Injection Lines

The injection lines to the damping rings from the booster linacs are relatively straightforward transport lines. They have five primary functions:

- Provide diagnostics to monitor the beam energy, energy spread, transverse positions, and emittances.
- Provide transverse betatron matching for injection into the rings.
- Compress the incoming energy spread to match the longitudinal phase space to the damping rings.
- Rotate the longitudinal polarization of the electron beam into the vertical plane for injection into the electron damping ring.
- Include a beam dump after the diagnostics but before injection into the rings.

The spin rotation requires at least a 20° arc to rotate the longitudinal spin into the horizontal plane. We have designed a 60° arc (270° spin rotation) which is more suitable for the energy compressors. Finally, although the positron beam is not polarized, we are designing the positron system so that it could be converted to operate with polarized electrons for future $\gamma - \gamma$ or $e^- - e^-$ collisions. Thus, the geometrical constraints imposed by the spin rotation are applied to both the electron and positron injection lines.

Extraction Lines

The extraction lines from the damping rings have two purposes: they match the beams into the beginning of the spin rotator/bunch compressor beam lines that are described in Chapter 5, and they contain final elements for the extraction systems.

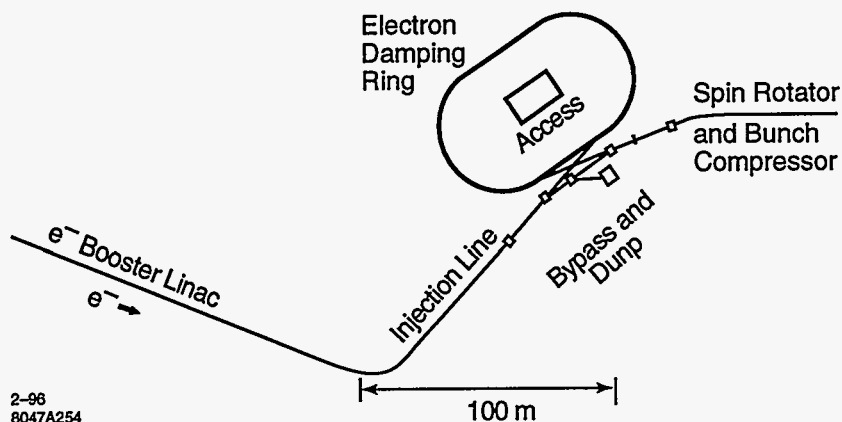


Figure 4-1. Layout of electron damping ring system along with the two bunch compressors and the electron source.

Bypass and Transfer Lines

There are four additional bypass and transfer lines that allow each of the rings to be bypassed and transfer the beams from the positron pre-damping ring to the main damping ring. These contain emittance diagnostics and beam dumps to allow tuning of the injector systems without operating portions of the ring complex.

4.2.2 Damping Ring Complex Layout

The electron and positron damping ring systems are located at the low-energy ends of the respective linacs. The two systems are separated by roughly 20 km. On the extraction side, the systems are constrained by the prelinacs, the spin rotator in the low-energy bunch compressor which performs a 20° bend, and the bunch compressor turn-around (180° arc). At the injection end, the systems are constrained by the source linacs; the electron source is roughly 300 m in length while the positron source is in excess of 1 km.

The electron damping ring system includes an injection line with a 60° bend, and the ring injection and extraction sections which yield a net bending of roughly 20°. Figure 4-1 is a schematic of a possible layout.

The positron damping ring system also includes an injection line with a 60° bend, and the injection and extraction sections for both the pre-damping ring and the main damping rings. Figure 4-2 is a schematic of a possible layout which allows for the long positron source system.

4.2.3 Requirements

At this point, we will enter a more detail description of the damping ring requirements and the parameter determination. The primary requirements of the NLC damping rings are summarized in Table 4-2 where the limiting parameters are listed for each of the NLC energy upgrades. The rings must produce electron and positron beams with emittances of $\gamma\epsilon_x \leq 3 \times 10^{-6}$ m-rad and $\gamma\epsilon_y \leq 3 \times 10^{-8}$ m-rad at a repetition rate as high as 180 Hz. The beams in the damping rings consist of multiple trains of 90 bunches with a maximum

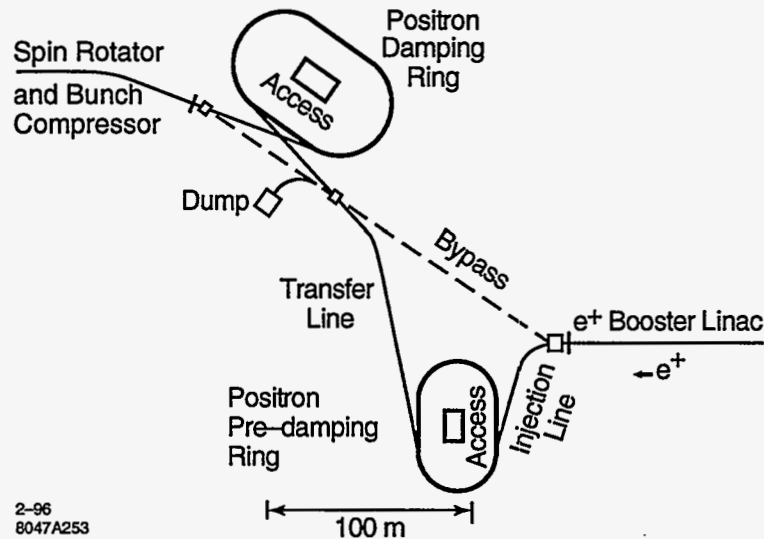


Figure 4-2. Layout of positron damping ring complex along with the two bunch compressors and the positron source.

	NLC-Ic (500 GeV)	NLC-IIc (1 TeV)	NLC-III (1.5 TeV)
$\gamma\epsilon_{x ext}$ (10^{-6} m-rad)	3	3	3
$\gamma\epsilon_{y ext}$ (10^{-8} m-rad)	3	3	3
Charge/Bunch (10^{10})	0.89	1.31	1.31
Bunches/Train	90	90	90
Bunch Spacing (ns)	1.4	1.4	1.4
Repetition Rate (Hz)	180	120	120

Table 4-2. Damping ring beam requirements for NLC designs.

single bunch charge of 1.31×10^{10} (this is 5% higher than the required charge at the IP to allow for beam loss due to collimation).

To satisfy these requirements, the damping ring complex is designed to operate with the parameters listed in Table 4-3 which exceed the requirements of all presently considered NLC upgrades. To provide operational flexibility, we are designing the rings to operate with a peak current roughly 20% higher than the nominal peak current. Many of the limiting requirements (damping times and bunch train lengths) are set by the NLC-Ic (500-GeV-c.m.) design and not the higher energy upgrades. The only parameter that increases in difficulty as the center-of-mass energy is upgraded is the beam charge. This is relevant for the design of the rf system and the vacuum chamber, and the study of collective effects (many of which depend upon the rf and chamber designs).

Table 4-4 lists the parameters of the beams assumed from the electron and positron injectors. The incoming electron emittance is specified as an rms value while the incoming positron emittance is specified as an edge emittance. The transverse injection errors are specified in units of the normalized actions and the permissible energy errors are given in %; the injection errors correspond to oscillation amplitudes that are equal to the

$\gamma\epsilon_{x\,eq} / \gamma\epsilon_{x\,ext}$ (10^{-6} m-rad)	3.0 / 3.0
$\gamma\epsilon_{y\,eq} / \gamma\epsilon_{y\,ext}$ (10^{-8} m-rad)	2.0 / 3.0
Charge/Bunch	1.57×10^{10}
Bunches/Train	90 bunches/train
Bunch Spacing (ns)	1.4
Repetition Rate (Hz)	180

Table 4-3. Requirements for NLC damping ring complex.

	Injected Electrons	Injected Positrons
Charge/Bunch	1.9×10^{10}	2.5×10^{10}
$\gamma\epsilon_{x,y}$ (m-rad)	1×10^{-4} (rms)	0.06 (edge)
$\sigma_{\Delta E/E}$ (%)	1 (FWHM)	2 (FWHM)
$\Delta\gamma J$ (m-rad)	0.5×10^{-4} (rms)	0.03 (edge)
$\Delta E/E$ (%)	0.2 (rms)	0.2 (rms)

Table 4-4. Electron and positron beams at entrance to damping rings.

rms and edge beam sizes for the electrons and positrons, respectively. Both of these values are set by the damping time requirements and not by the dynamic aperture or the multibunch sensitivity to transients both of which have looser tolerances.

4.2.4 Parameters: Damping Times and Equilibrium Emittances

At this point, we can discuss the parameters of the damping rings, in particular, the beam emittances and the required number of damping times. In a damping ring, the required number of damping times and the extracted emittances determine the primary parameters of the design. The emittances from the injectors are summarized in Table 4-4 for both the electrons and positrons and the requirements for the extracted beams are listed in Table 4-3. In examining these parameters, two points are immediately obvious.

First, the requirements for the positron and electron beams are extremely different. Because of the large incoming emittance, the injected positron beam needs substantially more damping and a much larger vacuum aperture. Therefore, we will use a pre-damping ring to damp the injected positron emittance to the level of the incoming electron beam. This allows us to partially separate the problems of large dynamic aperture, small equilibrium emittance, and fast damping. In addition, it allows us to design identical main damping rings for the electrons and positrons while the pre-damping ring is optimized for just the incoming positrons.

Second, the main damping rings must produce beams with a 100:1 emittance ratio, the vertical emittance being much smaller than the horizontal. Thus, the main rings will have to operate far from the coupling resonance. In a ring designed to produce flat beams, the vertical damping time is more critical than the horizontal and there is only one method of decreasing it: increased synchrotron radiation due to high-bending fields or damping wigglers. We will briefly discuss and discard other options subsequently.

In contrast, the pre-damping ring can operate on the difference coupling resonance since the extracted emittances of the pre-damping ring do not need to be asymmetric; the SLC damping rings operated in this

	Main Damping Rings	Pre-damping Ring
Max. Injected $\gamma\epsilon_x, \gamma\epsilon_y$ (m-rad)	$1.5 \times 10^{-4}, 1.5 \times 10^{-4}$	0.09, 0.09 (edge)
Extracted $\gamma\epsilon_x, \gamma\epsilon_y$ (m-rad)	$3 \times 10^{-6}, 3 \times 10^{-8}$	$1.5 \times 10^{-4}, 1.5 \times 10^{-4}$
Equil. $\gamma\epsilon_{eqx}, \gamma\epsilon_{eqy}$ (m-rad)	$3 \times 10^{-6}, 2.0 \times 10^{-8}$	$5 \times 10^{-5}, 5 \times 10^{-5}$
$N_{\tau y}$	4.8	3.2
τ_{eff} (ms)	1.16	1.74

Table 4-5. Damping time requirements for NLC damping rings.

mode until 1992 when it was decided to collide flat beams at the IP. Operating on the coupling resonance reduces the equilibrium emittance by a factor of two and it couples the horizontal damping partition into both planes, effectively increasing the vertical damping rate at the expense of the horizontal.

Now, we can specify the damping times and equilibrium emittances. Ideally, these determine the emittance of the extracted beam as expressed by:

$$\epsilon = \epsilon_i e^{-2N_r} + \epsilon_{eq}(1 - e^{-2N_r}) \quad , \quad (4.1)$$

where ϵ_i is the injected emittance, ϵ_{eq} is the equilibrium emittance, and N_r is the number of damping times the beam has been stored. Because the damping needed in the vertical plane is greater than or equal to that in the horizontal while the damping rate in the vertical is less than or equal to that in the horizontal ($J_x \geq J_y$), the number of damping times is determined from the vertical emittances. Table 4-5 lists the injected emittances from Table 4-4 assuming that the injection-offsets fully filament and add to the beam emittance. Then, we calculate the required number of vertical damping times for the pre- and main damping rings. We have assumed that the pre-damping ring is operating on the coupling resonance so that the extracted emittances are equal and we have assumed equilibrium vertical emittance of $\gamma\epsilon_{y eq} = 2.0 \times 10^{-8}$ m-rad for the main damping ring. Obviously, assuming a larger equilibrium vertical emittance in the main ring increases the required damping and therefore the difficulty of the design. Although requiring smaller a equilibrium emittances imposes stricter magnet and alignment tolerances, it is felt that the necessary alignment tolerances can be attained using beam-based alignment methods.

The NLC main damping rings will damp an injected beam vertical emittance of 1×10^{-4} to 7×10^{-9} . At the same time, we will design the rings to attain an equilibrium vertical emittance less than 2×10^{-8} m-rad; the tolerances are being specified to attain an expected vertical emittance of 1.5×10^{-8} m-rad. Thus, we are providing more damping than necessary. We believe that it is worthwhile investing in the additional damping capability since it provides stability against fluctuations in the incoming beam. Specifically, it allows for injection mismatches or other effects¹ that can increase the effective injected emittance by 50%. This additional damping will be reflected in the injection tolerance of $\gamma J_y \leq 0.5 \times 10^{-4}$. Finally, if necessary, the damping rates can be increased by operating the rings at a higher energy; the rings are being designed to operate at an energy between 1.8 GeV and 2.2 GeV with the nominal energy being 1.98 GeV.

Similar arguments apply to the pre-damping ring. Again, we want to keep the equilibrium emittance small to reduce the damping requirements. Because the pre-damping ring is coupled, the horizontal and vertical emittances and the horizontal and vertical damping rates are equal. In this case, we have chosen to design to coupled emittances of

$$\gamma\epsilon_{x,y eq} \leq 5 \times 10^{-5} \text{ m-rad} \quad (\text{pre-DR}) \quad . \quad (4.2)$$

¹In the SLC electron damping ring, the injected beam does not appear to damp at the expected damping rate during the first millisecond. The cause of this problem is unknown.

Although we have not included any margin in the damping time, we should note that in calculating the required number of damping times for the positron beam, we have used an effective rms injected emittance equal to 70% of the edge emittance.² At the time of this writing, we did not have details of the incoming positron beam distribution but this is undoubtedly an over-estimate of the effective rms emittance and therefore provides a margin on the damping requirements.

Finally, we can specify the required equilibrium horizontal emittance in the main damping rings. Since the rings are uncoupled and $J_x \geq J_y$, the horizontal damping time is less than or equal to the vertical. Therefore, the residual injected horizontal emittance is negligible and the horizontal emittance of the extracted beam is very nearly equal to the horizontal emittance of the ring:

$$\gamma\epsilon_{x\text{eq}} \leq 3 \times 10^{-6} \text{ m-rad} \quad (\text{MDR}) \quad . \quad (4.3)$$

Now we can calculate the required damping times of the rings. The damping times are determined from the desired repetition rate (f_{rep}), the required number of damping times per bunch train (N_τ), and the number of trains stored simultaneously in the rings (N_{train}):

$$\tau_{x,y} \leq \frac{1}{f_{\text{rep}}} \frac{N_{\text{train}}}{N_\tau} \quad . \quad (4.4)$$

The maximum number of trains stored in the rings depends upon the length of the bunch trains and the rise and fall times of the injection and extraction kickers. The kicker rise and fall times depend upon the required kicker amplitude and stability [Mattison 1995]. The SLC damping ring kickers have rise and fall times of 60 ns. Although the stability requirements are tighter in the NLC main damping rings than in the SLC rings, the amplitude and physical design constraints are looser. Thus, it is thought that 60 ns will be sufficient for the rise and fall time of the NLC main damping ring kickers. The situation is different in the pre-damping ring. Here the amplitude requirements are more severe than those in the SLC rings but the stability requirements are comparable and again the physical design constraints are looser. Thus, again we feel that 60 ns will be sufficient for the rise and fall time of the pre-damping ring kickers.

Note that when damping multiple trains of bunches at the same time, the damping time *per se* is not the relevant parameter. Instead, we are concerned with the damping time scaled by the number of bunches in the ring which is roughly proportional to the ring circumference; two rings, one with twice the damping time but storing twice as many trains, will have the same damping performance. Thus, we define an effective damping time:

$$\tau_{\text{eff}} \equiv \frac{\tau}{N_{\text{train}}} = \tau \frac{T_{\text{train}}}{T_0} \quad , \quad (4.5)$$

where T_{train} is the length required per bunch train including the gap between the trains, and T_0 is the ring circumference. The effective damping time then depends upon the repetition rate and the number of damping times per bunch. In the NLC main damping rings, the effective damping time is:

$$\tau_{\text{eff}} \leq \frac{1}{f_{\text{rep}} N_\tau} = 1.16 \text{ ms} \quad (\text{EDR, PDR}) \quad , \quad (4.6)$$

while in the pre-damping ring

$$\tau_{\text{eff}} \leq 1.74 \text{ ms} \quad (\text{PPDR}) \quad . \quad (4.7)$$

²When a beam is damped in a ring, the injected distribution is not modified until the emittance is damped close to the equilibrium emittance of the ring. Since an aperture limited beam, such as the incoming positrons, will not have a gaussian distribution, it is not reasonable to parameterize the emittance with the rms value. Instead, because we are interested in the core density of the beam, we will define the effective emittance using the FWHM: $\sigma_{\text{eff}} = 0.4 \text{ FWHM}$. Using this parameterization and assuming that the initial distribution is uniform, $\epsilon_{\text{eff}} \approx 0.7\epsilon_{\text{edge}}$. This is the value assumed for the pre-damping ring design.

4.2.5 Scaling Relations

Equations 4.2, 4.3, 4.6, and 4.7 determine the basic parameters. Initially to study these parameters we ignored the option of damping wigglers, assuming an isomagnetic ring, and we neglect the effect of intrabeam scattering. In this case, we can write simple expressions for $\gamma\epsilon_{x\text{ eq}}$ and $\tau_{y\text{ eff}}$, the two quantities we wish to calculate:

$$\tau_{y\text{ eff}} = 1.69 \times 10^{14} \frac{T_{\text{train}}}{\gamma^3 G_B} = \frac{2.88 \times 10^{12} T_{\text{train}}}{B_0 [kG] \gamma^2} \quad (4.8)$$

$$\gamma\epsilon_{x\text{ eq}} = 3.84 \times 10^{-13} \frac{\gamma^3}{J_x} \langle \mathcal{H} \rangle_B G_B = \frac{65 T_{\text{train}} \langle \mathcal{H} \rangle_B}{\tau_{y\text{ eff}} J_x} \quad (4.9)$$

Here, G_B is the inverse bending radius of the bending magnets, $\langle \mathcal{H} \rangle_B$ is the average of \mathcal{H}_x over the bending magnets, B_0 is the magnetic field in kGauss, and we have assumed that $J_y = 1$. Finally, T_{train} is the train length which is determined by the length of the bunch train and the injection and extraction kickers.

Equations 4.8 and 4.9 show that the emittance of a ring can be decreased by reducing the dispersion in the bending magnets, reducing the strength of the bends, or decreasing the energy of the ring. Unfortunately, the damping times are increased by reducing the bending magnet strength or decreasing the energy of the ring. This implies that the dispersion in the bends is the only free parameter. Unfortunately, it is also constrained.

In the NLC design, we would like to limit the ring energy to roughly 2 GeV; reasons for this choice are discussed in Section 4.2.6. If we then apply these formula to the main damping rings, we find that we need a 30-kGauss bending field to attain the desired damping. This is not reasonable and therefore we consider additional methods of increasing the damping.

The most obvious method of increasing the damping is to use damping wigglers. Another method of increasing the damping is to change the horizontal damping partition. Unfortunately, this has no effect on the vertical damping if the ring is not coupled. Regardless, changing the horizontal damping partition will decrease the equilibrium horizontal emittance which is another quantity we need to reduce. The damping partition can be changed with a defocusing gradient in the bending magnets—Robinson wigglers are not effective because of the high dispersion that is needed [Raubenheimer 1988]. Unfortunately, damping wigglers reduce the change of J_x . Thus, to change J_x significantly, one is forced to use very high gradients in the bending magnets which makes the option less desirable.

The scaling formulas Eqs. 4.8 and 4.9 can be modified to include the effects of damping wigglers:

$$\tau_{y\text{ eff}} = \frac{2.88 \times 10^{12} T_{\text{train}}}{B_0 (kG) \gamma^2 (1 + F_w)} \quad (4.10)$$

$$\gamma\epsilon_{x0} = \frac{65 T_{\text{train}}}{\tau_{y\text{ eff}} (J_{x0} + F_w)} \frac{(\langle \mathcal{H} \rangle_B + 6 \overline{\beta_x} F_w \rho_0 / 5 \pi k_w^2 \rho_w^3)}{(1 + F_w)} \quad (4.11)$$

where J_{x0} is the damping partition without wigglers and the parameter F_w is a measure of the effectiveness of the wigglers,

$$F_w \equiv \frac{L_w}{\pi} \frac{B_w^2}{B_0} \frac{1}{B \rho} = \frac{L_w}{\pi} \frac{\rho_0}{\rho_w^2} \quad (4.12)$$

In addition, L_w and B_w are the length and peak field of the wiggler; $\overline{\beta_x}$ is the average beta function in the wiggler, and k_w is the wiggler wave number, $k_w = 2\pi/\lambda_w$ where λ_w is the wiggler period. Also, ρ_0 and ρ_w

are the bending radii of the main bends and the wiggler. Both bending radii are proportional to the energy over the respective magnetic fields. We have assumed sinusoidal wigglers, and thus the average of $B_w^2(s)$ over the wiggler is equal to $\frac{1}{2}\hat{B}_w^2$. In addition, we assume that $\overline{\beta_x} \gg \lambda_w/2\pi$ so that the $\eta_x^2\beta_x$ term dominates in the excitation term from the wiggler.

As described in Section 4.2.7, in the NLC main damping ring design we have decided to equalize the contributions from the wigglers and the arcs to the radiation damping. This specifies that the term F_w is equal to 1. At this point, we can discuss the Halbach scaling formula for hybrid wigglers [Halbach 1985]:

$$B_w \leq 3.44 \exp \left[-\frac{g}{\lambda_w} \left(5.08 - 1.54 \frac{g}{\lambda_w} \right) \right] , \quad (4.13)$$

which is roughly valid for $0.08 < g/\lambda_w < 0.7$. This suggests that one can achieve a peak field of $B_w = 22$ kGauss (close to the saturation point of Vanadium Permendur) in a wiggler with a gap of 2 cm and a period of 20 cm. In practice, this scaling result is optimistic when close to saturation but it provides a starting point from which one can determine the wiggler parameters.

4.2.6 Ring Energy

There are a number of considerations when determining the ring energy. First, the desire to maintain high-spin polarization while damping the beams suggests that the nominal ring energy should be chosen so that the spin tune is a half integer. This limits the energy to

$$E = (n + 0.5)440 \text{ MeV} = 1.10, 1.54, 1.98, 2.42, \dots \text{ GeV} . \quad (4.14)$$

Second, we would prefer to keep the ring energy low for two primary reasons: it keeps the ring cost lower and it keeps the normalized longitudinal emittance small, making the bunch compression easier. The NLC requires that the damping ring bunch be compressed longitudinally by roughly a factor of 40. We do not want an uncorrelated energy spread much greater than 1% in the linac and thus we need to perform at least a portion of the bunch compression at an energy five times that of the damping ring. Unfortunately, at higher energies it becomes more difficult to perform the compression without degrading the beam emittances.

The problem with a low-energy ring is that it is harder to attain the required damping using reasonable magnet designs. We can understand the choices using the scaling formula. First, using Eqs. 4.10 and 4.12 and assuming that the fraction of damping due to the wigglers F_w and the wiggler peak field B_w are fixed, we find that, to meet the damping time requirements, the main bending field and the required length of wiggler scale as

$$B_0 \sim \frac{1}{\gamma^2} \quad \text{and} \quad L_w \sim \frac{1}{\gamma} . \quad (4.15)$$

Thus, as the ring energy is increased, the bending magnets and wigglers become easier to design and construct.

Next, using Eq. 4.11 and noting that the dispersion invariant scales as $\langle \mathcal{H} \rangle_B \sim \Theta^3 \rho_0 \sim \Theta^3 \gamma / B_0$, we find that, to maintain the equilibrium emittance,

$$N_{\text{cell}} \sim \gamma \quad \text{and} \quad L_{\text{bend}} \sim \gamma^2 . \quad (4.16)$$

Finally, given these relations, the length of the ring, the momentum compaction, and the synchrotron radiation power must scale as

$$L_{\text{ring}} \sim \gamma^3 \quad \text{and} \quad \alpha_p \sim 1/\gamma^2 \quad \text{and} \quad P_{\text{SR}} \sim U_0 \sim \gamma , \quad (4.17)$$

where we assumed that the cell length scales in the same manner as the length of the bends. The cost of the rings will tend to increase with the length, while the cost of the rf systems will increase with the power required; both of these costs will increase with higher energy. In addition, the momentum compaction decreases with the square of the ring energy while rough scaling for the longitudinal microwave threshold scales as $\gamma\alpha_p$. This suggests that longitudinal stability may be more difficult at higher energy.

Thus, the determination of the nominal ring energy becomes an optimization between the difficulty of the bending and wiggler magnets versus the decrease in momentum compaction, and the increase in size and cost of the ring. We should attempt a cost optimization, but for this iteration of the NLC damping ring design, we have picked an energy of 1.98 GeV and a spin tune of roughly 4.5. This is the lowest energy that appears to yield reasonable designs for the bending magnets and wigglers. Of course, during operation, we may want to vary the ring energy to optimize for a lower repetition rate or a larger injected emittance. For this reason, we are designing the rings to operate over the 1.8–2.2-GeV range; this range extends between the two nearby integer spin resonances.

Finally, it is worth noting that intrabeam scattering does not present justification for increasing the ring energy. *When the effective damping times are held constant*, the emittance growth due to intrabeam scattering does not decrease with the ring energy [Raubenheimer 1991]. Using very simple scaling formula, the emittance growth depends upon the intrabeam scattering growth rate compared to the synchrotron radiation damping. The intrabeam scattering growth rate scales roughly as

$$\tau_{x\text{ IBS}}^{-1} \sim \frac{N\langle\mathcal{H}\rangle}{\gamma\epsilon_x\gamma\epsilon_y\gamma\epsilon_z} \quad (4.18)$$

which, for given normalized emittances, is independent of energy, while the damping rates scale inversely with the ring length which increases as γ^3 . Thus, emittance growth due to intrabeam scattering actually becomes worse as the design energy is increased.

4.2.7 Wigglers vs. Arcs

At this point, we can discuss the difference between designing a wiggler with arcs or a ring with wigglers. In the former, the radiation damping in the wiggler dominates the radiation damping in the arcs, *i.e.*, the parameter F_w is much greater than 1. In this case, the contribution of the quantum excitation in the arcs is suppressed by roughly a factor of $(1 + F_w)^2$. This allows one to design the arcs with a much larger dispersion which leads to a larger contribution to the momentum compaction and makes the chromatic correction easier. Unfortunately, the gains in the momentum compaction and chromatic correction are partially offset by the additional length of wiggler that is required.

The Japan Linear Collider (JLC) damping rings [JLC] are an example of this design style. There, roughly 80% of the damping is performed in the wigglers and the requirements on the arcs are substantially reduced. But, the JLC design requires 140m of high-field wiggler and the momentum compaction and dynamic aperture, if larger at all, do not appear to be significantly larger.

For the NLC main damping ring design, we have decided to pursue another approach: we want to divide the radiation damping equally between the arcs and the damping wiggler. We feel that this is a more efficient use of magnets and space. It exchanges some of the difficulties of dealing with a very long wiggler system with the arcs. Preliminary comparisons between the JLC and NLC rings show that they both have similar performance expectations.

4.2.8 Lattice Specification

At this point, we can apply the scaling formula to estimate the parameters for the NLC damping rings. First, we can estimate the bending field required in the pre-damping ring to meet the damping time requirements. The pre-damping ring needs to attain an effective damping time of $\tau_{y\text{eff}} = 1.74\text{ms}$ (Eq. 4.7). Assuming that damping wigglers are not used, limiting the change to the horizontal damping partition to $J_x = 1.3$, and allowing 60 ns for the rise and fall times of the injection and extraction kickers, Eq. 4.10 shows that the bending field must be $B_0 = 17.5\text{kGauss}$; this is comfortably below the saturation point of standard magnet iron. Two points to note: first, the required field is independent of the number of trains stored in the ring at once, and second, without changing J_x , the required field would be 20 kGauss which is quite high.

A similar procedure can be used to estimate the bending fields and wigglers fields required in the main damping rings. Assuming that wigglers are used to perform half the required damping and that the bunch trains are separated by 60 ns, Eq. 4.10 shows that the bending field must be $B_0 = 15.1\text{kGauss}$. If we limit the peak wiggler field to 22 kGauss, Eq. 4.12 shows that we need 26 m of wiggler.

Now, we have to specify a lattice that will meet the emittance requirements. For the main damping ring, we have considered four different lattice cell structures: a FOBO cell, which is a FODO cell where the defocusing quadrupole is replaced by a bending magnet with a defocusing gradient, a Chasman-Green lattice, a Triple Bend Achromat (TBA) lattice, and a Theoretical Minimum Emittance (TME) lattice. The advantages and disadvantages of each are summarized below:

- FOBO
 - + Simple FODO-like structure with well-constrained beta-functions
 - Uses three quadrupoles per bending magnet (assuming symmetric form)
 - Less efficient at generating emittance
 - Difficult combined function bending magnet
- Chasman-Green
 - + Fairly efficient at generating emittance
 - + Two quadrupoles per bending magnet
 - + Excellent dynamic aperture behavior in R. Brinkmann's comparison [Brinkmann 1990].
 - + Presently used at ESRF and ELETTRA
- TBA
 - + Fairly efficient at generating emittance
 - + Two quadrupoles per bending magnet
 - + Presently utilized at ALS and PLS
- TME
 - + Very efficient at generating emittance (fewer bends)
 - + Easy to optimize ratio of α_p and \mathcal{H}
 - + Excellent dynamic aperture in studies

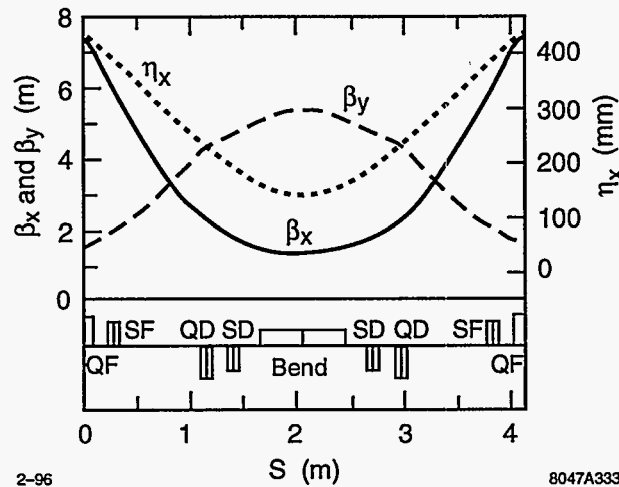


Figure 4-3. Lattice functions in a FOBO cell.

Lattice (GeV)	Energy (10^{-6} m-rad)	$\gamma\epsilon_{x\text{eq}}$ (10^{-3})	α_p (m)	Circ.	N_{bends} (10^{-3} m-rad)	Norm. Accept. X/Y
FOBO	2.2	4.4	1.4	133	80	36 / 17
Chasman-Green	2.0	3.0	0.6	154	72	4 / 14
TBA	2.0	3.4	0.7	177	72	14 / 10
TME	2.0	3.2	0.7	158	40	36 / 26

Table 4-6. Parameters for different lattice structures [Moshhammer, 1993].

– Three quadrupoles per bending magnet

To study the different structures, we made preliminary designs for the NLC main damping rings using each of these four lattices [Moshhammer 1993]; the rings were designed in a race-track form with two arcs, including dispersion suppressors, and roughly 10m of straight section which could be expanded into injection and extraction and wiggler sections. Parameters and tracking results for the four designs are listed in Table 4-6 and the cell lattice functions are plotted in Figures 4-3, 4-4, 4-5, and 4-6. Notice that the dispersion is not matched to zero at the ends of the Chasman-Green and TBA cells; zero dispersion is not necessary after most cells in the ring and one can obtain smaller emittances by matching to nonzero values. The only advantage these preliminary results indicated was that for equal ring energy, the TME design used fewer and longer bending magnets with lower field gradients. This was thought to be sufficiently important that it outweighed the advantage of using a more standard lattice such as the Chasman-Green or TBA. Thus, we decided to complete a design based upon the TME structure and study the other lattices further in the future.

The optimization is different in the positron pre-damping ring. Here, the equilibrium emittance is easily attained and the primary issues become attaining the desired dynamic aperture and constraining the beta-functions to keep the required vacuum aperture relatively small. The FOBO lattice which is basically a simple FODO structure seems to be the best choice in this case; typical lattice functions are plotted in Figure 4-3. The FOBO structure was felt to be superior to the more standard FODO structure because it

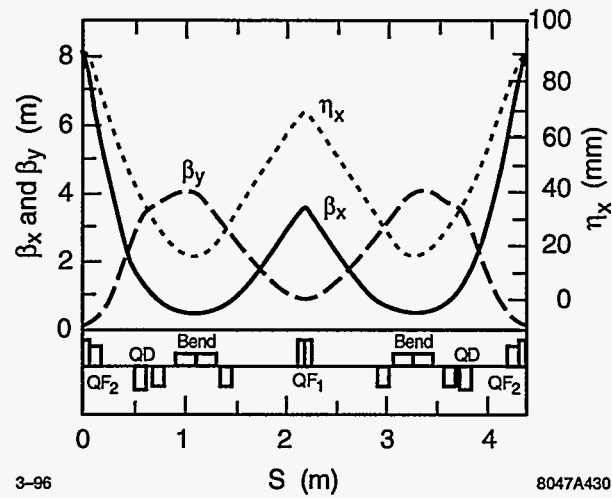


Figure 4-4. Lattice functions in a Chasman-Green cell.

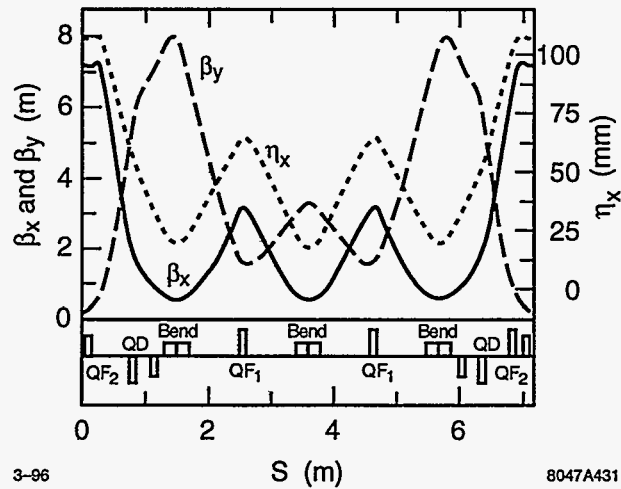


Figure 4-5. Lattice functions in a TBA cell.

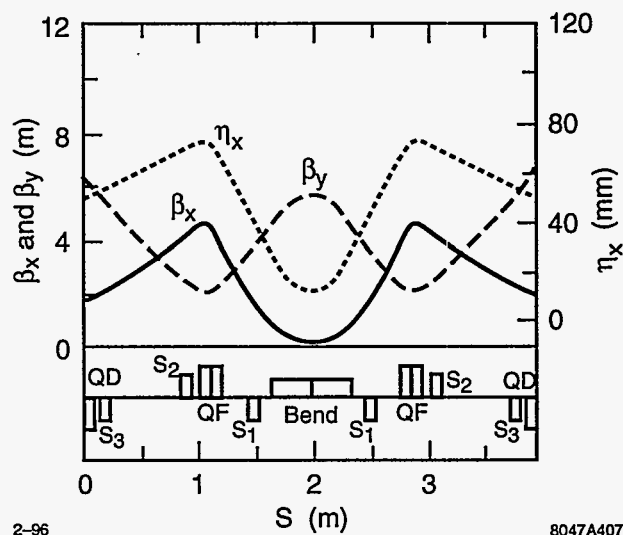


Figure 4-6. Lattice functions in a TME cell.

allows one to increase the horizontal damping partition and thus increase the transverse damping rates when the ring operates on the betatron coupling resonance.

4.2.9 RF Parameters

In both the pre-damping ring and the main damping rings, the rf is chosen to be 714 MHz. This is as low as consistent with the bunch spacing of 1.4 ns. There are several advantages of the low-frequency choice. First, for a given rf voltage, the lower frequency has a higher stored energy in the cavities thereby reducing the beam loading and the bunch-to-bunch synchronous phase shift. Second, the coupled-bunch instability driven by the fundamental mode of the cavities has a smaller growth rate. Finally, two other advantages of the lower frequency is the increased bunch length in the main damping rings and the larger energy acceptance in the pre-damping ring.

The minimum rf voltage is determined by the synchrotron radiation, HOM losses, and the height of the energy bucket. In the pre-damping ring, we would need an rf voltage in excess of 3.5 MV to capture the full $\pm 2\%$ incoming energy spread. Instead, we use an energy compressor to reduce the injected energy spread at the expense of increasing the bunch length. We expect the compressor will be able to reduce the incoming energy spread by a factor of two. With the compressor, an rf voltage of 2.0 MV should be sufficient; this provides an energy bucket of $\pm 1.5\%$.

In the main damping rings, we are designing for an rf voltage of 1.0 MV. This is the lowest voltage that is consistent with the energy loss per turn of roughly 700 kV. The main rings have a very small momentum compaction and we want to keep the voltage low to keep the bunch length relatively long. Space is being left in the design to allow for future upgrades of the rf system to 1.5 or 2.0 MV.

Finally, the harmonic number of the rings is chosen to allow operation with fewer, but possibly longer, bunch trains at a reduced repetition rate. Since one would like to place the trains symmetrically in the ring, this requires that the harmonic number be a multiple of all the different numbers of trains being considered.

Thus, while the PPDR has been designed to damp three trains of bunches at the same time, we have chosen an even harmonic number so that it could also operate with two evenly spaced bunch trains. Similarly, the EDR and PDR have been designed to operate with four trains of bunches at a 180-Hz repetition rate. To allow for operation with three bunch trains at 120 Hz, the harmonic number should be a multiple of 4 and 3. Unfortunately, the present design has a harmonic number of 532 which is not ideal. In the next design iteration, the rings will be modified to have an harmonic number of 540.

Finally, it should be noted that the harmonic numbers of the rings do not need to be related from timing considerations because only single bunch trains are injected on any machine cycle. In particular, the PPDR has a slightly larger gap between bunch trains allow more time for the injection and extraction kickers to rise and fall.

4.3 Lattice Design

In this section, we will describe the layouts and optics of the main damping rings, the pre-damping ring, the injection and extraction transport lines, and the PPDR to PDR transport line. After describing the optical designs, we will discuss the lattice related accelerator physics issues. This includes trajectory correction, emittance control and matching, dynamic and energy apertures, and polarization. These are all low-current effects. Collective effects are discussed in Section 4.4 and the rf and vacuum systems are described in Sections 4.5 and 4.6. In addition, the feedback systems and support and alignment systems are described in Sections 4.7 and 4.9 and the magnet and diagnostics designs are describe in Sections 4.10 and 4.11.

At the time of this writing, the design of the main damping ring is fairly complete. We do not feel that there are any significant flaws in the design although a lot of detailed engineering is still required; this is particularly true of the rf cavities and the bending magnets. The only significant modification currently planned is increasing the ring circumference to increase the harmonic number from 532 to 540; this will facilitate operation with either 4 or 3 bunch trains. The circumference change will be made by increasing the length of the two straight sections by roughly 1.7 meters which will have the side benefit of making the vacuum chamber design simpler in the wiggler region.

The design of the pre-damping ring has not yet been investigated in the same depth as the main damping ring design. At this time, we have a design that appears to meet all of the requirements but many of the component designs have not yet been considered. As stated in the introduction, our belief is that the pre-damping ring is significantly more straightforward than the main damping rings except for two issues: the injection and extraction systems and the dynamic aperture. Both of these arise from the very large injected beam emittances and both of these are addressed in our design.

4.3.1 Main Damping Rings

As described, the Electron and Positron Damping Rings (EDR and PDR) are designed to damp beams with an injected emittance of $\gamma\epsilon_{x,y} = 1 \times 10^{-4}$ m-rad to an emittance of $\gamma\epsilon_x = 3 \times 10^{-6}$ m-rad and $\gamma\epsilon_y = 3 \times 10^{-8}$ m-rad. The damping and emittance requirements on the rings are described in Section 4.2.3. The determination of the design parameters is discussed in Sections 4.2.6–4.2.9; these parameters are summarized in Table 4-7.

Energy	1.8 ~ 2.2 GeV; 1.98 GeV nominal
Circ.	223 m
Max. Current	1.2 A
Max. N_{bunch}	1.57×10^{10}
Trains	4 trains of 90 bunches
Train Separation	60 ns
Bunch Separation	1.4 ns
Max. Rep. Rate	180 Hz
ν_x, ν_y, ν_z	23.81, 8.62, 0.004
$\gamma\epsilon_x$	2.56×10^{-6} m-rad
$\gamma\epsilon_x, \gamma\epsilon_y$ with IBS	3.1×10^{-6} m-rad, 1.5×10^{-8} m-rad
σ_ϵ	0.09%
σ_z	4.0 mm
$\xi_{x\text{ uncorr}}, \xi_{y\text{ uncorr}}$	-41.8, -22.4
τ_x, τ_y, τ_z	4.06 ms, 4.62 ms, 2.50 ms
U_{SR}	644 KV/turn
J_x	1.14
α_p	0.00047
V_{RF}	1.0 MV
f_{RF}	714 MHz
Lattice	40 TME Cells

Table 4-7. Parameters for main damping ring (vers. 6.11)

The lattice is based on detuned Theoretical Minimum Emittance (TME) cells which were chosen because of eased requirements on the bending magnets. The chromaticity is corrected with three families of sextupoles and the dynamic aperture is more than sufficient. The damping is performed using both high-field bending magnets and a damping wiggler. The bunch trains are injected onto and extracted from the closed orbit using pulsed kickers and DC septa. Finally, all of the quadrupoles and all of the sextupoles will have independent power supplies. This facilitates beam-based alignment as well as matching of the lattice functions; both of these are important for attaining the desired vertical emittance.

In the next sections, we will describe the ring layout and then details of the ring lattice: the arcs and the dispersion suppressors, the wiggler and injection and extraction straight sections, and the placement of the rf cavities. In addition, the rf and vacuum systems are described in Sections 4.5 and 4.6 while the feedback systems and support and alignment systems are described in Sections 4.7 and 4.9. Finally, the magnet and diagnostics designs are describe in Sections 4.10 and 4.11.

Layout

The NLC main damping rings are roughly 223 m in circumference and measure 50 m by 80 m. They have a nominal energy of 1.98 GeV and required damping is achieved using both high field bending magnets and roughly 26 m of damping wiggler. The rings are designed in a race-track form with two arcs separated by straight sections; the layout is illustrated in Figure 4-7. Each arc consists of 19 TME cells plus dispersion matching sections. The straight sections are roughly 30 m in length. On one side of the ring, the straight section is devoted to the damping wigglers while the other straight section contains the injection and extraction components and the rf cavities. The arc cells, which are roughly 4 m in length, have one

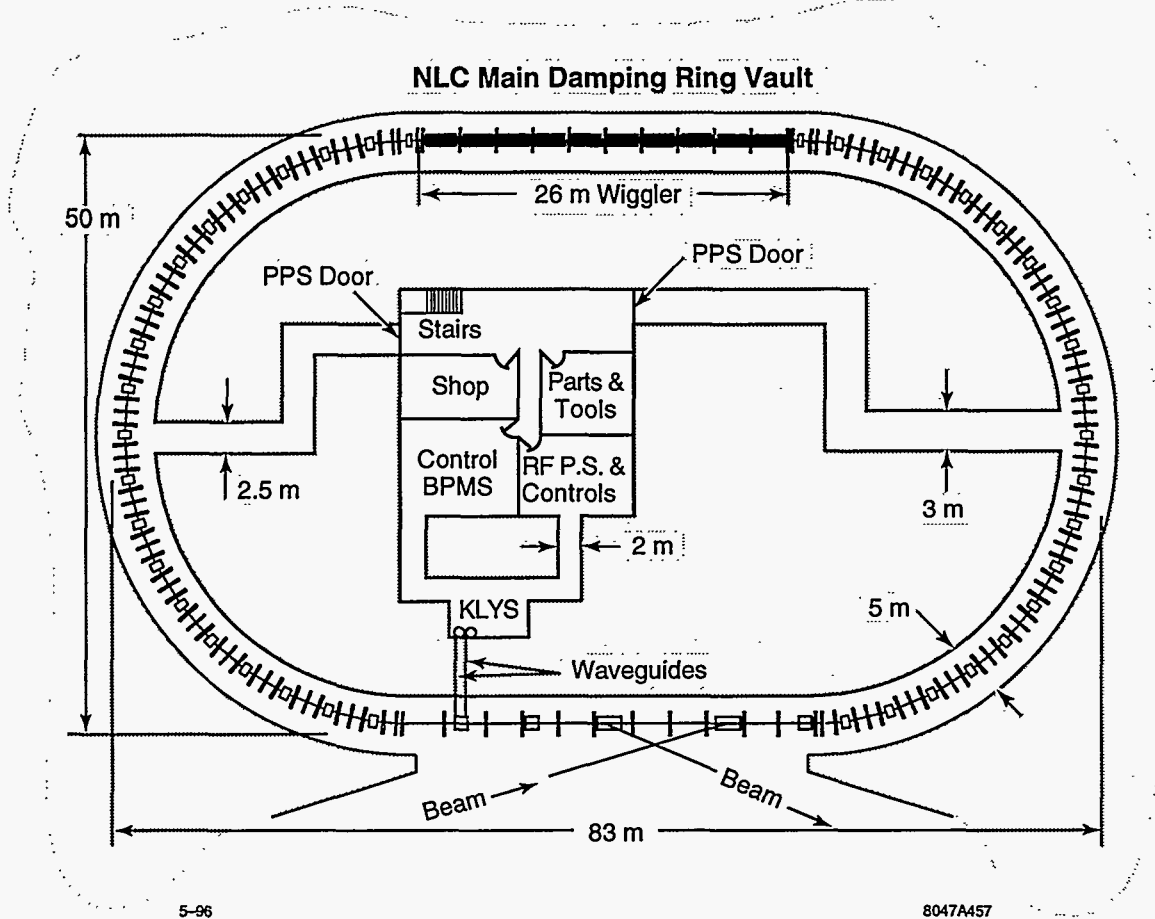


Figure 4-7. Layout of main damping ring.

bending magnet, six sextupole magnets, three quadrupoles, and their own integral vacuum chamber. The wiggler straight section consists of 10 separate wiggler sections. The injection and extraction straight section contains: two kicker magnets and two septa for injection and extraction, two rf cavities, feedback striplines, and thirteen quadrupoles. Other components such as polarization monitors, optical monitors, and wire scanners will be added to this section.

At this time, we have not investigated the civil construction of the damping ring enclosures. Ideally, to minimize the disturbance to the ground, the ring enclosure will be constructed as a tunnel and not a vault. Although only schematically illustrated in Figure 4-7, the design goal will be to place all electronics, power supplies, kicker thyratrons, and rf klystrons in an accessible shielded region at the center of the ring. This will minimize cable and waveguide distances while allowing for maintenance and repair during operation.

Arcs

Each arc consists of 19 TME cells plus dispersion matching sections. Optimized TME cells are designed to attain the minimum emittance that is possible in a bending magnet. To do this, three quadrupoles are

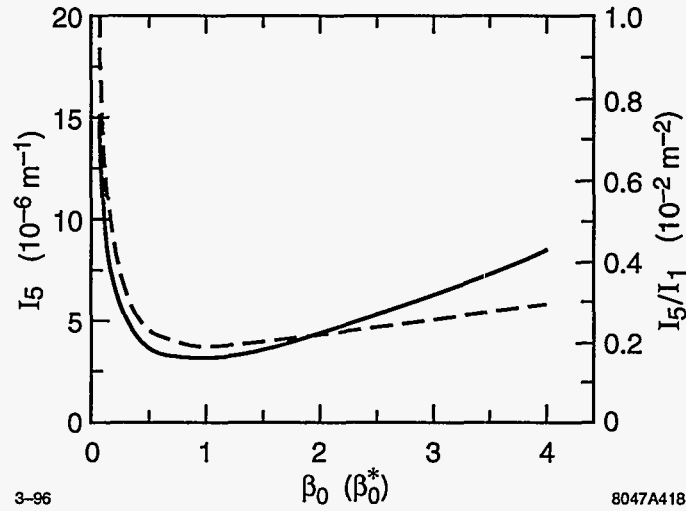


Figure 4-8. I_5 (solid) and I_5/I_1 (dashes) versus β_0 for TME cells.

placed between the bending magnets and are used to minimize the average dispersion invariant \mathcal{H} through the bending magnets. In general, this minimum is found when the dispersion and horizontal beta functions have minima at the center of the dipoles. Explicitly, the minimum emittance should be found when [Teng 1985]

$$\beta_{x0}^{TME} \approx \frac{L_B}{\sqrt{60}} \quad \eta_{x0}^{TME} \approx \frac{L_B^2}{24\rho} \quad (4.19)$$

where β_0 and η_0 are the values at the center of the dipole and L_B is the length of the dipole.

Unfortunately, minimizing $\langle \mathcal{H} \rangle$ also implies a small value of the momentum compaction. We would like to keep the momentum compaction large since this eases the requirements on the longitudinal impedance due to the longitudinal microwave instability and it leads to a longer bunch length which is also desirable. Thus, we chose parameters in the cells to optimize the ratio of I_1/I_5 for a given bending angle rather than \mathcal{H} (or I_5). In this case, the optimal values of the dispersion at the center of the bending magnet is equal to

$$\eta_0^* \approx -\frac{L_B^2}{24\rho} + \frac{L_B}{\sqrt{15}} \sqrt{2L_B^2 + 5\beta_0^2} \quad (4.20)$$

This value is actually close to the optimal TME value.

In Figure 4-8, we plot the variation of I_5 (solid), which is proportional to \mathcal{H} , and I_5/I_1 (dashes), which is proportional to the ratio of \mathcal{H} to α_p , versus β_0 for the case when $\eta_0 = \eta_0^*$. Notice that both curves have minima near the optimum beta function but do not increase very rapidly as β_0 is increased. In practice, we detune the cell so that $\beta_0 \approx 2\beta_0^{TME}$; this reduces the chromaticity. In Figure 4-9, we plot the variation of I_5 (solid) and I_5/I_1 (dashes) against η_0 for $\beta_0 = 2\beta_0^{TME}$. In this case, the optimum \mathcal{H} occurs at roughly η_0^{TME} while the optimum \mathcal{H}/α_p occurs around $\eta_0 \approx 2\eta_0^{TME}$. We have chosen to optimize the cells to this latter value.

Each TME cell consists of two QF quadrupoles, a single QD quadrupole, and a single bending magnet with a defocusing gradient. The defocusing gradient in the bending magnets increases both the quantum excitation and J_x . In a ring without damping wigglers, the increase in J_x is larger than the increase in the excitation and the equilibrium emittance can be decreased by as much as a factor of two. But, the emittance and

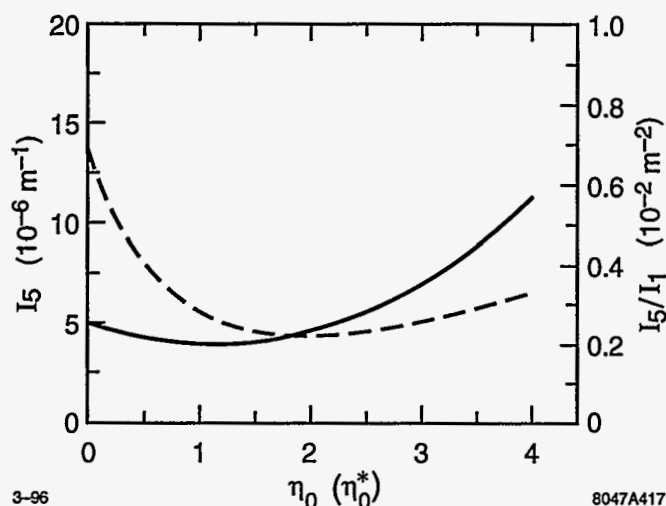


Figure 4-9. I_5 (solid) and I_5/I_1 (dashes) versus η_0 for TME cells.

damping time reduction is less when damping wigglers are included since they reduce the change to J_x for a given gradient. Because the main damping rings do not need the additional horizontal damping and because it takes large gradients to achieve a significant reduction in the emittance, we have chosen a gradient that optimizes the matching through the cells while producing $J_x = 1.14$.

The length of each cell is roughly 3.9 m. The vacuum chamber is circular with a 1.25-cm inner radius and an ante-chamber is needed to handle the intense synchrotron radiation. The lattice functions for a cell are plotted in Figure 4-10 and the component layout is illustrated in Figure 4-11. The magnets and vacuum system are described in Sections 4.10 and 4.6.1, respectively.

The dipole steering correction is performed using trim windings on the sextupoles. There are two horizontal correctors and one vertical corrector in each cell. In addition, there are three button BPMs per cell. These are located at the sextupole magnets on either side of the bending magnet and one of the sextupoles adjacent to the defocusing quadrupole.

The chromatic correction is performed using three sextupole families in the arcs as illustrated in Figure 4-10. There is one defocusing family placed on either side of the bending magnets and a focusing and defocusing sextupole placed adjacent to the focusing and defocusing quadrupoles. Thus, there are six sextupoles per cell. At this time, it is not believed that additional sextupoles located in nondispersive regions or additional families of sextupoles are needed. The three sextupole families allow us to correct the chromaticities while also minimizing the tune shift with amplitude terms. This yields a dynamic aperture that is more than sufficient (Section 4.3.9).

Finally, the dispersion is matched to zero at the end of the arcs for the two straight sections. The matching is performed using the three upstream quadrupoles and a bending magnet with an integrated strength that is half of the arc bending magnets. We have assumed that the magnetic field of the matching bends is decreased to reduce excessive fringing fields. The gradient is scaled at the same time so that the matching bends can be constructed using the same pole shape as the main ring bends.

The horizontal and vertical dispersion matching will be tuned using the matching quadrupoles, which have individual power supplies, and trim windings on the adjacent sextupoles that will be wired as skew quadrupoles. Four additional skew quadrupole windings are located in each arc for local correction of the

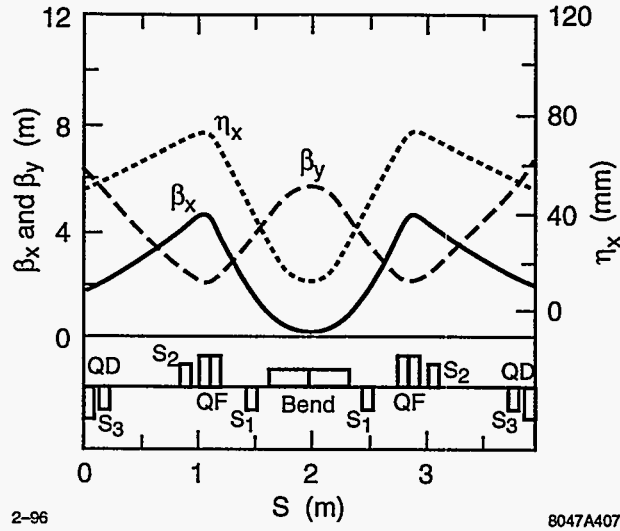


Figure 4-10. β_x (solid), β_y (dashes), and η_x (dots) in main damping ring cell.

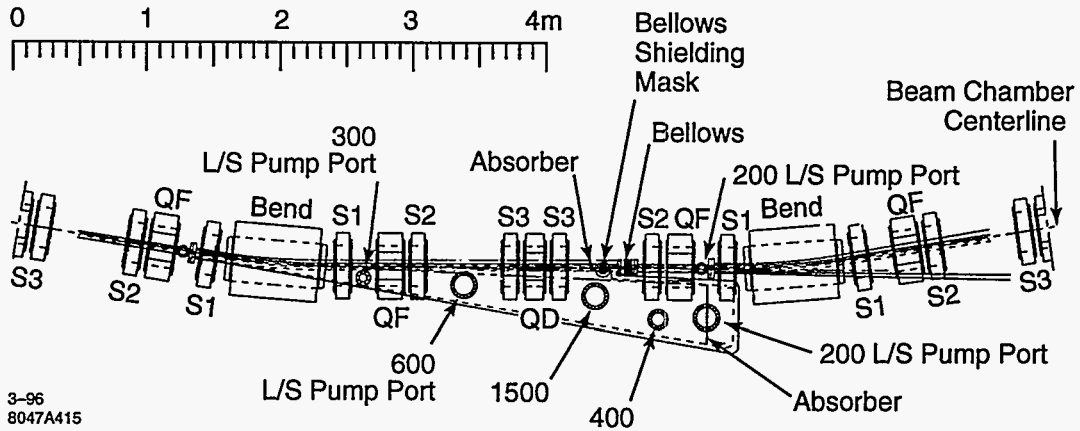


Figure 4-11. Cell layout in a main damping ring cell showing magnet and vacuum chamber components; note the bending magnets are drawn as "H" magnets although the present design utilizes "C" bending magnets.

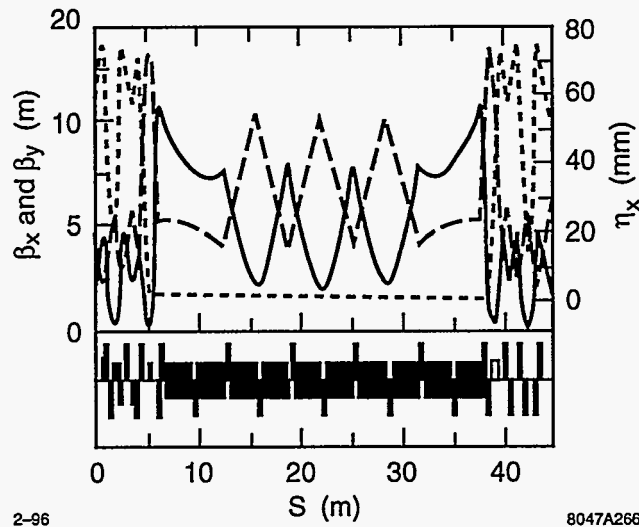


Figure 4-12. β_x (solid), β_y (dashes), and η_x (dots) in main damping ring wiggler region.

vertical dispersion which is the most important contribution to the vertical emittance; this is discussed further in Section 4.3.8.

Wiggler Region

The wiggler region consists of five FODO cells with 3.0-m drifts between the quadrupoles. There are ten 2.6-m wiggler sections to be placed within the region with roughly 21 cm of space between the wiggler ends and the quadrupoles. The wigglers have a 2-cm full gap. To handle the intense synchrotron radiation, the vacuum chamber will have integrated pumping in ante-chambers on both sides of beam chamber. The adjacent quadrupoles have a 3-cm pole-tip radius so that they fit around the chamber. The wiggler magnet sections are described in Section 4.10.1: "Wiggler Magnets".

To minimize the emittance growth in the wigglers, we need to minimize the average horizontal beta function through the region. The average beta function is minimized at a phase advance of roughly 101.5° per cell, but this is a flat minimum and the chromaticity per cell increases rapidly as the phase advance increases. Thus, we have chosen horizontal and vertical phase advances of roughly 90° and 60° per cell.

The lattice functions are matched from the dispersion suppressors with two quadrupoles immediately following the suppressor and the first two quadrupoles at either end of the wiggler region. This allows the region to remain matched if the wiggler strength is varied. The lattice functions from the last TME cell through the wiggler region are plotted in Figure 4-12.

The dipole steering correction will be performed using trim windings on the quadrupoles wired as dipoles and button BPMs located next to the quadrupoles. The BPMs will be shielded to protect them from the large angle (low energy) synchrotron radiation.

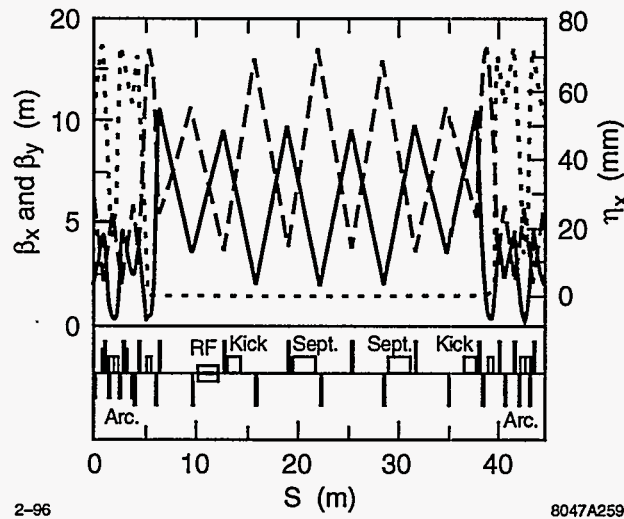


Figure 4-13. β_x (solid), β_y (dashes), and η_x (dots) in main damping ring injection and extraction region.

Injection-Extraction Region

The beams are injected and extracted in the injection-extraction straight section. To reduce the rf transients, beams are injected and extracted simultaneously. In this way, the beam current through the rf cavities is not interrupted.

The injection-extraction region is simply a mirror image of the wiggler region. It consists of five FODO cells with 3.0-m drifts between quadrupoles. The matching of the lattice functions is performed with four matching quadrupoles at either end of the region. The placement of the kickers and septa is illustrated in Figures 4-13 and 4-14 and the extracted beam trajectory, along with the position of the septum blade, is illustrated in Figure 4-15.

The steering correction in this region will be performed using air-core dipole magnets. Experience with the SLC damping rings has illustrated the need for orthogonal horizontal and vertical angle and position closed orbit bumps through each of the septa as well as control of the injected and extracted beam trajectories.

The kickers are 1.2m in length and provide a 2.5-mr horizontal deflection; these are described further in Section 4.10.3.

The septa are DC current sheet septa constructed in two pieces. The first septum is 83-cm long and provides a 25-mr deflection. The blade has a thickness of 5 mm and lies 9 mm from the stored beam where the residual field is negligible. The injected and extracted beam trajectories have 4.5-mm clearance from the blade; assuming an emittance of 10^{-4} m-rad, the 3-sigma horizontal beam size is 1.5 mm. The second septum is 1-m long and it provides a 90-mr deflection. The blade has a thickness of 15 mm and lies 9 mm from the stored beam where again the residual field is negligible. Both sections of the septum magnet are described further in Section 4.10.1.

The adjacent focusing quadrupoles need to have a 3-cm pole-tip radius to provide room for the injected or extracted beams, while the adjacent defocusing quadrupoles may need to include an entrance or exit beam line; at the adjacent defocusing quadrupoles, the injection and extraction trajectories are roughly 25 cm from the stored beam trajectory.

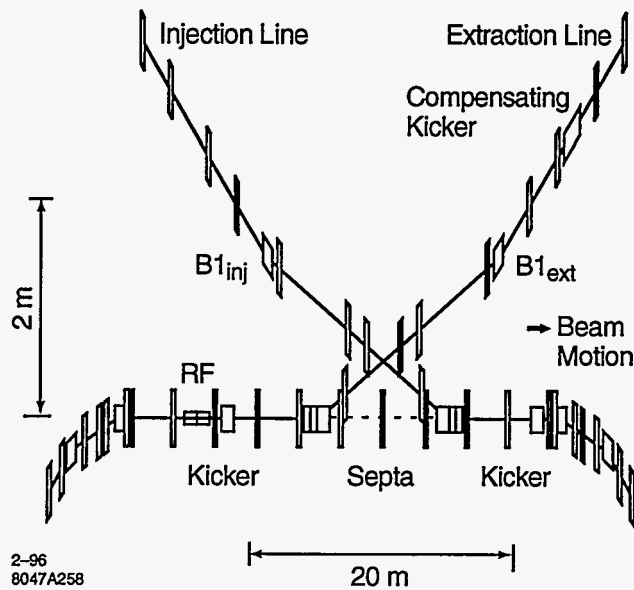


Figure 4-14. Component layout in the main damping ring injection and extraction region.

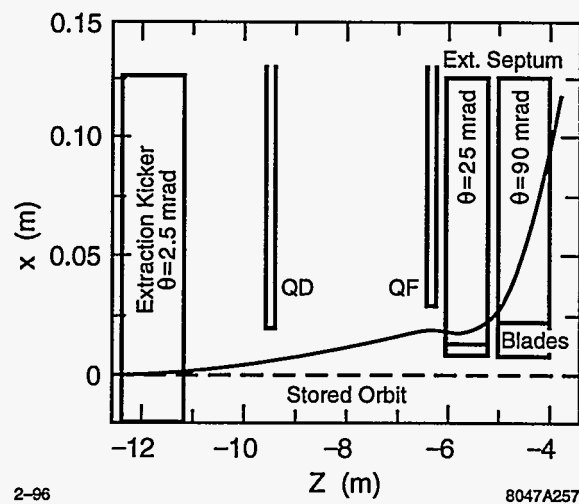


Figure 4-15. Extracted beam trajectory from kicker through septum.

The injection and extraction lines cross about 60 cm from the stored beam trajectory. Initial calculations of the effect of the crossing suggest that the effect of the beams passing through each other is not insignificant. Thus, a vertical chicane will probably be used to deflect the incoming beam trajectory away from the extracted beam. The closest magnets are 1.2-m away from the crossing and thus there is plenty of longitudinal space for the chicane but attention will need to be given to the effect of the fringing fields on the extracted beam.

To reduce the tolerances on the septum field stability, a compensating bend B_1 , which is powered in series with the septum, is located after the beam crossing on both the injection and extraction lines. Four quadrupoles are used to match the R_{22} transport element so that field fluctuations will cancel. This will ease the septum field tolerances by roughly an order of magnitude to $\Delta I/I \sim 5 \times 10^{-5}$.

In the same manner, the effects of kicker jitter on the extracted beam will be reduced using an achromatic (double) kicker scheme. Here, a compensation kicker is located in the extraction line after the septum compensation bend. Two additional quadrupoles are used to match the compensation kicker so that it is separated from the extraction kicker by a $+I$ transform in the horizontal plane. The compensation kicker is powered from the same thyatrons as the extraction kicker and is expected to reduce the sensitivity to kicker jitter by at least a factor of four. This will ease the tolerance $\Delta\theta/\theta$ on the extraction kicker from 0.0005 to 0.002. A similar achromatic kicker system will be tested at the ATF damping ring at KEK.

In addition, the sensitivity of the stored beam to the trailing edge of the kicker pulses is reduced by separating the injection and extraction kickers by $+I$ and adjusting the falling edge of the injection kicker to compensate for that of the extraction kicker; this can be done using a separate pulser as discussed in Section 4.10.3. Furthermore, the bunch trains will be ordered in the ring so that the trailing edge of the kicker pulse only effects the most recently injected bunch train allowing any residual deflection to be damped.

Finally, we should note that this injection and extraction region requires fairly difficult septa and kicker magnets. Although the magnets are thought to be possible, we also considered an alternate design that would require weaker kicker magnets. The alternate design consisted of two FODO cells with 5-m drift sections between quadrupoles. In this case, there is only one septum, a septum quadrupole, which both the injected and extracted beams use. Two of the disadvantages of this design were that the two beams must pass through each other and the resulting deflects of the extracted bunches can be as large as $0.2\sigma_y$ and the field tolerances in the septum quadrupole were very tight. For these reasons, we are not considering this design further.

RF Cavities

The rf cavities are located in a 3-m drift section before the extraction kicker; the cavity placement is illustrated schematically in Figures 4-13. The present rf design specifies two rf cavities, but the rf cavities and associated tapers are roughly 50 cm in length and thus additional cavities could be installed if necessary. In these sections, the dispersion is zero and the horizontal and vertical beta functions are roughly 6 m. It is expected that the cavity aperture will be roughly twice the nominal vacuum chamber radius and thus special masks will not be needed to protect the cavities from beam loss during injection or synchrotron radiation.

Detuned Lattice

We have studied a detuned version of the lattice for the main damping rings. The optics has an equilibrium emittance and a momentum compaction that are both roughly twice as large as the nominal lattice. In addition, the quadrupole and sextupole strengths are reduced by 30% while the dynamic aperture is increased

by roughly 50% and the ring tunes are changed to $\nu_x = 20.185$ and $\nu_y = 6.385$. Such a lattice may prove useful during the initial commissioning stages.

4.3.2 Pre-Damping Ring

As described, the Positron Pre-Damping Ring (PPDR) is designed to damp the large emittance positron beam from the positron source to an emittance of roughly $\gamma\epsilon_{x,y} = 1 \times 10^{-4}$ m-rad. At this point, the positrons are injected into the positron main damping ring (PDR), described in Section 4.3.1 where they are damped to the desired final emittances. The pre-damping ring allows us to decouple the large aperture requirements for the incoming positron beams from the final emittance requirements of the linear collider.

The damping and emittance requirements on the PPDR are described in Section 4.2.3. The determination of the design parameters is discussed in Sections 4.2.6–4.2.9; these parameters are summarized in Table 4-8.

The pre-damping ring does not need to produce flat beams. Thus, to maximize the damping of the transverse phase space, the ring has $J_x \approx 1.4$ and operates on the coupling difference resonance. This increases the damping in both the horizontal and vertical planes. Furthermore, like the main damping ring, the ring damps multiple trains of bunches at once, the number of which is determined by the ring circumference. The initial design was only 114m in circumference and stored only two trains. The present design is roughly 50% larger and stores three bunch trains. Although this increase in circumference will certainly increase the cost of the ring, the previous design was very tightly packed making the component design and maintenance substantially more difficult; experience with the SLC damping rings strongly suggests that the increase in circumference is cost-effective.

The magnets and vacuum system are being designed to provide sufficient aperture to accept a 2-GeV beam with an edge emittance of $\gamma\epsilon_{x,y} = 0.09$ m-rad and $|\delta p/p| \leq 1.5\%$ plus 2-mm clearance for misalignments and mis-steering. Given the nominal injected edge emittance of $\gamma\epsilon_{x,y} = 0.06$ m-rad, this provides a substantial margin for injection and internal mismatches.

Like the main damping rings, all of the quadrupoles and all of the sextupoles will have independent power supplies. This will facilitate beam-based alignment as well as matching of the lattice functions which is especially important in the pre-damping ring because of the limited aperture.

In the next sections, we will describe the ring layout and then details of the ring lattice: the arcs and the dispersion suppressors, the wiggler and injection and extraction straight sections, and the placement of the rf cavities. Issues such as trajectory correction, dynamic aperture, and matching are described later in this section (Section 4.3), while collective effects are discussed in Section 4.4. In addition, the rf and vacuum systems are described in Sections 4.5 and 4.6 while the feedback systems and support and alignment systems are described in Sections 4.7 and 4.9. Finally, the magnet and diagnostics designs are describe in Sections 4.10 and 4.11.

Layout

The design of the pre-damping ring looks very similar to the SLC damping rings, except the lengths are scaled by a factor of five. The ring has a race-track form with dispersion-free straight sections for injection and extraction. The ring is roughly 60 meters by 40 meters and is illustrated schematically in Figure 4-16.

Energy	1.8 ~ 2.2 GeV; 1.98 GeV nominal
Circ.	171 m
Max. Current	1.2 A
Max. N_{bunch}	1.57×10^{10}
Trains	3 trains of 90 bunches
Train Separation	64 ns
Bunch Separation	1.4 ns
Max. Rep. Rate	180 Hz
ν_x, ν_y, ν_s	10.18, 8.18, 0.018
$\gamma\epsilon_x$	7.7×10^{-5} m-rad
$\gamma\epsilon_{x,y}$ (coupled)	4.5×10^{-5} m-rad
σ_ϵ	0.1%
σ_z	7.5 mm
ξ_x uncorr, ξ_y uncorr	-13.9, -10.0
τ_x, τ_y, τ_z	4.44 ms, 6.15 ms, 2.73 ms
U_{SR}	371 KV/turn
J_x	1.39
α_p	0.0051
V_{RF}	2.0 MV
f_{RF}	714 MHz
Lattice	30 FOBO Cells

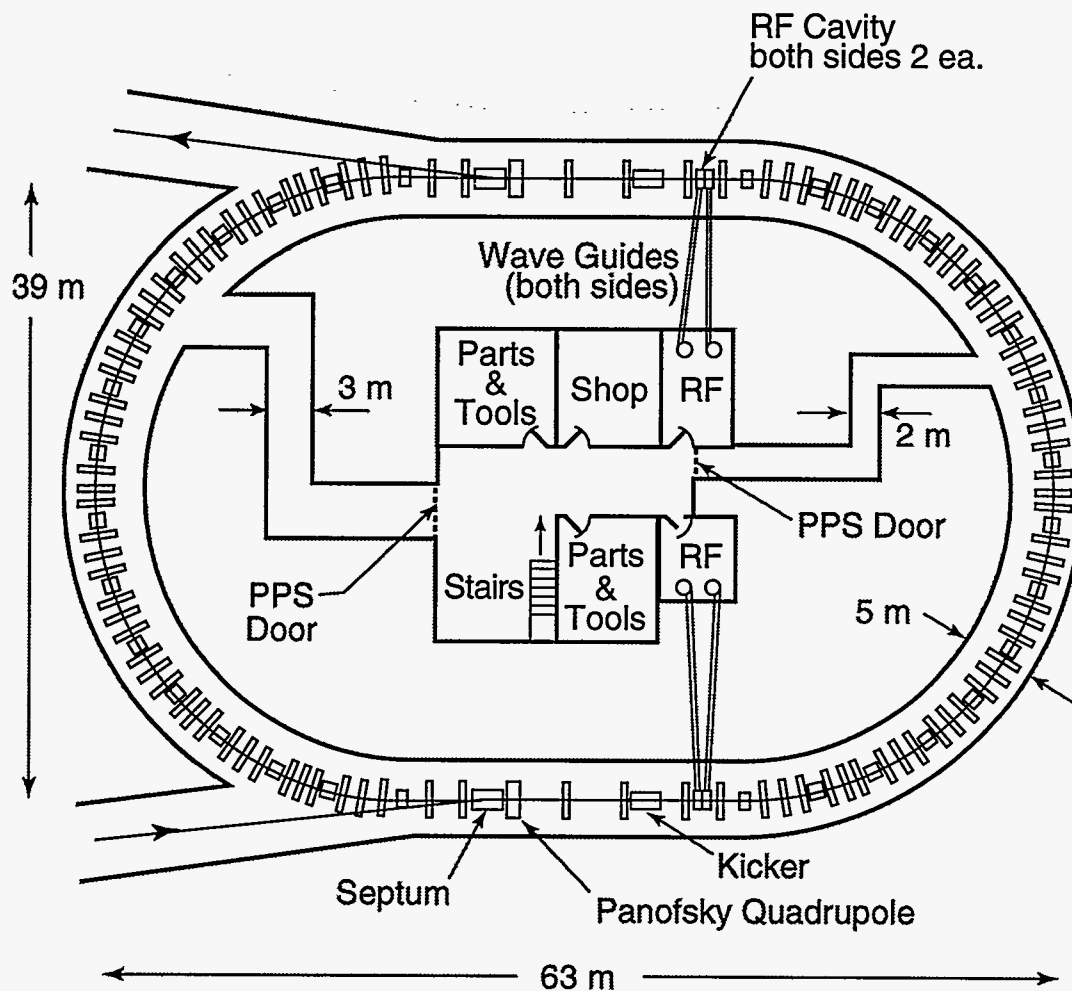
Table 4-8. Parameters for pre-damping ring (vers. 3.4)

In the design, the injection and extraction regions are in the straight sections on opposite sides of the ring. To reduce the requirements on these components, the systems are designed to occupy most of these regions. To minimize rf transients during injection and extraction, a new bunch train will be injected one half turn after a train is extracted. Furthermore, the rf cavities are placed downstream of the injection kicker and upstream of the extraction kicker so that the injection/extraction process will not interrupt the beam current seen by the rf cavities.

Arcs

Each arc is constructed from 14 FOBO cells plus dispersion suppressors. The FOBO cells are similar to FODO cells except a bend with a defocusing gradient is used instead of the defocusing quadrupole. This lattice structure was chosen because it keeps the lattice functions well constrained and it is simple. It has significantly better emittance performance than the normal FODO lattice and the single central bending magnet has smaller fringing field losses than if it were split as in a normal FODO cell.

Although the bending magnet has a defocusing gradient and could, in theory, completely replace the defocusing quadrupole, small defocusing quadrupoles are included at either end of the bending magnet. These provide additional vertical focusing to reduce the aperture and gradient requirements in the bend and they provide additional tuning control to optimize the lattice. Thus, each cell contains a single bending magnet, a single QF magnet, and two QD magnets. These magnets are described in Section 4.10. The cells are 4.1-m in length and the horizontal and vertical phase advances per cell are roughly 0.29 and 0.20. These tunes were chosen to balance the emittance contribution against the chromaticity generated by the cells while constraining the vertical beta function in the bending magnet. Finally, the lattice functions and magnet locations are plotted in Figure 4-17.



5-96
8047A516

Figure 4-16. Layout of pre-damping ring.

The dipole steering correction is performed using trim windings on the sextupoles. There is one horizontal corrector and one vertical dipole corrector in each cell. In addition, there are two BPMs per cell: one located adjacent to the bending magnet and one located next to the focusing quadrupole.

The chromatic correction is performed using two families of sextupoles: a set of defocusing sextupoles located between the bending magnet and the defocusing quadrupoles and a set of focusing sextupoles located between the defocusing and focusing quadrupoles. The symmetric placement of the sextupoles optimizes the dynamic aperture although it doubles the required number of sextupole magnets; this should be further investigated in the future.

The required vacuum aperture is determined from $X, Y = \sqrt{2\beta\epsilon_{x,y} + \eta_{x,y}\delta p/p}$. To provide sufficient aperture for an edge emittance of $\gamma\epsilon_{x,y} = 0.09$ m-rad and $|\delta p/p| = \pm 1.5\%$ plus 2-mm clearance around the beam for misalignments and mis-steering, the inner chamber size must be 5.8 by 1.8 cm at the focusing quadrupoles

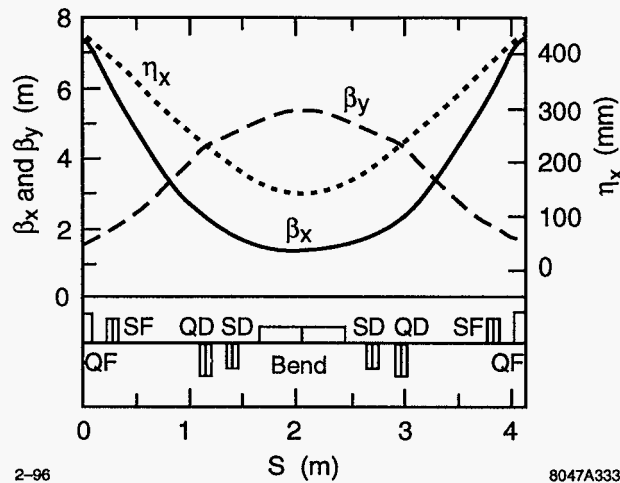


Figure 4-17. β_x (solid), β_y (dashes), and η_x (dots) in the pre-damping ring FOBO cell.

and 2.0 by 3.6 cm at the bending magnet. To minimize the impedance of the chamber, we will use a uniform elliptical cross section of an inner aperture of 6 cm by 3.6 cm; this will be discussed further in Section 4.6.2.

Finally, the dispersion is matched to zero at the end of the arcs for the two straight sections. The matching is performed using the two upstream quadrupoles and a bending magnet with an integrated dipole strength that is half that of the arc bending magnets. These matching bends have the same magnetic field as the main arc bends and half the effective length, but they have no field gradient to ease the field requirements and the fringing fields. As in the main damping ring, the horizontal and vertical dispersion matches will be tuned using the dispersion matching quadrupoles and trim windings on the sextupoles wired as skew quadrupoles.

Injection/Extraction

The injection and extraction regions are constructed from FODO cells in the dispersion-free straight sections. The two regions are located on opposite sides of the ring and utilize most of the respective straight sections to reduce the requirements on the kickers and the septa. Both systems are identical except for the number of kicker modules that are used; the extraction line needs fewer because of the smaller out-going beam. The lattice functions and component placement in the injection linac are illustrated in Figure 4-18.

The injection kickers are constructed in six segments with a total length of 2 m and provide an 8-mr horizontal deflection. The large deflection is needed because of the very large injected beam emittances. The extraction kicker is similar except it would be constructed from five of the kicker segments and would provide a 6.6-mr horizontal deflection. Both of these are described further in Section 4.10.3.

The septa are DC Lambertson septa that deflect the beam vertically. They are 2-m in length and have 5-kGauss fields providing a 150-mr deflection. The return blades are 2.3-cm thick and are located 3.3-cm from the stored and injected beam trajectories and 1.8-cm from the extracted beam trajectory; the extracted beams sizes are smaller and thus less space is required. In all cases, this leaves >1-cm clearance from the edge of the beam to the blade, assuming an injected edge emittance of 0.09 m-rad and an extracted beam emittance of 1×10^{-4} m-rad; the septa are described further in Section 4.10.2.

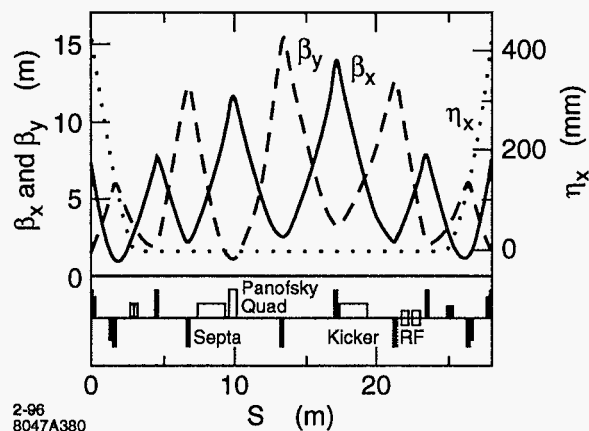


Figure 4-18. β_x (solid), β_y (dashes), and η_x (dots) in the pre-damping ring injection region.

The focusing quadrupoles, adjacent to the septa, are constructed as dual Panofsky quadrupoles. This is necessary to make optimal use of the kickers. Both halves of the dual quad have the same strength and the same polarity. They are 50-cm in length and provide an integrated gradient of 28 kGauss. The horizontal aperture of each quadrupole is 6.2 cm. The center current sheet is 2-cm thick and, assuming an injected edge emittance of $\gamma\epsilon_{x,y} = 0.09$ m-rad, the blades are 8 mm from the stored and injected beams; these quadrupoles are described further in Section 4.10.2.

Finally, the adjacent defocusing quadrupoles may need to include an entrance or exit beam line; at the adjacent defocusing quadrupoles, the injection and extraction trajectories are roughly 30 cm from the stored beam trajectory.

After the beam has cleared the ring, it is deflected horizontally and then vertically to return to the plane of the damping ring. The optics of this section has not yet been developed but no significant problems are expected. Beyond this point the injection and extraction lines will be similar to those of the main damping rings.

Using the same technique as in the main damping rings, the effects of kicker jitter on the extracted beam will be reduced using an achromatic (double) kicker scheme. Here, a compensation kicker is located in the extraction line after the septum compensation bend. Six quadrupoles are used to match the compensation kicker so that it is separated from the extraction kicker by a $+I$ transform in the horizontal plane. The compensation kicker is powered from the same thyratrons as the extraction kicker and is expected to reduce the sensitivity to kicker jitter by at least a factor of four. This will ease the tolerance $\Delta\theta/\theta$ on the extraction kicker from 0.0016 to 0.0064. A similar achromatic kicker system will be tested at the ATF damping ring at KEK.

RF Cavities

The PPDR uses four 714-MHz rf cavities to provide the 2-MV rf field; the rf system is described in Section 4.5. To eliminate the transient beam loading when bunch trains are injected and extracted, one pair of rf cavities is placed in a 2-m drift section after the injection kicker and the other pair is located in a similar drift before the extraction kicker; these are illustrated in Figure 4-18. Although the cavity aperture is large compared to

the vacuum chamber radius, additional masking will probably be needed to protect the cavities from beam loss at injection.

4.3.3 Injection Line

The injection lines transport the beams from the source linacs to the damping rings. The damping ring injection components from the septum compensation bend through the injection kicker, are considered part of the damping rings and are described in Sections 4.3.1 and 4.3.2. The injection lines have five primary functions:

- Provide diagnostics to monitor incoming the beam energy, energy spread, transverse position, and emittance.
- Provide transverse betatron matching for injection into the rings.
- Compress the incoming energy spread and match the longitudinal phase space to the damping rings.
- Rotate the longitudinal polarization of the electron beam into the vertical plane for injection into the electron damping ring.
- Include a beam dump just before injection into the rings.

Although the positron beam is not presently polarized, we are designing the positron injection line so that it could be easily upgraded to operate with polarized beams, *i.e.*, either polarized positrons or polarized electrons which would be needed for $\gamma\text{-}\gamma$ or e^+e^- collisions. Thus, the geometrical constraints imposed by the spin rotation are applied to both the electron and positron injection lines and the two lines are very similar.

Layout

The layout of the electron injection line is plotted in Figure 4-19; the positron line is similar, although there is a longer rf section after the arc instead of the solenoid. Both injection lines are roughly 70m in length. They include an arc of 60° which:

- Generates the R_{56} for the energy compressor.
- Provides for the energy diagnostics.
- Rotates the polarization vector by 270° in the $x\text{-}z$ plane so that it is oriented in the x direction.

Following the arc, a 2.5-m S-band (2.856 GHz) rf (electrons) or 4-m L-band (1.428 GHz) rf (positrons) accelerator section is used to perform the energy compression. The L-band rf is needed in the positron line because the incoming positron beam emittance is very large and the aperture of the S-band structure is not sufficient; unfortunately, one needs twice the energy gain from the L-band structure as would be needed from an S-band structure.

Next, the electron side includes a solenoid to rotate the polarization from the horizontal plane to the vertical. This is followed by a series of FODO cells with five conventional wire scanners for emittance measurement; these wire scanners would be similar to those used throughout the SLC.

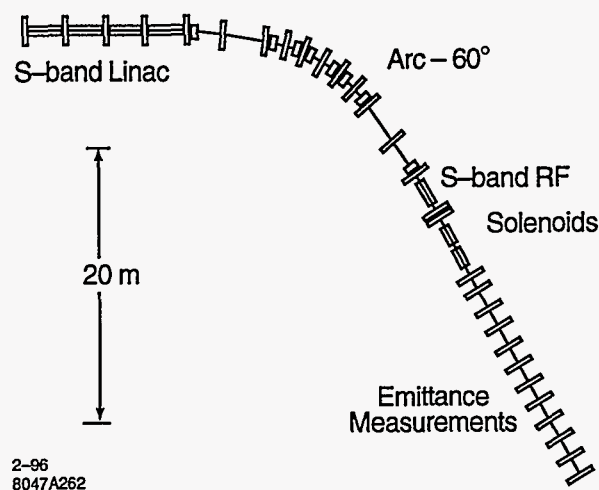


Figure 4-19. Component layout of the electron injection line.

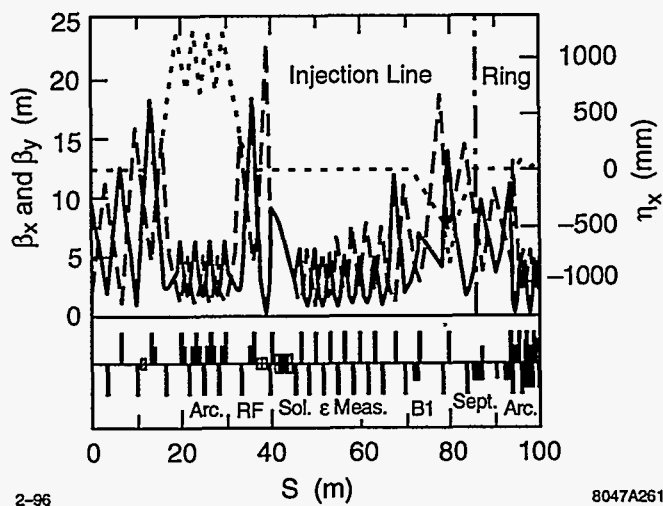


Figure 4-20. β_x (solid), β_y (dashes), and η_x (dots) in the electron injection line with the solenoid on; the damping ring boundary is denoted by the vertical dashed line.

Finally, the beam is matched from the injection line into the ring. This section includes the septum compensation bend which generates a high dispersion that is ideal for a final energy and energy spread measurement. This portion of the line is described in Sections 4.3.1 and 4.3.2 and the component placement is illustrated in Figures 4-14 and 4-18. The bypass line, which includes a pulsed beam dump, intersects the injection line just before the septum compensation bend. A bending magnet is used to direct the beam to either the bypass line and beam dump or to the damping ring.

Optical Design

The electron injection line optical functions with the solenoids on are plotted in Figure 4-20; the positron line is similar. The lines are matched from the electron or positron source linacs into an arc that rotates

the longitudinal spin polarization into the horizontal direction and acts as an energy diagnostic. The arc consists of three cells with a horizontal phase advance of 60° and a peak dispersion of 1.2 m.

This arc provides an $R_{56} = 0.8$ m for the energy compression and allows for a very accurate measurement of the beam energy by separating two BPMs by 180° and summing the horizontal measurements; the sum of the two measurements is independent of incoming betatron oscillations. The high dispersion also allows for accurate measurements of the electron and positron beam energy spread using wire scanners. For the electron beam, the dispersive beam size is roughly 1 cm while the betatron beam size is roughly 0.4 mm while in the positron system the expected energy spread extends between $\pm 2\%$ with a corresponding beam size of 2.4 cm at the high-dispersion points in the arc while the beam edge emittance of $\gamma\epsilon = 0.06$ m-rad corresponds to a size of 1 cm at the same location. Although this resolution is thought to be sufficient, if it is not, the dispersion can be increased in the design by increasing the length of the arc cells; this will be evaluated in the future.

In the electron line, the arc is followed by a 2.5-m S-band rf section which completes the energy compression and then two 1.5-m solenoids to complete the spin rotation. To prevent emittance dilution due to betatron coupling, the beta and alpha functions are set to be equal through the solenoid. The matching quadrupoles before and after the solenoid allow the betatron match to be maintained as the solenoid excitation is varied. The positron line differs in that it uses a 4-m L-band acceleration section and the solenoid is not needed.

Following the solenoids there is an emittance measurement section which consists of four FODO cells with five wire scanners interspersed. These wires will be used to measure the beam emittance, the betatron match, and the coupling mismatch from the solenoid; the matching quadrupoles can then be used to adjust the matching which when properly set will minimize the coupling mismatch as well as the betatron mismatch.

Finally, the beam line is matched past the septum compensation bend and into the ring; details of this are described in Sections 4.3.1 and 4.3.2. There is a dispersion maximum of 80 cm roughly halfway between the septum and the compensating bend where the final energy and energy spread will be measured just before injection into the rings.

Energy Compressors

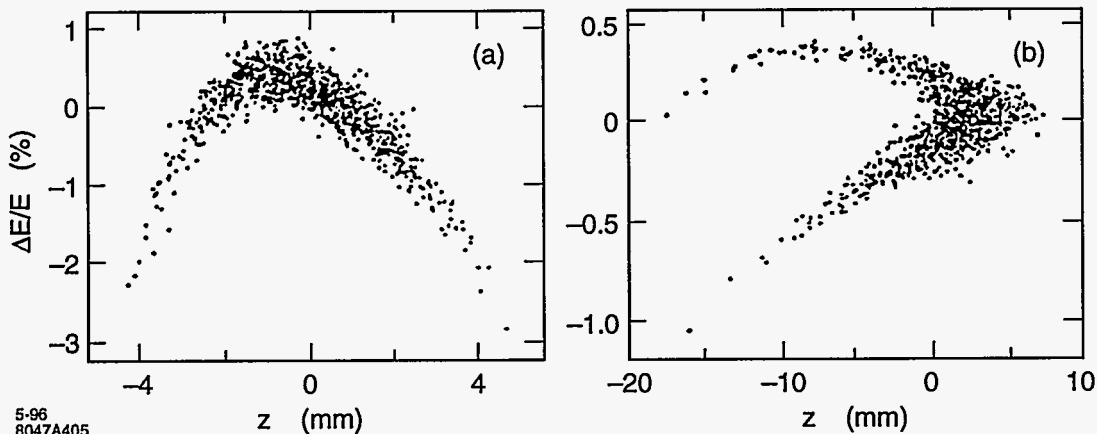
The energy compressors reduce the incoming energy spread and the incoming energy jitter while increasing the bunch length. The compressor is required for the positron system because the pre-damping ring rf bucket height is only $\pm 1.5\%$ while the incoming beam has an energy deviation extending between $\pm 2\%$. The compressor also matches the beam to the rf bucket in the ring, reducing the amplitude of the longitudinal quadrupole oscillation at injection.

In the case of the electron beam, the compressor is not completely necessary since the rf bucket height is sufficient to accept the incoming beam. Regardless, the compressor will reduce the sensitivity to energy jitter and improve the longitudinal match at injection. In both cases, the compressors are designed to compress the energy spread and increase the bunch length by a factor of two. Parameters of the two compressors are given in Table 4-9 and the incoming and outgoing longitudinal phase spaces for the electrons and positrons are plotted in Figures 4-21 and 4-22, respectively.

Details of the energy compressor rf design can be found in Chapter 6. In both the S-band (electron) and L-band (positron) compressors, the structures will be Damped-Detuned Structures similar to those developed for the X-band main linacs. The L-band rf power will be provided by two 35-MW klystrons and a SLED rf pulse compressor. In the S-band case, the rf will be provided by a single 56-MW klystron which is similar to the SLAC 5045 klystrons. In both cases, the multibunch loading will be compensated using the ΔT

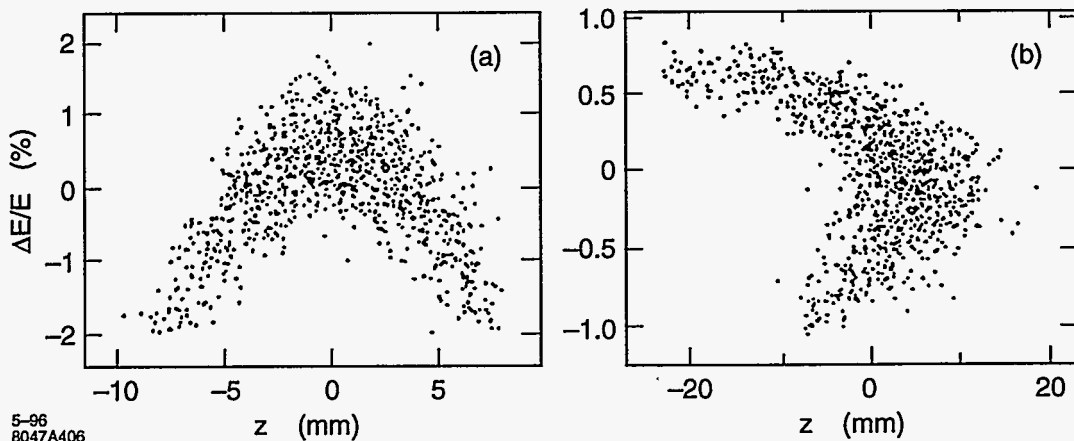
	Electron	Positron
$(\Delta E/E)_{inj}$ (95%) (%)	± 0.6	± 1.8
$\sigma_{z inj}$ (mm)	1.5	3.7
R_{56} (m)	0.8	0.8
T_{566} (m)	2.0	2.0
f_{RF} (MHz)	2856	1428
V_{RF} (MV)	42	80
L_{RF} (m)	2.5	4
$(\Delta E/E)_{ext}$ (95%) (%)	$\pm 0.4\%$	$\pm 1.0\%$
$\sigma_{z ext}$ (mm)	3.33	6.97

Table 4-9. Parameters of electron and positron energy compressors.



5-96
8047A405

Figure 4-21. Longitudinal phase space of electrons before (a) and after (b) energy compressor.



5-96
8047A406

Figure 4-22. Longitudinal phase space of positrons before (a) and after (b) energy compressor.

(early injection) method. The positron compressor has been specified to compensate for a maximum beam current of 2.75 A (2.4×10^{10} per bunch) which is roughly 85% greater than the charge needed at the IP to provide for beam loss through the injector system. The electron compressor has been designed to compensate for maximum beam current of 2.2 A (1.9×10^{10} per bunch) which is roughly 50% greater than the charge needed at the IP. In both cases, the beam loading should be compensated to an error less than a few 10^{-4} relative energy deviation; the tuning of the beam loading compensation will be done using either the energy spectrometer in the beam dumps or the dispersion in the arcs of the rings.

Polarization

The longitudinal polarization of the electron beam must be rotated into the vertical plane before injection into the main damping ring. This is performed using the 60° arc which rotates the polarization vector through 270° in the x - z plane at the nominal beam energy of 1.98 GeV. A solenoid is then used to rotate the polarization into a vertical orientation. The rotation in the solenoidal field is given by

$$\theta_s = \left[1 - \frac{g-2}{2} \right] \frac{B_z L_{sol}}{B\rho} \quad (4.21)$$

To perform the 90° rotation at 1.98 GeV requires an integrated field of 103.9 kGauss-m. We assumed two superconducting solenoids with lengths of 1.5 m and fields of 34.62 kGauss; these are similar to the superconducting solenoids used in the SLC damping ring injection and extraction lines.

4.3.4 Extraction Line

The main damping ring extraction lines only extend through the end of the achromatic kicker systems; the achromatic kicker system is discussed in Section 4.3.1. The extraction line optics is shown in Figure 4-23 and the component layout is illustrated in Figure 4-14 which is in Section 4.3.1.

The beam line downstream of the extraction line is part of the spin rotator and bunch compressor section and is described in Chapter 5. Regardless, it is worthwhile noting the requirements from the damping ring viewpoint.

- Energy and energy spread measurement: This will be done using the dispersion in the 20° arc which is part of the spin rotator system and is described in Chapter 5. In the same manner as in the injection line arc, BPMs located 180° apart in horizontal phase advance can provide a very accurate measure the the beam energy deviations.
- Bunch length measurement: It will be desirable to have a continuous parasitic measurement of the bunch length from the damping rings. This will be done by measuring the beam size in the bends of the bunch compressor. The calibration depends upon the compressor rf voltage and the dispersion in the bending magnet; this is discussed in Chapter 5.
- Transverse phase space measurement: The present design has a laser wire scanner located after the beta-matching quadrupoles at the end of the extraction line. This will provide a continuous parasitic diagnostic of the damping ring performance and can be used for quad-scan emittance measurements when necessary. In addition, there are four laser wire scanners in the prelinac at the end of the first bunch compressor. The emittance from the damping rings can be measured by turning off the bunch

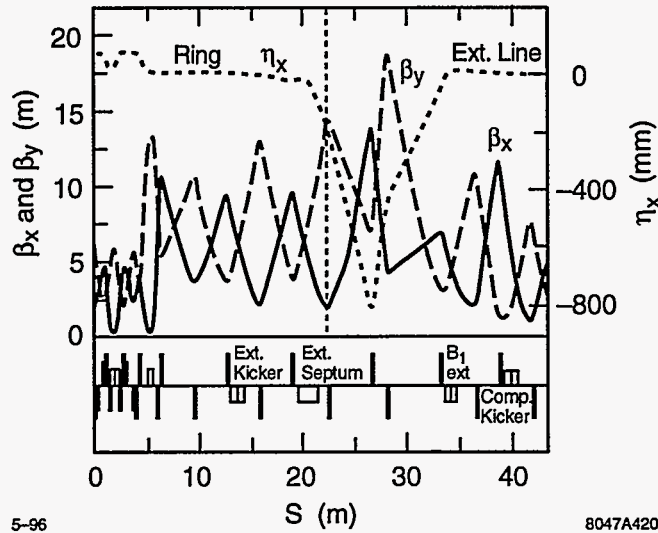


Figure 4-23. β_x (solid), β_y (dashes), and η_x (dots) in the main damping ring extraction line; the damping ring boundary is denoted by the vertical dashed line.

compressor spin rotation solenoids and the bunch compressor rf. This will be the main diagnostic for most tuning operations.

- **Matching:** The beta-matching will be performed using six quadrupoles at the end of the extraction line and the beginning of the bunch compressor system which is described in Chapter 5. The dispersion-matching will be performed using both trim quadrupoles and trim skew quadrupoles located in the extraction line and trim quadrupoles located in the 20° arc of the spin rotator system. Finally, the residual betatron coupling will be corrected with a skew correction system located between the spin rotators and the first bunch compressor; this is also described in Chapter 5.
- **Pulsed dump line:** A pulsed dump line will be located in the prelinac following the emittance diagnostics at the end of the first bunch compressor. This will allow full operation of the damping ring complex for commissioning and tuning.

4.3.5 PPDR-to-PDR Transfer Line

The design of the PPDR-to-PDR transfer line has not been completed yet. In concept it will combine the pre-damping ring extraction line, described in Section 4.3.2, with the main damping ring injection line, described in Section 4.3.1. In addition, the line should include a single wire scanner with a variable quadrupole to perform a quad-scan emittance measurement and a beam dump before the main damping ring. If the beams are polarized, the spin polarization will already be oriented vertically and no further manipulation is necessary.

4.3.6 Bypass Lines

The design of the damping ring bypass lines has not been completed yet. As illustrated in Figures 4-1 and 4-2, the primary component of the bypass lines will be the beam dumps. Since the bypass lines will branch off after the emittance diagnostics, these will allow tuning of the electron and positron sources while the damping rings are being maintained. These beam dumps will need to absorb the full beam power of roughly 130 kW.

4.3.7 Trajectory Correction

The main damping rings and downstream systems all have very tight alignment and field tolerances to prevent dilution of the transverse emittances. In all cases, these tolerances will be attained using beam-based alignment techniques where the alignment accuracy depends on beam measurements and not mechanical systems; the techniques to be used in the damping rings are described in Section 4.9.

In the downstream systems, the alignment will be implemented using remote magnet movers. The tolerances are sufficiently loose in the damping rings that there is some question as to whether magnet movers are required; once the alignment is known, one could mechanically perform the differential moves to attain the desired alignment. This question will be determined in the future, for this design, we have assumed magnet movers.

In this section, we will describe the placements and required strengths of the trajectory correctors. These correctors must be able to provide sufficient steering to store beams before the beam-based alignment procedures are started. In addition, they must correct for residual alignment errors after beam-based alignment. In most cases, the corrector strengths required to simply store the beams are very weak compared to those required to steer the trajectory and minimize the BPM readings.

Main Damping Rings

In the main damping rings, each arc cell (Figure 4-10) contains two horizontal dipole correctors, a single vertical dipole corrector, and three BPMs. The horizontal correctors will be located at the S1 sextupole magnets (the sextupoles adjacent to the bending magnet). The vertical corrector will be located at either one of the S3 sextupoles (the sextupoles adjacent to the QD magnet). Both horizontal and vertical dipole correctors will consist of trim windings on the sextupole magnets and are discussed in Section 4.10.1.

Like the horizontal correctors, two BPMs will be located between the S1 sextupole magnets (the sextupoles adjacent to the bending magnet) and the QF quadrupole magnets. At this time, we have not determined how the BPMs are mounted but, ideally, they would be constrained transversely at either the sextupole or the quadrupole magnet. The sextupoles are the preferred choice because they are separated by roughly 108° in horizontal phase advance while the QF magnets are separated by 144° and the orbit relative to the magnetic center of the sextupoles is more important than that of the quadrupoles. The third BPM would be located at the QD magnet; it is not strictly necessary for the trajectory correction or emittance control, but it provides redundancy if one of the other BPMs in the cell fails.

Sextupoles ($X/Y/\Theta$) ($\mu\text{m}/\mu\text{r}$)	100 / 50 / 1000
Quad. QFH ($X/Y/\Theta$) ($\mu\text{m}/\mu\text{r}$)	100 / 100 / 600
Quad. QM2 ($X/Y/\Theta$) ($\mu\text{m}/\mu\text{r}$)	100 / 100 / 600
Other Quad. ($X/Y/\Theta$) ($\mu\text{m}/\mu\text{r}$)	100 / 100 / 1000
Bends ($X/Y/\Theta$) ($\mu\text{m}/\mu\text{r}$)	200 / 200 / 1000
BPMs ($X/Y/\Theta$) ($\mu\text{m}/\mu\text{r}$)	100 / 100 / 1000
All magnets have 0.1% rms strength errors.	

Table 4-10. Rms errors for EDR and PDR orbit and emittance simulations.

	Rms Θ_X (μrad)	Max Θ_X (μrad)	Rms Θ_Y (μrad)	Max Θ_Y (μrad)
Arcs	155	433	132	468
Straights	60	201	54	223

Table 4-11. Corrector strengths from 100 simulations in the EDR and PDR with errors from Table 4-10.

In both straight sections, BPMs will be located at every quadrupole, while horizontal dipole correctors will be located at the focusing quadrupoles and vertical dipole correctors will be located at the defocusing quadrupoles. Here, the dipole correctors will consist of trim windings on the quadrupoles.

Finally, additional horizontal and vertical dipole correction elements will be needed in the injection/extraction region to allow optimal control of the trajectory through this region. Small air core dipoles will be used for this function.

The orbit correction has been simulated using a standard set of errors listed in Table 4-10. All errors have Gaussian distributions truncated at ± 2.5 sigma. For the simulations, the arc BPMs and horizontal correctors were placed at the non-optimal QF magnets. After correction, the residual trajectory at the monitors was roughly 100- μm rms. The rms and maximum corrector strengths found from 100 simulations are listed in Table 4-11. The correctors are subdivided into arc correctors and straight section correctors. It is suggested to design the arc correctors for a maximum deflection of 0.50 mr (33 G-m field) and the straight section correctors for a maximum deflection of 0.25 mr (16 G-m field). These strengths will be more than sufficient to store beams after the preliminary conventional alignment where the expected errors are roughly four times those in Table 4-10. In addition, if during normal operation, the errors are significantly larger and many of the correctors are at maximum strength, the rings must be realigned.

Pre-Damping Ring

In the pre-damping ring, each arc cell (Figure 4-17) contains one horizontal dipole corrector, a single vertical dipole corrector, and two BPMs. The horizontal corrector will be located at one of the SF sextupole magnets (the sextupoles adjacent to the focusing quadrupole). The vertical corrector will be located at either one of the SD sextupoles (the sextupoles adjacent to the bending magnet). Both horizontal and vertical dipole correctors will consist of trim windings on the sextupole magnets and are discussed in Section 4.10.2.

Like the correctors, one BPM will be located between the SF sextupole magnets and the adjacent QF quadrupole magnets. The other BPM would be located between the bending magnet and one of the SD

Sextupoles ($X/Y/\Theta$) ($\mu\text{m}/\mu\text{r}$)	200 / 200 / 2000
Quadrupoles ($X/Y/\Theta$) ($\mu\text{m}/\mu\text{r}$)	200 / 200 / 2000
Bends ($X/Y/\Theta$) ($\mu\text{m}/\mu\text{r}$)	200 / 200 / 1200
BPMs ($X/Y/\Theta$) ($\mu\text{m}/\mu\text{r}$)	200 / 200 / 2000
All magnets have 0.1% rms strength errors.	

Table 4-12. Rms errors for PPDR orbit and matching simulations.

Rms Θ_X (μrad)	Max Θ_X (μrad)	Rms Θ_Y (μrad)	Max Θ_Y (μrad)
166	532	347	1104

Table 4-13. Corrector strengths from 100 simulations in the PPDR with errors from Table 4-12.

magnets. At this time, we have not determined how the BPMs are mounted but, ideally, they would be constrained transversely at either the sextupole or the quadrupole magnet.

In both straight sections, BPMs will be located at every quadrupole while horizontal dipole correctors will be located at the focusing quadrupoles and vertical dipole correctors will be located at the defocusing quadrupoles. Here, the dipole correctors will consist of trim windings on the quadrupoles.

The orbit correction has been simulated using a standard set of errors listed in Table 4-12. All errors have Gaussian distributions truncated at ± 2.5 sigma. For the simulations, the arc BPMs and horizontal correctors were placed at the non-optimal QF magnets while the defocusing correctors were placed at one of the QD magnets. After correction, the residual trajectory at the monitors was roughly $110\text{-}\mu\text{m}$ rms while the actual trajectory had an rms and maximum values of roughly $130\text{ }\mu\text{m}$ and $269\text{ }\mu\text{m}$ in the horizontal plane and $390\text{ }\mu\text{m}$ and $1014\text{ }\mu\text{m}$ in the vertical plane. These trajectory offsets are consistent with the 2-mm steering allowance provided in the aperture calculations.

The rms and maximum corrector strengths found from 100 simulations are listed in Table 4-13. It is planned to design the correctors for a maximum deflection of 1.0 mr (67 G-m field). These strengths will be more than sufficient to store beams after the preliminary conventional alignment where the expected errors are comparable to those in Table 4-12.

Transfer Lines

No simulations have been performed at this time. The primary issues will be the aperture issues in the positron injection line, injection onto the closed orbit in both rings, trajectory control through the extraction septa. The aperture issues in the positron injection line will be resolved by including a $\pm 5\text{-mm}$ clearance for steering and including numerous BPMs and dipole correctors. The injection and extraction trajectories will be adjusted with additional steering correctors in the injection/extraction regions. The apertures of the septa have been chosen so that there should be plenty of room to optimize the trajectories.

4.3.8 Emittance Control and Matching

In addition to causing orbit deviations, alignment and field errors generate dispersion and betatron mismatches. In all of the damping rings, these increase the horizontal and vertical emittances but are only significant in the main damping rings where the equilibrium emittances are very small. In fact, in the main damping rings, the vertical emittance requirement determines alignment tolerances; other effects such as steering and dynamic aperture have looser tolerances.

In the pre-damping ring, which operates on the betatron coupling difference resonance, the tolerances for emittance control are relatively loose; other effects such as physical and dynamic aperture limitations are more important. Thus, the matching into- and in the pre-damping ring needs to be controlled. In addition, the pre-damping ring has a problem which is opposite that in the main damping rings, namely, the width of the coupling resonance is extremely small and, for stable operation, this will probably need to be increased with skew quadrupoles or vertical orbit bumps through the sextupoles.

In the transport lines, similar effects will increase the effective emittances injected into the rings, thereby increasing the time needed to damp to the desired emittances, and possibly leading to particle loss if the mismatched beam exceeds the aperture. We will first describe the issues for the main damping rings where the very small vertical equilibrium emittance determines the alignment tolerances; the tolerances needed to attain the vertical emittance are more severe than those due to the dynamic aperture limitations. Next, we will discuss the pre-damping ring and finally we will discuss the injection and extraction matching requirements.

Although these effects will set tolerances, this section does not discuss how these tolerances will be attained and maintained stably. This will be discussed in Sections 4.9 and 4.8.

Main Damping Rings

In the NLC main damping rings, the primary sensitivity of the equilibrium emittances arises from dispersion mismatches; this is true in both the horizontal and vertical planes. Other effects such as betatron mismatches and betatron coupling are less important. In particular, the expected vertical emittance dilution from vertical dispersion due to random errors is roughly five times greater than the dilution due to coupling from the same errors.

The three elements that have the greatest contribution to the emittances are the horizontal and vertical misalignments of the arc sextupoles, rotational misalignments of the arc focusing quadrupoles, and rotational misalignments of the bending magnets. To reduce the emittance dilutions, it is most efficient to set lower tolerances on these sources and have more relaxed tolerances on the other elements.

We have performed 100 simulations using the errors listed in Table 4-10. As before, all errors have Gaussian distributions truncated at ± 2.5 sigma. Orbit correction was performed as discussed in the previous section. Without any other correction of the lattice, we found an average horizontal emittance of $\gamma\epsilon_x = 2.69 \times 10^{-6}$ m-rad and an average vertical emittance of $\gamma\epsilon_y = 2.92 \times 10^{-8}$ m-rad; for comparison, the design values for horizontal and vertical emittance are $\gamma\epsilon_x = 2.6 \times 10^{-6}$ m-rad and $\gamma\epsilon_y = 1.5 \times 10^{-8}$ m-rad. Histograms of the resulting emittance values are plotted in Figure 4-24.

In general, the dispersion generated by the alignment errors is easily corrected. The mismatch will oscillate much like an uncorrected close orbit and a few dispersion correctors can reduce the rms value significantly. The horizontal dispersion can be corrected using weak quadrupoles in regions of large horizontal dispersion

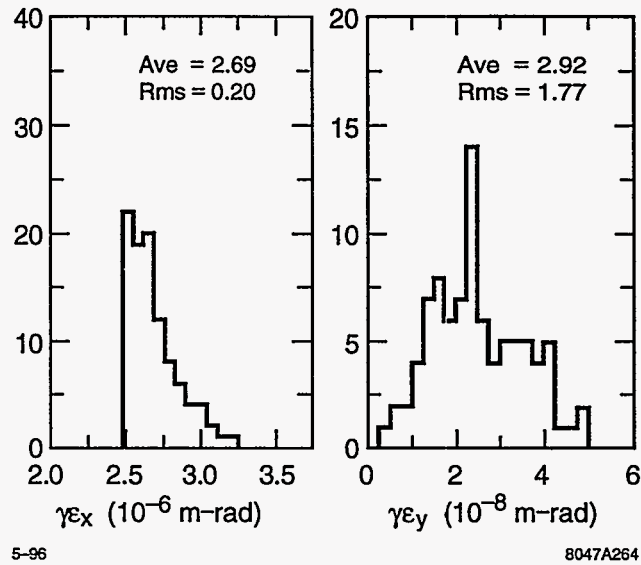


Figure 4-24. Horizontal and vertical emittances from 100 simulations of errors and only using orbit correction; the average horizontal emittance is $\gamma\epsilon_x = 2.69 \times 10^{-6}$ m-rad and the average vertical emittance is $\gamma\epsilon_y = 2.92 \times 10^{-8}$.

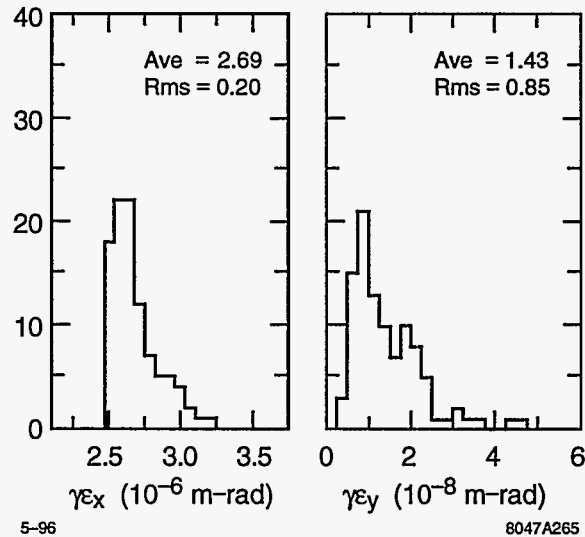


Figure 4-25. Horizontal and vertical emittances from 100 simulations of errors where two weak skew quadrupoles were used to reduce the vertical dispersion; the average vertical emittance is $\gamma\epsilon_y = 1.43 \times 10^{-8}$.

and the vertical dispersion can be corrected using weak skew quadrupoles in regions of large horizontal dispersion.

In Figure 4-25, we plot the residual emittance after using just two skew quadrupoles, located in the dispersion suppressor cells, to minimize the rms vertical dispersion. Notice that both the average of the vertical emittance and the width of the distribution are decreased. In this case, the average vertical emittance is $\gamma\epsilon_y = 1.43 \times 10^{-8}$ m-rad and 95% of the simulations have emittances below $\gamma\epsilon_y = 3 \times 10^{-8}$ m-rad; further correction would be possible with additional elements. This minimization can be performed either by directly measuring the dispersion or by optimizing the emittance of the extracted beam; in the simulation, we optimized the extracted beam emittance. Finally, as mentioned, a similar procedure can be used to correct the horizontal dispersion. We have not yet implemented such a solution but it will be straight-forward.

The current design for the main damping rings specifies individual power supplies for all the quadrupoles and sextupoles. Thus, there are numerous quadrupoles that can be used to correct betatron mismatches and horizontal dispersion mismatches. In addition, we are considering using magnet movers on most of the quadrupoles and sextupoles. If remote magnet movers are adopted then skew correctors to correct the vertical dispersion will exist all around the ring, *i.e.*, vertical motion of the sextupoles. If we do not choose to use the remote magnet movers, then eight sextupoles in each arc will have trim windings wired as skew quadrupoles.

As discussed previously, the alignment tolerances will be attained using beam-based alignment practices which are discussed in Section 4.9 while the tolerances required to maintain the required stability are discussed in Section 4.8.

Pre-Damping Ring

As stated, the issues are completely different in the pre-damping ring. Here, because the aperture is tight, the primary problem becomes maintaining the matched beta and dispersion functions. With the individual quadrupole power supplies it is straight-forward to both measure and correct any betatron mismatches that may exist. Similar arguments apply to correcting dispersion mismatches which are easily measured by storing the beam and varying the rf frequency.

Finally, because of the accurate alignment that is required to attain the desired dynamic aperture, the width of the betatron resonance is relatively small. This will make reliable operation on the coupling resonance difficult and so skew quadrupoles will be used to increase the width of the resonance; this technique was also used on the SLC Positron Damping Ring.

Injection Line

The injection lines have relatively loose alignment and field tolerances. The primary issue is matching the beams to the damping rings. This is required to prevent emittance growth due to filamentation and possible beam loss if the mismatched beam exceeds the damping ring aperture.

Both injection lines have emittance diagnostics just upstream of the rings so that incoming mismatches can be corrected. The fine tuning of the beam match will be performed using gated synchrotron light cameras, located in the rings, to measure the beam size on different turns after injection. This technique has been used to successfully match the incoming phase space to the SLC damping rings [Minty 1995] and we expect to be able to match the incoming beam sizes to better than 10%.

Extraction Line

In the extraction lines from the main damping rings, the beam emittances are asymmetric and very small. Thus, betatron coupling and dispersive errors can lead to significant emittance growth. The betatron coupling will set tolerances on the allowable magnet roll and skew fields. This is particularly true for the extraction septa which tend to have nonlinear fields close to the septa blades. Similarly, the dispersive errors will set tolerances on the allowable orbit deviations, magnet alignment, and matching of the dispersion.

In the NLC damping rings, we are including multiple steering correctors to optimize in the injection and extraction trajectory through the septa. In addition, we are designing the septa with substantial clearance between the beam trajectory and the septa blades to minimize the nonlinearity seen by the beams.

The extraction lines will include six matching quadrupoles to match the beta functions into the spin rotators beam lines which follow; these are described in Chapter 5. In addition, residual betatron coupling from the damping rings or the extract lines will be corrected in the first bunch compressor skew correction section; this is also described in Chapter 5. In simulations, this correction section has had no difficulty removing large coupling from the extracted beams. We do not plan on installing any additional skew quadrupoles to control the betatron coupling in the extraction lines.

Trim quadrupole and skew quadrupoles will be located in the dispersive region of the extraction lines (Figure 4-23) to correct for residual dispersion leaking from the damping rings. In addition, correcting quadrupole elements will be placed in the 20° arc which is part of the spin rotator that follows the damping ring extraction lines.

Most tuning of the extracted beam will be performed using the emittance diagnostic station at the end of the first bunch compressor; this is described more fully in Chapter 5. To measure the extracted beams, the compressor rf and spin rotators will be turned off. In addition, a single laser wire will be located in the extraction line to monitor the ring performance. It will be possible to perform quad-scan emittance measurements on this wire for further tuning of the extracted beam.

Transfer Line

At this time, we have not yet designed the PPDR-PDR transfer line. It is expected that the beam line will be a combination of the injection and extraction lines just discussed and is not thought to present any significant problems. The line will include a single conventional wire scanner to monitor the pre-damping ring performance. In addition, quad-scan emittance measurements could be made on this wire when desired.

4.3.9 Dynamic Aperture

The dynamic aperture is usually a limitation in low-emittance strong-focusing rings such as the NLC main damping rings. It is of particular concern in these cases, because the the rings must be designed to have minimal injected beam loss and the injected beam emittances are many orders of magnitude larger than the extracted emittances. The dynamic aperture is also a limitation for the pre-damping ring because of the very large injected beam emittances.

At this time, we have developed solutions for both the main damping rings and the pre-damping ring with very satisfactory performance. The tolerances in the main damping rings to attain a dynamic aperture that is in excess of $10\sigma_{x,y}$ of the injected beams are looser than the tolerances that are required to attain the

Source	Error	Rms Magnitude
All Elements except Bends	X, Y (μm)	100, 100
All Bends	X, Y (μm)	200, 200
All Elements	Z [mm], Θ (mr)	1, 1
All Magnets	$\Delta B/B$ (10^{-3})	1

Table 4-14. Rms errors for main damping ring dynamic aperture simulations.

desired extracted vertical emittance. We believe that these tolerances will be attained using beam-based alignment techniques and do not present a limitation.

In the pre-damping ring, the tolerances to attain a dynamic aperture in excess of the physical aperture are even looser. Here, the alignment tolerances could probably be attained using conventional alignment practices although the ability to use beam-based alignment will exist.

Finally, the multipole tolerances on the magnets in both rings are also straightforward. The tolerances on the main and pre-damping ring magnets are looser than the multipoles components that are being measured on the KEK ATF damping ring magnets and are comparable to those of the PEP-II LER ring magnets.

Main Damping Rings

The goals for the dynamic aperture are an aperture in excess of 10 sigma for an injected beam with the nominal injected emittance of 1×10^{-4} m-rad and a momentum aperture of $\pm 1\%$. This will allow the rings to operate during the commissioning phases where the injection beam properties will likely be poor and it will reduce the sensitivity to injection trajectory errors. Of course, this goal far exceeds the aperture requirements. The electron and positron injectors are being designed assuming a 10% loss of charge at injection into the main damping rings for which an aperture of 3 sigma of the injected beam size would more than suffice.

The dynamic aperture studies have been performed using MAD (Vers. 8.1) and TRACY; it should be noted that both of these codes use large ring approximations and the validity of this should be verified. The results, including energy errors of $|\delta p/p| \leq 1\%$, are illustrated in Figure 4-26. The outer curve shows the acceptance of the bare lattice while the inner curve is the goal of 10 times the injected beam size. One can see that the bare rings have an acceptance that is more than double the desired aperture.

The five middle curves in Figure 4-26 show the aperture when alignment and multipole errors are included, each curve corresponding to a different seed of random errors. In each case, the ring orbits were corrected with the dipole correctors and the tunes were corrected back to the nominal values using the arc quadrupoles.

The rms alignment errors that were used are listed in Table 4-14; these are looser than the tolerances required to attain the desired vertical emittance. In addition, all magnets were assumed to have strength errors of 10^{-3} and higher-order multipole errors.

The quadrupole magnet multipoles that were included are shown in Figure 4-27. Here, the bars represent the systematic multipoles while the solid line is the magnitude of the random multipoles. In both cases, the harmonic fraction shown is the multipole component relative to the quadrupole component at $2/3$ of the the magnet bore; the bore varies from 15 mm to 30 mm for the different quadrupole families.

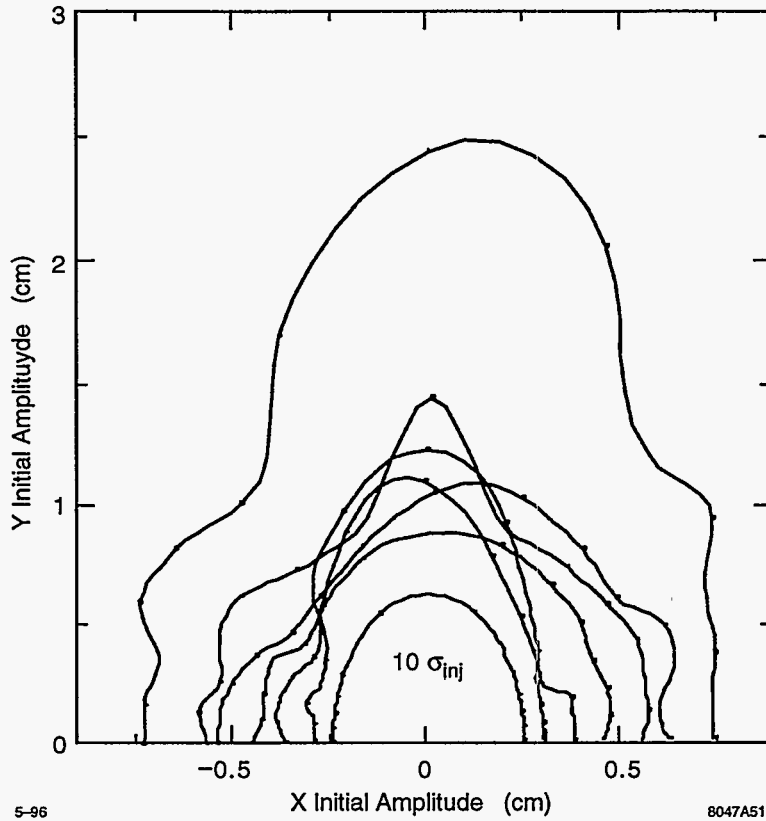


Figure 4-26. Main damping ring dynamic aperture with multipole and alignment errors; the outer solid curve is the aperture of the bare lattice while the middle five curves are the aperture with different sets of errors and the inner solid curve is 10 sigma of the injected beam.

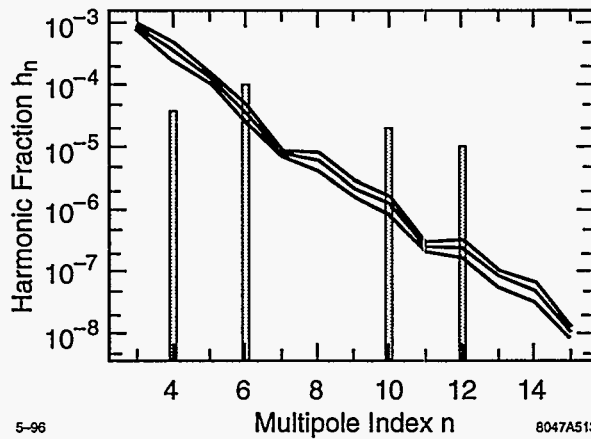


Figure 4-27. Systematic (bars) and random (solid line) multipoles in the quadrupoles where the harmonic fraction is evaluated at 2/3 of the quadrupole bore.

Source	Error	Rms Magnitude
All Elements	X, Y (μm)	200, 200
All Elements	Z (mm), Θ (mr)	2, 2
All Magnets	$\Delta K/K$ (10^{-3})	1

Table 4-15. Rms errors for PPDR dynamic aperture simulations.

In order to evaluate the magnitude of the random multipoles in the quadrupole magnets, we assumed that the quadrupoles would be constructed in two pieces, as was done for both the ALS and the APS synchrotron light sources. The random contribution arising from fabrication errors then has two components: an uncorrelated pole-to-pole piece (significantly reduced relative to four-separate-pole construction), which we take to be 0.77 mils ($20\ \mu\text{m}$) rms in the pole placement in the transverse plane; and the two-pole correlated contribution which can be characterized in terms of a relative translation (in the transverse plane) and rotation of the two halves. The former we take to be 1.5 mils ($40\ \mu\text{m}$) in each of the two dimensions, and the latter to be 1.1 mr, corresponding to a linear displacement of 8.9 mils ($225\ \mu\text{m}$) at a 20 cm arm length.

These pole-to-pole errors contribute to all multipoles and yield a symmetric (but non-uniform) multipole orientation angle distribution, while half-magnet translation errors generate even index pole contributions (*i.e.*, 8, 12, ...), and rotation errors generate odd index poles (*i.e.*, 6, 10, ...). Neglecting fringe fields and assuming ideal pole shapes, the anomalous multipoles generated by the above pole misplacements are precisely determined (to first order) by two dimensional magnetostatics [Halbach 1969].

The estimated systematic components are based on preliminary designs and experience from similar magnet designs. The 8- and 24-pole contributions occur only in the magnets which must accommodate a wide vacuum ante-chamber and thus necessarily deviate from reflection symmetry around each pole. The detailed design alternatives that affect the systematic multipoles have been given minimal attention; thus these systematic multipoles should be viewed as representative rather than definitive.

Finally, similar random and systematic multipoles have been included in the combined function dipoles. The systematic multipoles tentatively adopted are slightly looser than those achieved in prototyping the KEK ATF combined function magnet. It will be possible to extend the analysis of random multipoles done above for quadrupoles once a sufficiently definite design of the combined function pole shape is achieved.

With the errors, the dynamic aperture still exceeds the goal aperture although it is significantly smaller than the bare aperture of the ring. Of course, the dynamic apertures are sensitive to the correction that has been performed. As a trivial example, we considered the seed that led to the worst aperture and corrected the tunes with the straight section quadrupoles rather than the arc quadrupoles. In this case, the aperture improves by roughly 60%; in other cases, correcting the tunes with the straight section quadrupoles rather than the arc quadrupoles has little effect. Finally, we have also studied the aperture for tune variations of 0.01 about the nominal tunes and saw no noticeable change.

Finally, we have not yet included the multipoles from the sextupole magnets or the effect of the nonlinearity due to the wigglers. Both of these are expected to have a small effect but still need to be added.

Pre-Damping Ring

In the pre-damping ring, the goal for the dynamic aperture is an acceptance in excess of the nominal injected edge emittance of 0.09 m-rad with a momentum aperture of $\pm 2\%$. This corresponds to a normalized

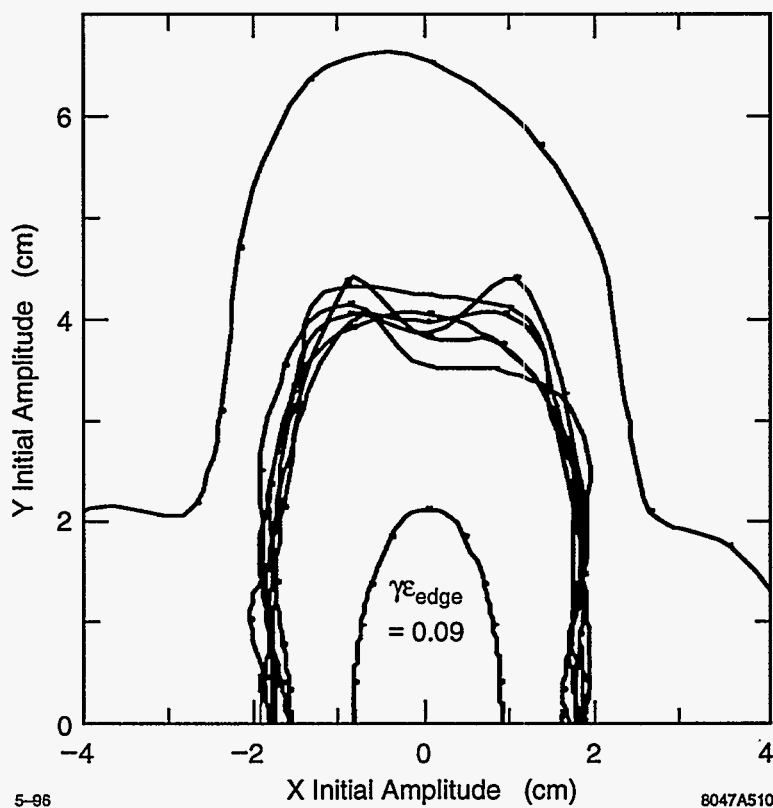


Figure 4-28. Main damping ring dynamic aperture with multipole and alignment errors; the outer solid curve is the aperture of the bare lattice while the middle six curves are the aperture with different sets of errors and the inner solid curve is that required for an edge emittance of $\gamma\epsilon_{x,y} = 0.09$ m-rad.

acceptance of 0.09 m-rad where the acceptance is defined in terms of the particle action:

$$J_x = \frac{1}{2}(\gamma x^2 + 2\alpha x x' + \beta x'^2) \quad (4.22)$$

It should be noted that this is much larger than the aperture required. The positron source has been specified assuming 20% beam loss during injection into the pre-damping ring.

Again, the aperture studies have been performed using MAD (Vers. 8.1) and TRACY. We have studied the effect of alignment and magnet multipole errors. The results, including energy errors of $|\delta p/p| \leq 2\%$, are illustrated in Figure 4-28. The outer curve shows the acceptance of the bare lattice while the inner curve is the goal aperture of $\gamma J = 0.09$ m-rad. One can see that the bare rings have an acceptance that is more than three times the required aperture.

The six middle curves in Figure 4-28 show the aperture when alignment and multipole errors are included, each curve corresponding to a different seed of random errors. In each case, the ring orbits were corrected with the dipole correctors and the tunes were corrected back to the nominal values using the arc quadrupoles.

The rms alignment errors that were used are listed in Table 4-15; these are relatively loose tolerances and could be expected to be attained using conventional alignment practices. In addition, all magnets were assumed to have strength errors of 10^{-3} and higher-order multipole errors.

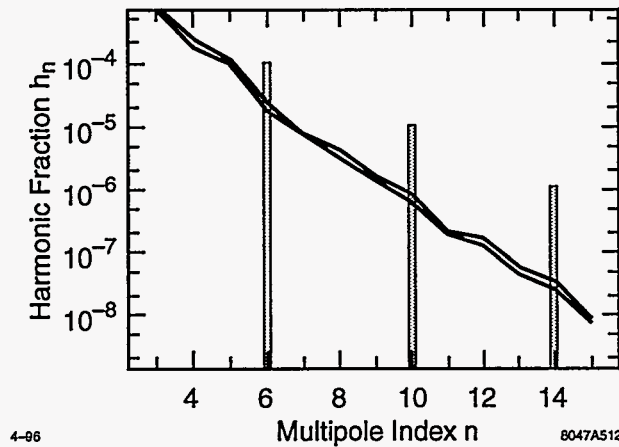


Figure 4-29. Systematic (bars) and random (solid line) multipoles in the quadrupoles where the harmonic fraction is evaluated at $2/3$ of the quadrupole bore.

The quadrupole magnet multipoles that were included are shown in Figure 4-29. Again, the bars represent the systematic multipoles while the solid line is the magnitude of the random multipoles. In both cases, the harmonic fraction shown is the multipole component relative to the quadrupole component at $2/3$ of the the magnet bore; the bore varies from 30 mm to 40 mm for the different quadrupole families.

As was done for the main rings, we assume that the quadrupoles would be constructed in two pieces with tolerances on 0.77 mils ($20 \mu\text{m}$) on the relative placement of the two poles on one piece and 1.5 mils ($40 \mu\text{m}$) on the placement of the two pieces. We also assumed random and systematic multipoles in the combined function dipoles that are based on those achieved in the prototype KEK ATF combined function magnet.

With these errors, we find that the aperture is almost double the required aperture. In the future, we will improve our estimates of the multipoles in the bending magnets and include multipoles in the sextupole magnets but we do not expect the aperture to change significantly.

4.3.10 Polarization

The polarization is assumed to be longitudinal at the exit of the electron source linac. It is rotated into the vertical plane in the injection line for injection into the electron main damping ring. The rotation is performed using the 60° arc followed by a solenoid. A similar arc is included in the positron injection line to allow the line to be easily upgraded for future polarized beams.

The polarization loss in the injection line due to the 1% energy spread in the beam is less than 1%. In contrast, if the injection line energy is changed, there will be large losses in polarization. This loss arises because the 60° arc no longer rotates the polarization by 270° . The fractional polarization loss is equal to:

$$\frac{\Delta P}{P} = (1 - \cos \Delta\Theta) \quad (4.23)$$

where $\Delta\Theta$ is the deviation from the 270° rotation: $\Delta\Theta = 270^\circ \Delta E / 1.98 \text{ GeV}$. Thus, changing the ring energy by 100 MeV to 1.9 GeV or 2.1 GeV would result in a 2.7% loss in polarization through the injection line; the loss would increase to roughly 10% at 1.8 or 2.2 GeV.

At this time, we have not looked in detail at polarization issues in the damping rings. At the nominal operating energy of 1.98 GeV, the rings have a spin tune of 4.5; at this operating point, the depolarization is expected to be small. The operating energy range of roughly ± 220 MeV corresponds to shifts of ± 0.5 in spin tune. At these points, the spin tunes would be integral and we would expect full depolarization. Many other resonances exist that will limit the polarization within the ± 200 -MeV operating range; these have not yet been studied although it would likely be possible to minimize their effect by modifying the ring tunes. We also have yet to study the effect of the beam emittance and the synchrotron radiation on the beam polarization. Both of these effects are expected to be negligible but have yet been considered.

Finally, after extraction from the damping rings, the polarization is rotated to the desired orientation in the bunch length compressors; these spin rotators are described in Chapter 5.

4.4 Collective Limitations

The NLC damping rings will operate with long trains of bunches at a high average beam current and thus coupled-bunch instabilities are an important limitation. In addition, to obtain the desired magnetic fields, the vacuum apertures are relatively small and the broad-band impedance sources can be large. Thus, both single and multibunch instabilities are potential limitations in the NLC damping rings.

Furthermore, because the performance requirements on the damping rings are tight, it is important to avoid instabilities of all sorts. This is also true of the so-called "benign" instabilities. For example, the "strong" longitudinal microwave instability, usually considered benign, sometimes exhibits a bursting mode that has been observed in a number of storage rings; such uncivilized behavior is not acceptable in a damping ring.

In this section, we review "collective" limitations for the main damping rings. We start by describing the impedance model for the ring. This is based upon MAFIA [Klatt 1986] calculations of the bellows, slots, masks, and BPMs, the resistive wall impedance, and the rf cavities; the rf cavities and the vacuum system are described in greater detail in Sections 4.5 and 4.6. Next, we discuss the single bunch instabilities, the synchronous phase variation along the bunch trains, and the coupled bunch instabilities. Finally, we address other effects including beam-gas scattering, intrabeam scattering, lifetime limitations, and ion trapping.

In addition to the usual series of instabilities, the damping rings may also be subject to some new effects that have been predicted theoretically but have not yet been seen experimentally. In particular, there are a photoelectron-positron instability, referred to as the "Ohmi effect," and a fast beam-ion instability that have been postulated. We address both of these issues although, at this time, the true implications are not clear.

In general, there are no known limitations in the main damping rings. The coupled-bunch instabilities require HOM damped rf cavities and a transverse coupled bunch feedback system but these technologies are being well developed for the new B-factories as well as for the KEK ATF damping ring. In addition, the broad-band impedance must be kept minimal to avoid the microwave instability but this should be possible with careful vacuum chamber design.

The two unknowns, the fast beam-ion instability and the electron-positron instability, will be verified in the near future. If they do present a limitation, there are a number of ways to ameliorate the effects; these are addressed in the respective sections.

Finally, this section deals primarily with the main damping ring. In most respects, the issues are less severe in the pre-damping ring since the bunch length is roughly twice as long, the vacuum aperture is much

larger, and the beam emittances are much larger. The collective issues in the PPDR is are summarized in Section 4.4.11.

4.4.1 Main Damping Ring: Impedance Model

The ring impedance determines the beam stability and heating due to excitation of the higher-order modes (HOMs). The short damping ring bunches have a bunch spectrum that starts rolling off at 10 GHz, which is comparable to the 9-GHz cutoff frequency of the 1.25-cm-radius beam pipe. With such a broad bunch spectrum, even small irregularities of the beam pipe cross-section can give noticeable contribution to the beam impedance. Therefore, a careful design and analysis of the vacuum system and other impedance sources is required.

The total longitudinal impedance can be written as the sum of the narrow-band impedance (NB) and the broad-band impedance (BB):

$$Z_i^{tot} = Z_i^{NB} + Z_i^{BB} \quad (4.24)$$

The narrow-band impedance is primarily determined by the rf cavity HOMs and a few NB HOMs of the BPMs and bellows:

$$Z_i^{NB} = i \sum_m \frac{\omega_m}{2} \left(\frac{R}{Q}\right)_m \left[\frac{1}{\omega - \omega_m + i\omega_m/(2Q_m^L)} + \frac{1}{\omega + \omega_m + i\omega_m/(2Q_m^L)} \right] \quad (4.25)$$

The broad-band impedance is determined by the high frequency modes of the cavities and small discontinuities of the beam pipe such as the slot of the ante-chamber, bellows, BPMs, rf contacts, shallow tapers, etc. We can estimate the impedance by scaling from the inductance of the PEP-II. Scaling proportional to the machine circumference $2\pi R$ gives $L = 12$ nH. However, this scaling implies that the total number of inductive components in the ring scales as machine radius and that the inductive character of a component is not changed, *i.e.*, the dimensions of the elements scales in proportion to the rms beam size. A more accurate estimate can be obtained by modeling the vacuum components with the code MAFIA [Klatt 1986] as will be described below.

The broad-band impedance can be expressed:

$$Z_i^{BB} = -i \frac{Z_0}{(1 - i\omega a/c)^{3/2}} \frac{\omega L}{4\pi c} + (1 - i)1.05 \sqrt{\frac{\omega R}{c}} + (1 + i) \frac{R_{cav}}{\sqrt{\omega}} \theta(\omega - \omega_c) \quad [\Omega] \quad (4.26)$$

The impedance of the inductive components also have a small resistive part in addition to the inductance. This is included in the first term in Eq. 4.26; the pure inductive impedance is modified to roll off at high frequencies as $1/\sqrt{\omega}$ which corresponds to the behavior of a cavity impedance at high frequencies. Such a model well describes the dependence of the loss factor on the bunch length. The parameter a defines the roll-off frequency and can be obtained from the loss factor of a bunch with the nominal rms length $\sigma_z = 4$ mm.

RF Cavities

The main contribution to the narrow-band impedance comes from the two rf cavities. As a first estimate, we modeled the cavities after the PEP-II rf cavity, scaled to the desired 714-MHz frequency. Since it is desirable to increase the beam pipe radius b at the cavity location to minimize the transverse kick factor, we considered three models with different beam pipe radii b and nose cone radii r :

Model	freq (MHz)	R_s [M Ω]	R/Q [Ω]	E_p (kV/m)	H_p (A/m)	k_l V/pC	k_{\perp} V/pC/m
1	728.06	3.99	114.14	74.1	66.46	1.21	10.1
2	726.88	4.89	137.01	88.7	61.99	2.99	75.6
3	717.33	4.54	132.21	71.2	68.73	2.78	72.0

Table 4-16. RF cavity models considered for MDR with $\sigma_z = 3.3$ mm.

- 1) $b=3.1$ cm, $r=0.66$ cm
- 2) $b=1.4$ cm, $r=0.66$ cm
- 3) $b=1.4$ cm, $r=1.86$ cm.

Table 4-16 gives frequency, shunt impedance R_s , R/Q , and the maximum E and H fields at the surface of the cavity, E_p and H_p , for the fundamental mode.

Cavity model 1, with 3.1-cm beam-pipe radius, has a total loss factor of $k_l = 1.21$ V/pC for an rms bunch length $\sigma_z = 3.3$ mm; this is shorter than the expected damping ring bunch length of $\sigma_z = 4.0$ mm. The maximum longitudinal impedance is $\Re Z_l = 0.21$ k Ω at 1 GHz while the maximum transverse impedance is $\Re Z_{\perp} = 170$ k Ω/m^2 at 2 GHz. The total loss factor of cavity model 2, with the 1.4-cm beam pipe, is $k_l = 3.0$ V/pC for the same 3.3-mm bunch length. The transverse kick factor is increased from $k_{\perp} = 10.2$ V/pC/m for cavity model 1 to $k_{\perp} = 75.6$ V/pC/m for cavity model 2 without a substantial gain in the shunt impedance of the fundamental mode.

The larger radius $r_c = 3.1$ cm of the beam pipe at the cavity location reduces the impedances which is preferable. The two rf cavities could be mounted on the same large radius beam pipe, which may be tapered to the regular 1.25-cm beam pipe at both ends. Separation of the cavities and the distance from a cavity to the nearest taper has to be optimized to avoid reduction of the Q factor of the fundamental mode and cross-talk between the cavities. The longitudinal loss and transverse kick factors for a model with a shallow 15-cm-long taper on both sides gives $k_l = 1.725$ V/pC and $k_{\perp} = 39.43$ V/pC/m; these numbers may be reduced by using longer tapers.

Such a design, however, leaves a large number of HOMs with frequencies up to the 9-GHz cutoff frequency trapped between the tapers. They can be damped by using absorbers placed on the tapers, adding wave guide dampers loaded with ferrite, or by using wave guides with ridges matched to coaxial cables. Similar designs have been used at KEK B-factory and DAFNE Φ -factory. The first method may be difficult to use because the absorber efficiency deteriorates at high frequencies and because the absorbers themselves would be sources of the resistive-wall impedance, outgassing, and dust.

A conceptual design using the wave-guide dampers is shown in Figure 4-30. A cylindrical coaxial wave guide, having a zero cutoff frequency, is connected to a taper. The outer radius of the wave guide is 3.1 cm and the inner radius of the wave guide was chosen to optimize the damping while minimizing the transverse kick to the beam. The wave guide is terminated with absorbers. The effect of the dampers on the Q -factor of the fundamental mode may be reduced by placing a choke on the wave guide.

Preliminary studies using MAFIA demonstrate that the fundamental mode is not affected by the wave guide damper as shown in Figure 4-30. The longitudinal wakefield for this design is shown in Figure 4-31; it is thought that the short-range wake can be further minimized with optimization of the parameters. At this time, we are performing 2- and 3-D MAFIA studies of the cavity to optimize the placement of the waveguide on the taper and those on the cavity body.

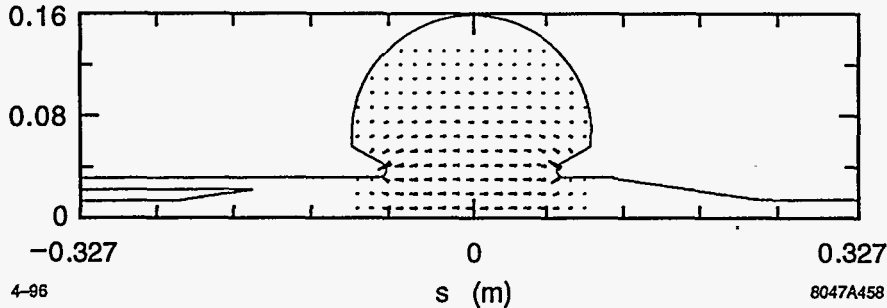


Figure 4-30. Rf cavity model showing coax damping waveguide in the taper but not showing the damping waveguides on the cavity.

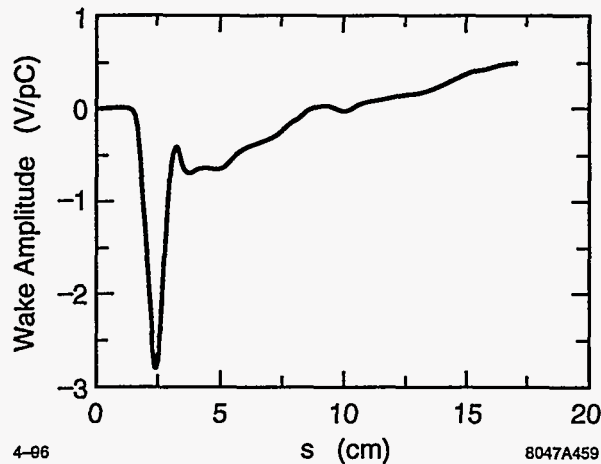


Figure 4-31. Longitudinal wake for the rf cavity.

The high frequency contribution of the rf cavities to the broad-band impedance, Eq. 4.26, can be estimated comparing the loss factors of the modes with frequencies $\omega < \omega_c$ with the total loss factor of a cavity. The difference, Δk_l ,

$$\Delta k_l = \frac{2R_{cav}}{Z_0} \sqrt{\frac{\omega_c}{c\sigma_z}} [\Gamma(1/4) - 4\sqrt{\frac{\omega_c\sigma_z}{c}}] \quad (4.27)$$

defines the coefficient which appears in Eq. 4.26

$$R_{cav} = \frac{Z_0 \Delta k_l}{2\Gamma(1/4)} \sqrt{c\sigma_z} \quad (4.28)$$

for $f_c = 5.34$ GHz. The sum of the NB contribution from the modes $f < f_c$ and the BB tail from $f > f_c$ has a weak dependence on the choice of f_c .

Resistive Wall

The resistive-wall impedance for a round 223-m Al beam pipe is

$$Z_l = (1 - i) 1.05 \sqrt{n} \Omega \quad (4.29)$$

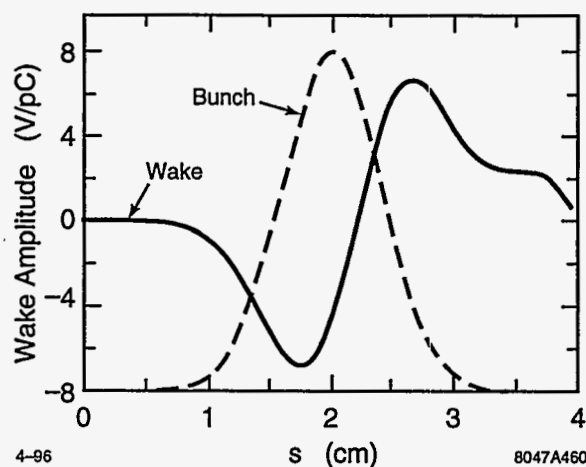


Figure 4-32. Longitudinal wake of the slot termination.

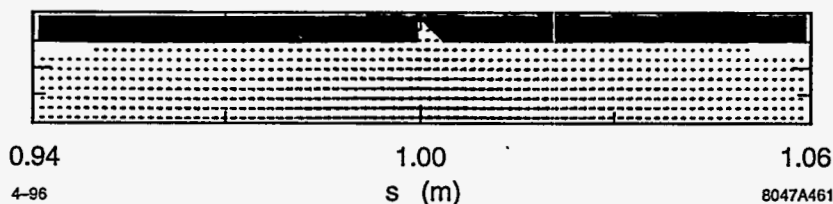


Figure 4-33. MAFIA model of the bellows rf contact showing the trapped mode.

$$Z_{\perp} = (1 - i) \frac{0.48 M\Omega}{\sqrt{n}} \frac{m}{m} \quad (4.30)$$

where n is the harmonic number, $n_{max} = R/\sigma_z = 9000$ for $\sigma_z = 4.0$ -mm bunch. The conductivity $\sigma_c = 3.8 \times 10^7 \Omega^{-1}m^{-1}$ and the beam pipe radius $b = 1.25$ cm were taken in this estimate. Note, that the skin depth is $\delta = 69.5/\sqrt{n} \mu\text{m}$.

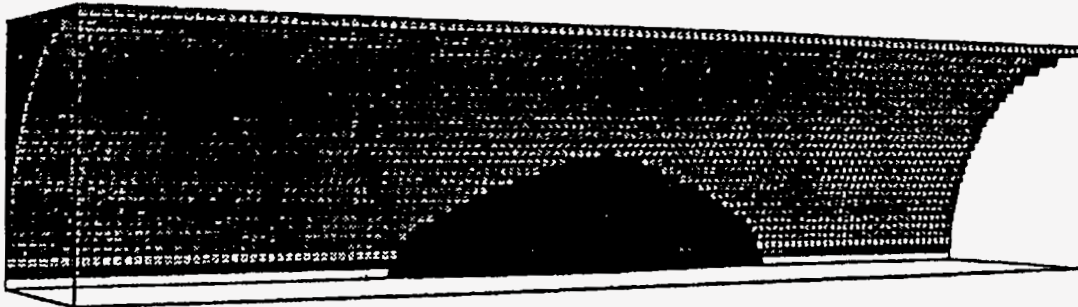
The loss factor of the resistive wall is

$$k_l = \frac{\Re Z_{\perp}}{\sqrt{n}} \frac{2\Gamma(3/4)}{Z_0 \sigma_z} \sqrt{\frac{R}{\sigma_z}} \quad (4.31)$$

and, in this case, is equal to $k_l = 1.4$ V/pC. It should be noted that this estimate does not include the smaller vacuum aperture in the wiggler region where the full gap is only 16 mm. This is partially offset by the larger chamber in the injection/extraction region, and the average loss factor is not changed significantly.

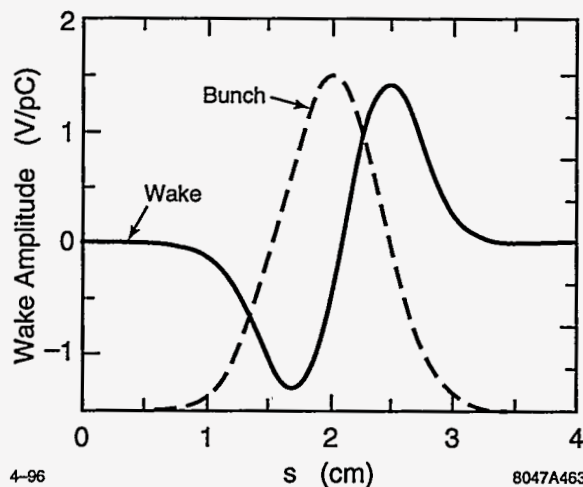
Ante-Chamber Slots and Bellows

To provide adequate pumping with the minimum impedance and to reduce heating and adverse effects of the secondary photon and electron emission, the beam chamber is connected with the ante-chamber by a narrow slot 5-mm wide and 20-mm deep. The slot is terminated with a 25° taper at the masks for the bellows. The impedance of the slot is inductive, see Figure 4-32. The inductance is 0.001 nH for the $\sigma_z = 4$ -mm bunch length. The total inductance of 50 slots per ring is 0.05 nH, a very small contribution to the impedance budget.



4-96
8047A462

Figure 4-34. MAFIA model for the bellows mask.



4-96

8047A463

Figure 4-35. Longitudinal wake for the bellows mask.

The impedance of the shielded bellows is given by slots between shield fingers, and by a small cavity of 4-mm length near the ends of the fingers. The contribution of the slots can be estimated analytically and is negligibly small. The 2D MAFIA simulations of the small cavity showed that there is a trapped mode, see Figure 4-33, with frequency 9.099 GHz, which is below the beam pipe cutoff frequency of 9.186 GHz. The mode is localized in the region with length longer than length of the cavity. The trapped mode has a high $Q_0 = 15000$ and $R/Q = 0.23 \Omega$. The power loss by 360 bunches with 1.5×10^{10} particles per bunch is 6.7 W but, only 25%, *i.e.*, 1.7 W, is deposited within the cavity region. This estimate is conservative because the beam pipe is interrupted by the chamber slot within the localization length of the trapped mode reducing the loaded Q factor of the mode.

Masks

A mask, that is 25-mm long and 2-mm thick, is located at the downstream end of the chamber slot to shield the bellows from the synchrotron radiation. The wakefield of the mask, modeled as shown in Figure 4-34,

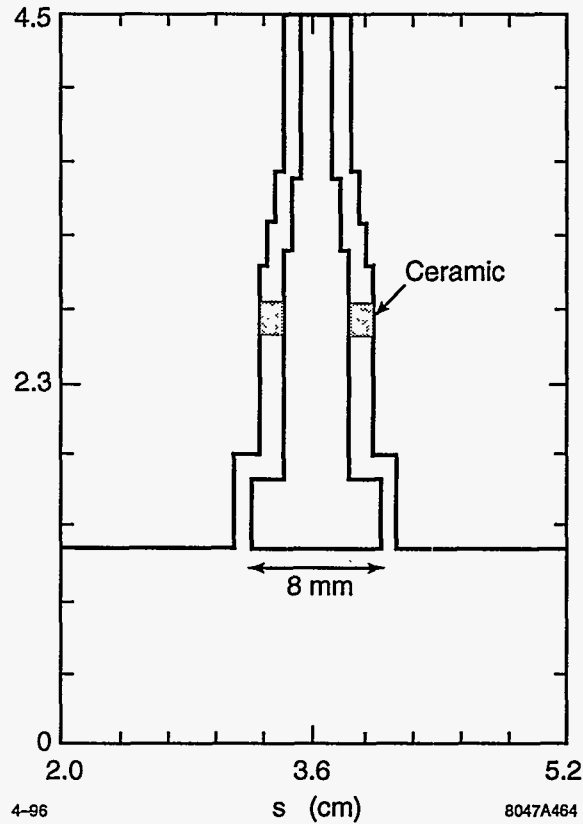


Figure 4-36. 2D projection of 3D MAFIA model for the BPMs.

is depicted in Figure 4-35. The wakefield is mostly inductive but with a substantial resistive component of roughly 5×10^{-3} V/pC. The inductance of a mask is 0.0048 nH which agrees roughly with analytic estimates. The total inductance of the 50 masks and slots is 0.24 nH; the inductance will increase to 1.71 nH if the mask thickness is increased from 2 mm to 4 mm.

BPMs

The design of the BPMs in a high current ring is difficult because of the need to avoid trapped modes that can lead to excessive heating. The BPMs in the NLC damping ring consist of four buttons placed symmetrically around the beam pipe. In the initial design, the buttons have diameters of 8 mm and a ceramic ring of 2 mm thickness for vacuum seal is located at a distance of 9-mm away from the button. Calculations with 3D MAFIA were used to determine the impedance and signal sensitivity of the BPM. The MAFIA model of the BPM is outlined in Figure 4-36.

The total loss parameter of a four-button BPM is found to be $k_l = 2.03 \times 10^{-2}$ V/pC. The longitudinal wakefield of a BPM has a long tail of oscillations at large distances related to several trapped modes. The impedance spectrum is shown in Figure 4-37. Two prominent peaks in the relevant frequency range appear. The field pattern of the resonant mode of high Q at 9.1 GHz corresponds to a mode which is localized mostly in the beam pipe and extends to long distances around a BPM, (Figure 4-38(a)). For 150 BPMs, the

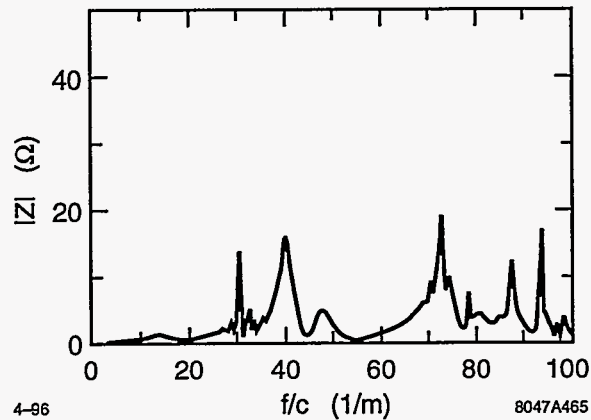


Figure 4-37. Longitudinal impedance of a four button BPM.

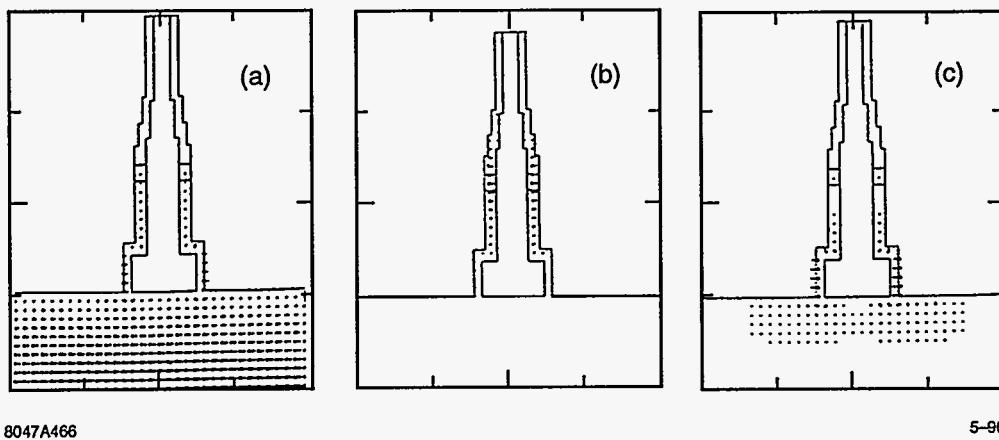


Figure 4-38. Trapped modes in the BPMs.

total impedance of this mode is $2.1 \text{ k}\Omega$, which is small compared with the stability limit of $6.5 \text{ k}\Omega$ which is calculated from Eq. 4.41 assuming that its frequency is resonant with the revolution frequency (f_b); this is the worst case. The actual frequency of the mode in units of the revolution frequency of 714 MHz , $f_r/f_b = 12.7$, is far from an integer value. Hence, the coupled-bunch effects of this mode will be small. Additionally, due to large spatial extent, the heating, produced by the mode at the BPM button, is small. Another resonance at 12.0 GHz is the TE_{11} is localized inside of a button, see Figure 4-38c. The total impedance for all the BPMs for this mode is $2.4 \text{ k}\Omega$, which is small compared with the stability limit of $7.5 \text{ k}\Omega$. The Q value of this resonance is about 50, and, hence, the heating effect arising from coupled bunches is negligible. Furthermore, there is a small peak at around 9.8 GHz between these two resonances. It is identified as the ceramic mode (Figure 4-38b). Since the ceramic is situated far away from the button, this mode is not strongly excited by the beam.

Thus, in the present design, there are a number of narrow-band impedances which appear to be below the coupled bunch stability limits. Detailed heating effects in the BPM need to be addressed further. Finally, the signal at the coaxial cable as a function of time is shown in Figure 4-39 and the transfer impedance for the signal is shown in Figure 4-40. Further investigation is needed to determine whether the output signal satisfies the resolution requirements.

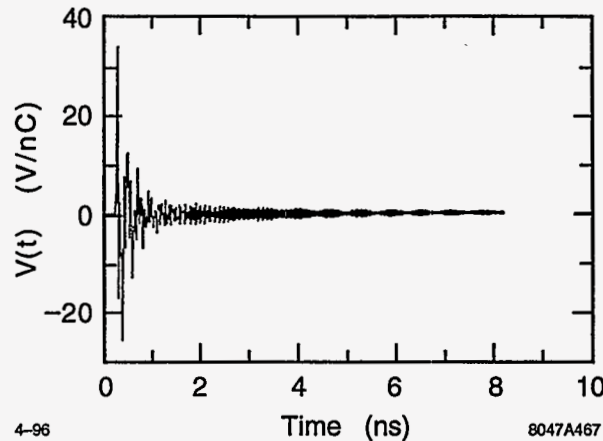


Figure 4-39. BPM response to a passing bunch.

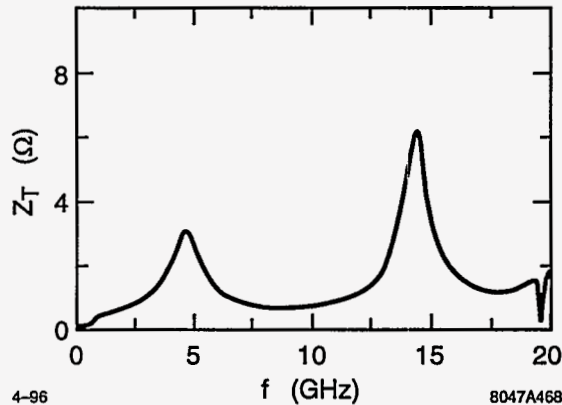


Figure 4-40. Transfer impedance for the BPMs.

Summary

The contributions to longitudinal loss factor are listed in Table 4-17. The main contribution comes from two rf cavities, BPMs, and resistive walls. The other components of the ring are mostly inductive but, for short bunches, still have noticeable loss factors. The main source of the inductance is the synchrotron radiation masks, 50 of them give $L = 0.24$ nH. Some components, such as feedback, injection and extraction kickers, diagnostics, dampers, etc. are not yet included. We expect that they will not substantially change the total (high frequency) impedance.

The transverse impedance is dominated by the HOMs of the cavities and the resistive wall.

The total HOM power can be estimated from the total loss factor k_l as

$$P = I_{beam}^2 \frac{Z_0 k_l s_b}{4\pi} \quad (4.32)$$

which gives a rough estimate that does not take into account the real beam spectrum and an enhancement for the modes at frequencies equal to multiples of the bunch spacing frequency.

	number	k_l V/pC
RF cavities	2	3.45
Res. Wall		1.44
Ante-chamber		0.0225
Bellows	50	0.365
4-button BPMs	150	3.04
Masks	50	0.25
Total:		8.5

Table 4-17. Loss factor summary for the main damping rings.

This yield $P = 15.4$ kW for $k_l = 8.5$ V/pC, maximum beam current $I_{beam} = 1.2$ A, and the $s_B/c = 1.4$ -ns bunch spacing; the HOM power propagating in the beam pipe is smaller due to the narrow-band modes trapped in the rf cavities and BPMs. This is not expected to present a limitation but needs further investigation.

4.4.2 Single-Bunch Potential Well Distortion and Longitudinal Microwave Instability

The two important questions concerning the single bunch longitudinal phase space are (a) What is the average bunch shape and energy spread in the ring? and (b) What is the threshold current to the microwave instability? The answer to the first question is needed in order to know the longitudinal phase space properties of the bunch in subsequent parts of the collider. As for the second question, it is known that the microwave instability is accompanied by an increase in beam energy spread (which increases the longitudinal emittance) and, more importantly, that it can also be accompanied by unpredictable transient beam behavior (*e.g.*, the “saw-tooth” variation in bunch length that has been observed in the SLC damping rings [Krejčík 1993]), a phenomenon that can greatly degrade the performance of the linear collider as a whole.

The microwave instability is also known to come in at least two forms: One, which we call the “strong” type of instability, has a high growth rate that depends only weakly on the synchrotron radiation damping rate, a threshold that can be roughly approximated by the Boussard criterion [Boussard 1975], and that can be thought of as generated by the coupling of two synchrotron modes with different azimuthal mode numbers. The other, a type that has only recently been identified [Oide 1994, Chao 1995, Bane 1995a], we call the “weak” type of instability; it has a growth rate that is sensitive to the radiation damping time, has a threshold that has no connection to the Boussard criterion, and can be described as the coupling of two modes with the same azimuthal but different radial mode numbers. The weak type of instability is found in storage rings with a predominantly resistive impedance.

In this section, we find that for the NLC damping rings at our highest design current ($N = 1.57 \times 10^{10}$) we may be running near the threshold of the weak instability but we are significantly below that of the strong instability. However, the weak instability is not a serious problem like the strong instability.

Consider, the SLC damping rings. In 1994 a completely redesigned vacuum chamber was installed. Before this time a strong type of instability was observed, with the current—due to the microwave instability—limited to the threshold value [Krejčík 1993]; since the upgrade only a weak type of instability has been seen, and the SLC runs routinely a factor of 3 above the threshold current [Bane 1995b]. We also believe the weak

instability is less serious in that, unlike the strong instability, it is very sensitive to the tune spread within the bunch; by slightly increasing the tune spread (such as, for example, by adding a modestly powered, higher harmonic cavity to the ring [Chao 1995]), through Landau damping, the threshold to this kind of instability can be increased substantially.

In this section, we first obtain the wakefields of the main vacuum chamber objects, driven by a bunch that is significantly shorter than the nominal bunch length, using the computer program MAFIA [Klatt 1986]. These individual wake functions are then summed in the correct proportion to give a wakefield representing the entire ring. Finally, this wakefield is used as a Green function for calculating the effect of potential well distortion and for obtaining the threshold to the microwave instability. To obtain the bunch shape below threshold this wakefield is applied to the Haïssinski formula [Haïssinski 1973]; for locating the threshold current it is applied to the Vlasov equation, which is solved in a perturbative manner using K. Oide's computer program [Oide 1990].

Calculations

One cannot predict the average bunch properties nor the threshold current of a ring without knowing the vacuum chamber geometry, from which they can calculate the wakefield or the impedance. As was the case for the SLC damping rings small changes in vacuum chamber cross-section—such as those connected to bellows, transitions, and masks—can dominate in their contribution to bunch lengthening and the microwave instability over larger objects such as the rf cavities [Bane 1988]. Therefore, it is important to know the details of the geometry of the vacuum chamber before beginning this work (as it is important to build the vacuum chamber to tight specifications during the construction phase). For the NLC damping rings, the main contributors to the longitudinal impedance have been designed: they are the 2 rf cavities, the 150 beam position monitors (BPMs), the longitudinal resistive-wall wakefield, the 50 synchrotron radiation masks, and the 50 tapers and pumping slots. It is assumed that the bellows that allow the ring to be assembled are shielded, leaving an impedance that is insignificant. Furthermore, it is assumed that the kicker chamber and septum region also do not contribute significantly to the impedance (Note that the important objects are all described in detail in Section 4.4.1).

The nominal rms bunch length in the NLC damping ring is 4 mm; for all our wakefield calculations we take a gaussian bunch with rms $\sigma_z = 1$ mm as the driving bunch and calculate the wakefield to 15 mm behind the bunch center (due to the large number of mesh points required for finding the wake of the rf cavities and the BPMs we could not easily use a shorter driving bunch). We begin with the rf cavities. There are two single-cell cavities; each cavity is set back from the beam tube by a pair of gradual tapers. The total wakefield of the two rf cavities, as calculated by MAFIA, is shown in Figure 4-41 (the solid curve). We see contributions of both the setbacks and the cavity itself in the shape of the wake. The BPMs are of the button type; each BPM consists of four cylindrical, 8-mm-diameter electrodes that are set symmetrically (about the axis) into the beam tube wall; the impedance is due to the annular space that electrically isolates each button from the tube wall. The wakefield of the 150 BPMs is given by the dashed curve in Figure 4-41. We notice ringing at a frequency beyond 20 GHz.

The longitudinal resistive-wall wakefield can normally be ignored in impedance calculations of storage rings; for the NLC, however, its contribution is significant. For a gaussian bunch the resistive-wall wakefield is given by [Piwinski 1972]

$$W_z(s) = \frac{C}{4b\sigma_z^{3/2}} \sqrt{\frac{c}{2\pi\sigma}} f(s/\sigma_z) \quad , \quad (4.33)$$

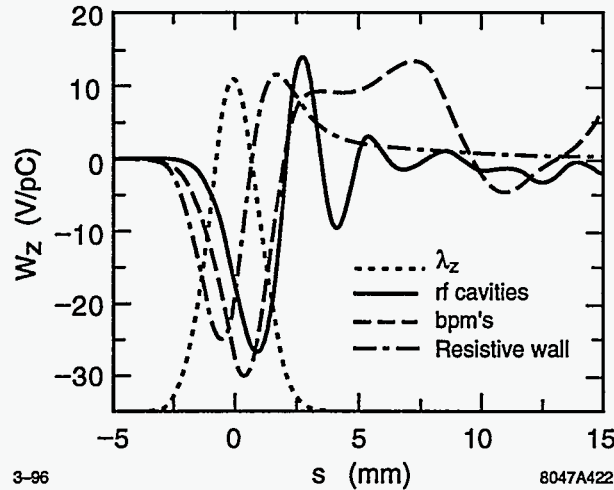


Figure 4-41. The longitudinal wakefield left by a gaussian bunch, with $\sigma_z = 1$ mm, due to the rf cavities (the solid curve), the BPMs (the dashed curve), and the resistive-wall wakefield (the dot-dashes). The driving bunch shape is given by the dotted curve, with the head to the left.

with C the machine circumference, b the tube radius, σ_z the rms bunch length, σ the conductivity of the vacuum chamber walls; with

$$f(u) = |u|^{3/2} e^{-u^2/4} (I_{1/4} - I_{-3/4} \mp I_{-1/4} \pm I_{3/4}) |u^{2/4} \quad . \quad (4.34)$$

In Eq. 4.34 the upper signs apply for $u < 0$, the lower signs for $u > 0$; the modified Bessel functions I are evaluated at $u^2/4$. For the NLC damping ring we take $C = 223.5$ m, $b = 1.25$ cm, $\sigma_z = 1$ mm, and $\sigma = 3.2 \times 10^{17} \text{ s}^{-1}$ (aluminum). The resulting resistive-wall wakefield is given by the dot-dashed curve in Figure 4-41. We note that, in amplitude, the cavities, the BPMs, and the resistive-wall contribute about equally to the total wakefield of a 1-mm bunch. As final ingredients we have also obtained the wakefields of the 50 synchrotron radiation masks and the 50 tapers and pumping slots; these contributions are small compared to the wakefields discussed above.

Summing all the contributions we obtain the wakefield that we will use as a Green function to represent the entire NLC damping ring (see Figure 4-42). One important subtlety is that, since it has a leading tail, our Green function is not causal. To obtain a causal Green function we will consider two ways of modifying the leading tail. The first method, which we call the capacitive approximation, is obtained by flipping the leading tail to the back, about $s = 0$, and adding it to the wake. The second method, which we call the resistive approximation, is obtained by replacing the leading tail by a delta function at the origin that has the same area as the leading tail. In the following we will compare the results using these two versions of the Green function. If the bunch used to calculate the Green function is sufficiently short, then the results for the two cases should be nearly the same.

To obtain the longitudinal bunch distribution λ_z we apply the total wake function to the Haïssinski equation [Haïssinski 1973]

$$\lambda_z(s) = K \exp \left(-\frac{s^2}{2\sigma_{z0}^2} + \frac{1}{V_{rf}' \sigma_{z0}^2} \int_0^s V_{ind}(s') ds' \right) \quad , \quad (4.35)$$

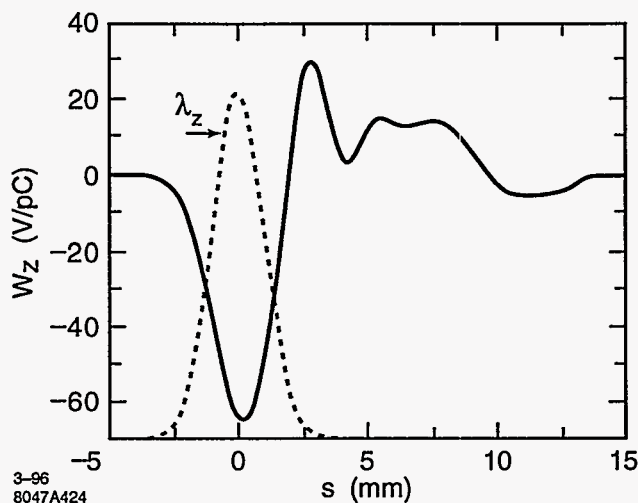


Figure 4-42. The total longitudinal wakefield left by a gaussian bunch, with $\sigma_z = 1$ mm, on each turn in the NLC damping ring. The driving bunch shape is given by the dotted curve, with the head to the left.

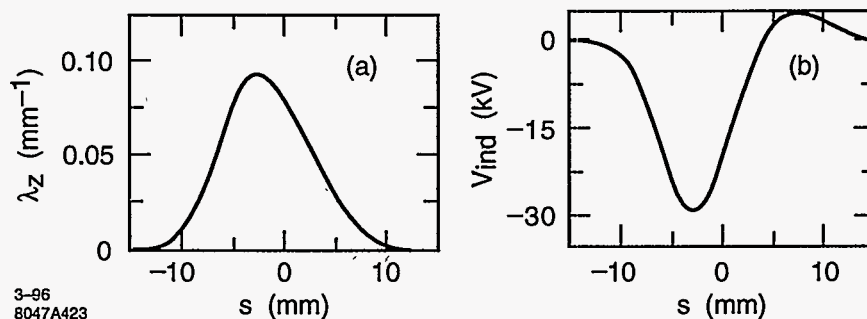


Figure 4-43. The NLC damping ring bunch shape (a) and the induced voltage (b) when $N = 1.57 \times 10^{10}$, $V_{rf} = 1$ MV, $\phi = 50^\circ$. The head of the bunch is to the left.

with K a constant that gives $\int_{-\infty}^{\infty} \lambda_z(s) ds = 1$, σ_{z0} the nominal (zero current) bunch length, V'_{rf} the slope of the rf voltage at the synchronous phase, and

$$V_{ind}(s) = eN \int_0^{\infty} \lambda_z(s-s')W_z(s') ds' \quad , \quad (4.36)$$

with eN the total bunch charge. For $N = 1.57 \times 10^{10}$, $\sigma_{z0} = 4$ mm, $V_{rf} = 1$ MV, rf frequency $f_{rf} = 714$ MHz, and synchronous phase (from the peak) $\phi = 50^\circ$, we obtain the bunch shape and induced voltage shown in Figure 4-43 (the head of the bunch is to the left). [The result is essentially the same for both the capacitive and the resistive approximation to the Green function.] We note that the impedance is clearly resistive in character, *i.e.*, V_{ind} is roughly proportional to λ_z , and that the bunch shape is hardly perturbed from the nominal, gaussian one. The rms bunch length is increased by 6% to 4.23 mm and the centroid is shifted forward by 1.46 mm, to make up for the higher mode losses.

To estimate the threshold for the strong microwave instability we use the Boussard criterion [Boussard 1975]:

$$\frac{e\hat{I}|Z/n|}{2\pi\alpha_p E\sigma_\delta^2} \lesssim 1 \quad , \quad (4.37)$$

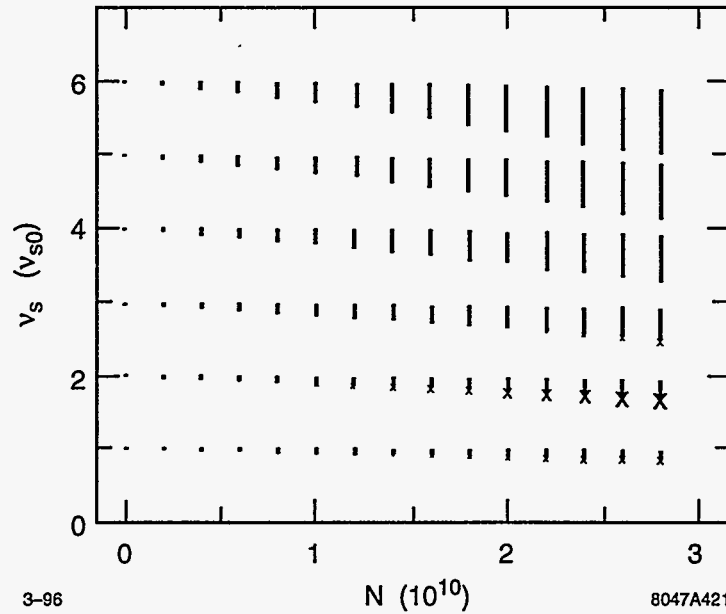


Figure 4-44. The modes obtained by the Vlasov method when the capacitive model to Green function is used. Stable modes are represented by a dot, unstable modes by an 'X', with the size proportional to the growth rate.

with \hat{I} the peak current; $|Z/n| = |Z|\omega_0/\omega$ where Z is the impedance at frequency ω and ω_0 is the revolution frequency (for an inductive impedance $|Z/n|$ is a constant); α_p is the momentum compaction, E the beam energy and σ_δ the rms relative energy spread. The above criterion, if satisfied, indicates that the beam is stable. Note, however, that the Boussard criterion is only a very rough criterion, used to obtain an approximate idea of where the threshold to the strong instability might be. For the NLC, since the impedance is resistive it can be characterized by a resistance R , with the induced voltage given by $V_{ind} = -eNcR\lambda_z$. Fitting to this equation we find that the effective resistance of the damping ring $R \approx 250 \Omega$. Let us take as typical bunch frequency $\omega \sim c/\sigma_z$, which gives $|Z/n| \approx R\sigma_z\omega_0/c = 0.03 \Omega$. Then, using the same parameters as above, and taking $\alpha_p = 4.7 \times 10^{-4}$, $E = 2 \text{ GeV}$, and $\sigma_\delta = 9 \times 10^{-4}$, we find that the left hand side of Eq. 4.37 equals 0.5, suggesting that, at the highest envisioned current, we are still below the threshold for a strong instability.

To get a better estimate of the instability threshold, we have applied our wakefield to K. Oide's computer program that solves the linearized, time-independent Vlasov equation [Oide 1990]. This program uses a perturbation approach to find the threshold; it includes the potential well distortion as a zeroth order effect. This program solves for the modes of the system, and finds the mode that first becomes unstable. (For the SLC damping ring, the results of this program have been shown to agree very well with turn-by-turn tracking using a large number of macro-particles [Bane 1995a, Bane 1993]). For our simulation, we take as nominal synchrotron frequency $\nu_{s0} = 0.004$, and truncate the system matrix to six mode numbers in the azimuthal direction and 60 in the radial direction.

The results are shown in Figure 4-44 where we plot the dependence of mode frequency on current for the capacitive approximation to the Green function. Stable modes are represented by a dot (note that at $N = 0$ for every azimuthal mode number there are 60 dots with the same frequency); unstable ones are indicated by an 'X', with the size of the symbol proportional to the growth rate (synchrotron radiation damping is not included in the calculation). We see that for each azimuthal mode number, at least up to the nominal

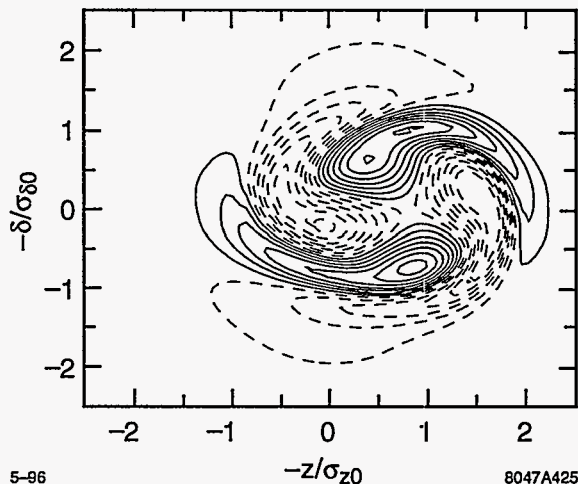


Figure 4-45. The shape of the weak mode found at $N = 2 \times 10^{10}$ when the capacitive approximation to the Green function is used.

maximum current ($N = 1.57 \times 10^{10}$), the frequencies are spread and depressed only slightly, which is typical behavior for a resistive impedance. The synchrotron radiation damping time of the NLC damping ring is $t_z = 2.5$ ms. The growth rate of an unstable mode first matches this value at $N = 1.65 \times 10^{10}$. The unstable mode is a quadrupole mode of the weak type, with frequency $1.8\nu_{s0}$ (its shape is plotted in Figure 4-45). In this example, the nearest strong instability is at $N = 7 \times 10^{10}$.

If, instead, we take the resistive approximation to the Green function we find that the growth rate of the weak instability is below the synchrotron radiation damping all the way up to the threshold of the strong instability, which, in this case, we find at $N = 8 \times 10^{10}$. The true result for our model damping ring is probably somewhere between the results given by the capacitive and the resistive model to the Green function, which suggests that at the highest design current no microwave instability will be encountered in the NLC damping rings. To obtain a more precise result of the location of the instability thresholds we need to get the wakefields for the NLC damping ring vacuum chamber due to a bunch with an rms that is significantly shorter than the current value of 1 mm.

4.4.3 Single-Bunch Transverse Mode Coupling

Transverse coupling will set a limit on the maximum single bunch beam current. In addition, the mode coupling threshold will be modified by the coupling between the bunches [Berg 1995]. In this section, we calculate the single bunch mode coupling threshold and then describe the modification of the results due to the bunch trains; the coupled-bunch instabilities are described in a later section.

In the NLC damping ring, the vertical plane results are universally worse than those for the horizontal plane, so only the vertical plane will be discussed here. The details of these calculations is given in Ref. [Berg 1995].

We use the broadband model of the transverse impedance and the transverse cavity higher-order modes given in Section 4.4.1. Note that the cavity higher-order modes as well as the part of the broadband impedance due to cavity tails must be enhanced by a factor of the β -function at the cavities (taken to be 6.5 m) over the average β -function (4-m vertical).

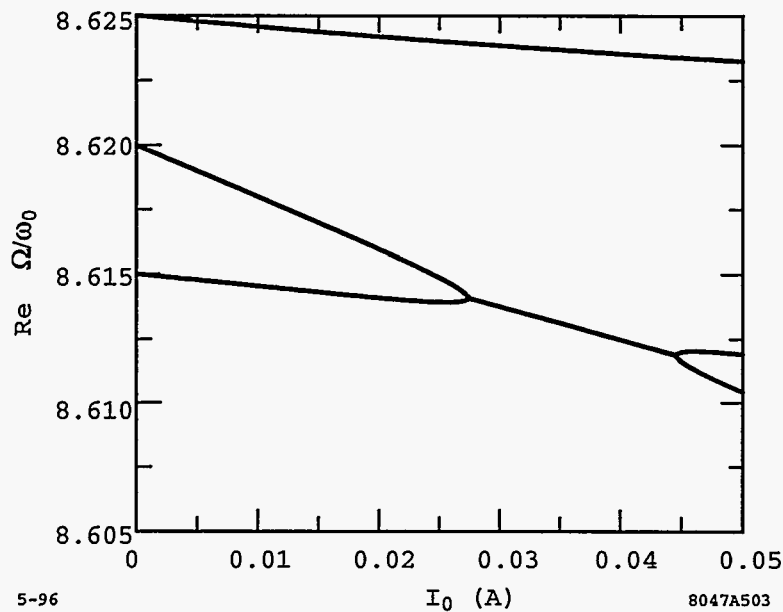


Figure 4-46. Single-bunch vertical mode coupling.

If only a single bunch is considered, transverse-mode coupling is seen at around 28 mA, as shown in Figure 4-46; the threshold is almost identical whether the rf cavities are deQed to 100 or 3000. For comparison, the damping ring single bunch current is much less, roughly 3.3 mA.

If we consider 532 symmetrically placed bunches, we find that the rigid ($m = 0$) coupled-bunch motion is only very slightly affected by mode coupling at the typical currents but the $m = 1$ coupled-bunch growth rates are strongly affected. If the rf cavities are deQed to around 100, the resulting growth rates are well below radiation damping at a beam current of 1.2 A. If the some cavity modes are left with Qs around 3000, the growth rates can become comparable to to the radiation damping rate. Additional details will be discussed in the section on transverse coupled-bunch instabilities.

4.4.4 Bunch-to-Bunch Synchronous Phase Variation

At any given time, there will be four trains of 90 bunches in the main damping rings. Within a train, the bunches populate adjacent buckets and between trains there is a gap that extends over 43 buckets. A consequence of an uneven filling scheme is that within each train the synchronous phase will vary from bunch to bunch. After extraction the beam enters the bunch compressors and then the X-band linac. The phase variation in the ring, if uncompensated, will lead to a phase variation in the X-band linac which, in turn, will result in an unacceptable spread in the final energy of the bunches in a train. The synchronous phase variation, however, can be compensated, either in the damping ring itself or in the bunch compressors that are described in Chapter 5. The present NLC design assumes that later method of compensation and the bunch compressors have been designed to accommodate a ± 20 ps variation in the synchronous phase.

In this section, we first find the synchronous phase variation across the bunch trains of the NLC damping rings, and then we study a method of compensating this variation—one employing passive sub-harmonic

cavities—in the damping ring itself. More details of this compensation technique can be found in Ref. [Bane 1995c].

The Variation in Synchronous Phase

Consider a damping ring filled with bunch trains, with N bunches per train, and let us suppose that we can ignore the effects of higher cavity modes. Let us further assume that the bunch gap is short, *i.e.*, $|\Delta\bar{\omega}T_g| \ll 1$, with T_g the gap time interval, and

$$\Delta\bar{\omega} = \Delta\omega + i\frac{\omega_{rf}}{2Q_L} \quad , \quad (4.38)$$

where $\Delta\omega$ is the frequency detuning, ω_{rf} the fundamental frequency, and Q_L the loaded Q of the cavity. Then the steady-state phase difference between the first and last (N^{th}) bunch in each train is given by [Lambertson 1995]

$$\Delta\phi_{1N} \approx -\frac{2kI_0T_g}{V_c \sin\phi} \quad , \quad (4.39)$$

with k the loss factor ($= \frac{1}{2}\omega_{rf}R/Q$), I_0 the average beam current, V_c the peak voltage, and ϕ the nominal synchronous phase ($\phi = \cos^{-1}[U_0/eV_c]$, where U_0 is the energy loss per turn). The average beam current I_0 is given by

$$I_0 = \frac{Nq}{NT_b + T_g} \quad , \quad (4.40)$$

with q the charge per bunch and T_b the bunch-to-bunch time interval within a train. The negative sign in Eq. 4.39 indicates that the synchronous phase of the last bunch is more forward (toward the crest) than the first bunch. Note also that in the NLC damping rings not only is the gap short but also the bunch train itself, *i.e.*, $|\Delta\bar{\omega}NT_b| \ll 2\pi$; it can easily be shown [Bane 1995c] that in such a case the synchronous phase varies linearly with bunch number within each bunch train.

For the NLC damping rings the rf frequency is 714 MHz and the R/Q for the two rf cavities combined is 240 Ω ; therefore, $k = 0.54$ V/pC. We take $N = 90$, $q = 2.5$ nC, $T_b = 1.4$ ns, and $T_g = 60.2$ ns; therefore, $I_0 = 1.2$ A. Taking $V_c = 1$ MV and $\phi = 50^\circ$ we obtain $\Delta\phi_{1N} = -5.8^\circ$. We have also numerically simulated this problem using turn-by-turn tracking [Thompson 1991]. The unloaded Q of the cavities was taken to be $Q_0 = 25500$; for minimum reflected power $Q_L = 2200$ and $\psi = -44.5^\circ$ (remember: $\tan\psi = 2Q_L\Delta\omega/\omega_{rf}$). The results are shown in Figure 4-47. Plotted are the shift in synchronous phase $\Delta\phi$ versus bunch number. We see that, over each train, the variation is linear with bunch number, and that the total phase shift is -5.9° , in good agreement with our analytical results. Note that both the length of the gap and the length of the bunch train are short according to our criteria: $|\Delta\bar{\omega}T_g| = 0.003 \ll 1$ and $|\Delta\bar{\omega}NT_b| = 0.2 \ll 2\pi$.

It may occasionally happen that one bunch train has a slightly different charge than the others. To study the sensitivity to this we have repeated the numerical tracking but with the bunches of the first train having only 95% of the nominal charge. The results are shown in Figure 4-48. In this case the maximum phase deviation in the first train has been reduced to 80%, in the other three trains to 95%, of the value found for equally populated trains. Note, however, that the average value of $\Delta\phi$ for all trains has changed by 3° . This average change, however, can easily be corrected by a phase feedback system in the damping ring.

Compensating the Variation in Synchronous Phase

Given a sufficient amount of extra power and bandwidth in the klystron, the synchronous phase variation discussed above can be compensated by properly varying the generator voltage as a function of time; this

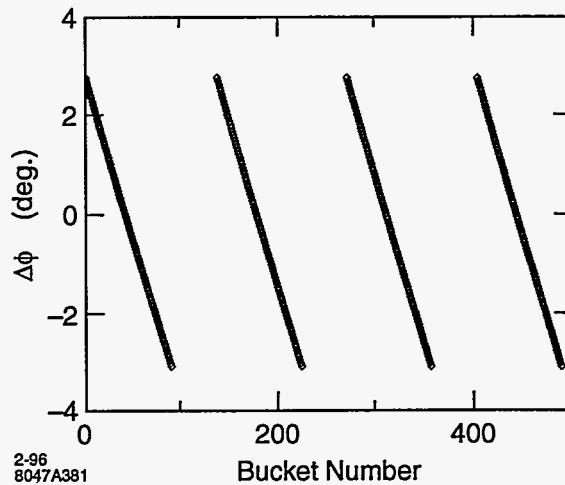


Figure 4-47. The steady-state, bunch-to-bunch synchronous phase variation vs. bunch number for the NLC damping rings. Note that a more negative value of phase is more toward the front (toward the rf crest).

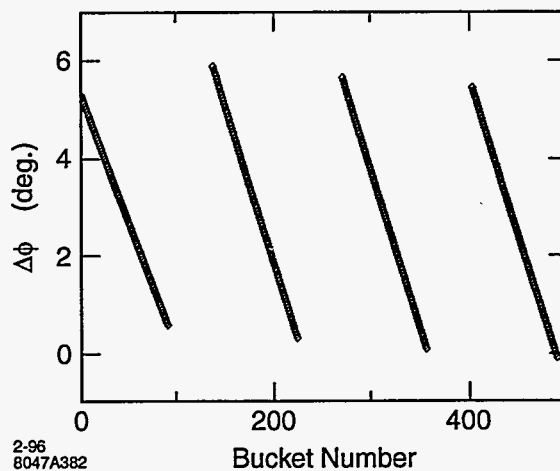


Figure 4-48. The synchronous phase variation vs bunch number for the case when the bunches of the first train have only 95% of the nominal bunch population while the rest are unchanged.

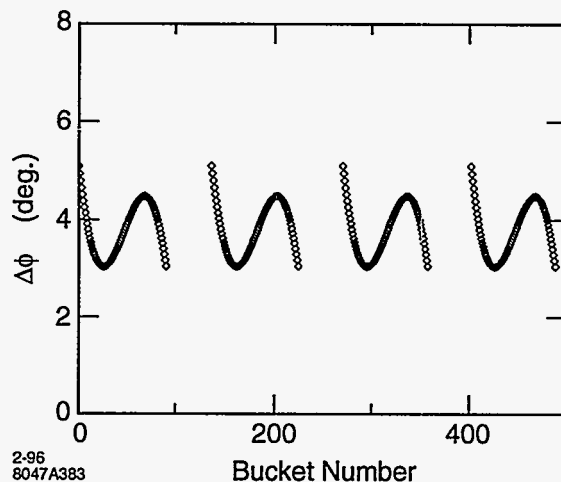


Figure 4-49. The synchronous phase variation that can be achieved when one passive, lower harmonic cavity is used.

method will be studied in future work. However, here we will discuss a method of compensation described in Ref. [Kubo 1993], where the authors find that a properly tuned, passive, lower harmonic cavity can be used to compensate the phase variation due to bunch trains. The frequency of the compensation cavity must be equal to $\omega_{rf} - 2\pi n N_t / T_0$, with n an integer, N_t the number of bunch trains, and T_0 the revolution time. This method of compensation works quite well when the gap length is larger than the length of a bunch train. In our case, however, the gap length is only about half the train length. We will, therefore, also investigate the effect that can be obtained using two lower-harmonic cavities to compensate the synchronous phase variation.

Figure 4-49 gives the tracking results when an optimally-tuned, passive cavity with frequency $\omega_{rf} - 8\pi/T_0$ is included in the damping ring. The parameters of this cavity were optimized numerically. They are: $R/Q = 34 \Omega$, $Q_0 = 3.43 \times 10^4$, $Q_L = 1.14 \times 10^4$, and $\psi = -85^\circ$. We see from the figure that the maximum phase deviation has been reduced to 2.1° , which is only a factor of 3 smaller than we had initially. Adding a second, passive cavity, with frequency $\omega_{rf} - 16\pi/T_0$, $R/Q = 18 \Omega$, $Q_0 = 3.43 \times 10^4$, $Q_L = 1.0 \times 10^4$ and $\psi = -82^\circ$ gives the results shown in Figure 4-50. Now the maximum phase deviation has been reduced to 0.65° , which is a factor of nine smaller than we started with. Finally, note that the R/Q s of the compensation cavities are very small, so they should not contribute to an instability. One negative point, however, might be that the residual phase variation is nonlinear with bunch number, an effect which may have its own negative ramifications.

At this time, we have decided not to compensate the loading in the rings. The $\pm 3^\circ$ L-band variation across the bunch train can be easily accommodated in the bunch compressors as described in Chapter 5. Furthermore, because the variation is linear across the bunch train, it may be straightforward to correct the resulting energy variation in the prelinac before the second compressor. This would allow a simpler design for the second compressor system.

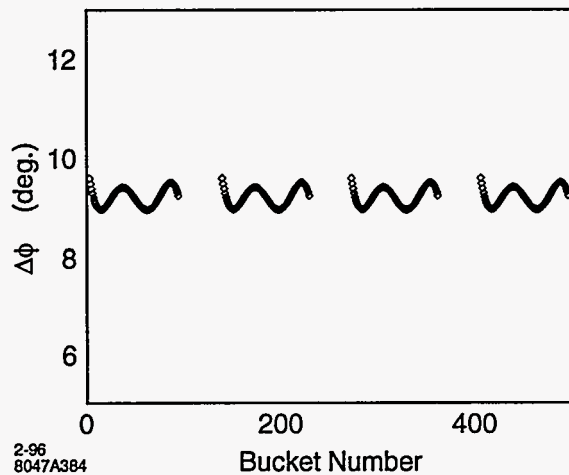


Figure 4-50. The synchronous phase variation that can be achieved when two passive, lower harmonic cavities are used.

4.4.5 Coupled Bunch Instabilities

The close spacing of bunches (1.4 ns) within a train in the main damping rings allows for the possibility that bunch wakefields will influence the motion of consecutive bunches. In general, such wakefields arise from narrow-band resonances in the rf cavities and from the finite conductivity of the vacuum chamber wall. Under certain conditions, the wakefields can generate a transverse or longitudinal coherent structure in the relative motion of the bunches which grows exponentially, leading to a loss of beam quality and/or loss of the beam itself. This is referred to as a coupled-bunch instability. The wakefields can also create static offsets in either the transverse or longitudinal position along the bunch train due to the nonuniform filling pattern of the ring. Furthermore, the restraints on beam size and bunch phase at extraction require control of beam oscillation transients from injection errors. These effects are generally proportional to the total beam current and thus are a concern for the 1.2-A design current for the main damping rings.

At the time of this study, the HOMs of the damping ring cavities were not available. Thus, we have estimated these various effects for the main damping rings assuming a scaled-down version of the PEP-II rf cavity as the primary source of narrow-band resonances, where the cavity size has been reduced such that the fundamental mode frequency has increased from 476 to 714 MHz. The strongest monopole and dipole higher-order-modes (HOMs) are given in Tables 4-18 and 4-19. It is also assumed that all HOMs are damped to $Q < 200$. The effects are calculated for two identical rf cells with a total voltage of 1 MV.

Longitudinal

In the longitudinal plane, coupled-bunch oscillations are driven only by the monopole HOMs of the rf cavities. Assuming a uniformly filled ring, the growth rate for dipole oscillations is given by

$$\frac{1}{\tau} = \frac{1}{2} \frac{I_0 \alpha_p f_{rf}}{(E/e) Q_s} [Z_{||}]_{\text{eff}} \quad (4.41)$$

f_r (MHz)	R_s (k Ω)
3060.85	2.6
1941.55	1.8
2291.94	1.8
4563.48	0.66
1487.27	0.52
4150.84	0.52
3368.43	0.46
3554.05	0.36
5180.54	0.32

Table 4-18. Strongest rf cavity monopole HOMs.

f_r (MHz)	R_{\perp} (k Ω /m)
1193.2	85
2499.8	72
1988.2	36
2397.2	11.2
2310.6	9.7
4861.2	7.8
3755.4	7.0
3603.0	4.8
3423.6	3.8
4736.2	3.8
3346.5	2.6

Table 4-19. Strongest rf cavity dipole HOMs.

where the effective impedance is

$$[Z_{\parallel}]_{\text{eff}}^I = \sum_{p=-\infty}^{p=+\infty} \frac{\omega_p}{\omega_{rf}} e^{-(\omega_p \sigma_r)^2} Z_{\parallel}(\omega_p). \quad (4.42)$$

The effective impedance and the corresponding growth rate are shown in Figure 4-51. For $Q < 200$ the fastest growth rate falls approximately a factor of two below the radiation damping rate, indicating stable oscillations. The above applies strictly to a uniform fill pattern with every rf bucket filled. The effects of instabilities are typically lessened by nonuniform fill patterns. More detailed simulations are required to study transient effects including the gaps between bunch trains.

The growth rates are insensitive to tuning of the HOM frequencies because of the relatively large bandwidth of the HOMs as compared to the revolution frequency. Landau damping from a tune spread within the bunch is not effective because of the short bunch length. Coupled-bunch shape oscillations, *i.e.*, $m > 0$, are not driven by the HOMs at a significant level. Also, with the nominal detuning, the fundamental mode impedance does not drive any coupled-bunch instabilities at a rate comparable to the radiation damping rate.

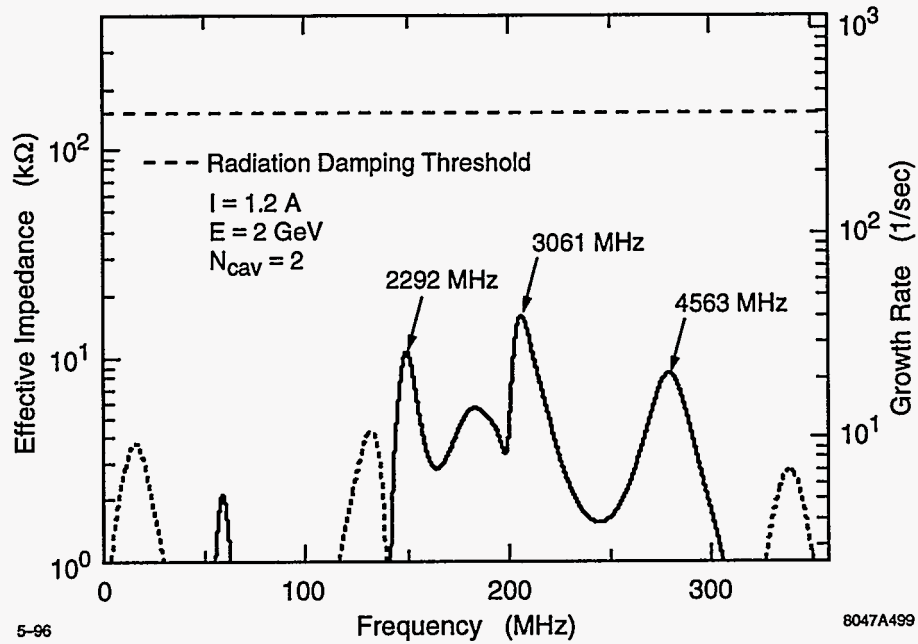


Figure 4-51. Longitudinal coupled-bunch growth rates.

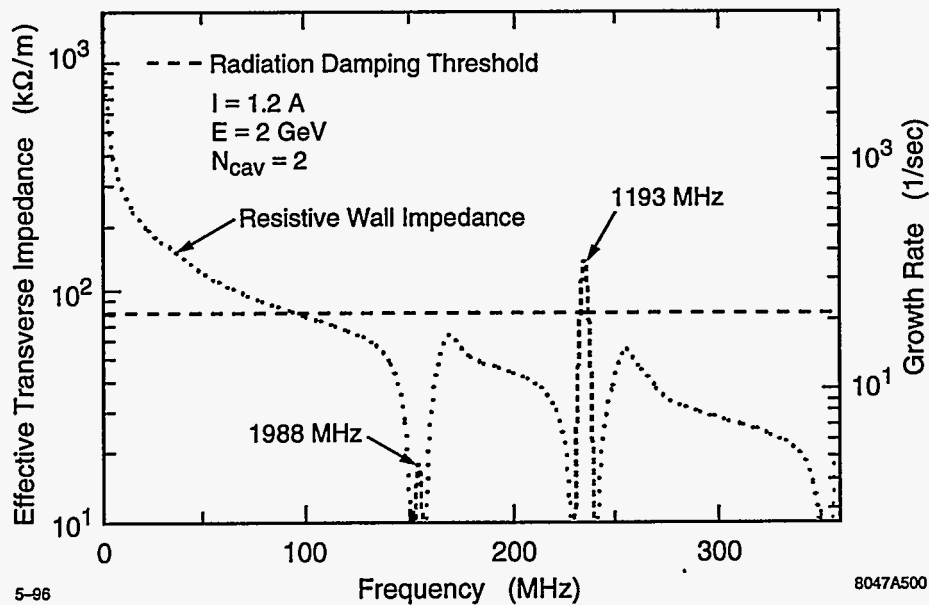


Figure 4-52. Transverse coupled-bunch growth rates.

Transverse

Coupled-bunch oscillations in the transverse planes are driven by dipole rf cavity HOMs and by the resistive-wall impedance. The HOMs given in Table 4-19 are assumed to be equally strong in the horizontal and vertical planes. The resistive-wall impedance results from the finite conductivity of the vacuum chamber wall and for a round pipe of radius b and resistivity ρ is given by

$$Z_{\perp}(\omega) = (1 + j) \frac{cL}{\pi b^3} \sqrt{\frac{\rho\mu_0}{2}} \frac{1}{\sqrt{\omega}} \quad (4.43)$$

For a 1.25-cm-radius Al beam pipe, the net resistive-wall impedance is given as

$$Z_{\perp,RW} = (1 - j) \frac{0.48}{\sqrt{n}} \text{ M}\Omega/\text{m} \quad (4.44)$$

where $n = \omega/\omega_0$.

Assuming a uniformly filled ring, the coupled-bunch growth rate for dipole oscillations of the beam is given by

$$\frac{1}{\tau} = \frac{1}{2} \frac{I_0 f_0}{(E/e)} \beta_{\perp} j [Z_{\perp}]_{\text{eff}} \quad (4.45)$$

where the effective impedance is given by

$$[Z_{\perp}]_{\text{eff}} = \sum_{p=-\infty}^{p=+\infty} e^{-(\omega_p \sigma_{\tau})^2} Z_{\perp}(\omega_p) \quad (4.46)$$

The effective impedance and the corresponding growth rates are shown in Figure 4-52. The resistive-wall impedance dominates mainly because of the small vacuum chamber. The large growth rate in excess of radiation damping will require a feedback system to damp transverse beam oscillations; this is described in Section 4.7. Higher-order head-tail modes are not driven at a significant level by the HOMs for $Q < 3000$.

There is a transient beam loading of the transverse impedance analogous to that of the longitudinal which could possibly result in a variable transverse offset along the length of the bunch train. This effect has not yet been studied in detail but it not expected to be significant.

4.4.6 Ion Trapping

The cross section for ionization of the residual gas is larger than that of elastic scattering or bremsstrahlung (compare Section 4.4.9). For carbon monoxide CO and a beam energy of 50 GeV, it is about 2 Mbarn [Rieke 1972]. The main effect of the residual gas on the beam is thus due to the creation of ions. The ions are produced at a rate of about $2 p[\text{nTorr}] \text{ s}^{-1}$ or $6.5 p[\text{Torr}] \text{ m}^{-1}$ ions per electron. The large bunch gap of 60 ns prevents ions from being trapped between bunch trains. Computer simulations may need to be performed to determine the fraction of ions which remains trapped during the gap but this is expected to be extremely small $\lesssim 10^{-3}$.

At the end of a single bunch train the longitudinal density of ions created by the train is $9 \times 10^4 \text{ m}^{-1}$ at a pressure of 10^{-8} Torr , assuming 90 bunches of 1.5×10^{10} electrons each. Particles in the trailing bunches

then suffer a vertical tune shift of $\Delta Q_y \approx 0.02$. To limit this effect, we are designing the main damping ring vacuum system to achieve a pressure less than 5×10^{-9} Torr.

It has been predicted that the interaction of beam and ions also gives rise to a fast transverse beam-ion instability [Raubenheimer 1995a]. It is because of this instability that the present target for the Damping Rings is a vacuum level as low as 10^{-9} Torr. For an electron beam, the instability mechanism is the following. Ions created by the first bunches perturb the tail of the bunch train. The mutually driven transverse oscillations of beam and ions result in a fast multi-bunch instability. The growth time of this instability at the end of the bunch train is given by

$$\tau_{\text{asym,e-}}^{-1} [\text{s}^{-1}] \approx 5p [\text{Torr}] \frac{N_b^{\frac{3}{2}} n_b^2 r_e r_p^{\frac{1}{2}} L_{\text{sep}}^{\frac{1}{2}} c}{\gamma \sigma_y^{\frac{3}{2}} (\sigma_x + \sigma_y)^{\frac{3}{2}} A^{\frac{1}{2}} \omega_\beta} \quad (4.47)$$

where A denotes the atomic mass number of the ions, n_b the number of bunches, N_b the number of particles per bunch, L_{sep} the bunch spacing, r_p and r_e the classical proton and electron radius, respectively, c the velocity of light, and $\omega_\beta \approx 1/\beta_y$. The rise time τ_{asym} in Eq. 4.47 refers to the asymptotic equation (for large times t)

$$J_y \approx \frac{J_{y0}}{8\pi \sqrt{t/\tau_{\text{asym}}}} \exp\left(2\sqrt{t/\tau_{\text{asym}}}\right) \quad (4.48)$$

where J_y denotes the vertical action of the trailing bunch. The instability amplifies the Fourier component of the vertical bunch-to-bunch displacement which corresponds to the ion-oscillation frequency. Assuming the initial displacements are due to the finite number of electrons, the vertical action at time zero is given by $J_{y0} \approx \sigma_y^2 / (N_b n_b 2\beta_y) \sim 3 \times 10^{-24}$ m. The rise time of Eq. 4.47 depends strongly on the number of bunches, the number of particles per bunch and the beam size. Due to the small vertical beam size and the rather large number of electrons, the growth times expected for the different NLC subsystems are exceedingly short.

In the electron damping rings, the predicted rise time for the trailing bunches is 100 ns at a pressure of 10^{-8} Torr. At 10^{-9} Torr the rise time would be $1 \mu\text{s}$, which is still too short for a feedback system. However, when the instability grows from Schottky noise, about 200 rise times are required before the oscillation amplitude becomes of the order of the beam size. Moreover, decoherence and filamentation of the ions, not included in the derivation of Eq. 4.47, may lead to a further increase of the rise time by about a factor of two [Stupakov 1995]. Therefore, for the NLC damping rings a pressure of 10^{-9} Torr may be barely acceptable. An analytical treatment of the instability mechanism, computer simulations, possible remedies, and open questions are discussed in Ref. [Raubenheimer 1995a]. Figure 4-53 shows an example of the simulation results. The vertical action for different bunches of the train is depicted as a function of the traversed distance, for a pressure of 10^{-8} Torr. The rise times deduced from Figure 4-53 and the analytical estimate, Eq. 4.47, agree within a factor of two.

A positron bunch train deflects the equally charged ions and does not show the same ion-driven multibunch instability. However, single positron bunches may interact with the ionized electrons, which results in a similar instability, albeit with larger rise times. In this case, the asymptotic growth rate at the bunch tail can be written as

$$\tau_{\text{asym,e+}}^{-1} [\text{s}^{-1}] \approx 7p [\text{Torr}] \frac{N_b^{\frac{3}{2}} r_e^{\frac{3}{2}} \sigma_z^{\frac{1}{2}} c}{\gamma \sigma_y^{\frac{3}{2}} (\sigma_x + \sigma_y)^{\frac{3}{2}} \omega_\beta} \quad (4.49)$$

where σ_z is the rms bunch length. At a pressure of 10^{-9} Torr, the expected instability rise time for the positron Damping Ring is $120 \mu\text{s}$. Since this is comparable to the synchrotron period (about $150 \mu\text{s}$), the synchrotron motion will prevent the buildup of the instability.

Several possible remedies have been suggested for the multibunch instability [Raubenheimer 1995a]. First, additional gaps in a bunch train will alleviate the effect. Second, it may be possible to design lattices in

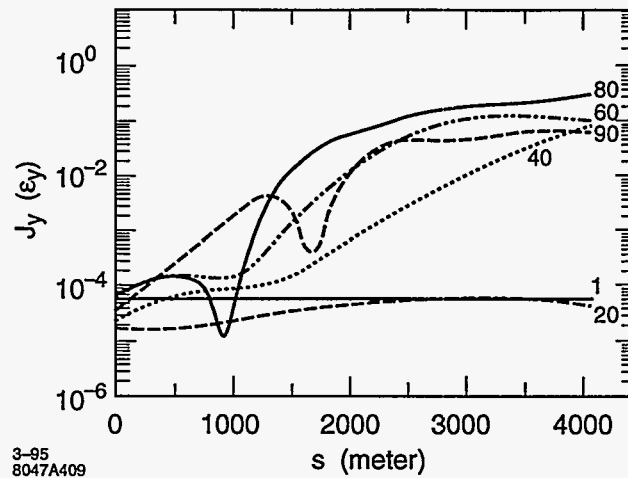


Figure 4-53. Growth of the action for every twentieth of 90 bunches in the NLC damping ring for a pressure of 10^{-8} Torr, an atomic mass of 28 (carbon monoxide), and 1.5×10^{10} particles per bunch.

which the ion frequency is strongly location-dependent. If the instability saturates at an amplitude of about one sigma, it is also conceivable to design damping rings in which the equilibrium emittance is about half the desired emittance. Preliminary simulation results indicate, however, that the saturation is not complete and that further amplitude growth at a smaller rate is possible. Finally, after extraction from the ring, fast kickers could realign the trailing bunches. Until the suitability of such schemes has been demonstrated, it will be assumed that in the damping rings of the NLC an average pressure of or below 10^{-9} Torr has to be maintained, to preserve the vertical emittance.

4.4.7 Positron-Electron Instability

Another instability that has been discussed is the positron-electron instability [Ohmi 1995]. This arises when an intense, positively charged bunched beam produces an electron cloud (or plasma) inside the vacuum chamber in which it travels. The basic mechanism is as follows: photons emitted due to synchrotron radiation hit the inside of the vacuum chamber and create photoelectrons. These, in turn, are accelerated transversely by the positively charged bunches and hit the wall on the opposite side of the vacuum chamber. Depending on their energy, these photoelectrons can be absorbed or can create secondary electrons. In this latter case, the secondaries are, in turn, accelerated, and the process is iterated, as sketched in Figure 4-54.

There are two effects from these electrons: they desorb gas molecules from the walls of the vacuum chamber and possibly ionize them, and they create an electron cloud. The gas desorption effect decreases in importance as the chamber gets "scrubbed" with increased use. But the electron cloud, of course, remains.

For high-enough current, a resonance occurs when the typical traversal time of the electrons across the chamber is equal to the time spacing of the bunches, leading to beam-induced multipactoring [Grobner]. But even for currents well below this threshold, as in the case of the NLC damping ring, the electron cloud still exists and couples the transverse motion of the bunches, leading to a potential coupled-bunch instability.

Experimental evidence of such an electron-cloud instability has been reported at the KEK Photon Factory [Izawa 1995]. A related phenomenon has also been observed at CESR [Rogers 1995], in which case the

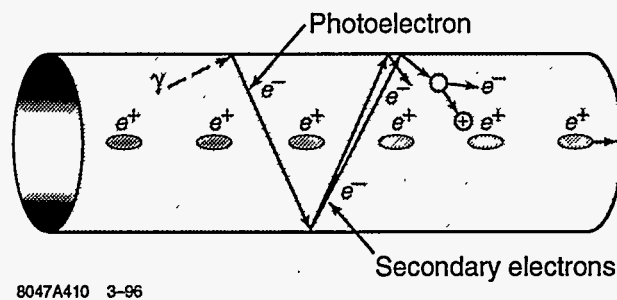


Figure 4-54. Sketch of the beam-induced electron plasma.

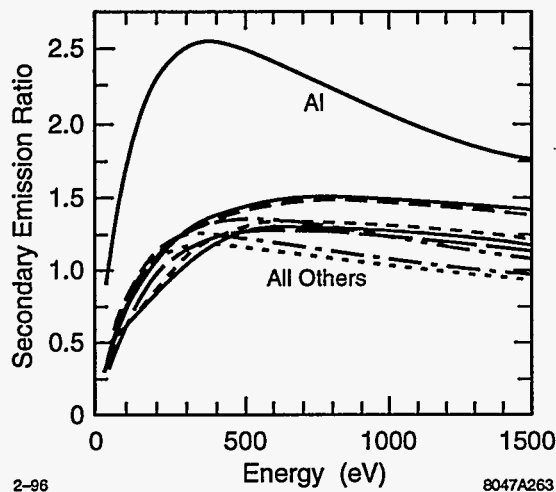


Figure 4-55. The secondary emission ratio for various metals as a function of the incident electron energy in eV.

electron cloud is not produced by the mechanism described, but by the trapping action of the combined electric and magnetic leak fields of the ion pumps. Although in this case the electron cloud occupies only a very small fraction of the vacuum chamber, it is enough to produce coupled-bunch motion. A theoretical explanation of the coupled motion based on the plasma idea has been put forward [Ohmi 1995], which predicts fairly fast growth rates for the instability. The predicted value for the onset of the instability is in rough agreement with the observations.

We have developed a simulation code [Furman 1995] and analytic calculations [Heifets 1995] to study this phenomenon at the NLC damping ring and the PEP-II positron beam. An important ingredient of the simulation is secondary electron emission. Figure 4-55 shows experimental measurements of the emission ratio for various metals (these curves are incorporated into the simulation code). Aluminum has the highest ratio, and that all other metals are not too different from each other.

Preliminary simulation results show that, for the nominal main damping ring parameters, an uncoated Al vacuum chamber would lead to a fast avalanche of electrons following injection into the machine. This avalanche would eventually stop due to the repulsive nature of the space-charge force of the electron cloud [Heifets 1995]. Even so, it is likely that the resultant instability would be difficult to control. On the other hand, if the vacuum chamber is coated with any of the other metals indicated in Figure 4-55, the simulation shows that the electron cloud density reaches saturation even if space-charge effects are not taken into

consideration. The reason for this equilibrium state is a balance between the predominant absorption of the electrons upon hitting the walls, and the creation of photoelectrons following the passage of every bunch through the bending magnets.

For the nominal Main Damping Ring current and bunch spacing, the characteristic time of the plasma is < 10 ns. Thus a beam gap equivalent to a few bunch spacings makes the plasma disappear altogether. This implies that there will be no turn-to-turn coupling. If a leading bunch oscillates transversely, the electron plasma will act as a coupler and drive the trailing bunches. The amplitude of the driven bunches will grow linearly with time with a characteristic time scale estimated at 0.2ms. Thus the feedback system will need to be able to damp instabilities of this time scale. However, we should point out that this is a subject of ongoing research and the correct answer may differ substantially.

There have been a number of solutions proposed for this effect. One such solution would place strips of ceramic, coated with thin conducting layer, along the edges of opening of the ante-chamber. Biased with a low DC voltage, such a design may prohibit production of the photo-electrons and eliminate the photo-electron driven instability of the positron storage rings.

Finally, this effect may be important in the pre-damping ring as well as in the positron main damping ring. At this time, we have not evaluated the effect for those parameters.

4.4.8 Intrabeam Scattering

Intrabeam scattering is a very significant effect in the main damping rings because of the small normalized emittances; it has negligible effect in the pre-damping ring. In the main damping rings, intrabeam scattering has been calculated with ZAP [Zisman 1986]. Figure 4-56 is a plot of the horizontal emittance and the vertical damping time versus the ring energy. The vertical damping time is the dotted curve and there are three curves for the horizontal emittance: $N = 1.57 \times 10^{10}$ (solid), $N = 0.7 \times 10^{10}$ (solid), and $N = 0$ (dashes). The intrabeam scattering emittance growth was calculated by ZAP. Notice that the emittance decreases to a minimum as the ring energy is decreased to roughly 1.8 GeV. Unfortunately, the vertical damping time increases rapidly as the energy is decreased and, at an energy of 1.7 GeV, the damping time would only allow operation at 120 Hz.

At the nominal energy of 1.98 GeV for 180-Hz operation, ZAP estimates the horizontal emittance as roughly 3.30×10^{-6} m-rad at a charge of 1.5×10^{10} and 2.96×10^{-6} m-rad at a charge of 0.7×10^{10} . But, ZAP calculates the rms growth of the beam size. Because of the fast damping times, a significant fraction of the rms growth is actually contributions to the beam halo and not an increase of the beam core [Raubenheimer 1994]. This results in a correction for the growth of the core that, for the NLC main damping ring parameters, is roughly 30%. Thus, at 1.98 GeV, with the maximum beam charge, we expect the horizontal core emittance to increase to 3.1×10^{-6} m-rad; at lower charge, the growth is less.

It is important to note that the scattering in the vertical plane will be less than in the horizontal plane [Raubenheimer 1993b]. This arises because intrabeam scattering emittance growth occurs due to changes in the longitudinal particle energy from the scattering. It is similar to the emittance growth from synchrotron radiation, except the intrabeam scattering occurs throughout the ring while the synchrotron radiation only occurs in the bending magnets. In a storage ring, the horizontal dispersion is minimized at the bends while the vertical dispersion, which is due to errors, is relatively uniform in magnitude around the ring. Thus, the intrabeam emittance growth has a much larger relative contribution to the horizontal emittance than the vertical emittance. We have not yet calculated the vertical growth for the NLC parameters, but experience with the KEK ATF damping ring suggests that the vertical emittance growth should be roughly 30% of

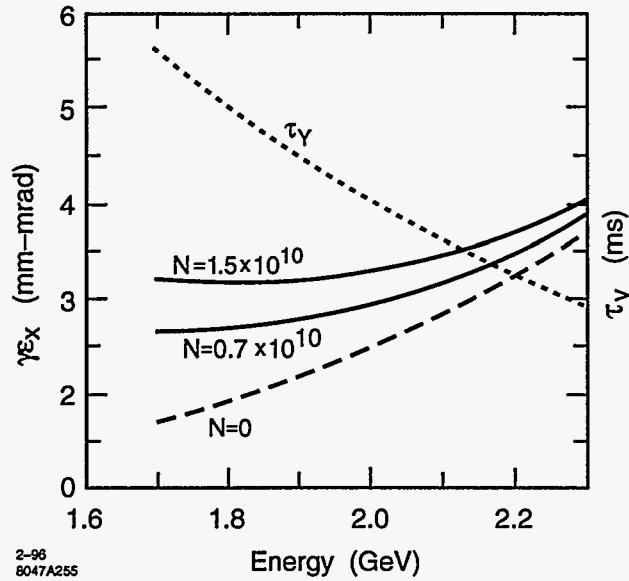


Figure 4-56. Horizontal equilibrium emittance and vertical damping time versus ring energy for different single bunch charges.

the horizontal growth. In this case, the vertical emittance growth due to intrabeam scattering will not be significant.

4.4.9 Beam-Gas Scattering

The vacuum pressure in the NLC damping rings will be less than 10^{-8} Torr. This is low enough so that scattering with residual gas atoms does not limit the beam lifetime or dilute the vertical emittance. The tolerable vacuum level is determined from several different effects. First, elastic scattering on atomic nuclei may increase the equilibrium emittance. The cross section for this process is about

$$\sigma_{\text{scatt}} \approx \sum_i 4\pi\alpha^2 Z_i^2 (1.4a_0 Z_i^{-\frac{1}{3}})^2 \quad (4.50)$$

where α denotes the fine structure constant, a_0 Bohr's radius, and Z_i the atomic number. The sum is over all atoms of a molecule. For carbon monoxide, CO , a common molecule in accelerator vacuum systems, we have $\sigma_{\text{scatt}} \approx 0.5$ Mbarn. At a pressure of 10^{-8} Torr, an electron undergoes no more than 5 collisions per second, and, therefore, during a vertical damping time of 4.8ms only a small halo is created around the undisturbed beam core [Hirata 1992, Raubenheimer 1992]. Figure 4-57 shows the beam distribution due to gas scattering for several vacuum pressures [Raubenheimer 1992].

Second, the beam lifetime is reduced by bremsstrahlung in the field of the atomic nuclei [Piwinski 1985]. In this case the cross section is

$$\sigma_{\text{brems}} \approx \sum_i \frac{4}{3} 4r_e^2 Z_i^2 \alpha \ln \frac{E}{\Delta E} \ln \frac{183}{Z_i^{-\frac{1}{3}}} \quad (4.51)$$

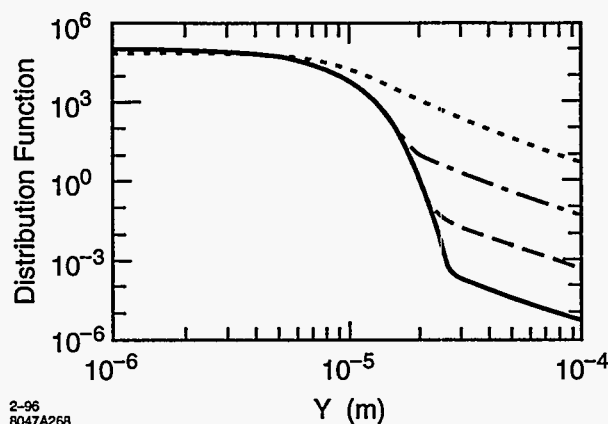


Figure 4-57. Beam distribution in the NLC damping ring with CO gas pressures of 10^{-12} Torr (solid), 10^{-10} Torr (dashed), 10^{-8} Torr (dot-dash), and 10^{-6} Torr (dotted).

where r_e is the classical electron radius, and $\Delta E/E \approx 10^{-2}$ the energy acceptance of the ring. Again for CO, the cross section is $\sigma_{\text{brems}} \approx 6$ barn, which translates into a beam lifetime of 5 hours at a pressure of 10^{-8} Torr.

4.4.10 Lifetime Limitations

In a damping ring, it is unlikely that the beam lifetimes could limit the operation of the ring since the beams are stored for a very short time. But, poor beam lifetimes could make commissioning and studying the ring difficult. The primary beam lifetime limitations are excessively small apertures, beam-gas scattering, and the Touschek effect; the latter refers to large-angle collisions between particles within the beam that lead to particle loss.

With adequate design and tolerances, one should be able to avoid the first limitation. In addition, with reasonable vacuum pressures, the lifetime due to beam-gas scattering should not be significant. Assuming a pressure of 10^{-8} Torr in the NLC damping rings, the lifetime due to beam-gas scattering is roughly four hours; this is more than sufficient.

In contrast, the Touschek lifetime will tend to be severe in the main damping rings since it depends inversely upon the particle density in the beam. In the NLC main damping rings, the Touschek lifetime is roughly two minutes. While this is long compared to the operating beam storage time of 22 ms, it may be too short to study the properties of a stored beam. In this case, one can increase the vertical beam size or decrease the number of particles per bunch, thereby decreasing the beam density and increasing the lifetime.

4.4.11 PPDR Collective Limitations

Collective effects are not expected to be significant in the Positron Pre-Damping Ring. The PPDR has a longer bunch length and a larger vacuum chamber, reducing the contributions to the broadband impedance and the resistive-wall impedance. Thus, the growth rates of the coupled-bunch instabilities, that are driven by

the resistive-wall impedance, should be well below the radiation damping rate. In addition, the longitudinal microwave threshold should be increased substantially due to the lower impedance and the larger momentum compaction. Finally, issues such as the Touschek lifetime and intrabeam scattering are not relevant because of the large beam emittances.

The one collective issue that may be significant in the pre-damping ring is the positron-electron instability, referred to as the "Ohmi Effect." This may be partially ameliorated by using an ante-chamber to absorb most of the radiation and by covering the inside of the vacuum chamber with titanium nitride or similar coating. In the future, we will verify the importance of the other effects and, hopefully, will have additional data with which to evaluate the "Ohmi Effect."

4.5 RF Systems

There are four distinct rf systems in the damping ring complex: the S-band and L-band energy compressors, and the pre-damping ring and main damping ring rf systems. As discussed in Section 4.2.9, the ring rf systems will be based on 714-MHz cavities with HOM damping. The present design is based on the PEP-II cavity design but there are many laboratories around the world working on rf cavities with damped HOMs and we will gain from their experience.

In the pre-damping ring, the total rf voltage is 2.0 MV which leads to an energy bucket of $\pm 1.5\%$. Although this is not sufficient to capture the full $\pm 2\%$ energy spread, the L-band energy compressor will reduce the incoming energy spread by at least a factor of two (Section 4.3.3). The injection line rf systems are based on the electron and positron source linac rf systems while, as stated, the damping ring rf systems are based on the PEP-II rf systems.

In the next sections, we will describe the rf systems for the main damping rings and then the pre-damping ring. Next, we discuss the low-level rf control system for the main damping ring. The low-level rf controls are extremely important in these damping rings because of the high beam-loading and very tight stability tolerances on the extracted bunches. To achieve the stability, the low-level rf system requires many layers of feedback but, as has been realized in the SLC damping rings, it is extremely important to understand the interactions between these feedback loops. This is described in Section 4.5.3. Finally, we will outline the energy compressor rf systems; these systems are described in greater detail in Chapter 6.

4.5.1 Main Damping Rings RF Systems

The rf systems of the NLC main damping rings have to provide sufficient voltage to the beam to compensate for losses due to synchrotron radiation (from the dipole magnets and from the wigglers), losses into higher-order modes (HOMs) of the rf cavities, and parasitic losses to vacuum chamber components. The large synchrotron radiation losses, HOM, and parasitic losses result in an rf system with a large power throughput to the beam. The beam current in the cavity is a factor of 11 greater than the generator current needed to provide the gap voltage.

In addition, the large beam current makes the suppression of HOM impedances more important, to avoid uncontrollable coupled-bunch and single-bunch instabilities. Therefore, in addition to providing the required voltage, the systems should present a low-impedance environment to the beam to maximize instability threshold currents, and avoid the necessity for or minimize the power requirements of beam feedback systems.

The frequency of the damping ring rf systems is determined by the bunch spacing in the main linac—the bunches within a train are separated by 1.4 ns—thereby requiring a minimum rf frequency of 714 MHz. Four trains, 90 bunches each, occupy the damping ring at any one time, with 1.57×10^{10} particles per bunch and an average current of 1.2 A.

The accelerating voltage requirement of 1 MV is achievable using conventional copper cavity construction techniques. To alleviate the problems of coupled-bunch instabilities driven by cavity higher-order modes, some type of suppression of the HOMs is required. There are several suitable such monochromatic cavity designs currently being used or designed, which could find application in the NLC damping rings. For example, the ATF cavity being built for KEK uses a cylindrical body, to which end plates are brazed. These plates have nose cone structures and coupling apertures to which the damping waveguides attach, two on each end of the cavity [Sakanaka 1995]. A different design has been developed for DAΦNE, using a bell-shaped cavity structure with a rounded cavity and enlarged beam-pipe apertures to allow modes to propagate past the ends of the cavity. Long tapers connect the cavity to the smaller diameter beam pipe, resulting in a decreased R/Q value for many modes. Damping waveguides are attached to the cavity body, and to the adjacent tapers [Barry 1993].

For this study we choose a cavity based on a design developed for the PEP-II B-factory project. This cavity has a rounded body and reentrant nose cones, providing a large shunt impedance, and three waveguide loads mounted on the cavity body to efficiently suppress the HOMs. Tapers from the cavity nose cone region to the straight section vacuum chamber provide a smooth transition from the scaled PEP-II cavity to the small vacuum chamber, help to minimize the cavity broadband impedance, and also support additional damping waveguides.

Other cavity designs are feasible, such as reducing the aperture at the nose cones to the nominal vacuum chamber dimensions, avoiding the use of tapers. This is expected to increase the strength of many HOMs, but the damping waveguides may still provide the required attenuation for these modes and the increase in broadband impedance may be acceptable. A more detailed optimization, including factoring in the cost of different options, will take place in the future.

The main parameters of the NLC damping ring rf systems are listed in Table 4-20. To determine the power requirements of the rf systems, we need to estimate the losses to parasitic modes in the vacuum chamber components. This we have done by scaling from measurements and calculations performed for other, recently designed or built, low-impedance storage rings. As discussed subsequently, the klystron power requirements, two klystrons each rated at 600 kW, appear to be within the capabilities of manufacturers at this frequency.

In addition, transients in the rf system excited by the gaps in the circulating beam and by injection timing mismatches cause a shift in synchronous phase and timing errors along the bunch train. These transients may be suppressed by the use of feedback systems around the rf klystrons and cavities. The required low-level rf system is described in Section 4.5.3.

Cavity Design

The determination of the number of cavities required involves a compromise between their power-handling capabilities and the beam impedance presented by the cavities. Power-handling capabilities of the rf window and coupler, and the problems of heat dissipation in the cavity walls and apertures are the limitation to the power into each cavity. These problems have been extensively studied for the PEP-II B-factory rf systems, and we choose to follow their lead and use a cavity design based on the PEP-II B-factory cavities.

Energy	1.98 GeV
Circumference	223 m
RF	714 MHz
Harmonic Number	532
σ_ϵ	0.09%
σ_z	3.9 mm
α	0.000465
$U_{s.r.}$	644 keV/turn
U_{HOMs}	7.5 keV/turn
$U_{parasitic}$	25 keV/turn
V_{RF}	1.0 MV
# Cavities	2
# Klystrons	2
Cavity Wall Dissipation	41.6 kW/cavity
Klystron Power	600 kW/klystron
Shunt Impedance	3.0 M Ω /cavity
Beam Current	1.2 A
Coupling Factor	11
Unloaded Q	25500
Synchronous Phase Angle	42.6°
Optimum Detuning at Full Current	148 kHz
Synchrotron Frequency	5 kHz
Loaded Q	2170
Energy acceptance	$\pm 1.5\%$

Table 4-20. Rf system parameters for the NLC main damping rings.

The basic cavity shape is a reentrant structure with nose cones, similar to the cavities currently used at the KEK Photon Factory, Daresbury SRS, and the ALS at Berkeley. A conventional copper construction is used, with aperture coupling to the feeder waveguide. Re-entrant nose cones are used to optimize the shunt impedance of the fundamental mode. We scale the dimensions of the PEP-II cavities to achieve a resonant frequency of approximately 714 MHz, with a beam-pipe aperture of 6.2-cm diameter at the nose cones. As discussed in Section 4.4.1, the large aperture at the nose cones reduces the broadband impedance of the cavity and is clearly advantageous. To mate the cavity to the adjacent beam pipe, we use long tapers, while maintaining a total cavity length (including tapers) of less than 0.5 m.

Figure 4-58 shows a half section of the cavity model illustrating the coax damping waveguides on the taper but not showing the damping waveguides on the cavity. Calculations with the electromagnetic design code URMEL give a shunt impedance of $R_s = 4.35 \text{ M}\Omega$, $Q_0 = 36000$. For the B-factory cavities the addition of the damping waveguides reduced the shunt impedance and unloaded Q value by 30% (compared to the URMEL values). Using the same scaling, we calculate a shunt impedance of $R_s = 3.0 \text{ M}\Omega$, $Q_0 = 25500$, and $R/Q = 120 \Omega$ for the NLC damping-ring rf systems.

The total loss parameter for each cavity is computed by ABCI to be $k_{\text{total}} = 1.75 \text{ V/pC}$ for a bunch length of 4.0 mm, of which the fundamental mode contributes 0.27 V/pC , giving the contribution from higher-order modes $k_{HOMs} = 1.48 \text{ V/pC}$ per cavity.

Three waveguides are attached to the cavity body to damp the higher-order modes. These waveguides are dimensioned to have a cut-off frequency above the frequency of the accelerating mode of the cavity, but

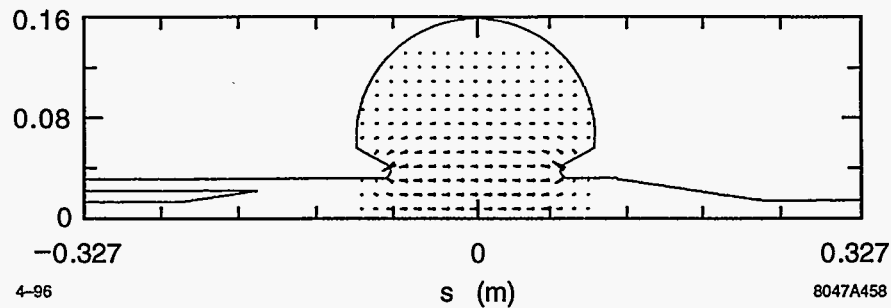


Figure 4-58. Half section of the rf cavity, without cavity damping waveguides.

below the frequency of the lowest HOM. Thus the power in HOMs may couple through the apertures in the cavity wall to the waveguides, where it is absorbed in a cooled lossy dielectric material. The location of these waveguides is at 30° from the center of the radius of the cavity body, this position being optimized to couple to the strongest HOMs in the cavity [Rimmer 1992]. The waveguides are located equidistantly in azimuth. The location of the lossy material within the waveguide is at a sufficient distance from the cavity aperture to exclude dissipation of the fundamental mode power from evanescent fields in the waveguide. Experience with the PEP-II cavities shows that Q values of HOMs are damped by two orders of magnitude in most cases, and three orders for targeted modes [Rimmer 1992].

Many higher-frequency cavity modes will spread into the tapers, where the delocalizing effect generally decreases their impedance through a reduction in the transit time factor. These modes may be further damped by locating additional damping waveguides on the tapers. There are many modes at relatively high frequencies, capable of driving within-bunch instabilities which are difficult to combat with feedback systems. Effective broadband damping eliminates these problematic modes. At this time, we are performing 2- and 3-D MAFIA studies of the cavity to optimize the placement of the waveguide on the taper and those on the cavity body.

The PEP-II cavities are designed for a maximum power dissipation of 150 kW. To maintain the same power per unit area in the damping ring cavities, we scale by the frequency ratio of the two rings' rf systems squared to obtain 67 kW per cavity maximum power dissipation in the NLC damping rings cavities. De-rating by 30% gives a conservative dissipation goal of 47 kW per cavity or less.

Higher-Order Mode and Parasitic Losses

Cavity HOM losses are determined from the loss parameter k_{HOMs} and the charge per bunch q ; U_{HOMs} is the loss per turn to the cavity HOMs

$$U_{\text{HOMs}} = k_{\text{HOMs}}q \quad (4.52)$$

giving $U_{\text{HOMs}} = 3.7 \text{ keV}$ per cavity per turn.

We scale from measurements and calculations of other machines, parasitic losses to vacuum chamber components other than the rf cavities, such as bellows shields, BPMs, kicker magnets, and resistive wall. With careful attention to the design of components, using sophisticated electromagnetic design codes and careful measurements, the parasitic losses can be minimized in modern machines. We choose PEP-II and the ALS as examples of clean, low-impedance machines from which to obtain an estimate of the loss parameter for the NLC damping rings.

For the PEP-II B-factory, the total loss parameter for vacuum chamber components excluding the rf cavities has been estimated to be 6 V/pC , for a bunch length of 10 mm [PEP-II 1993]. Scaling the loss parameter with bunch length as $k \sim \rho^{-1.5}$, with machine circumference as $220/2200$, and with the ratio of the vacuum chamber diameters as $6.2/2.8$, gives $k_{\text{parasitic}} = 6.9 \text{ V/pC}$.

The ALS is a very similar machine to the NLC damping rings, in that the circumference and the bunch length are almost identical in the two machines. The vacuum chamber radius in the ALS is larger than in the NLC damping rings. Measurements of the ALS vacuum chamber components indicate a loss parameter of approximately 5.8 V/pC (excluding cavities) [Corlett 1993]. Scaling to the NLC damping ring vacuum chamber radius, we estimate $k_{\text{parasitic}} = 15 \text{ V/pC}$. Finally, the calculations in Section 4.4.1 give a $k_{\text{parasitic}} = 5 \text{ V/pC}$. Assuming a value of 10 V/pC , yields losses of $U_{\text{parasitic}} = 25 \text{ keV}$ per turn. Of course, it should be noted that the parasitic losses are very small compared to the synchrotron radiation losses and thus the design is insensitive to the exact value.

Voltage Requirements

The voltage required to compensate for the synchrotron radiation loss, due to both dipole bend magnets and the wigglers, is $U_{\text{SR}} = 644 \text{ keV}$ per turn. In addition, the vacuum chamber parasitic losses are $U_{\text{parasitic}} = 25 \text{ keV}$ per turn, and the rf cavity HOM losses $U_{\text{HOMs}} = 3.7 \text{ keV}$ per turn per cavity. For two rf cavities, the total loss per turn is 677 keV . In order to provide an energy acceptance of $\pm 1\%$, the cavity voltage must be at least $V_{\text{rf}} = 0.85 \text{ MV}$. To provide some contingency for additional energy acceptance and bunch length control, we take the cavity voltage requirement to be $V_{\text{rf}} = 1.0 \text{ MV}$.

Power Requirements

The cavity power dissipation is given by

$$P_c = \frac{V_{\text{RF}}^2}{2R_s} \quad (4.53)$$

and each cavity dissipates 41.6 kW , based on two cavities, giving a total $P_c = 83 \text{ kW}$. This is within the estimated power-handling capability of 47 kW per cavity.

The power delivered to the beam is determined from the synchrotron radiation, HOM losses, and parasitic losses is

$$P_b = I_o(U_{\text{SR}} + U_{\text{HOMs}} + U_{\text{parasitic}}) = I_o U_{\text{losses}} \quad (4.54)$$

where $U_{\text{losses}} = 677 \text{ keV}$ per turn, $I_o = 1.2 \text{ A}$ for an average beam current, and the power to the beam $P_b = 812 \text{ kW}$.

The total rf power required $P_{\text{rf}} = P_b + P_c = 895 \text{ kW}$. Feeding each cavity independently would require two klystrons rated at least 450 kW . Providing a 20% overhead for rf feedback, and 10% for losses in transmission to the cavities, each klystron would be rated at 600 kW .

Coupling Factor and Loaded Q

To be able to obtain the condition of a matched cavity with full beam loading, the cavity coupling factor β_o is determined from

$$\beta_o = 1 + \frac{P_b}{P_c} \quad (4.55)$$

# Cavities	3
U_{HOMs}	11.3 keV/turn
Cavity Wall Dissipation	18.5 kW/cavity
# Klystrons	3
Klystron Power	350 kW/klystron
Coupling Factor	15.7
Synchronous Phase Angle	42.8°
Optimum Detuning at Full Current	222 kHz
Loaded Q	1529

Table 4-21. Rf system parameters with three cavities.

and we find $\beta_o = 10.7$. The loaded quality factor of a cavity is then

$$Q_d = \frac{Q_o}{1 + \beta_o} \quad (4.56)$$

and $Q_l = 2170$. The filling time $2Q_l/\omega = 0.97 \mu\text{s}$. The synchronous phase angle ϕ_s is determined from the total loss per turn U_{losses} and the rf voltage

$$\sin \phi_s = \frac{U_{\text{losses}}}{V_{\text{rf}}} \quad (4.57)$$

which gives $\phi_s = 42.6^\circ$. The optimum cavity detuning frequency δ_f is determined from

$$\delta_f = \frac{f_{\text{rf}}}{2Q_o} \frac{P_b}{P_c} \cot \phi_s \quad (4.58)$$

where $\delta_f = -148 \text{ kHz}$, which is small compared to the orbit frequency of 1.36 MHz. Growth times of coupled-bunch modes driven by the accelerating cavity mode are likely to be long.

RF Parameters with Three Cavities

The possibility of using three rf cavities instead of two has been investigated, to reduce the power dissipation in the cavities, the throughput rating of the rf vacuum windows, and the power rating of the klystrons. Table 4-21 lists the parameters changed from the two-cavity case. Klystron power requirements are reduced to 350 kW per klystron, including 20% overhead for feedback systems. Window throughput power is also reduced by 40% to 350 kW. The cavity wall losses are reduced from 42 kW per cavity to less than 20 kW per cavity. Optimal cavity detuning increases to 222 kHz, and the coupling factor is increased to almost 16.

Transient Suppression Using Feedback or Feedforward

The nonuniform bucket population generates transients in the rf system, and the beam sees a nonuniform accelerating voltage. Each bunch in a train has its own individual synchronous phase angle, and the spacing between bunches changes to accommodate this. The use of sub-harmonic cavities, feedback around the rf system, and feedforward in the rf system are being evaluated to reduce the spread in bunches along the rf waveform.

Klystrons and accessories

The necessary rf power at 714 MHz will be provided by high-power klystrons. Depending upon the number of cavities and the overhead required for feedback and feedforward, the power could be supplied by three klystrons feeding three cavities, two klystrons feeding two cavities or one super-power klystron driving a pair of cavities. The choice will depend on economic as well as technical considerations. Klystrons exist with up to 1.2-MW CW output in the 350-508-MHz region and power supplies, circulators and loads have been developed to handle this power level. This technology can be readily adapted to the higher frequency and there is already R&D underway in the industry on 1-MW tubes in the 700-MHz frequency range for applications such as tritium production.

There is considerable commercial activity in this frequency range for the television broadcast industry and many mature products exist at the 50-70-kW CW power level. For one- or few-off applications it is possible to combine the output from several of these tubes to produce a higher-power supply such as that used at the SPS at CERN. This station used eight 60-kW TV klystrons (Phillips YK1190 series), producing 450 kW at 800 MHz (newer, higher-power tubes are now available). Given the relatively high volume of production of these transmitter tubes it may be cost-effective to build a high-power source this way with minimal R&D investment.

RF cavity windows

Approximately 600 kW per cavity (into two cavities) will be required to support 1.2 A of beam current at 1 MV total voltage, and overhead (in peak voltage) is required for feedback systems, so the rf window will be a critical component. Both coaxial and disk-type windows routinely operate on high-power klystrons at 1-1.2-MW CW, and cavity windows have been developed for PEP-II and other machines for up to 500 kW throughput. These technologies can be readily scaled to 714 MHz. Additional safety margin could be achieved by supplying the power through two windows per cavity which would provide a very reliable system. Using three cavities per ring would also reduce the power per window significantly.

4.5.2 Pre-Damping Ring RF Systems

The rf systems of the NLC pre-damping rings are based on "monochromatic" cavities as described for the main damping rings in Section 4.5.1. These systems serve to provide sufficient voltage to the beam to compensate for losses due to synchrotron radiation, losses to higher-order modes (HOMs) of the rf cavities, parasitic losses to vacuum chamber components, and to provide a sufficient rf potential well to capture the injected beam. The resulting accelerating voltage requirement of 2 MV is achievable using four conventional copper cavities.

In order to determine the power requirements of the rf systems, we estimate the losses to parasitic modes in the vacuum chamber components by scaling from the losses estimated for the main damping rings, as described in Section 4.5.1. For the pre-damping ring, with smaller machine circumference and larger beam pipe diameter than the main damping rings, we estimate $k_{\text{parasitic}} = 7 \text{ V/pC}$.

We choose to use four cavities and two klystrons, with pairs of cavities fed from a single klystron. The klystron power rating of 440 kW appears to be within the capabilities of manufacturers at this frequency.

Table 4-22 lists the main parameters of the NLC pre-damping ring rf systems.

Voltage Requirements

The voltage required to compensate for the synchrotron radiation losses is $U_{s.r.} = 371$ keV per turn. In addition, the vacuum chamber parasitic losses are $U_{parasitic} = 17$ keV per turn, and the rf cavity HOM losses $U_{HOMs} = 3.7$ keV per turn per cavity. For four rf cavities, the total loss per turn is 404 keV.

A larger cavity voltage is required to capture the injected beam, and at a nominal cavity voltage $V_{rf} = 2.0$ MV, a sufficient energy acceptance of $\pm 1.46\%$ is obtained.

Power Requirements

The cavity power dissipation is given by

$$P_c = \frac{V_{rf}^2}{2R_s} \quad (4.59)$$

and 41.6 kW is dissipated in each cavity, based on 4 cavities, giving a total $P_c = 167$ kW. This is within the estimated power handling capability of 47 kW per cavity (see Section 4.5.1).

The power delivered to the beam is determined from the synchrotron radiation, HOM losses, and parasitic losses:

$$P_b = I_o(U_{s.r.} + U_{HOMs} + U_{parasitic}) = I_o U_{losses} \quad (4.60)$$

$U_{losses} = 404$ keV per turn, and for an average beam current $I_o = 1.2$ A the power to the beam $P_b = 485$ kW.

The total rf power required $P_{rf} = P_b + P_c = 652$ kW. Feeding two cavities from one klystron requires two klystrons rated at 326 kW. Providing approximately 20% overhead for rf feedback, and 10% for losses in transmission to the cavities, each klystron would be rated at 440 kW.

Coupling Factor and Loaded Q

To be able to obtain the condition of a matched cavity with full beam loading, the cavity coupling factor β_o is determined from

$$\beta_o = 1 + \frac{P_b}{P_c} \quad (4.61)$$

and we find $\beta_o = 3.9$. The loaded quality factor $Q_l = 5190$, and the filling time $2Q_l/\omega = 2.3$ μ s.

The synchronous phase angle ϕ_s is determined from the total loss per turn U_{losses} and the rf voltage

$$\sin \phi_s = \frac{U_{losses}}{V_{rf}} \quad (4.62)$$

which gives $\phi_s = 11.7^\circ$. The optimum cavity detuning frequency δf is determined from

$$\delta f = \frac{f_{rf}}{2Q_o} \frac{P_b}{P_c} \cot \phi_s \quad (4.63)$$

$\delta f = -197$ kHz, which is small compared to the orbit frequency of 1.75 MHz, therefore growth times of coupled-bunch modes driven by the impedance of the accelerating cavity mode are likely to be long.

Energy	1.98 GeV
Circumference	171 m
RF Frequency	714 MHz
Harmonic Number	408
σ_ϵ	0.0977%
σ_z	7.5 mm
α	0.00511
$U_{s.r.}$	371 keV/turn
U_{HOMs}	16 keV/turn
$U_{parasitic}$	17 keV/turn
V_{rf}	2.0 MV
# Cavities	4
# Klystrons	2
Cavity Wall Dissipation	42 kW/cavity
Klystron Power	440 kW/klystron
Shunt Impedance	3.0 M Ω /cavity
Beam Current	1.2 A
Coupling Factor	3.9
Unloaded Q	25500
Synchronous Phase Angle	11.7°
Optimum Detuning at Full Current	197 kHz
Synchrotron Frequency	31.5 kHz
Loaded Q	5190
Energy acceptance	$\pm 1.46\%$

Table 4-22. Rf system parameters for the NLC pre-damping ring.

4.5.3 Low-Level RF Systems

The low-level system includes various regulating feedback loops, controls, and protection interlocks. Most of these constituents are common to other storage ring and damping ring rf systems and therefore pose no unusual design challenges. The design goal is to ensure ease in diagnosis of rf-related problems while minimizing the complexity of the rf system: anticipated error sources are corrected for locally and regulation of each klystron-beam-cavity interaction is independently maintained. The function of the low-level rf system is

- to regulate the cavity voltage and beam phase, and
- to minimize the effects of transient beam loading caused by injection and extraction.

Cavity voltage and beam phase regulation is maintained by passive feedback while transient loading in the cavities will be minimized using feedforward at injection. Similar beam-loading compensation techniques will be tested and used at PEP-II [PEP-II 1993] and the KEK Accelerator Test Facility (ATF) damping ring [ATF 1995]. The feedforward algorithm, which is discussed in detail below, also allows beam injection at a high duty cycle.

The stability of the rf system and the particle beam in the main damping rings has been studied using a numerical model of the beam-cavity interaction with multiple feedback loops. The study has yet to be applied

to the positron pre-damping ring, however, the low-level rf system designs are expected to be quite similar. Unique to the NLC damping rings are the high beam currents (about a factor of 10 increase compared to the SLC). Analyses of transient loading at injection have therefore been performed. The simulations will be extended to study synchronous phase transients due to the gaps between bunch trains, which are discussed in Section 4.4.4.

Low-Level Controls

A block diagram of the low-level control system is shown in Figure 4-59. The rf from the main NLC oscillator is phase-shifted using feedback from the interaction point (IP) collision time (as determined by the arrival time of e^+ in one linac and the e^- in the other). This global phasing of the front end (source, injector linac, etc.) is required since the single-turn injection/extraction scheme, which minimizes beam phase and bunch length variations in steady-state operation of the damping rings, disallows independent phasing of beam phase at injection to and extraction from the damping rings. The phase-shifted rf from the main oscillator is frequency-divided to 714 MHz, amplified as necessary, and used as the phase reference for the damping ring rf system. A separate voltage-controlled oscillator (VCO) is provided to allow the ring frequency to be varied (for measurement of the chromaticity, for example).

Beam Phase Loop. Deviations in damping ring timing are corrected using a phase feedback loop which uses the beam phase measured with a damping ring BPM and adjusts the phases of the source, prelinac, and damping ring. The bandwidth of this loop is limited by the minimum frequency for coherent synchrotron oscillations (≈ 2 kHz at full current).

Referring to Figure 4-59, a common local oscillator provides rf input to the two klystrons. Each klystron powers a one single-cell cavity with higher-order mode damping for coupled-bunch modes. A circulator upstream of each cavity isolates the klystron from reflected power arising from cavity detuning or the sudden absence of beam. Additional protection is provided by an rf switch upstream of each klystron which is activated by standard protection interlocks. There are slow interlocks including those for cavity vacuum and for water flow and temperatures in the klystrons, cavities, and circulator loads. Fast interlocks protect against reflected power faults and arcs in the klystrons and circulators.

Five feedback loops are used to stabilize the beam and accelerator. These include loops to regulate the klystron output, the cavity resonant frequency, and the cavity phase and amplitude. In the heavily beam-loaded limit, the cavity amplitude and phase loops should ideally correct for beam-induced transients. Using feedforward, however, because the phasor voltage of the cavity is maintained independent of the beam current or the change in beam current, the gain requirements of these loops is significantly reduced. The precise gain and bandwidth requirements in the feedback design have yet to be determined.

Klystron Amplitude and Phase Loops. Slow, high gain feedback loops are used to correct for klystron high-voltage power supply ripple and other sources of phase or amplitude error. The input to both loops is a measure of the klystron forward power. The phase of this signal is compared with the input rf phase and the difference is used to shift the phase of the input rf. In the klystron amplitude loop, the rf signal is converted to DC with an amplitude detector. The difference in this amplitude from the error signal of the cavity amplitude feedback is used to adjust an rf attenuator upstream of the klystron.

Cavity Amplitude Loops. To regulate against slow changes in the cavity voltage, due to long-term thermal variations for example, the amplitude of each cavity is maintained at an externally specified level,

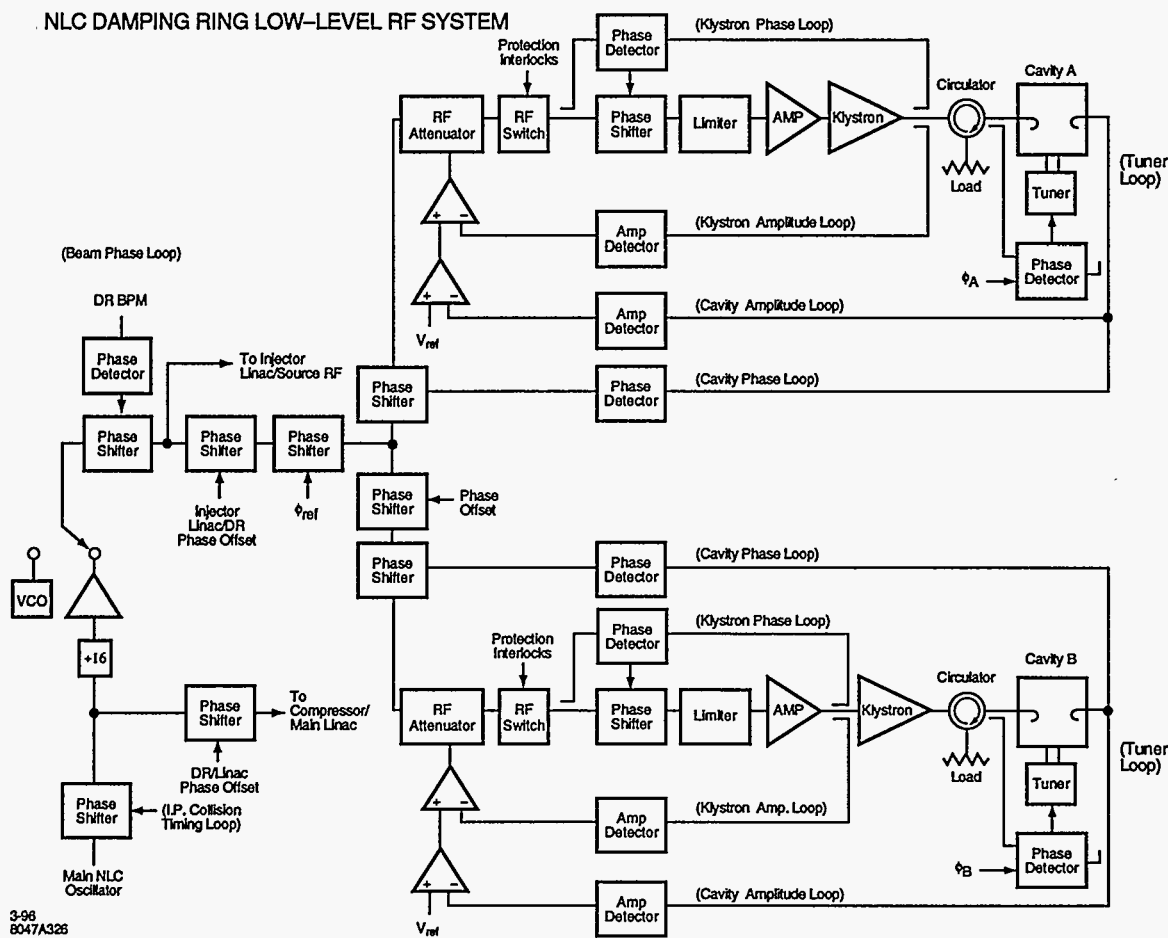


Figure 4-59. Block diagram of the low-level control system for the NLC damping rings.

V_{ref} . The error signal is used to adjust an rf attenuator upstream of the klystron. The bandwidth is high and limited by the minimum frequency for coherent beam oscillations (≈ 2 kHz at full current).

Cavity Phase Loop. This loop maintains the phase of the net cavity voltage with respect to phase of the input rf by adjustment of an rf phase shifter. The bandwidth is limited to ≈ 2 kHz at full current.

Cavity Tuner Loops. A single loop per cavity is used to correct for thermal variations and reactive loading by the beam. For fast filling of the ring (see below), the tuner positions are fixed at externally specified angles, ϕ_a and ϕ_b , to minimize the reflected power from the cavities when operating at full current. The bandwidth of these loops is limited by the speed of the mechanical plungers (≈ 1 Hz).

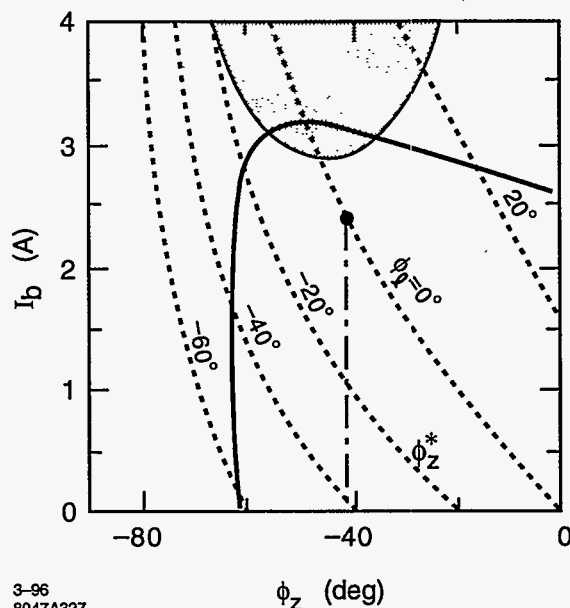


Figure 4-60. Parameter space for voltage regulation for the main damping ring with 1.2 MW rf power. Here, the beam current $I_b = 2I_{dc}$ is plotted versus the tuning angle ϕ_z . The shaded region is that limited by Robinson instability and the dotted lines are contours of constant loading angle. The nominal operating point is shown at $\phi_l = 0$.

Feedforward Algorithm for Beam Injection

Because of the very high beam currents, beam-induced loading of the cavities at injection is a concern in the damping ring rf system design. Studies have shown that without compensation (either feedforward or direct feedback [Pedersen 1975]), beam-loading of the rf system could result in beam loss and instabilities in the regulation. A feedforward algorithm was devised to correct the injection transients. While the beam-loading limit was not a concern for the steady-state operation of the damping rings, direct feedback was also considered to help damp the transients.

Shown in Figure 4-60 is the parameter space for voltage regulation for the NLC main damping ring. The beam current I_b , which is twice the total DC current, is plotted as a function of the cavity tuning angle ϕ_z , which is the angle between the total current and total cavity voltage and is a measure of how far off resonance the cavity is being driven. The steady-state full current operating point is shown by the circle. The shaded area shows Robinson's region of instability [Robinson 1962] in the high-current limit. (The low current limit corresponds to $\phi_z > 0$.) The dotted curves are contours of constant loading angle, ϕ_l ; along the line $\phi_l = 0$ the reflected power is minimized. The solid curve corresponds to a maximum total klystron output power of 1.2 MW. In the steady-state, the cavity voltage will be maintained at the nominal value of 1 MV for operation anywhere within the region bounded by the klystron power curve and the lower right quadrant of Figure 4-60. Operation outside this region results in loss of regulation of the cavity voltage, due to insufficient klystron power, and eventually beam loss. Transient loading or klystron nonlinearities may reduce the stable operating region. The klystrons are specified to deliver a maximum of 1.2-MW peak power to ensure linearity of the klystron response.

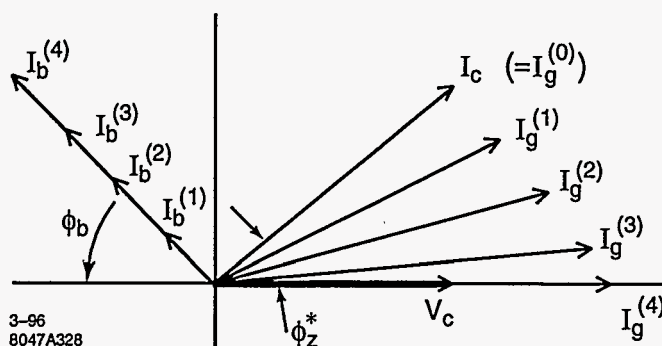


Figure 4-61. Feedforward algorithm illustrated using phasors.

There are two possible schemes for injecting to full current. To minimize the total reflected power in the injection process, the tuning angle ϕ_z could be preset just before each train is injected such that $\phi_l = 0$ after the train is injected. This corresponds to moving along the $\phi_l = 0$ line in Figure 4-60. However, this scheme is time consuming since it is limited by the slow motion of the tuners. A faster scheme involves one preset of the tuners to ϕ_z^* , when the beam is absent, followed by consecutive injection of all 4 trains. While the reflected power is not insignificant during initial detuning without beam, it is within the specifications of the circulators. In the interest of maintaining a high duty cycle and allowing for maximum flexibility and compatibility to the remainder of the accelerator, the fast injection scheme has been developed. (However this does not preclude the alternative.)

Two techniques for correcting for the beam-induced transients at injection have been studied. Based on recent experiences and success at the SLC, the use of direct feedback was considered first. While it is possible to inject all the trains, there are a number of disadvantages introduced by the loop:

- The required gain places a tight tolerance on the total delay (less than 210 ns for an open loop gain of 2.5) and hence on the delay time in the klystron.
- The required gain introduces coupled-bunch modes that are supported by the cavity.
- Because the transient is corrected *after* it is detected, residual cavity voltage and phase oscillations still persist.

The second technique is based on pre-conditioning the cavity phase and amplitude based on knowledge of the incoming charge. Using this feedforward algorithm, the total cavity current and voltage as well as the phase angle between them are held constant during the injection process. The process is depicted using phasors in Figure 4-61. Here V_c is the total cavity voltage (which is the vector sum of the generator and beam voltages), I_c is the total cavity current, $I_b^{(k)}$ and $I_g^{(k)}$ are respectively the beam and generator currents for train k , ϕ_b is the synchronous phase angle measured with respect to the crest, and ϕ_z^* is the cavity tuning angle for which the loading angle is zero at full current.

The principle of the injection procedure, using feedforward, is as follows (for the case of a zero-to-full-current ramp):

1. With beam off, deactivate tuner loops and detune for $\phi_l = 0$ at maximum current; that is, set the tuner position to ϕ_z^* .

2. Set the external references (see Figure 4-59) $V_{\text{ref}} = SI_g$ for the desired cavity voltage, where S is the transconductance of the klystron, and $\phi_{\text{ref}} = \phi_z^*$.
3. Inject train 1.
4. Increment V_{ref} by $\Delta V_{\text{ref}} = S\Delta I_g$ and ϕ_{ref} by $\Delta\phi_{\text{ref}}$ and inject train 2.
5. Repeat step 4 until all trains have been injected.
6. Reactivate tuner loops.

This procedure can be executed at maximum duty cycle so that the total time for injection is 4 cycles, or 22.2 ms at 180 Hz. Similar procedures are used for initial turn on with low beam currents or with low repetition frequencies. These are described in the section on the machine protection system (MPS) in Chapter 16.

The required changes in the reference voltage and reference phase are:

$$\Delta I_g = \frac{V_c/R + I_b^k \cos \phi_b^k}{\cos \phi_b^k} - \frac{V_c/R + I_b^{k+1} \cos \phi_b^{k+1}}{\cos \phi_b^{k+1}}, \quad (4.64)$$

and

$$\Delta\phi = \tan^{-1} \left[\frac{\tan \phi_z^* + \frac{I_b^k R}{V_c} \sin \phi_b^k}{1 + \frac{I_b^k R}{V_c} \cos \phi_b^k} \right] - \tan^{-1} \left[\frac{\tan \phi_z^* + \frac{I_b^{k+1} R}{V_c} \sin \phi_b^{k+1}}{1 + \frac{I_b^{k+1} R}{V_c} \cos \phi_b^{k+1}} \right] \quad (4.65)$$

A potential systematic error associated with feedforward is that the cavity voltage will be regulated to the specified value, V_{ref} ; if the incoming charge is of different current than anticipated, then the amplitude feedback loop would regulate to an incorrect voltage.

Simulations of Low-Level rf System

Numerical simulations of the low-level rf system were performed by modifying existing software used in SLC rf system analysis [Minty 1995b]. In the simulations, the parameters of Table 4-20 are used. The model includes two (linear) klystrons, two rf cavities, and various feedback loops which include realistic nonlinear elements such as time delays and filters. At present, the cavity is modeled as a narrow-band resonator so that only beam interactions with the fundamental cavity mode are analyzed. Synchrotron radiation damping has not been taken into account.

The simulated response of the cavity voltage and beam phase to the injection of the first train is shown in Figure 4-62 for three cases: no transient loading compensation (solid), correction with direct feedback using a loop gain of 2.5, and correct phasing of the loop to minimize the transients (dot-dashed), and correction with feedforward (dashed). The results are summarized in Figure 4-63, in which the peak-to-peak cavity voltage and phase oscillations are plotted as a function of train number using direct feedback (a) or using feedforward (b). As can be seen, the correction of the beam-transients is substantially improved with the feedforward algorithm.

Figure 4-64 shows simulation results for the injection procedure outlined above for a zero to full current ramp. The feedforward references, as calculated from Eqs. 4.64 and 4.65, are also shown, along with the required generator and reflected powers. Notice that the Robinson damping time is shorter for the higher the current;

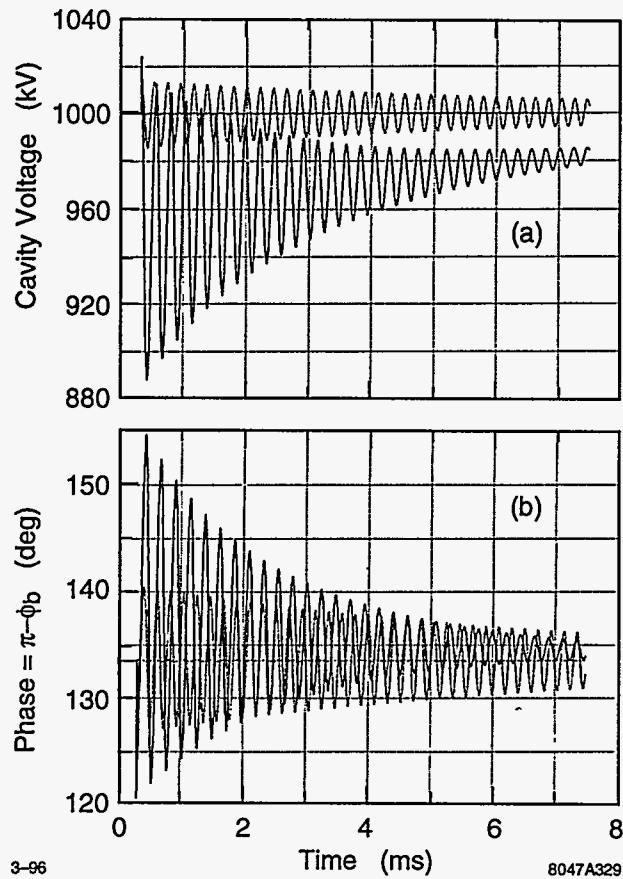


Figure 4-62. Simulations of injection transients in the cavity voltage (a) and beam phase (b) at injection of the first train. The largest oscillations arise without feedback or feedforward; the direct rf feedback reduces the amplitude of both the voltage and phase oscillations but reduces the damping of the oscillations; the feedforward system reduces the oscillations to essentially zero.

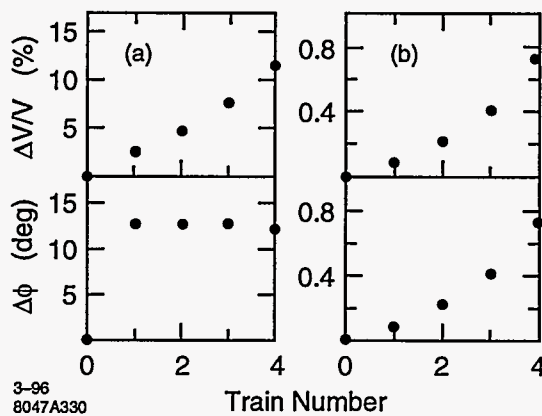
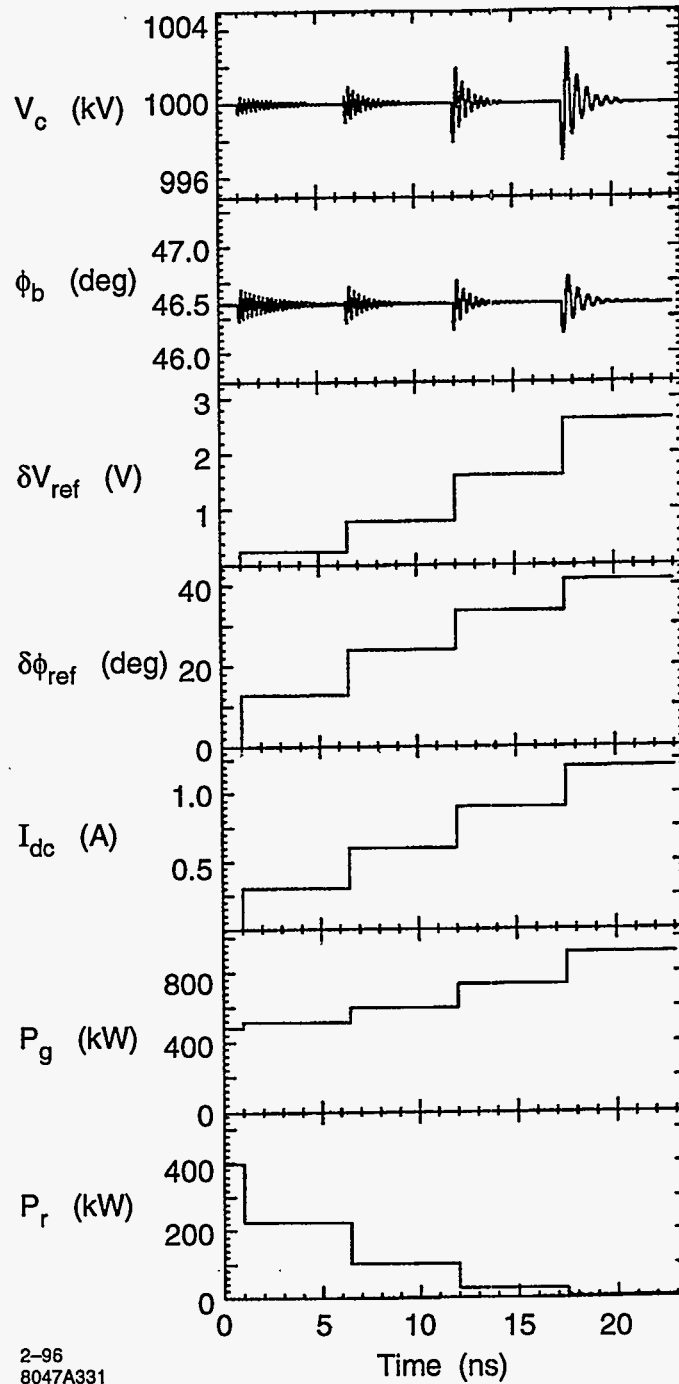


Figure 4-63. Simulated peak-to-peak cavity voltage and phase oscillations as a function of train number. The transients are corrected either with direct feedback (a) or feedforward (b).



2-96
8047A331

Figure 4-64. Simulated current ramp from no beam to full current. Plotted are the cavity voltage V_c [kV], the beam phase ϕ_b [deg], the change in reference voltage V_{ref} [V], the change in reference phase ϕ_{ref} [deg], the DC beam current I_b [A], the generator power P_g [kW], and the reflected power P_r [kW].

	Electron	Positron
f_{rf} (MHz)	2856	1428
V_{rf} (MV)	42	80
L_{rf} (m)	2.5	4
Gradient (MV/m)	21	20
Structure Type	DDS	Detuned
Multibunch loading Comp.	ΔT	ΔT

Table 4-23. Parameters of the rf systems for the electron and positron energy compressors.

this arises because of the fixed tuning angle. Also worth noting is the decrease in the coherent synchrotron oscillation frequency with current; as the beam current is increased the phase of the beam with respect to the generator crest becomes smaller resulting in a reduced restoring force for coherent phase perturbations. This effect must be taken into account in the feedback loop designs. Further analysis of stability tolerances imposed by the feedforward algorithm are in progress.

4.5.4 Energy Compressors

The electron and positron injection lines include rf sections that are used to reduce the incoming beam energy spread and energy jitter. Parameters of the energy compressors are given in Section 4.3.3. The electron compressor uses an S-band rf system while the positron system uses an L-band system; the L-band rf system is needed for the positron line because the beam emittance and beam size are too large for the apertures in the S-band structures.

The structures are shortened versions of those used in the electron and positron source linacs and are described in Chapter 6. The parameters for the injection line rf structures are listed in Table 4-23. In both cases, S-band and L-band, we use the ΔT (early injection) multibunch beam-loading compensation technique described in Chapter 6. This is the preferred method since it does not require additional off-frequency structures or klystrons. The technique can compensate for the full range of beam current by adjusting the klystron output.

4.6 Vacuum Systems

4.6.1 Main Damping Ring

The main damping ring vacuum system has been designed to attain a vacuum pressure less than 10^{-9} Torr. Because of the small vacuum chamber aperture and the large amount of synchrotron radiation, attaining such a pressure by simply pumping the beam chamber is unreasonable. Just to attain a pressure of 10^{-8} Torr in the arcs without an ante-chamber would require placing a 400 L/s pump every 20 cm.

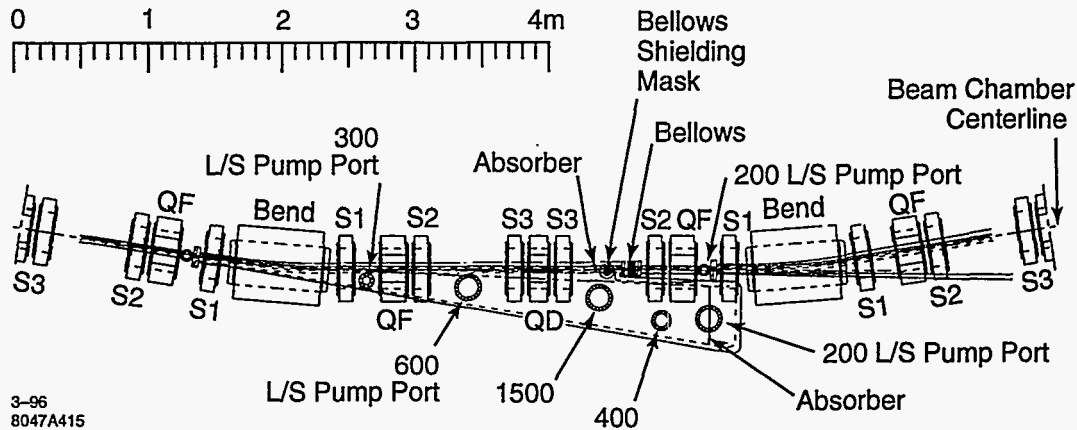


Figure 4-65. Arc vacuum chamber in the NLC main damping ring.

For these reasons, the arc and wiggler vacuum chambers have ante-chambers where the pumping is performed. At this time, we have a fairly advanced design for the arc chamber—this has allowed us to make accurate estimates of the ring impedance—and are working on the design of wiggler vacuum system.

Arcs

The NLC arc vacuum chamber is patterned after the Advanced Light Source (ALS) vacuum system. The vacuum chamber in each 4-m-arc cell will be constructed from two chamber sections and connected with a single bellows to the next arc cell chamber. The chambers will be machined in two halves from aluminum and then welded. Constructing the chamber from machined-aluminum rather than extrusions readily allows for complicated shapes while maintaining very high construction tolerances.

The arc beam chamber is circular with a 12.5-mm radius and a 5-mm-high slot that couples it to an ante-chamber. Because of the small chamber radius, the 5-mm slot subtends a relatively large angle and allows 99.8% of the synchrotron radiation power to escape the beam chamber. This is actually a greater percentage of the radiation than escapes the ALS vacuum chamber which uses a 1-cm slot. Of course, because of the smaller dimensions, the alignment and construction tolerances will be tighter than those on the ALS chambers.

The chamber of a single arc section is illustrated in Figure 4-65 and a cross-section of the vacuum chamber inside a quadrupole magnet is shown in Figure 4-66. The chamber will be machined to accommodate the magnet poles and the arc magnets are designed as "C" magnets, allowing the ante-chamber to exit the sides of the magnets. The minimum wall thickness is 2.5 mm at the quadrupole poles, leaving 0.5 mm between the chamber and the magnet poles for alignment purposes. In the magnets, the 5-mm coupling slot is tapered to 8 mm in the ante-chamber and the wall thickness is increased to 11 mm.

The primary photon stop is at the end of the ante-chamber. The ante-chamber is designed with two vertical aperture constrictions to which reduce the flow of desorbed gas from the photon stop to the beam chamber.

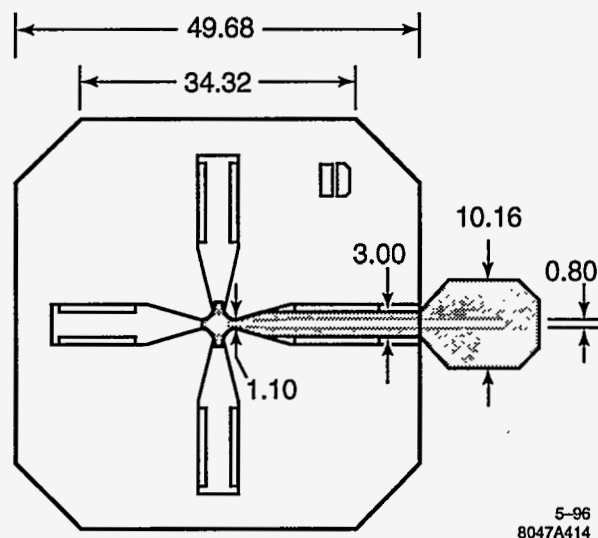


Figure 4-66. Arc vacuum chamber in a quadrupole magnet.

This allows for differential pumping which greatly reduces the pumping requirements. The vertical cross-section of the chamber in the photon stop region is shown in Figure 4-67.

The design of the beam chamber bellows is illustrated in Figure 4-68. The design is based on the ALS bellows. A smooth rf coupling within the bellows is achieved by maintaining the thin BeCu flex band under tension between either end of the internal plates. Thermal expansion of the beam pipe (1 mm for an 11°C in the 4-m chamber sections) is easily accommodated by fold-over fingers bridging a slot between the end of the flex band and the upstream end flange. During installation, when larger compression is required, the flex band is allowed to bow outward from the beam chamber centerline.

The rf liner in the bellows has the same dimensions and profile as the beam chamber, and, to simplify the design, the slot and ante-chamber are terminated just upstream. A mask which extends 2 mm into the beam chamber shields the bellows from the synchrotron radiation. The linear power density on the bellows mask and absorbers is kept just under 100 W/cm, which compares favorably with PEP and PEP-II values. The impedance of the slot termination, mask, and bellows have been calculated using MAFIA and are discussed in Section 4.4.1.

The initial vacuum design was based on NonEvaporable Getter (NEG) vacuum pumps that were supplemented with small ion pumps. Presently, we are considering using titanium sublimation pumps similar to those that are used in the ALS and will be used in the PEP-II Low Energy Ring. Assuming a desorption rate of 2×10^{-6} molecule per photon (thermal desorption is negligible), the total pumping per cell to attain a vacuum pressure of 10^{-9} Torr is 3200 L/s. The pressure profile in the beam chamber is illustrated in Figure 4-69.

Finally, it is anticipated that the arc vacuum system will be baked once before installation. At this time, we have not decided if it is necessary to install the capability for *in-situ* baking. Catastrophic vacuum vents are rare. If one does occur, it is likely that the chamber could be scrubbed using the intense synchrotron radiation from the beams. Of course, while the chamber is being scrubbed, the ring performance would likely be very poor, but the scrubbing should not take very long. This is the procedure that is used in the SLC

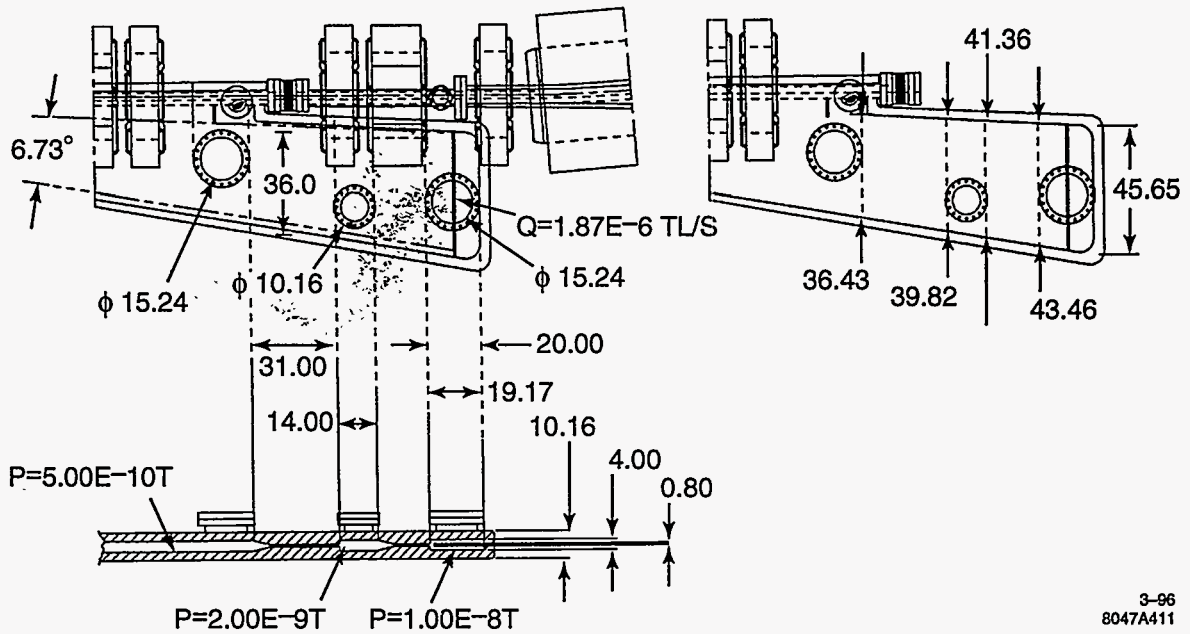


Figure 4-67. End of arc cell chamber with photon stop and bellows and associated mask. The vertical ante-chamber profile shows aperture constrictions to reduce pumping requirements.

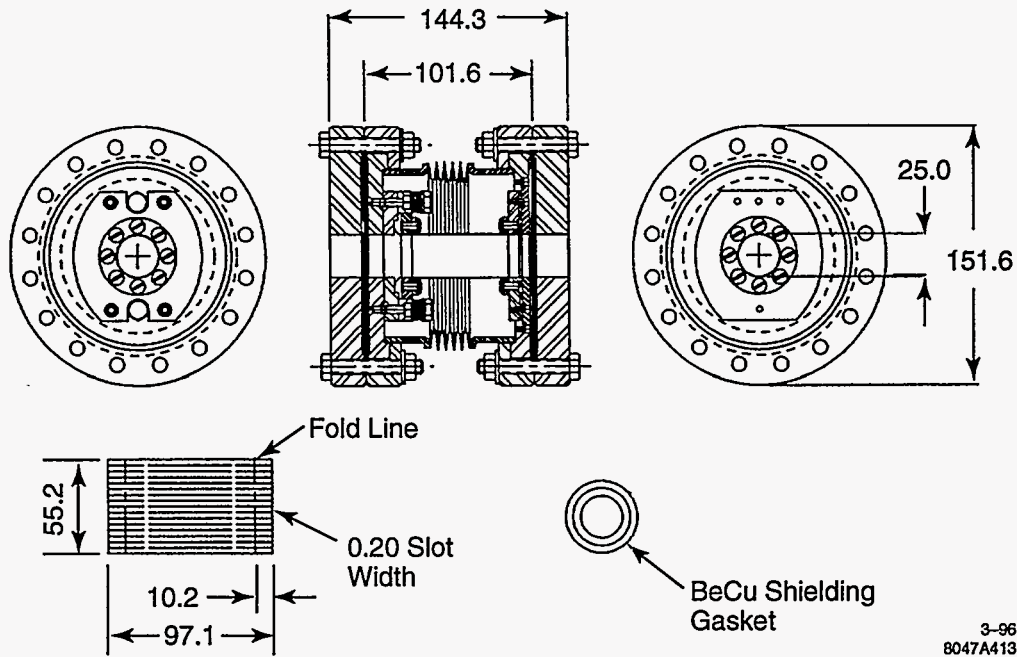


Figure 4-68. Arc vacuum chamber bellows design.

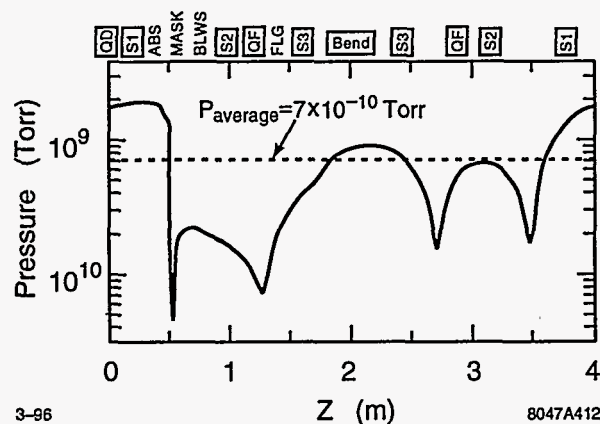


Figure 4-69. Vacuum pressure in the arc beam chamber.

damping rings and it was also the procedure used in the ALS to recover after the only unplanned vacuum vent experienced thus far.

Wiggler Regions

The wiggler straight section vacuum chamber is approximately 35-m long. It extends inside the arc from one side of the straight section to allow the absorption of the synchrotron radiation from the last wiggler magnets. The vacuum chamber is aluminum and is designed to absorb approximately 400 kW of synchrotron radiation power. The cross section of the vacuum chamber together with a cross section of a wiggler magnet and the supporting frame is shown in Figure 4-70. As is seen from the picture, the vacuum chamber has a beam chamber that is roughly 45 mm by 16 mm and an antechamber on either side with a slot height of 10 mm. The antechamber slots are sloped at 0.25 radian angle, forming a water cooled dump to absorb the synchrotron radiation generated by the wiggler magnets. The vacuum pumping is performed by distributed Nonevaporable Getter (NEG) pumps which are located behind the dump surfaces at the end of each slot.

The design of the distributed NEG pumps is a departure from conventional NEG designs and follows the approach adopted for a vacuum chamber of the wiggler straight section of the Low Energy Ring of PEP-II B-Factory [Heim 1995]. Here, an SAES ST707 strip is cut into individual 'wafers' using a laser sheet metal cutting machine. The cutting is performed under an argon purge to prevent oxidation. The NEG wafers are then slipped over a 9-mm diameter steel tube which is a combination of vacuum barrier and support rod. Between each wafer there is a 2-mm-thick stainless-steel wire-ring spacer. Each pump contains approximately 11 m of NEG strip per meter of length. This provides a distributed pumping speed of 385 liters per second per meter with a getter capacity of 1.1 Torr-liters per meter. The NEG pump is activated by a commercial tubular heater inserted inside the tube. The heater is outside of the vacuum space and it doesn't require an electrical feed-through. In addition, replacement of a failed heater does not require venting the wiggler vacuum chamber. The stainless steel rf screen separates the dump area from the NEG pumps. The purpose of the screen is to block rf TE modes from propagating down the slots and heating the NEG. The distributed NEG pumps will be supplemented by discrete ion pumps to pump hydrogen during NEG activation and methane during machine operation.

The wiggler vacuum chamber will be fabricated from two aluminum plates. Two pieces make up the top and bottom halves of the chamber. Each plate is machined on the outside first to form the water cooling

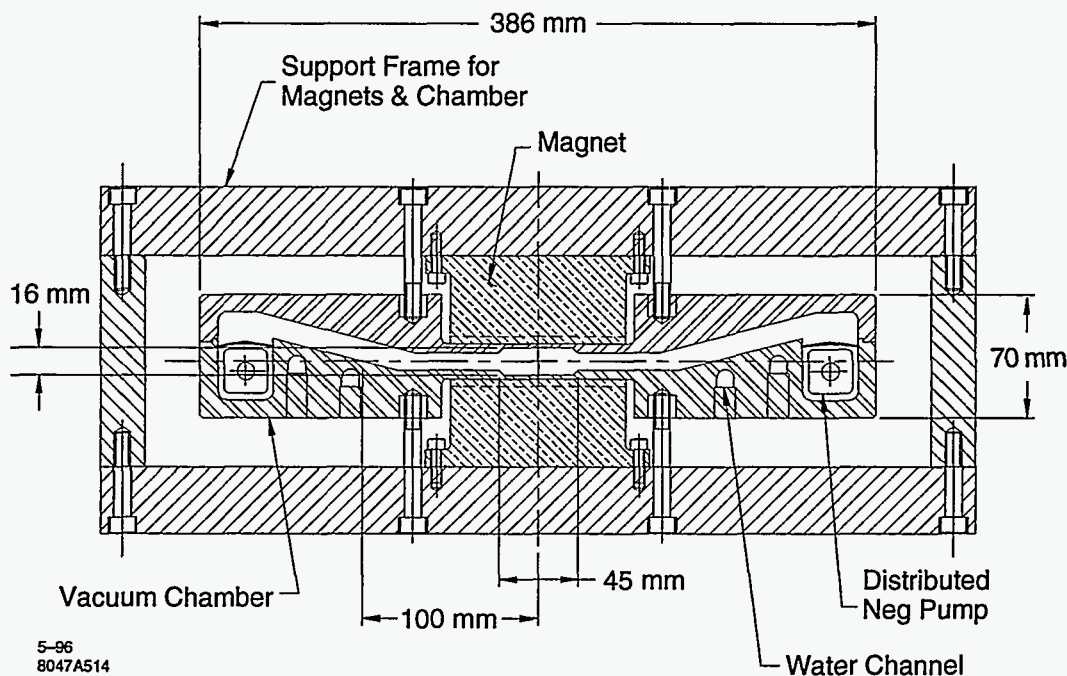


Figure 4-70. Schematic of the cross section of the wiggler vacuum chamber, the cross section of the wiggler magnet, and the supporting frame.

passages and the magnet pole pockets. After the water cooling passages have been TIG closure welded, the interior aperture and dump surfaces are machined. A second TIG welding operation is required to join the top and bottom plates and to attach an aluminum-to-steel adapters to each end. Finally, the stainless steel end flanges are welded to the adapters.

The chamber will be vacuum baked at 150° for one or two days, then argon gas glow-discharge cleaned and, finally, coated with the layer of the titanium nitride to reduce photoelectron emission.

Injection/Extraction Region

At this point, we do not have a design for the vacuum system through the injection/extraction region of the main damping ring but we do not expect it to present significant difficulties. In concept, the arc ante-chamber will be terminated after the last matching bend. The circular 1.25-cm-radius beam chamber will continue for roughly 3 m to the rf cavities. In the present design, the aperture is increased before the cavities in a 15-cm taper to a 3.1-cm radius. After the two rf cavities, the chamber would taper back to the 1.25-cm radius to pass through the ceramic chamber of the extraction kicker system. Following the extraction kickers, the chamber would be increased to a 1.6-cm radius and then would become elliptical as the horizontal half width is increased to 2.5 cm to allow for the extracted beam. The chamber will maintain this elliptical profile between the two septa and then taper back down to pass through the injection kickers. Finally, the arc ante-chamber will resume at the matching bend.

Effort will be needed to maintain smooth transitions from one cross-section to the next. We will also need to consider how to minimize the impedance due to the septa which will be mounted in large vacuum canisters.

Finally, we will need to design the coated ceramic chambers for the kickers and the numerous pumping ports that will be required to maintain the 1-nTorr vacuum pressure in this conductance-limited system.

4.6.2 Pre-Damping Ring

The vacuum system for the pre-damping ring has not been designed yet but the vacuum requirements are relatively loose; a pressure of 10^{-8} Torr will be sufficient. It has been assumed that the chamber would be constructed from aluminum like the main damping ring chambers. Of course, since the tolerances are much looser, it would probably be formed by extrusion rather than be machined from aluminum stock.

As noted in Section 4.3.2, the chamber aperture in the arcs must have inner dimensions of 6 cm by 3.6 cm to accommodate the edge emittance of 0.09 m-rad and leave ± 2 -mm clearance for steering. Although it is not required from the vacuum point of view, an ante-chamber will probably be used though the arcs because it eases the handling of the radiation power. In addition, the ante-chamber would reduce the number of secondary electrons which may cause the positron-electron instability discussed in Section 4.4.7. To further reduce the number of secondary electrons, the aluminum chamber could be coated.

4.6.3 Transport Lines

The vacuum system in the injection, extraction, and transfer lines has not been completed. The system must include valves to isolate the damping rings from the source linacs and the bunch compressors. The vacuum pumping is primarily needed to counter the thermal outgassing. In these sections, the vacuum pressure should be less than 10^{-8} Torr.

4.7 Feedback and Feedforward Systems

The damping rings will require numerous feedback and feedforward systems. Some of the rf feedback systems were described in the section on the low-level rf control, Section 4.5.3. This includes feedback loops around the klystrons and cavities as well as timing feedback loops from the bunch compressors and feedforward loops from the sources. In this section, we describe the transverse coupled bunch feedback systems and some of the transverse feedbacks needed to maintain the beam trajectory. In addition, we will review the requirements on some of the other global feedback and feedforward systems.

4.7.1 Coupled Bunch Transverse Feedbacks

As described in Section 4.4, the transverse coupled-bunch growth rates in the main damping rings require feedback damping. This section describes a bunch-by-bunch feedback for the main rings that is similar to that planned for the PEP-II rings.

The fastest growing coupled-bunch modes in the main damping ring are those driven by the transverse resistive-wall impedance. Because the pre-damping ring vacuum aperture is much larger than that in the

main damping rings, the resistive-wall impedance is not expected to be significant and thus a coupled-bunch feedback system will probably not be necessary in the pre-damping ring; this will be verified in the future.

Main Damping Ring Feedback Design

The coupled-bunch growth rates calculated for the main damping rings indicate that a feedback system will be required to maintain stability of transverse beam oscillations. It is expected that the longitudinal oscillations will be stable and will not require a feedback system.

As shown in the calculations of coupled-bunch growth rates, the transverse impedance excites a fairly broadband spectrum of beam modes, although the dominant modes are driven by the resistive-wall impedance up to about 50 MHz. We propose a bunch-by-bunch system that acts independently on each bunch, damping all possible coupled-bunch modes. For a bunch spacing of 1.4 ns, this implies that the minimum system bandwidth be at least 357 MHz. This bandwidth requirement poses the most difficult design restrictions on the system.

The transverse feedback system (TFB) can, in principle, be operated in any one of many frequency bands (0–357 MHz, 357–714 MHz, etc.). To minimize expensive wide-band high-power driver amplifier power, we chose to operate in the 0–357-MHz frequency band, where the impedance of a stripline-pair kicker is greatest. In addition, the kicker impedance is largest at the lower frequencies of the dominant coupled-bunch modes.

The design of the main damping ring TFB system follows the design of a system recently commissioned at the Advanced Light Source [Barry 1993] and one planned for PEP-II [Barry 1995]. The main damping ring TFB system would differ only in the frequency bandwidth and the total power required. A block diagram of the system is shown in Figure 4-71. Two sets of button pickups, located approximately 90° apart in betatron phase, are used to detect beam moments $I\Delta x$ and $I\Delta y$. The individual button signals are processed at 2.84 GHz ($4x f_{rf}$) to benefit from greater button sensitivity at higher frequency, combined via hybrids, and demodulated to baseband. The baseband-moment signals are combined in proportion according to the Twiss parameters at the pickups and the phase advance from pickups to kicker. The signal is delayed the appropriate amount for coincidence with the bunch at the kicker. Not shown in the figure is an element for rejection of an orbit offset at the pickup. The offset rejection can be implemented in several ways, for example, as a notch filter.

As mentioned, the kicker is a 50- Ω stripline pair operated in difference mode with a length of one-half the bunch spacing (21 cm). The kicker impedance is given by

$$R_{k,\perp} = 2 Z_L \left(g_{\perp} \frac{l \sin(\omega l/c)}{b (\omega l/c)} \right)^2, \quad (4.66)$$

where $Z_L = 50 \Omega$, $l=21$ cm, and $b=1.5$ cm is half of the stripline separation, and g_{\perp} is the coverage factor and assumed to be close to unity. This configuration yields a kicker impedance of 19.6 k Ω (at $\omega = 0$). The broadband power required is given by

$$P_{k,\perp} = \frac{V_k^2}{2R_{k,\perp}}, \quad (4.67)$$

where V_k is the kicker voltage. Specification of this voltage is discussed in the following section on computer simulations.

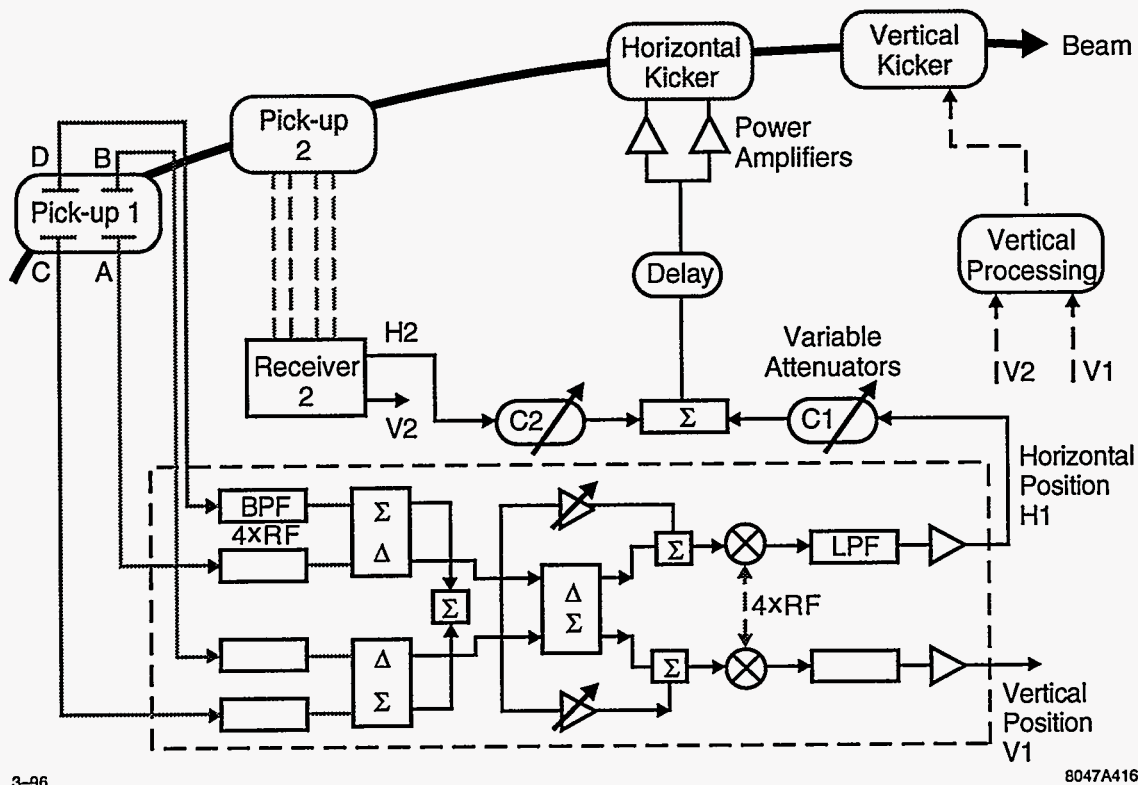


Figure 4-71. Schematic of the coupled-bunch feedback system.

Computer Simulations

This section describes computer simulations of the coupled-bunch oscillations and the corresponding feedback system used to damp the oscillations. The purpose of performing these simulations is twofold. The first is to determine the growth rates for the actual filling pattern which are difficult to calculate analytically. The second is to empirically determine how much power is required for the system to satisfactorily damp coupled-bunch oscillations. To this end, we can include effects such as injection beam transients, pickup and kicker noise, DC orbit offsets, etc.. In particular, the simulations include the limiting of the feedback response at larger beam oscillation amplitudes. The results described here represent a first attempt to find an adequate feedback voltage for damping injection beam offsets assuming a perfect feedback system; further optimization will be performed in the future.

The beam dynamics in this study are simulated using common tracking techniques at a single point in the ring, where difference equations are used to describe the discrete time evolution of the beam oscillations and wake voltages [Siemann 1983, Thompson 1989]. This approximation is valid for all of the effects we wish to study, especially since most of the wake voltages are localized at the rf cavities. One notable exception is the distributed wake of the resistive-wall impedance, which results from the skin effect on the inner vacuum chamber wall. The local approximation for the resistive-wall wake is valid when the corresponding growth or damping rate is slow compared to the betatron oscillation period. This condition is true for all cases studied here. Tracking is done in both transverse directions, which we generically label x . The turn-by-turn

difference equations for x and x' for a linear lattice are given by

$$x_{i+1} = \cos 2\pi Q_x x_i + \beta_x \sin 2\pi Q_x x'_i (1 - 2\lambda_x) \quad (4.68)$$

$$x'_{i+1} = -\frac{1}{\beta_x} \sin 2\pi Q_x x_i + \cos 2\pi Q_x x'_i (1 - 2\lambda_x) + \frac{\Re(\tilde{V}_{w,i+1})}{E} \quad (4.69)$$

where the tracking is assumed to be at a symmetry point with $\beta' = 0$ and zero dispersion. The tunes and β functions are assumed to be constant as a function of amplitude and energy. Amplitude-dependent tunes generally lower the effective coupled-bunch growth rates but here we are restricting ourselves to a worst-case scenario with no nonlinearities.

The transverse wake voltage from dipole HOMs is found by summing the contributions from all previous bunch passages. Tracking of the wake voltage is done by treating it as a complex phasor, \tilde{V}_w . The difference equation for \tilde{V}_w is given by

$$\tilde{V}_{w,i+1} = \tilde{V}_{w,i} e^{(j\omega_r + \frac{\omega_r}{2Q})\Delta t} - j2k_{\perp} q x_{i+1} \quad (4.70)$$

where k_{\perp} is the transverse loss parameter, ω_r is the angular resonant frequency, and x is the transverse offset at the location of the HOM.

As mentioned above, the resistive-wall wake voltage is the only non-localized wake of concern. The approximate localized wake voltage for a round pipe is given by

$$V_{w,rw}(t) = qx \frac{lc}{\pi b^3} \sqrt{\frac{\mu_0 \rho}{\pi}} \frac{1}{\sqrt{t}} \quad (4.71)$$

where l is the length of the vacuum chamber (usually the ring circumference), ρ the material resistivity, and b the chamber radius. The voltage for bunch passage must be remembered and individually recalculated each iteration. The resistive-wall wake is cutoff after four turns.

Main Damping Ring Feedback Systems

The TFB system measures a transverse position error and produces the appropriate angular kick to correct the error which is applied to the beam on a subsequent turn. Because the tracking in this simulation is done at only a single point in the ring, we are currently using a linear combination of the transverse position measured on the two previous turns to calculate the correct kick given by

$$V_{fb} = G_{fb} E \left(\frac{x}{\beta_x \tan \phi_x} - \frac{x_{-1}}{\beta_x \sin \phi_x} \right) \quad (4.72)$$

where G_{fb} is the TFB gain and usually ranges from 0.03–0.3, x and x_{-1} are the positions on the current and previous turns, and $\beta_{\perp} = 6.5$ m in the NLC simulations. The feedback voltage limits at the maximum amplifier output voltage.

A simulation result for the case of 4 trains of 90 bunches, filled to a total beam current of 1.2 A, is shown in Figure 4-72. The injected train is offset at injection by 500 μm ; with the assumed value of $\beta_{\perp} = 6.5$ m, this corresponds to an injection offset that is $1.2\sigma_{x,y}$. Figure 4-72 shows the transverse offset of all bunches versus turn number, and Figure 4-73 shows the corresponding feedback voltage. The feedback voltage was limited to 1500 V for this case. The injected bunches saturate the feedback and damp linearly in time until the amplifier comes out of saturation, whereupon they damp exponentially. The stored bunches are excited to very small amplitudes but are quickly damped.

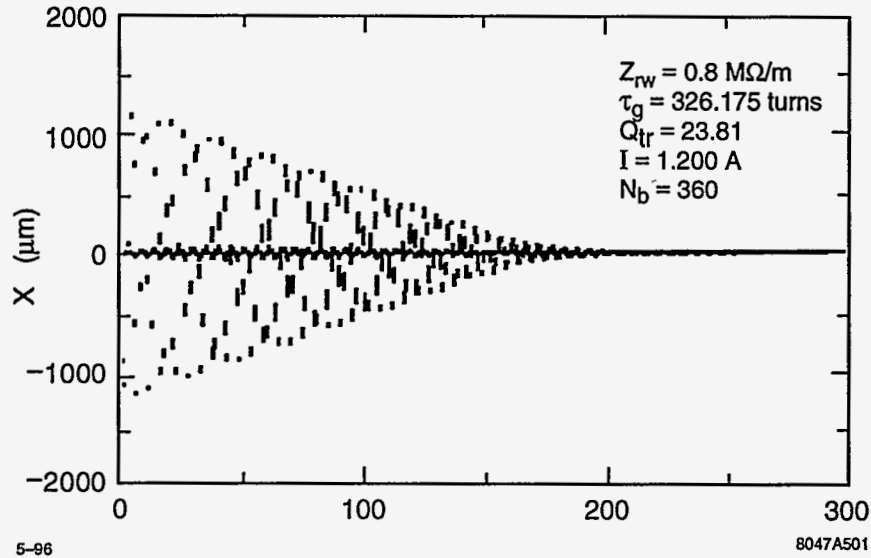


Figure 4-72. Bunch position after a train is injected into a main damping ring with a $500\text{-}\mu\text{m}$ offset; it is difficult to resolve the individual bunches in the trains.

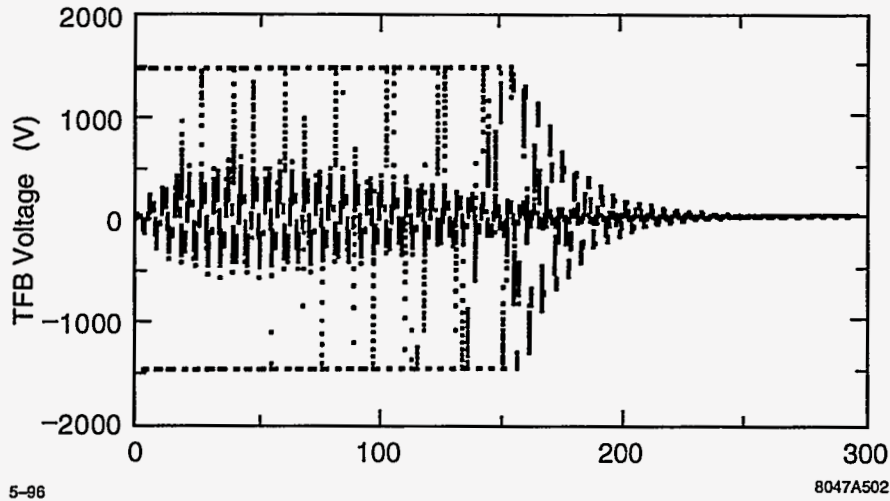


Figure 4-73. Feedback voltage after a train is injected into a main damping ring with a $500\text{-}\mu\text{m}$ offset (1.2 sigma); notice that the feedback saturates at roughly 1.5 kV .

A maximum voltage of 1500 V corresponds to broadband power of 60 W. Although this seems like a rather modest requirement, it is reasonable considering the relatively small offsets at injection. We expect the power to scale roughly as the square of the offset so considerably more power is needed for larger offsets. Furthermore, we have not yet considered the effects of residual orbit offset and noise which also consume power.

4.7.2 Stored Orbit Feedbacks

In addition to the coupled-bunch feedback system just described and the rf feedbacks described in Section 4.5.3, we plan to implement transverse position feedbacks in the damping rings. These will be used to maintain the beam orbit to prevent variations in the extracted beam trajectory and to prevent emittance growth or dynamic aperture reduction due to orbit shifts. Similar feedback systems are installed in most synchrotron light sources where the stability requirements are severe because of the long distances from the radiation source point to the experimental stations.

Because the revolution rate in the rings is roughly 1.3 MHz, these feedback systems are not limited by the sample rate like most other beam-based feedbacks in the linear collider. Of course, they are still limited by the corrector slew rate which depends upon the corrector magnets, the power supplies, and the vacuum chamber. Since most destabilizing effects are relatively low frequency, we do not believe that the feedbacks need to respond to frequencies above 30 Hz. In this case, the correctors can be simple air-core dipole magnets mounted around the normal vacuum chamber; they would be placed in the injection and extraction region where the vacuum chamber does not have an ante-chamber. Finally, although the feedback systems will be much more important in the main damping rings than in the pre-damping ring, they will likely be used to improve the operational stability in all three rings.

4.7.3 Injection Feedbacks

In addition, to the transverse position feedbacks in the damping rings, we will use fast beam-based feedbacks in the injection lines to stabilize the incoming trajectories, energy, and intensity:

- Bunch-by-Bunch Energy
- Bunch-by-Bunch Intensity
- Bunch Train Energy Spread
- Transverse Phase Space

These systems are similar to those used throughout the SLC and described in Appendix D.

4.7.4 Extraction Feedbacks

As in the injection lines, we will use fast beam-based feedbacks in the extraction lines to stabilize the outgoing trajectories. In addition, there will be a fast multibunch kicker system to correct for small (static) bunch-to-bunch position errors arising from the damping ring extraction kickers—these kickers are described in

Chapter 7. There will also be a feedback for the damping ring phase based on the extracted beam trajectory through the bunch compressor; this is described in Section 4.5.3.

Finally, there will be an intensity feedforward system that will adjust the beam loading compensation in the linacs to fluctuations in the bunch train charge; a similar system is used in the SLC to stabilize the electron beam energy. The bunch train charge will be measured near the end of the store cycle. Without a feedforward system, the tolerance on variations in the bunch train charge is 0.3% to limit the energy deviation at the IP to 0.1%. It is expected an intensity feedforward system will reduce the bunch train intensity jitter tolerance by over a factor of five by adjusting the linac beam loading compensation to the measured beam charge. In addition, the feedforward system would automatically trigger the beam dumps, either at the end of the linac or at the end of the first or second bunch compressor, if the deviation in bunch train charge exceeds specified limits; such a system is needed to limit backgrounds in the detector at the IP.

4.8 Vibration and Stability

4.8.1 Vibration

Vibrations of the quadrupole magnets due to the ground motion will cause the beam trajectory to vary. The two dominant sources of vibrations are ground motion that is transmitted and possibly amplified by the magnet supports, and a man-made noise, *e.g.*, generated by cooling water flow in the magnets [Turner 1995]. The latter, however, is more difficult to analyze, because much will depend on water cooling system and magnet supports design. Regardless, with proper design, the effect of cooling and other man-made sources should be minimal. For example, in the ALS synchrotron light source, the magnet cooling was measured to increase the magnet vibration by roughly 1 nm [Greene 1992]; motion at ten times this amplitude is still acceptable.

The effect of the vibrations on the beam trajectory depends crucially on the correlation from magnet to magnet. For high frequencies, when the wavelength of the ground waves is smaller than the distance between the quadrupole magnets, the magnet vibrations are uncorrelated. In this case, each magnet contributes independently in inverse proportion to the square of its focal length to the perturbation of the closed orbit. In the intermediate range corresponding to the wavelengths larger than the distance between the magnets, but smaller than the dimensions of the ring, one can expect resonant effects in the dependence of the closed orbit distortion on the frequency [Rossbach 1988]. At very small frequencies, when the wavelength becomes much larger than the size of the ring, the main components of the ground motion will be a rigid displacement and a tilt of the ring, which do not distort and displace the closed orbit relative to the magnets. However, the amplitude of the ground vibrations grows sharply when the frequency decreases.

The vertical perturbation of the closed orbit can be characterized by its deviation $y_B(s)$ from the ideal trajectory. We denote the value of this function at the location of i th quadrupole magnet by y_{Bi} . It is given by

$$y_{Bi} = \sqrt{\beta_i} \sum_j G_{ij} y_j \quad , \quad (4.73)$$

where β_i is the beta function and y_i is the displacement of the i th quadrupole, and the coefficients G_{ij} are computed from the known parameters of the lattice.

The matrix elements G_{ij} should satisfy the following sum rules,

$$1 = \sqrt{\beta_i} \sum_j G_{ij} \quad , \quad (4.74)$$

$$\begin{Bmatrix} x_i \\ z_j \end{Bmatrix} = \sqrt{\beta_i} \sum_j G_{ij} \begin{Bmatrix} x_j \\ z_j \end{Bmatrix} \quad . \quad (4.75)$$

The first of these two equations is due to the fact that if the entire ring shifts vertically as a rigid body by one unit, the closed orbit moves together with the ring by the same distance. The second equation expresses that the tilting of the ring in either x or z direction would also cause the same tilting of the orbit. These two sum rules are particularly important in the limit of low frequencies when the main components of the ground motion are the shifts and the tilts of the ring. Equations 4.74 and 4.75 guarantee that they do not produce distortions of the closed orbit relative to the magnets, and only the deformations of the shape of the ring would contribute to the closed orbit perturbation.

In order to eliminate rigid shifts and tilts of the closed orbit which go together with the ring and do not move the beam trajectory in the vacuum chamber, we consider the average square of the difference between the orbit and the magnet displacements,

$$\delta y_i^2 = \langle (y_{Bi} - y_i)^2 \rangle. \quad (4.76)$$

Using Eq. 4.74, we find that

$$\langle \delta y_i^2 \rangle = \sum_i G_{ij} G_{ik} [\langle y_i^2 \rangle - 2 \langle y_i y_j \rangle - \langle y_j y_k \rangle]. \quad (4.77)$$

The expectation value of the mixed product $\langle y_i y_j \rangle$ can be expressed in terms of the two-dimensional power spectrum of the ground motion, $P(\omega, k)$,

$$\langle y_i y_j \rangle = \int_0^\infty \frac{d\omega}{2\pi} \int_0^\infty P(\omega, k) \cos(k l_{ij}) \frac{dk}{2\pi} \quad , \quad (4.78)$$

where l_{ij} denotes the distance between the i th and the j th quadrupoles. We use the following representation for $P(\omega, k)$, $P(\omega, k) = P(\omega) \mu(\omega, k)$, where $P(\omega)$ is the integrated power density of the ground motion, and $\mu(\omega, k)$ describes the correlation of the ground motion at different points. In the model developed in Appendix C.2, this function is equal to

$$4 / \sqrt{\omega^2 / v(\omega)^2 - k^2} \quad , \quad (4.79)$$

where v denotes the velocity of the ground waves. In our calculations, we used a simpler model assuming that

$$\mu(\omega, k) = \begin{cases} 2\pi v(\omega) / \omega, & k < \omega / v(\omega) \\ 0, & k > \omega / v(\omega) \end{cases} \quad , \quad (4.80)$$

where $v(\omega)$ [m/s] $\approx 450 + 1900 \exp(-\omega/4\pi)$, and ω is measured in s^{-1} [Adolphsen 1995]. Qualitatively, this dependence tells that the contribution to the function $\mu(\omega, k)$ at the frequency ω comes, with equal weights, from the waves with the wavenumbers below $\omega/v(\omega)$ only. For the original model in Appendix C, the weights are not equal, with a larger contribution coming out from the vicinity of $k = \omega/v(\omega)$.

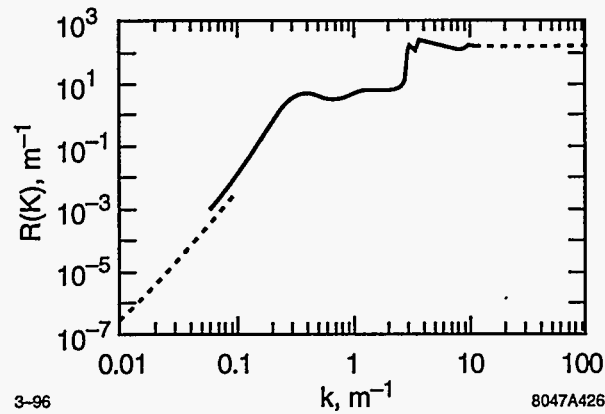


Figure 4-74. Plot of the averaged response function for the NLC damping ring.

The final expression for δy_i^2 takes the form

$$\langle \delta y_i^2 \rangle = \beta_i \int_0^{\infty} \frac{d\omega}{2\pi} P(\omega) R_i \left(\frac{\omega}{v(\omega)} \right) , \quad (4.81)$$

where $R_i(k)$ is the response function for the lattice at the location of the i th quadrupole. We average this function over the ring and denote it as $R(k)$; it is plotted in Figure 4-74.

For large ω , ($\omega > 2\pi \times 250$ Hz), R approaches the high-frequency limit of uncorrelated quadrupole vibrations. It is approximately constant in this region with a value of about $R \approx 160$ m^{-1} shown by the horizontal dashed line in Figure 4-74. For very small frequencies, one can prove that $R \approx Ak^4$, where $A \approx 30$ m^3 ; this asymptote is also shown in Figure 4-74 by a dashed line.

Assuming a spectrum of ground motion [Juravlev 1995]

$$P(\omega) \left[\frac{\mu m^2}{Hz} \right] \approx \frac{1.6 \times 10^{-3}}{\omega^4} , \quad (4.82)$$

where ω is given in s^{-1} , we found the following value for δy_i upon integration in Eq. 4.81 from zero to infinity,

$$\sqrt{\langle \delta y_i^2 \rangle} = 0.14 \text{ nm} . \quad (4.83)$$

This is negligibly small in comparison with a typical vertical size of the bunch of the order of $5 \mu m$.

The high frequency limit of the function R can easily be translated into the tolerance for the uncorrelated motion of the quadrupoles in order the beam trajectory vary less than 10% of the vertical size of the beam. For the nominal emittance $\gamma \epsilon_y = 2 \times 10^{-8}$ m-rad, the uncorrelated vibration of the quadrupoles should not exceed 18 nm.

Finally, if the trajectory motion is too large, one can use a global orbit feedback to stabilize the trajectory in the ring. Because of the high-revolution frequency, this is a straightforward feedback system (see Section 4.7).

4.8.2 Stability

In addition to the high frequency motion of the ground, there are alignment and electronic drifts that need to be controlled. To maintain the vertical emittance the closed orbit must not drift by more than $10\ \mu\text{m}$. This implies a tolerance on the magnet alignment and, more importantly, on the BPMs and BPM electronics. The primary sources of drift are thermal fluctuations and slow movement of the ground.

To estimate the effect of the ground fluctuations, we use the ATL-model which predicts that the rms difference in the displacement of any two points is given by $\Delta y^2 = ATL$ where A is a coefficient, T is the time, and L is the distance between the two locations. Using a coefficient of $A = 5 \times 10^{-7}\ \mu\text{m}^2\text{s}^{-1}\text{m}^{-1}$, which is an upper limit on the value that has been measured at SLAC (see the discussion in Appendix C), we find that the stored orbit will vary by $10\ \mu\text{m}$ after roughly 24 hours. This is not a significant limitation—it is reasonable to expect to correct the closed orbit every 24 hours. Furthermore, this trajectory variation would be substantially reduced by a global orbit feedback as discussed in Section 4.7.

Of course, it does not do any good to re-correct the closed orbit if the BPM readbacks are drifting due to either electronic variations or physics drifts. This is where the tolerance on the thermal stability is very important. To minimize the BPM drifts, we will anchor the BPMs to the magnets so that they are constrained transversely and temperature in the ring tunnel will be maintained to a fraction of a $^\circ\text{C}$, while that in the electronics racks will be stabilized to 1°C . With this thermal regulation, we would hope to limit the BPM drifts to less than $10\ \mu\text{m}$ over 24 hours.

4.9 Alignment and Supports

The main damping rings and downstream systems all have very tight alignment and field tolerances to prevent dilution of the transverse emittances. In all cases, these tolerances will be attained using beam-based alignment techniques where the alignment accuracy depends on beam measurements and not mechanical systems; the techniques to be used in the damping rings are described in Section 4.9.3.

To attain the desired vertical emittances and dynamic aperture, the magnets in the main damping rings must be aligned to the level of $50\sim 100\ \mu\text{m}$ in the vertical plane and $100\sim 200\ \mu\text{m}$ in the horizontal plane; these tolerances are specified in Sections 4.3.8 and 4.3.9. In addition, the vacuum chamber must be aligned at the level of $\sim 500\ \mu\text{m}$ to prevent synchrotron radiation from hitting the inside of the beam chamber. Of course, these tolerances refer to the alignment over a relatively short distance (1 or 2 cells) and not globally.

To attain these tolerances, we plan to rely on beam-based alignment of the quadrupoles and sextupoles. Unfortunately, one cannot do the same for the combined-function bending magnets; these need to be aligned using conventional techniques to $200\text{-}\mu\text{m}$ rms (see Section 4.3.8).

In the downstream systems (X-band linacs, final focus, etc.), the alignment will be implemented using remote magnet movers. In the damping rings the tolerances are sufficiently loose that there is some question as to whether magnet movers are required; once the alignment is known, one could mechanically perform the differential moves to attain the desired alignment. Mechanical alignment could only be considered if the alignment is stable at the $50\text{-}\mu\text{m}$ level for months—experience from the ALS and calculations using the “ATL” model would suggest that this is the case. Regardless, the mover question will be determined in the future; for this design, we have assumed magnet movers.

4.9.1 Girders and Supports

The girder and support systems are still being designed. The concept is similar to that adopted in the collimation section and the final focus. The supports would be mounted on a low concrete girder attached directly to the floor. The magnet movers would then be mounted on the girders and aligned using shims. Finally, the magnets would be mounted on the movers.

The movers could be similar to the linac movers, described in Chapter 7. These are based on the SLAC Final Focus Test Beam (FFTB) magnet movers and have a range in excess of ± 1 mm in x and y with a $0.3\text{-}\mu\text{m}$ step size. Of course, the damping rings do not such high precision and a simpler design would probably be adopted.

4.9.2 Mechanical Alignment

Mechanical alignment will be used to pre-align the quadrupoles and sextupoles in the damping rings and to align the elements that cannot be aligned using beam-based alignment, *i.e.*, the bending magnets, vacuum chamber, and rf cavities. The required alignment is $200\ \mu\text{m}$, which is well within the capabilities of modern equipment.

4.9.3 Beam-based Alignment

Attaining the required magnet alignment, in the main damping rings, through purely mechanical systems will be difficult. For this reason, we plan to use beam-based alignment to determine the positions of the quadrupoles and sextupoles with respect to the beam. Quadrupole beam-based alignment is being used at MAX-lab [Rojssel 1994], LEP [Barnet 1994], ALS [Robin 1995] and SSRL. In all these rings, it is possible to adjust the fields in each quadrupole individually, either with separate power supplies or with additional trim windings. All techniques vary the quadrupole field and measure the orbit variation; the magnitude of the orbit change is proportional to the quadrupole-to-beam offset.

The actual algorithm used to deduce the offsets is somewhat different in each of the laboratories, but once the quadrupole-to-beam offset is determined, it is referenced to the adjacent BPMs. The quadrupole-to-BPM offsets are then used to either re-align the magnets or to steer the beams through the center of the quadrupoles.

How accurately one can measure these quadrupole-to-BPM offsets depends upon several quantities: the reproducibility of the BPMs, stability of the correctors and other magnets, and physical motion of the machine. At the ALS, the quadrupole-to-BPM offset can be measured with a repeatability that is better than ± 5 microns [Robin 1995]. This is at the level of the BPM noise and is well within the necessary tolerances required in the NLC.

Sextupole beam-based alignment is being used at KEK [Kamada 1994] and at DESY [Herb 1995]. In these measurements, a local orbit bump is made in a section of the ring containing one sextupole. All the sextupoles in that family are then varied as a whole and the change in the resulting orbit is measured. The amplitude of the orbit bump is changed and the measurement is repeated. The horizontal deflection then depends

quadratically upon the orbit offset while the vertical deflection is linear in the offset:

$$\theta_x = 0.5K_2l(\Delta X + x_m)^2 \quad \theta_y = K_2l\Delta X y_m \quad , \quad (4.84)$$

where K_2l is the integrated sextupole strength, ΔX is the orbit offset, and x_m and y_m are the sextupole misalignments. By fitting the resulting oscillations, the sextupole center was inferred a resolution of several hundred microns in TRISTAN [Kamada 1994].

This process will be simplified in the NLC damping rings because all of the sextupoles will have individual power supplies and the BPMs will have $1\text{-}\mu\text{m}$ resolution. To estimate the resolution of technique, we assume that the orbit is moved in five steps by a total of $\pm 250\ \mu\text{m}$ in the sextupole while measurements are made of the closed orbit with the sextupole on and off; it is necessary to turn the sextupole on and off to isolate the individual magnet—alternately, one could use a remote magnet mover to move just the sextupole to be aligned. By using all of the ring BPMs to fit the resulting betatron oscillations to a single kick at the sextupole location, the effective BPM resolution should decrease to roughly $0.1\ \mu\text{m}$. Of course, systematic errors will degrade this effective resolution and thus we will assume a $0.5\text{-}\mu\text{m}$ effective resolution. In this case, one should be able to determine the vertical alignment of the sextupole with a resolution of roughly $20\ \mu\text{m}$; this is clearly sufficient, although higher resolution could be obtained with a larger orbit step size.

Unfortunately, this technique will be slow. To align all of the sextupoles in each of the main rings will probably take many hours. There are several possible directions in which one may try to improve the speed of the measurement. First, putting an additional winding on four of the six poles of the sextupole would provide a quadrupole field [Raubenheimer 1995b, Kikuchi 1995]. This would allow one to use the quadrupole beam-based alignment techniques to find the quadrupole center which should be close to the sextupole magnetic center; this should be significantly faster. Second, one could vary multiple sextupoles at once and fit for a number of kicks at the same time; this will degrade the resolution but it will still probably be sufficient. Third, one could vary the sextupole strength and measure the tune variation. For example, turning off a sextupole in which the beam is horizontally offset by $50\ \mu\text{m}$ will cause tune changes of roughly $\Delta\nu \approx 0.001$ —easily measurable. Unfortunately, applying this technique to the vertical alignment is more difficult, although it may be possible by operating on the difference coupling resonance and measuring the resulting tune separation. All such combined approaches require additional research.

At this point, we have not estimated the frequency with which beam-based alignment would have to be used. If it is required often (daily), the alignment system must be highly automated and the magnets would need to be mounted on movers. Fortunately, the alignment tolerances are relatively loose (compared to the rest of the collider) and it is expected that alignment would only need to be performed at the beginning of a run. Experience at the ALS suggests that the alignment is stable to better than $50\ \mu\text{m}$ over periods of six months or more [Robin 1995].

One of the important problems that needs to be resolved is how the BPMs are mounted to the magnets. At the ALS, the BPMs are mounted in the vacuum chamber and this is free move transversely. Thermal fluctuations then cause the BPM positions to drift by as much as $50\ \mu\text{m}$. Designs have been suggested that allow the BPMs to be mounted in the chamber but will constrain the transverse movement at the magnets; this is clearly desirable.

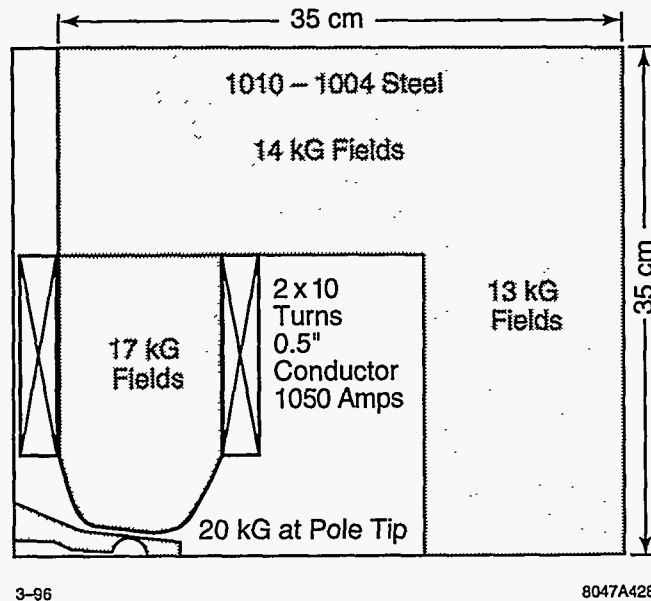


Figure 4-75. Main damping ring "C" bend magnet cross section.

4.10 Magnet Design and Power Supplies

4.10.1 Main Damping Rings

Bending Magnets

The required field parameters of the bending magnets are listed in Table 4-24 for nominal energy of 1.98 GeV. The magnet is a high-field combined-function magnet with a 15-kGauss field and a relatively strong quadrupole gradient. The full aperture at the beam pipe location is 3.2 cm and the required good field region is ± 0.5 cm.

To determine the feasibility of the bending magnets, we completed a first pass at the design of an "H" magnet using the 2D computer code POISSON and the 3D code TOSCA. Although the "H" style magnet seemed possible, the required fields and the geometry naturally lend themselves to a "C" style magnet. Thus, we have modeled a similar design with POISSON based on the "C" geometry; this magnet is illustrated in Figure 4-75 with a blowup of the pole in Figure 4-76.

In both cases, the required fields are attained using standard 1010 magnet iron with peak fields in the pole tip of 19.6 kGauss. The fields are sufficiently high that saturation effects cause the relative quadrupole and higher multipole components to vary as a function of excitation. The deviation of the magnetic field from a simple dipole field with a linear gradient is plotted in Figure 4-77 for three different excitation currents. The variation of the relative quadrupole is $\sim 1\%$ but it, as well as the variation in the sextupole component, is easily compensated; the higher-order multipoles are not significant.

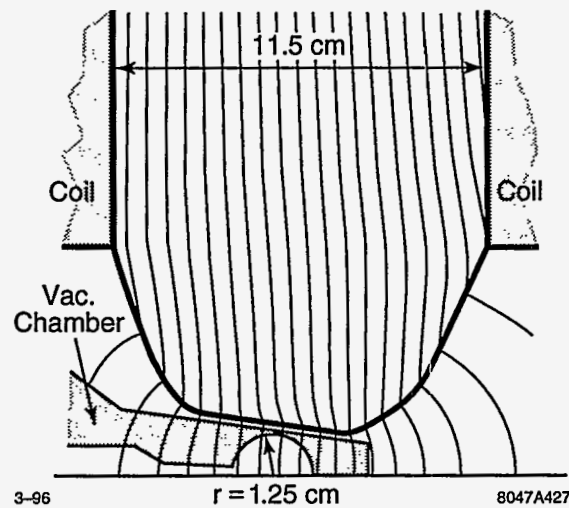


Figure 4-76. Main damping ring "C" bend magnet pole.

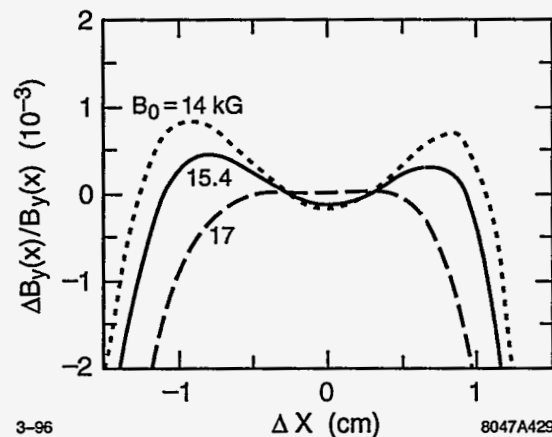


Figure 4-77. Main damping ring "C" bend magnet multipoles versus excitation for ring operation from 1.8 GeV to 2.2 GeV.

The magnet is a sector magnet and, because the sagitta is substantial (1.3 cm), the magnet pole must be curved along the beam trajectory. At this time, we have not considered construction techniques although it seems most likely that the magnets would be machined with solid cores to accommodate the curvature; the KEK ATF dipole magnets are being constructed in a similar fashion. We have estimated that a construction tolerance of $25 \mu\text{m}$ is needed to attain the required field quality.

The ends of the poles will be chamfered at a 60° angle. For convenience, we plan to use removable end pieces on the magnets. Here, the last 4 cm (or so) of the pole is removable to allow straightforward optimization of the fringing fields and future modifications; similar pole-ends are used on the SLC damping ring bending magnets. At this time, we have not studied the fringing fields at the magnet ends of the "C" magnet design. Although the "H" magnet design and other previous experience with combined function magnet design [Raubenheimer 1993a] leads us to believe that they should not be difficult, in the future, we will model the magnet in 3D and include the fringing fields in the dynamic aperture calculations.

Dipole Magnet Designs:	2
Main Bends:	
Number	38
Magnetic Length	68.4 cm
Half Gap	1.6 cm
Amp-turns	40,900
$B_{0\text{eff}}$	15.3 kGauss
$B_1 (dB_y/dx)$	126 kGauss/m
Matching Bends:	
Number	4
Magnetic Length	40 cm
Half Gap	1.6 cm
Amp-turns	34,500
$B_{0\text{eff}}$	13.0 kGauss
$B_1 (dB_y/dx)$	107 kGauss/m

Table 4-24. Dipole magnet parameters for main damping rings at 1.98 GeV.

It is also important to include the fringing field when calculating the radiation damping rate [Rivkin 1985]. To this extent, we have quoted the field in terms of $B_{0\text{eff}}$ which is defined as:

$$B_{0\text{eff}} \equiv \sqrt{\int_{-\infty}^{\infty} ds \frac{B_0^2}{L_B}} \quad (4.85)$$

and is the quantity that determines the synchrotron radiation damping. In general, the peak field in the center of the dipole will be slightly greater than $B_{0\text{eff}}$ because of the fringe fields.

The main dipole magnet coils will be constructed from two layers, with 10 turns per layer, of 0.5-in square water-cooled conductor to provide a total of 45,000 A-turns for operation at 2.2 GeV. The matching bends have half the integrated field and gradient of the main bending magnets. To reduce the fringing fields, we increased the length and decreased the fields. Since the magnets have the same ratio of field to gradient as the main bending magnets, they would be constructed with the same cross section as the main bends but powered with 38,000, rather than 45,000 A-turns, for 2.2-GeV operation. At this time, we have not considered whether an additional trim coil will be needed to account for the different saturation behavior of the matching the main bending magnets.

All of the bends in each ring will be powered by a single 100-kW power supply rated at 800 V and 1250 A. The stability of the main power supply is not very critical. Only low-frequency variations penetrate the vacuum chamber. Thus, the primary effect of bend power-supply fluctuations are slow shifts of the stored beam energy. This has three effects: (1) the bunch compressor converts the energy changes to changes in the beam phase and therefore energy fluctuations at the IP (this effect is discussed further in Chapter 5), (2) in regions of dispersion, the close orbit shifts, and (3) the betatron tunes change by an amount proportional to the uncorrected chromaticity.

In general, the most severe limitation is that on the extracted beam energy. To limit the fluctuations to 1/20 of the rms beam energy spread, the power supplies must regulate better than $\Delta I/I = 5 \times 10^{-5}$. This will cause tune variation at the level of 0.002 and 0.001 in the horizontal and vertical planes and it will cause the beam energy to fluctuate at the IP by roughly 0.05%. The horizontal and vertical orbit shifts at

the extraction point, which are proportional to the residual dispersion, will be much less than 1/10 of the respective beam sizes.

Quadrupole Magnets

The required parameters of the quadrupole magnets are listed in Table 4-25 for the at the nominal energy of 1.98 GeV. Five basic magnet designs are needed:

1. A 20-cm magnetic length with a maximum 10.3-kGauss pole-tip field (at 2.2 GeV) and a 1.5-cm radius aperture for the dispersion matching.
2. A 20-cm magnetic length with a maximum 9.3-kGauss pole-tip field (at 2.2 GeV) and a 1.5-cm radius aperture for the arc QFs.
3. A 15-cm magnetic length with a maximum 8.2-kGauss pole-tip field (at 2.2 GeV) and a 1.5-cm radius aperture for the arc QDs.
4. A 15-cm magnetic length with a maximum 5-kGauss pole-tip field (at 2.2 GeV) and a 2.0-cm radius aperture for the injection and extraction region.
5. A 15-cm magnetic length with a maximum 7-kGauss pole-tip field (at 2.2 GeV) and a 3.0-cm radius aperture for the wiggler region.

The larger-radius quadrupoles are needed in the wiggler and injection and extraction regions to accommodate the wiggler region vacuum chamber and the injected and extracted beam trajectories. The five families are summarized in Table 4-26.

As discussed in Section 4.3.9, we have assumed that the quadrupoles would be constructed in two pieces, as was done for both the ALS and APS synchrotron light sources; this will reduce the random multipoles arising from construction errors. Thus, we assumed an uncorrelated pole-to-pole error (significantly reduced relative to four-separate-pole construction) of 0.77 mils ($20\ \mu\text{m}$) rms in the pole placement in the transverse plane and the two-pole correlated contribution which can be characterized in terms of a relative translation (in the transverse plane) and rotation of the two halves. The former we assumed to be 1.5 mils ($40\ \mu\text{m}$) in each of the two dimensions, and the latter to be 1.1 mr, corresponding to a linear displacement of 8.9 mils ($225\ \mu\text{m}$) at a 20-cm arm length. The resulting multipoles are described in Section 4.3.9.

The design of the arc quadrupole magnets is further complicated by the vacuum ante-chamber. The ante-chamber is 3-cm high and in excess of 25-cm wide as illustrated in Figure 4-66. Thus, it is not reasonable to design the magnet around the chamber. We are pursuing two approaches of accommodating the ante-chamber: first, a symmetric design where iron is removed from the mid-plane on both sides of the magnet, and, second, the asymmetric case where iron is only removed from one side of the midplane. The former approach has been adopted at the APS storage ring and latter was adopted for the ALS ring. In both cases, the systematic magnet multipoles were corrected using shims to levels below our tolerances (see Section 4.3.9).

These two cases have been modeled with POISSON and the pole-tip field versus current for the symmetric case is plotted Figure 4-78.

The straight-section quadrupoles have larger apertures but are thought to be more straight-forward and we have not yet modeled them. In the injection/extraction magnets, there is no ante-chamber and the large bore wiggler magnets were sized to encompass the wiggler section ante-chamber easily; we will re-size these magnets after the wiggler vacuum chamber design is completed.

Magnet	Quan.	K1 (m ⁻²)	B _{pole} (kGauss)	Mag. Len. (cm)	Aper. (cm)
QFH (Arc Quad)	72	7.9	7.9	20	1.5
QDH (Arc Quad)	36	-6.0	6.0	15	1.5
QFHM (Arc Matching)	4	7.5	7.5	20	1.5
QDHM (Arc Matching)	4	-7.1	7.1	15	1.5
QM2 (Eta Matching)	4	8.9	8.9	20	1.5
QM3 (Inj/Ext Matching)	2	-5.3	5.3	15	1.5
QM4 (Inj/Ext Matching)	2	6.7	6.7	20	1.5
QM5 (Inj/Ext Matching)	2	-2.0	2.7	15	2.0
QM6 (Inj/Ext Matching)	2	2.0	2.7	15	2.0
QFX (Inj/Ext cells)	2	2.9	5.9	15	3.0
QDX (Inj/Ext cells)	2	-2.3	3.1	15	2.0
QM3W (Wiggler Matching)	2	-5.3	5.3	15	1.5
QM4W (Wiggler Matching)	2	6.3	6.3	20	1.5
QM5W (Wiggler Matching)	2	-0.4	0.8	15	3.0
QM6W (Wiggler Matching)	2	0.4	0.8	15	3.0
QFW (Wiggler cells)	2	2.8	5.6	15	3.0
QDW (Wiggler cells)	2	-1.0	2.0	15	3.0

Table 4-25. Quadrupole magnets for NLC main damping ring vers. 6.11 at 1.98 GeV.

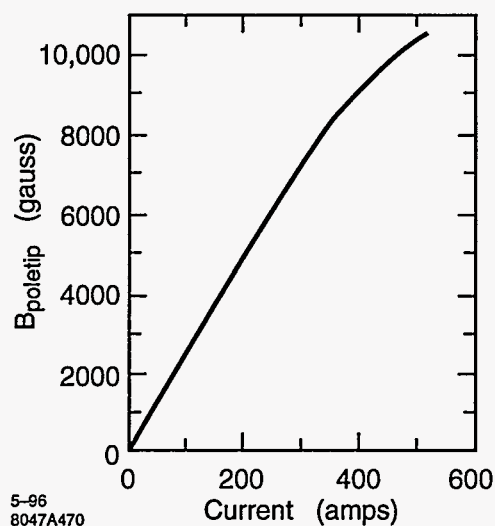


Figure 4-78. Pole-tip field versus current for symmetric arc quadrupole design.

Quadrupole Magnet Designs:	5
Arc QFs:	
Number	80
Magnetic Length	20 cm
Inscribed Radius	1.5 cm
Max. B_{pole}	9.3 kGauss
Main Coil	15 turns
Max. Current	410 A
η QFs:	
Number	4
Magnetic Length	20 cm
Inscribed Radius	1.5 cm
Max. B_{pole}	10.3 kGauss
Main Coil	17 turns
Max. Current	410 A
Arc QDs:	
Number	44
Magnetic Length	15 cm
Inscribed Radius	1.5 cm
Max. B_{pole}	8.2 kGauss
Main Coil	15 turns
Max. Current	350 A
Inj/Ext Quads:	
Number	6
Magnetic Length	15 cm
Inscribed Radius	2.0 cm
Max. B_{pole}	5 kGauss
Wiggler Quads:	
Number	10
Magnetic Length	15 cm
Inscribed Radius	3.0 cm
Max. B_{pole}	7 kGauss

Table 4-26. Quadrupole magnet parameters for NLC main damping rings at 2.2 GeV.

Magnet	Quan.	K2 (m ⁻³)	B _{pole} (kGauss)	Mag. Len. (cm)	Aper. (cm)
S1	76	-220	2.1	9	1.7
S2	76	+460	4.5	9	1.7
S3	76	-420	4.1	9	1.7

Table 4-27. Sextupole Magnets for NLC Main Damping Ring at 1.98 GeV.

Sextupole Magnet Designs:		1
Arc Sextupoles: Number		216
Magnetic Length		9 cm
Inscribed Radius		1.7 cm
Max. B _{pole}		5.5 kGauss
Main Coil		10 turns
Trim Coil		29 turns
Max. Current		260 A

Table 4-28. Sextupole magnet parameters for NLC Main Damping Ring.

Each quadrupole will have an independent power supply which adds substantial flexibility to the lattice design and simplifies the beam-based alignment procedures since an additional trim winding is not needed on each quadrupole. The disadvantage of the independent supplies may be the additional cost.

The primary effect of quadrupole power-supply fluctuations are changes in the betatron tunes and the orbits. We have calculated tolerances on the power supplies assuming independent power supplies which have uncorrelated fluctuations. The tolerance to limit the fluctuations in the tunes to 0.001 is $\Delta I/I = 2 \times 10^{-4}$. Further assuming an rms orbit displacement in the quadrupoles of 500 μm , this power-supply tolerance will cause horizontal and vertical orbit fluctuations of 0.5% and 5% of the respective beam sizes. Finally, if the quadrupoles were on string supplies or if the power supply fluctuations are correlated, the magnitude of the orbit errors does not change (assuming random orbit offsets) but the sensitivity to the tune variation increases by roughly a factor of 10, making the tolerance $\Delta I/I = 2 \times 10^{-5}$.

Sextupole Magnets

The required parameters of the sextupole magnets are listed in Table 4-27 for the nominal energy of 1.98 GeV. All the sextupole magnets have similar parameters and would likely be constructed from the same design; these parameters are summarized in Table 4-28.

Like the quadrupole magnets, the design of the sextupole magnets is complicated by the vacuum ante-chamber. Because we would like to use trim coils in the sextupoles to implement dipole and possibly skew quadrupole correction, we are only pursuing the asymmetric, where iron is only removed from one side of the mid-plane, approach of accommodating the ante-chamber; this philosophy has been adopted at the ALS ring.

This magnet has been modeled with POISSON and a plot of the pole-tip field versus current appears in Figure 4-79. In addition, a drawing of the whole magnet is shown in Figure 4-80.

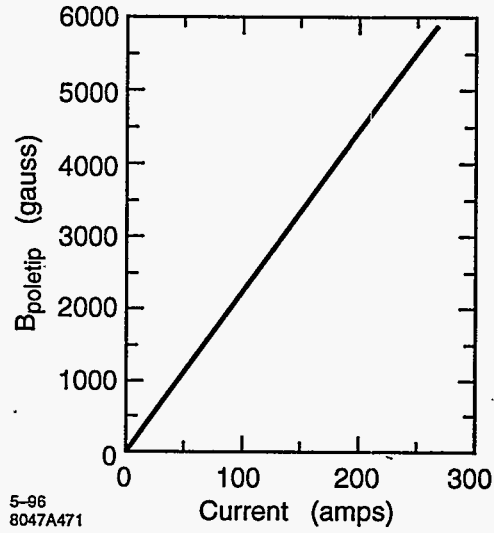


Figure 4-79. Pole-tip field versus current for asymmetric arc sextupole design.

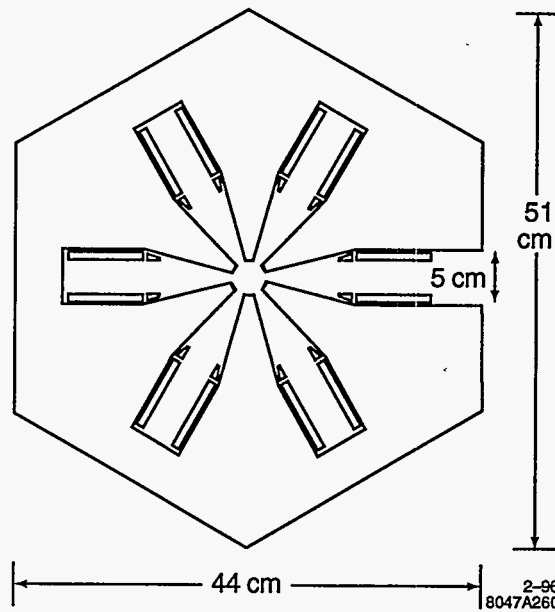


Figure 4-80. Main damping ring sextupole design.

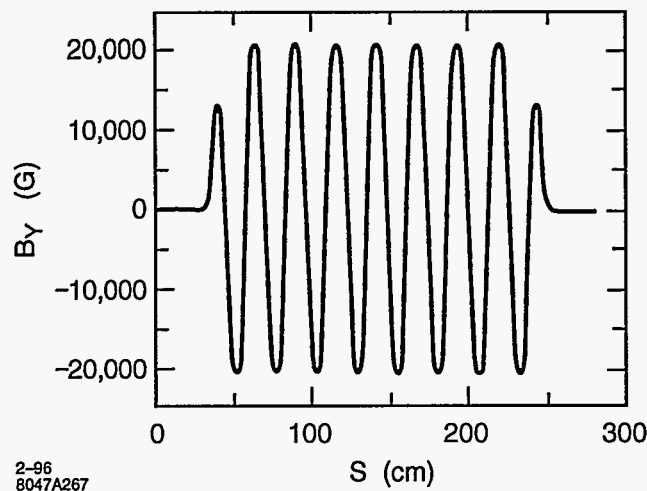


Figure 4-81. Measured wiggler field in SSRL BL-9 wiggler [Baltay].

In addition to the main coils, we are planning to use trim windings on some magnets as dipole correctors. The present magnet modeling has included a single trim winding capable of producing pole-tip fields of roughly 600 Gauss; this is more than sufficient for the dipole correction.

Wiggler Magnets

The main damping rings require roughly 25 m of strong wiggler to attain the desired damping times. The two parameters that are relevant for a damping wiggler are the integral of $B_y^2(s)$, which determines the damping, and the quantum excitation which is determined by the wiggler period and the field. To achieve the desired vertical damping time of 4.63 ms, the integral of B_y^2 over the length of the wiggler must be 6200 kGauss²-m, and to constrain the emittance dilution, the quantum excitation due to the wiggler should be less than that of the arcs.

We have chosen to consider a relatively short, high-field, short-period device. If we assume a sinusoidal field with a peak field of 22 kGauss (close to the saturation of Vanadium Permendur), then we need a length of 25.6 m and a period of roughly 25 cm. Using simple scaling laws, it is thought that such a device could either be constructed as an electro-magnetic wiggler or as a permanent magnet hybrid wiggler.

The SSRL Beam-Line 9 wiggler nearly meets our requirements [Baltay]. It is a hybrid wiggler with a length of 2.14 m, a 26-cm period, and a peak field of 20.5 kGauss. Because the wiggler poles were designed to optimize the total flux, the field is not sinusoidal and the integral of B_y^2 averaged over one period is within 1% of the required field in the main damping rings. When the matching poles at the ends of the wiggler are included, the field is within 3% of the required field. The measured field profile along the wiggler is plotted in Figure 4-81 and a comparison between the normal sinusoid field pattern and that of the wiggler is plotted in Figure 4-82 [Baltay].

Our goal in choosing the wiggler parameters was to minimize the length of wiggler needed and thereby the cost. It was thought that, for a given technology, the costs scaled with length. At a later time, it may be decided that this was not an optimal choice. In that case, we could increase the length, decreasing the peak field and increasing the wiggler period. For example, it might be more reasonable to consider a 30-m wiggler

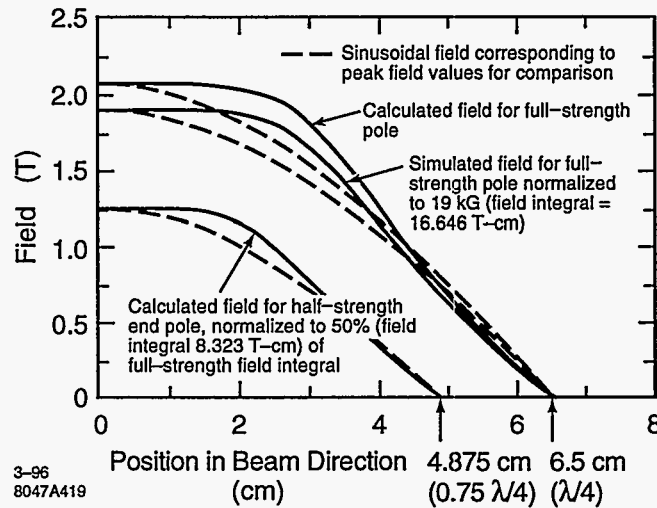


Figure 4-82. Field from SSRL BL-9 wiggler using shaped poles [Baltay].

with a peak field much less than 20 kGauss, and a 30-cm period. Alternately, we could increase the ring energy—the required peak field scales as $1/\sqrt{\gamma}$.

Injection and Extraction Septa

For the injection and extraction scheme shown in Figures 4-13 and 4-14, there are 3 m of space for the septa. As an initial design, we have assumed a DC current sheet septa that has a 1-cm vertical aperture and is composed of two pieces: an 83-cm segment and a 1-m section; the two sections are separated by 15 cm. The initial section has a 5-mm-thick blade and a 2-kGauss field while the second section has a 15-mm-thick blade which would consist of three turns of conductor and a 6-kGauss field. Both sections would be powered in series with roughly 1800 A, producing a total bend angle of 115 mrad. The current density in the blades is 36 Amps/mm² which is roughly one third the current density in the SLC damping-ring septa blades. The cooling channels have not been studied yet but the requirements are relatively loose; a coolant flow of roughly 1 GPM will limit the temperature rise to 6°C in the first section and 30°C in the second segment.

The dipole field quality along the injected and extracted beam trajectories is less than 2×10^{-4} over a radius of 3 mm; this is roughly 2 sigma of the injected beam. Finally, both septa require back-leg coils to decrease the field on the close orbit. A back-leg trim of 15 A-turns on the first segment will reduce the field on the closed orbit to much less than 0.5 Gauss with an insignificant gradient, and a back-leg trim of 150 A-turns will reduce the field from the second segment to similar levels.

The tolerance on the septum field is determined from the extracted beam angular divergence at the septum which is roughly $8 \mu\text{r}$. Thus, to limit the extracted beam fluctuations to less than 1/10 of the beam size, the septum field must be stabilized to roughly $\Delta I/I \sim 5 \times 10^{-6}$. This field tolerance should be eased by a factor of 10 by powering a compensation bend in series with the septum as is discussed in Section 4.3.1.

The compensation bending magnet has not been designed. It is required to have an integrated field of 7.7 kGauss-m. In the present design, we have assumed a magnetic length of 80 cm and a field of roughly 10 kGauss. The length and design of the magnets will be adjusted so that the current needed to excite these

compensation magnets will be equal to the current needed for the septa so that both can be powered in series.

Correction Coils

The ring will need dipole, quadrupole, and skew quadrupole correctors. The quadrupole correctors are required to optimize the dispersion match through the arcs and wiggler, and the skew quadrupole correctors are needed to correct the betatron coupling and vertical dispersion. The number, placement, and strength of the quadrupole and skew quadrupole correctors has not been determined. With independent power supplies, additional quadrupole trims will not be necessary and, with magnet movers on the quadrupoles or sextupoles, additional skew quadrupole trims will not be needed.

Each standard arc cell will require one vertical dipole corrector and two horizontal dipole correctors which we have nominally placed at the S1 and S3 sextupoles. These correctors should have maximum strengths of 33 G-m which corresponds to a 0.5-mr deflection. Simulations of the trajectory correction show that the typical strength of the correctors is roughly $120 \mu\text{r}$. Assuming uncorrelated variation, the corrector power supplies must regulate at the level of $\Delta I/I \lesssim 1 \times 10^{-4}$ to limit the vertical orbit jitter to one tenth of the vertical beam size.

As stated, in the arcs, we plan to use trim windings to the sextupoles to generate dipole fields as is done in the ALS. This choice saves space along the beam line, and makes it relatively easy to generate horizontal magnetic field for the vertical steering despite the vacuum ante-chamber. Also sextupole trims generate a more uniform dipole field than trim winding on the quadrupoles. Additional trim windings on the sextupoles could be used to generate skew quadrupole fields for correction if needed.

In the wiggler straight section, we plan to use trim windings on QFW and QDW quadrupoles for the horizontal and vertical correction. These quadrupoles have larger bore and smaller corrector strengths are required so we are not concerned about the sextupole fields introduced. These correctors should have maximum strengths of 16 G-m, which corresponds to a 0.25-mr deflection. The corrector power supplies must also regulate at the level of $\Delta I/I \lesssim 1 \times 10^{-4}$ to limit the vertical orbit jitter to one-tenth of the vertical beam size. In addition, we could add trims to the ends of each wiggler sections for additional horizontal correction. No estimate of the required strengths has been made.

In the injection and extraction straight section, we need additional orbit correction to optimize the trajectory through the septa. At this point, we have not studied these needs and have only assumed correctors located at the focusing and defocusing quadrupoles that are similar to the wiggler straight section. It will be straightforward to add additional dipole correctors in this region since the vacuum chamber will not include the ante-chamber and will be relatively clear.

4.10.2 Pre-Damping Ring

Bending Magnets

The bending magnets for the pre-damping ring are combined-functions magnets with a 17.5-kGauss effective field and a gradient of 33 kGauss/m; the required good field region is ± 2 cm. The vertical aperture is 4.4 cm which is 6-mm larger than the vacuum chamber height, leaving roughly 2.5 mm for the vacuum chamber wall. Parameters of the magnets are listed in Table 4-29.

Magnet	Quan.	$B_{0\text{ eff}}$ (kGauss)	dB_y/dx (kGauss/m)	Mag. Len. (cm)	$\frac{1}{2}$ Gap (cm)
BB (Main Bends)	28	17.5	33	80	1.9
BM (Matching Bends)	4	17.5	0	40	1.9

Table 4-29. Pre-damping ring bending magnets for Vers. 3.4.

At this time, we have not modeled the magnet and may have to modify the parameters subsequently. Because the magnet is a high-field gradient magnet, the fields may be difficult to attain without significant saturation. Although the magnet could be designed to operate with a saturated pole, the saturation will cause the relative field components to vary as a function of the excitation. This may make changing the ring energy difficult. If necessary, we could consider using additional trim magnets to provide the bending or we could construct the pole from Vanadium Permendur which saturates at a higher magnetic field.

Quadrupole and Sextupole Magnets

The quadrupoles and sextupoles in the pre-damping ring have larger apertures than in the main damping ring but similar construction issues apply. The arc magnets will need to accommodate the vacuum antechamber and thus will probably be constructed with an asymmetric design. The injection and extraction region quadrupoles have larger apertures. Although we have not yet started designs of the magnets, they are not expected to be difficult. Table 4-30 lists the magnets and requirements.

Corrector Magnets

The dipole correction fields will be generated in the arcs using trim windings on the sextupoles as is planned for the main damping rings. In the straight sections, the dipole fields would be generated with trim windings on the quadrupoles.

Injection/Extraction Septa

In the present design, the injection and extraction septa are vertically deflecting Lambertson septa. This is not considered a liability in the pre-damping ring because the vertical emittances are still large. A Lambertson septum can provide strong magnetic fields with greater reliability than a current-sheet septum. The fields in the septa are assumed to be 5 kGauss with a 2.3-cm-thick blade. At this time, no design exists but these parameters are quite relaxed.

Panofsky Quadrupoles

To ease the requirements on the injection and extraction kickers, we plan to use a dual Panofsky quadrupole as the horizontally focusing quadrupole next to the two septa. This provides horizontal focusing of both the stored and injected or extracted beams but does not deflect their trajectories. The dual quadrupole is 50-cm-long and has a gradient of 60 kGauss/m. The apertures are 6.2 cm by 6.2 cm with a 2-cm-thick central blade. The required current density is roughly 20 A/mm² which is a factor of six less than that in the SLC

Arc QFs:	
Number	42
Magnetic Length	26 cm
Inscribed Radius	3.5 cm
Max. B_{pole}	8.8 kGauss
Arc QDs:	
Number	56
Magnetic Length	15 cm
Inscribed Radius	3.5 cm
Max. B_{pole}	5.1 kGauss
Inj/Ext Quads:	
Number	6
Magnetic Length	20 cm
Inscribed Radius	4.0 cm
Max. B_{pole}	4.3 kGauss
Arc Sexts:	
Number	112
Magnetic Length	9 cm
Inscribed Radius	3.0 cm
Max. B_{pole}	2 kGauss

Table 4-30. Quadrupole and sextupole magnet parameters for NLC pre-damping rings at 2.2 GeV.

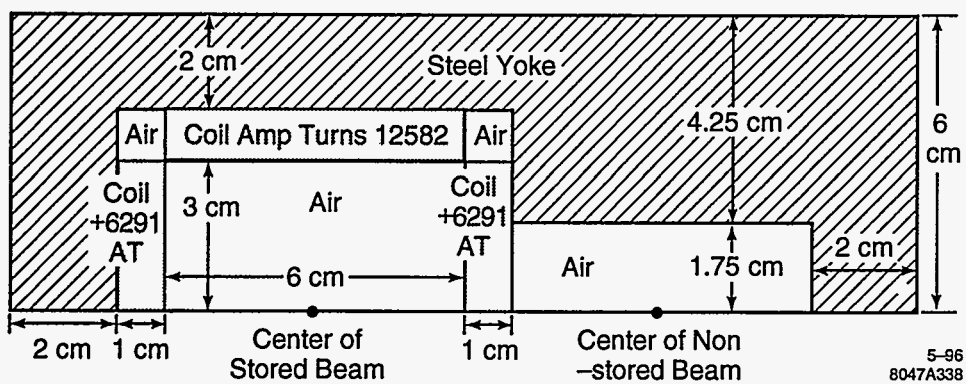


Figure 4-83. Upper half of a single Panofsky quadrupole for pre-damping ring injection and extraction regions; the present design uses a dual Panofsky quadrupole.

damping ring septa; these currents should be straightforward to attain. A preliminary single quadrupole design is illustrated in Figure 4-83.

4.10.3 Injection and Extraction Kickers

Damping ring injection is accomplished by bringing the beam toward a ring straight section at a large enough angle to clear the conventional magnets, bending it nearly parallel to the ring orbit with a DC septum magnet, and bending it onto the ring orbit with a pulsed kicker magnet at the point where the injected and stored orbits cross. Extraction is accomplished by analogous components, in the reverse order. The overall NLC design optimization requires that several trains of bunches must be damped simultaneously. The rise and fall times of the kicker magnetic field must be less than the gap between bunch trains, and the field must be flat for the duration of the train. The NLC parameters allow 60 ns for kicker rise and fall times, and require a 130-ns flattop.

These parameters are similar to those of the SLC damping rings. The SLC damping rings have revolution periods of 120 ns and each ring stores two bunches. The e^+ ring kickers extract and inject one bunch each cycle (the other bunch remains for more damping), while the e^- ring kickers inject and extract both bunches each cycle (one for collisions, one to produce more positrons). The SLC e^+ kickers demonstrate injection and extraction with 60-ns rise and fall times without disturbing other stored bunches. The SLC e^- kickers demonstrate injection and extraction with 60-ns rise or fall times of 60-ns-long bunch trains (albeit containing only two bunches) on a single pulse.

The SLC kickers are implemented with thyatron pulsers, discharging coaxial cables, or oil-filled Blumleins through cables into transmission line magnets with resistive terminations. The magnets use ferrite flux returns and distributed capacitance with loaded epoxy dielectric. The kicker beam pipes are ceramic, with a thin metallic coating to decouple the magnets from the beam at high frequencies. This basic topology, with some parametric changes, is also appropriate for the NLC kickers.

However, several iterations of design over several years were required to produce kicker systems that were operationally reliable and met the SLC performance specifications. Some additional development and demonstration will be required for the NLC. The large aperture (the result of the large emittance) in the NLC e^+ pre-damping ring poses quantitatively larger difficulties than in the SLC case. On the other hand, some of the NLC parameters are more favorable than for SLC, and allow straightforward solutions to the new problems.

Main Damping Rings

The e^- and e^+ main damping rings are identical, and there is little difference in the requirements for injection and extraction, so the same kicker system may be used in all four cases. (The e^+ pre-damping ring kickers are discussed elsewhere, since the requirements are somewhat different.) The requirements are listed in Table 4-31. The tolerances correspond to a centroid jitter of 10% of the beam sigma.

For a transmission line magnet, the field rise time is the sum of the electrical pulse rise time and the magnet transit time. We budget half of the 60-ns rise time to the electrical pulse, leaving 30 ns for the magnet transit time, as for the SLC. The kick angle and beam energy determine the product of field and length. Combined with the horizontal aperture, this determines the total magnetic flux. Combined with the transit time, this determines the voltage, independent of length. The height is fixed by the aperture requirement, then the length essentially determines the required current, or equivalently the magnet and pulser impedance. For

Parameter	Value
Rise time	60 ns
Falltime	60 ns
Flattop	130 ns
Repetition rate	180 Hz
Beam Energy	2.0 GeV
Injected Invariant Emittance	1.0×10^{-4} m-rad
Extracted Invariant Emittance	3.0×10^{-6} m-rad
Insertion Lattice	90° FODO
Insertion Quad Spacing	2.9 m
Beta at Kicker	5.0 m
R_{12} from kicker to septum	6 m
Kick Angle	2.5 mr
Injection Kick Tolerance	$\pm 3.5 \times 10^{-3}$
Extraction Kick Tolerance	$\pm 0.5 \times 10^{-3}$

Table 4-31. NLC main damping ring kicker requirements.

Parameter	Value
Electrical transit time	30 ns
Horizontal aperture	30 mm
Vertical aperture	30 mm
Length	120 cm
Field	139 Gauss
Current	332 A
Voltage	16.7 kV
Inductance	1.51 μ Henry
Capacitance	596 pF
Impedance	50 Ω

Table 4-32. NLC main damping ring kicker magnet parameters.

the SLC, the available length is short, resulting in an impedance of 12.5 Ω . This requires a large capacitance per unit length, and degrades the thyatron rise time. The kicker length of 1.2 m is chosen for the NLC to produce an impedance of 50 Ω , requiring 16 times less capacitance per unit length than for the SLC. Despite the higher impedance, the magnet voltage is less than half that required in the SLC (this is indirectly the result of the lower emittance). The SLC kicker magnets are 9-cell LC transmission lines with ferrite flux returns, and a similar construction (albeit physically longer) would have adequate bandwidth to meet the NLC requirements. The kicker magnet parameters are listed in Table 4-32.

Kicker Pulsers

Kicker pulsers very similar to those used in the SLC would probably be adequate for the NLC. For three of the four kickers in the SLC (all but e^- extraction), a simple pulser circuit with a charge-line discharged by a thyatron is operationally adequate, although it does not strictly rise from 0.0% to 100.0% or fall from 100.0% to 0.0% in 60 ns. The coherent damping time of the SLC damping rings is fast enough that the midstore kicks in the e^+ ring due to rise and fall times in excess of 60 ns does not degrade the stored beam

emittance (although it is operationally preferred to adjust the ring tune so the two midstore kicks tend to cancel). The rise time of the e^- injection kicker and the fall time of the e^- extraction kicker are irrelevant, because there are no other bunches in the ring at those times. Any kick on the turn after e^- injection from excessive fall time damps away rapidly. The case of SLC e^- extraction is more complex and is discussed below.

Since in the NLC, rise or fall times in excess of the 60-ns nominal would only affect bunches that remain in the rings, slight precursors or tails would presumably be tolerable. If this is the case, simple thyatron cable discharge pulsers would be adequate for the NLC main damping rings. With a continuous coaxial charge line, the pulse is intrinsically flat, with only a very slight droop from attenuation in the charge-line cable, plus any residual ringing from the thyatron switching.

Should the flatness of the pulse not meet the specification, it is possible to install an identical kicker magnet in the extraction line outside the ring, at a point related by a $\pm I$ transport matrix to the ring kicker. If the pulser feeds both magnets in parallel, and the cable delays are set appropriately, kicker pulse errors induced at the first magnet will be canceled by the second magnet. It is not unreasonable to expect an order of magnitude relaxation of the flatness tolerance by this technique.

Since the system impedance is higher than for SLC, the thyatron rise time should be somewhat better for the NLC. If the rise and fall times from a simple thyatron pulser are not adequate, several strategies are available. The budget for thyatron rise and fall time can be increased by reducing the magnet transit time. The rise and fall time of the thyatron pulse can be improved, at the expense of more complexity. Or thyatrons could be replaced by other switches, such as spark gaps or solid-state devices.

Cutting the magnet length in half gains 15 ns, but requires twice the current and voltage. Two half-length magnets fed in parallel also gains 15 ns, with no increase in voltage but a doubling of (total) current. Reducing the magnet capacitance per unit length by a factor of four would also gain 15 ns, but would double the impedance and thus the voltage. There is room in the lattice for two such magnets fed in parallel, which could operate at the same voltage and (total) current as the original design but still gain 15 ns of transit time.

In the SLC e^- ring, both bunches are extracted on a single pulse, so a degraded rise time results in one of the two bunches receiving a kick on the turn before extraction. The thyatron pulser is augmented by a saturating ferrite pulse-sharpening filter that removes thyatron prepulse (produced by the intermediate grids in the multistage thyatrons), and part of the slow early rise of the current waveform. This device does not degrade the pulse flatness, but does degrade the fall time. Also, a peaking capacitor in parallel with the charge-line is used to make the current overshoot initially, which makes the field reach the 100% level more quickly, but both degrades the flatness and the fall time (a smaller capacitance value would improve the rise time with minimal flatness degradation, but for the SLC rise time is more important). Since the "bunch train" only has two bunches in the SLC, a single pulse shape adjustment is adequate to make the kick magnitude equal at the two times of interest. It is implemented by oil-filled, motor-adjustable, variable-impedance insertions in the charge-lines.

All of the above pulser modifications degrade the fall time. For SLC e^- extraction, any fall time degradation is irrelevant and is not corrected. For the NLC, one could "use" bunch trains in such an order that the (trailing) train that is disturbed by a slow fall time is the one that will remain in the ring the longest for additional damping. If pulser modifications are used to improve the rise time for the NLC, another thyatron could also be added to the pulser, which would be fired to define the end of the pulse, circumventing the degradation in fall time. This technique is standard for long pulse kickers in proton machines.

Spark gaps, since they operate at high pressure rather than near-vacuum, have much higher dI/dt than thyatrons. With laser-triggering to reduce time jitter to tolerable values, and adequate engineering for

Parameter	Value
Rise time	60 ns
Fall time	60 ns
Flat top	130 ns
Repetition rate	180 Hz
Beam Energy	2.0 GeV
Injected Invariant Emittance (edge)	6.0×10^{-2} m-rad
Extracted Invariant Emittance (rms)	1.0×10^{-4} m-rad
Insertion Lattice	90° FODO
Insertion Quad Spacing	2.9 m
Beta at Kicker	5.0 m
R_{12} from kicker to septum	6 m
Injection Kick Angle	8.0 mr
Injection Kick Tolerance	$\pm 10 \times 10^{-3}$
Extraction Kick Tolerance	$\pm 1.6 \times 10^{-3}$

Table 4-33. NLC e^+ pre-damping ring injection kicker requirements.

erosion reduction and/or rapid replacement, spark gaps could be a thyatron alternative with better rise time and fall time.

Solid-state FETs are now available with rise times better than 10 ns, up to about 1000 V and about 100 A, and have the advantage that they can be turned off as well as on. They can be run in parallel for higher currents, and can be stacked in series for higher voltages. A series-switched FET pulser to produce a 20-kV pulse would require about 40 stages (since the charge voltage is twice the pulse voltage), each stage with several FETs in parallel to handle the current. It is not trivial to trigger a FET stack in such a way that none of the FETs is ever over-voltaged and destroyed, but it is not beyond the state of the art. The number of stages can be reduced by using a transformer, although more parallel FETs are needed in each stage, and the transformer loses some of the rise time improvement.

If the magnet is divided into enough segments fed in parallel (about 20), the voltage required is low enough that a few FETs in parallel could drive each segment directly. The engineering challenges with this approach are that the impedance becomes so low that the FETs must be located very close to the magnet, and the magnet is no longer a transmission line, so it is more difficult to obtain a flat pulse shape.

Pre-Damping Ring

The e^+ pre-damping ring must accept and rapidly reduce the large emittance of the undamped positrons. The pre-damping function is separated from the final damping largely due to the tradeoff between damping rate and final emittance, but the separation has the side benefit of making the kickers less difficult. The requirements for the injection kicker are listed in Table 4-33; the extraction kicker is similar except the required kick angle is 6.7 mr instead of 8 mr. The large emittance results in a large kick angle which require very high kicker power levels, but also relaxes the tolerances compared to the main damping rings.

Achieving a 30-ns magnet transit time in a single magnet would require 80 kV, which is far outside of the SLC experience, so the magnet is divided into four segments driven in parallel at roughly 20 kV. To keep the total length reasonable, the magnet impedance is chosen to be 16.6 Ω . This is 50% higher than the SLC

Parameter	Value
Electrical transit time	30 ns
Horizontal aperture	62 mm
Vertical aperture	45 mm
Number of feeds	6
Length per feed	28.9 cm
Field	308 Gauss
Current	1104 A
Voltage	18.4 kV
Inductance per feed	0.854 μ Henry
Capacitance per feed	3070 pF
Impedance	16.6 Ω

Table 4-34. NLC e^+ pre-damping ring kicker magnet parameters.

kickers, but requires roughly the same capacitance per unit length. The pre-damping ring kicker magnet parameters are listed in Table 4-34.

The pre-damping ring kicker pulser parameters are essentially identical to those for the main ring kicker pulsers, apart from the lower impedance level. However, six such pulsers are needed for injection, and five for extraction. The lower impedance makes the rise time and fall time requirement somewhat harder to meet, although by using two thyratrons in parallel for each pulser, the impedance per tube can be increased back to the same as for the main ring kickers. (The SLC e^- pulsers demonstrate the feasibility of parallel thyratrons.) The same types of magnet modifications and pulser modifications discussed in connection with the main ring kickers could be used for the pre-damping ring kickers, but the more relaxed tolerances may make them unnecessary.

4.10.4 Transport Lines

The magnets used in the injection, extraction, and other transport lines are straightforward and will not be described.

4.11 Instrumentation for the Main Damping Rings

The emphasis for the damping ring instrumentation is to provide sufficiently high-resolution monitoring to meet the performance requirements for emittance and stability. In particular, the main damping rings require precise control of the beam position in the ring magnets as well as high-resolution beam size measurements to monitor the damping process. The beam-based alignment procedures also require high resolution BPMs to determine small orbit shifts as magnets are varied and to track sources of beam jitter. Finally, the multibunch stability requirements demand accurate bunch-to-bunch measurements of bunch intensity, position, and phase.

4.11.1 Beam Position Monitors

The BPM system is scaled from the PEP-II BPM system using "button" BPM electrodes and BPM processors with a 10-MHz bandwidth that will average over roughly twenty bunches in a train. Each BPM module will contain on-board DSP and memory to allow for multi-turn averaging and other data manipulation. Using the present PEP-II ADC's, the maximum measurement rate would be once every $7 \mu\text{s}$ (roughly once every 10 turns).

The button-style BPMs have the advantage of lower beam impedance and simpler construction compared to stripline monitors. We have assumed buttons with an 8-mm diameter in a 1.25-cm-radius beam pipe as described in Section 4.4.1.

Three BPMs are required per arc cell to ensure coverage of all betatron phases and provide some redundancy in monitoring. This makes for 114 arc BPMs, plus eight matching section BPMs, nine wiggler section BPMs and seven straight-section BPMs, giving a total of 138 BPMs per ring. The arc BPMs will be centered in each of the S1 and one of the S3 sextupoles rather than in the quadrupoles, since the orbit tolerances are tightest in the sextupoles.

The tightest resolution requirement is in monitoring the position of the stored orbit since it impacts the vertical equilibrium emittance and is needed for the beam-based alignment of the magnets. Here, $1\text{-}\mu\text{m}$ resolution is required with a $1\text{-}\mu\text{m}$ rms stability over a few hours, and $10\text{-}\mu\text{m}$ stability over 24 hours. Similar requirements are found elsewhere in the NLC, but the stored orbit measurement is made easier by measuring over many turns and applying filtering and signal processing techniques in the BPM electronics to extract the beam signal. The proposed system should have a single turn resolution of

$$\sigma \sim 1 \mu\text{m} \sqrt{1 + \left(\frac{0.5 \text{ A}}{I_{\text{train}}}\right)^2} \quad (4.86)$$

for the average position of twenty adjacent bunches. This is more than sufficient for normal operation and for low current studies the $1\text{-}\mu\text{m}$ resolution could be obtained by averaging over many turns.

Of course, the stringent BPM stability requirement might only be met if remote sensing of magnet positions is also implemented in the ring. BPMs reveal relative changes between the beam and the magnet holding the BPM, but are blind to thermal and seismic drifts in magnet position. The stability issues were discussed in Section 4.8.2.

Specifications for single-turn measurement resolution are considerably looser $\sim 50 \mu\text{m}$ as it is used mainly for diagnosing injection errors. The more important criterion for the single-turn measurements is the resolution of individual bunches within each train. A small number (minimum two) of dedicated BPMs will be needed to resolve bunch-to-bunch injection errors. Similarly, bunch-to-bunch errors in the stored beam, which arise from instabilities, can be detected by the same two high-bandwidth BPMs. The bunch spacing in the train suggests a 1-GHz bandwidth is required to discriminate individual bunch motion. The high-bandwidth processor can be used in conjunction with a resonant stripline BPM, turned to have notches in the response at the revolution harmonics thereby enhancing the betatron sidebands.

The limited redundancy in the specified number of arc BPMs is rapidly consumed by the number of special-purpose BPMs: two BPMs are required for single-turn phase space reconstruction; sample-and-hold BPM sum signal is used for peak current monitoring of transient bunch length instabilities; high-bandwidth signal path ($\sim 30 \text{ GHz}$) is required from one BPM for spectral analysis of bunch length instability phenomena; several additional pickups are used for phase monitoring and rf feedback systems.

4.11.2 Beam Size Monitors

Measurement of the beam size in the ring is required to monitor the damping process and to verify that the desired equilibrium emittance is attained. Imaging of visible synchrotron radiation gives an immediate diagnostic of the injected beam size and condition. The gated cameras used in the SLC damping rings can resolve turn-by-turn changes in beam size but will not distinguish individual bunches in the NLC train.

Unfortunately, the fully-damped beam is too small to resolve by visible light. The diffraction-limited resolution is given by [Hofmann 1982]

$$\Delta y = 0.6\gamma\sqrt{2\lambda\lambda_c} \quad (4.87)$$

where $\lambda_c = \frac{4\pi}{3\gamma^3}$, giving at best a 26- μm resolution, whereas the vertical equilibrium beam size in the arc dipoles is 6 μm .

The visible synchrotron light will be an excellent diagnostic for the beam before it reaches the equilibrium beam size, but measurement of the final spot would require at least a factor 20 shorter wavelength. This would require a monitor operating in the XUV to soft X-ray regime, for which there is no easy design solution.

An alternative to a beam size monitor is to measure the equilibrium beam size with a scanning "laser wire" as proposed at many other points along the NLC. The scanning process probably loses the turn-by-turn beam size information, but this should not be an issue for the stored beam. It may also be possible to design a laser scanner that could scan the beam size quickly compared to the damping time, *i.e.*, $\lesssim 1$ ms.

4.11.3 Bunch Length Measurement

Streak camera measurements of the visible synchrotron radiation yield bunch length and bunch distribution data on a turn-by-turn basis and can further discriminate between individual bunches in the train. Additional confirmation of bunch length can be made with the extracted beam profile at a high-dispersion location downstream of the bunch compressor; this is discussed further in Chapter 5. Finally, transient bunch length behavior in the rings can be observed on the BPM signals, as mentioned above.

4.11.4 Polarization Measurement

Unfortunately, it may be difficult to measure the polarization in the ring because of backgrounds due to synchrotron radiation and particle loss. Regardless, the polarization of the electrons can be measured in the extraction line using a Compton laser polarimeter. Depolarizing resonances are only likely to be encountered in the ring if the energy is changed to achieve shorter damping times for faster repetition rate operation.

4.11.5 RF Diagnostics

The damping ring bunches should be phase-locked to the main linac rf system at the level of 0.1°. Beam loading introduces a phase offset across the bunch so high-bandwidth systems must be used to detect the phase of individual bunches. Stable operation of the rf system under the heavy beam loading will

require extensive monitoring of phase and power levels throughout the klystron and feedback systems; this is discussed further in Section 4.5.3.

4.11.6 Ion Measurements

Ion effects can be a serious performance limitation and may work in an unpredictable way. The onset of ion accumulation may be observed with gated beam loss monitors which detect electrons scattered from the ion cloud although this would likely be difficult due to backgrounds. The effect of the ions may be to cause tune shifts in the beam during the store time. Dynamic tune changes such as these can be monitored by gated excitation of the betatron tunes.

4.11.7 Conventional Diagnostics

This would include numerous betatron tune measurement systems based on turn-by-turn BPM analysis, spectrum analyzers, beam excitation systems, etc.. Also included are machine-protection systems that are routinely monitored, for example, during machine repetition rate changes.

4.12 Conclusions and Comments

In this chapter, we have described the damping ring complex for the NLC. The damping rings are designed to produce beams with emittances of $\gamma\epsilon_x = 3 \times 10^{-6}$ m-rad and $\gamma\epsilon_y = 3 \times 10^{-8}$ m-rad at a repetition rate of 180 Hz. With the present electron and positron injector designs, this requires damping the incoming electron emittance by over four orders of magnitude and the incoming positron emittance by roughly six orders of magnitude.

The damping is performed in three rings: a pre-damping ring for the positrons which damps the very large incoming positron emittance to roughly the same size as the incoming electron beam, and two main damping rings that damp the electrons from the injector and the positrons from the pre-damping ring to the desired final values. All three rings use high-field combined-function bending magnets and the main damping rings also have 26 m of wiggler magnets to attain the desired damping rates.

The design of the pre-damping ring is relatively straightforward—the primary difficulties are related to the very large incoming beam emittance, *i.e.*, the large transverse and energy apertures that are required and the injection and extraction systems. We presented a design with solutions for both of these issues. Although we have not yet started detailed engineering studies for the components of the ring, the tolerances and requirements appear reasonable. The alignment tolerances are well within the capabilities of conventional alignment practices (although we will include the ability to use beam-based alignment) and most magnet requirements are not dissimilar from those of the PEP-II LER or the ALS synchrotron light storage ring.

The main damping rings are more difficult and thus most of our studies have concentrated on them. Fortunately, the rings have a number of similarities with the present generation of synchrotron light storage rings and with the new flavor factories being constructed. In addition, many of the design and physics questions will be studied in the ATF prototype damping ring that is being constructed at KEK. Thus, many

of the accelerator physics questions that may arise in the NLC damping rings will be studied and verified in these other rings.

These similarities have also simplified the design process and provide confidence that most of the components could be constructed. In particular, the beam currents are less than those in the PEP-II LER and we have adopted rf cavities and a multibunch feedback system based on those being constructed for the LER. Likewise, the vacuum system is based on those of the ALS and PLS synchrotron radiation sources and the magnets designs are similar to those in these and other radiation sources. Although many of these components are the present state-of-the-art, we will benefit from operational experience of these other rings before the construction of the NLC is started. This will allow appropriate design modifications to ensure the required reliability for the NLC damping rings.

One exception are the combined-function bending magnets which have higher fields than in these other rings. We have performed some initial studies which show that the fields are attainable, but we still will need to build and measure a prototype before we can have complete confidence in the design. Fortunately, this is relatively inexpensive. If indeed the specifications cannot be met, it is straightforward to redesign the rings with looser requirements on the bending magnets although this is at the expense of some of the operating range.

Finally, the damping rings must provide a stable reliable platform for the rest of the collider. One of the lessons from the SLC is that we cannot expect optimal performance if all the components are operated at their limits. Thus, throughout the damping ring designs, we have provided substantial margin in the design performance over that actually required for the NLC. In particular, we have designed for higher currents than needed as well as apertures in excess that required. Similarly, we have provided for beam-based alignment and tuning systems that will provide much better accuracy than is actually needed. All of these overheads in the design should yield improved operations and reliability.

References

- [Adolphsen 1995] C. Adolphsen, private communication (1995).
- [Baltay] M. Baltay, private communication (1995).
- [Bane 1988] K. Bane, "The Calculated Longitudinal Impedance of the SLC Damping Rings", *Proc. of the 1st European Part. Acc. Conf.*, Rome, Italy, 637 (1988).
- [Bane 1989] K. Bane and R. Ruth, "Bunch Lengthening Calculations for the SLC Damping Rings", *Proc. of the 1989 Part. Acc. Conf.*, Chicago, IL, 789 (1989).
- [Bane 1993] K. Bane and K. Oide, "Simulations of the Longitudinal Instability in the SLC Damping Rings", *Proc. of the 1993 Part. Acc. Conf.*, Washington DC, 3339 (1993).
- [Bane 1995a] K. Bane and K. Oide, "Simulations of the Longitudinal Instability in the New SLC Damping Rings", *Proc. of the 1995 Part. Acc. Conf.*, Dallas, TX (1995).
- [Bane 1995b] K. Bane *et al.*, "High-Intensity Single Bunch Instability Behavior in the New SLC Damping Ring Vacuum Chamber", *Proc. of the 1995 Part. Acc. Conf.*, Dallas, TX (1995).
- [Bane 1995c] K. Bane and K. Kubo, "Bunch-to-Bunch Variation in the Synchronous Phase in the NLC Damping Rings", NLC-Note 19 (1996).
- [Barnet 1994] I. Barnet *et al.*, "Dynamic Beam Based Alignment", CERN-SL94-84 (BI), (1994).
- [Barry 1993] W. Barry *et al.*, "Design of the ALS Transverse Coupled Bunch Feedback System", *Proc. of the 1993 Part. Acc. Conf.*, Washington, DC (1993).
- [Barry 1995] W. Barry *et al.*, "Design of the PEP-II Transverse Coupled Bunch Feedback System", *Proc. of the 1995 Part. Acc. Conf.*, Dallas, TX (1995).
- [Bartalucci 1993] S. Bartalucci *et al.*, "Analysis of methods for controlling multibunch instabilities in DAFNE", LNF-93/067 (P), (1993).
- [Berg 1995] J. Scott Berg, "Transverse Coupled Bunch Mode Coupling and Growth Rates for the NLC Main Damping Ring", NLC-NOTE-10 (1995).
- [Boussard 1975] D. Boussard, CERN LABII/RF/INT/75-2 (1975).
- [Boussard 1983] D. Boussard and G. Lambert, "Reduction of the Apparent Impedance of Wide-Band Accelerating Cavities by RF Feedback", *IEEE Trans. Nucl. Sci.* **30**, 2239 (1983).
- [Brinkmann 1990] R. Brinkmann, "A Study of Low Emittance Damping Ring Lattices", DESY-M-90-09 (1990).
- [Chao 1995] A. Chao, B. Chen, and K. Oide, "A Weak Microwave Instability with Potential Well Distortion and Radial Mode Coupling", presented at the 1995 Part. Acc. Conf., Dallas, TX (1995).
- [Corlett 1993] J.N. Corlett and R.A. Rimmer, "Impedance Measurements of Components for the ALS", *Proc. of the 1993 Part. Accel. Conf.*, Washington, DC (1993).

- [Fox 1993] J. Fox *et al.*, "Feedback Control of Coupled Bunch Instabilities", *Proc. of the 1993 Part. Accel. Conf.*, Washington, DC (1993).
- [Furman 1995] M. Furman, "The Positron Beam Instability Code POSINST", to be documented (1995).
- [Grobner] O. Gröbner, "Bunch Induced Multipactoring", *Proc. Xth Int. Conf. on High Energy Acc.*, Serpukhov, USSR, 277 (1977).
- [Greene 1992] E. Greene, T. Warwick, "Environmental Vibration Measurements of the ALS Floor and Storage Ring", LSBL-144 (1992).
- [Halbach 1969] K. Halbach, *Nucl. Instr. and Methods* **74**, 147 (1969).
- [Halbach 1985] K. Halbach, *J. Appl. Phys.* **57**, 3605 (1985).
- [Haïssinski 1973] J. Haïssinski, "Exact Longitudinal Equilibrium Distribution of Stored Electrons in the Presence of Self-Fields", *Il Nuovo Cimento* **18B**, No. 1, 72 (1973).
- [Heifets 1994a] S. Heifets, "Bunch-to-Bunch Phase Variation in the NLC DR", NLC-NOTE-6 (1994).
- [Heifets 1994b] S. Heifets, "Study of the NLC DR Impedance and Collective Effects: the First Attempt", NLC-NOTE-9 (1994).
- [Heifets 1995] S. Heifets, "Study of an Instability of the PEP-II Positron Beam", PEP-II AP Note 95.21 (June 7, 1995).
- [Heim 1995] J. Heim *et al.*, "Wiggler Insertion of the PEP-II B-Factory," *Proc. of the 1995 Part. Acc. Conf.*, Dallas, TX (1995).
- [Herb 1995] S. Herb, G.B. Jaczko, and F. Willeke, "Beam-Based Calibration of Beam Position Monitor Offsets in the HERA Proton Ring using Strong Sextupole Fields", (1995).
- [Hirata 1992] K. Hirata and K. Yokoya, "Nongaussian Distribution of Electron Beams due to Incoherent Stochastic Processes", *Particle Accelerators* **39** 147-158; and KEK-Preprint-91-212 (1992).
- [Hofmann 1982] A. Hofmann and F. Meot, "Optical Resolution of Beam Cross-section Measurements by Means of Synchrotron Radiation", *Nucl. Instr. and Methods* **203**, 483-493 (1982).
- [Izawa 1995] M. Izawa, Y. Sato and T. Toyomasu, "The Vertical Instability in a Positron Bunched Beam", *Phys. Rev. Lett.* **74**, 5044 (1995).
- [JLC] KEK JLC damping ring design.
- [Juravlev 1995] V.M. Juravlev *et al.*, "Seismic Conditions in Finland and Stability Requirement for the Future Linear Collider" (1995).
- [Kamada 1994] S. Kamada, "Overview on Experimental Techniques and Observations", *Proc. of the Workshop on Nonlinear Dynamics in Particle Accelerators: Theory and Experiments*, Arcidosso, Italy (1994).
- [ATF 1995] "ATF Accelerator Test Facility Design and Study Report", KEK Internal 95-4 (1995).

- [Kikuchi 1995] M. Kikuchi *et al.*, "Beam-Based Alignment of Sextupoles with the Modulation Method", *Proc. of the 1995 Part. Acc. Conf.*, Dallas, TX (1995).
- [Klatt 1986] R. Klatt and T. Weiland, "Wake Field Calculation with Three-Dimensional SCI Code", *1986 Linear Acc. Conf. Proc.*, SLAC, 282 (1986).
- [Krejcik 1993] P. Krejcik *et al.*, *Proc. of the 1993 Part. Acc. Conf.*, Washington DC (1993).
- [Kubo 1993] K. Kubo, *et al.*, "Compensation of Bunch Position Shift Using Sub-RF Cavity in Damping Ring", *Proc. of the 1993 Part. Acc. Conf.*, Washington, DC, 3503 (1993).
- [Lambertson 1995] See, for example, G.R. Lambertson, "Update of RF Reaction During Beam Gap", PEP-II Tech Note 85 and CBP Tech Note 73, (1995).
- [Mattison 1995] T. Mattison, "Injection/Extraction Kickers for the NLC Damping Rings", talk given to NLC damping ring group 1/10/95.
- [Minty 1995] M.G. Minty, W.L. Spence, "Injection Envelope Matching in Storage Rings," *Proc. of 1995 Part. Acc. Conf.*, Dallas, TX (1995).
- [Minty 1995b] M.G. Minty and R.H. Siemann, "Heavy Beam Loading in Storage Ring RF Systems", SLAC-PUB-95-6801, submitted to *Nucl. Instr. and Methods*, (September 1995).
- [Moshhammer 1993] W. Moshhammer and T. O. Raubenheimer, presentation at LC93.
- [Murphy 1987] J. B. Murphy, "Storage Ring Lattice Considerations for Short Wavelength Single Pass FELs", *Proc. of the ICFE Workshop on Low Emittance e^+e^- Beams*, BNL-52090, Brookhaven, NY, 197 (1987).
- [Ohmi 1995] K. Ohmi, "Beam and Photo-Electron Interactions in Positron Storage Rings", KEK Preprint 94-198, (February 1995).
- [Oide 1990] K. Oide and K. Yokoya, "Longitudinal Single Bunch Instability in Electron Storage Rings", KEK Preprint 90-10, (1990).
- [Oide 1994] K. Oide, "A Mechanism of Longitudinal Single Bunch Instability in Storage Rings", KEK Preprint 94-138, (1994).
- [Pedersen 1975] F. Pedersen, "RF Cavity Feedback", *IEEE Trans. Nucl. Sci.* NS-22, no. 3 (1975), and NS-32, no. 3 (1985).
- [Pedersen 1992] F. Pedersen, SLAC-400, 192 (1992).
- [PEP-II 1993] LBL-PUB 5379, SLAC-418, in PEP-II Conceptual Design Report, June 1993.
- [Piwinski 1972] A. Piwinski, DESY Report 72/72 (1972).
- [Piwinski 1985] A. Piwinski, "Beam losses and lifetime", CERN Accelerator School, Gif-sur-Yvette, CERN85-19 (1985).
- [Raubenheimer 1988] T. O. Raubenheimer, L. Z. Rivkin, R. D. Ruth, "Damping Ring Designs for a TeV Linear Collider", *Proc. of the 1988 DPF Summer Study, Snowmass '88*, Snowmass, CO, 620 (1988).
- [Raubenheimer 1991] T.O. Raubenheimer, "Generation and Acceleration of Low Emittance Flat Beams for Future Linear Colliders", Ph.D. Thesis, Stanford University, SLAC-387 (1991).

- [Raubenheimer 1992] T.O. Raubenheimer and P. Chen, SLAC-PUB 5893, in "Tons in the Linacs of Future Linear Colliders", Proc. of LINAC92, Ottawa, vol. 2, 630-632 (1992).
- [Raubenheimer 1992] T. Raubenheimer, "Emittance Growth due to Beam Gas Scattering", KEK Report 92-7 (1992).
- [Raubenheimer 1993a] T.O. Raubenheimer, R. Early, T. Limberg, and H. Moshhammer, "A Possible Redesign of the SLAC SLC Damping Rings", Proc. of the 1993 Part. Acc. Conf., Washington DC, (1993).
- [Raubenheimer 1993b] T.O. Raubenheimer, K. Egawa, M. Kikuchi, K. Kubo, S. Kuroda, K. Oide, S. Sakanaka, N. Terunuma, J. Urakawa, "The Vertical Emittance in the ATF Damping Ring", Nucl. Instr. and Methods A335:1 (1993).
- [Raubenheimer 1994] T.O. Raubenheimer "The Core Emittance with Intrabeam Scattering in e^+/e^- Rings", Particle Accelerators 45:111 (1994).
- [Raubenheimer 1995a] T.O. Raubenheimer and F. Zimmermann, "A Fast Beam-Ion Instability: Linear Theory and Simulations", Phys. Rev. E 52, 5487 (1995).
- [Raubenheimer 1995b] T.O. Raubenheimer, private communication (1995).
- [Rieke 1972] F.F. Rieke and W. Prepejchal, "Ionization cross sections of gaseous atoms and molecules for high energy electrons and positrons", Phys. Rev. A 6, (1972).
- [Rimmer 1992] R.A. Rimmer, "RF Cavity Development for the PEP-II B-Factory", Proc. Intl. Workshop on B-Factories, KEK, Tsukuba, Japan (1992).
- [Rivkin 1985] L. Z. Rivkin, "Damping Ring for the SLAC Linear Collider", Ph.D. Thesis, Cal. Tech. (1985).
- [Robin 1995] D. Robin, G. Portmann, and L. Schachinger, "Automated Beam Based Alignment of the ALS Quadrupoles", NLC Note 18, (1995).
- [Robinson 1962] K.W. Robinson, CEA report, CEAL-1010 (1962).
- [Rojsel 1994] P. Rojsel, "A Beam Position Measurement System Using Quadrupole Magnets Magnetic Centre as the Position Reference", Nucl. Instr. and Methods in Phys. Rev. 343, (1994).
- [Rogers 1995] J. Rogers, "Photoelectron Trapping Mechanism for Horizontal Coupled Bunch Mode Growth in CESR", CBN 95-2 (1995).
- [Rossbach 1988] J. Rossbach, "Closed-Orbit Distortions of Periodic FODO Lattices Due to Plane Ground Waves", Particle Accelerators 23, 121 (1988).
- [Sakanaka 1995] S. Sakanaka *et al.*, "Design of a high power test cavity for the ATF damping ring", Proc. of the Part. Acc. Conf., Dallas, TX (1995).
- [Sands 1976] M. Sands, "Beam-Cavity Interactions", Orsay report, 2-76 (1976).
- [Siemann 1983] R. Siemann, "Computer Models of Instabilities in Electron Storage Rings", in *The Physics of Particle Accelerators*, AIP Conf. Proc. 127, 431 (1983).
- [Stupakov 1995] G. Stupakov, T.O. Raubenheimer and F. Zimmermann, "A Fast Beam-Ion Instability: Effect of Ion Decoherence", Phys. Rev. E 52, 5499 (1996).

- [Thompson 1989] K.A. Thompson, "Transverse and Longitudinal Coupled Bunch Instabilities in Trains of Closely Spaced Bunches", *Proc. of the 1989 Part. Acc. Conf.*, Chicago, IL (1989).
- [Thompson 1991] K.A. Thompson, "Simulation of Longitudinal Coupled-bunch Instabilities", ABC-24, (1991).
- [Teng 1985] L.C. Teng, "Minimum Emittance Lattice for Synchrotron Radiation Storage Rings", LS-17 Argonne (1985).
- [Turner 1995] J.L. Turner *et al.*, "Vibration Studies of the Stanford Linear Collider", *Proc. of the 1995 Part. Acc. Conf.*, Dallas, TX, (1995).
- [Wilson 1994] P. Wilson, private communication (1994).
- [Zisman 1986] M. Zisman, S. Chattopadhyay, J. Bisognano, "ZAP Users Manual", LBL-21270 (1986).

Contributors

- Karl Bane
- Lou Bertolini
- John Byrd
- Yunhai Cai
- John Corlett
- Dick Early
- Miguel Furman
- Sam Heifets
- Kwok Ko
- Patrick Krejcik
- Tom Mattison
- Bobby McKee
- Michiko Minty
- Cho Ng
- Tor Raubenheimer
- Robert Rimmer
- David Robin
- Ben Scott
- Steve Smith
- Bill Spence
- Cherril Spencer
- Gennady Stupakov
- Perry Wilson
- Sasha Zholents
- Frank Zimmermann

Bunch Compressors and Prelinac

Contents

5.1	Introduction	258
5.2	Requirements and Design Options	260
5.2.1	Design Goals	260
5.2.2	Beam Requirements	260
5.2.3	Spin Rotator Options	261
5.2.4	Bunch Compressor Options	262
5.2.5	RF Frequency Choices	264
5.2.6	Tuning and Diagnostics	264
5.3	System Design	265
5.3.1	Layout	265
5.3.2	Ring Extraction	265
5.3.3	Spin Rotator	266
5.3.4	Low-Energy Compressor	272
5.3.5	Prelinac	274
5.3.6	High-Energy Compressor	276
5.4	Longitudinal Dynamics	281
5.4.1	Optical and RF Nonlinearities	282
5.4.2	The T_{566} -Matrix Element	284
5.4.3	Single Bunch Longitudinal Wakefields	285
5.4.4	Multibunch Wakefields	285
5.4.5	Bunch Shaping	285
5.4.6	Longitudinal Phase Space at the End of the Linac	285
5.4.7	Multibunch Dynamics	286
5.5	Transverse Dynamics	298
5.5.1	Spin Rotator and Low-Energy Bunch Compressor	298
5.5.2	Prelinac	301
5.5.3	High-Energy Bunch Compressor	301
5.5.4	Space Charge and Coherent Radiation	307
5.5.5	Ion Effects	308
5.5.6	Synchrotron Radiation	309
5.6	Tolerances	310
5.6.1	Alignment and Field Tolerances	310
5.6.2	Tolerances on RF Phase, Energy, and Intensity	310
5.7	Conclusions and Comments	314

5.1 Introduction

This chapter describes the NLC bunch compressors, which compress the 4-mm-long bunches from the damping rings to the 100 ~150- μm bunch lengths required in the main linacs and final foci. It also describes the S-band prelinacs that accelerate the beams from the damping rings at roughly 2 GeV to an energy of 10 GeV and the spin rotators that provide control over the particle spin orientation. These systems are part of the low-energy injector complex that prepares the beams for injection into the X-band main linacs. Thus, it is essential that they provide a stable and reliable platform for the tuning of the linacs and final foci. In the next paragraphs, we briefly summarize the status of each of these subsystems before delving into greater detail in the body of the chapter.

The first items in the compressor systems are the spin rotators which are located at the exit of the damping rings. We plan to install a spin rotator on the electron side and leave space for an installation on the positron side. This is to allow for a future upgrade to polarized positrons or polarized electrons which would be wanted for $\gamma\text{-}\gamma$ or e^+e^- collisions. The rotators are based on pairs of solenoids separated by a horizontal arc to allow full control over the spin orientation; this is similar in concept to the original SLC spin rotator system. Solenoids were chosen to control the spin because the other alternate, namely a snake, requires a vertical bending chicane which must be unreasonably long to prevent synchrotron radiation from increasing the vertical emittance. Of course, the problem with solenoids is that they couple the beam which, with flat beams, leads to an increase in the projected vertical emittance; this is the reason the original solenoid system is not presently used in the SLC. Our present design uses pairs of solenoids which are optically separated so that the coupling is fully canceled. There are very tight tolerances on the quadrupole fields between the sextupoles but an extensive skew correction system has been included to ease the tolerances as well as correct any residual coupling from the damping rings.

Next, the NLC bunch compressors must compress the bunches from the damping rings with 4-mm lengths to the 100 ~150- μm bunch lengths required in the main linacs and final foci. To perform the compressions, a two-stage compressor system has been designed: the first stage follows the damping rings and the second stage operates at a beam energy of 10 GeV at the exit of the 8-GeV S-band prelinacs.

The two-stage system has a number of advantages over a single stage compressor. In particular, it keeps the rms energy spread less than roughly 2%, it is optically more straightforward, and the bunch lengths are more logically matched to the acceleration rf frequency so that the energy spread due to the longitudinal wakefields can be canceled locally. The disadvantage of the two-stage design is that it is more complex and lengthy than a single-stage compressor. The first stage rotates the longitudinal phase by $\pi/2$ while the second stage performs a 2π rotation. In this manner, phase errors due to the beam loading in the damping rings and energy errors due to imperfect multibunch energy compensation in the 8-GeV S-band prelinacs do not affect the beam phase at injection into the main linac.

One of the driving philosophies behind the NLC compressor design has been to utilize naturally achromatic magnetic lattices wherever the beam energy spread is large. In particular, the optics is chosen so that quadrupoles are not placed in regions of large dispersion and strong sextupoles are not needed. This choice arises from experience with the SLC bunch compressors which are based on second-order achromats where quadrupoles are located in dispersive regions and strong sextupoles are used to cancel the chromatic aberrations. Unfortunately, the SLC design is extremely difficult to operate and tune because of the large nonlinearities and the sensitivity to multipole errors in the quadrupoles; over the years additional nonlinear elements have been added (skew sextupoles and octupoles) to help cancel the residual aberrations but the tuning is still difficult. To further facilitate the tuning in the NLC design, we have explicitly designed

orthogonal tuning controls and diagnostics into the system. We feel confident that these considerations will make the system relatively straightforward to operate and tune.

Finally, the rf acceleration throughout the compressor system, *i.e.*, the bunch compressor rf and the 8-GeV prelinac, is performed with relatively low frequency rf. In particular, the first bunch compressors use L-band (1.4 GHz) rf and the prelinac and second bunch compressor use S-band (2.8 GHz) acceleration. Although these systems are, in general, longer and more expensive than higher frequency accelerator systems, we feel that they are needed at the low beam energy. In particular, we have designed the systems so that they have small beam loading and relatively loose alignment tolerances. This is important to provide the reliability and stability that is desired in the bunch compressor system. Of course, such lightly-loaded systems are inefficient and could not be used to accelerate the beams to very high energy.

To minimize the long-range transverse wakefields, all of the accelerator structures are Damped-Detuned Structures (DDS), similar to those developed for the X-band main linacs. In addition, the beam loading is primarily compensated using the ΔT (early injection) method. This has the advantage of canceling the bunch-to-bunch energy deviations locally within an accelerator structure thereby minimizing the transverse emittance growth due to dispersive and chromatic effects. Details of the multibunch beam loading compensation, the accelerator structures, and power sources is presented in Chapter 6.

The design described in this chapter appears to meet, or even to surpass, all requirements; the requirements are detailed in Section 5.2. At the same time, the present design still allows for improvements and optimization. First, because the designs were being made concurrently, we overestimated the errors in the beams from the damping rings that we should expect—assuming a more reasonable input beam could significantly change the optimization and potentially decrease the length and complexity of the compressor system. Second, an option of simplifying the second stage to only perform a $\pi/2$ rotation in longitudinal phase space should be explored. This also could provide a substantial saving in length and S-band rf components, but it will require tighter tolerances on the phase variation in the damping rings and the energy compensation in the 8-GeV S-band prelinac. Third, another path, that should be further investigated, is the possibility of optically compensating the longitudinal nonlinearities. The present design uses additional rf systems in the second compressor to compensate the longitudinal nonlinearities introduced in the dispersive regions. It would certainly be desirable to compensate these effects locally without having to resort to the additional rf systems.

In the next section (Section 5.2), we review the requirements of the system and the assumed beam from the damping ring. We then provide an overview of the design choices that were made and some of the alternate options. Next, in Section 5.3, we describe the various components of the compressor in more detail and in Sections 5.4 and 5.5, we discuss the longitudinal and transverse dynamics which are relevant to the design, and the tuning schemes that are needed to attain the desired performance. The tolerances and tuning schemes are described in Section 5.6, and the chapter concludes with a summary and an outlook on further studies.

Finally, it should be noted that, at the time of this study, not all of the damping ring or the low frequency rf system parameters were finalized. Thus, in many of the dynamics studies, performed for the bunch compressors, we intentionally over-estimated the expected errors to provide a margin. The example of the synchronous phase offsets has already been mentioned. Similarly, we assumed SLAC S-band wakefields when calculating effects of the accelerator structures. Because the present design calls for structures that have roughly twice the group velocity, the SLAC transverse single bunch wakefield is roughly a factor of two too strong and the longitudinal wakefield is roughly a factor of $\sqrt{2}$ too strong. Thus, the system will perform even better than has been calculated. We will note sections that have these errors.

5.2 Requirements and Design Options

In this section, we will describe the design goals of the bunch compressor systems and beam requirements. We will also outline the design choices that were made and some of the alternate options.

5.2.1 Design Goals

The NLC bunch compressor system is designed with six goals:

- The compressor system must compress a bunch with $\sigma_z \approx 4$ mm from the damping rings to the $\sigma_z = 100 \mu\text{m} \sim 150 \mu\text{m}$ needed in the main X-band linacs and the final foci. This requires compressing the bunch length, and correspondingly increasing the energy spread, by a factor of 30–40.
- The bunch compressor system should be able to compensate for bunch-to-bunch phase offsets induced by the beam loading in the damping rings; if not corrected, these phase errors would become energy errors at the end of the linacs. This requires that the compressor system rotate the longitudinal phase space by $\pi/2$, translating the phase errors into injection energy errors.
- The bunch compressor system should provide a trombone-like arm, reversing the direction of the beam before injection into the main X-band linacs. This allows extension of the linac lengths to upgrade the beam energy at the IP without significant modification to the injection systems. It also allows for abort systems to dump the beam and feed-forward systems to correct the beam trajectory, phase, and energy before injection into the main linacs.
- The compressor system must include a spin rotator system that can rotate the polarization vector of the electron beam from the vertical plane to any arbitrary orientation. This is easiest at lower beam energy.
- The compressor system must be able to correct for coupling mismatches from the damping rings; dispersive mismatches from the damping rings will be corrected in the ring extraction line, described in Chapter 4.
- The compressor systems are the injectors into the main linac and they need to provide a stable and reliable platform to allow tuning of the linac and final focus systems. The system should have reasonable tolerances and limit the horizontal and vertical emittance dilutions to 20% and 30% respectively.

5.2.2 Beam Requirements

In this section, we describe the injected and extracted beam requirements; these are summarized in Table 5-1. The damping rings are designed to produce beams with a relative energy spread of $\sigma_\delta \sim 1 \times 10^{-3}$ and a bunch length of $\sigma_z \approx 4$ mm. The beam emittances are damped to $\gamma\epsilon_x = 3 \times 10^{-6}$ m-rad and $\gamma\epsilon_y = 3 \times 10^{-8}$ m-rad and the spin is oriented vertically to preserve the polarization in the rings.

The compressor system has been designed to accept beams whose incoming phase varies due to the transient beam loading in the damping rings. The present design allows for phase errors of ± 20 ps while limiting the

Inj. Energy	1.8-2.2 GeV
Inj. Bunch charge/Beam current	$< 1.31 \times 10^{10} / < 1.5$ A
Inj. Phase error Δz	< 6 mm (4 mm expected)
Inj. Bunch length σ_z	< 5 mm (4 mm expected)
Inj. Energy error $\Delta E/E$	$< 0.01\%$
Inj. Energy spread σ_δ	0.1%
Inj. Emittances $\gamma\epsilon_x, \gamma\epsilon_y$	$3 \times 10^{-6}, 3 \times 10^{-8}$
Ext. Energy	10 GeV
Charge loss	$< 1\%$
Ext. Phase error Δz	< 15 μ m
Ext. Bunch length σ_z	100 – 150 μ m
Ext. Energy error $\Delta E/E$	$< 3\%$
Ext. Energy spread σ_δ	$< 1.5\%$
Ext. Emittances $\gamma\epsilon_x, \gamma\epsilon_y$	$3.6 \times 10^{-6}, 4 \times 10^{-8}$

Table 5-1. Input and extracted beam requirements for compressor system.

phase error of the extracted beams to less than $\pm 0.2^\circ$ of X-band. This will limit the resulting energy error at the end of the main linac to less than 0.1% and will limit the luminosity loss due to shifts of the collision point to less than 1%. It should be noted that, in the present damping ring design, the phase variation is less than ± 12 ps (Chapter 4).

The compressor system will operate with a train of 90 bunches having bunch charges of 0.68×10^{10} particles for NLC-Ia and 1.31×10^{10} particles for NLC-IIc; these values are 5% higher than the design bunch charges at the IP to provide overhead in the bunch charge. The higher charge for NLC-IIc coincides with longer bunches in the main linacs ($\sigma_z = 150$ μ m) while the lower charge in NLC-Ia corresponds to a shorter bunch length (100 μ m).

In all cases, the expected beam loss through the compressor system is much less than 1%. To provide an additional margin, the compressor system has been designed to accept beams with an initial bunch length of 5 mm. Because there are no quadrupoles in regions of large dispersion, this has minimal impact on the design requiring only slightly larger horizontal apertures in the bending magnets and vacuum system. All apertures have been specified in excess of $\pm 5\sigma_{x,y}$ plus an allowance for the injected phase error of ± 6 mm and an additional allowance for steering errors of 2 mm; the allowance of 2 mm for steering errors is based on present SLC operation.

Finally, the bunch compressor system has been designed to have minimal emittance dilutions. In particular, the system needs to limit the horizontal emittance dilution to 20% and the vertical dilution to 30% while providing a stable platform for the tuning of the downstream systems. Wherever possible we have chosen technologies that, while more expensive or less efficient, will ease the tolerances. We believe the added cost and inefficiency is acceptable for these relatively small sections.

5.2.3 Spin Rotator Options

The spin rotator system must orient the spin so that the polarization is longitudinal at the IP. Because there is net bending in the collider to provide for the multiple IPs with a 20-mr crossing angle and because the beam energy at the IPs will be varied, it is necessary to provide full control over the orientation of the spin

vector. To control the orientation of the spin vector, one can either use solenoids or a snake or serpent design that consists of interleaved horizontal and vertical bending magnets.

The choice of a rotator system is determined by emittance dilution constraints and limitations on the momentum compaction (R_{56}). In the NLC, it would be difficult to preserve the vertical emittance of $\gamma\epsilon_y = 3 \times 10^{-8}$ m-rad through a "half-serpent" system [Fieguth 1987] which necessarily includes vertical bending. To limit the vertical emittance dilution due to synchrotron radiation to 2%, one can show that the length of the vertical dipole magnets is related to the beam energy as [Emma 1994].

$$L[\text{m}] > 190E[\text{GeV}] \quad . \quad (5.1)$$

Even at the minimum beam energy of 2 GeV, the bending magnets must become excessively long. For this reason, a solenoid-based rotator system was chosen. It is located immediately after damping ring extraction where the beam energy is low and the beam energy spread is small. The betatron coupling introduced by the solenoids is corrected by using pairs of solenoids separated by an optical transformation so that the coupling is canceled.

5.2.4 Bunch Compressor Options

For the NLC design, we are currently planning to use a two-stage compressor design which is outlined in Ref. [Raubenheimer 1993]. The first stage, located after the spin rotator, compresses the bunch from the damping rings to $\sigma_z = 500 \mu\text{m}$ for injection into an S-band prelinac. There, the beam is accelerated from the damping ring energy of roughly 2 GeV to an energy of 10 GeV where it is injected into the second stage of the compressor. This second stage compresses the bunch to the final bunch length of $\sigma_z = 100 \mu\text{m}$ – $150 \mu\text{m}$, before injection into the X-band main linac. The first compressor stage rotates the phase space by roughly $\pi/2$ and the second stage rotates the longitudinal phase space by 2π so that the beam phase in the X-band main linac is independent of the phase in the damping rings.

While the linear design of such a two-stage bunch compressor system is conceptually straightforward, the design is complicated by the large longitudinal nonlinearities introduced in both the bending sections and the rf sections. The solution we have adopted is to use the nonlinearity of an additional sinusoidal rf to cancel the nonlinearity introduced in the bending sections, but this is difficult and is potentially dangerous; systems where one large effect cancels another large effect are inherently extremely sensitive. We have investigated some options of decreasing the optical longitudinal nonlinearities by adding sextupoles but these made the transverse phase space unacceptable. These issues will be discussed further in Section 5.4.

Alternate Approaches

Unfortunately, the second-stage bunch compressor is complicated because of the required 2π rotation in longitudinal phase space. One possible alternate approach would be to use a $\pi/2$ compressor for the second stage *if the S-band linac can be used to compensate the bunch-to-bunch energy deviations*. This would have two advantages: first, it simplifies the design of the second stage compressor; the required R_{56} (the R_{56} is the (5,6) element in the linear transfer matrix) in the second compressor would be 0.05 m which would be easily achieved with a simple FODO arc. Second, such a system might allow one to tune the bunch-to-bunch energy deviation of the beam after the X-band linac by making small phase changes in the second compressor. The allowable phase changes must be small compared to the final beta function of $100 \mu\text{m}$, *i.e.*, $\Delta\phi \ll 1^\circ$ X-band.

It is also possible to consider designing a single-stage bunch compressor system at the exit of the damping rings, but the large energy spreads and large space charge forces at the exit of the compressor are thought to make preservation of the transverse emittances difficult; a systematic study of the required tolerances has not been performed. In addition, the nonlinearity in the longitudinal phase space would seem to complicate if not preclude this option (see the discussion in the next section).

Alternatively, one could consider accelerating the uncompressed beam from the damping rings in a low-frequency structure and then use a single-stage compressor. This option would reduce the relative energy spread and the space charge forces, but, because of the nonlinearity of both the rf and the T_{566} , it is more difficult to perform the 90° rotation. This system does not appear to have significant advantages over the present design and thus we will not consider it further.

Single-Stage vs. Multistage

At first glance, a single-stage compressor has several advantages compared with the two-stage solution. It is simpler, contains less elements, and, perhaps most importantly, avoids the significant wakefield effects in the prelinac, thereby improving the longitudinal dynamics at high intensity. It has also been argued that a single-stage compressor may ease the compensation of multibunch effects [Oide 1994].

The main disadvantages of a single-stage compressor are the increase of the final energy spread to 5%, which enhances the harmful effects of the T_{566} and U_{5666} and the much larger sensitivity to incoming phase variations; the T_{566} and U_{5666} are the TRANSPORT notation for the higher-order dependences of the path length on the energy deviation: $x\text{-}\delta^2$ and $x\text{-}\delta^3$. The nonlinearity of the rf alone is already significant. Assuming an L-band rf system, an initial phase error $z_0 \approx \sigma_{z0} \approx 5$ mm would change the final phase at the exit of the compressor by $\Delta z_f \approx k^2 z_0^3 / 6 \approx 20$ μm , where, as before, $k \equiv 2\pi/\lambda$. Such a change is too large to be tolerable, considering that the beam in the main linac will be off crest by about $10\text{--}15^\circ$ and that the energy change at the end of the linac has to be small.

As a concrete example, we have performed simulations of the longitudinal dynamics for a single compressor consisting of 750-MV L-band rf and a wiggler (or chicane) with $R_{56} \approx 9$ cm. In the ideal case of perfectly compensated U_{5666} and T_{566} , an initial phase error of ± 6 mm increases the final bunch length to 155 μm (from 100 μm for no initial phase offset). If the T_{566} is included, without compensation, the final rms bunch length for zero initial phase error is as large as 58 mm. Applying a compensating S-band rf, as discussed for the double-stage compressor, the minimum final bunch length as a function of compensating voltage V_c was found to be 400 μm , for $V_c \approx 195$ MV and no initial phase error. Such a single-stage compressor does not fulfill our specifications.

To make a single-stage compressor a viable and attractive option, the T_{566} -matrix-element has to be smaller than about a third of the R_{56} -matrix-element (for a generic wiggler or chicane, $|T_{566}|$ is 1.5 times R_{56}). If the T_{566} -matrix-element is of this size, the residual nonlinearity can be compensated by a decelerating rf as in the double-stage scheme, without introducing other intolerable aberrations. A small T_{566} -matrix-element may be realized by manipulating the second-order dispersion via quadrupoles at dispersive locations and/or via additional sextupoles. A further complication arises, however, in the transverse phase space, where dilutions of the transverse emittance have to remain tolerable for an rms energy spread as large as 5%. These two requirements, small T_{566} and tolerable transverse emittance dilution, appear to be in conflict with each other, as changes to the second-order dispersion also generate higher-order dispersion and chromaticity, which affect the transverse emittances.

For these reasons, attempts to design a single-stage compressor with satisfactory performance in all phase-space dimensions have not yet been successful.

5.2.5 RF Frequency Choices

The choice of rf frequency depends upon the bunch length and the expected phase variations from the damping rings, the sensitivity to multibunch beam loading, the alignment tolerances, and the length and cost of the rf system. The tolerances due to all of these effects are significantly eased by using lower rf frequency with lightly beam-loaded structures. The disadvantage of lower-frequency rf is the system cost and poorer efficiency.

For example, in the low-energy compressor, one can use 139 MV of L-band rf, which requires roughly 10 m of accelerator structure, or 70 MV of S-band rf which could be provided with roughly 3 m of accelerator structure. But, the multibunch loading is more difficult to compensate in the S-band system and would require using the ΔF compensation technique. Therefore, we would need three different structures with slightly different rf frequencies and three klystrons to power the structures. Furthermore, for the same transverse emittance dilution, the transverse alignment tolerances on the S-band structure are more than five times tighter than on the L-band structures. Since the bunches are long in the bunch compressors the alignment tolerances are tight anyway and the factor of five is significant. For these reasons and because the additional cost is not a significant limitation in these short rf sections, the present design is based on the lower-frequency rf systems. In particular, we use L-band rf (1.4 GHz) in the low-energy compressors and S-band rf (2.8 GHz) in the prelinacs and the high-energy compressors.

In all cases, we will use Damped-Detuned Structures similar to those developed for the X-band main linacs. These minimize the long-range transverse wakefields as well as provide a straightforward method of measuring the induced dipole modes which are used to align the structures to the beam. The structures, power sources, rf pulse compressors, and details of the beam-loading compensation are all described in Chapter 6.

5.2.6 Tuning and Diagnostics

Although the tolerances on components in the bunch compressor systems are not nearly as tight as in the main linacs or the final foci, we have chosen to adopt the same methods of beam-based alignment and tuning. In particular, to ease the alignment procedures, all of the quadrupoles will be mounted on remote magnet movers and will be powered by individual power supplies. In addition, each quadrupole will contain a BPM with a resolution of $1 \mu\text{m}$. Similarly, all of the accelerator structures will be instrumented with an rf BPM to measure the induced dipole modes and each girder will be remotely movable; depending on location, the girders will support either one or two structures. All of these components: the $1 \mu\text{m}$ resolution BPMs, the magnet and structure movers, and the structure BPMs, are described in Chapter 7 which discusses the design of the main X-band linacs.

Finally, there are three emittance diagnostic stations located through each compressor system: one after the low-energy compressor, one after the prelinac, and one after the high-energy bunch compressor. Each diagnostic station will contain four laser wire scanners so that emittance measurements can be made without disrupting the collider operation. Lastly, there will be a pulsed beam dump after each diagnostic station so that the various subsystems can be tuned before sending the beams further downstream.

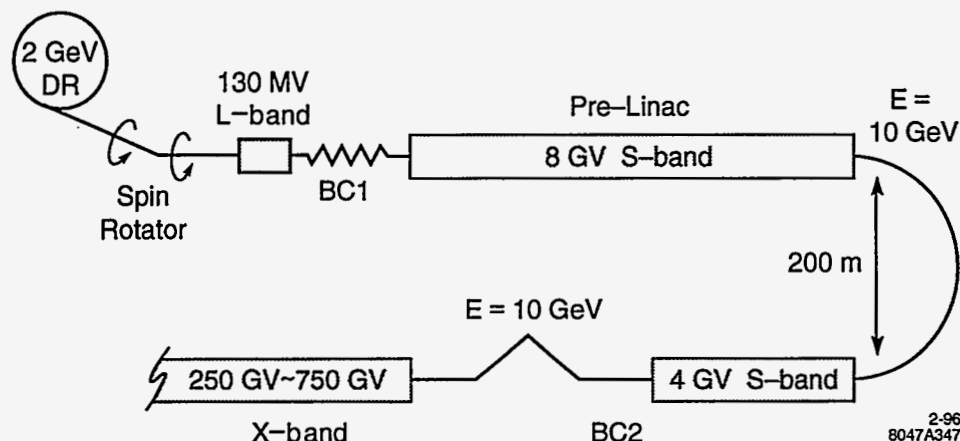


Figure 5-1. Schematic of the NLC bunch compressor system.

5.3 System Design

In this section, we will describe the present design of the bunch compressor system. We start with a description of the overall layout and then describe the various subsystems in sequence. A discussion of the longitudinal and transverse dynamics in the compressor system can be found in Sections 5.4 and 5.5, respectively. Finally, the system tolerances are discussed in Section 5.6.

5.3.1 Layout

The bunch compressor system starts at the end of the extraction lines from the main damping rings where the beam energy is between 1.8 and 2.2 GeV. It includes the matching and spin rotation sections, the first bunch compressor, and subsequent diagnostics. It also includes the S-band prelinac that accelerates the beam from roughly 2 GeV to 10 GeV. Finally, it includes the second bunch compression system which contains a 180° arc, a compressor rf section, a chicane, and the matching and diagnostics beyond the end of the chicane for injection into the main linac. The compressor system also includes three pulsed beam dumps to allow tuning of the various subsystems before taking the beam further down the collider.

The length of the spin rotator and first bunch compressor is roughly 170 m while the prelinac is roughly 450-m long. Finally, the 180° arc is roughly 330 m and the second compressor rf and chicane are 350-m long. Thus, the overall system is 1.3 km in length. A schematic view is given in Figure 5-1.

5.3.2 Ring Extraction

The beams are extracted from the main damping rings using an achromatic kicker system and achromatic extraction septum. These are described in Chapter 4 and the component layout is illustrated in Figure 4-14. The bunch compressor beam line begins after the compensation kicker. It starts with six quadrupoles to match the lattice functions into the spin rotator system. A single laser wire scanner is included in this section

to provide a continuous diagnostic on the ring performance and quad-scan emittance measurements when necessary. This wire will be used to verify the beta match and minimize any residual dispersion leaking from the damping ring. Finally, there will be a fast-feedback system to control the extraction positions and angles from the damping rings. Similar feedback systems are used in many places through the SLC and are described in Appendix D.

5.3.3 Spin Rotator

The spin rotator system is located immediately after the damping rings. It consists of four paired superconducting solenoids and an intermediate short arc that bends the beam by roughly 20° . The system is designed to operate over the energy range of 1.8 GeV–2.2 GeV. At the nominal energy of 2 GeV, it allows complete control over the spin orientation; at other energies, some of the tuning range is lost but it should still be sufficient. The betatron coupling introduced by the solenoids is canceled by using pairs of solenoids separated by an I transform in X and a $-I$ transform in Y . Although such a cancelation system is sensitive to errors, tuning simulations show that it is straightforward to correct the system; the tuning studies are described in Section 5.5. In this section, we describe the rotator optical design and performance.

Cross-plane Coupling Compensation in a Solenoid Rotator

Solenoid magnets can be implemented to rotate the electron spin about the longitudinal axis by ψ ; however, they radially focus the beam and unfortunately introduce a roll about the beam axis [Fieguth 1989]. The damped, flat beam is rolled through an angle ψ_b , which is roughly one-half that of the spin precession.

$$\psi_s = \left[1 - \left(\frac{g-2}{2} \right) \right] \frac{B_z L_s}{(B_0 \rho)} \approx \frac{B_z L_s}{(B_0 \rho)} = 2\psi_b \quad (5.2)$$

In Eq. 5.2, L_s is the effective solenoid length, B_z is the longitudinal magnetic field and $(B_0 \rho)$ is the usual magnetic rigidity. For electrons, $(g-2)/2 \approx 1.16 \times 10^{-3}$, is the anomalous magnetic moment and can be ignored. The large $x-y$ coupling introduced when passing the solenoid can potentially destroy the vertical emittance. It can be shown that the vertical projected emittance at the end of a solenoid of strength ψ_s is

$$\epsilon_y^2 = \epsilon_{x_0}^2 S^4 + \epsilon_{y_0}^2 C^4 + \epsilon_{x_0} \epsilon_{y_0} C^2 S^2 (\beta_x \gamma_y - 2\alpha_x \alpha_y + \beta_y \gamma_x) \quad , \quad (5.3)$$

where $C \equiv \cos(\psi_s/2)$, $S \equiv \sin(\psi_s/2)$, and $\beta_{x,y}$, $\alpha_{x,y}$, $\gamma_{x,y}$, ϵ_{x_0,y_0} are the beam Twiss parameters and initial emittances at the solenoid entrance. For $\psi_s = \pi/2$, equal Twiss parameters in the two planes and a horizontal-to-vertical emittance ratio of 100 as in the NLC, the vertical emittance after the solenoid increases as

$$\frac{\epsilon_y}{\epsilon_{y_0}} = \frac{\epsilon_{x_0}}{\epsilon_{y_0}} S^2 + C^2 \approx 50 \quad . \quad (5.4)$$

A coupling compensation system needs to be included which is able to reliably correct this large emittance increase. A system of skew quads can be imagined but has the undesirable character of requiring new skew quad settings for each new solenoid setting. A more robust correction scheme can be designed by splitting the solenoid in half and introducing a canceling symmetry between the two halves [Spence 1991]. The first half-solenoid rotates the beam about the longitudinal axis by $\psi_s/2$ while the spin rotates by ψ_s . If this is followed by a transfer matrix which is $+I$ in the x -plane and $-I$ in the y -plane, the beam is reflected about the y -axis where another half-solenoid of equal strength rotates the beam to its flat state again and a net

spin precession of $2\psi_s$ is accomplished. If $k \equiv \psi_s/2L_s = B_z/2(B_0\rho)$, the transfer matrix of the solenoid [Brown 1980] is

$$R_s = \begin{pmatrix} C^2 & SC/k & SC & S^2/k \\ -kSC & C^2 & -kS^2 & SC \\ SC & -S^2/k & C^2 & SC/k \\ kS^2 & -SC & -kSC & C^2 \end{pmatrix}. \quad (5.5)$$

Inserting the reflector beam line between the two solenoids produces a system transfer matrix of

$$R_s \begin{pmatrix} 1 & 0 & 0 & 0 \\ 0 & 1 & 0 & 0 \\ 0 & 0 & -1 & 0 \\ 0 & 0 & 0 & -1 \end{pmatrix} R_s = \begin{pmatrix} \cos \psi_s & k^{-1} \sin \psi_s & 0 & 0 \\ k \sin \psi_s & \cos \psi_s & 0 & 0 \\ 0 & 0 & \cos \psi_s & k^{-1} \sin \psi_s \\ 0 & 0 & k \sin \psi_s & \cos \psi_s \end{pmatrix}. \quad (5.6)$$

As long as the solenoids have equal strength ($\pm \sim 1\%$ in this case), all $x-y$ coupling is canceled independent of solenoid settings; the solenoid pairs will be powered in series to insure comparable strengths. Finally, the focusing dependence can be compensated with matching quadrupoles.

Location of the Rotator

Solenoid rotator systems are limited to low-energy applications due to the necessary scaling of solenoid strength with energy. For the NLC, this may seem like a major disadvantage since the second bunch compressor at 10 GeV includes a 180° arc and the beam delivery section (Collimation-Final Focus) includes a 10-mr arc at 500 GeV to achieve the 20-mr crossing angle. These bends will rotate a non-vertically oriented spin vector many times, potentially depolarizing the beam due to the incoming energy spread. However, a calculation of this depolarization shows it to be small. If the bunch compressor arc at 10 GeV bends the beam by π , the spin will be rotated by $\psi_s = \alpha\gamma_0(1+\delta)\pi$ (11.4 turns) while the beam delivery arc at 500 GeV will rotate the spin vector by 1.8 turns. The change in the spin magnitude will be $P(\delta)/P_0 = \cos(\alpha\gamma_0\delta\pi)$ and the mean polarization over a beam with a Gaussian energy spread σ_δ is

$$\bar{P}/P_0 = \frac{1}{\sqrt{2\pi}\sigma_\delta} \int_{-\infty}^{\infty} e^{-\delta^2/2\sigma_\delta^2} \cos(\alpha\gamma_0\delta\pi) d\delta = e^{-(\alpha\gamma_0\pi\sigma_\delta)^2/2}. \quad (5.7)$$

For an energy spread of $\sigma_\delta = 0.25\%$ in the 10-GeV 180° arc, the relative depolarization is 1.6%; it is roughly five times smaller through the beam delivery system. Therefore, the solenoid-based rotator system can be placed at 2 GeV immediately after damping ring extraction with little spin diffusion. Note that the net spin rotation in the low-energy compressor wiggler and the high-energy compressor chicane are zero since there is no net bending and thus these sections cause no depolarization.

Rotator Flexibility

A fully flexible rotator can be made by placing a short horizontal bending section between two split-solenoid segments as previously described. If the four solenoids are each capable of providing a maximum $\pm 45^\circ$ of spin rotation around the longitudinal axis and the bend section provides 90° around the vertical axis, the system will provide arbitrary control of the IP spin orientation as long as the spin sign is reversible by some means prior to damping. The net spin rotation through the system is symbolized in Eq. 5.8.

$$\Omega_{\text{tot}} = \Omega_{\text{sol}/34} \Omega_{\text{bend}} \Omega_{\text{sol}/12} = \begin{pmatrix} c_3 & -s_3 & 0 \\ s_3 & c_3 & 0 \\ 0 & 0 & 1 \end{pmatrix} \begin{pmatrix} c_2 & 0 & s_2 \\ 0 & 1 & 0 \\ -s_2 & 0 & c_2 \end{pmatrix} \begin{pmatrix} c_1 & -s_1 & 0 \\ s_1 & c_1 & 0 \\ 0 & 0 & 1 \end{pmatrix} \quad (5.8)$$

Here $c_i \equiv \cos(\psi_i)$, $s_i \equiv \sin(\psi_i)$, where ψ_i is the spin rotation of the i th section and $i = 1, 2, 3$ indicates the first solenoid pair, the bend section, and the second solenoid pair respectively. Since the input spin vector from damping ring extraction will be vertical, the spin vector after the full system is

$$\bar{s} = \Omega_{\text{tot}} \begin{pmatrix} 0 \\ \pm 1 \\ 0 \end{pmatrix} = \begin{pmatrix} \mp(\sin(\psi_3) \cos(\psi_1) + \cos(\psi_2) \cos(\psi_3) \sin(\psi_1)) \\ \pm(\cos(\psi_3) \cos(\psi_1) - \cos(\psi_2) \sin(\psi_3) \sin(\psi_1)) \\ \pm \sin(\psi_2) \sin(\psi_1) \end{pmatrix}. \quad (5.9)$$

If the solenoid fields are reversible, then any arbitrary spin orientation is achievable at the nominal beam energy of 2 GeV where $\sin(\psi_2) = 1$; there is a slight loss in the tunable orientation when the damping ring energy is raised or lowered but this is not expected to be significant.

Rotator Beam Line Optics

The reflector beam line (between solenoids) is built with four FODO cells each with 90° betatron phase advance in x and 45° in y . Three cells of 120° , 60° are possible; however, the chromaticity of the 120° cells is larger than desirable. The short bend section (mini-arc) is a simple missing magnet scheme containing six horizontal bend magnets and four 90° x and y FODO cells. The net horizontal bend angle at 2 GeV is $\pi/2\alpha\gamma = 19.83^\circ$. The peak horizontal dispersion is 260 mm and the total R_{56} is 40 mm.

The solenoids are 1.50 m in length with a maximum field strength of ± 38.5 kGauss; this will rotate the spin by 45° at a beam energy of 2.2 GeV. There is also a four-quadrupole beta matching section between the first solenoid pair segment and the mini-arc, and another matching section between the mini-arc and the second solenoid pair segment. These matching sections are used to maintain the periodic beta functions in the mini-arc through all possible solenoid settings. This is necessary since the solenoids radially focus the beam. The reflector sections provide coupling cancelation while the matching sections provide constant beta functions at the output of the entire system. Figure 5-2 shows the lattice functions for the combined spin rotator and first bunch compressor while Figure 5-3 shows the beta functions of the spin rotator system with (a) solenoids off and (b) solenoids on. With the solenoids at full strength, the x and y beta functions between them are strongly coupled creating very large vertical beta functions due to the locally rolled beam. The dispersion functions are shown in Figure 5-3c.

Chromaticity of the Rotator System

It is important to cancel the large solenoid coupling over a range of particle energies which is comparable to the beam energy spread. The reflector beam line transfer matrix will break down at some level for off-energy particles resulting in energy dependent-coupling. By locating the solenoid rotator system immediately after damping ring extraction and before the first bunch compressor rf section, the energy spread in the solenoids is small ($\sim 0.1\%$ rms). This bandpass is easily achieved in the worst case (all four solenoids at maximum strength) by using FODO cells with $\leq 90^\circ$ phase advance. Figure 5-4 shows the mono-energetic system bandpass with all four solenoids at full strength, $\psi_s(\text{pair}) = \pi/2$. Figure 5-5 shows the emittance as the Gaussian rms energy spread is increased. The vertical emittance increase at 0.1%-rms Gaussian energy spread is $< 0.5\%$.

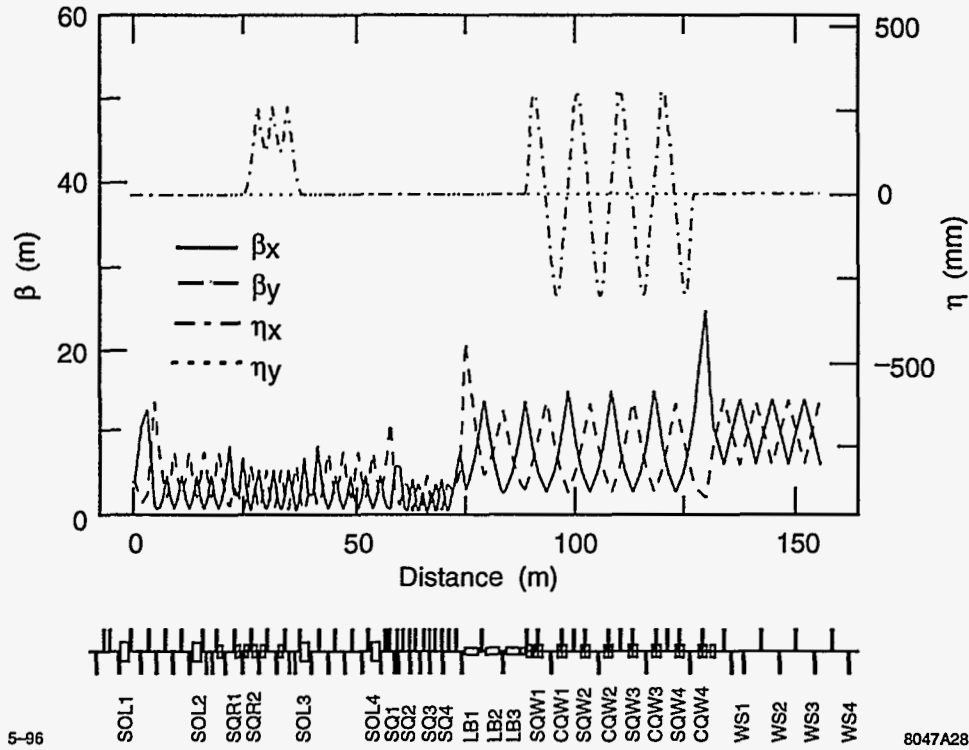


Figure 5-2. Dispersion and beta functions for the entire low-energy bunch compressor and spin rotator system. Tuning elements and major component locations are indicated. Notation is explained in Section 5.5.

Longitudinal Phase Space and Synchrotron Radiation

The rotator system has very little impact on the performance of the first bunch compressor. The longitudinal transfer matrix of the first bunch compressor, not including the spin rotator, is (see Section 5.3.4)

$$\mathbf{R}_{bc1} = \begin{pmatrix} 1 + fR_{56} & R_{56} \\ f & 1 \end{pmatrix} \quad (5.10)$$

To minimize the final bunch length after compression, the rf parameter, f , is chosen so that $1 + fR_{56} = 0$. In this case, adding the spin rotator system with $\alpha \equiv R_{56}(\text{rot})$ changes only the R_{66} element of the the total transfer matrix.

$$\mathbf{R}_{bc1}\mathbf{R}_{rot} = \begin{pmatrix} 0 & R_{56} \\ f & 1 \end{pmatrix} \begin{pmatrix} 1 & \alpha \\ 0 & 1 \end{pmatrix} = \begin{pmatrix} 0 & R_{56} \\ f & 1 + \alpha f \end{pmatrix} \quad (5.11)$$

The bunch length after the first compression is unchanged by the rotator and the energy spread after compression is insignificantly smaller ($f = 2\text{ m}^{-1}$, $\alpha = -0.04\text{ m}$).

$$\sigma_{zf} = \sigma_{\delta i} R_{56} \quad , \quad \sigma_{\delta f} = \sqrt{\sigma_{z i}^2 f^2 + \sigma_{\delta i}^2 (1 + \alpha f)^2} \quad (5.12)$$

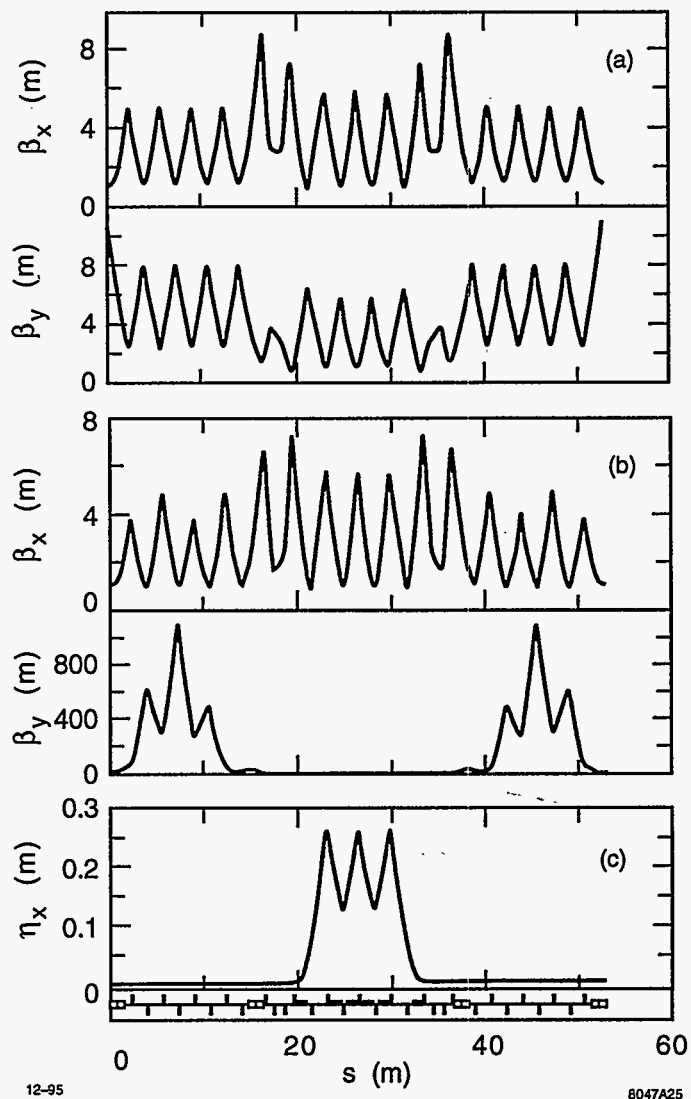


Figure 5-3. (a) Horizontal and vertical beta functions for spin rotator system with all four solenoids switched off. (b) Beta functions with all solenoids at maximum field, $\phi_s(\text{pair}) = \pi/2$. (c) Horizontal dispersion function for spin rotator system (same for solenoids off or on); the vertical dispersion is zero.

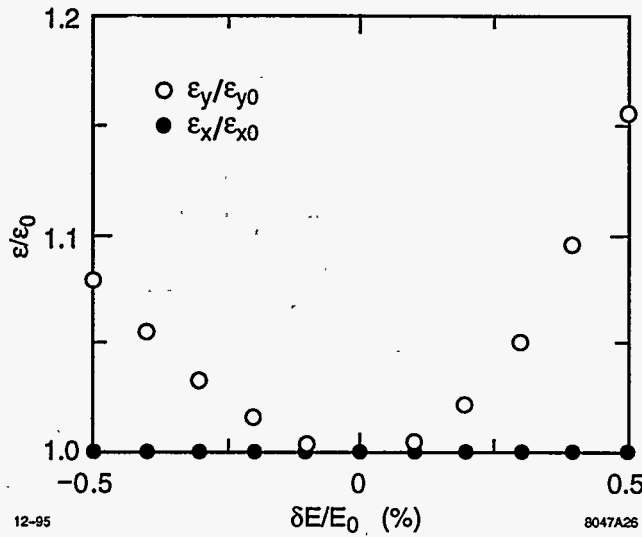


Figure 5-4. Energy bandpass of the complete solenoid-based rotator system for a mono-energetic beam. The emittance values used are $\gamma\epsilon_{x0} = 2.3 \times 10^{-6}$ m, $\gamma\epsilon_{y0} = 2.3 \times 10^{-8}$ m.

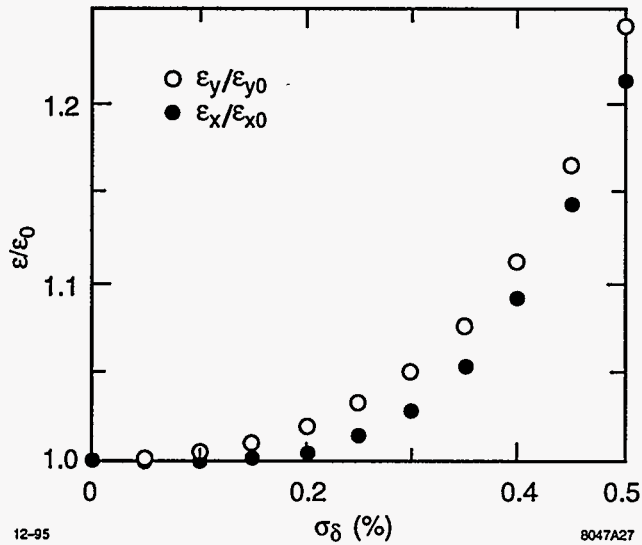


Figure 5-5. Gaussian rms energy spread dependence of relative chromatic emittance growth.

Energy	2 GeV
σ_z	5 mm \rightarrow 500 μ m
σ_ϵ	0.1% \rightarrow 1.0%
V_{rf}	139 MV
f_{rf}	1.4 GHz
L_{rf}	10 m
ϕ_{rf}	-101°
R_{56}	0.5 m
$\Delta\epsilon_{SR}/\epsilon$	\sim 1.3%
Bend Hor. Aperture	4 cm
Quad. Aperture	1 cm
Length	100 m

Table 5-2. Parameters for 2-GeV compressor.

Feedback, Tuning, and Diagnostics Sections

The tightest tolerances on this system are in the construction of the reflector beam line. Without any tuning correction, one of the eight quadrupoles in the reflector would have to be built with a gradient which meets the absolute specification to an accuracy of \sim 0.2% to limit the vertical emittance increase to 2%; most other quadrupoles are significantly looser in this tolerance. In any case, a small tunable coupling correction section is already needed to minimize damping ring extraction coupling and this same correction section can be used to cancel any residual coupling due to reflector imperfections.

The tuning of the spin rotator optics, *i.e.*, the betatron match and coupling, will be done with the bunch compressor rf off and use an emittance diagnostic section located at the end of the first bunch compressor—this is described in Section 5.3.4; this procedure is similar to that used in the SLC bunch compressors. The tunability of this system has been studied in some detail using the *Final Focus Flight Simulator* program [Woodley 1994]. To facilitate the tuning, four skew quadrupoles are placed at the end of the rotator system in locations with appropriate phase advances so they are, at least initially, orthonormal to each other [Emma 1995]. In addition, two more skew quadrupoles are placed in the 20° arc to correct any residual vertical dispersion. This system can then be easily compensated for random quadrupole gradient errors of 1% rms and is discussed further in Section 5.5.

Because of the small incoming energy spread, the alignment tolerances are relatively loose, \sim 50 μ m. Regardless, the alignment of the solenoids and quadrupoles will be adjusted using remote magnet movers similar to those developed for the FFTB. All of the quadrupoles have internally-mounted BPMs and independent power supplies to facilitate the alignment; the tolerances are discussed further in Section 5.6.

Finally, as described earlier, there will be a fast-feedback system in the ring extraction line to control the extraction positions and angles from the damping rings. Because the alignment and vibration tolerances are relatively loose, no other feedback systems are expected in this region.

5.3.4 Low-Energy Compressor

The low-energy bunch compressors follow the spin rotators. Assuming an rms energy spread of $\sigma_\delta = 1 \times 10^{-3}$, they compress the damping ring beam to a bunch length of 500 μ m. The final bunch length is roughly

independent of the incoming bunch length and the system has been designed to accept an initial bunch length of 5 mm; this is 25% larger than expected from the damping ring. The bunch compressors consist of a 139-MV L-band (1.4 GHz) rf section followed by a long period wiggler which generates the R_{56} needed for the bunch compression; parameters are listed in Table 5-2.

The compressors are designed to rotate the longitudinal phase space by roughly $\pi/2$. This prevents synchronous phase errors, originating due to the transient beam loading in the damping rings, from becoming phase errors, and thereby extraction energy errors, in the linacs. Of course, the phase tolerance is then reflected on the phase stability of the compressor rf system—one reason for choosing the L-band rf frequency is that it is much less sensitive to the multibunch loading which manifests itself as a phase error.

A " $\pi/2$ " compressor can be constructed from an rf section introducing a $\delta - z$ correlation and a bending system where the path length is energy-dependent. The linear equations determining the parameters are simple. The transfer matrix is:

$$\mathbf{R} = \begin{pmatrix} 1 + fR_{56} & R_{56} \\ f & 1 \end{pmatrix}, \quad (5.13)$$

where

$$f \equiv \frac{d\delta}{dz} = -\frac{Vk \sin \psi}{E_o + V \cos \psi}. \quad (5.14)$$

Here, R_{56} is the R_{56} of the bending system, V is the rf voltage, k is the rf wave number, and ψ is the rf phase where 0° corresponds to running on the rf crest. Finally, the compressed phase, energy, bunch length, etc., are given by:

$$z_f = z_i(1 + fR_{56}) + \delta_i R_{56} \quad (5.15)$$

$$\delta_f = z_i f + \delta_i \quad (5.16)$$

$$\sigma_{z_f}^2 = \sigma_{z_i}^2(1 + fR_{56})^2 + 2\langle \delta_i z_i \rangle R_{56}(1 + fR_{56}) + \sigma_{\delta_i}^2 R_{56}^2 \quad (5.17)$$

$$\sigma_{\delta_f}^2 = \sigma_{z_i}^2 f^2 + 2\langle \delta_i z_i \rangle f + \sigma_{\delta_i}^2 \quad (5.18)$$

$$\langle \delta_f z_f \rangle = \sigma_{z_i}^2 f(1 + fR_{56}) + \langle \delta_i z_i \rangle (1 + 2fR_{56}) + \sigma_{\delta_i}^2 R_{56} \quad (5.19)$$

For full compression, the R_{56} is determined by the initial energy spread and the desired bunch length. The rf parameters are chosen so that $f = -1/R_{56}$. In such a design, the only free parameters are the rf frequency and the rf phase—all other parameters are determined by the input beam. Finally, note that such a compressor does not really rotate the longitudinal phase space by $\pi/2$, but the final phase is independent of the initial phase as desired.

Wiggler

The bending system used to generate the R_{56} for the low-energy compressor is constructed as a very long period wiggler. Quadrupoles are placed between the dipoles in locations where the dispersion passes through zero. In this manner, they can constrain the beta functions but they will not generate any second-order dispersion and do not need large apertures. This eliminates the need for strong sextupole magnets which would have tight vertical alignment tolerances due to the coupling they introduce—sextupole correctors and other multipole fields will still be required for tuning purposes. Four wiggler cells are used with a 90° phase advance per cell to reduce the sensitivity to systematic errors in the bending magnets. The optical functions for the entire low-energy compressor, including spin rotator, rf section, and diagnostics section are plotted in Figure 5-2.

The bending magnets and quadrupoles for the low-energy compressor are straightforward. The required apertures are listed in Table 5-2. The main bending magnets are 1.2 m in length with a magnetic field of

14 kGauss; they will be powered as a string by a single power supply to reduce the regulation tolerance on the supply. The quadrupoles are 15 cm in length and have pole-tip fields that are less than 7 kGauss. They will be powered by independent power supplies and mounted on remote magnet movers to facilitate the beam based tuning.

RF Section

The rf section consists of two 5-m L-band rf structures that provide a total rf voltage of 139 MV and operate at a phase of -101° which is slightly past the nominal -90° ; this is to compensate the T_{566} generated in the wiggler. These structures are located in FODO cells just prior to the beginning of the wiggler. The multibunch beam loading compensation is accomplished using the ΔT method (early injection) and is discussed in Chapter 6. To facilitate the alignment, both structures will be instrumented with rf BPMs and will be mounted on remote movers.

Feedback, Tuning, and Diagnostic Sections

Because of the small beam emittances, the alignment and field tolerances in the compressor would be tight. Fortunately, it is straightforward to use simple tuning techniques to ease the tolerances substantially. The quadrupoles will be powered with independent power supplies and will be mounted on remote movers to facilitate the alignment and the optical tuning will be performed using an emittance diagnostic section consisting of four laser wires located after the compressor wiggler. This is followed by a beam dump that will allow full operation of the damping rings and compressor systems for tuning and commissioning purposes.

Four weak skew quadrupoles and four weak normal quadrupoles will be placed in the dispersive regions of the wiggler to facilitate the tuning of the horizontal and vertical dispersion. In addition, four skew sextupoles will be added to control the vertical second order dispersion. All of the tuning elements and procedures are described in Section 5.5.

The rf voltage and phase of the L-band cavity can be calibrated by varying the rf phase and measuring the beam centroid offsets in the wiggler section. It is more difficult to tune the beam loading compensation in the rf structures. This will be done using a beam phase monitor located at the end of the bunch compressor with a phase resolution of 0.1° S-band. Finally, there will be a phase feedback system that will measure the bunch train centroid through the wiggler and adjust the damping ring synchronous phase; this is discussed in Chapter 4.

5.3.5 Prelinac

Optical Design

The optical design of the prelinac consists of simple FODO cells with an initial quadrupole spacing of 3.1 m to accommodate the 3-m S-band structures. As the beam energy is increased, the quadrupole spacing is increased to a 6-m spacing, accommodating two accelerator structures between quadrupoles. The matching across this transition has been tuned to have a bandwidth in excess of 20%. Finally, note that the horizontal and vertical phase advances are separated by roughly 5%. This reduces the sensitivity to systematic skew quadrupole fields and the nonlinear betatron coupling due to the beam space charge field and trapped ions [Raubenheimer 1992]. The lattice functions are plotted in Figure 5-6.

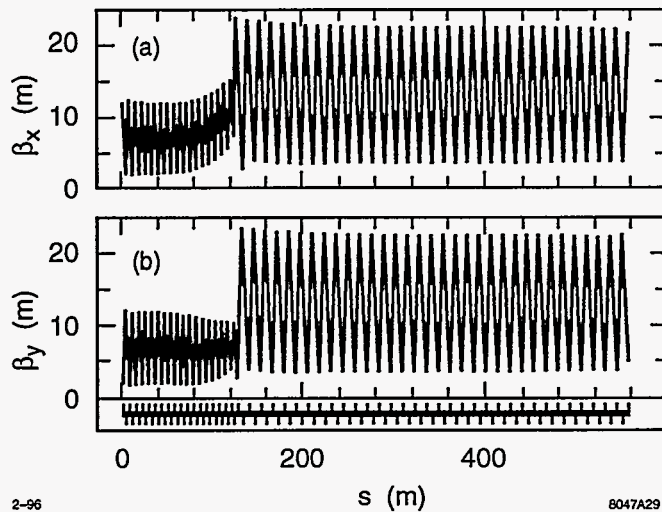


Figure 5-6. Optical functions in S-band prelinac.

The quadrupoles are 10 cm in length and have a 1-cm radius with pole-tip fields less than 7.6 kGauss. As is standard practice in the NLC, all of the linac quadrupoles will have internal BPMs and will be mounted on remote magnet movers. In addition, all of the quadrupoles are powered by independent power supplies. This will allow the electrical centers of the BPMs to be accurately determined with respect to the magnetic centers of the quadrupoles and then the quadrupoles can be aligned by adjusting the movers.

RF System

The S-band prelinac consists of 3-m DDS S-band accelerating structures—the structures, klystrons, and rf pulse compressors are described in greater detail in Chapter 6. The linac consists of 33 rf modules with four accelerator structures per module. Each module is powered with two 5045 klystrons and a SLED pulse compressor to produce a net acceleration of 254 MeV. Thus the linac can provide 8.4 GeV of acceleration and would normally operate with one rf module in standby. The multibunch beam loading is compensated using the ΔT method (early injection) so that the bunch-to-bunch energy deviations are corrected locally in each structure; this minimizes the emittance growth due to dispersive and chromatic effects. The expected bunch-to-bunch energy variation is less than 10^{-4} ; this is discussed in Chapter 6.

Finally, all of the accelerator structures will have rf BPMs and will also be mounted on girders that can be remotely aligned; there is one structure support girder between quadrupoles and thus at the beginning of the prelinac there is only one structure per girder while at the end of the linac there are two structures per girder. This will allow the structures to be aligned to the beam trajectory. The alignment techniques are described in Section 5.5.

Feedback, Tuning, and Diagnostic Sections

As noted earlier, there is a diagnostic section, consisting of four laser wire scanners, after the low-energy bunch compressor at the beginning of the prelinac. This is followed by a pulsed dump which can absorb a

	NLC-I a	NLC-I c	NLC-II a	NLC-II c
Energy	10 GeV			
Initial σ_z	500 μm			
Final σ_z	100 μm	150 μm	125 μm	150 μm
Initial σ_ϵ	0.25 %			
Final σ_ϵ	1.5 %	1.2 %	1.3 %	1.4 %
180° arc R_{56}	0.211	0.147	0.184	0.162
Arc Length	330 m			
$\Delta\epsilon_{SR}/\epsilon$ (arc)	2.2%	1.5%	2.0%	1.6 %
V_{rf} (GV)	3.85	3.50	3.73	3.61
f_{rf}	2.8 GHz			
L_{rf}	250 m			
$V_{rf c}$ (MV)	274	226	256	240
$f_{rf c}$	11.4 GHz			
$L_{rf c}$	7.6 m			
Chicane R_{56}	36 mm			
Chicane Length	100 m			
$\Delta\epsilon_{SR}/\epsilon$ (chicane)	~ 0.05%			
Bend Hor. Aperture	10 cm			

Table 5-3. Parameters for 10-GeV compressor.

full bunch train at the nominal repetition rate so that the damping rings and first bunch compressors can be tuned before the beams are sent through the prelinacs.

A second diagnostic section, again consisting of four laser wire scanners, is located at the end of the prelinac. To save space, this section is integrated into the linac lattice. It is followed by another pulsed beam dump to facilitate the tuning of the prelinac. As described, the transverse alignment of the quadrupoles and accelerator will be performed using remote magnet movers; details are described in Section 5.5.

The rf phases and the beam loading compensation will be tuned using the spectrometer in the beam dump or using the 180° arc as a spectrometer. The BPMs in the arc have a resolution of 1 μm and will be able to resolve relative energy variations of roughly 10^{-5} ; this is more than sufficient to optimize the klystron phases and the beam loading compensation.

Finally, one fast-feedback system will be used to control the transverse position and angle of the bunch train as it is injected into the prelinac and another will be located at the transition region where the quadrupole spacing is increased from 3 to 6 m. In addition, an energy feedback will be used to stabilize the beam energy; this will adjust the phases of the two klystrons feeding one of the rf modules to vary the beam voltage.

5.3.6 High-Energy Compressor

The high-energy bunch compressors follow the prelinacs. Assuming an rms bunch length of $\sigma_z = 500 \mu\text{m}$, they compress the beam to a bunch length between 100 and 150 μm depending on the NLC parameters. The bunch compressors consist of a 180° arc which is followed by a 4-GeV S-band (2.8 GHz) rf section and a chicane. Parameters of the high-energy bunch compressors are listed in Table 5-3 for four different NLC scenarios.

As described, the second compressor is designed to rotate the longitudinal phase space by 2π ; it is a telescope in longitudinal phase space. This requires two rf sections and two bending regions. We can use the prelinac as the first rf region. Then, a 180° arc will be used for the first bending region, followed by an rf section and then a magnetic chicane as the second bending region. The linear equations that determine the compressor are:

$$\mathbf{R} = \begin{pmatrix} 1 + f_2 R_{562} + f_1(f_2 R_{561} R_{562} + R_{561} + R_{562}) & R_{561} + R_{562} + f_2 R_{561} R_{562} \\ f_1 + f_2 + f_1 f_2 R_{561} & - - - \end{pmatrix}, \quad (5.20)$$

where R_{561} and R_{562} are the R_{56} s of the first and second bending regions and f_1 and f_2 are the rf parameters for the first and second rf regions. Finally, the (2,2) matrix element can be found from the other (the determinant equals 1) but it is not relevant for our study.

To make the final phase independent of the incoming energy and only sensitive to the incoming phase, we require that the (1,2) matrix element equal zero. In addition, to compress the bunch by a factor m , we require that the first matrix element be equal to $\pm 1/m$. Finally, to perform a full $n\pi$ rotation, we require that the (2,1) element also be zero, but this is not actually very important for us since the incoming phase errors should be small. Thus, no restriction needs to be placed on the rf of the prelinac and the two constraints on the compressor design are:

$$1 + f_2 R_{562} = \pm 1/m \quad R_{561} = \mp m R_{562} \quad (5.21)$$

where the upper sign corresponds to a 2π rotation and the lower signs are for a π rotation of the phase space.

Because the NLC collider geometry suggests using a 180° arc and a chicane which have opposite values of R_{56} , we have designed the compressor to perform a 2π rotation. Now, given a value of the R_{56} in the chicane and a chosen rf frequency (S-band), the R_{56} of the arc and the parameters of the rf section between the arc and the chicane are determined. To reduce nonlinearities of the longitudinal phase space, the R_{56} of the chicane should be as small as possible. However, a smaller R_{56} increases the required rf voltage, so a compromise had to be found. According to longitudinal single-bunch simulations, an R_{56} of 100 mm is too large and impairs the performance of the compressor. In the present design, therefore, the R_{56} of the chicane is chosen as 36 mm, which implies a 200-m-long S-band rf section.

Arc

The bending system used to generate the R_{56} for the 180° arc is constructed from a series of FODO cells. Although one could reduce the emittance growth through this section using combined-function bending magnets, we have chosen separated-function magnets so that one can use beam-based alignment techniques to align the quadrupole magnets.

We have studied several versions of the arc, with different numbers of cells. In all cases, the R_{56} is easily adjusted with the horizontal phase advance and the choice of the number of cells depends upon the tuning range desired. The present arc design consists of 68 FODO cells, and has an average radius of about 100 m. Variation of the horizontal phase advance per cell from 90° to 135° changes the R_{56} from 29 cm to 15 cm, which results in an increase of the final bunch length from $100 \mu\text{m}$ to $150 \mu\text{m}$. This variability covers the entire NLC operating plane. While the horizontal phase advance is varied, the vertical phase advance per cell is held constant at 90° . Figure 5-7 illustrates the tuning range of the R_{56} in the arc and the corresponding emittance growth due to synchrotron radiation. In addition, the beta functions and dispersion functions are plotted in Figures 5-8 and 5-9. Finally, the arc parameters are summarized in Table 5-4.

The arcs are constructed using bending magnets that are 1.25 m in length and have a maximum field of 6 kGauss and quadrupole magnets that are 32-cm long and have a 1-cm radius with pole-tip fields of

Parameter	Symbol	Unit	$\psi_x = 90^\circ$	$\psi_x = 108^\circ$	$\psi_x = 135^\circ$
Momentum compaction	R_{56}	m	-0.286	-0.208	-0.150
Synch. rad. emit. growth	$\Delta\epsilon_{SR}/\epsilon_0$	%	3.7	2.4	1.6
Max. hor. beta function	β_x^{\max}	m	7.27	7.67	10.35
Max. hor. dispersion function	η_x^{\max}	m	0.133	0.102	0.078
F-quad pole-tip magnetic field	B_{QF}	kGauss	+7.15	+8.08	+9.26
D-quad pole-tip magnetic field	B_{QD}	kGauss	-7.15	-7.32	-7.50
F-sext. pole-tip magnetic field	B_{SF}	kGauss	+1.18	+1.74	+2.63
D-quad pole-tip magnetic field	B_{QD}	kGauss	-2.06	-2.98	-4.43
# FODO cells	N_{cell}	—		68	
Energy	E	GeV		10	
Total arc length	L_{tot}	m		295	
Total bend angle	θ	°		180	
Mag. length of quadrupoles	L_Q	m		0.32	
Mag. length of dipoles	L_B	m		1.25	
Mag. length of sextupoles	L_S	m		0.10	
Drift between every magnet	L_{BPM}	m		0.3	
Vert. betatron phase adv. per cell	ψ_y	°		90	
Quadrupole magnet pole radius	r_Q	mm		10	
Sextupole magnet pole radius	r_S	mm		10	
Bend angle of dipole	θ_B	°		1.304	
Bend radius of dipole	ρ	m		54.9	
Spin advance per cell	Φ_{Spin}	°		59.2	

Table 5-4. Parameters for 180° arc of high-energy compressor for several momentum compaction factors adjusted by varying the x -betatron phase advance per cell, ψ_x .

8 kGauss. To relax the stability and voltage requirements on the bending magnet power supplies, 18 bends are powered as a string by a single power supply. As stated, all of the quadrupoles have independent power supplies to facilitate the beam-based alignment.

Sextupole compensation is also included in the optical design to desensitize the arc to the generation of dispersion due to incoming betatron oscillations. This also desensitizes the arc to the generation of second order dispersion due to a dispersion oscillation through the entire arc. Without sextupole compensation a vertical betatron oscillation (jitter) which propagates through the entire arc will generate vertical dispersion due to the chromaticity of the quadrupoles. For an initial oscillation amplitude of $\eta_\sigma = y_0/\sqrt{\beta_y\epsilon_{y0}}$ in the first QD ($y'_0 = 0$) which oscillates through an arc with $N(\gg 1)$ FODO cells of phase advance per cell μ and rms energy spread σ_δ , the vertical emittance dilution due to dispersion is approximately (thin lens QDs only)

$$\frac{\Delta\epsilon}{\epsilon_0} \approx \frac{1}{2} \left(n_\sigma N \sigma_\delta \frac{1 + \sin \mu/2}{\cos \mu/2} \right)^2 \quad (5.22)$$

For the high-energy bunch compressor (BC2) arc parameters without sextupoles, an initial vertical oscillation of $n_\sigma = 1$ ($y_0 = 3.3 \mu\text{m}$) would induce a 10% emittance dilution due to vertical dispersion. Likewise, a small vertical dispersion error of 1 mm (at QDs) through the entire arc would generate second-order dispersion which dilutes the emittance by 10%. The inclusion of sextupoles opens these oscillation tolerances by more than a factor of 10 and actually allows full recovery of the emittance using the simple linear tuning schemes discussed in Section 5.5.3, even for extreme vertical emittance dilution cases of $\Delta\epsilon_y/\epsilon_{y0} \sim 30$. The

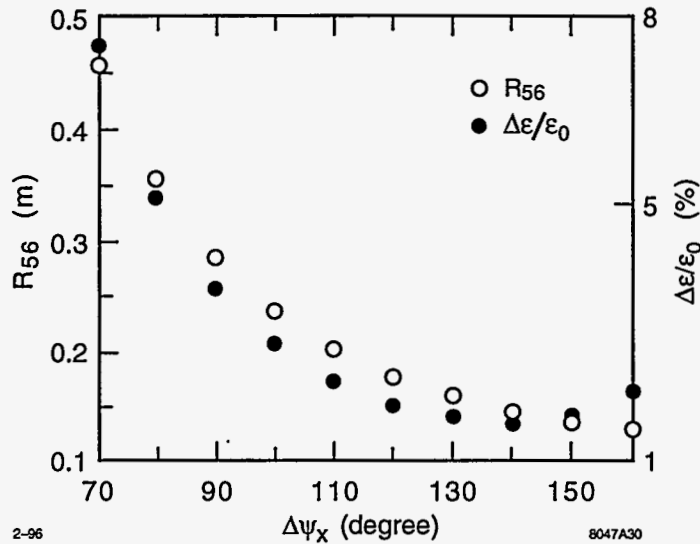


Figure 5-7. R_{56} (solid) and $\Delta\epsilon_x$ (dashes) for 68-cell arc.

sextupoles are 10-cm long with 1-cm pole radius and 1.7 and -3.0 kGauss pole-tip fields for the ‘focusing’ (SF) and ‘defocusing’ (SD) sextupoles, respectively. Their alignment tolerances are similar to the quadrupole alignment tolerances of roughly $60 \sim 100 \mu\text{m}$ and are discussed in Section 5.5.3.

Figure 5-10 is a plot of the emittance dilution, without synchrotron radiation effects, at the end of the 68-cell arc as a function of the incoming energy spread for a horizontal phase advance of 108° . For the nominal operation parameters, the emittance growth is less than 0.5%.

RF Section

The high-energy bunch compressor rf sections consist of roughly 4 GeV of S-band linac. The linacs are similar to the S-band prelinacs, consisting of 3-m DDS S-band accelerator structures. They differ from the prelinacs in that the multibunch beam loading is compensated using a combination of the ΔT method (early injection) and the ΔF method; this is necessary to attain the required compensation. The linacs consist of 16 rf modules with a net acceleration of 253 MeV per module. Thus, they can provide 4 GeV of acceleration and would normally operate with at least one rf module in standby; see the parameters in Table 5-3. Each module has five accelerator structures, four tuned to the nominal frequency and one structure that is either 1.1 MHz above the nominal 2.856 GHz or 1.1 MHz below 2.856 GHz; the sign of the frequency compensation alternates between modules. The four normal structures in each module are powered with two 5045 klystrons and a SLED pulse compressor while the off-frequency structure is powered with a single 42-MW klystron. The structures, klystrons, rf pulse compressors, and beam loading compensation are described in greater detail in Chapter 6.

Because the bunch length is long in these rf sections, the transverse wakefields are significant. Furthermore, because the chicane will rotate the longitudinal phase space, the transverse emittance dilutions will not be correctable after the beam passes the chicane. To reduce the emittance dilution, this rf section has strong focusing with a 3.1-m quadrupole spacing. To attain the required fields, the quadrupoles are 15 cm in length with a 1-cm aperture and maximum pole-tip fields of 7 kGauss.

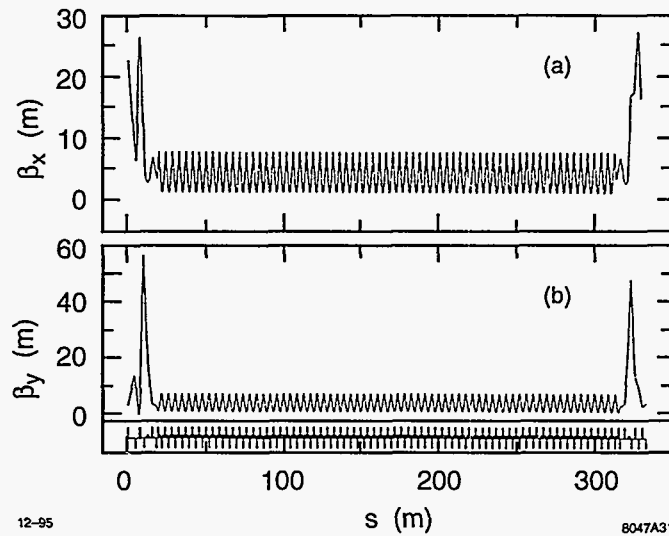


Figure 5-8. Beta functions for 68-cell arc.

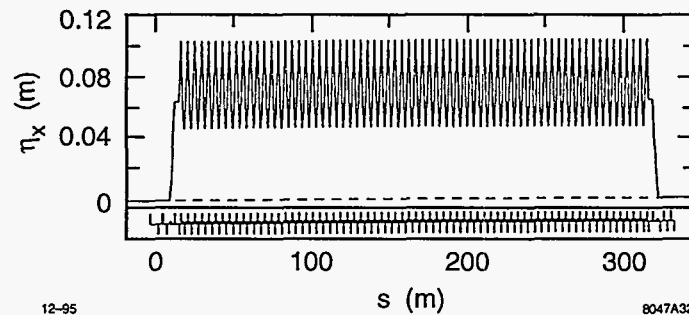


Figure 5-9. Dispersion function for 68-cell arc.

Finally, the high-energy compressor also needs a higher frequency rf to compensate the T_{566} from the chicane. The present design requires roughly 275 MV of X-band rf provided in three 1.8-m structures.

Chicane

The chicane is constructed from sixteen 2.5-m bending magnets having a 1.1-kGauss field; the beta functions and the dispersion function are plotted in Figures 5-11 and 5-12. The lengths and spacing are chosen so as to achieve the R_{56} of 3.6 cm in a reasonable length, without generating substantial emittance dilution due to synchrotron radiation; all of these are subjective constraints and the parameters might be optimized in another manner.

One potential issue is the peak value of the dispersion which is roughly 65 cm. This means that the horizontal good field aperture of the bending magnets must be large (~ 10 cm full width) to provide an aperture in excess of ± 5 sigma and without tuning correction, the alignment and field tolerances will be severe. The

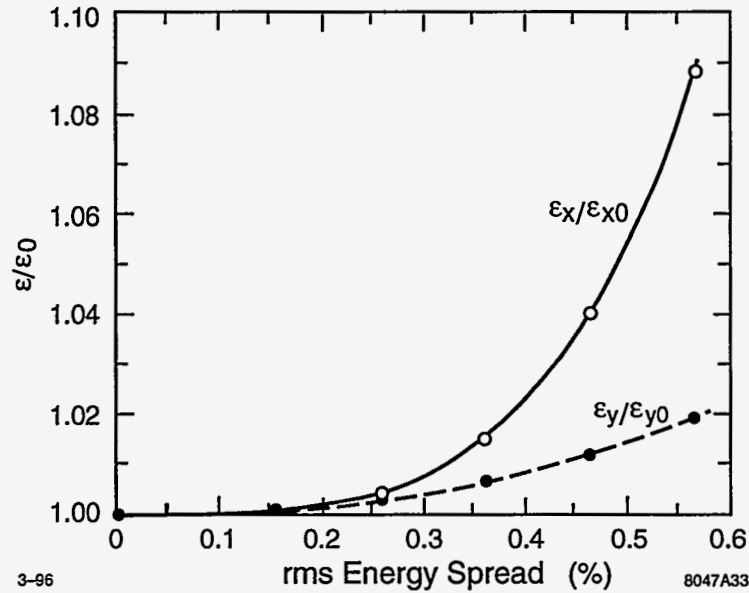


Figure 5-10. Chromatic emittance growth for nominal operation, ($R_{56} = 210$ cm).

field tolerances can be attained by using large aperture magnets and careful construction techniques and, fortunately, the tuning of the errors is straightforward as described in Section 5.5.

Feedback, Tuning, and Diagnostic Sections

A diagnostic section consisting of four laser wires is located at the end of the chicane so that the chromatic properties of the chicane can be tuned properly for injection into the main X-band linacs. Presently, it is thought that the 180° arc and the rf section can be tuned by turning the compressor rf off to minimize the beam energy spread and using the diagnostic section at the end of the chicane. If necessary, an additional diagnostic section can be integrated into the end of the high-energy compressor rf section before the chicane. Finally, there are pulsed beam dumps just before the beginning of the main linacs that allow the whole injector complex to be tuned before accelerating the beams to high energy; the tuning elements and procedures are described in Section 5.5.3.

5.4 Longitudinal Dynamics

The primary purpose of the bunch compressor system is to rotate the longitudinal phase space from the damping rings by $\pi/2$ while compressing the bunch length. In this process, nonlinearities distort the phase space, changing the bunch shape and the sensitivity to incoming phase errors from the damping rings. In this section, we discuss the sources of nonlinearity and their compensation and we present simulation results illustrating the longitudinal beam distributions at the IP.

Finally, it should be noted that most of these simulations were performed before the structure parameters were finalized. Thus, the wakefields that were used in the simulations are stronger than those expected and

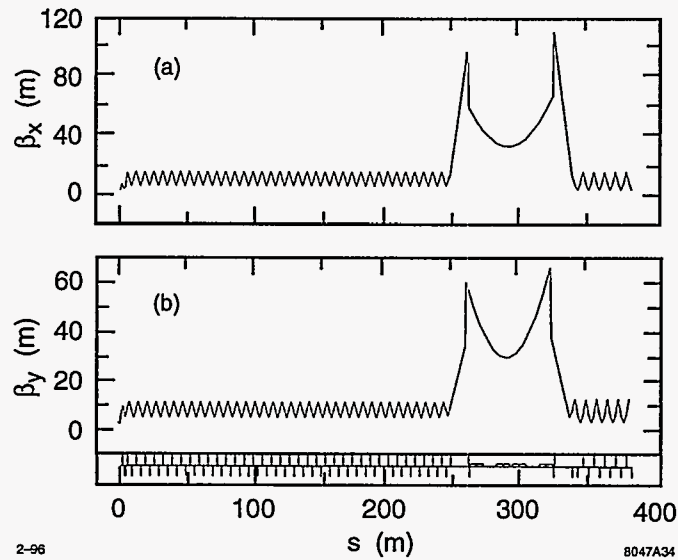


Figure 5-11. Beta functions for chicane.

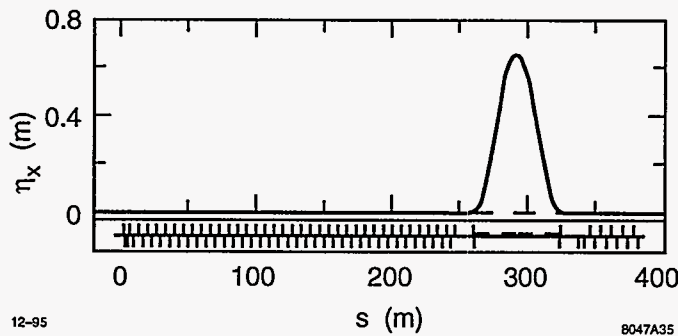


Figure 5-12. Dispersion function for chicane.

only the ΔF technique was used for the beam loading compensation. Both of these differences will cause the simulations to *over-estimate* the sensitivities and errors. Since this document is primarily a feasibility study and the feasibility is clearly demonstrated, we have not yet re-calculated the effects.

5.4.1 Optical and RF Nonlinearities

Having been given all parameters as described and having generated the desired linear transfer matrix for the longitudinal phase space, the tracking simulations still show a fairly large variation of rms energy spread, and, in particular, of the mean energy at the end of the main linac as a function of initial phase error. For instance, a 6-mm initial phase error causes a change of the final beam energy by about 0.2%–0.3%, which is too large to be tolerable. Furthermore, the mean energy and energy spread show a very asymmetric dependence on positive and negative phase errors.

An important nonlinear aberration of the system is due to the quadratic dependence of the final longitudinal phase on the incoming energy (the T_{566} transfer-matrix element in TRANSPORT notation [Brown 1977]) for the different subsystems. It is straightforward to see (compare Section 5.4.2) that for wiggler and chicane we have

$$T_{566}^{w,c} = -\frac{3}{2}R_{56}^{w,c} \quad (5.23)$$

while for the present lattice of the arc we find

$$T_{566}^a \approx 1.9 \cdot R_{56}^a \quad (5.24)$$

It is the nonzero $T_{566}^{w,c}$ coefficient of wiggler and chicane which causes the intolerably large variation of the final energy at the end of the main linac as a function of initial phase error. (The T_{566}^a of the arc is not significant.)

There are two effects that are important. First, initial phase errors give rise to energy errors δ_1 after the first compressor rf, which in turn, due to the T_{566}^w of the wiggler, cause a phase offset in the prelinac. The result is an additional energy change $\Delta\delta_{pl}$ which may either add to or cancel the energy error δ_1 , dependent on the sign of the offset. The second compressor further enhances the energy error and, due to the T_{566}^c of the chicane, generates a significant phase error in the main linac. A second effect is that, if the bunch is longitudinally off-set, the T_{566} can either increase or counteract the nonlinearity of the rf, giving rise to an asymmetry in bunch length versus phase error, for each compressor stage separately.

The simulation results show that it is desirable to compensate the sensitivity to initial phase errors caused by the $T_{566}^{w,c}$ of wiggler and chicane. A compensation can be performed, for instance, with an additional, decelerating rf [Raubenheimer 1994b], whose purpose is to cancel the quadratic dependence of the final phase z_f on the longitudinal position (the phase error) at the compressor rf. Consider the main compressor rf

$$V \cos(\psi + kz) \quad (5.25)$$

and a compensating rf

$$V_c \cos(\psi_c + k_c z) \quad (5.26)$$

with V_c small compared with the beam energy E , $V_c \ll E$, followed by a chicane or a wiggler. The phase z_f at the exit of this system depends on the initial phase z_{rf} at the rf as

$$\begin{aligned} z_f = & (1 - R_{56}^{w,c}(f + f_c))z_{rf} + T_{566}^{w,c}(f + f_c)^2 z_{rf}^2 \\ & + \frac{1}{2}R_{56}^{w,c}(fk \cot \psi + f_c k_c \cot \psi_c)z_{rf}^2 \end{aligned} \quad (5.27)$$

where we have omitted a constant shift as well as higher-order terms, $f_c \equiv V_c k_c \sin \psi_c / (E + V \cos \psi)$ for the compensating rf, and $f \equiv V k \sin \psi / (E + V \cos \psi)$ is the corresponding value for the main compressor rf; $k \equiv 2\pi/\lambda$ is the wave number. The sum of the quadratic terms in Eq. 5.27 is zero if we choose

$$T_{566}^{w,c}(f + f_c)^2 = \frac{1}{2}R_{56}^{w,c}(fk \cot \psi + f_c k_c \cot \psi_c) \quad (5.28)$$

which, for the special case $\psi = -\pi/2$ and $\psi_c = \pi$, simplifies to

$$V_c = -2 \frac{T_{566}^{w,c} k^2 V^2}{R_{56}^{w,c} k_c^2 E} = 3 \frac{\lambda_c^2 V^2}{\lambda^2 E} \quad (5.29)$$

where we have used Eq. 5.23. Alternately, assuming no additional compensating rf system and only changing the rf phase, we find:

$$\cot(\psi) = 3 \frac{f}{k} \quad (5.30)$$

In the first compressor stage, we can simply change the L-band rf phase from -90° to -101° to perform the compensation. Unfortunately, in the second compressor this is more difficult; the S-band rf would have to be run roughly -50° from the zero crossing to provide sufficient curvature. Instead, we plan to use 275 MV of X-band rf operating at a phase of -180° to perform the compensation.

With the compensation, the residual longitudinal aberrations are now third order and higher. An initial phase error or multibunch beam loading may cause an energy offset δ of the entire bunch at the entrance to the high-energy compressor (BC2). In addition, the longitudinal wakefields in the prelinac induce a (mainly) quadratic δ - z -correlation, where z is the longitudinal position of a single particle with respect to the bunch center. Due to the R_{56}^a of the arc, this energy error translates into a position error at the two rf systems of BC2, which is transformed once more into energy by the rf, and back into longitudinal phase by the T_{566}^c of the chicane. The final phase z_f of a single particle at the exit of BC2 is

$$z_f \approx az - bz^4 - c\delta^2 z^2 - d\delta z^2 - e\delta z^4 + \dots \quad (5.31)$$

where $a \approx 1/5-1/7$ is the desired linear compression ratio, and the four nonlinear terms on the right-hand side are about the same size ($10-20 \mu\text{m}$), for typical values $\delta \approx \pm 0.004$ and $z \approx 500 \mu\text{m}$. These four terms are negligibly small if the prelinac wakefields are absent.

5.4.2 The T_{566} -Matrix Element

Let the trajectory of an arbitrary particle be described by a general dispersion function η as $x = \eta\delta$, where δ is the relative momentum deviation. The dispersion function may be expanded as a power series in δ :

$$\eta\delta = \eta_0\delta + \eta_1\delta^2 + \dots \quad (5.32)$$

For a system of bending magnets and quadrupoles with bending radius ρ and gradient k , the functions η_0 and η_1 fulfill the differential equations [Delahaye 1985]

$$\eta_0'' + \left(\frac{1}{\rho^2} + k\right)\eta_0 = \frac{1}{\rho} \quad (5.33)$$

$$\eta_1'' + \left(\frac{1}{\rho^2} + k\right)\eta_1 \approx -\frac{1}{\rho} + \left(k + \frac{2}{\rho^2}\right)\eta_0 \quad (5.34)$$

which, for $\eta_0 \ll \rho$, may be further approximated by

$$\eta_0'' + k\eta_0 \approx \frac{1}{\rho} \quad (5.35)$$

$$\eta_1'' + k\eta_1 \approx -\frac{1}{\rho} + k\eta_0 \quad (5.36)$$

The R_{56} - and T_{566} -matrix-elements may be expressed in terms of $\eta_{0,1}$ [Delahaye 1985]

$$R_{56} = -\int \frac{\eta_0}{\rho} ds \quad (5.37)$$

$$T_{566} \approx -\int \left(\frac{\eta_1}{\rho} + \frac{1}{2}\eta_0'^2\right) ds \quad (5.38)$$

In case of wiggler and chicane $k\eta_{0,1} = 0$ and, therefore, $\eta_1 = -\eta_0$. Since $\eta_0'' \approx 1/\rho$, the second term in the expression for T_{566} can be integrated by parts, with the final result

$$T_{566} \approx -\frac{3}{2}R_{56} \quad (\text{for wiggler and chicane}) \quad (5.39)$$

To reduce the T_{566} -matrix-element, the value of the second-order dispersion needs to be reduced. Ideally, one would like to have $T_{566} = 0$, which requires a sign reversal of η_1 such as to cancel the contribution from η_0^2 . This can be accomplished by adding quadrupoles at locations with nonzero η_0 , as evident from Eq. 5.36, or by adding sextupoles (not included in the above equations). Unfortunately, such changes to η_1 may adversely affect the transverse emittances.

5.4.3 Single Bunch Longitudinal Wakefields

Longitudinal wakefields in the S-band accelerator seriously modify the longitudinal phase space. For our calculations we have assumed the SLAC wakefield. The actual wakefield for the NLC will be roughly $\sqrt{2}$ smaller because of the increased iris aperture. Thus, we have over-estimated the tolerances and sensitivities.

5.4.4 Multibunch Wakefields

Thus far, the simulations have included only the fundamental longitudinal mode for the different S-band, L-band, and X-band rf sections. Parameters were provided by R. Miller [Miller 1995] and are listed in Table 5-6; these parameters differ slightly from the structure design parameters described in Chapter 6.

5.4.5 Bunch Shaping

At this time, we have not investigated the option of deliberately shaping the longitudinal profile of the bunch to reduce the energy spread induced by the longitudinal wakefields and/or the transverse emittance dilution. However, a two-stage bunch-length collimation section is part of the bunch-compressor and linac design; it is discussed in Chapter 9. This system, by itself, already reduces the beam energy spread, and it would be an integral part of any bunch-shaping strategy. More studies on this topic are left for the future.

5.4.6 Longitudinal Phase Space at the End of the Linac

To determine the optimum parameters of the system, we have considered four NLC scenarios, corresponding to different bunch lengths and energies (see Table 5-5). The parameters chosen enclose the NLC operating plane as described in Chapter 1.

Computer simulations of the longitudinal single-bunch dynamics have been performed with the code LITRACK [Bane]. In these simulations, a distribution of particles as extracted from the damping rings is tracked through the different compressor subsystems and the main X-band linac. The parameters of the bunch compressor are optimized such that the final average energy and the energy spread at the end of the main linac are insensitive (*i.e.*, vary by less than 0.1%–0.2%) to initial phase errors up to 20° S-band, or ± 6 mm.

In the latest simulation studies, the phase of the main X-band linac was adjusted to obtain a final full-width, half-maximum (FWHM) energy spread of about 0.8%. This energy spread is slightly smaller than the energy bandwidth of the final focus (see Chapter 11) and it might be reduced further by tuning the rf properties in the X-band linac. Figures 5-13 through 5-16 present tracking results for two different bunch lengths in either

	NLC-I		NLC-II	
Cms energy	500 GeV	500 GeV	1 TeV	1 TeV
Bunch length	100 μm	150 μm	125 μm	150 μm
Single-bunch gradient	33.25 MV/m	29.13 MV/m	60.19 MV/m	53.97 MV/m
L_{acc}	8130 m	8130 m	8900 m	8900 m
N/bunch (10^{10})	0.65	0.85	0.95	1.25
E_{max} (GeV)	267	233	534	473
Average ϕ_{rf} ($^\circ$) ^a	-14.4	-15.1	-7.2	-11.0

^a with respect to beam center, for 0.8% FWHM energy spread.

Table 5-5. Four different NLC scenarios considered in the bunch-compressor simulations.

NLC-I and NLC-II. Shown is the longitudinal distribution at the exit of the bunch compressor and, for five different initial phases, at the end of the main linac. Figure 5-17 presents the dependence of the average energy on the initial phase error, for the same four NLC scenarios. Figures 5-18 and 5-19 show equivalent pictures for the rms and FWHM energy spread, respectively. In all cases, the beams are acceptable for the final focus.

5.4.7 Multibunch Dynamics

The real purpose of the bunch compressors is not to reduce the length of a single bunch, but the length of each bunch in the train of 90 bunches. This task is complicated by the longitudinal long-range wakefields and the pertinent multibunch beam loading in the various accelerator sections of the compressor.

In this section, we will evaluate the ΔF compensation technique for the multibunch beam loading which adds two additional rf systems with slightly different frequencies to each acceleration section [Kikuchi 1992]. These rf systems generate an additional voltage which increases almost linearly along the bunch train, and which can be adjusted to cancel the linear part of the multibunch beam loading. It should be noted that the present rf system design actually uses a combination of ΔT and ΔF techniques that is much more effective than just the ΔF technique described here.

A simulation study has been performed to test this multibunch energy compensation scheme and the interplay of longitudinal single- and multibunch dynamics in the bunch compressor. For the purpose of this study, the long-range wakefields have been confined to the fundamental mode. The wakefield of a structure is then characterized by three numbers: the loss factor k , the mode frequency f , and the quality factor Q . In terms of these quantities, the wakefield at a distance z reads

$$W(z) = 2k \cos\left(\frac{2\pi fz}{c}\right) e^{-\frac{2\pi fz}{2Q}} \quad (5.40)$$

where c denotes the velocity of light. Also taken into account in the simulation is the group velocity of the fundamental mode, which introduces a small nonlinear component to the beam loading and makes perfect beam-loading compensation impossible—at least for the compensation scheme presently chosen. Wakefield parameters for the different structures were provided by R. Miller [Miller 1995]. They are compiled in Table 5-6.

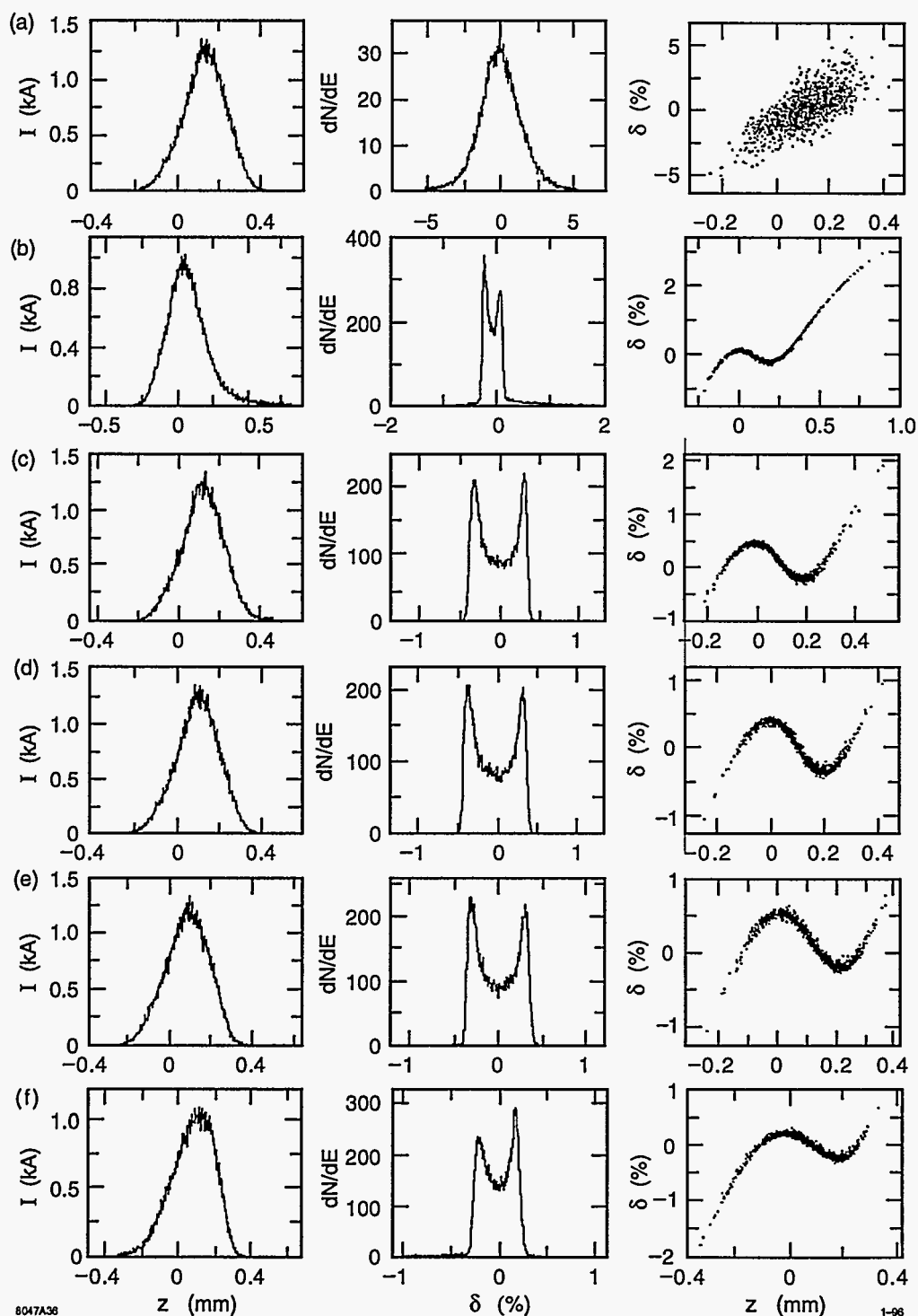


Figure 5-13. Longitudinal phase space distributions for NLC-Ia, $N = 6.5 \times 10^9$ and a final bunch length of $100 \mu\text{m}$: a) after the bunch compressor; and at the end of the main linac for an initial phase error of b) -12, c) -6, d) 0, e) 6, f) 12 mm.

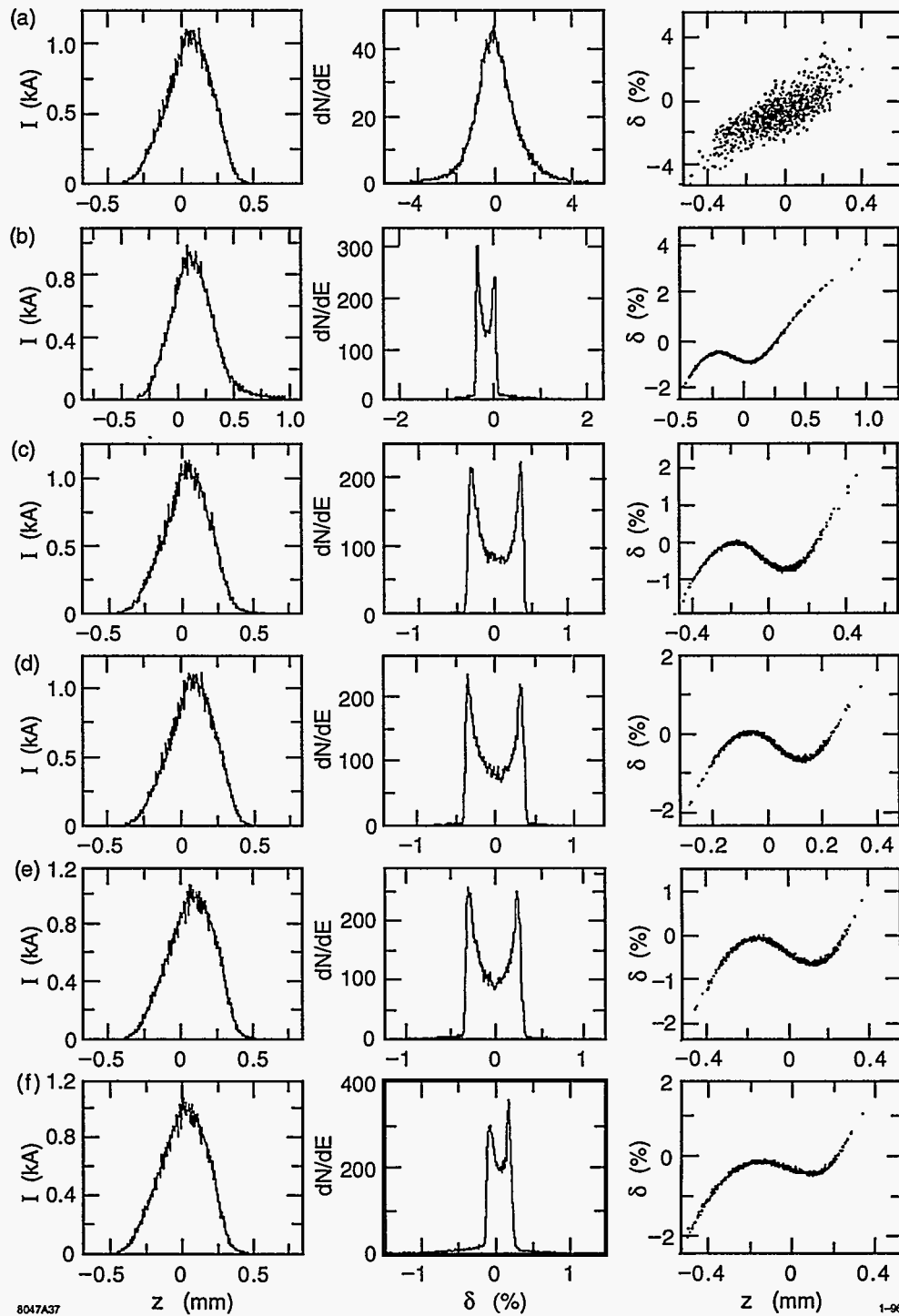


Figure 5-14. Longitudinal phase space distributions for NLC-I c, $N = 8.5 \times 10^9$ and a final bunch length of $150 \mu\text{m}$: a) after the bunch compressor; and at the end of main linac for an initial phase error of b) -12 , c) -6 , d) 0 , e) 6 , f) 12 mm.

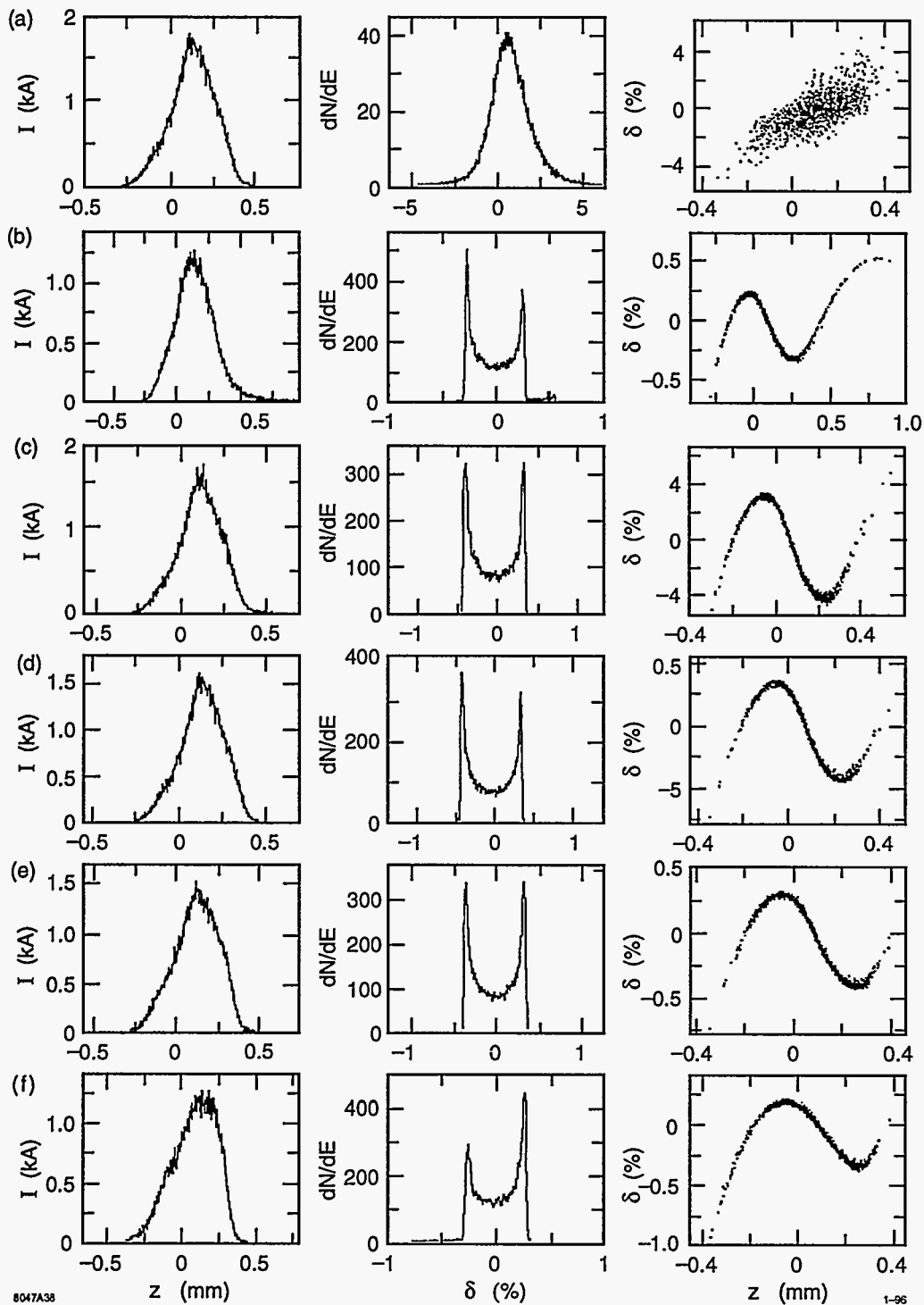


Figure 5-15. Longitudinal phase space distributions for NLC-IIa, $N = 9.5 \times 10^9$ and a final bunch length of $125 \mu\text{m}$: a) after the bunch compressor; and at the end of the main linac for an initial phase error of b) -12 , c) -6 , d) 0 , e) 6 , f) 12 mm.

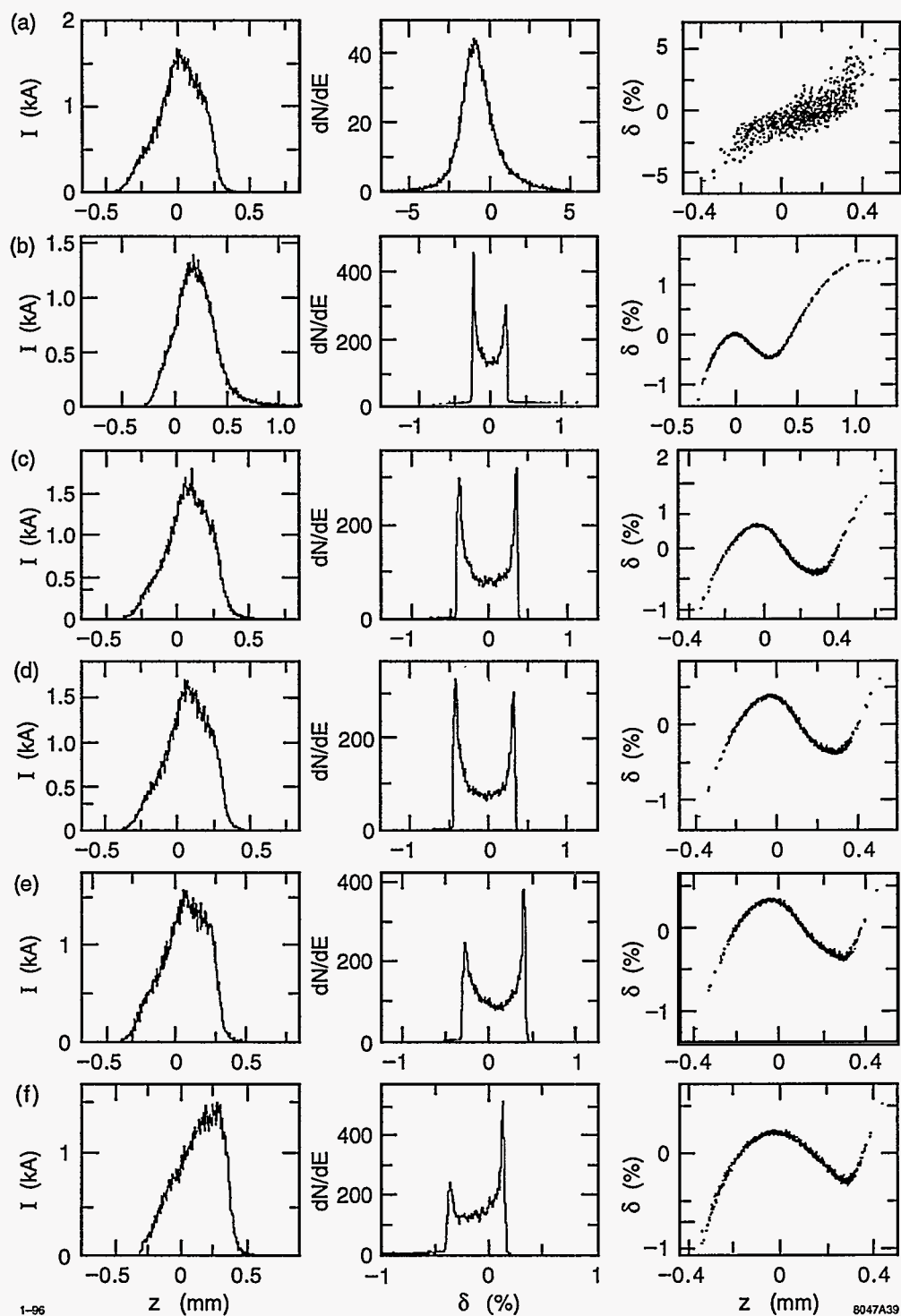


Figure 5-16. Longitudinal phase space distributions for NLC-IIc, $N = 1.25 \times 10^{10}$ and a final bunch length of $150 \mu\text{m}$: a) after the bunch compressor; and at the end of the the main linac for an initial phase error of b) -12, c) -6, d) 0, e) 6, f) 12 mm.

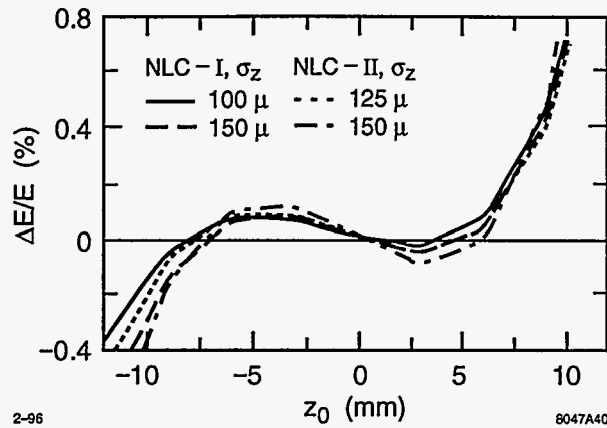


Figure 5-17. Variation of average energy with initial phase error, for two different bunch lengths in the NLC-I and NLC-II.

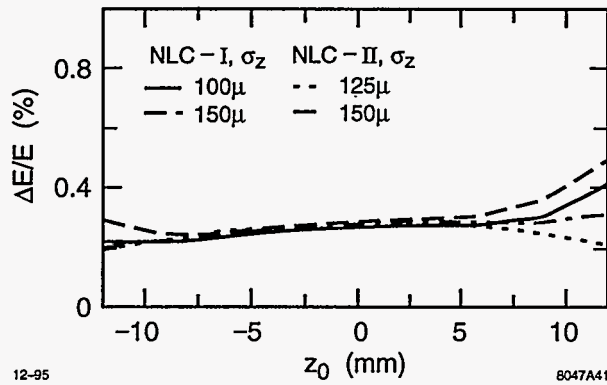


Figure 5-18. Variation of rms energy spread with initial phase error, for two different bunch lengths in the NLC-I and NLC-II.

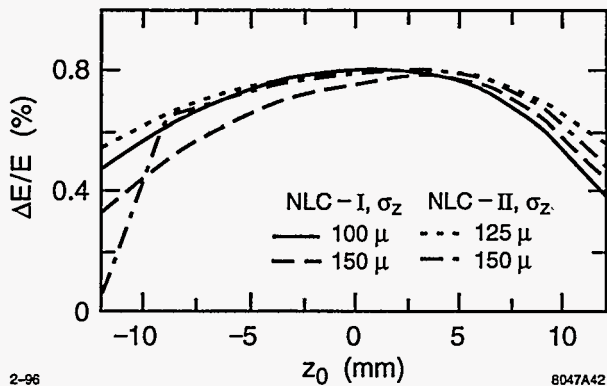


Figure 5-19. Variation of FWHM energy spread with initial phase error, for two different bunch lengths in the NLC-I and NLC-II.

Parameter	L-Band	S-Band	X-Band	Comment
f (GHz)	1.428	2.856	11.424	frequency
$2k$ (V/C/m)	1.8×10^{13}	3.7×10^{13}	2.0×10^{14}	loss factor $\times 2$
v_g/c	0.012	0.012	0.08	group velocity
Q	18,000	13,000	7000	quality factor
l (m)	6	3	1.8	structure length

Table 5-6. Wakefield and structure parameters for the different accelerating sections in the bunch compressor.

The short-range wakefields used in the multibunch simulations are the same as those which were employed in the single-bunch case: The short-range wakefield for the X-band structure was derived by K. Bane [Bane 1995]. The wakefields for other frequencies were estimated from an approximative formula in Ref. [Palmer 1990].

The multi-bunch energy compensation scheme of choice was proposed by Kikuchi [Kikuchi 1992]. If two rf structures are driven at frequencies $f_0 \pm \Delta f$, the effective total voltage for the n th bunch is

$$\Delta V_n = V_c \sin\left(\frac{2\pi(f_0 + \Delta f)z_n}{c}\right) - V_c \sin\left(\frac{2\pi(f_0 - \Delta f)z_n}{c}\right) \quad (5.41)$$

$$\approx 4\pi V_c \frac{\Delta f}{c} \cos\left(\frac{2\pi f_0 z_n}{c}\right) \quad (5.42)$$

where z_n denotes the longitudinal position of the bunch, and $2\pi \Delta f z_n/c \ll 1$ was assumed. The required compensation voltage V_c is [Kikuchi 1992]

$$V_c = qc \frac{k_m L_m + 2k_c L_c}{b 2\pi \Delta f} \quad (5.43)$$

where $(k_m L_m)$ and $(2k_c L_c)$ are the beam-loading voltage in the main rf structure and compensating cavities, respectively, and b is the bunch spacing.

For all subsystems a compensation frequency in the S-band region was chosen, detuned from the main S-Band frequency by $\Delta f \approx \pm 1$ MHz. Several considerations determined the optimum choice of Δf . In general, a larger Δf reduces the required compensation voltage and the additional beam loading. The compensation, however, becomes less linear for larger beam frequency. It seems best to choose the frequency difference so as to partially cancel the nonlinear component of the beam loading. In the simulation, this is done empirically by minimizing the rms energy variation (or phase variation) as a function of Δf .

The initial setup of the multibunch compensating rf was performed by considering only one macroparticle per bunch in order to increase the computational speed. Subsequently, the main rf-voltages and phases were re-optimized for the single-bunch dynamics. This is necessary because of additional short-range wakefields in the compensation structures. Finally, a train of 90 bunches, 50 macroparticles each, was tracked through the entire system, and through the X-Band main linac. No long-range wakefields in the X-Band linac were considered, assuming that they are perfectly compensated by rf-pulse shaping.

The simulation includes an initial linear phase variation of ± 3 mm along the bunch train, as caused by beam loading in the damping rings. There is no need for a particular rf system to compensate this initial phase variation, since the compressor was designed to handle single-bunch phase errors up to ± 6 mm or larger.

Table 5-7 summarizes the compressor parameters used in the simulation. Note that the active length of the prelinac is about 320 m, and thus about 30% shorter than in the present ZDR design. The 320-m length assumes an unrealistic gradient of 30 MV/m (or up to 36 MV/m for the compensating rf) but the performance is not expected to be much different for a greater length.

Results of the simulation study are summarized in Figures 5-20 and 5-21 and in Table 5-8. Note that the bunch-to-bunch variation of energy, position, and bunch length, apparent in the two figures, arises from the finite number of macroparticles per bunch (50), and is much larger than the expected actual bunch-to-bunch variation. On the other hand, the slow change of energy, position, and bunch length over several bunches represents the effect of the long-range wakefields, and is the quantity of interest here. Table 5-8 lists the longitudinal bunch-to-bunch phase variation, the bunch-to-bunch energy spread, the intrabunch energy spread, and the rms bunch length at the end of the main linac, for different NLC scenarios. The longitudinal bunch position varies by 30–40 μm about the average value. The bunch length fluctuates by $\pm 10 \mu\text{m}$. Changes of phase and bunch length give rise to a bunch-to-bunch rms energy variation of roughly 0.1–0.2%, and a total variation of 0.8% for the NLC-I and 0.6% for the NLC-II. The rms intrabunch energy spread is 0.3–0.4% in all cases.

We conclude that the ΔF multibunch energy compensation is straightforward and, in the simulation, its performance is adequate and satisfactory. The primary disadvantage of the ΔF technique is that the compensation is not local and thus the dispersive and chromatic emittance dilutions are larger. In the NLC injectors, we have adopted a combination of the ΔT and ΔF techniques that should perform far better than the ΔF scheme reported here—this is described in Chapter 6.

Parameter	Collider Version				Comment
	NLC-Ia	NLC-Ic	NLC-IIa	NLC-IIc	
V_{LB} (MV) ϕ_{LB} (°) L (m)	136.0 -89.88 8.5	136.5 -89.88 8.5	136.0 -89.92 8.5	136.0 -89.88 8.5	Main L-band RF 1st stage $f = 1.428$ GHz
V_{SB} (MV) ϕ_{SB} (°) L (m)		6.9 -180.0 0.4			Comp. S-band RF 1st Stage $f = 2.856$ GHz
V_{SB} (MV) Δf (kHz) ϕ_{SB} (°) L (m)	± 26.7	± 34.4 ± 856.8 -90. 2×3.0	± 38.4	± 50.5	Multibunch Comp. S-band RF 1st Stage $f_c = f_0 \pm \Delta f$, $f_0 = 2.856$ GHz
V_{SB} (MV) ϕ_{SB} (°) L (m)	8050 -4.0 270	8049 -3.0 270	8054 -3.0 270	8068 -3.0 270	Prelinac S-Band RF $f = 2.856$ GHz
V_{SB} (MV) Δf (kHz) ϕ_{SB} (°) L (m)	± 805	± 1037 ± 856.8 -90. $2 \times 27 / 2 \times 39$	± 1159	± 1525	Multibunch Comp. S-band RF Prelinac $f_c = f_0 \pm \Delta f$, $f_0 = 2.856$ GHz
V_{SB} (MV) ϕ_{SB} (°) L (m)	3850 -89.6 130	3500 -88.5 130	3730 -89.7 130	3610 -89.7 130	Main S-band RF 2nd Stage $f = 2.856$ GHz
V_{XB} (MV) ϕ_{XB} (°) L (m)	274	276 -183.0 8	256	240	Comp. X-band RF 2nd Stage $f = 11.424$ GHz
V_{SB} (MV) Δf (kHz) ϕ_{SB} (°) L (m)	± 338	± 440 ± 1142.4 -90. 2×15.0	± 492	± 647	Multibunch Comp. S-band RF 2nd stage $f_c = f_0 \pm \Delta f$, $f_0 = 2.856$ GHz
V_{XB} (GV) ϕ_{XB} (°) L (m)	270.32 -15.7 8130	236.83 -16.1 8130	535.69 -8.3 8900	480.33 -12.0 8900	Main Linac X-band RF $f = 11.424$ GHz

Table 5-7. Rf parameters of compressor subsystems, as used in the multibunch simulation study.

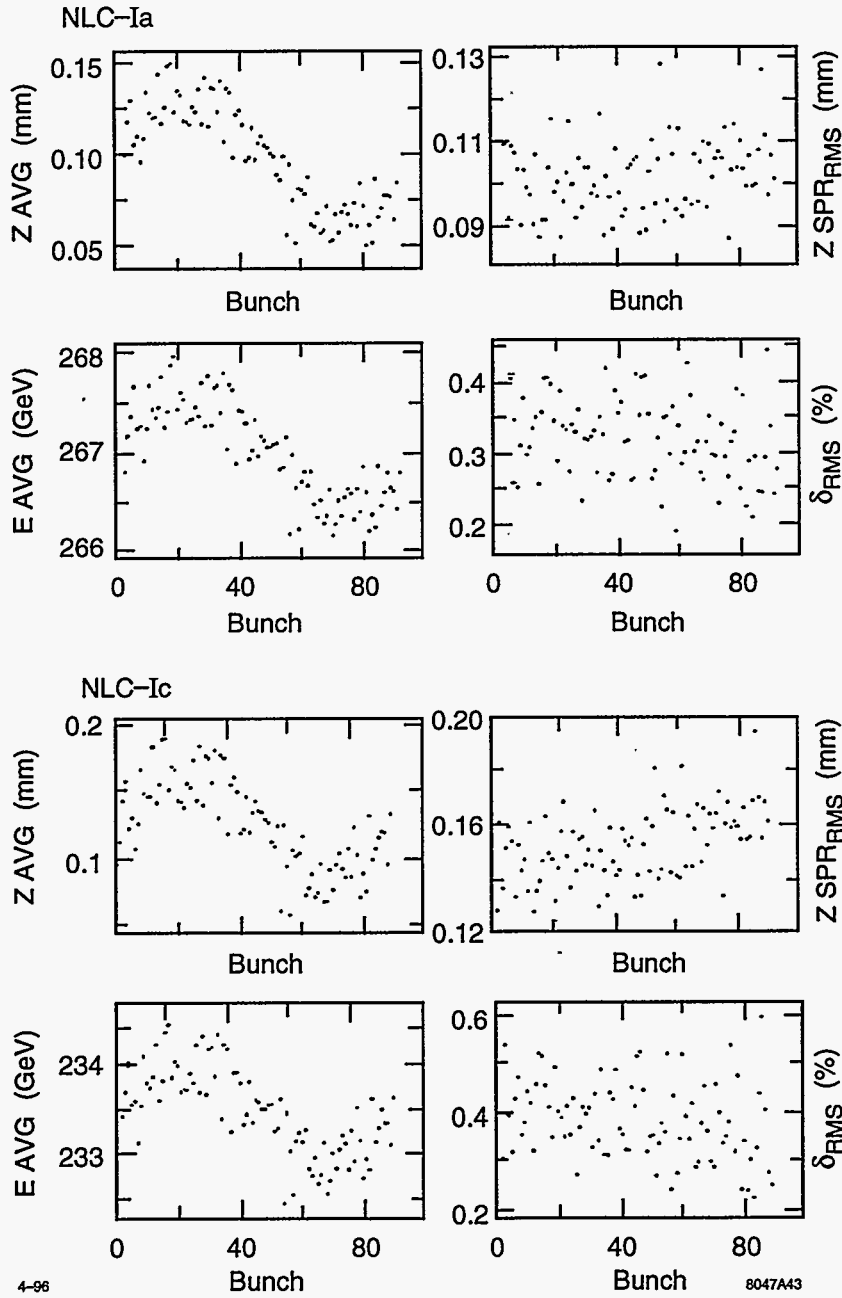


Figure 5-20. Bunch centroid position, rms bunch length, average bunch energy, and rms energy spread, as a function of bunch number in a train of 90 bunches, for two different versions of NLC-I.

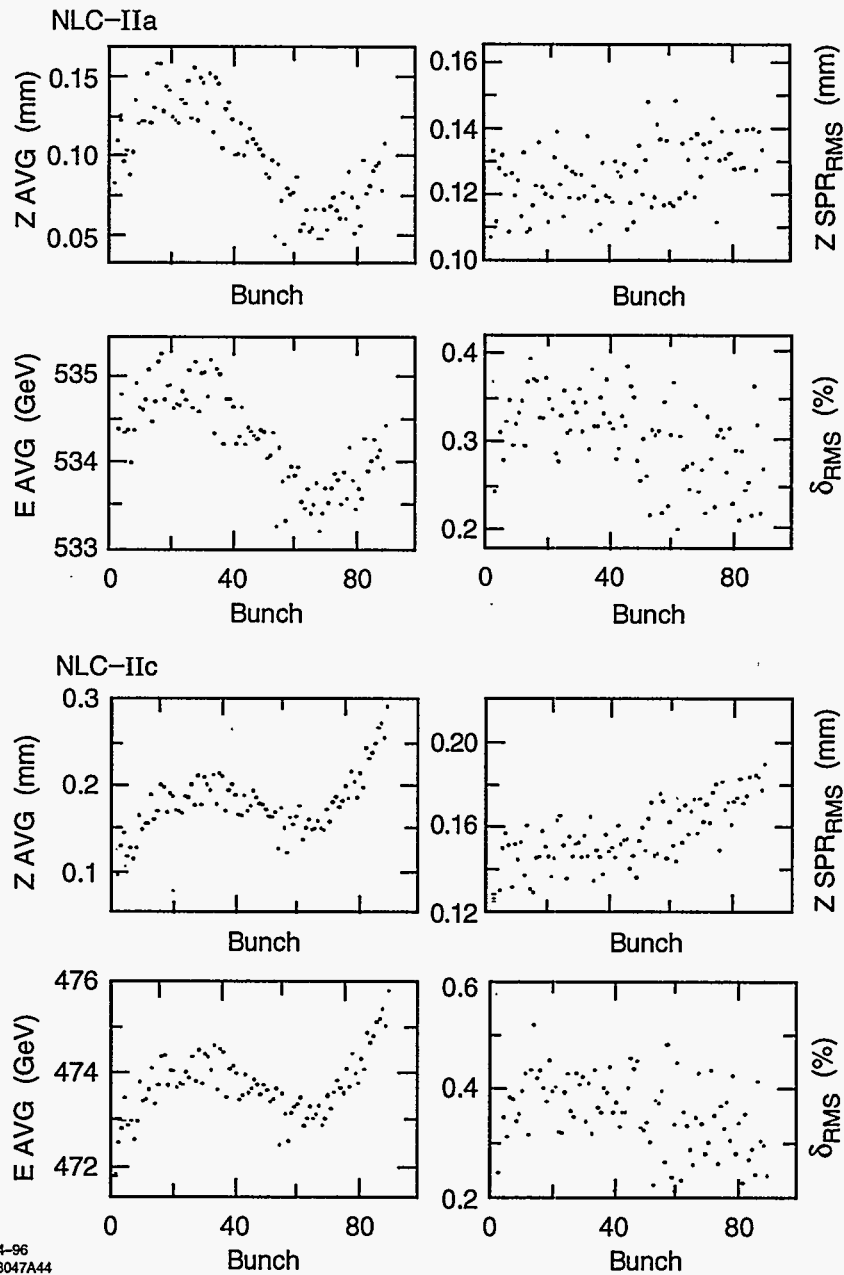


Figure 5-21. Bunch centroid position, rms bunch length, average bunch energy, and rms energy spread, as a function of bunch number in a train of 90 bunches, for two different versions of NLC-II.

Parameter	Collider Version				Comment
	NLC-Ia	NLC-Ic	NLC-IIa	NLC-IIc	
$z_{b, rms}$ (μm)	28	33	31	36	Rms phase variation
$\sigma_{z, ave}$ (μm)	100 ± 9	153 ± 13	125 ± 10	156 ± 15	Average bunch length
$\delta_{b, rms}$ (%)	0.18	0.20	0.09	0.14	Rms energy variation
$\sigma_{\delta, ave}$ (%)	0.31	0.38	0.31	0.36	Intrabunch rms energy spread
E_b (GeV)	266.9	233.46	534.2	473.7	Average energy

Table 5-8. *Inter- and intrabunch energy spread, rms bunch length, and longitudinal phase variation at the end of the X-band main linac, for a train of 90 bunches in two different versions of the NLC-I and NLC-II. Numbers were obtained by a macroparticle simulation, which includes the effect of short- and long-range wakefields, multibunch energy compensation, and an initial phase variation of 6 mm along the train.*

5.5 Transverse Dynamics

In this section, we will examine the effects that can dilute the transverse emittances. The primary source of dilution are optical aberrations in the spin rotator and compressors and single bunch wakefields in the linacs. We will describe these effects and the respective tuning compensation systems in three regions which are organized according to the respective diagnostic sections. Thus, we will describe the tuning in the spin rotator and low-energy bunch compressor, in the prelinac, and in the high-energy bunch compressor. Next, we will discuss the effect of the multibunch transverse wakefields and then finally we will describe the effects of: space charge fields and coherent radiation, ion trapping, and synchrotron radiation. All of these later effects impose weak constraints on the system design.

5.5.1 Spin Rotator and Low-Energy Bunch Compressor

Given the small vertical emittance at damping ring extraction ($\gamma\epsilon_y = 3 \times 10^{-8}$ m), it is crucial that tuning elements and algorithms be provided which will allow full correction of the inevitable fabrication and alignment errors of the first bunch compressor (BC1). This is especially necessary when considering the large energy spread incurred after the BC1 rf structures ($\sim 1\%$ rms) as well as the large cross-plane coupling generated and canceled again between spin rotator solenoids. The following section describes dispersion correction elements, coupling correctors, beam matching, and diagnostics necessary for preserving the damped transverse emittance. In addition, the results from a full tuning simulation are presented.

Tuning Elements and Aberrations

Dispersion Correction Elements. The large energy spread of the bunch compressor sets very tight tolerances on residual dispersion, especially in the vertical plane. The relative emittance dilution due to residual spatial, η , and angular, η' , dispersion is expressed in Eq. 5.44 including subsequent chromatic filamentation.

$$\frac{\delta\epsilon}{\epsilon_0} = \frac{\eta^2 + (\eta\alpha + \eta'\beta)^2}{2\epsilon_0\beta} \sigma_s^2 \quad (5.44)$$

The tolerable vertical spatial dispersion at a point $\beta = 10$ m, $\alpha = 0$, is $175 \mu\text{m}$ (2% emittance dilution at $\gamma\epsilon_y = 3 \times 10^{-8}$ m and 1% rms energy spread). To correct at this level, four small skew quadrupoles are placed in the wiggler section of the BC1 at points of large horizontal dispersion. These are tiny correction elements (10-cm long, 30-mm pole-tip radius, ± 1 kGauss pole-tip field). They are paired at $-I$ (transfer matrix) intervals so that coupling is not generated and the pairs are separated by 90° . In this way, orthogonal η and η' knobs are available. A similar system of four normal quadrupoles is used for horizontal dispersion correction. Figure 5-22 shows the placement of these skew and normal elements (SQW1,...4, CQW1,...4), as well as other elements discussed below.

In addition to dispersion correction after the BC1 rf structures, it is useful to include two more skew quadrupoles (SQR1, SQR2) in the mini-arc section of the spin rotator to provide correction of residual vertical dispersion generated before the rf sections. The net emittance dilution is a linear combination of the two residual dispersion functions weighted by their respective energy spreads (1% post-compression and 0.1% pre-compression). Although post-compression dispersion is much more intolerable, any significant pre-compression dispersion will not be correctable by the wiggler section skew quadrupoles. The two skew

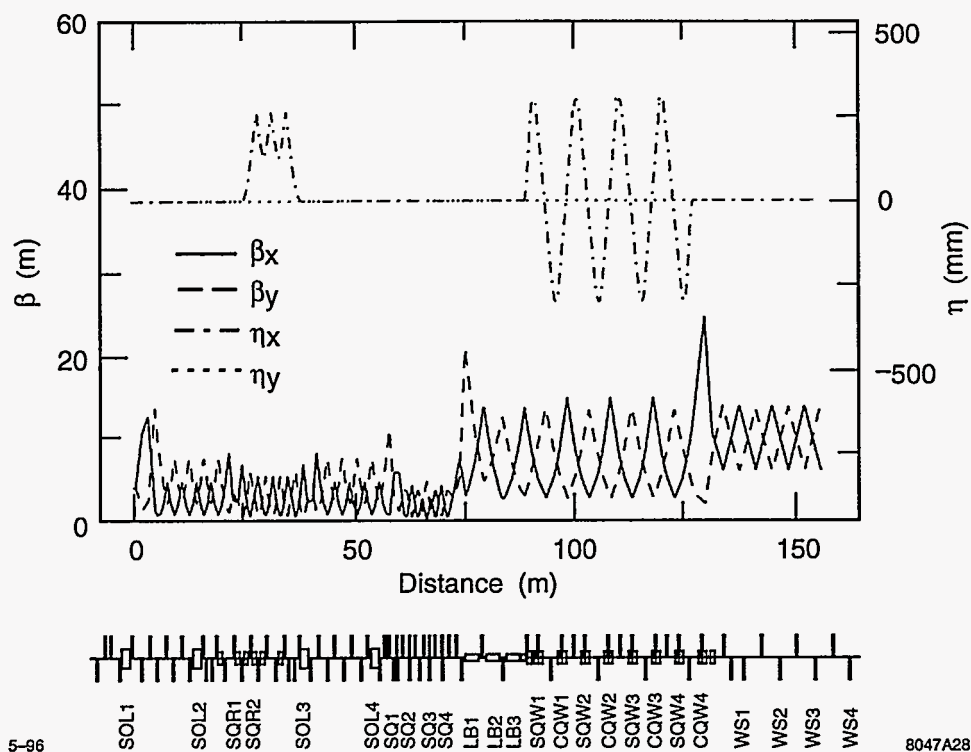


Figure 5-22. Dispersion and beta functions for the entire low-energy bunch compressor and spin rotator system. Tuning elements and major component locations are indicated.

elements in the mini-arc are separated by 90° to provide spatial and angular pre-compression vertical dispersion correction. The ratio $(\eta_x \sigma_\delta)^2 / \beta_x \epsilon_x \gg 1$ so that paired coupling cancellation is not necessary.

Coupling Correction. The spin rotator solenoids (SOL1,...4) are nominally separated by optics which will cancel their cross-plane coupling. However, imperfections in the cancellation optics will result in emittance dilution. Furthermore it may be necessary to correct coupling generated within the damping rings. Therefore, a skew correction section is included following the spin rotator. This section contains four skew quadrupoles (SQ1,...4) in a non-dispersive section which is placed at ideal phase advance points so that they are initially orthonormal. The vertical emittance is minimized with each of these four skew elements. At the end of this process, and allowing for some reiteration, the coupling is completely corrected.

Beam Matching. Several provisions exist in the BC1 to compensate for matching errors. There are four variable strength quadrupoles which match the extracted beam to the spin rotator optics. There are also matching quadrupoles within the spin rotator to compensate for the focusing effect of the solenoids. Finally there are several matching quads between the skew correction section and the wiggler and also after the wiggler section. The BC1 rf may be switched off in order to distinguish more clearly between dispersion errors and matching errors.

Second-Order Corrections. Although it is not necessary to include local sextupole chromatic corrections for the design optics, simulations have shown (Section 5.5.1, Tuning Simulations) that for large vertical

RMS Quadrupole Strength Errors ($\Delta k/k$)	1.0%
RMS Dipole Magnet Roll Errors (θ)	0.25°
Initial Cross-Plane Coupling (DR output)	$\epsilon_y/\epsilon_{y0} = 2.2$
All Four Solenoids at Full Field	35 kGauss

Table 5-9. Errors and conditions for bunch compressor and spin rotator tuning simulations.

dispersion corrections ($\epsilon_y/\epsilon_{y0} \gg 10$) some second-order dispersion arises. If this situation develops, it is a simple matter to include four skew sextupoles adjacent to the wiggler skew quadrupoles to provide T_{366} and T_{466} knobs which are paired so that vertical chromaticity is not generated.

Phase Space Diagnostics. To measure the BC1 extracted beam, four wire scanners (WS1,...4) are placed at ideal phase advance intervals (45°) at the end of the wiggler. The corrections described above are applied by minimizing the measured emittance. It is not necessary to actually measure the cross-plane coupling. It is fully corrected by minimizing the projected vertical emittance. The matched beam size is the same at each wire ($\sim 10 \mu\text{m}$ vertically by $\sim 65 \mu\text{m}$ horizontally) and therefore the matched condition is easily recognizable. Wire scanner roll tolerances are readily achievable ($\sim 1^\circ$). In addition, a wire scanner placed at a high-dispersion point ($\sim 220 \text{mm}$) in the spin rotator mini-arc will be useful to measure the extracted damping ring energy spread ($\sim 0.1\%$). The ratio of the dispersive beam size to the betatron beam size is $\sim 4:1$ here. Finally a wire scanner at a peak dispersion point ($\sim 240 \text{mm}$) in the wiggler will be useful to measure the damping ring extracted bunch length (similar size ratio $\sim 4:1$).

Tuning Simulations

Tuning simulations have been run for the many corrections described above using the *Final Focus Flight Simulator*. Table 5-9 summarizes the set of errors and conditions introduced to the bunch compressor and spin rotator system for these simulations.

These errors produce extreme conditions that result in a vertical emittance which is a factor of >200 times larger than the initial intrinsic emittance $\gamma\epsilon_{y0} = 2.3 \times 10^{-8} \text{m}$. In this case, the vertical beam profiles measured on the wire scanners will increase from the nominal $\sim 10 \mu\text{m}$ to $>130 \mu\text{m}$.

The simulations are run to test the tuning algorithms, especially in this extreme case. In the tuning process, a realistic measurement resolution is not attempted. The emittance measurements are infinitely precise and the initial diluted vertical emittance is $\gamma\epsilon_{y0} = 540 \times 10^{-8} \text{m}$. Although it may not be the optimal procedure, the following describes the tuning procedure used:

- Step 1. With L-band rf switched on, scan both vertical dispersion knobs to minimize projected vertical emittance (some iteration useful at this extreme stage).
- Step 2. With L-band rf switched on, scan both horizontal dispersion knobs to minimize projected horizontal emittance.
- Step 3. With L-band rf switched off, scan the four coupling correction skew quadrupoles to minimize projected vertical emittance.
- Step 4. With L-band rf switched off, match horizontal and vertical beta functions with damping ring extraction quadrupoles (not actually tested here).
- Step 5. Repeat Steps 1 and 2 (most dilution caused by dispersion).

Step 6. With L-band rf switched on, scan both second-order vertical dispersion knobs to minimize projected vertical emittance (only necessary for these extreme conditions).

Step 7. With L-band rf switched off, scan pre-compression vertical dispersion knobs.

The simulation of this procedure with the conditions of Table 5-9 has proven very successful and results in a final emittance dilution of <2% in both planes. Quadrupole alignment errors were not included in the simulation; however, this should simply add to vertical dispersion errors which are already extreme due to the large dipole magnet roll errors. It is estimated that such a procedure will probably require approximately 16 hours of real machine time.

5.5.2 Prelinac

The prelinac quadrupoles will be aligned using the standard quadrupole beam-based alignment procedure used in the main linacs and the beam-delivery sections. Each quadrupole will be powered with an individual power supply. Then, the power supply can be varied making it straightforward to determine the alignment of the quadrupole magnetic center with respect to the electrical center of the BPM captured in the magnet. Each quadrupole will be mounted on a remote magnet mover to facilitate the alignment. In addition, the accelerator structures will also be mounted on remote movers and will contain BPMs that will measure the induce dipole modes in the structures. This will allow the structure to be accurately aligned to the beam trajectory established by the quadrupoles. Finally, additional tuning, using oscillation bumps similar to those used in the SLC linac, could be performed using the emittance diagnostic station located at the end of the prelinac.

Simulations of the transverse emittance dilution were performed with the LInear Accelerator Research simulation program described in Chapter 7. In simulations, the residual vertical emittance dilution was less than 15% assuming errors due to 10 μm quad-BPM resolution, 40 μm structure BPM resolution, 200 μm initial quadrupole offsets, and 1 μm mover step size. The dilution is dominated by the dispersive dilution due to the large incoming energy spread (1%) of the beam. These are very loose tolerances. The expected errors are 2 μm quad-BPM misalignments, 20 μm structure BPM resolution, and 0.3 μm mover step size. These would yield a vertical emittance dilution that is less than 1%.

5.5.3 High-Energy Bunch Compressor

The high-energy bunch compressor can be separated into 3 stages: the 180° arc, the compressor rf, and the chicane. The quadrupoles in the arc and the compressor rf section will be aligned using the standard beam-based techniques that will also be used in the pre-linac, the main linac, and the beam-delivery section of the collider. Here, each quadrupole is powered with an individual power supply and the power supply is varied to determine the magnetic center of the quadrupole with respect to a BPM captured within the bore. The quadrupoles are then aligned with remote magnet movers; this algorithm is described in greater detail in Chapter 7. and the preceding section on the prelinac alignment. The arc was explicitly designed using separated function magnets to facilitate this form of alignment.

The 4-GeV compressor rf section has strong focusing to reduce the sensitivity to wakefields. To keep the vertical emittance dilution due to transverse wakefields to less than 1%, the accelerator structures must be aligned within 45 μm of the beam trajectory. This will be accomplished using structure BPMs ("S"-BPMs)

Name	Quantity	Roll (mrad)	$\Delta B/B_0$ (10^{-4})	b_1/b_0 (%)	b_2/b_0 (%)
BB	138	4.7	1.2	0.3	5

Table 5-10. BC2 arc dipole magnet single element tolerances for 8% emittance growth each ($\gamma\epsilon_{x0} = 3 \times 10^{-6} m$, $\gamma\epsilon_{y0} = 3 \times 10^{-8} m$, $\sigma_\delta = 0.25\%$). Quadrupole and sextupole field harmonics (b_1/b_0 and b_2/b_0) are evaluated at a radius of 4 mm. They generate 1st and 2nd order x -dispersion.

Name	Quantity	Roll (mrad)	Δx offset (μm)	Δy offset (μm)	Δx_{rms} vibrate (μm)	Δy_{rms} vibrate (μm)	$\Delta B/B_0$ (%)	b_2/b_1 (%)
QF	69	1.12	920	230	2.3	0.58	0.9	10
QD	68	1.10	2930	100	7.3	0.25	4.8	120

Table 5-11. BC2 arc quadrupole magnet single element tolerances for 8% emittance growth each ($\gamma\epsilon_{x0} = 3 \times 10^{-6} m$, $\gamma\epsilon_{y0} = 3 \times 10^{-8} m$, $\sigma_\delta = 0.25\%$). Sextupole field component tolerances (b_2/b_1) are evaluated at a radius of 4 mm and are very loose for the QDs (120%).

to measure the induced dipole mode and the remote movers to align the structures to the beam path. Given this loose tolerance, no significant dilution is expected.

As in the low-energy bunch compressor, tuning elements must also be included in the high-energy compressor. The most likely mechanisms for emittance dilution are rolled dipoles and quadrupoles, misaligned quadrupoles and sextupoles, as well as quadrupole gradient errors, all of which generate mostly anomalous dispersion which phase mixes in the main linac (see Eq. 5.45). Cross-plane coupling and beta-mismatch errors are much less likely since the horizontal beam size in the arc and chicane is dominated by dispersion (*i.e.*, $\{\eta_x \sigma_\delta\}^2 / \beta_x \epsilon_x \gg 1$) (see Table 5-4 and Figures 5-11 and 5-12). The next sections describe the tuning elements and algorithms for controlling anomalous dispersion in the arc and chicane; the tuning of the rf section was described earlier.

180° Arc Section

In order to estimate the dispersion correction range needed we first examine the single element tolerances for the arc. These tolerances are then scaled to estimate the emittance dilution associated with an achievable set of alignment and quadrupole gradient tolerances. This estimated emittance dilution is used to choose the necessary correction range and the scheme is tested for induced non-linear aberrations. The single element tolerances for the 180° arc FODO magnets are listed below in Table 5-10 (dipoles), 5-11 (quadrupoles), and 5-12 (sextupoles). Each tolerance represents a 2% luminosity loss for that single element's effect on one beam (8% emittance increase for one beam in one plane). The effects of these errors increase the IP beam size except for dipole field regulation and quadrupole transverse vibration which steer the beams out of collision. In this case, the betatron phase to the IP is not calculated so phase averaging is applied.

The important vertical emittance dilution mechanisms include vertical misalignments of the quadrupoles and sextupoles and roll errors of quadrupoles and dipoles. Horizontal dilution mechanisms include horizontal misalignments and gradient errors of the QF quadrupoles. The magnetic multipole tolerances in the tables, when scaled down by \sqrt{N} , are easily achievable, as are the horizontal alignment and gradient errors of the

Name	Quantity	Roll (mrad)	Δx offset (μm)	Δy offset (μm)	Δx_{rms} vibrate (μm)	Δy_{rms} vibrate (μm)	$\Delta B/B_0$ (%)
SF	68	325	800	160	800	160	>50
SD	68	325	1740	86	1740	86	>50

Table 5-12. BC2 arc sextupole magnet single element tolerances for 8% emittance growth each ($\gamma\epsilon_{x0} = 3 \times 10^{-6}$ m, $\gamma\epsilon_{y0} = 3 \times 10^{-8}$ m, $\sigma_\delta = 0.25\%$). The field regulation and roll tolerances are not important (for aligned sextupoles) because the chromaticity of the arc is insignificant.

QD quadrupoles and the roll and field errors of the sextupoles. Static field strength errors of the dipoles can be encompassed in the horizontal alignment of the quadrupoles. Regulation and vibration tolerances are not addressed by the tuning schemes discussed here. These non-static problems will need to be corrected by orbit feedback systems or, as in the case of dipole field regulation, all dipoles or groups of dipoles will be powered in series to significantly loosen these tolerances. An achievable set of alignment and quadrupole gradient tolerances is now chosen and the associated emittance dilution is tabulated for each mechanism in Table 5-13.

For these tolerances, the total emittance dilution factor for the vertical plane may be ~ 12 , whereas the horizontal may be ~ 2 . Dispersion correctors should handle at least this range and should also not affect beta functions or introduce betatron coupling. The quadrupole roll tolerances of 0.5mr and sextupole vertical alignment tolerances of $60 \mu\text{m}$ were chosen so that cross-plane coupling will not be a problem and therefore no betatron-coupling correction is required (*i.e.*, for a monochromatic beam, 69 QF and 68 QD magnets with 0.5mr rms roll errors plus 68 SF and 68 SD magnets with $60 \mu\text{m}$ rms vertical misalignments will produce a 2% luminosity loss for the one beam due to betatron coupling). The sextupoles may easily be beam-based aligned if vertical movers are included with ± 1 mm range. If an SD's pole-tip field is temporarily raised to -4 kGauss (from -3 kGauss) and its vertical position is scanned in ~ 5 steps over the range ± 1 mm while the horizontal beam centroid offset is recorded on a < 4 - μm resolution BPM near the next QF, then each sextupole may be aligned to < 60 - μm resolution. This resolution may be improved by using more than one BPM. Note that energy jitter will vary the BPMs reading due to the ~ 100 -mm x -dispersion there. However, all arc x -BPMs may be used together to correct the data for this energy jitter down to $\delta E/E_0 = (4 \mu\text{m}/\sqrt{68})/(100 \text{ mm}) \sim 5 \times 10^{-6}$. Figure 5-23 shows a simulated sextupole (SD) alignment scan using one 4- μm resolution x -BPM.

Dispersion Correctors for the Arc. Vertical dispersion correction at the end of the arc can be provided by adding four small skew quadrupoles (of zero nominal field)—one per cell in the last four cells (cells 65–68). This scheme takes advantage of the 90° vertical phase advance per cell by pairing skew quadrupoles at $-I$ transfer matrix (2 cell) separation so that, for equal and opposite skew quadrupole settings, no betatron cross-plane coupling is generated. The two asymmetrically powered pairs of skew quadrupoles are shifted by one cell ($\Delta\psi_y = 90^\circ$) with respect to each other so that both betatron phases are correctable (η_y and η'_y). Betatron coupling is also correctable, if necessary, if one skew quadrupole is also added to each of cells 61–64. In this way four symmetric pairs may be formed (61/63, 62/64, 65/67 and 66/68) which correct betatron coupling without introducing vertical dispersion so that, given the unequal x and y tunes of the arc, all four cross plane correlations are removable within skew quadrupole field limits (not possible for $\Delta\psi_x = 90^\circ/\text{cell}$). The range of vertical dispersion correction for one pair of 10-cm-long, ± 1 kGauss pole-tip field, 30-mm pole-tip radius skew quadrupoles located 10-cm upstream of the QD at $\beta_y = 6.5$ m, $\eta_x = 50$ mm is $\Delta\epsilon_y/\epsilon_{y0} \sim 12$ at 0.25% rms energy spread for $\gamma\epsilon_{y0} = 3 \times 10^{-8}$ m (or the peak vertical dispersion induced

Rms magnet roll angles	Rms vertical misalignments	Rms horizontal misalignments	Rms static gradient errors	$\Delta\epsilon_y/\epsilon_{y0}$	$\Delta\epsilon_x/\epsilon_{x0}$
0.5 mrad QF/QD/BB	100 μm QF/QD 60 μm SF/SD	200 μm QF/QD 200 μm SF/SD	0.5% QF/QD	—	—
68 QDs 69 QFs 138 BBs				1.1 1.1 0.1	~ 0 ~ 0 ~ 0
	68 QDs 69 QFs 68 SDs 68 SFs			5.4 1.0 2.6 0.8	0 0 ~ 0 ~ 0
		68 SDs 68 SFs 68 QDs 68 QFs		0 0 0 0	0.1 0.3 ~ 0 0.2
			68 QDs 69 QFs	~ 0 ~ 0	0.1 1.7
Total Expected Dilution <i>without</i> Tuning =				12.1	2.4

Table 5-13. Chosen set of rms alignment tolerances and quadrupole static gradient tolerances for the BC2 arc and their impact on emittance dilution for each plane ($\gamma\epsilon_{x0} = 3 \times 10^{-6}$ m, $\gamma\epsilon_{y0} = 3 \times 10^{-8}$ m, $\sigma_\delta = 0.25\%$). Vertical alignment of SDs and QDs is most critical.

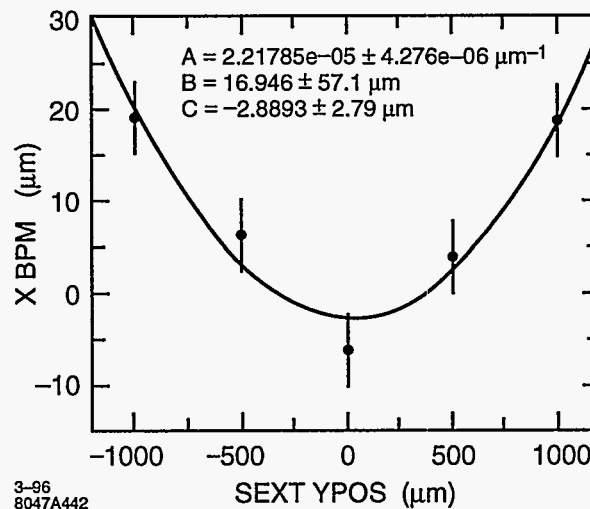


Figure 5-23. Simulated sextupole (SD) alignment scan using one 4- μm -resolution x -BPM located at the next QF. The SD's pole-tip field is set to -4 kGauss (from -3 kGauss) for the alignment.

Quad type	Quantity	Length (m)	Pole radius (mm)	Max. field (kGauss)	2% lum. step size (kGauss)	$\Delta\eta_{x,y}^{\max}$ at $\beta_{x,y}^{\max}$ (mm)	Max. $\varepsilon_y/\varepsilon_{y0}$
Skew	4-8	0.1	30	± 1.0	± 0.08	7	12
Normal	7	0.1	30	± 2.3	± 0.42	28	2.4

Table 5-14. BC2 arc dispersion correction magnet specifications for 0.25% rms energy spread, $\gamma\varepsilon_{x0} = 3 \times 10^{-6}$ m and $\gamma\varepsilon_{y0} = 3 \times 10^{-8}$ m. There is one skew quadrupole (or SD vertical mover) in each of the last four (or eight) FODO cells 10-cm upstream of each QD and one normal quadrupole in each of cells 54 through 60, 10-cm upstream of each QF (or QF trim supplies).

at the center of the next QD magnet is as much as ± 7 mm per pair). No significant coupling or beta beat is generated over this range. For betatron coupling, one of the four symmetric pairs of skew quadrupoles at ± 2 -kGauss pole-tip field will correct a 50% vertical emittance dilution due to coupling. These four coupling correctors may be easily added if betatron coupling becomes a problem. Their inclusion will effectively loosen sextupole vertical alignment tolerances by nearly a factor of 2. Of course the skew quadrupoles may also be replaced, with some loss in correction speed, by QD roll-movers with ± 10 -mm range or SD vertical movers of ± 1 -mm range (SD vertical mover steering in the x -plane, is small and can be removed with a post-arc launch feedback system); the magnet movers planned exceed these ranges.

The horizontal dispersion may similarly be controlled by adding two pairs of small normal quadrupoles (of zero nominal field). Due to the nominal 108° horizontal phase advance per cell, these quad pairs must be spaced by 5 cells in order to provide a $-I$ separation. It is probably best not to nest the skew and normal correction quads. If cell 54 and 55 as well as cell 59 and 60 include a 10-cm-long, ± 2.3 -kGauss, 30-mm radius quadrupole which is 10-cm upstream of the QF at $\beta_x = 6.4$ m, $\eta_x = 93$ mm, the emittance correction range per pair will be $\Delta\varepsilon_x/\varepsilon_{x0} = 2.4$ (or the additional horizontal dispersion induced at the center of a QF magnet is as much as ± 28 mm per pair). If cells 56, 57 and 58 also include a 10-cm-long normal quadrupole, then the horizontal dispersion correction scheme will also work for $90^\circ/\text{cell}$ and $135^\circ/\text{cell}$ horizontal phase advance configurations if the appropriate correction quadrupole (CQ) pairs are tuned for a given R_{56} configuration (*i.e.*, $\psi_x = 90^\circ/\text{cell}$: CQ pairs 57/59 and 58/60, $\psi_x = 108^\circ/\text{cell}$: CQ pairs 54/59 and 55/60, $\psi_x = 135^\circ/\text{cell}$: CQ pairs 55/59 and 56/60; see Table 5-4). Since the vertical transfer matrix between paired normal quadrupoles (5 cells for $108^\circ/\text{cell}$) is not $-I$ there will be an insignificant perturbation to the vertical beta function which amounts to a $< 0.2\%$ vertical beta beat amplitude at full horizontal dispersion correction (± 2.3 -kGauss quadrupole fields). Of course these CQ quadrupoles may also be replaced by independent QF trim supplies of $\pm 5\%$ range (SF horizontal movers would require a large ± 2.5 -mm range and may steer too much). The dispersion correction specifications are summarized in Table 5-14.

This scheme of skew and normal quadrupole dispersion correction has been tested over various vertical emittance dilution mechanisms ranging to $\Delta\varepsilon_y/\varepsilon_{y0} \sim 30$. The dispersion was easily corrected with the skew/normal quadrupole pairs and then the arc was tracked with 3000 particles. The emittance dilution was corrected to within 4% without any coupling correction necessary. The remaining 4% dilution was due to betatron coupling which is also correctable as described above. There are also two quadrupoles placed in the dispersion suppressor section at the beginning and end of the arc which can be used to vary the horizontal dispersion function. However, these variable quadrupoles are included to properly match/suppress the arc dispersion function over the various R_{56} configurations (different horizontal phase advance per cell).

Dispersion Measurements. Dispersion correction for the arc can be accomplished in practice by correlating arc and post-arc BPM readings with prelinac energy variations and applying calculated corrections to the skew and normal quadrupole pairs, and/or by switching off the bunch compression rf between the arc and chicane (so that chicane dispersion errors are minimized), then minimizing the measured emittance on the post-chicane wire scanners using simple orthogonal combinations of the dispersion correction quadrupole pairs.

Beta Matching Corrections for the Arc. There are four matching quadrupoles placed at both entrance and exit of the arc which may be used for empirical beta matching into the post-chicane wire scanner section (with pre-chicane rf switched off to minimize dispersion effects). If the arc dispersion is first matched using the BPM correlation technique described above, then dispersion errors from the arcs should not bias the beta matching process significantly. The tolerance on the beta match into the arc is fairly loose. It can be shown that the synchrotron radiation (SR) emittance increase approximately scales with the amplitude of the incoming beta mismatch.

$$\Delta\epsilon_{SR} \approx B_{mag}\Delta\epsilon_{SR-nom}. \quad (5.45)$$

Here $B_{mag}(\geq 1)$ is the beta mismatch amplitude in the horizontal plane and $\Delta\epsilon_{SR-nom}(\ll \epsilon_{x0})$ is the nominal SR emittance increase for a matched incoming beam. A very large mismatch of $B_{mag} = 2(\beta_x \approx 4\beta_{x0}, \alpha_x = \alpha_{x0} = 0)$ will increase a nominal 2.4% SR emittance increase to 4.8%. The vertical match has no such constraint.

Steering Correctors for the Arc. Horizontal and vertical dipole correctors at each QF and QD, respectively, will be required (depending on the availability of quadrupole movers) to initially steer the beam line and to use in fast feedback applications. Correctors with ± 0.4 -kGauss fields and 10-cm length will be adequate to displace the beam nearly ± 1 mm at the next similar quadrupole. The horizontal correctors will then need to regulate at $\sim 5 \times 10^{-4}$ over the 100-ms (10 pulse) range while similar vertical correctors will need $\sim 4 \times 10^{-5}$ regulation ($\sim 0.5\%$ luminosity loss due to all correctors in both arcs for both planes). Quadrupole movers will be used to realize the vertical alignment tolerances using beam based alignment techniques.

Chicane Section

As in the BC2 arc, the chicane presents mostly a dispersion correction problem. Since the chicane includes no quadrupoles at dispersion points, emittance dilution mechanisms will include dipole magnet roll errors and dipole field quality effects. Dipole roll errors should be correctable with vertical steering. Table 5-15 shows the approximate single element tolerances (2% luminosity reduction per error per beam) for the two chicane dipole locations; two B1 dipoles at chicane start/end and the two B2 dipoles at chicane center.

If these tolerances are not met, small correction quadrupoles and skew quadrupoles at the half-way point of the B1 dipoles (split at $\eta_x = 40$ mm, $\beta_{x,y} = 50$ m) can be added to control horizontal and vertical dispersion. These quadrupoles would need to be ~ 10 cm in length, with ~ 50 -mm radius and ± 1 -kGauss fields. Both dispersion phases can be handled by placing these correctors at the first and last B1 chicane dipole centers which are separated by $\sim \pi/2$ in phase. Betatron coupling and beta-mismatch effects will not be significantly generated due to the large dispersion here (*i.e.*, $\{\eta_x\sigma_\delta\}^2/\beta_x\epsilon_x \sim 50$). If the sextupole field harmonic tolerances are not met, then small tuner normal sextupoles will also need to be included here to correct second order horizontal dispersion.

Name	Quantity	Length (m)	Roll (mrad)	$\Delta B/B_0$ (10^{-5})	b_1/b_0 (10^{-4})	b_2/b_0 (10^{-3})
B1	2	10	0.14	2.1	33.5	377.0
B2	2	10	0.18	2.6	2.8	2.1

Table 5-15. BC2 chicane dipole single element tolerances for 8% emittance growth each ($\gamma\epsilon_{x0} = 3 \times 10^{-6}$ m, $\gamma\epsilon_{y0} = 3 \times 10^{-8}$ m, $\sigma_\delta = 1.5\%$). Quadrupole and sextupole field harmonics (b_1/b_0 and b_2/b_0) are evaluated at a radius of 100 mm. They generate 1st and 2nd order dispersion.

5.5.4 Space Charge and Coherent Radiation

The space-charge field of the beam is not insignificant when it exits the low-energy and the high-energy bunch compressors. This field can drive coupling resonances and increase the beam emittance or add to the beam halo. However, estimates of these effects indicate that they are small because the beams are rapidly accelerated and the optics has been chosen to avoid the most significant resonance, namely $2\psi_x \approx 2\psi_y$.

The space-charge fields in the bending magnets manifest themselves in a slightly different manner. There have been a few estimates of these effects which can be separated into a centrifugal space charge force (CSCF) and a coherent synchrotron radiation force (CSR). A calculation of the CSCF in bunched beams [Carlsten 1995] shows that this should not be a limitation in the NLC. In contrast, the CSR may be significant. Here, the longitudinal electric field of the coherent synchrotron radiation induces an energy variation along the bunch [Derbenev 1995]; the coherent radiation field is similar to a longitudinal wakefield except that the field travels faster than the bunch and acts on leading particles rather than a normal wakefield which acts on trailing particles. In the wigglers and chicanes, this field will destroy the achromaticity of the compressors, thereby causing an increase in the horizontal emittance; the effect is not important in the 180° arcs where the dispersion is smaller and bends are shorter.

If we neglect the shielding effects of the vacuum chamber, the induced energy spread is predicted to be roughly [Derbenev 1995]

$$\sigma_\delta \approx 0.2 \frac{N r_0 L_d}{\gamma R^{2/3} \sigma_z^{4/3}}, \quad (5.46)$$

where N is the bunch charge, L_d and R are the bending magnet length and bending radius, and r_0 and γ are the classical electron radius and the relativistic factor.

As stated, this induced energy spread will break the chromatic cancelation of the wiggler or chicane. The increase in the horizontal emittance is roughly [Raubenheimer 1995b]

$$\Delta\gamma\epsilon_x \approx 0.5\alpha^2 \sigma_x \frac{I}{17kA} \left(\frac{R}{\sigma_z} \right)^{1/3} \quad (5.47)$$

where α is the bend angle and I is the bunch current. In both the NLC low- and high-energy compressors, this predicts roughly 5% horizontal emittance growth.

Finally, the long-wavelength radiation is suppressed by boundary conditions imposed by the vacuum chamber. The point where shielding becomes important can be estimated as:

$$\sigma_z \gtrsim \sqrt{\frac{h^2 w}{\pi^2 R}} \quad (5.48)$$

where h and w are the full height and width of the chamber and R is the bending radius. In the low- and high-energy bunch compressors, we find that shielding is important for bunch lengths greater than $500\ \mu\text{m}$ and $150\ \mu\text{m}$, respectively. These values are close to the fully-compressed bunch lengths and thus the chamber shielding may reduce the predicted emittance dilution.

At this time, this emittance dilution has not been observed experimentally and thus there is some uncertainty in the calculations. Regardless, it does not appear that the coherent radiation will be a significant limitation to the NLC compressors. It should be noted that this might be one reason not to consider a single stage compressor as the predicted dilution becomes much more important.

5.5.5 Ion Effects

At the start of the prelinac, all ions created by the beam are stably trapped within a single bunch train, except for hydrogen ions which are over-focused between bunches. An upper limit on the critical ion mass is obtained for the maximum current of 90 bunches with 1.5×10^{10} particles each. In this case the critical ion mass is six proton masses at the start and 29 at the end of the prelinac.

The ions will, first, increase the rate of filamentation, due to the additional focusing experienced by the trailing bunches, and, second, cause a nonlinear octupole-like coupling of horizontal and vertical betatron motion [Raubenheimer 1992]. At a pressure of 10^{-8} Torr, the focusing along the bunch train varies by $\Delta Q_y \approx 10^{-4}\ \text{m}^{-1}$ assuming 90 bunches of 1.5×10^{10} particles each. To attain an additional filamentation due to ions which is comparable to that caused by the intrinsic energy spread, a pressure of less than 10^{-9} Torr has to be achieved. Finally, a separation of the horizontal and vertical phase advances by about 5% effectively eliminates the effect of nonlinear coupling.

As in the damping rings and main linacs, the ionization of the residual gas may give rise to a transverse multibunch instability of the electron bunch train in the prelinac. At a pressure of 10^{-8} Torr, the estimated growth time τ_{asym} of this instability is about 90 ns [Raubenheimer 1995a], assuming 90 bunches of 1.5×10^{10} particles each and ignoring decoherence of the ion oscillations. The ion-driven instability causes an increase of the Fourier component at the ion-oscillation frequency of the vertical bunch positions. Traversing the 500-m-long prelinac at a pressure of 10^{-8} Torr amplifies an initial bunch-to-bunch displacement at this Fourier component, characterized by an action value J_{y0} , by a factor 3×10^4 . As an example, if the original perturbation is due to the finite number of electrons in the train, the initial action value is about $J_{y0} \approx \sigma_y^2 / (2\beta_y N_b n_b) \approx 3 \times 10^{-24}$ m-rad, which yields a negligible emittance growth of $\Delta(\gamma\epsilon_y) \approx 2 \times 10^{-15}$ m-rad.

However, assuming that the initial perturbation is due to a realistic bunch-to-bunch orbit jitter of about 1% σ_y , the emittance blow-up can be as large as 500%. Fortunately, ion decoherence, due to the variation of the vertical ion oscillation frequency with the horizontal position, increases the rise time of the instability by about a factor of two or three, thereby relieving the pressure tolerance by the same factor [Stupakov 1995].

Taking the decoherence into account, and assuming a partial pressure of 5×10^{-9} Torr of CO , the emittance increase resulting from an initial 1% σ_y harmonic bunch-to-bunch offset at the ion frequency would be about 10%. Because the main constituent of the vacuum is hydrogen, which is not trapped in the beam, this is a relatively loose vacuum requirement.

Until further studies and experiments improve our understanding of the ion-driven instability and possible cures, it is assumed that the required pressure in the prelinac is below 10^{-8} Torr of which more than 70% would be H_2 .

	Wiggler	Arc	Chicane
N_γ	99	662	28
E_c (keV)	3.5/4.6	25	7.4
ΔE_{rad} (keV)	134	5300	66
$\Delta\delta_{rms}$ (%)	$1.3 \cdot 10^{-3}$	$4 \cdot 10^{-3}$	$8 \cdot 10^{-5}$
$\Delta(\gamma\epsilon_x)$ (10^{-6} m-rad)	0.039	0.038	0.0015
$\Delta(\epsilon_x)/(\epsilon_{x0})$ (%)	1.3	1.3	0.05

Table 5-16. *Effects of synchrotron radiation in wiggler, arc, and chicane.*

5.5.6 Synchrotron Radiation

Incoherent synchrotron radiation in bending and quadrupole magnets may increase the energy spread and, more importantly, dilute the horizontal and (if linear coupling or vertical dispersion is nonzero) the vertical emittance. The total emittance growth in the bunch compressor should be smaller than 5% horizontally, and less than 1-2% vertically. The latter number translates into a tolerance for the tuning procedures and the diagnostics. In addition, the induced energy-spread should be small compared with the original energy spread of the bunch.

The effects of synchrotron radiation in the longitudinal and the horizontal phase space are summarized in Table 5-16 for wiggler, arc, and chicane. In all cases, the number of radiated photons per electron, N_γ , is much larger than one so that the resulting net effect can be described by a Gaussian distribution. The critical energy $E_c \equiv 3\hbar c\gamma^3/(2\rho)$ is only a few keV. Therefore, the radiating particles stay inside the energy acceptance of the system. The average energy loss, ΔE_{rad} , and the additional rms momentum spread due to synchrotron radiation, $\Delta\delta_{rms}$, are both small. The change of the horizontal emittance can be estimated from [Raubenheimer 1994a]

$$\Delta(\gamma\epsilon_x) \approx 4 \cdot 10^{-8} \left(\frac{E}{\text{GeV}} \right)^6 I_5 \quad (5.49)$$

where I_5 denotes the fifth synchrotron radiation integral [Helm 1973]. A mismatch between the synchrotron radiation effects and the original beam distribution can lead to an emittance growth which is larger than predicted by Eq. 5.49 [Spence 1993]. This difference could be especially important for the chicane, since the phase advance over the four bending magnets is only about 90° . To estimate the actual emittance growth, a simulation study has been performed using the computer code MAD [Grote 1990]. The simulations show an emittance growth of approximately $\Delta(\gamma\epsilon_x) \approx 2 \times 10^{-9}$ m-rad in the chicane, which is consistent with the simple estimate of Eq. 5.49, and indicates that the effect of the radiation-lattice mismatch is small. The total increase of the horizontal normalized emittance in the bunch compressor is then about 2.6%. We conclude that the effects of incoherent synchrotron radiation appear insignificant.

5.6 Tolerances

5.6.1 Alignment and Field Tolerances

These are discussed in the text. In general, all transverse alignment and magnet tolerances in the bunch compression system are relatively loose. The only field tolerances that are tight are those in the spin rotator system and the bending magnet multipoles in the chicane. Both of these tolerances are eased using simple tuning techniques similar to those routinely used in the SLC bunch compressors. All of the magnet alignment tolerances are substantially larger than the expected resolution from the beam-based alignment; the alignment techniques are discussed in greater detail in Chapter 7.

5.6.2 Tolerances on RF Phase, Energy, and Intensity

Some of the tightest tolerances in the bunch compressor system are those on the (relative) rf phase stability. The tolerance on the phase difference of electron and positron compressor rf is set by the loss of luminosity when the beams do not collide at the minimum waist position. A collision which is longitudinally offset by $\Delta s = 0.2\beta_y^*$ leads to a 2% loss of luminosity, which translates into a maximum tolerable rf phase difference $\Delta\phi_{SB,e+e-}$ or $\Delta\phi_{LB,e+e-}$ between the S-band and L-band rf systems, respectively, on the electron and positron side. This tolerance can be as tight as 0.17° (Table 5-17) and may be difficult to meet because the compressors are located more than 20-km apart.

Even tighter tolerances on relative-phase stability have to be achieved, on either side of the IP, between different compressor and linac rf systems. If the beam is injected into the main linac at a wrong phase, the final beam energy changes. This energy change sets a tolerance on the relative rf phase stability of linac and compressor rf, and on the allowed bunch-to-bunch energy variation due to multibunch beam loading or intensity variation in the various compressor subsystems.

In case the beam is nominally off-crest by an X-band phase angle ϕ_{XB} , the maximum allowed phase error $\Delta\phi_{XB}$ (in degree), which causes a 0.1% average energy change, is given by

$$\Delta\phi_{XB} \leq \frac{10^{-3} 360}{2\pi \tan \phi_{XB}} \quad (5.50)$$

and the corresponding longitudinal position error (meter) in main linac and second compressor is

$$\Delta z_{XB} \leq \frac{10^{-3} \lambda_{XB}}{2\pi \tan \phi_{XB}} \quad (5.51)$$

where λ_{XB} denotes the wavelength of the X-Band rf (26 mm). The maximum phase error $\Delta\phi_{SB}$ for the S-band rf of the second compressor is equal to

$$\Delta\phi_{SB} (^\circ) \leq \frac{\Delta z_{XB} 360}{\lambda_{SB}}, \quad (5.52)$$

and the maximum single-bunch energy variation due to multi-bunch beam loading in the S-Band rf section is

$$\left. \frac{\Delta E}{E} \right|_{SB} \leq \frac{\Delta z_{XB}}{R_{56}^c} \quad (5.53)$$

		NLC-Ia	NLC-Ic	NLC-IIa	NLC-IIc
E_{\max}	(GeV)	267	233	534	473
N_{part}	(10^{10})	0.65	0.85	0.95	1.25
Final σ_z	(μm)	100	150	125	150
σ_y^*	(nm)	4.52	7.00	3.57	5.35
θ_y^*	(μrad)	36.17	35.02	28.59	26.75
$\Delta\phi_{SB}^{e^+e^-}$	($^\circ$)	0.17	0.27	0.17	0.27
$\Delta\phi_{LB}^{e^+e^-}$	($^\circ$)	0.50	0.56	0.44	0.62
$\Delta z_{e^+e^-}$	(μm)	50	80	50	80
ϕ_{XB}	($^\circ$)	-14.4	-15.1	-7.2	-11.0
ϕ_{PL}	($^\circ$)	-4	-5	-5	-8
$\Delta\phi_{XB}$	($^\circ$)	0.22	0.21	0.45	0.30
$\Delta\phi_{SB}$	($^\circ$)	0.055	0.053	0.112	0.073
$\Delta\phi_{LB}$	($^\circ$)	0.16	0.11	0.29	0.16
$\Delta\phi_{PL}$	($^\circ$)	0.32	0.22	0.57	0.33
Δz_{XB}	(μm)	16	15	33	21
Δz_{SB}	(μm)	16	15	33	21
Δz_{LB}	(μm)	95	63	167	96
Δz_{PL}	(μm)	95	63	167	96
$\frac{\Delta E}{E} _{XB}$	(10^{-3})	1.0	1.0	1.0	1.0
$\frac{\Delta E}{E} _{SB}$	(10^{-3})	0.45	0.43	0.91	0.59
$\frac{\Delta E}{E} _{LB}$	(10^{-3})	0.19	0.13	0.33	0.19
$\frac{\Delta E}{E} _{PL}$	(10^{-3})	4.0	4.7	6.1	5.3
$\frac{\Delta N}{N} _{XB}$	(%)	6.4	4.5	8.1	5.7
$\frac{\Delta N}{N} _{SB}$	(%)	30	21	40	20
$\frac{\Delta N}{N} _{LB}$	(%)	290	148	351	154
$\frac{\Delta N}{N} _{PL}$	(%)	116	105	121	80

Table 5-17. Tolerances on rf phase, single-bunch energy, and intensity in the various compressor subsystems for four different NLC scenarios, corresponding to either 2% loss of luminosity or to a 0.1% change of average bunch energy, at the end of the main linac. Subindices *XB*, *SB*, *LB* and *PL* refer to main X-band linac, S-band rf of the second compressor, L-band rf of the first compressor, and the prelinac (S-band rf), respectively.

The tolerances for the first (L-Band) compressor are obtained in a similar way, taking account of the compression ratio $-R_{56}^c/R_{56}^a$ of the second stage. We thus have

$$\Delta z_{LB} \leq -\frac{\Delta z_{XB} R_{56}^a}{R_{56}^c}, \quad (5.54)$$

$$\Delta \phi_{LB} (^\circ) \leq \frac{\Delta z_{LB} 360}{\lambda_{LB}}, \quad (5.55)$$

$$\left. \frac{\Delta E}{E} \right|_{LB} \leq \frac{\Delta z_{LB}}{R_{56}^w}. \quad (5.56)$$

There is also a tolerance on the bunch-to-bunch energy variation in the prelinac. A relative energy error δ_{PL} at the end of the prelinac causes a change of the longitudinal position Δz_{XB} of the bunch center at the exit of the second compressor, which in lowest order is given by

$$\Delta z_{XB} \approx \frac{1}{2} f_{2,c} k_{2,c} R_{56}^a{}^2 R_{56}^c \delta_{PL}^2 + T_{566}^c (-f_{2,c} R_{56}^a + 1)^2 \delta_{PL}^2 + \mathcal{O}(\delta_{PL}^3) \quad (5.57)$$

from which the maximum allowed energy variation $\Delta E/E|_{PL} \equiv \delta_{PL, max}$ in the prelinac can be estimated:

$$\left. \frac{\Delta E}{E} \right|_{PL} \leq \frac{3}{4} \left[\frac{\Delta z_{XB}}{\frac{1}{2} f_{2,c} k_{2,c} R_{56}^a{}^2 R_{56}^c + T_{566}^c (-f_{2,c} R_{56}^a + 1)^2} \right]^{\frac{1}{2}} \quad (5.58)$$

where the factor 3/4 in front is an empirical correction due to finite bunch length and higher-order contributions.

A phase error in the prelinac causes both an energy error at the exit of the prelinac and a phase error in the main linac. Both these effects lead to a change of the final energy, but the latter effect is ten times as severe as the former. For this reason, the energy error at the end of the prelinac may be ignored, and the tolerance on the longitudinal position in the prelinac is the same as that for the L-Band compressor, while the phase tolerance (in degree S-Band) is simply twice that of the L-Band rf.

A limit on single-bunch intensity variation arises from the above tolerances on energy and from the single-bunch beam loading. Denoting the relative energy change per 10^{10} particles due to longitudinal wakefields by δ_{10} , the intensity tolerance for an rf section may be written as

$$\frac{\Delta N}{N} \leq \frac{\Delta E}{E} \cdot \frac{10^{10}}{\delta_{10} N}, \quad (5.59)$$

where $\Delta E/E$ designates the allowed energy variation.

Finally, if the ΔF beam loading compensation is used in either of the two compressor stages or the prelinac, then there are two additional rf systems which are used for multibunch beam loading compensation. The tolerance on the phase stability for these rf systems follows directly from the tolerable energy error ΔE in the pertinent compressor subsystem:

$$\Delta \phi_{mbc} \leq \Delta E / V_{mbc} \quad (5.60)$$

where V_{mbc} is the amplitude of the compensating rf voltage. The limit on the energy deviation, ΔE , is taken from Eqs. 5.53, 5.56 or 5.58, respectively. Similarly, the allowed frequency error for the compensating rf is determined by the corresponding phase (or energy) error at the end of the bunch train, *i.e.*,

$$\frac{\Delta f}{f} \leq \frac{c \Delta E}{2\pi V_{mbc} l_{train} f} \quad (5.61)$$

		NLC-Ia	NLC-Ic	NLC-IIa	NLC-IIc
$\Delta\phi_c, BC2$	(°)	0.76	0.56	1.06	0.53
$\Delta\phi_c, BC1$	(°)	0.81	0.42	0.99	0.44
$\Delta\phi_c, PL$	(°)	0.17	0.20	0.26	0.23
$\Delta f _c, BC2$	(kHz)	17	12	23	12
$\Delta f _c, BC1$	(kHz)	18	9	22	10
$\Delta f _c, PL$	(kHz)	3.7	4.5	5.7	5.0

Table 5-18. Tolerances on phase and frequency stability for the additional rf systems which are employed to compensate multibunch beam loading, considering four different NLC scenarios. Tolerances correspond to a 0.1% change of average bunch energy, at the end of the main linac. Subindices BC2, BC1, and PL refer to the second compressor, first compressor, and prelinac, respectively. The subindex 'c' indicates the compensating nature of the rf.

Table 5-17 compiles tolerances on main rf and T_{566} -compensating rf for all compressor subsystems and four different NLC scenarios. Some tolerances shown in the table are easy to achieve, for instance those on the intensity. Other tolerances may need more attention. For example, the phase-stability tolerance for the second compressor is less than a tenth of a degree S-Band.

Table 5-18 lists tolerances on phase and frequency stability for the three double rf systems which compensate for multibunch beam loading in the different compressor subsystems. In this case, the tolerances are tightest for the prelinac, where a phase stability of about 0.2° S-band needs to be achieved. By comparison, the phase tolerances for the compensating rf of the two compressor stages are at least 0.4° S-band. They are, thus, looser than those of the corresponding main rf systems.

5.7 Conclusions and Comments

A design of a two-stage bunch compressor has been described that meets all specifications, as far as single- and multibunch dynamics is concerned. The bunch compressor has been designed in view of NLC-I and NLC-II, *i.e.*, for a c.m. energy of 0.5 and 1 TeV, and may have to be reevaluated once a specific operating range for NLC-III, with 1.5 TeV-c.m. energy, is determined.

Possible topics of further study in the bunch-compressor design are the following: First, if attempts are successful to correct the synchronous phase variation in the damping rings, the bunch compressor may be simplified and shortened. Second, a final value has to be chosen for the $R_{56}^{a,c}$ matrix elements of arc and chicane. A reduction of the present values would reduce the (significant) length of the rf system in the second compressor, at the expense of increased sensitivity to the incoming beam conditions. In particular, the choice of $R_{56}^{a,c}$ depends, of course, on the assumed initial phase variation. Third, the possibility of and schemes for bunch shaping need to be explored. Also, the design of two 90° compressor stages as an alternative to the present "90°/360°" scheme could be investigated. Next, one or both compressor stages may be redesigned so as to reduce the T_{566} -matrix elements. This would improve the performance in the longitudinal phase space, and could also reduce the length of the bunch compressor.

As a final point, we note that a single-stage compressor remains the most attractive alternative to the present design. A single stage would be shorter, easier to tune, and would improve the longitudinal dynamics at high intensity. The main disadvantage is that the nonlinearities in the longitudinal phase space are more severe, because of the much larger energy spread. Consequently, for a single stage, the T_{566} -matrix element has to be reduced to about a third of the R_{56} -matrix element. The residual nonlinearity can then be compensated by a decelerating rf as in the double-stage scheme. A small T_{566} -matrix element may be realized by placing quadrupoles at dispersive locations and/or by adding sextupoles. In reducing the T_{566} , care has to be taken, since the emittance dilution in the transverse phase space has to remain acceptable for an rms energy spread as large as 5%. So far, attempts to design a single-stage compressor with satisfactory performance in all phase-space dimensions have not been successful. Nevertheless, this option should be pursued further.

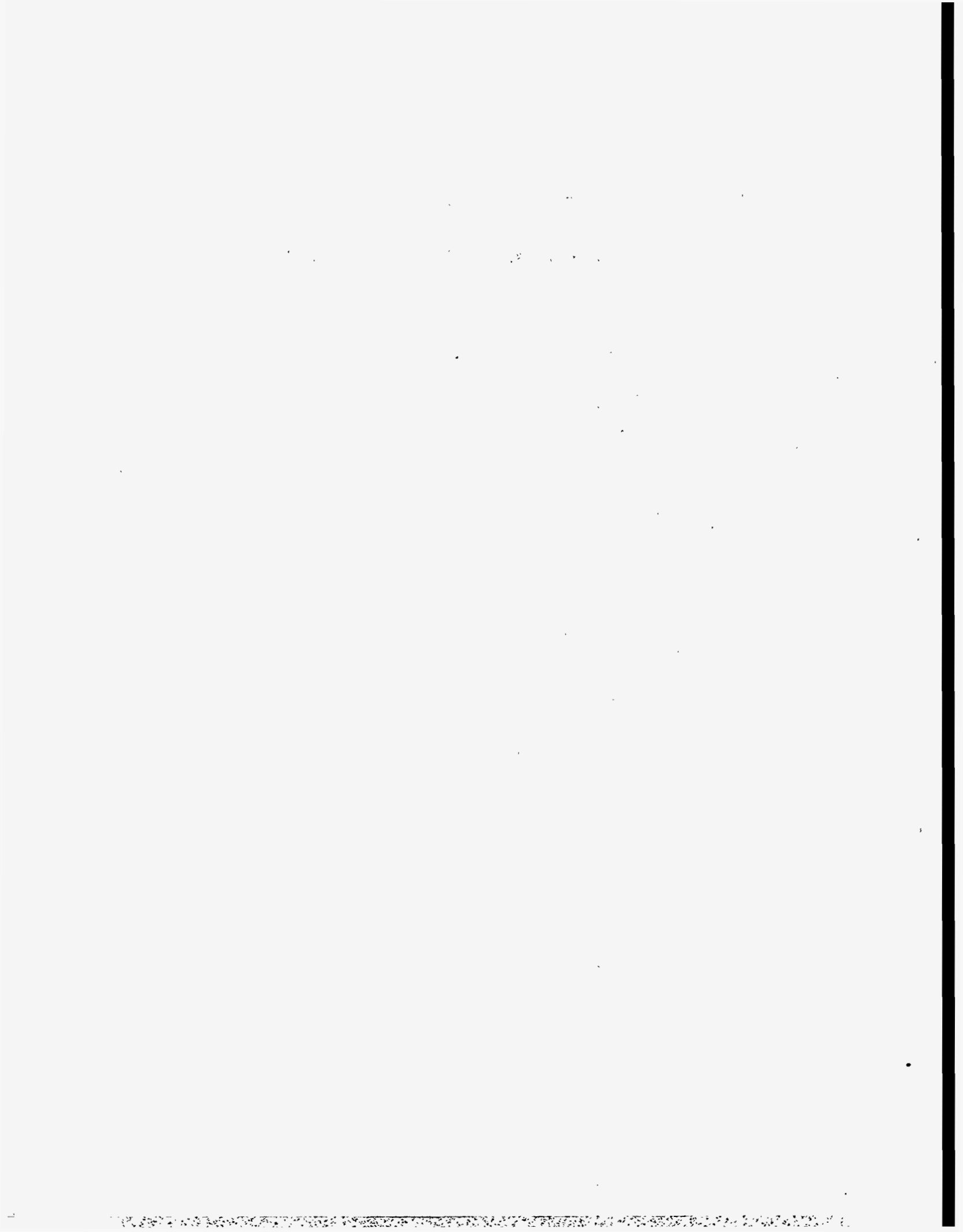
References

- [Bane] The program LITRACK for simulating longitudinal wakefield effects in linear accelerators has been written by K. Bane.
- [Bane 1995] K. Bane, "The Short-Range Wake Field for the NLC X-Band Structure", NLC-Note-9 (1995).
- [Brown 1977] K. Brown, F. Rothacker, D. Carey, C. Iselin, "TRANSPORT - A Computer Program for Designing Charged Particle Beam Transport Systems", SLAC-91 (1977).
- [Brown 1980] K.L. Brown *et al.*, CERN 80-04, (March 1980).
- [Burke 1995] D. Burke, "Proposal for New NLC Operating Plane", SLAC memorandum, unpublished (1995).
- [Carlsten 1995] B.E. Carlsten and T.O. Raubenheimer, "Emittance Growth of Bunched Beams in Bends," *Phys. Rev. E* 51:1453 (1995).
- [Delahaye 1985] J.P. Delahaye and J. Jäger, "Variation of the Dispersion Function, Momentum Compaction Factor and Damping Partition Numbers with Particle Energy Deviation", *Particle Accelerators* 18, 183 (1986).
- [Derbenev 1995] Y.S. Derbenev, J. Rossbach, E.L. Saldin, V.D. Shiltsev, "Microbunch Radiative Tail-Head Interaction", (DESY) TESLA-FEL 95-05 (1995).
- [Emma 1994] P. Emma, "A Spin Rotator System for the NLC", NLC-Note-7 (1994).
- [Emma 1995] P. Emma, "A Skew Correction and Diagnostic Section for Linear Colliders", in preparation (1995).
- [Fieguth 1987] T. Fieguth, "Snakes, Rotators, Serpents and the Octahedral Group", SLAC-PUB-4195 (January, 1987).
- [Fieguth 1989] T.H. Fieguth, "The Optical Design of the Spin Manipulation System for the SLAC Linear Collider", *Proc. of the 1989 Part. Acc. Conf.*, Chicago, IL (1989).
- [Grote 1990] H. Grote and F. C. Iselin, *The MAD Program, Version 8.1, User's Reference Manual*, CERN/SL/90-13 (AP) (1990).
- [Helm 1973] R.H. Helm, M.J. Lee and P.L. Morton, M. Sands, "Evaluation of Synchrotron Radiation Integrals", *Proc. of the 1973 Part. Acc. Conf.*, San Francisco, CA; *IEEE Trans. Nucl. Sci.* NS-20, 3, 900 (1973).
- [Kikuchi 1992] M. Kikuchi, "Multi-Bunch Energy Compensation in Bunch Compressor of Linear Colliders", *Proc. of the 1992 High Energy Acc. Conf.*, Hamburg, Germany, 864 (1992).
- [Miller 1995] R. Miller, private communication (1995).
- [Oide 1994] K. Oide, discussed at XLC miniworkshop, SLAC, Dec. 1994 (1994).
- [Palmer 1990] R. Palmer, "Prospects for High-Energy e^+e^- Linear Colliders", *Ann. Rev. Nucl. Part. Sci.* 40, 529-592 (1990).

- [Raubenheimer 1992] T.O. Raubenheimer and P. Chen, "Ions in the Linacs of Future Linear Colliders", *Proc. of LINAC 92*, Ottawa, Canada (1992).
- [Raubenheimer 1993] T.O. Raubenheimer, P. Emma, S. Kheifets, "Chicane and Wiggler Based Bunch Compressors for Future Linear Colliders", *Proc. of the 1993 Part. Acc. Conf.*, Washington, DC (1993).
- [Raubenheimer 1994a] T.O. Raubenheimer, "Bunch Compressor Parameters", NLC-NOTE-2 (1994).
- [Raubenheimer 1994b] T.O. Raubenheimer, private communication (1994).
- [Raubenheimer 1995a] T.O. Raubenheimer and F. Zimmermann, "A Fast Beam-Ion Instability: Linear Theory and Simulations", *Phys. Rev. E* **52**, 5487 (1995).
- [Raubenheimer 1995b] T.O. Raubenheimer, "Summary of the Linac Working Group", *Proc. of the MicroBunches Workshop*, Brookhaven, NY (1995).
- [Rogers 1991] R. Rogers and S. Kheifets, "Misalignment Study of the NLC Bunch Compressor", *Proc. of the 1991 IEEE Part. Acc. Conf.*, San Francisco, CA (1991).
- [Spence 1991] W. Spence, private communication (1991).
- [Spence 1993] W. Spence, "Phase Space and Synchrotron Radiation in High Energy Electron Transport Lines", *Proc. of the Emittance 93 Workshop*, KEK **93-13** 362 (1993).
- [Stupakov 1995] G. Stupakov, T.O. Raubenheimer and F. Zimmermann, "A Fast Beam-Ion Instability: Effect of Ion Decoherence", *Phys. Rev. E* **52**, 5499 (1996).
- [Woodley 1994] M. Woodley, private communication (1994).
- [Zimmermann 1994] F. Zimmermann, "Longitudinal Single-Bunch Dynamics and Synchrotron Radiations Effects in the Bunch Compressor", NLC-Note-3 (October 1994).

Contributors

- Paul Emma
- Zenghai Li
- Tor Raubenheimer
- Kathy Thompson
- Frank Zimmermann



Low-Frequency Linacs and Compressors

Contents

6.1	Introduction	320
6.2	Beam-Loading Compensation	320
6.3	Numerical simulation of beam-loading compensation	324
6.3.1	The e^+ Drive, the e^- Booster and the (e^- , e^+) Prelinacs	324
6.3.2	The e^+ Capture Linac	325
6.3.3	The e^+ Booster Linac	327
6.3.4	L-band (e^- , e^+) Bunch Compressors	329
6.3.5	S-band (e^- , e^+) Bunch Compressors	329
6.3.6	The (e^- , e^+) energy compressors	332
6.3.7	Beam-loading Compensation in the Spare Modules	332
6.3.8	Summary of the Beam-loading Compensation	332
6.4	Klystrons	333
6.4.1	S-band S65 klystron	333
6.4.2	L-band L75 klystron	334
6.5	Dipole Wakefields	335
6.5.1	Detuned Structure	335
6.5.2	Damped Detuned Structure	335

6.1 Introduction

The NLC complex has seven S-band linacs and four L-band linacs. The main L-band linac accelerates the positron beam from the positron target to 2 GeV where it enters the damping ring. In addition there are one 80-MeV L-band linac associated with the positron energy compressor at the output of the positron booster linac and two 134-MeV L-band linacs associated with the electron and positron first stage compressors at the output of the two damping rings. These linacs are run in phase quadrature with the beam to introduce the linear correlation between time and energy within each bunch which is required for compression. The seven S-band linacs are:

- 1) The Positron Drive Linac which accelerates the electrons which strike the positron target.
- 2) The Electron Booster Linac which accelerates the electron beam to 2 GeV where it enters the Electron Damping Ring.
- 3) 42-MeV electron energy compressor at the output of the electron booster linac.
- 4,5) The Electron and Positron Preaccelerators which accelerate the beams from the damping rings to 10 GeV where the second bunch compression occurs.
- 6,7) 3.85-GeV S-band linacs to produce the linear energy correlation required for each of the second-stage compressors.

These linacs share enough common characteristics and design problems that it is appropriate to discuss the rf design of these linacs together in this chapter. The principal design issues confronting the rf design of these linacs are beam loading and dipole wakefields. Except for the first 250-MeV portion of the Positron L-band linac which is inside a 0.5-T solenoid, all of these linacs must be capable of accelerating about 2-A beams with about 100-ns macropulse length. The part of the Positron L-band linac inside the solenoid needs to accelerate a total effective current of about 14 A since both electrons and positrons get captured onto their respective accelerating crests, $\lambda/2$ apart. Because the electrons are produced by ionization as well as by pair production, there are about 65% more electrons than positrons. Furthermore, the solenoid transports many particles which are outside the phase and energy range acceptable to the pre-damping ring. These excess particles will be scraped off in the energy analyzing slits after the bend immediately after the solenoid, but in the two capture sections within the solenoid they create extremely heavy beam loading.

6.2 Beam-Loading Compensation

All of these linacs are fairly heavily loaded by a beam with a pulse length much shorter than the reasonable filling times of the structures, which are in turn shorter than the ringing time, $2Q/\omega$, for the structure. In this situation, the energy of the beam will drop approximately linearly with time during the pulse as a result of beam loading. For this case there are two natural choices for beam-loading compensation: 1) ΔT (or Early Injection), *i.e.*, injecting the beam into the structure before the structure is full; 2) ΔF , *i.e.*, having one or more accelerator structures running at a frequency 1 to 2 MHz above or below the nominal frequency and roughly in phase quadrature from the accelerating phase. Thus the beginning of the pulse can be decelerated by the off-frequency section(s), while the end of the pulse is accelerated. The advantage of ΔT compensation is that the compensation occurs in every accelerator section, so that the energy spectrum can be good throughout the linac, thus minimizing emittance growth from dispersion and chromatic effects.

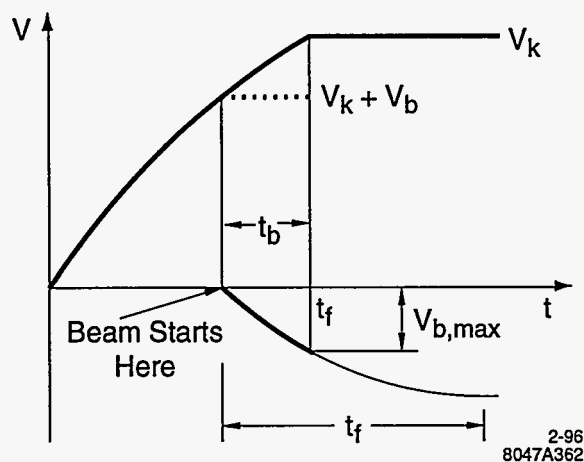


Figure 6-1. ΔT beam-loading compensation for rectangular rf input pulse.

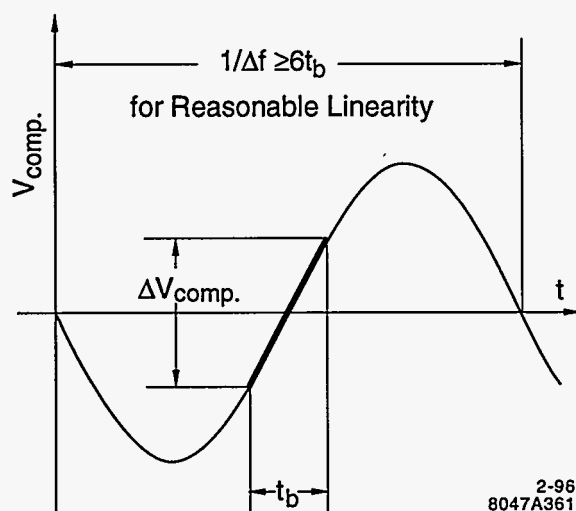


Figure 6-2. Energy gain, $V_k(t)$, in a ΔF compensation section.

The way ΔT compensation works is shown in Figure 6-1 in which the voltage $V_k(t)$ produced by a step-function rf pulse is plotted as a function of time for a traveling-wave linac section. Also plotted is the beam-induced voltage $V_b(t)$. The resultant sum of $V_k(t)$ and $V_b(t)$ is plotted for the case where the beam is turned on before the linac structure is full. To illustrate the principle of ΔF compensation, the voltage gain $V_{\text{comp}}(t)$ of a beam with an F_0 bunch structure in a ΔF -compensation section operating at a frequency $F_0 \pm \Delta F$ is plotted in Figure 6-2. The beam is bunched with a bunch-repetition frequency of 714 MHz, a subharmonic of the accelerator frequency F_0 . In an accelerator section powered by rf at a frequency $F_0 \pm \Delta F$, the bunches see a field which appears to vary with the difference frequency ΔF as shown in Figure 6-2. If the beam pulse length satisfies the relation $t_b \leq \frac{1}{6\Delta F}$ and is phased as shown, the energy gain will vary quite linearly with time.

It is instructive to calculate the power required for compensation by early injection for a rectangular rf pulse (non-sledded) in the approximation that $t_b \ll t_f \ll 2Q/\omega$, where t_b is the beam pulse length and t_f is the

structure filling time.

$$\frac{dV_b}{dt} = -\frac{i \omega r}{2 Q} L \quad (6.1)$$

$$\frac{dV_k}{dt} = \left(\frac{P v_g \omega r}{Q} \right)^{1/2} \quad (6.2)$$

$$V_k^2 = L^2 \frac{P \omega r}{v_g Q} \quad (6.3)$$

where V_b = beam-induced voltage
 i = beam current
 L = accelerator length
 V_k = voltage produced by klystron power
 P = klystron power
 v_g = average group velocity in the structure

Setting $\frac{dV_k}{dt} = -\frac{dV_b}{dt}$ and multiplying by Eq. 6.3 we find that

$$P = \frac{i V_k}{2} \quad (6.4)$$

This remarkable result says that for compensation by early injection the klystron power has to be approximately equal to half the power absorbed by the beam *and is independent of the shunt impedance of the structure and the length of the linac* under the inequalities stated above. For compensation by early injection with the approximation used here the filling time must satisfy the relation:

$$\frac{t_b}{t_f} = \frac{V_b}{V_k} \quad (6.5)$$

With ΔF compensation one is free to pick the filling time. In the approximation that $t_b \ll t_f$, and that r/Q is independent of group velocity, the beam-induced voltage is independent of filling time (see Eq. 6.1). For filling times short compared with $2Q/\omega$ the peak power required varies inversely with filling time. One can also reduce the power required by decreasing the gradient. For a given required voltage, the power varies linearly with gradient, however the beam-induced voltage varies linearly with length or inversely with gradient. Increasing the beam-induced voltage tightens the tolerance on the compensation and increases the fraction of the overall length and the fraction of the total rf power which must be dedicated to the off-frequency compensating sections. One finds that for either ΔT or ΔF compensation there is an optimum product Lr/Q which minimizes the power required for accelerating the beam to a given voltage and compensating for beam loading. The optimum is very broad and changing the product by a factor of two in either direction only raises the power required by about 15%. We have chosen an unloaded gradient of 25 to 30 MeV/m for the S-band accelerators to minimize dark current problems. This determines the length of the accelerator required for a given beam energy. For a fixed length the beam loading for a short pulse varies linearly with r/Q , so we pick a value about half of the optimum which increases the power required about the 15% mentioned above the minimum. With these choices the power and lengths required for ΔT compensation are somewhat greater (about 10%) than for ΔF . Our present feeling is that the ΔF system is probably easier to operate. Depending on the percentage beam loading and the energy spread after compensation, a total phase shift of 1/2 to one radian is likely to be acceptable. Thus an off-frequency

Frequency	2856 MHz
Structure type	DDS disk-loaded ^a
Structure length	3 m
# sections per module	4
Filling time	371 ns
Group velocity	0.05 c to 0.0125 c
# klystrons per module	2
Klystron power	65 MW
Rf pulse length (flattop)	4 μ s
Pulse compression	SLED I

^aDamped Detuned Structure

Table 6-1. S-band linac rf parameters.

compensating section can correct for a beam-loading voltage V_b between 1/2 and one times the peak voltage of the section.

The principal disadvantage of the ΔF compensation, is that the beam energy spread reaches half of the compensation of a single off-frequency section. The compensation section then overcorrects by a factor of two which reverses correlation of energy with time during the pulse. In order to maintain a small enough energy spread to achieve an acceptable emittance growth it appears necessary to distribute the power from one klystron running off frequency to a number of short accelerator sections, so that each correction is acceptably small. The compensation sections should be placed so that the beam-loaded particles have the same total betatron phase advance as the first particles in the bunch train which have no beam loading. This is approximately equivalent to saying that they should spend as much time (or distance along the accelerator axis) high in energy as they do low in energy. That is the spatial average along the accelerator axis of the difference in energy between the first particle and the last particle should vanish. One can either choose to have short ΔF sections after each regular sections or to have one or two long ΔF sections in each of the accelerator modules. It appears to us that the high power microwave distribution system to many short ΔF compensation sections becomes unreasonably complicated and expensive. Using long ΔF sections will, however, result in poor energy spectrum and associated emittance growth. Therefore, we have chosen to use ΔT compensation for most of the low frequency linacs. The positron capture linac (inside the solenoid) requires ΔF compensation to achieve a acceptable multibunch energy spread because of the extremely high current. It is desirable to use ΔF compensation on the S-band bunch compressors, because the tuning to minimize the energy spread is very straightforward for ΔF compensation.

Table 6-1 presents the preliminary parameters for the S-band structure and rf system. The klystrons are assumed to be like the 65-MW 5045 klystrons, 240 of which power the existing SLAC linac. The useful power at the load is assumed to be 60 MW to allow for attenuation.

L-band Positron Linac: The initial acceleration of the positrons, from the target to the Positron Damping ring at 2 GeV, is done in a L-band linac with 1428-MHz rf power. The reason for this is that the four-dimensional phase space acceptance of a linac varies as λ^4 . Thus, accelerating in a 1428-MHz linac instead of a 2856-MHz linac increases the phase volume acceptance of the linac by a factor of 16. This makes the production of the high-intensity ($\approx 10^{12}$ e^+ per rf pulse) positron beam required for NLC comfortable for a conventional electromagnetic shower positron source. The beam-induced voltage per unit length for a beam pulse length much less than the filling time varies inversely as λ^2 , so beam loading becomes less of a problem. 75-MW klystrons are used for accelerating the beam. For the first 200 MeV, the beam is focused by a solenoid. In this region we assume the beam loading is produced by a beam current of up to 14 A,

Frequency	1428 MHz
Structure type	Gaussian detuned
Structure length	5 m
# sections per module	4
Filling time	675 ns
Group velocity	0.046 c to 0.0115 c
# klystrons per module	2
Klystron power	75 MW
Rf pulse length (flattop)	5 μ s
Pulse compression	SLED I

Table 6-2. *L-band linac rf parameters.*

since both electrons and positrons will be captured on the appropriate E field crests. The L-band linac rf parameters are given in Table 6-2.

6.3 Numerical simulation of beam-loading compensation

The low-frequency linacs can be grouped into four groups based on their commonalities in structure and beam loading. In the following subsections we discuss the beam-loading compensation of each of the linac groups.

Two kinds of klystrons, S65 and L75, will be used to power the low-frequency linacs. The S65 klystron will be SLAC 5045 65-MW-like klystrons (see Section 6.4.1 for details), and capable of delivering 60-MW useful power, allowing for about 10% loss in the rf components. The L75 klystrons are L-band 75-MW klystrons (see Section 6.4.2 for details) which can deliver 67.5-MW useful power. We assume that the klystrons run at full power except when otherwise specified.

The numerical simulations in this section assume that the accelerator structures are dispersionless, which, we believe, is a good approximation. In this section, "energy spread" refers to the relative rms energy spread, and it is relative to the energy gain of that linac, except when otherwise specified. The actual energy spread will be a factor of $\Delta E_{\text{gain}}/(\Delta E_{\text{gain}} + E_0)$ smaller, where E_0 is the initial beam energy. The energy spread obtained in this section is the residual of the beam-loading compensation. The total energy spread of the beam should be obtained by adding in quadrature the initial energy spread to the energy spread obtained in this section.

6.3.1 The e^+ Drive, the e^- Booster and the (e^- , e^+) Prelinacs

The e^+ drive linac, the e^- booster linac, and the (e^- , e^+) prelinacs use the same kinds of klystrons and acceleration structures. It is adequate to discuss the beam-loading compensation together in this section. The only differences among these linacs are the final energy and the beam current, as shown in Table 6-3. The acceleration structure will be S-band Damped Detuned Structure (DDS) ($F = 2.856$ GHz). The beam-loading voltage is compensated by use of the ΔT compensation method.

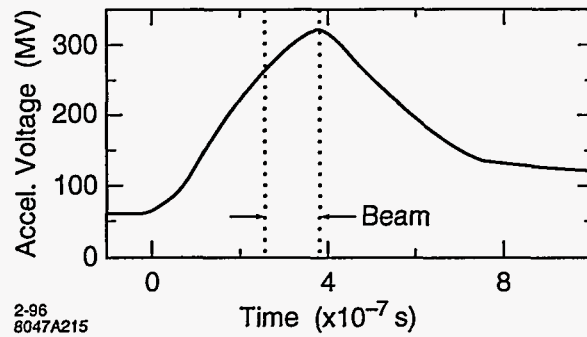


Figure 6-3. Acceleration voltage of a SLED-I driven structure.

The ΔT compensation requires that the beam be injected before the structure is full. The condition

$$\frac{dV_k}{dt} = -\frac{dV_b}{dt} \quad (6.6)$$

is essential for compensating the beam-loading voltage for the later bunches. The profile of the acceleration voltage, as a function of time, of a SLED-I driven structure is as shown in Figure 6-3. The bunch train occupies the region marked by the dotted lines. The slope of the voltage is inversely proportional to the filling time of the structure and depends on the profile of the SLED-I output. In order that Eq. 6.6 be satisfied, the filling time of the structure needs to be chosen properly, and the SLED output may also need to be modulated. The filling time of the structure in concern is chosen to be $0.371 \mu\text{s}$, which is about three times the length of the bunch train. The beam loading is about 30% of the acceleration for a beam current of 2.2 A. Amplitude modulation of the SLED-I output is required to increase the derivative of the acceleration voltage. The amplitude modulation of the SLED-I output is obtained by amplitude modulating the klystron output. Our design uses a pair of klystrons to drive one SLED-I cavity. The phases of the two klystrons are modulated in opposite directions to obtain a combined amplitude modulated output. The klystrons will be S65 klystrons. A schematic drawing of an accelerator module is shown in Figure 6-4.

The energy spread due to the beam loading of a 2.2-A beam current can, in principle, be compensated to less than 2.4×10^{-5} , and less than 1.1×10^{-5} for a 1.5-A beam current. Since the energy spread is relative to the energy gain of the linac, the actual energy spread will be lower if the initial energy of the beam is not zero. The average gradients in the structure for the two cases are 17.3 MV/m and 21.2 MV/m respectively. The energy spectrum and the SLED-I wave form used for compensating the beam loading of a 2.2-A beam current are shown in Figure 6-5.

6.3.2 The e^+ Capture Linac

The accelerator structure for the e^+ capture linac will be detuned L-band structure ($F=1.428 \text{ GHz}$) in order to have a large acceptance. The total energy gain of this linac is about 240 MeV. The beam is focused by a solenoid. We assume the beam loading in this linac is produced by a beam current of up to 14 A. For a typical disk-loaded L-band accelerator structure, the beam-loading voltage can be over 50% of the acceleration. The ΔF compensation is necessary for compensating such a high beam loading.

Since the linac is heavily loaded, short accelerator length is desirable, which can cut the power requirement for the klystrons as well as the cost of building the wrap-round solenoid. However, the length of the accelerator

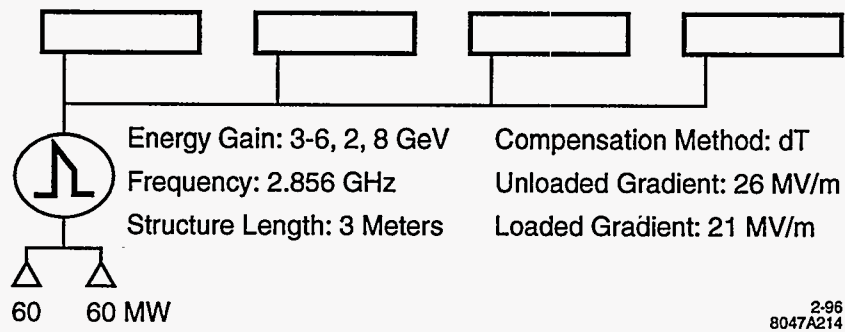


Figure 6-4. An accelerator module for the e^+ drive, e^- booster, and the (e^-, e^+) prelinacs.

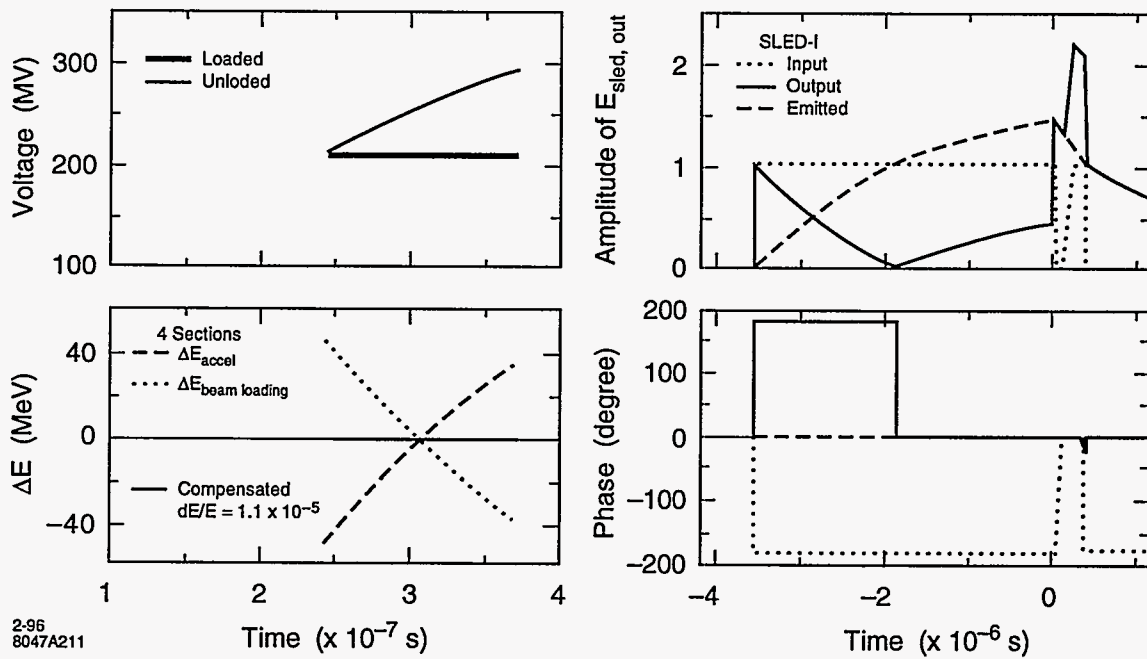


Figure 6-5. Beam-loading compensation for a 2.2-A beam current in S-band linac by using amplitude modulation of the SLED-I wave form.

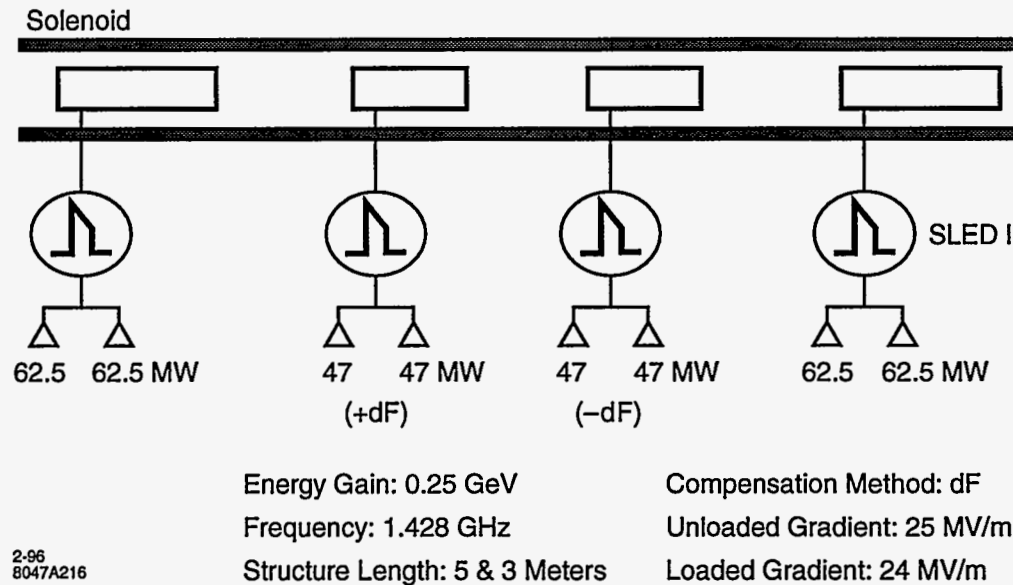


Figure 6-6. The e^+ capture linac.

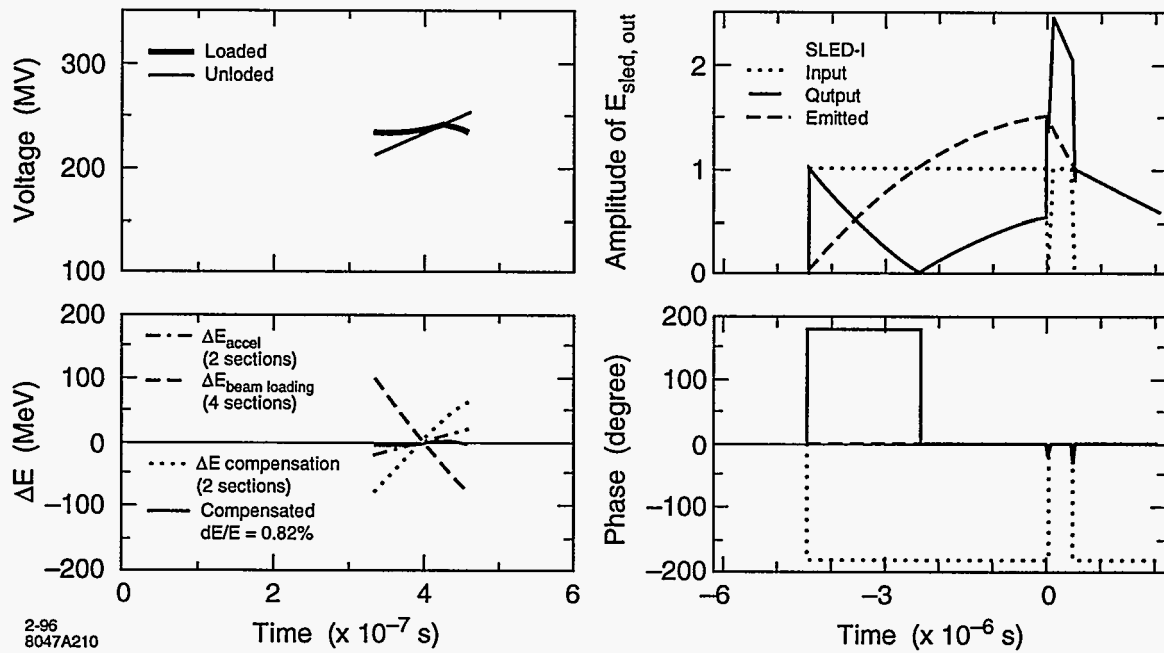
is limited by the maximum average gradient of the structure. Our criterion is that the average gradient in the L-band linac may not exceed 25 MV/m. In our design, we use two 5-m structures for acceleration and two 3-m structures for ΔF compensation. Two compensation sections operate at 1428 ± 1.428 MHz respectively to reduce the single-bunch effect. The filling time of the acceleration and compensation structures as simulated are $0.463 \mu\text{s}$ and $0.422 \mu\text{s}$ respectively. The compensation sections are required to have certain acceleration in order to reduce the gradient requirement for the acceleration sections. Each of the acceleration and compensation sections will be driven by two L75 klystrons and one SLED-I cavity. A schematic drawing of the e^+ capture linac is shown in Figure 6-6.

The acceleration klystrons will operate at 62.5-MW useful power while the compensation klystrons will operate at 47-MW useful power. This produces an average gradient for both the acceleration and compensation sections of about 25 MV/m, and a total energy gain of about 240 MeV. The center bunch runs 45° off-crest in the compensation sections, which provides a 53-MeV acceleration in each of the compensation sections. With the ΔF compensation, the beam-loading energy spread can be reduced to 0.82%, which is only a small fraction of energy spread in a single bunch. In Figure 6-12 are shown the energy spectrum of the beam-loading compensation and the SLED-I wave form for the capture linac.

6.3.3 The e^+ Booster Linac

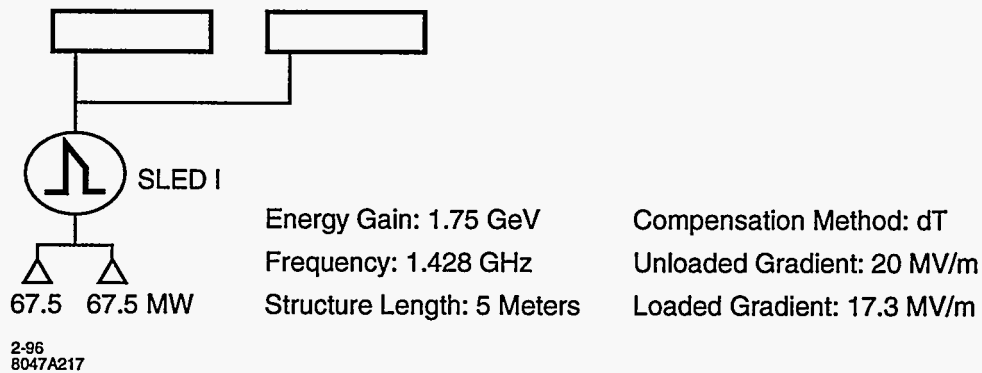
The e^+ booster linac accelerates the positron beam up to 2 GeV. The acceleration structure will be a detuned L-band structure ($F = 1.428$ GHz). The beam current in the linac is 2.75 A. The beam-loading compensation method is ΔT .

While the beam loading in the L-band structure is lower than in the S-band structure, beam-loading compensation still prefers a short filling time. The filling time of the L-band structure is chosen to be $0.675 \mu\text{s}$. The beam loading is about 14% of the acceleration for a beam current of 2.75 A. Amplitude



2-96
8047A210

Figure 6-7. Beam-loading compensation for the e^+ capture linac.



2-96
8047A217

Figure 6-8. An accelerator module for the e^+ booster linac.

modulation of the SLED-I output is required to increase the derivative of the acceleration voltage. Two L75 klystrons will be used to drive one SLED-I cavity, which in turn drives two accelerator structures. An accelerator module is shown in Figure 6-8. The SLED-I wave form for the L-band accelerator is similar to Figure 6-5. The energy spread after beam-loading compensation is less than 5×10^{-5} . The loaded gradient of the structure is 17.3 MV/m.

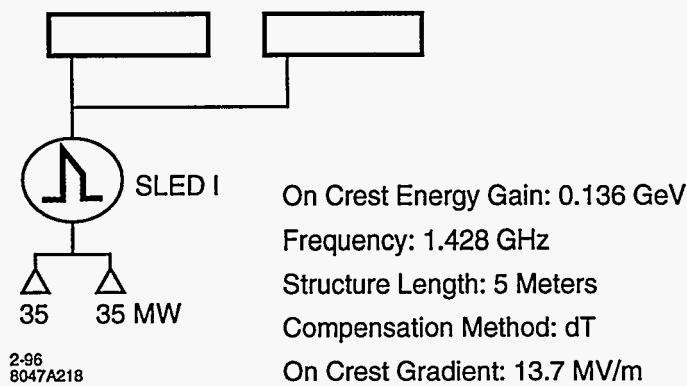


Figure 6-9. An accelerator module for the L-band compressor linacs.

6.3.4 L-band (e^- , e^+) Bunch Compressors

After the damping rings, the bunch length of the (e^+ , e^-) beams is compressed. Two L-band linacs are used to produce the linear energy spread required for bunch length compression. The beam current is 1.6 A. The bunches run in phase quadrature with the rf crest phase. The compression voltage, which is the unloaded zero phase acceleration, is required to be 136 MeV and with less than 5% variation along the bunch train. The 5-m L-band detuned structures, same as the one used in the e^+ booster linac, will be used. Each compressor linac only needs two of such acceleration structures. Two L75 klystrons running at 35-MW useful power and one SLED-I cavity will be used to drive the whole L-band compressor linac. A schematic drawing is shown in Figure 6-9.

The beam-loading voltage is 90° off the rf voltage. Simple ΔT compensation method cannot be used for beam-loading compensation. A scheme that combines the ΔT method and phase modulation was studied, and shown to be effective for beam-loading compensation. The ΔT -amplitude modulation will be used for obtaining a uniform compression along the bunch train. A phase offset to the SLED-I output during the beam time is introduced to compensate the beam-loading voltage, which is 90° off-crest. The phase offset provides an in-phase (actually 180° -out-of-phase) component of rf voltage that cancels the beam-loading voltage.

Figure 6-10 shows the energy spectrum of the compressor linac and the SLED-I input and output wave forms. The amplitude and phase modulation of the SLED-I input can be obtained by properly phase-modulating the two klystrons. The amplitude modulation is obtained by modulating the phases of the two klystrons in opposite directions. Whereas, the phase offset is obtained by phase modulating the two klystrons in the same direction. The beam loading in these linacs can be reduced to $6 \times 10^{-2}/E_0$. The compression voltage deviates less than 3% along the bunch train.

6.3.5 S-band (e^- , e^+) Bunch Compressors

Before entering the main X-band linacs, the (e^+ , e^-) beams are further compressed in bunch length in each of the respective accelerators. S-band linacs are used to produce the linear energy spread required for bunch length compression. The beam current in these linacs is 1.5 A. The compression voltage, or the unloaded

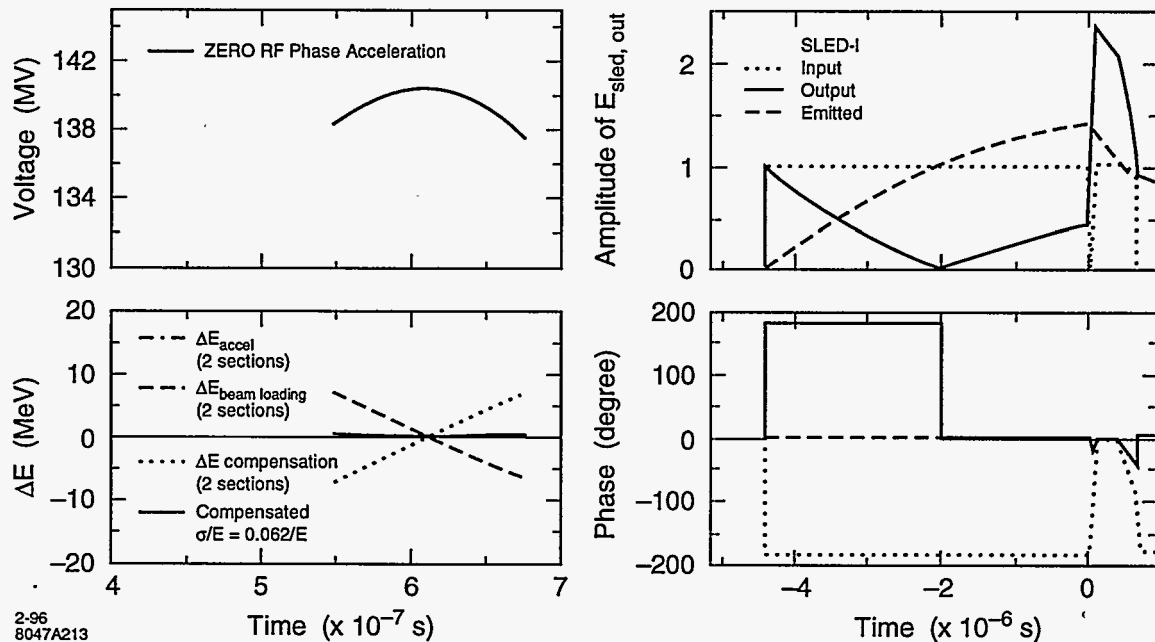


Figure 6-10. Beam-loading compensation for the L-band compressor linacs.

zero phase acceleration, is required to be 3850 MeV, and the deviation of the compression along the bunch train should be less than 5%. The beam loading in these linacs is relatively high. The ΔF sections will be used for beam-loading compensation, while the ΔT scheme will be used in the regular sections to obtain a uniform compression voltage. Both the ΔF and ΔT sections will be 3-m S-band DDS structures.

Two L65 klystrons and one SLED-I cavity will be used to drive four regular acceleration sections. Amplitude modulation of SLED-I output is needed to generate a uniform compression. The SLED-I wave form for the regular sections is shown in Figure 6-12. One L65 klystron and a SLED-I cavity will be used to drive one ΔF compensation section. The compensation klystron only needs to run at 42-MW useful power for an optimal beam-loading compensation. No amplitude modulation is needed for the compensation SLED-I. The ΔF sections operate alternatively at 2856 ± 1.1424 MHz through the linac to reduce the single bunch effect. A schematic drawing of an accelerator module as described above is shown in Figure 6-11.

In Figure 6-12 are shown the compression voltage and the beam-loading compensation results for an accelerator module. The optimal rf phase for the ΔF sections is 44° off-crest. At this rf phase, the ΔF sections also provide some acceleration that nearly cancels the deceleration (half the beam-loading voltage) due to the beam loading. With ΔF compensation, the beam-loading energy spread can be reduced to 0.62×10^{-3} at an energy of 10 GeV. The average gradient in the structure is about 22 MV/m.

An alternative ΔT compensation method, similar to the one used in the L-band compressors, was also investigated. It has been shown that the ΔT compensation can give better energy spectrum compared to the ΔF compensation. However, the ΔF method is more straightforward and operationally more convenient.

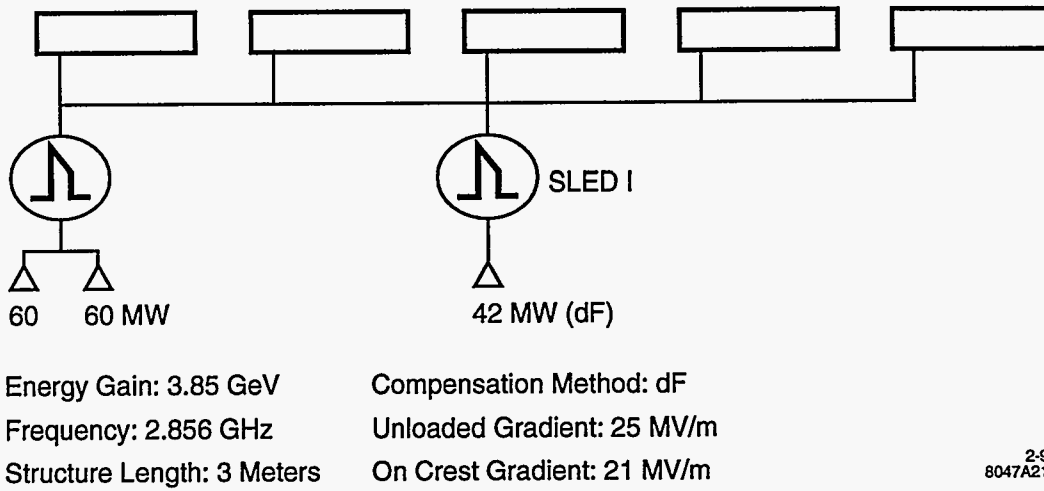


Figure 6-11. An accelerator module for the S-band compressor linac. The four regular sections are used to generate a linear correlated energy spread within a bunch. One ΔF section is used to compensate the beam loading.

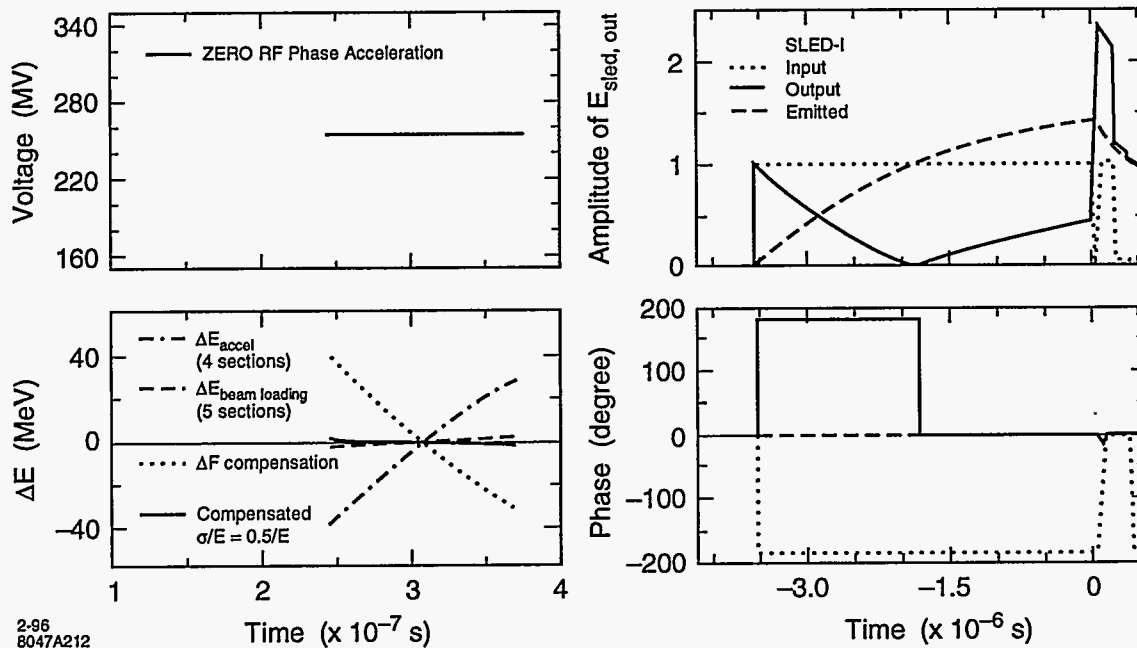


Figure 6-12. Beam-loading compensation for the S-band compressor linacs.

6.3.6 The (e^- , e^+) energy compressors

There are energy compressors associated with the electron and positron beams before they enter the damping rings. The compressor will be S-band for the electron beam and L-band for the positron beam. The compression voltage requirements for the S-band and L-band compressors are 42 MeV and 80 MeV respectively. The deviation of the compression voltage along the bunch train is required to be less than 10%, and the compensated beam-loading energy spread less than 0.1% in full width. Both compressors will use ΔT and phase modulation method to obtain a uniform compression voltage and beam-loading compensation.

S-band e^- energy compressor. The beam current in the electron energy compressor is 2.2 A. A single 2.5-m S-band accelerator section is used to generate the energy correlation needed for energy compression. The filling time of the structure is 0.371 μs . The compressor will be driven by one unsledded S65 klystron, with a 130-ns rising time in amplitude. The maximum phase offset for beam-loading compensation is 60°. The resultant full energy spread along the bunch train is 0.73×10^{-3} , and the deviation of the compression voltage is less than 5%.

L-band e^+ energy compressor. The beam current in the positron energy compressor is 2.75 A. The compressor will be composed of one 4-m L-band accelerator section. The compressor will be driven by two L75 klystrons with SLED-I pulse compression. The filling time of the structure is 0.537 μs . The maximum phase offset for beam-loading compensation is 80°. With ΔT and phase modulation, the full energy spread can be reduced to less than 0.49×10^{-3} and the compression voltage is within 5% deviation.

6.3.7 Beam-loading Compensation in the Spare Modules

Each of the linacs discussed in this chapter is designed to have about 10% spare accelerating modules. The beam induces the same transient beam-loading voltage in these spare accelerator sections as in a powered section. In order to maintain localized compensation, we will drive one of the two klystrons which drives a module with a switched drive signal at $F_0 \pm \Delta F$. With appropriate choice of ΔF , 1.428 MHz for L-band and 1.1424 MHz for S-band, this drive frequency will produce enough voltage in the standard accelerating structures when powered by one klystron to compensate for the beam loading in the same structure. Since it is very unlikely that both klystrons in a module will fail at the same time, this technique will usually maintain localized beam-loading compensation even with failed klystrons. Since ΔF is greater than the bandwidth of the SLED-I cavities, they will behave as if they are detuned.

6.3.8 Summary of the Beam-loading Compensation

A summary of the beam-loading compensation is shown in Table 6-3. In the compensation sections, the frequency offset ΔF is 1.428 MHz for the e^+ capture linac and is 1.1424 MHz for the S-band compressor linac. The notation, such as $2 \times 60/4$, in the klystron power specification means to use two klystrons running at 60-MW useful power to drive one SLED-I cavity, and the SLED-I cavity drives four accelerator sections.

	e^+ drive e^- booster	(e^-, e^+) prelinac	e^+ capture	e^+ booster	(e^-, e^+) L-band compressor		(e^-, e^+) S-band compressor	
					Bunch	Energy	Bunch	Energy
Frequency (GHz)	2.856	2.856	1.428	1.428	1.428	1.428	2.856	2.856
E Gain (GeV)	3-6, 2	8	0.250	1.75	0.136	0.080	3.85	0.042
Current (A)	2.2	1.5	14	2.75	1.6	2.75	1.5	2.2
L_{struct} (m)	3	3	5	5	5	4	3	2.5
T_f (μs)	0.371	0.371	0.464	0.675	0.675	0.537	0.371	0.371
N Struct/module	4	4	2	2	2	1	4	1
$P_{klystron}$ (MW)	2 \times 60/4	2 \times 60/4	2 \times 62.5/1	2 \times 67.5/2	2 \times 35/2	2 \times 35/1	2 \times 60/4	56 ^b /1
Klystron Pulse (μs)	4	4	5	5	5	5	4	0.5
Average Gradient (MV/m)	17.3	21.2	24.2	17.3	13.7	20.0	21.1	16.8
(MV/module)	208	254	242	173	137	80.0	253	42
Compensation Method	ΔT	ΔT	$\Delta T/\Delta F$	ΔT	ΔT	ΔT	$\Delta T/\Delta F$	ΔT
L_{struct} (m)			3				3/3	
T_f (μs)			0.422				0.371	
N Struct/module			2				1	
$P_{klystron}$ (MW)			2 \times 47/1				42/1	
Klystron Pulse (μs)			5				4	
$\sigma/(\Delta E$ (MeV))	2.4×10^{-5}	1.1×10^{-5}	8×10^{-3}	5×10^{-5}	$\frac{0.062}{E_0}$	$\frac{0.49^c}{E_0}$	$\frac{6.2}{E_0}$	$\frac{0.73^a}{E_0}$

^aMaximum energy spread.

^bNot SLEDed.

Table 6-3. A summary of low-frequency linac beam-loading compensation.

6.4 Klystrons

6.4.1 S-band S65 klystron

Klystrons operating at 2856 MHz with 65 MW of available rf output power will be required for the NLC. Such klystrons already exist at SLAC as the 5045 klystron tubes. The 5045 klystrons will need slight modifications to improve pulsewidth (from 3.5 μs to 4 μs) and average power handling capability. Table 6-4 summarizes the parameters for NLC S-band klystrons.

Beam voltage	350 kV
Beam current	400 A
Rf pulsewidth @ rep rate	4 μ s @ 180 Hz
Cathode loading	2:1 (8 A/cm ² max)
Cathode convergence	18:1 (3.525" dia.)
Rf output power	65 MW
Saturated gain	~55 dB
Efficiency	\geq 40%
Operating frequency	2856 \pm 1.4 MHz
3 dB Bandwidth	15 MHz
Solenoidal focusing field	1400 Gauss

Table 6-4. Design parameters for a 65-MW S-band klystron

Beam voltage	388 kV
Beam current	483 A
Rf Pulsewidth @ rep rate	5 to 6 μ s @ 180 Hz
Cathode loading	2:1 (6 A/cm ² max)
Cathode convergence	11:1 (4" dia.)
Rf output power	75 MW
Saturated gain	~55 dB
Efficiency	\geq 40%
Operating frequency	1428 \pm 1.4 MHz
3 dB Bandwidth	8 MHz
Solenoidal focusing field	980 Gauss

Table 6-5. Design parameters for a 75-MW L-band klystron.

6.4.2 L-band L75 klystron

Klystrons operating at 1428 MHz with 75 MW of available rf output power will also be required for the NLC. Table 6-5 summarizes the parameters for NLC L-band klystrons. A conventional klystron as described above would be approximately 123-in long and weigh approximately 900 lb. Such a klystron can be built and operated using technology currently available and proven. Indeed, 150-MW klystrons operating at twice the frequency have already been built at SLAC. However, interesting designs for multiple-beam klystrons have been studied at SLAC which indicate a substantial reduction in beam voltage without sacrificing efficiency. For example, a 10-beam klystron operating at only 273 kV would have 114 A in each beam which leads to a theoretical efficiency of 64% (giving 200 MW).

6.5 Dipole Wakefields

The S-band accelerator sections will be detuned by about 6% in a Gaussian density distribution to diminish the effect of dipole wakefields. This will cause the structure to be what might inarticulately be called "over-constant-gradient", *i.e.*, the gradient rises from the input to the output. Damping will be desirable. A manifold damped structure similar to the X-band damped detuned structure is being studied and it appears to have dipole wakefields greatly reduced from the structure without damping. Figure 6-13 shows a MAFIA [Mafia Collab.] representation of 1/4 of a cell in the proposed three-m S-band structure. In order to enhance the damping, the S-band structure was modified from a simple scaling from the X-band design: a narrow (5-mm-wide) slot extends from each manifold into each disk, extending about half the distance from the manifold to the iris in the disk. This greatly enhances the coupling to the TM_{11} -like mode which is predominant in the lowest dipole band for the parameters chosen for the S-band structure. The ringing time of microwave structure scales as $\lambda^{3/2}$, and consequently the natural scaling for accelerator structure length is $\lambda^{3/2}$. However, this scaling from the NLC X-band structure would give a cumbersome 14-m-long S-band accelerator section. Instead, a 3-m length has been chosen tentatively. With the filling time chosen for ΔT compensation, we get an average group velocity which is a factor of 2.2 smaller for the S-band structure. This change makes the lowest passband dipole predominantly TM_{11} -like, even at the zero phase advance of the passband. Slots in the disks were added to improve the coupling. Narrow slots have negligible effect on the fundamental mode shunt impedance since they are parallel to the current for that mode.

A preliminary study indicates that just detuning will be adequate for the positron L-band linac because of the strong focusing produced by the many wrap-around quads and because of the very low dipole impedance of the large aperture L-band linac.

6.5.1 Detuned Structure

The most important wakefield in the S-band structure is the first passband dipole wakefields. One finds that by detuning the dipole frequency in a Gaussian density distribution, the wakefield can be dramatically suppressed. The NLC S-band structure will be detuned by about 6% in full width with a three-sigma cutoff. The detuning can be obtained by properly varying the iris aperture and the cell radius while keeping the fundamental frequency unchanged. Figure 6-14 shows a preliminary estimation of the dipole spectrum for the S-band structure. Each frequency shown in the spectrum corresponds to one cell in the structure.

The dipole wakefield estimated by using a equivalent circuit model [Thompson] for a S-band Gaussian detuned structure is shown in Figure 6-15. It is shown that the detuned structure can strongly suppress the wakefield. However, since the dipole spectrum is a discrete and truncated Gaussian, the decoherence among the modes only helps to reduce the short-term wakefields. At a longer time scale, but shorter than the pulse length, the modes re-cohere, which results in strong long-term wakefields. Certain damping scheme is needed to minimize the long-term wakefields.

6.5.2 Damped Detuned Structure

A damping scheme similar to the X-band damping manifold will be used to damp the long-term dipole wakefield. In addition to the damping manifold, a narrow slot extends from each manifold into each disk is

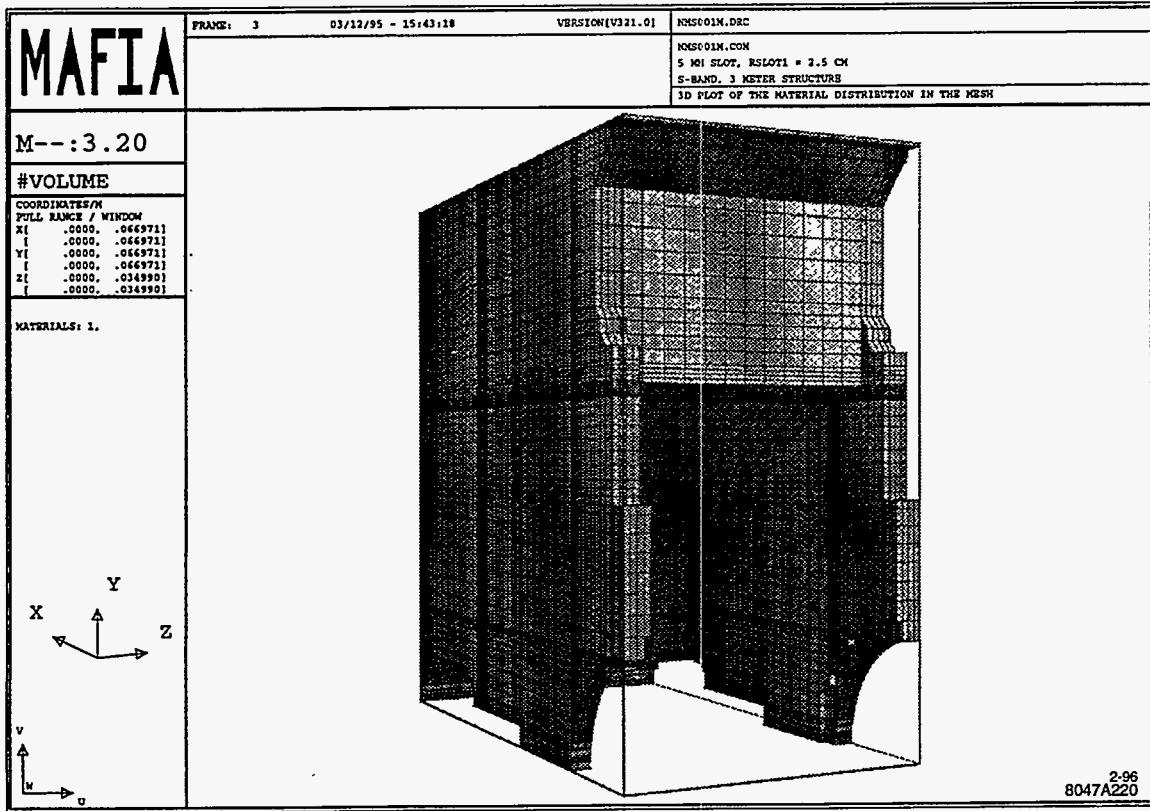


Figure 6-13. The 1/4 cell of the S-band structure.

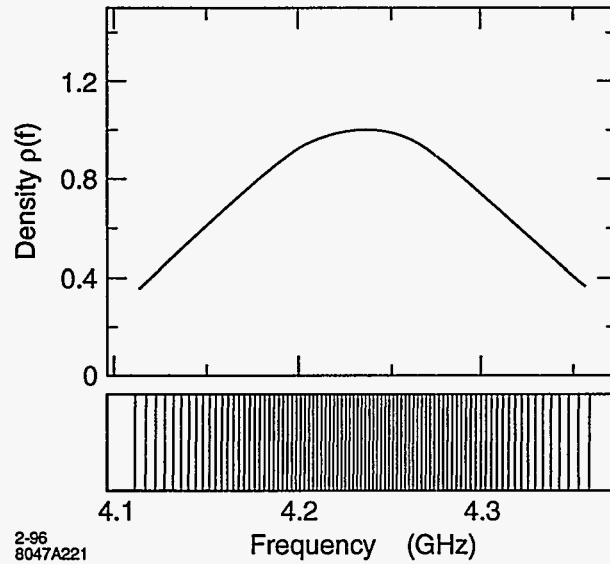


Figure 6-14. Gaussian detuned dipole spectrum for the S-band structure.

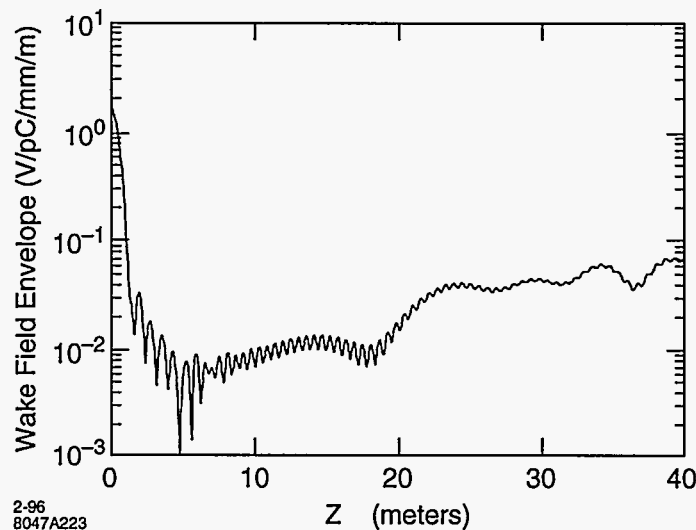


Figure 6-15. Wakefields for a detuned S-band structure.

added to enhance the coupling, see Figure 6-16. The manifold runs parallel to the structure, and is 1.39-cm wide and 2.12-cm high. The wall between the cell and the manifold is cut open with the full manifold width. The narrow slot, 0.5 cm in full width, cuts about halfway into the disk. The full height of the slot-manifold is about 3.834 cm.

The coupling between the slot-manifold and the cell is estimated by use of the 3-D MAFIA and code MDAMP [Kroll 1994] derived from the equivalent circuit model. For a Gaussian detuned structure, the iris radii a and the cell radii b are tapered. With the additional slot-manifold, the structure is three-dimensional. It is not practical to model the whole structure by use of the 3-D MAFIA. However, since the tapering is gradual and smooth, we can use a cell-to-cell approach, *i.e.*, to model the structure cell by cell. For each cell, the two irises at the two ends of the cell are assumed to have the same radius, which takes the average of the two actual radii of the irises. Periodic boundary conditions are applied to the two ends, which is equivalent to model an infinitely long constant impedance structure. The 3D MAFIA is used to model a number of selected cells along the structure. Interpolation method is used to obtain the parameters for the rest of the cells.

In Figure 6-17 is shown a MAFIA result of the dispersion relation for a cell with $a = 1.150$ cm and $b = 4.071$ cm. At zero phase advance, the lower frequency mode is the manifold mode and the upper mode is the dipole mode of the cell. As the phase advance increases, the two modes come closer to each other. The modes, however, do not cross. At a particular phase advance, 120° for this case, the field patterns of these modes switch and the dispersion curves start to separate further apart. The frequency separation of the modes at the avoided crossing point indicates the coupling strength, with large separation corresponding to large coupling. The simulation shown in Figure 6-17 has about 6% of coupling.

The coupling is insensitive to the width of the slot. In Figure 6-18 are shown the couplings for different slot widths. As one can see that the coupling only increases by 0.5%, from 5% to 5.5%, as the slot width increases from 3 mm to 5 mm. On the other hand, the coupling is sensitive to the depth of the slot. We calculated the couplings for different slot positions while keeping the whole slot-manifold geometry unchanged. Figure 6-19 shows the coupling as a function of the nearest distance of the slot to the axis. The coupling varies almost linearly to the distance and the slope is about 1% per millimeter.

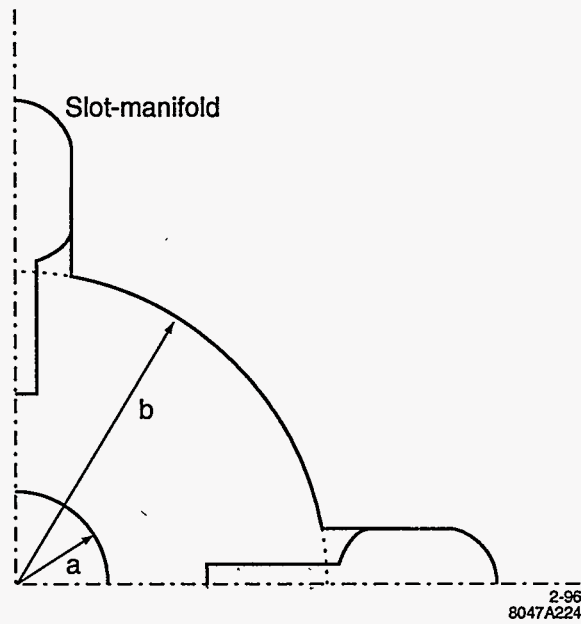


Figure 6-16. Slot-manifold damping structure for the S-band accelerator.

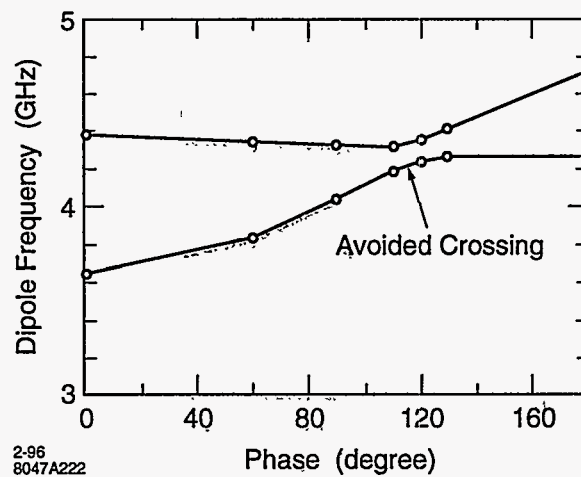


Figure 6-17. MAFIA simulation of the dispersion curve of a slot-manifold coupled S-band accelerator cell. The avoided crossing indicates the strength of the coupling.

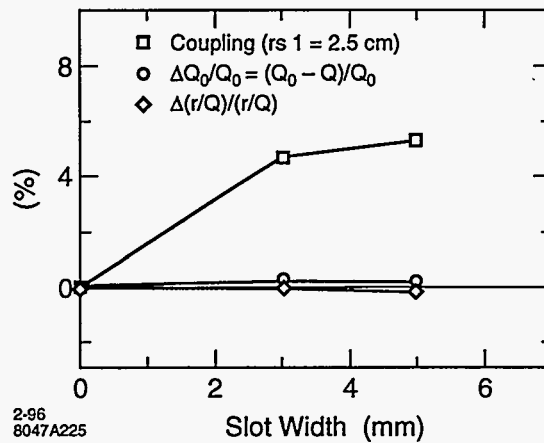


Figure 6-18. Cell-slot-manifold coupling, $\Delta Q_0/Q_0$ and $\Delta(\tau/Q_0)/(\tau/Q_0)$ for different slot width.

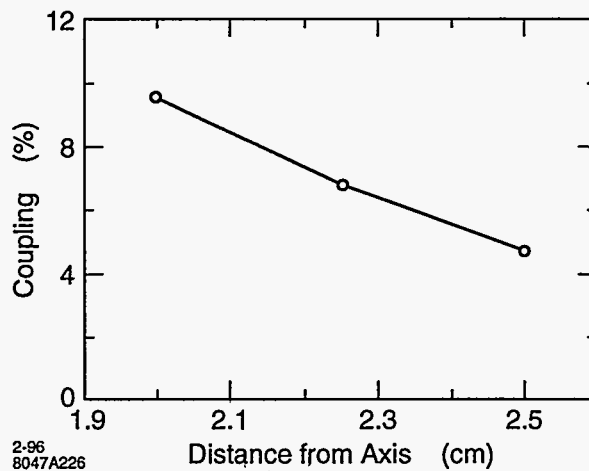


Figure 6-19. Cell-slot-manifold coupling as a function of the distance of the slot from the axis.

The coupling not only depends on the depth of the slot, but also depends on the iris opening. The iris opening is tapered in the detuned S-band structure, with large opening in the front and smaller opening toward the end. The radial position of the slot will also be tapered to get similar coupling for all cells.

The slot-manifold also preserves the Q_0 and the shunt impedance (τ) of the structure, as shown in Figure 6-18. The reason underlying this is the small wall loss of the fundamental mode induced by the slot. Even though the slot-manifold couples strongly to the TM_{11} dipole field, it has very weak coupling to the fundamental mode which is a TM_{01} mode. For the TM_{01} mode, the current in the disk is in the radial direction. The narrow radial slot in the disk has small perturbation to this current. The E and B fields of the fundamental mode are weak in the slot, which results in small wall loss and associated Q_0 and τ loss.

The dipole wakefield, estimated by using equivalent circuit model, for a damped-detuned structure with 6% cell-manifold coupling is shown in Figure 6-20. The long-term wakefield is strongly minimized by the damping structure. This indicates that the slot-manifold can provide the coupling needed for damping the wakefields.

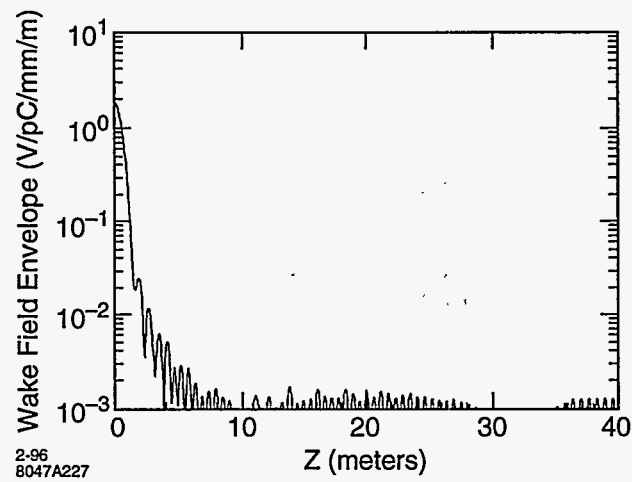


Figure 6-20. Wakefields for a damped-detuned S-band structure.

It is worthwhile to mention that the equivalent circuit model used so far is the single-band model. Recently, a multi-band equivalent circuit model has been developed, which promises to give better accuracy for wakefield estimation. Nevertheless, the single-band model has been proven experimentally in the X-band damped-detuned structure measurements to give reasonably good results.

References

- [Mafia Collab.] The Mafia Collaboration, MAFIA—The ECAD System.
- [Thompson] K. Thompson, private communications.
- [Kroll 1994] N. Kroll *et al.*, “Manifold Damping of the NLC Detuned Accelerating Structure”, SLAC-PUB-6660 (1994), in Proc. of the Sixth Workshop on Advanced Accelerator Concepts, Lake Geneva, WI, June 12-18, 1994.

Contributors

- David Farkas
- Kwok Ko
- Zenghai Li
- Roger Miller
- Tor Raubenheimer
- Daryl Sprehn
- Huan Tang
- Kathy Thompson
- Dian Yermian

Main Linacs: Design and Dynamics

Contents

7.1	Introduction	345
7.2	Parameters and Specifications	346
7.2.1	System Boundaries	346
7.2.2	Main Linac Parameters and Requirements	347
7.3	System Design	349
7.3.1	Design Overview	349
7.3.2	Linac Optics	350
7.3.3	Beam Line Layout: Normal Sections	355
7.3.4	Beam Line Layout: Special Diagnostic and Control Sections	358
7.3.5	Site Requirements and Tunnel Layout	362
7.4	Emittance Dynamics	366
7.4.1	Short-range Wakefields	367
7.4.2	Long-Range Wakefields	370
7.4.3	Single-Bunch Longitudinal Phase Space	372
7.4.4	Single-Bunch Transverse Phase Space	375
7.4.5	Multibunch Longitudinal Phase Space	384
7.4.6	Multibunch Transverse Phase Space	390
7.5	Alignment, Stability, and Feedback	392
7.5.1	Error Sources and Timescales	393
7.5.2	Alignment Procedures	397
7.5.3	Fast Transverse Feedback	399
7.5.4	Bunch-by-bunch Transverse Feedback	402
7.5.5	Linac Energy Management and Energy Feedbacks	403
7.6	Simulation Studies	406
7.6.1	Simulation Program	406
7.6.2	Objectives	408
7.6.3	Simulation Parameters	409
7.6.4	BNS Configuration	409
7.6.5	Static Imperfections and Their Correction	412
7.6.6	Full Simulation	420
7.6.7	Stability	423
7.6.8	Summary and Outlook	429
7.7	Tolerances	429
7.8	Operations and Machine Protection System	431
7.9	Linac Components	432
7.9.1	Supports and Movers	432

7.9.2	Quadrupole Magnets	437
7.9.3	Quadrupole Power Supplies	438
7.9.4	Multibunch Kicker	439
7.9.5	Chicanes	440
7.9.6	Beam Dumps	440
7.10	Instrumentation	440
7.10.1	Quadrupole and Feedback Beam Position Monitors	441
7.10.2	Feedback BPMs	443
7.10.3	Structure Beam Position Monitors	445
7.10.4	Laser Wire Scanners	448
7.11	Discussion	449

7.1 Introduction

The main linacs will accelerate electrons and positrons from an energy of 10 GeV to 250 GeV in the initial stage of running, and from 10 GeV to 500 GeV after upgrades to the rf system. For initial (upgraded) operation, trains of 90 bunches with 0.75×10^{10} (1.1×10^{10}) particles per bunch, and a 1.4-ns spacing between bunches, will be accelerated at a repetition rate of 180 (120) Hz.

There are two major design issues for the main linacs: the efficient acceleration of the beams and the preservation of the small beam emittances that are required to achieve the desired collision luminosity. The acceleration of the beams will be accomplished using X-band rf technology which is described in detail in Chapter 8. In this chapter, we discuss the design and operation of the linacs with the emphasis on the underlying beam dynamics that have driven the choices made in these regards.

The NLC linac design builds on the experience that has been gained over the last ten years from the operation of the SLC, in particular, in the development of beam-based alignment, tuning, and feedback techniques. Information from beam measurements are now routinely used in the SLC to align magnets, tune dispersion and chromaticity, compensate for accelerator structure misalignments, and to stabilize beam energy and orbits, including the beam-beam offset at the collision point. Such methods will also be crucial for the NLC operation as will become clear in this chapter. Their success in the SLC has given us confidence they will work in the NLC as well.

The NLC design also draws on the SLC operation experience in such areas as the transport of flat beams, the use of BNS damping, and linac energy management. From this, we have identified many things that need to be improved for the NLC. For example, drifts in the energy profile along the SLC linac have made tuning difficult, so in the NLC we are considering the use of beam-derived signals to keep the rf phases synchronous with the beams.

In areas where we cannot directly verify NLC operational issues with the SLC, we have built test facilities. These include ASSET for X-band structure wakefield measurements, ASTA and NLCTA for X-band accelerator technology testing, and the FFTB for final focus evaluation, although some of its features, such as quad movers, test linac concepts as well. Of these facilities, the NLCTA will provide the most direct test of the basic linac design in its ability to accelerate multibunch beams and to control the effects of beam loading. These facilities are discussed further in Chapters 8 and 11.

In this chapter, we begin with a discussion of parameters and specifications for the main linacs, followed by an overview (Section 7.3) of their design and layout. Many of the issues touched upon here (*e.g.*, alignment and stability, design of individual components, and instrumentation) will be treated in greater detail later in the chapter and elsewhere in this report, but Section 7.3 will provide a general orientation to the main issues and tradeoffs that have led to the present design.

Following the section on design and layout, we begin a detailed discussion of linac dynamics issues most closely related to emittance preservation. Of major importance are issues associated with the wakefields generated in the X-band accelerator structures by the beams. Although these structures will provide a high accelerating gradient, they will also heavily load the bunch train and will generate strong short- and long-range transverse wakefields when the bunches travel off-axis through them. Of particular concern is the long-range wakefield, which if not heavily suppressed, will resonantly amplify the betatron motion of the bunch train by many orders of magnitude. Much work to date has been devoted to solving this problem, the outcome of which is an accelerating structure that incorporates both detuning and damping of the wakefield. Most of the details of the structure design are given in the next chapter: here, at the beginning of Section 7.4, we review how the wakefields, both longitudinal and transverse, were computed for this structure.

With this foundation, we next consider the dynamics issues associated with single-bunch and multibunch phase space, both longitudinal and transverse. These include operational issues such as the optimal single-bunch energy spread profile for BNS damping and the methodology used to compensate long-range beam loading. Most of the discussion, however, is devoted to the tolerances required to prevent significant emittance dilution from such sources as misalignments and jitter (the latter can be thought of as producing a dilution of the time-averaged emittance). In particular, we consider only bare tolerances in that we assume no benefit from a beam-based types of correction, including feedback.

In the next section, 7.5, we consider issues of alignment, stability, and feedback, with emphasis on the beam-based methods that will be required in cases where the bare tolerances cannot be met. Where data is available on error sources, we compare their size to the tolerances presented in Section 7.4. We will see, for example, that beam jitter due to ground motion should not be a major problem for the linacs.

Maintaining the quadrupole and accelerator structure alignment, however, will be a key aspect of NLC operation. Quad offsets will lead to dispersive emittance growth while the structure offsets will lead to wakefield related emittance growth. In both cases, beam-based methods will be required as the bare tolerances would be impossible to meet otherwise. The proposed methods will require accurate measurements the beam position. How this will be achieved is discussed later in this chapter.

The quad and structure alignment algorithms are examples of local types of correction in that they correct the problem at the source. Also discussed are non-local correction methods where trajectory bumps, kickers, etc., are used to cancel the dilutions after they have accumulated. We generally consider them fall-back methods since they are sensitive to variations in beam transport properties between the sources of the dilution and the correction point.

Another important feature of the NLC operation will be the use of feedback systems to maintain stability on timescales of seconds and longer. They will be used to stabilize both bunch energies and trajectories at various locations along the linac. Because of their importance, we review the performance of the SLC feedback systems.

The remaining sections of the chapter contain information on beam transport simulations, tolerances, operations, linac components, and instrumentation. Of particular interest, due to the very large number of components in the main linacs, is to quantify the reliability of the various systems; studies of this are just beginning and will be discussed in future revisions of this chapter.

7.2 Parameters and Specifications

7.2.1 System Boundaries

The main linac systems boundaries are from the exit of the bunch compressor complex to the entrance of the collimation system that leads to the final focus. The main linacs consist basically of X-band acceleration sections, interspersed with quadrupoles to focus the beam, along with the necessary diagnostics and supporting systems. The rf system feeding the main linac accelerating structures and the details of the design of those structures are discussed in the next chapter.

On each rf pulse, a train of up to 90 bunches enters the main linacs from the bunch compressor. The two main tasks of the main linacs are to accelerate the bunches to high energy and to minimize the growth of the beam emittance. Even with care taken to minimize emittance growth and development of transverse "tails"

	NLC-I			NLC-II		
	a	b	c	a	b	c
N (10^{10})	0.65	0.75	0.85	0.95	1.10	1.25
Bunches/Train		90			90	
Repetition Rate (hz)		180			120	
σ_z (μm)	100	125	150	125	150	150
Unloaded Gradient (MV/m)		50			85	
Multibunch Loading (%)	25.5	29.4	33.34	22.0	25.5	28.9
Multibunch Loading (MV/m)	-12.8	-14.7	-16.7	-18.7	-21.5	-24.6
Single-bunch Loading ^a (MV/m)	-0.2	-0.3	-0.4	-0.4	-0.5	-0.6
Average ϕ_{rf}^b ($^\circ$)	-15	-15.5	-16	-7.5	-8.2	-11.2
BNS Overhead (%)	3	3	3	3.5	3.5	3.5
Feedback Overhead (%)	2	2	2	2	2	2
Repair Margin (%)	3	3	3	3	3	3
L_{acc} (m)		8150			8834	
Number Structure		4528			4908	
L_{total} (m)		8807			9550	
E_{max}^c (GeV)	266.7	250	232.2	529	500	468

^aSingle-bunch loading only includes HOM contribution.

^bAverage rf phase for 0.8% FWHM energy spread.

^cIncluding 10-GeV initial energy.

Table 7-1. NLC linac parameters.

on the beam, it will be necessary to clip the tails to minimize backgrounds in the detector; the collimation systems needed to do this are discussed in Chapter 9.

7.2.2 Main Linac Parameters and Requirements

Parameters of the main linacs are listed in Table 7-1 for NLC-I, which has a 500-GeV center-of-mass energy, and NLC-II, which has a 1-TeV center-of-mass energy. The length of each of the two main linacs in NLC-I is 8.8km. This will increase only slightly in the upgrade to NLC-II, with the bulk of the energy gain coming from an increase in the unloaded gradient from 50 to 85 MeV/m. This increase in gradient will be performed adiabatically by upgrading and doubling the number of klystrons which supply the rf power. It will be accompanied by an increase in beam charge which will leave the fractional beam loading roughly constant. However, the repetition rate will be decreased to keep total site power consumption from becoming too large. Since the total linac length required for NLC-II is not much longer than that for NLC-I, we will probably construct the full NLC-II linac length initially and use the additional length in NLC-I to attain beam energies slightly higher than 250 GeV.

For both NLC-I and NLC-II, three different parameter sets are listed. These correspond to the same rf power and linac length, but assume different bunch charges and bunch lengths. This leads to different loading through the linacs and therefore different final beam energies. The total beam energy is determined from the accelerating gradient, $Grad_{\text{rf}}$, the average beam phase, ϕ_{rf} , and the single and multibunch beam loading:

$$\Delta E = L_{\text{acc}} Grad_{\text{rf}} \cos \phi_{\text{rf}} (\% fdbk) (\% BNS) (\% off) - L_{\text{acc}} q (k_{\parallel \text{multi}} + k_{\parallel \text{single}}) \quad (7.1)$$

	NLC-I			NLC-II		
	a	b	c	a	b	c
$N (10^{10})$	0.65	0.75	0.85	0.95	1.10	1.25
$\sigma_z (\mu\text{m})$	100	125	150	125	150	150
$\gamma\epsilon_{x \text{ inj}} (10^{-6} \text{ m-rad})$	3.6			3.6		
$\gamma\epsilon_{y \text{ inj}} (10^{-8} \text{ m-rad})$	4			4		
$\sigma_{\epsilon \text{ inj}} (\%)$	<1.5			<1.5		
$\gamma\epsilon_{x \text{ ext}} (10^{-6} \text{ m-rad})$	4			4		
$\gamma\epsilon_{y \text{ ext}} (10^{-8} \text{ m-rad})$	7	9	11	9	11	13
$\Delta E/E_{FWHM \text{ ext}}$ single bunch (%)	0.8			0.8		
$\Delta E/E_{FWHM \text{ ext}}$ train (%)	1.0			1.0		

Table 7-2. NLC linac emittance requirements

In addition, there must be sufficient energy overhead for the energy feedback systems, the phase profile required for BNS damping, and the energy loss from klystron stations that have to be repaired. The value assumed for the klystron repair margin is roughly 50% larger than that needed in the SLC linac. The overhead assumed for the energy feedback is similar to that used in the SLC. Finally, the additional energy needed for BNS damping arises because the linac will not be operated at a constant rf phase. Instead, the rf phases are set in the first part of the linac to produce the desired BNS bunch energy spread; in the remainder of the linac, they are set to achieve a final energy spread that is within the final-focus bandwidth. This will be discussed further in Subsection 7.4.3.

The design-normalized emittance of the bunches entering the main linacs is $\gamma\epsilon_x = 3.6 \times 10^{-6}$ m-rad, $\gamma\epsilon_y = 4.0 \times 10^{-8}$ m-rad, and the energy is 10 GeV. It is the task of the main linacs to accelerate the bunches to ~ 250 GeV (NLC-I) or ~ 500 GeV (NLC-II), while preserving the low transverse emittance and maintaining the small final beam energy spread; these requirements are listed in Table 7-2.

The three parameter sets listed for NLC-I and NLC-II reflect a tradeoff in bunch charge versus beam size where the luminosity is kept nearly constant. As discussed in the introduction to this document, this is the main tradeoff that remains in a linear collider design when all constraints are taken into account. Larger beam sizes are desirable since they loosen many of the tolerances. However, increasing the beam charge to compensate the loss in luminosity produces problems related to beam power, and generally leads to tighter wakefield-related tolerances. The three parameter sets each represent compromises among these competing effects: together they span the range of operating conditions that we consider reasonable.

In this chapter, we will concentrate the mid-range parameters, that is, sets NLC-Ib and NLC-IIb. Note that we have allowed for over 100% vertical emittance growth in the linacs in these cases. This lets us set fairly conservative tolerances on the accelerator structure alignment. However, we believe that we will do better than these tolerances as we gain more experience with X-band accelerator construction and operation.

7.3 System Design

7.3.1 Design Overview

Although the layout of the main linacs is fairly simple, an array of X-band accelerator structures interleaved with a FODO quadrupole lattice, one faces a number of challenges to accelerate low-emittance bunch trains without significantly degrading the beam phase space. The X-band structures that provide a high-acceleration gradient also heavily load the beam, so careful control of the rf pulse shape will be needed to achieve the small beam energy spread that is required at the end of the linac. The X-band structures also have the drawback that large transverse wakefields, both long-range (bunch-to-bunch) and short-range (intra-bunch), are generated when the bunch train passes off-axis through the structures. Although damping and detuning of the dipole modes of the structure will be used to suppress the long-range wakefield, and autophasing will be used to offset the short-range wakefield effect on betatron motion, the structures will still have to be aligned precisely to limit emittance growth from both short-range and long-range wakefield effects. The small bunch sizes also make the beam sensitive to other emittance growth mechanisms such as dispersion from quadrupole misalignments, focusing from the ions generated in the residual gas of the beam-line vacuum chambers, and dilution from beam trajectory jitter, like that caused by vibrations of the quadrupole magnets.

Most of the deleterious effects will be limited by design. For example, the quadrupole magnet power supplies will be chosen to be stable enough not to cause significant beam trajectory jitter. For some of the effects, however, we will rely mainly on measurements of the beam properties to control emittance growth. In particular, beam trajectory measurements will be used to adjust the positions of the quadrupoles and structures to minimize the emittance growth caused by their misalignment. For this purpose, each quadrupole and structure in the linacs will contain a beam position monitor (BPM), and will be supported by movers that can be remotely controlled (*e.g.*, like the magnet movers in the FFTB).

A beam-based approach will also be used in a trajectory feedback system to suppress low-frequency jitter of the bunch train as a whole, and if necessary, bunch-to-bunch position variations within the train (special multibunch BPMs will be used in this case). These feedbacks will be included in each of five instrumentation regions that will be located along the linacs. These regions will also include high-dispersion sections so that bunch energy and energy spread can be measured and used for rf control feedback. As with the operation of the SLC, if the feedback and alignment algorithms fail to suppress emittance growth to the desired level, non-local types of tuning will be used, such as orbit bumps. To aid in this tuning, and to monitor the beam phase space, the instrumentation regions will also contain beam size monitors.

Finally, we note some of the machine protection strategies that will be used to deal with the high-power beams. Initial tuning and recovery from beam shut-off will be done by running with a single bunch per pulse, and with a larger than nominal emittance so that the bunch will not damage the beam pipe if it were steered into it. A series of thin spoilers, one per structure, will be the first material intercepted by the bunch, and will disperse the resulting shower of secondary particles to prevent damage to other beam line elements. For nominal beam operation, a series of safeguards will be used to shut off the beam before it hits the beam pipe, and to prevent fast changes ($<$ pulse period) that could steer the bunches into the beam pipe.

7.3.2 Linac Optics

The linac focusing system is designed to contain the beam transversely as it is accelerated. In the NLC linacs, there are many effects that will dilute the transverse projected emittance of the beams. The three primary sources of emittance dilution are:

- Short- and long-range transverse wakefields.
- Dispersive and chromatic effects.
- Transverse jitter induced by quadrupole vibration.

Ideally, one would like to design a lattice that will minimize all three of these effects without significantly increasing the length of the linac. Unfortunately, these three sources of dilution impose opposing constraints on the focusing lattice. The wakefield dilutions are minimized by increasing the focusing strength, while the other dilutions are increased by the stronger focusing. In the NLC main linacs, we will use beam-based alignment of the quadrupoles and BPMs to minimize the dispersive emittance growth; the technique for this is straightforward. Thus, in principle, the optimization becomes a balance between the dispersive and jitter dilutions and the wakefield dilutions.

In practice, the optimization is actually a balance between the additional length due to the strong focusing and the wakefield dilutions. That is, we want to have a sufficiently strong focusing system so that the wakefield dilutions are small but not an excessively strong lattice that would unnecessarily increase the length of the linacs due to the additional quadrupole magnets that would be required. A parameter that characterizes the strength of the wakefield relative to the focusing is the BNS energy spread needed for autophasing: autophasing is the condition where the chromatic growth of a beam performing a coherent betatron oscillation exactly cancels the wakefield growth and thus the beam oscillates as a rigid body.

The energy spread required for autophasing can be estimated from a two-particle model as:

$$\sigma_{\delta \text{ BNS}} \approx \frac{N r_0 W_{\perp} (2\sigma_z) L_c^2}{8\gamma} \left(1 + \frac{3}{2} \text{ctn}^2 \frac{\psi_c}{2} \right), \quad (7.2)$$

where N , r_0 , and W_{\perp} are, respectively, the number of particles per bunch, the classical electron radius, and the transverse wakefield. In addition, L_c and ψ_c are the FODO focusing cell length and the betatron phase advance through the cell. A shorter cell length and larger phase advance yield stronger focusing and smaller BNS energy spreads.

In the NLC linacs, we have limited the BNS energy spread to less than 1.6%. This yields tolerances on the trajectory control and alignment of the accelerating structures that are reasonable using high-resolution BPMs and a beam-based alignment technique for the structures. For comparison, in most of the SLC linac $\sigma_{\delta \text{ BNS}} \gtrsim 4\%$.

Lattice Design

The main linacs are based upon simple FODO cells where the quadrupoles are separated by an integral number of pairs of accelerator structures—see discussion in Section 7.3.3. Two structures are paired together since this simplifies the waveguide routing that is required. For the NLC linacs, we considered two basic approaches: (1) placing quadrupoles, all having the same length, after every structure pair and (2) increasing

the number of structure pairs between quadrupoles as $(E/E_0)^\alpha$ where α typically varies between 0.2 and 0.8.

While the first option has the most flexibility, allowing one to set the “optimal” lattice regardless of the final beam energy, it is very space inefficient. This arises because many quadrupoles are located in regions where the horizontal and vertical beta functions are nearly equal. Thus these quadrupoles do not contribute to the net focusing and are wasting space.

In the cases we studied, the length of the linac occupied by the quadrupoles was more than 15% with the first option while it was roughly 7% with the second option. For this reason and because we feel that it can provide sufficient flexibility, we have chosen to adopt the second approach.

For NLC-I and NLC-II, the primary center-of-mass energy range that needs to be considered is between 500 GeV and 1 TeV. We have designed a lattice where the quadrupole spacing is increased by pairs of accelerating structures such that the cell length scales with $\alpha \sim 0.5$ when the center-of-mass energy is roughly 700 GeV; this is a compromise between the 500-GeV center-of-mass energy and the 1-TeV center-of-mass energy. This lattice will provide sufficient focusing at even lower center-of-mass energies, and the focusing can be decreased at the higher energies to decrease the sensitivity to quadrupole vibration.

To decrease the final beam energies much below 250 GeV while constraining the beam emittance dilution due to the transverse wakefields would be difficult. In this case, one would likely add a bypass line to skip part of the linac. For example, to operate the collider at 92 GeV to study the “ Z_0 ” boson would only require the first fifth of the accelerating structures. The wakefields in the remaining structures simply increase the longitudinal and transverse emittance dilution and thereby decrease the performance of the collider.

In the lattice, the cell lengths increase in five steps, from roughly 8-m cells to 40-m cells, and the beta functions must do the same. We have matched across these transition regions without any significant increase in sensitivity. The horizontal and vertical beta functions for the NLC-II linacs are plotted in Figures 7-1 and 7-2. Notice that immediately following a transition point, the lattice contains a diagnostic section where the focusing is slightly weaker and is less uniform to provide optimal conditions for the emittance measurements; these diagnostic sections are discussed in Section 7.3.4. Figure 7-3 shows the horizontal and vertical phase advance per cell, and Figure 7-4 shows the horizontal and vertical BNS autophasing energy spreads. Figure 7-5 shows the location of the diagnostic stations on a plot of the horizontal dispersion.

The integrated quadrupole strengths required for the NLC-IIb lattice are plotted in Figure 7-6. The quadrupoles are assumed to have a 0.7-cm pole-tip radius. To keep the pole-tip fields reasonable, the quadrupole lengths are increased as the cell lengths are increased. The linac lattice uses five different quadrupole lengths: 0.2 m, 0.3 m, 0.4 m, 0.6 m, and 0.8 m in the regular lattice, while the final energy diagnostic section assumes a 1-m quadrupole with a 5-mm pole-tip radius; these longer quadrupoles are similar to those required in the collimation and final focus sections. The assumed lengths and the corresponding pole tip fields are plotted in Figure 7-7; note that some of the matching quadrupoles in the diagnostic sections are far too strong and must be lengthened.

Finally, we have studied the bandwidth of the linacs assuming that injection energy was correct but the accelerating gradient was too high or too low. The results are plotted in Figure 7-8 as a function of $B_{\text{mag}} - 1$. The parameter B_{mag} is equal to:

$$B_{\text{mag}} = \frac{1}{2} \left[\frac{\beta^*}{\beta} + \frac{\beta}{\beta^*} + \left(\alpha \sqrt{\frac{\beta^*}{\beta}} - \alpha^* \sqrt{\frac{\beta}{\beta^*}} \right)^2 \right], \quad (7.3)$$

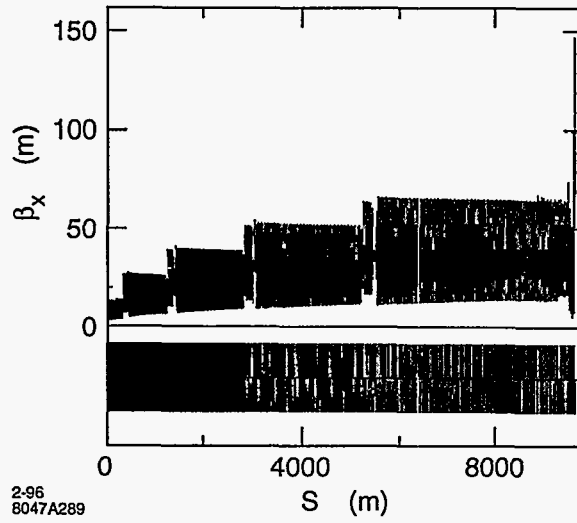


Figure 7-1. Horizontal beta function in the NLC-II linacs.

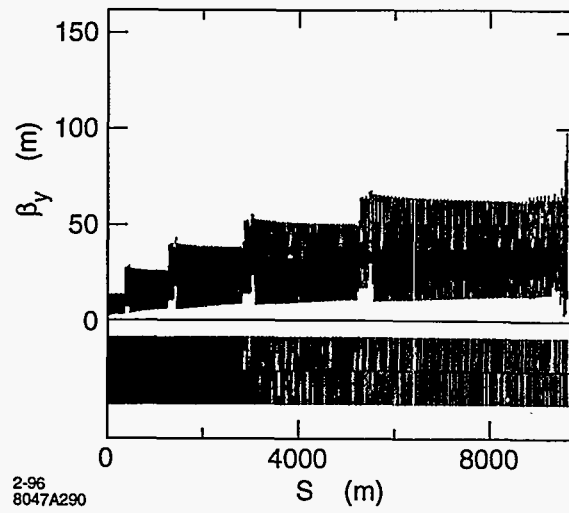


Figure 7-2. Vertical beta function in the NLC-II linacs.

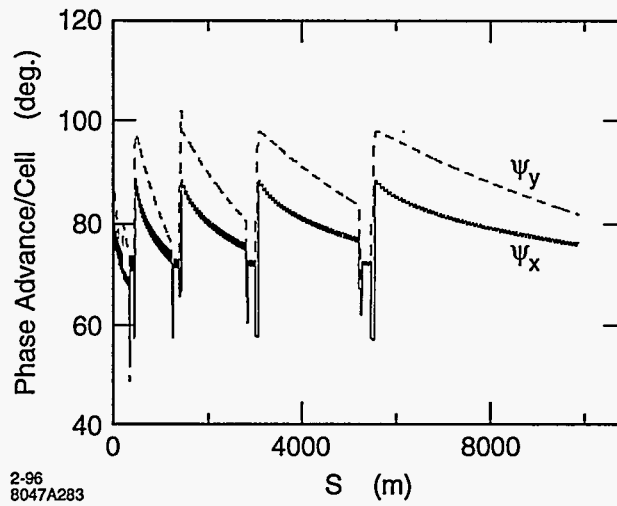


Figure 7-3. Horizontal and vertical phase advance in the NLC-II linacs; the vertical phase advance is larger than the horizontal to optimize the focusing in the vertical plane.

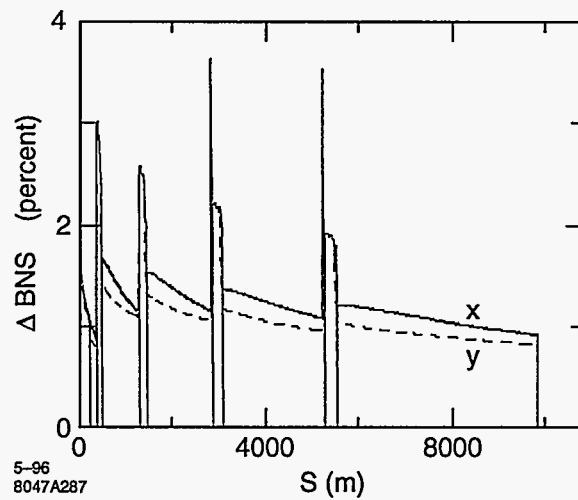


Figure 7-4. Horizontal and vertical BNS autophasing energy spreads for NLC-IIb; the large values occur in the diagnostic regions.

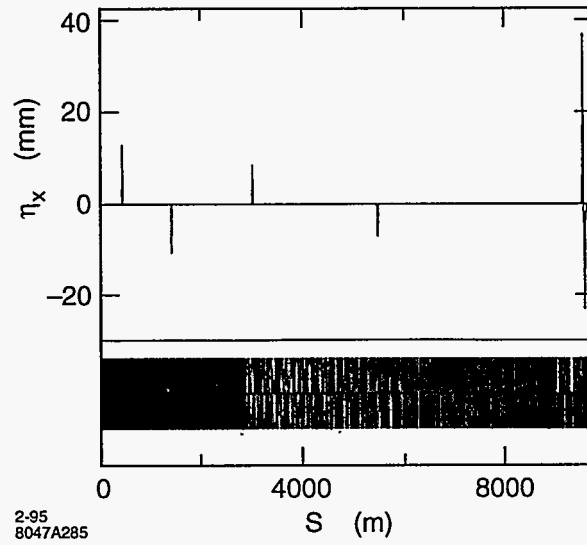


Figure 7-5. Horizontal dispersion function in the NLC-II linacs; note that the diagnostic stations are located at the non-zero dispersion regions.

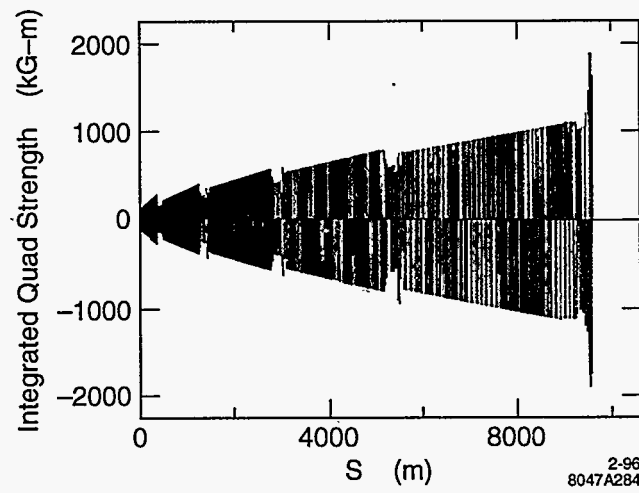


Figure 7-6. Integrated quadrupole strengths in NLC-IIb lattice.

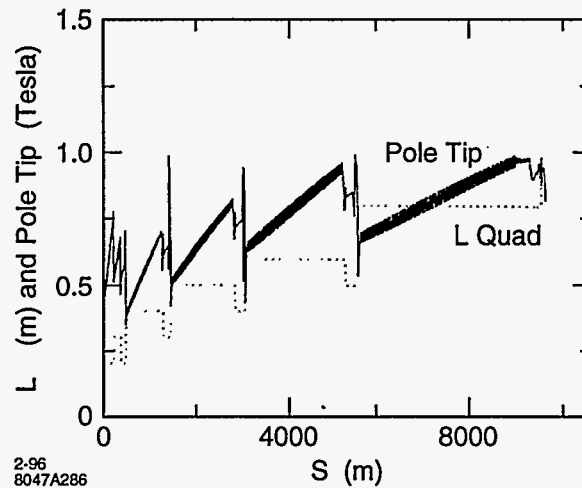


Figure 7-7. Quadrupole lengths (dotted) and pole-tip fields (solid) in NLC-IIb lattice.

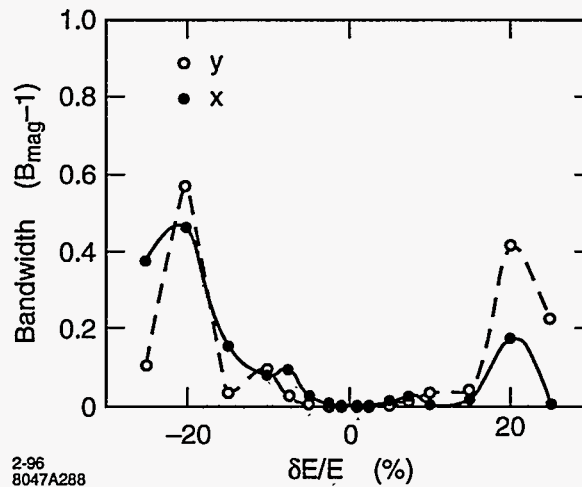


Figure 7-8. Bandwidth of the NLC-II linacs plotted in terms of $B_{\text{mag}} - 1$ which is proportional to the emittance increase after filamentation. The energy deviation is due to an increased or decreased acceleration gradient.

where β^* and α^* describe the beam ellipse and are equal to the lattice functions β and α when the beam is “matched” to the lattice. With this definition, B_{mag} times the beam emittance is equal to the emittance after filamentation. Thus, when $B_{\text{mag}} - 1$ equals one, there is 100% emittance growth. Figure 7-8 indicates that the optical bandwidth of the linacs is more than sufficient.

7.3.3 Beam Line Layout: Normal Sections

The main linacs are basically an array of X-band accelerator structures interleaved with a FODO quadrupole lattice. In this section, we describe the general layout and components of these “normal” beam line regions.

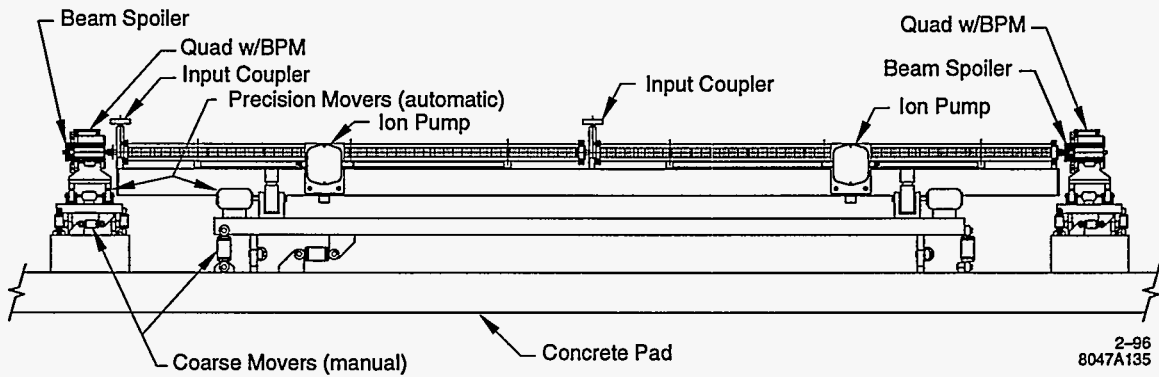


Figure 7-9. Side view of linac components near the beginning of the linacs, where there is a quadrupole between each pair of accelerator components.

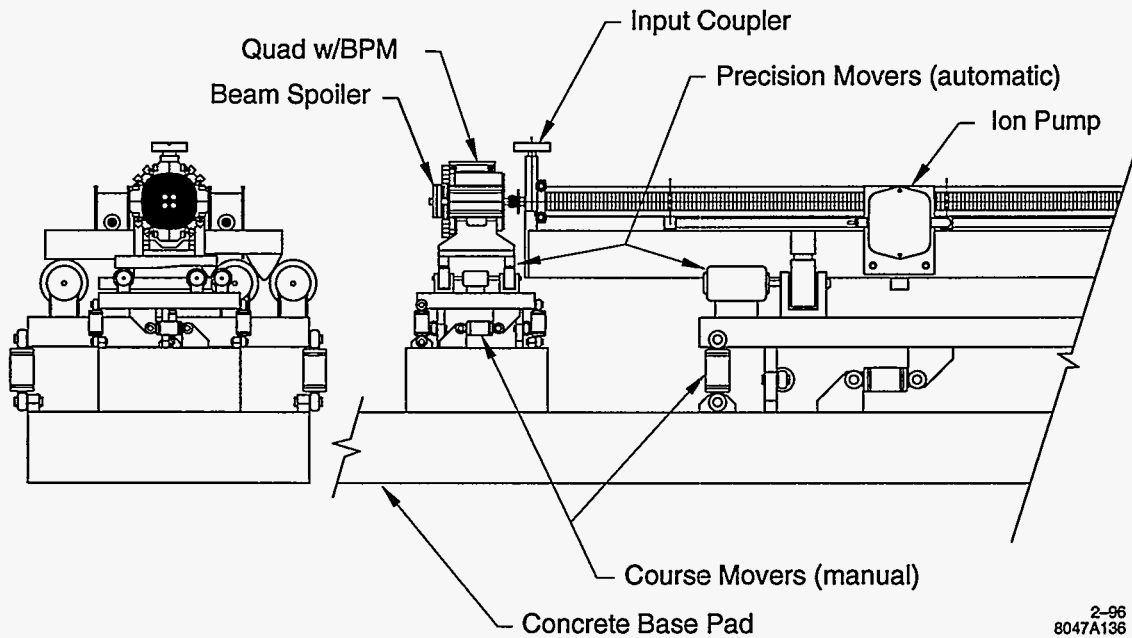


Figure 7-10. End view and close-up side view of the linac components.

The special diagnostic regions of the main linacs are described in Section 7.3.4. Further details on components and instrumentation are given in Sections 7.9 and 7.10, including newer concepts for the support system for the beam line components.

Structures

Figure 7-9 shows the beam-line layout near the beginning of the linacs where there is a quadrupole between each pair of accelerator structures; Figure 7-10 shows the end view and a close-up side view of the linac components. Note that the accelerator structures are supported in pairs on a common strongback, and that the strongback itself is supported by mechanical movers, which we call structure movers. Grouping the

structures in pairs is motivated by the fact that they have a common rf feed and therefore are mechanically constrained, at least for large movements. The two structures will each be supported on the strongback at six locations and will be aligned on the strongback before installation (five of the six supports can flex to allow for thermal expansion of the structure along the beam axis). It will still be possible to adjust the six supports *in situ*, although not easily, given that an alignment precision of about $10\ \mu\text{m}$ will be required.

The structure mover system will be similar to that used to move the SLC final focus triplet. The movers will provide independent horizontal and vertical positioning control at two points along the strongback, and will be used to remotely align the two structures as a whole relative to the beam trajectory. The alignment correction will be based on measurements of beam-induced signals from the structures, and the position changes will be made via five stepper motors that drive off-axis cams. Steps as small as $1\ \mu\text{m}$ will be achievable over a range of $\pm 1\ \text{mm}$. Structure roll can be adjusted as well but will not be changed. This capability is a byproduct of using a mounting system that does not over-constrain the object that is being supported.

The structure movers will be attached to a common girder that will be attached to the beam line support pedestal via manually adjustable supports. These girder supports will be used to set the initial position and orientation of the structure pairs, and will have a $\pm 1\text{-cm}$ range of travel. They will also be used if a global realignment of the beam line is necessary due to ground settling.

Quadrupoles

Near the beginning of each linac, there will be a quadrupole magnet after each structure pair (Figure 7-9). However, the separation of the quadrupoles will increase in two-structure increments along the linac, from one pair of structures to five pairs at the end of the linac. These quadrupoles will form a FODO optical array as discussed in Section 7.3.2.

The quadrupoles, each of which will contain a BPM, will be moved as one unit for alignment purposes. Each quadrupole/BPM unit will be mounted on a magnet mover, which in turn will be mounted on a manually adjustable support. This system will have the same adjustment capability as was described for the structures, but the movers will be similar to those used in the FFTB.

BPMs

A stripline BPM will be located inside each quadrupole and will contain four strips at an inner radius of 5 mm with strip lengths of 105 mm. This length was chosen because it makes the period between the forward and reflected pulses from a single bunch equal to half of the bunch spacing, which is optimal for multibunch measurements. Since this length is shorter than the minimum quadrupole length, the addition of the BPMs will not significantly increase the beam-line length.

Spoilers

After each structure, there will be a spoiler that will be the first material hit if the beam is steered far off-axis. The spoiler will be a titanium disk that is 0.2-radiation-lengths long (about 8 mm), with a 2-mm inner radius and a 1-cm outer radius. For normal beam operation, it will do little to prevent damage to the beam pipe, but for tuning, it allows a single high-emittance bunch to intercept the beam pipe without causing damage; the Machine Protection System (MPS) is discussed further in Section 7.8. The integrated

transverse wakefield kick due to a spoiler is about 10% that of the wakefield due to a single accelerator structure.

7.3.4 Beam Line Layout: Special Diagnostic and Control Sections

In a linac, it can be difficult to localize sources of emittance dilution, optical errors, and beam energy errors. If these errors propagate a sufficient distance, the emittance dilutions and optical errors will filament into unrecoverable emittance dilution and the beam energy errors will lead to large variations in the betatron phase. The relevant length scale is the number of betatron oscillations. The NLC linacs are sufficiently long (roughly 80 betatron wavelengths compared to 30 wavelengths in the SLC linac) that it is important to measure the beam emittance and energy at multiple points along the linacs. In addition, because trajectory errors will also filament into unrecoverable emittance dilution, it is important to provide fast feedbacks that will stabilize the trajectory at multiple points along the linacs.

To monitor the beam emittance, energy, and trajectory, there are four diagnostic stations located in each linac and one station located at the end of each linac. The stations within the linacs are located at 400, 1300, 2900, and 5300m; they are concentrated more closely at the beginning of the linacs because the beam is more sensitive at the low-energy end. In terms of betatron phase advance, these placements (including the station at the end of the linac) are located at 10, 22, 36, 54, and 78 oscillations. The diagnostic stations will provide five main functions:

- Beam emittance measurements.
- Energy and energy spread measurements.
- Fast feedback correctors.
- Bunch-by-bunch measurement and trajectory control.
- Beam dump.

Each of these will be described after briefly discussing the layouts.

The diagnostic stations are constructed from six FODO cells, each of which is roughly one-m longer than a normal FODO cell. This additional space is used by the diagnostics and kickers which are located near the quadrupole magnets. The accelerating structures occupy the middle of the cells just as they do in normal FODO cells. The quadrupole and accelerating section supports and girders are also identical to those of the main linac sections.

In addition to the six lengthened FODO cells, each of four diagnostic sections within each main linac includes a chicane which introduces dispersion for the energy and energy spread measurements; the length of the chicanes and matching quadrupoles is roughly equal to that of a single FODO cell. Finally, a much higher-resolution energy diagnostic section with a length of roughly 100 m is located at the end of each linac. This final energy diagnostic section also provides a net bending angle to compensate for the collimation section that follows the linac.

Station		Energy (GeV)	S (km)	σ_x (μm)	σ_y (μm)
NLC-Ib	Diag 1	20	0.4	26	7
	Diag 2	45	1.3	21	6
	Diag 3	90	2.9	18	5
	Diag 4	154	5.3	15	4
	Diag 5	245	8.6	12	3
NLC-IIb	Diag 1	30	0.4	22	6
	Diag 2	75	1.3	17	5
	Diag 3	155	2.9	14	4
	Diag 4	280	5.3	11	3
	Diag 5	490	9.4	8	2

Table 7-3. Beam sizes at laser wire scanners in linac diagnostic stations for the NLC-I and NLC-II.

Emittance Measurement

The beam emittance measurements are performed using laser wire scanners located at different betatron phases which allows the beam matrix to be measured without changing the optics between scans. Only three independent X and Y wire scanners are needed to reconstruct the uncoupled 2×2 X and Y beam matrices. This effectively measures the projected horizontal and vertical emittances along with the beta and alpha parameters that describe the beam. If one also wants to measure the off-diagonal X and Y coupling terms, then at least four scanners with X , Y , and diagonal wires (U-wires) are needed since there are ten rather than six independent parameters that describe the beam. In this case, the horizontal and vertical phase advances must be separated to get independent measurements of the coupling terms.

In the NLC linacs, we do not expect betatron coupling to be a significant source of emittance dilution; the roll tolerances on the quadrupoles are relatively loose. Regardless, when commissioning the linacs or tracing sources of emittance dilution, it is important to be able to verify the degree of coupling in the beams. Finally, experience with the SLC emittance measurements suggests using an additional wire scanner to over-constrain the measurement and provide an estimate of the measurement error; this additional scanner also provides a backup if one scanner fails. Thus, each of the diagnostic stations includes five laser wire scanners which can measure the emittances and coupling while providing an estimate of the measurement accuracy.

The wire scanners are located near maxima of the vertical beta function where the vertical beam size is largest and the aspect ratio σ_x/σ_y is smallest. The beam energy and beam sizes at the wire scanners are listed in Table 7-3 assuming normalized emittances of $\gamma\epsilon_x = 3.6 \times 10^{-6}$ m-rad and $\gamma\epsilon_y = 4 \times 10^{-8}$ m-rad; these emittances are smaller than those expected through most of the linacs. To optimize the diagonal measurements, the U-wires should be aligned at an angle given by the inverse tangent of the beam aspect ratio. For the NLC linacs, this corresponds to an angle of roughly 15 degrees. The laser wire scanners should be optimized to measure vertical beam spots in the range $1.6 \mu\text{m} \lesssim \sigma_y \lesssim 20 \mu\text{m}$; these spot sizes correspond to a vertical emittance ranging from $\gamma\epsilon_y \lesssim 6 \times 10^{-7}$ m-rad at 20 GeV to $\gamma\epsilon_y \gtrsim 3 \times 10^{-8}$ m-rad at 500 GeV.

Energy and Energy Spread Measurement

The beam energy and energy spread is determined by measuring the trajectory and beam size in dispersive regions. The dispersion is generated by chicanes in the linacs and by short arc sections at the end of the

Station	E (GeV)	η_x (mm)	Length (m)	R_{56} (μm)	I_5 (1/m)	$\Delta\epsilon_x/\epsilon_x$ (%)
Diag 1	32	13	8	-125	1.6×10^{-10}	0.1
Diag 2	80	11	16	-41	4.7×10^{-13}	0.1
Diag 3	165	8.6	23	-17	1.5×10^{-14}	0.3
Diag 4	290	7.0	30	-9	8.4×10^{-16}	0.4
Diag 5	500	37	110	-4	7.9×10^{-17}	1.2

Table 7-4. Parameters of linac energy diagnostic stations in the NLC-II.

linacs. The chicanes produce a maximum transverse displacement of roughly 1 cm and do not have a net bending angle or net transverse displacement. The arc sections at the ends of the linacs provide a total bending angle of roughly 0.5 mr to compensate for bending in the collimation sections that follow the linacs.

The locations, maximum dispersion values, and lengths of the energy diagnostic sections are listed in Table 7-4 for the NLC-II; the stations have the same length and dispersion in the NLC-I, but the beam energy differs because of the lower accelerating gradient. In all cases, the lengths and strengths of the systems were adjusted to limit the emittance growth due to synchrotron radiation to $\sim 1\%$. Finally, the sections will cause the beam phase and bunch length to change as a function of the beam energy and energy spread. These changes are quantified by the value of the R_{56} and are very small. Assuming a 10% energy error through the entire linac, the bunch length will be increased by less than 2% and the beam phase will be changed by 0.3° which is insignificant compared to the 10% energy error. The values of the R_{56} , as well as the emittance growth due to the synchrotron radiation, are also listed in Table 7-4; in the NLC-I, the R_{56} values are the same, but the emittance growths are negligible since the growth depends upon the sixth power of the beam energy.

In the chicanes, the beam energy measurement will be performed using a single BPM located at the maximum of the dispersion, and several BPMs located in nearby nondispersive regions. These latter BPMs will be used to remove the dependence on the incoming trajectory. The BPMs at the high dispersion points will differ from the normal linac BPMs in that they will need roughly twice the horizontal aperture. The primary purpose of the energy measurement is to track changes in the beam energy over time. These energy changes lead to variations in the phase advance along the linacs which can lead to changes in the beam emittances and trajectories, and the feedback system efficiencies. In the NLC, we would like to limit the phase advance variations to roughly 15° . This requires limiting the beam energy changes to 0.5% at the beginning of the linacs and 0.25% at the end of the linacs.

The expected resolution of the energy measurements is listed in Table 7-5 for the NLC-I and NLC-II, assuming a systematic error of $10 \mu\text{m}$ on the BPM measurement. This error is assumed to arise from both the stability of the BPM measurement and the resolution on determining the incoming trajectory from the surrounding BPMs which are in nondispersive regions. These different measurements are insensitive to the absolute value of the bending fields or the horizontal alignment of the BPM. In addition, assuming that the bending fields have been measured with a relative error of 10^{-3} , the absolute beam energy can be calibrated to less than 1% by varying the chicanes.

In the final energy diagnostic, the absolute beam energy can be calibrated much more accurately by measuring the angular separation of the synchrotron radiation generated at the beginning and end of the bending magnets. In this case, it should be straightforward to attain an absolute measurement with a relative error less than 10^{-3} . A similar procedure is used in the SLC final focus beam dump with a relative accuracy of roughly 2×10^{-4} .

Station	η_x (mm)	$\delta E/E$ Res. (%)	$\sigma_{x\beta}$ (NLC-I)(μm)	σ_ϵ Res. (%) (NLC-I)	σ_ϵ Nom. (%)
Diag 1	13	0.08	37	0.34	0.8
Diag 2	11	0.09	28	0.30	1.0
Diag 3	8.6	0.12	25	0.32	1.1
Diag 4	7.0	0.14	24	0.34	0.8
Diag 5	37	0.03	21	0.06	0.3

Table 7-5. Energy resolution of energy diagnostic stations for NLC-I and NLC-II.

Station	Energy (GeV) (NLC-I/NLC-II)	Corrector Strength [G-m] (NLC-I/NLC-II)
Diag 1	20 / 30	3 / 4
Diag 2	45 / 75	4 / 6
Diag 3	90 / 155	6 / 10
Diag 4	155 / 280	8 / 14
Diag 5	245 / 490	12 / 25

Table 7-6. Fast Feedback corrector strength in the NLC-I and NLC-II

In addition to the beam energy measurements, the chicanes and arc sections will provide energy spread measurements. The energy spread will be determined from either the synchrotron light spot size or a laser wire scanner. The resolution, estimated from the ratio of the dispersion to the betatron spot size for a horizontal emittance of $\gamma\epsilon_x = 4 \times 10^{-6}$ mr, is listed in Table 7-5 for the NLC-I; the values for the NLC-II are roughly 30% smaller. The nominal beam energy spread, which is much larger than the expected resolutions, is also listed.

It is envisioned that the chicanes will be used during normal operation to continuously measure the energy and energy spread. Regardless, the vacuum chamber through the chicanes will be designed to allow the bending fields to be varied continuously from zero to full excitation and to accept beams with an energy as low as 50% of nominal. This range of conditions requires a horizontal aperture that exceeds twice the nominal beam displacement in the chicane. In a chicane, the maximum displacement is equal to the peak dispersion function which is listed in Table 7-5 and varies between 13mm and 7mm. A vacuum chamber aperture of 3 cm by 1 cm in cross-section is more than sufficient.

Fast Feedbacks

At each diagnostic station, there are fast trajectory feedbacks that will control the horizontal and vertical trajectories. The feedback systems consist of horizontal and vertical pairs of dipole correctors followed by 10 high-resolution BPMs. The horizontal correctors are located at the first two horizontally focusing quadrupoles in the diagnostic sections while the vertical correctors are located at the adjacent defocusing quadrupoles. The BPMs are located at the subsequent focusing and defocusing quadrupoles.

To prevent the dipole correctors from driving the beam into the vacuum chamber, the corrector strength will be limited so the maximum trajectory deflections are less than 100 μm ; the maximum required strengths are listed in Table 7-6. The feedback systems need to operate at the full 180-Hz repetition rate. Thus, the correctors and the vacuum chamber should be designed so the fields attain a consistent slew rate.

For more details of the fast feedback system see Section 7.5.3.

Bunch-by-Bunch Trajectory Control

In addition to the fast feedback for the bunch train trajectory, we will implement high-speed vertical kickers to realign the bunches in a train. This system is designed to compensate for the long-range transverse wakefields induced by accelerator structure offsets. The high frequency kickers will be short striplines separated by roughly 90° in betatron phase; details are described in Section 7.5.4. Because the system is designed to correct static offsets of the structures, it will be controlled by a slow feedback system.

Beam Dumps

At this time, the only beam dumps we are planning for the linacs are ones that will be located at the ends. Beams would be deflected to the dump by a 180-Hz kicker magnet so that the beam direction can be switched from the dump line to the collimation section in a single interpulse period. The dump line begins in the beta matching section for the collimation region; this is located after the final energy diagnostic station and consists of drifts roughly 100m in length. Although a detailed design does not yet exist, at 500 GeV, an integrated field of 5.6 kg-m will deflect the beam by 2 cm after a drift of 60 m. This would allow a simple septum to further deflect the beam into the dump line. The kicker field of 5.6 kg-m is roughly 75% larger than the field of the 2-9 single-beam dumper in the SLC.

For more details of the beam dump, see Chapter 11.

7.3.5 Site Requirements and Tunnel Layout

Since the main linacs are the largest components of the NLC, the impact of the site on their cost and operation will be the dominant factor in choosing a location to build the accelerator. Although a systematic study of the site requirements has yet to be done, several factors that will impact the site selection can be readily identified. For example, the beam line must be located at least 20 ft below ground to provide radiation shielding. Access shafts to the surface will probably be required about every kilometer to provide cooling tower and substation connections, and to allow maintenance crews to reach the beam line. A flat terrain is desirable to minimize the depth of such access shafts and would also facilitate the establishment of a global coordinate system for alignment on the surface and the subsequent transfer of the reference system to the beam line.

There are a number of ground composition issues that will influence the site location. The general experience in constructing long beam line tunnels such as LEP is that the ground should be compact, homogeneous, hard and dry. The hardness of the ground has a number of tradeoffs. Tunnels bored in hard rock, such as granite, will generally be more stable in terms of ground vibrations and long-term settling than those bored in softer rock. However, the tunneling costs may be prohibitive and the site would likely be located in a mountainous region. Areas with softer rock such as sandstone and limestone, which are likely to have flatter terrain, would make the tunneling easier, but the tunnel would have to be better reinforced, which may offset much of the cost savings. Also, ground water variations are likely to have a bigger effect on the alignment of a tunnel built in softer rock. In this regard, the tunnel movement over several years should be < 1 cm on kilometer-length scales. Much larger variations will require that a global realignment of the beam line be performed.

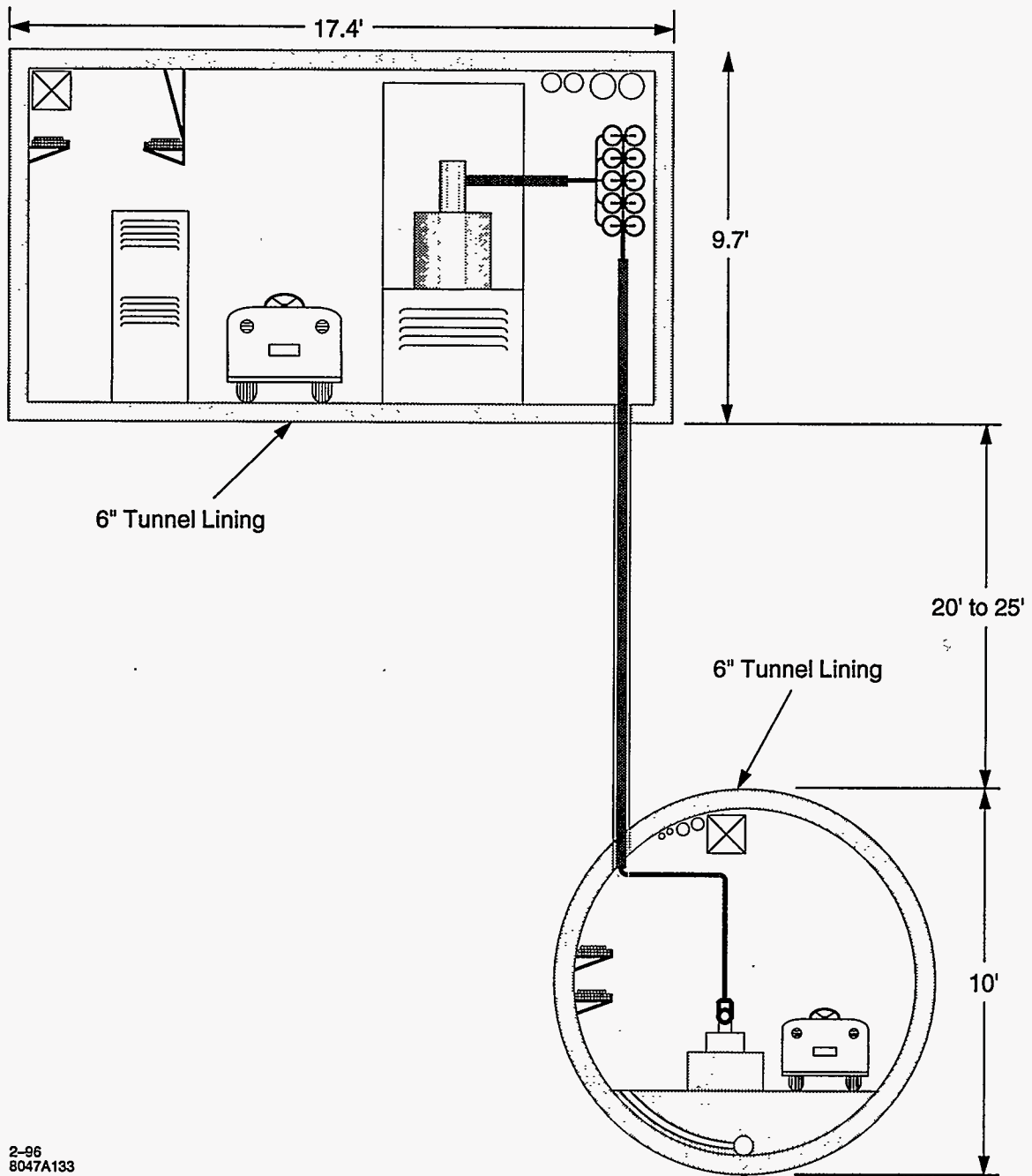
Seismic activity on all scales will be a factor in the site selection. While one certainly wants to avoid areas with a high-rate of major earthquakes, even areas with low seismic activity should be carefully considered

since minor fault lines may act as "slip-joints" for any geo-mechanical forces. On a smaller amplitude scale, ground motion will impact the machine operation due to the pulse-to-pulse beam position jitter generated by the movements of the quadrupole magnets. The ground motion frequencies of concern are those above about 0.1 Hz where the feedback systems that will be used to stabilize the beam may not produce the suppression that is required. The large micro-seismic activity (≈ 0.14 Hz) that originates from ocean waves tends to be fairly directional so its effect on beam motion can be minimized by orienting the beam line perpendicular to the direction of these ground waves (*i.e.*, a correlated motion of all quadrupoles produces less net beam motion). At higher frequencies, where the correlation lengths generally become shorter, the beam motion becomes more sensitive to quadrupole vibrations although the amplitude of ground motion tends to decrease as well. The tolerances in this regard depend on several factors and are discussed in Section 7.4. In general, however, the preference is for a naturally "quiet" site that is not subject to large "cultural" noise such as that produced by heavy machinery.

So far we have considered the site requirements without a specific model of the tunnel layout. However, the tunnel layout will influence the site selection, and vice-versa. The minimal requirement for the cross-sectional tunnel layout is that there be two areas, one that houses the beam line, and one that houses the klystrons, modulators and control electronics, which we call the gallery. We want to be able to inhabit the gallery while the beam line is in operation which will require that the two areas be separated by at least an equivalent of 10 ft of concrete for shielding purposes. With these constraints, we have begun to examine more seriously the two layout configurations shown in Figures 7-11 and 7-12. The KEK-type, so named because the JLC group at KEK has proposed this design, houses both the gallery and beam line areas in one tunnel, but with a 10-ft-wide concrete wall separating them. The semicircular shape of this tunnel would require the use of specialized boring machines. The second design is modeled after the SLAC linac in which the gallery is separated from the beam line with the ground in between serving as shielding. In its construction, the gallery would be located just below the surface and would follow the terrain where possible. It would be built using a "cut-and-cover" method whereas the beam line area would be constructed with circular tunnel boring machines. Having the gallery underground will aid in stabilizing the gallery air temperature to within the 1°C requirement. In the beam-line area, we want a 0.1°C stability, which should not be too difficult to achieve with either design since the beam line tunnels will be well isolated.

Careful evaluation of a number of tradeoffs will be required prior to selecting a tunnel design. The SLAC design will likely be cheaper to build and will allow easier access to the gallery where most of the maintenance work will be done. The beam line is also better isolated, thus reducing the vibrations there due to the maintenance work, pumps, and pulsed-power systems in the gallery. The impact of the shielding requirements on the design, including the complications caused by the numerous penetrations to the beam line, will also be less significant. However, the SLAC design requires longer rf runs with more bends between the pulse compression system and the structures, which will reduce the rf power transmission efficiency by a few percent. Also, the long penetrations through the ground between the two tunnels will have to be well-sealed to prevent water seepage into the beam line.

For costing purposes, we have developed in more detail the SLAC-type layout, including the utility distribution. This is presented in Chapter 18 which describes the conventional facilities.



2-96
8047A133

Figure 7-11. Klystron gallery and beam line tunnel layout ("SLAC type").

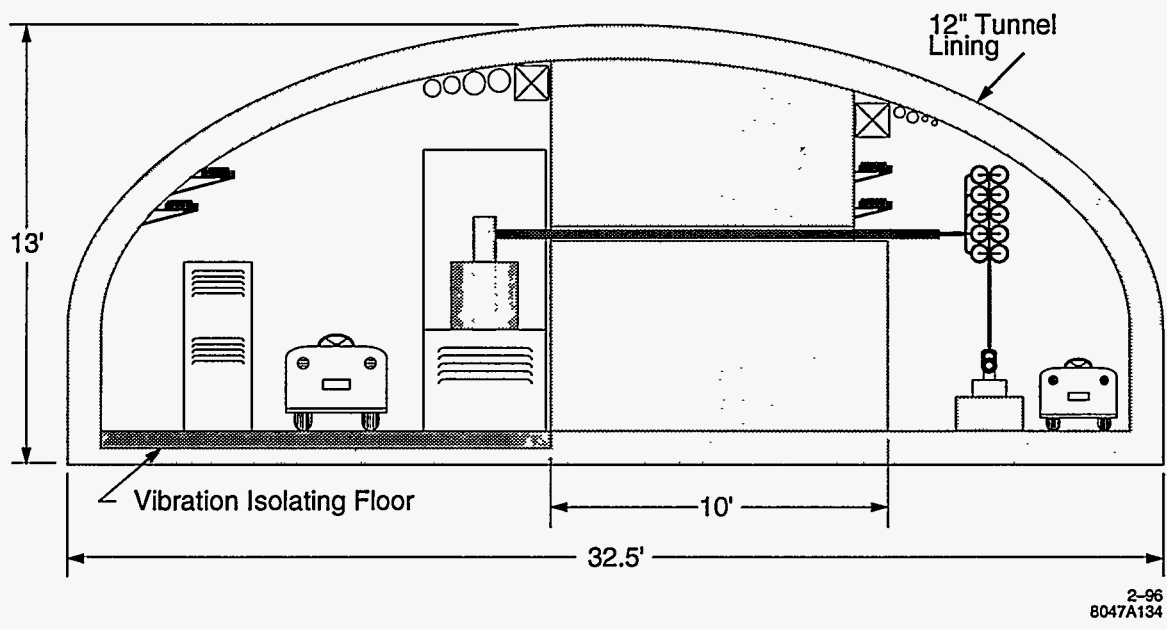


Figure 7-12. Semi-elliptical highway-style tunnel layout ("KEK-type").

7.4 Emittance Dynamics

The preservation of the transverse beam emittances and the control of the beam energy spread in the main linacs will require tight alignment and rf control tolerances. In this section, we describe these tolerances with an emphasis on the underlying dynamical effects. We consider only the bare tolerances which are derived assuming no benefit from beam-based correction methods, including feedback. In the next section, we continue with discussions of stability, alignment, and feedback, where the emphasis is on the error sources that set the scale of the problem, and the beam-based methods that will be required in cases where the bare tolerances cannot be met by other means.

We start this section by discussing the calculation of the short-range and long-range wakefields for the X-band accelerator structures. Although the intra-bunch dynamical effects of the wakefields in the NLC linacs are weak when compared with the SLC linac, they are still very important. Control of long-range wakefield effects is crucial to the operation of the NLC, due to its multibunch beam. Following the discussion of wakefield calculations, we discuss single bunch phase space issues (longitudinal and transverse), then multibunch phase space issues (longitudinal and transverse).

The discussion of single-bunch longitudinal phase space focuses on the need to adjust the average rf phase of the linac so the final energy spread is within the final-focus bandwidth. This average phase puts constraints on the energy spread profile in the linac which impacts wakefield and dispersive effects.

We next turn to single-bunch transverse effects where we present the bare tolerances for injection jitter, ground motion, power supply stability, quad, BPM and structure alignment, and rf deflections. In the case the quad and structure alignment, the results clearly indicate that conventional techniques will not be applicable as micron-level alignment will be required on lengths scales over 100 m.

For simplicity, the single bunch tolerances were computed assuming that the linac is autophased, that is, the energy spread of the bunches are adjusted so that the effect of the differential focusing along the longitudinal bunch profile exactly cancels the head-to-tail driving effect of the short-range transverse wakefields (using a correlated energy spread to offset resonant betatron growth is generally referred to as BNS damping). Because this requires energy spreads that are larger than the final-focus energy bandwidth, we will not be able to achieve this condition everywhere in the linac. Thus we consider how to optimize the rf phase profile along the linac to minimize betatron growth and yet keep the final bunch energy spread within the final-focus bandwidth.

Another option, that of using rf quadrupoles instead of (or in addition to) introducing a correlated energy spread to produce BNS damping, is also discussed. This would bring the linac closer to being autophased, but would require either a more complicated accelerating structure design or the introduction of special lossy rf quadrupole cells that would increase the length of the linacs.

The discussion of multibunch longitudinal phase space focuses upon the compensation of the multibunch beam loading, which varies from 20% to over 30% for the various linac parameters. The compensation scheme that has been chosen is "local" in that the rf input pulse is shaped to keep the energy of all the bunches in a train the same to within a few tenths of a percent throughout the linacs. The bunch-to-bunch charge variations and the ripple in the rf phase and amplitude must be well-controlled; simulation studies to set tolerances on these and other parameters are discussed in this subsection.

The discussion of multibunch transverse phase space includes the effects of the long-range transverse wakefield on emittance growth due to injection jitter and structure misalignments. The structure alignment tolerances

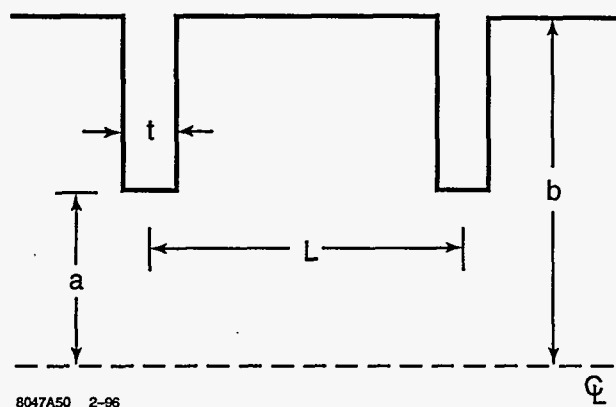


Figure 7-13. The model of one cell of the NLC structure that is used in the calculations.

are characterized by the length scale of the misalignments and are compared to the tolerances due to single-bunch effects. Finally, tolerances associated with the effect on ions on multibunch transport are presented.

7.4.1 Short-range Wakefields

Accelerator Structures

The accelerator structures in the main linacs will each consist of 206 cells and will operate at a frequency of 11.424 GHz. The structure design incorporates damping and detuning which is described in detail in Chapter 8. When computing the short-range wakefields generated in these structures, we ignore the manifolds that are used for damping but not the cell geometry variation that produces the detuning. Figure 7-13 illustrates the cell geometry (note the actual irises are rounded). Each cell is slightly different from its neighbors. The cell period is fixed at $L = 8.75$ mm and the cavity radius varies slightly but is roughly $b = 11$ mm. As one moves from the beginning to the end of the structure the iris radius varies from $a = 5.90$ mm to $a = 4.14$ mm and the iris thickness from $t = 1.26$ mm to $t = 2.46$ mm. The average value of a/λ for the cells is 0.187 where $\lambda = 26.25$ mm is the wavelength of the fundamental mode.

For our wakefield calculations we locally approximate the structure by a periodic model. The calculation method is as follows [Bane 1980a]: For the geometry of five representative cells, numbers 1, 51, 103, 154, and 206, we use the computer program KN7C [Keil 1972] to obtain the synchronous frequencies and loss factors of the first 250 or so monopole modes, which give us the low-frequency impedance. We approximate the high frequency contribution using the Sessler-Vainsteyn optical resonator model [Keil 1972, Brandt 1982]. Fourier-transforming these two contributions, we obtain the longitudinal wakefield for the given geometry. To calculate the wakefield of the entire NLC linac structure, we average the wakes obtained in this way for each of the five representative cells. The transverse (dipole) wakefield is obtained in an analogous manner, but using the computer program TRANSVRS [Bane 1980b] to obtain the dipole mode frequencies and loss factors. We first obtain the longitudinal dipole wakefield $W_z^{(1)}(s)$, then applying the Panofsky-Wenzel theorem [Panofsky 1956], we obtain the transverse dipole wakefield: $W_x(s) = \int_0^s W_z^{(1)}(s') ds'$.

The short-range longitudinal wakefield for cells 1, 51, 103, 154, and 206 of the NLC structure are shown in Figure 7-14 as a function of the distance behind the particle that is generating the wake. We should point out that the values at the origin, which should equal $W_z(0) = Z_0 c / (\pi a^2)$ [Palmer 1990, Gluckstern 1989]

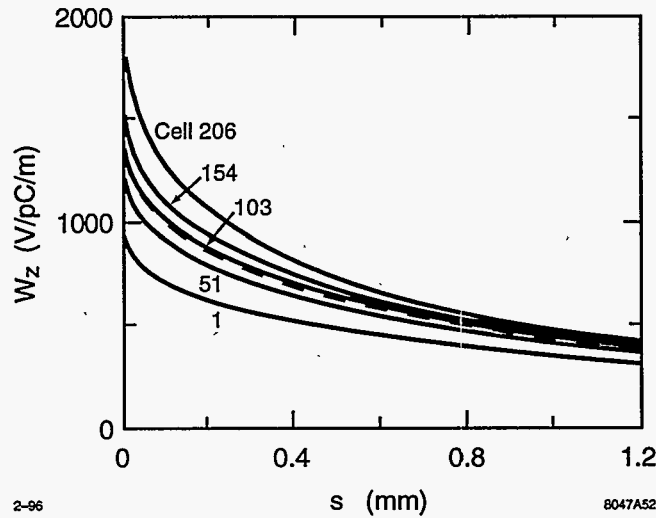


Figure 7-14. The longitudinal wakefield of cells 1, 51, 103, 154, and 206 of the NLC structure. The average is the same as that of cell 103. The dashed curve represents the average wake, the dots, the empirical fit (see text).

are about 5%–10% low, indicating some calculation error. The average wakefield for the entire structure is given by the dashed curve. A fit to the average wakefield, given by

$$W_z = 1388(V/pC/m) \cdot \exp[-1.16(s/mm)^{0.55}] \quad , \quad (7.4)$$

is shown by the dots. The net intra-bunch wakefield is obtained by convoluting this function with the longitudinal charge profile of the bunch. To set the length scale, the rms bunch length in the NLC will be in the 100- to 150-micron range.

The short-range transverse wakefield for the representative cells are given in Figure 7-15. In this case, the slopes at the origin should equal $W'_x(0) = 2Z_0c/(\pi a^4)$; our results are slightly higher, but in no case by more than 4%. The average wakefield for the entire structure is indicated by the dashed curve in Figure 7-15. A fit to the average wakefield, given by

$$W_x = 88(V/pC/mm/m) \cdot (1 - \exp[-0.89(s/mm)^{0.87}]) \quad , \quad (7.5)$$

is indicated by the dots.

MPS Spoilers

There is one 8-mm-long MPS spoiler with an iris radius of 2 mm following every accelerator structure. Because the aperture is roughly a factor of two smaller than that of the accelerator structures, the transverse wakefield of these spoilers can be significant even though there is only one per structure. Figures 7-16 and 7-17 show the spoiler geometry and transverse wakefield kick on a 100- μ m-long bunch; this kick is roughly 10% of the kick due to a single accelerator structure and thus has a small, but noticeable, effect on the dynamics. Finally, the relative magnitude of the longitudinal wakefield and the long-range wakefields are much smaller than those of the structures and can be neglected.

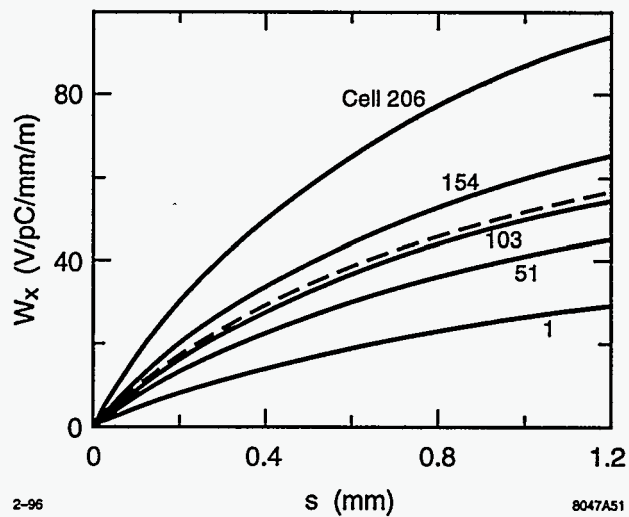


Figure 7-15. The transverse (dipole) wakefield of cells 1, 51, 103, 154, and 206 of the NLC structure. The dashed curve gives the average wakefield; the dots, the empirical fit.

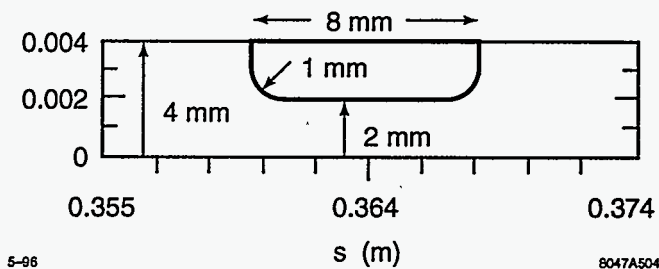


Figure 7-16. Geometry of MPS spoiler located at the ends of the accelerator structures.

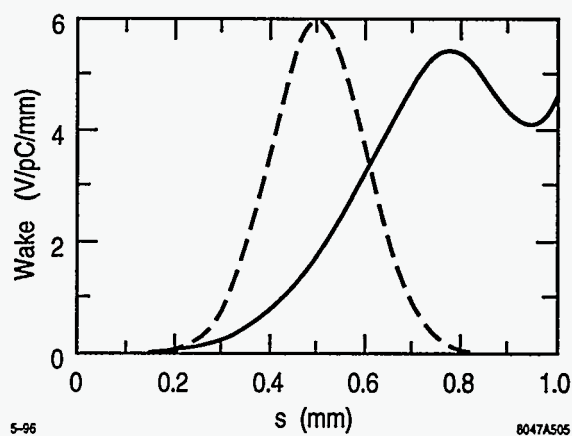


Figure 7-17. Transverse wakefield (solid) due to a 100- μm -long bunch passing an MPS spoiler; this is roughly 10% of the transverse wakefield due to a single 1.8-m accelerator structure. Dashed curve is bunch profile with 100- μm σ_z .

7.4.2 Long-Range Wakefields

In this section we discuss how the wakefield produced by a single bunch varies on the length scale of the bunch train. Given the transverse positions of the bunches in the train, these results can be used to compute the net wakefield acting on any bunch.

Detuned Structures

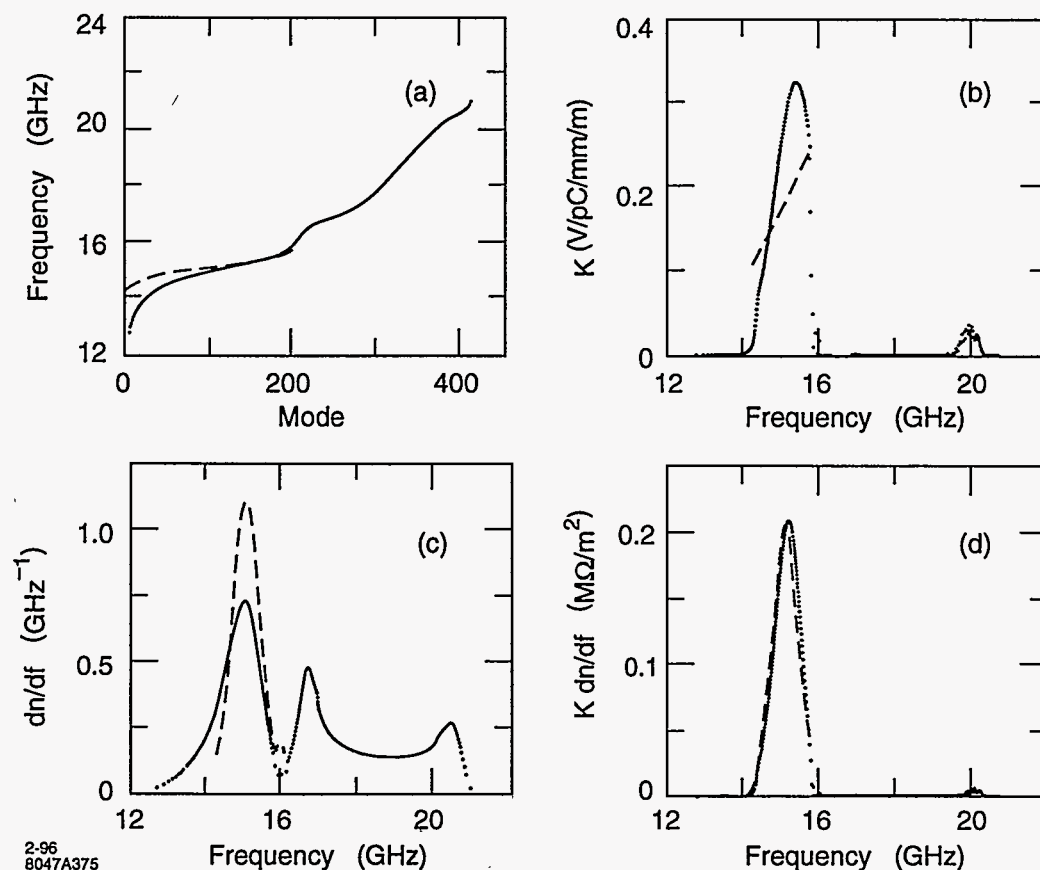
We first discuss the calculation of the long-range wakefield for a structure with detuning alone [Bane 1993]. The detuning involves varying the cell geometry to produce a Gaussian distribution in frequency of the product of the dipole mode density and the mode coupling strength to the beam. This yields an initial Gaussian fall-off of the integrated wakefield through the structure, which eventually levels off due to the discreteness of the modes. Further details of the detuning are given in Section 8.2. Here we outline the computational methods used to obtain the wakefield.

In this derivation, we consider each cell to be excited in some combination of cell modes (in practice, from the lowest or the lowest two dipole bands) and that the coupling holes determine the relation between the coefficients of these modes in two adjacent cells. Since the longitudinal electric field vanishes on the axis, we expect the coupling to be magnetic. We represent the structure by a single or double chain of circuits, where each circuit corresponds to a single-cell mode.

The uncoupled frequencies and the coupling parameters are obtained by applying the program TRANSVERS to periodic structures with the local cell dimensions at several points in the structure, and interpolating to obtain the values of these parameters at each cell. The coupled-circuit equations, supplemented by the appropriate boundary conditions in the first and last cells, are solved numerically by matrix inversion. The kick factors are then calculated from the resulting eigenfrequencies and eigenfunctions.

Most of the modes are localized in the structure in the lowest band. The results are shown in Figures 7-18 and 7-19 for the double-band model where only the two lowest bands are modeled. Note that the modes of the second band (roughly, those above 17 GHz) have low-kick factors and therefore do not contribute significantly to the wakefield. The wakefields obtained from the single- and double-band models do not differ greatly.

So far we have considered only the lowest two bands of dipole modes. When we perform a calculation that ignores cell-to-cell coupling but includes the effects of the modes of bands 3-8 [Bane 1994], we find that the wakefield amplitude is now an unacceptable 10% at the position of the second bunch, and it decreases only slowly as we move further back in the bunch train. This results from lack of detuning in some of the higher bands, especially the third and the sixth. Running URMEL [Weiland 1983], we find that near the light line, band 3 is a TM₁₁₁-like mode and band 6 is a TM₁₂₁-like mode. This suggests that by varying the iris thicknesses along the structure, with the thinner irises in cells with the larger radii—*i.e.*, near the beginning of the structure, and the thicker ones in cells with smaller radii—*i.e.*, near the end of the structure, we could detune these modes more. This variation has been incorporated in our structure designs: a Gaussian distribution of iris thicknesses with an average of 1.5 mm, an rms of 0.25 mm, and a total variation of 1 mm is used. This is expected to reduce to 1% the contribution of Bands 3-8 to the wakefield at the subsequent bunch locations.



2-96
8047A375

Figure 7-18. Results of double-band coupled model: (a) the mode spectrum, (b) the kick factor, (c) the mode density (normalized so that the integral of dn/df over the first half of the modes is one), and (d) the product of kick factor and mode density. For comparison, dashed lines show the results from a model that does not include the effect of cell-to-cell coupling.

Damped Detuned Structure

Although the structure detuning significantly reduces the long-range wakefield, the amplification of the betatron motion of the bunches in an NLC built with these structures would be larger than can be tolerated. One solution would be to use different structure types with interleaved modes to improve the long-range decoherence of the wakefield. Another solution is to also damp the dipole modes, which has the added benefit of loosening the internal alignment tolerances for the structure. This approach is being actively pursued; the basic method is to channel the dipole mode energy to an external load through four manifolds that run along structure and couple to each of the cells (see Chapter 8 for details).

The equivalent circuit models used for the detuned structure may be extended to this damped detuned structure (DDS). Although the theoretical treatment of this problem is still being refined, the results so far are encouraging. The initial calculations were performed using a single-band model for the accelerating structure and coupling it to a transmission line representation of each manifold mode that is included. The Q s of the modes from this treatment are shown in Figure 7-20 and the envelope of the resulting wake function

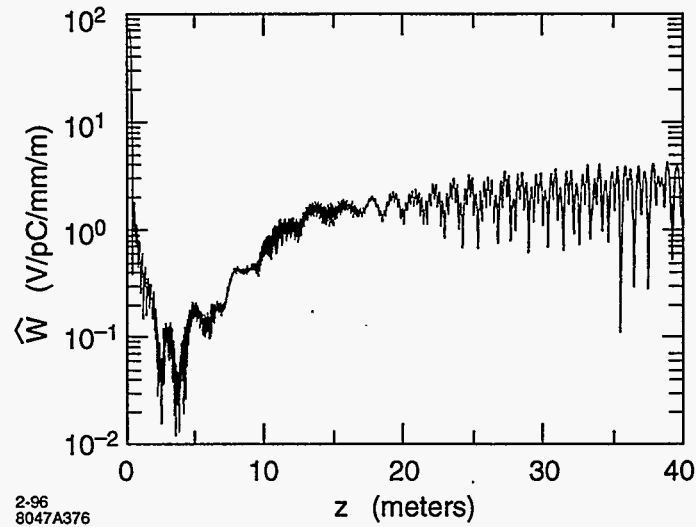


Figure 7-19. The envelope of the wake function calculated using the double-band model.

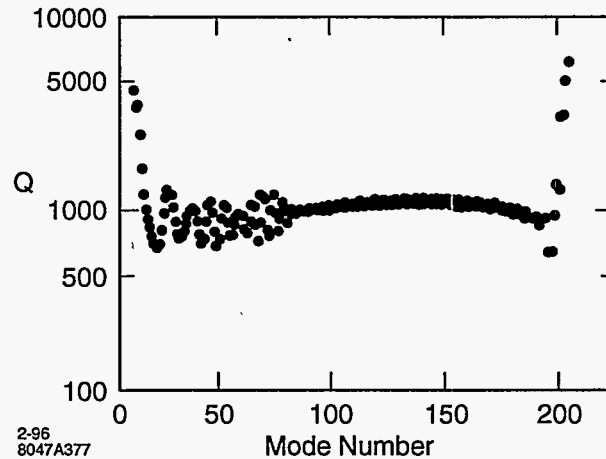


Figure 7-20. The Q s of the modes in the lowest dipole passband, calculated for the damped detuned structure (DDS).

is shown in Figure 7-21. The effect of copper losses have been included by combining the Q values shown in Figure 7-20 with an assumed copper loss value of 6500.

7.4.3 Single-Bunch Longitudinal Phase Space

The bunches will enter the NLC linacs with a 1% rms energy spread, which will be uncorrelated with longitudinal position along each bunch. In the linacs, the bunches will acquire a longitudinally-correlated component of energy spread due to the short-range wakefields and the curvature of the rf wave. Whereas

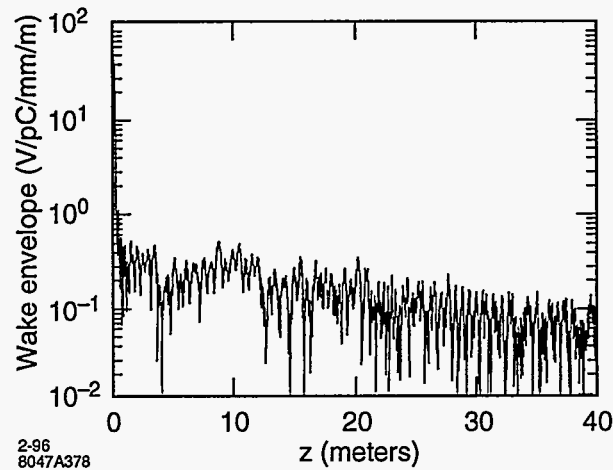


Figure 7-21. The envelope of the wakefield function calculated for the damped detuned structure (DDS).

the uncorrected component decreases inversely with energy, the correlated component will vary depending on how the phases of the accelerating rf field are set with respect to the beam timing.

There are three main constraints that one must consider when choosing the rf phase profile along the linacs. (1) The final energy spread of the beam must fit within the energy bandwidth of the final focus systems that are downstream of the linacs. (2) A correlated energy spread is needed in each bunch, with the bunch head at a higher energy than the tail, to counteract the amplifying effect of the short-range wakefield on the betatron motion of the bunch. This approach to suppressing resonant growth is usually referred to as BNS damping; using an energy spread to exactly cancel the resonant driving term, so all parts of the bunch oscillate uniformly, is generally referred to as autophasing [Balakin 1983]. We want to run as close to the autophasing condition as possible. (3) rf power is precious so the phasing must be done efficiently to maintain a high accelerating gradient.

Satisfying these constraints will require some compromises. For example, in our linacs where the beta function scales roughly as the \sqrt{E} , the optimal energy spread for autophasing is nearly constant along the machine. This could be achieved by running the beams at a constant phase behind the rf crest but the resulting final energy spread would be larger than the final-focus bandwidth. Thus the beams will need to run more forward on the crest, on average, than is optimal for autophasing. The proposed solution is to run the beams somewhat behind the crest early in the linacs, and then sufficiently in front of the crest near the end to reach the desired final energy distribution, as is done in the SLC. This method requires some extra energy overhead so we must be efficient in selecting the phase profile.

The tradeoffs in this regard are discussed in Section 7.4.4 where we examine single-bunch transverse phase space effects in general. Another approach to this problem that uses rf quadrupoles is also described. Below we discuss the constraints on the average rf phase due to the final-focus bandwidth.

The Average Linac RF Phase

Let us consider the NLC-I parameters: initial energy $E_0 = 10$ GeV, final energy $E_f = 250$ GeV, and total structure length $L_{acc} = 8150$ m. Let us assume that the bunches have a Gaussian longitudinal profile with rms length $\sigma_z = 125$ μ m, a population $N = 0.75 \times 10^{10}$ particles, and an initial uncorrelated energy spread of

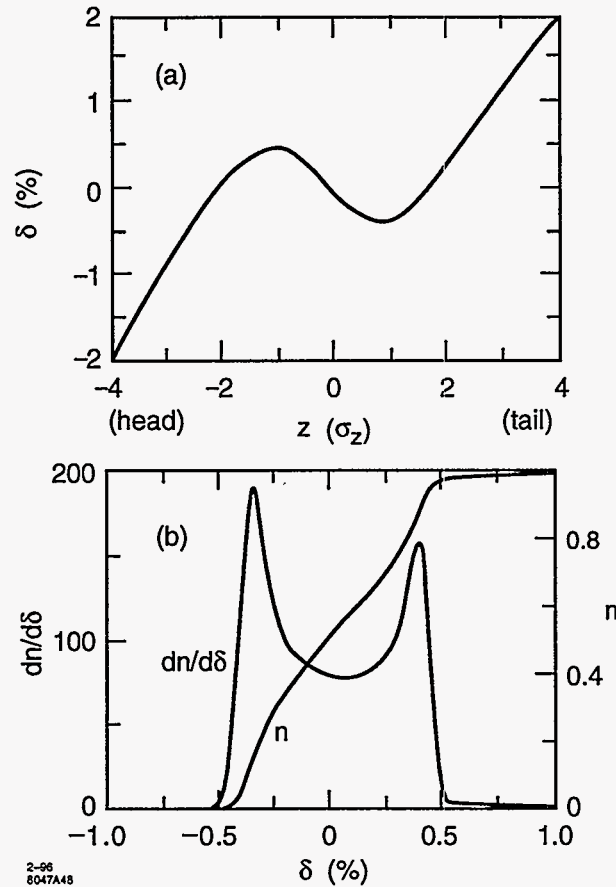


Figure 7-22. For the NLC-I when $\langle\phi\rangle = -15.5^\circ$: the correlated energy variation along the bunch (a), and the energy distribution and its integral (b).

1%. For this case, the single-bunch loading is 590 keV/m. Also, the minimum rms energy spread is obtained when the average linac rf phase $\langle\phi\rangle = -18.0^\circ$ (a negative phase represents a position in front of the rf crest); in this case the energy distribution is double-horned, with an rms spread of 0.27% and a horn spacing of 0.56%. Taking advantage of the larger energy bandwidth of the final focus systems, we choose to run the beams at $\langle\phi\rangle = -15.5^\circ$, where the horn separation becomes 0.81%. In this way we introduce a slight, longitudinally correlated, energy variation, which will reduce the energy overhead needed for autophasing. Figure 7-22 shows the resulting energy distribution and energy correlation at the ends of the linacs.

For NLC-II with $E_f = 500$ GeV, $L_{\text{acc}} = 8150$ m, $\sigma_z = 150$ μm and $N = 1.1 \times 10^{10}$, the single-bunch loading is 830 keV/m. In this case, we will run with $\langle\phi\rangle = -8.5^\circ$ to achieve the energy distribution width of 0.8%.

7.4.4 Single-Bunch Transverse Phase Space

To transport the micron-size bunches through the main linacs without significantly degrading the bunch emittances will require that certain tolerances be met in regard to stability and alignment. In this section we discuss those tolerances that result from effects which degrade the transverse emittances of the all bunches equally, and ignore those effects which degrade the emittance of the bunch train as a whole (*e.g.*, kicks from long-range transverse wakefields). In doing so, we effectively treat the linacs as if only a single bunch were being transported per rf pulse. With this caveat, we examine jitter tolerances on injection and quadrupole motion; alignment requirements for the quadrupoles, BPMs, and accelerator structures; and limits on the transverse components of the rf field. In particular, we present only the bare requirements in that no beam-based alignment or feedback techniques are assumed to be used. In some cases, we will see that the bare tolerances will be nearly impossible to meet, and so the use of these techniques will be essential. A description of these techniques and their effect on the tolerances are presented in Section 7.5.

To compute the tolerances, a number of simplifying assumptions were made. An important one is that the linacs are operated in the autophased condition so that the effect of short-range transverse wakefields on betatron motion can be ignored. For the linac lattice, it was assumed that the beta function and the spacing between quadrupoles scale as \sqrt{E} , and that the horizontal and vertical phase advance is 90° per cell. For the NLC Ib (NLC I Ib) configuration, an initial quadrupole spacing of 4.2m (3.2m) was assumed which yields a beta function profile and quadrupole magnet count that are similar to that of the proposed optics (Section 7.3.2). Only the NLC I Ib results for the vertical plane are presented here: the vertical tolerances for the NLC Ib configuration are generally about 35% looser, and the tolerances for the horizontal plane in either configuration are about a factor of three looser. The emittance growth values that are quoted are averages and are relative to $\gamma\epsilon_y = 4 \times 10^{-8}$. In most cases, the emittance growth is distributed as χ^2 with two degrees of freedom, which is exponential.

We next turn to a more detailed consideration of how one implements the desired BNS damping, *i.e.*, how one obtains as nearly as possible the autophased condition while staying within acceptable bounds of energy overhead and final energy spread. Also we examine the use of rf quadrupoles as a possible alternative to achieving autophasing.

Injection Jitter

Pulse-to-pulse variations of the bunch trajectories at injection to the linacs will degrade the machine performance in two ways. In traversing the linacs, the energy spread of the off-axis bunches will lead to filamentation, and thus increase the bunch emittances. Even in the absence of this effect, the bunches will collide off-center at the IP, thus reducing the collision luminosity. The effect of this jitter can be characterized by an equivalent increase in the bunch emittance, but requires an assumption about the transverse phase space of the jitter. If we assume that the jitter phase space is matched to the beam, as is generally seen in the SLC, then the emittance growth is equal to the square of the ratio of rms jitter to beam size. Hence, to keep the emittance growth below 3%, one must limit the jitter to less than 17% of the beam size.

Including the effect of filamentation does not change this result since the jitter phase space is matched to the beam. However, its effect would be a limiting factor if one could remove the jitter in a feed-forward manner between the end of the linacs and the IP. If the filamentation in the linac was complete, the jitter tolerance would not change, but we expect only partial filamentation, about 50° rms assuming a 0.1% uncorrelated energy spread that is independent of energy, plus a 1% uncorrelated energy spread component at the beginning of the linacs that decreases as $1/E$ (note the BNS energy spread can be ignored for this

calculation if the beams are autophased). With this partial filamentation, the injection jitter tolerance would increase to about 26% of the beam size, which would hardly justify an effort at a feed-forward correction.

Quadrupole Vibration and Ground Motion

Another source of bunch trajectory jitter is from quadrupole magnet vibrations. If the transverse position of a quadrupole is displaced, it will kick the beam by an angle equal to the offset divided by the focal length of the quadrupole. If all quadrupole positions vary pulse-to-pulse, then the bunch trajectories at the end of the linacs will vary as the sum of the betatron trajectories produced by the individual kicks during each pulse. The size of this jitter depends on the spectrum of the individual quadrupole motions as well as the correlations of the quadrupole motions. As a simplification, we assume isotropy in that we suppose that all quadrupole motion spectra are equal and that the correlations depend only on the distance between quadrupoles.

A major concern in the NLC design is the effect that ground motion will have on beam transport via the quadrupole vibration it generates. When computing ground motion tolerances in this regard, one can treat each region of the NLC, such as the electron linac, independently from the rest of the machine to a good approximation. The quantity of interest is the deviation of the beam motion from the ground motion at the end of the region when the initial beam trajectory follows the ground motion at the beginning of the region. When computing the effect on luminosity, the deviation at the end of the region is assumed to remain unchanged relative to the beam size as the beam travels to the IP, where by symmetry, it can be shown to be related to that of the opposing beam. Thus the effect of ground motion on luminosity can be computed for both halves of the machine from the relative beam motion it induces in one half.

If the ground motion is uncorrelated quad-to-quad, then the tolerance one finds on the vertical rms motion is 6 nm for a 1.5% reduction in the time-averaged luminosity ($\gamma\epsilon_y = 4 \times 10^{-8}$ is assumed at the IP). In the NLC linac tunnels, the rms vertical ground motion, when computed over periods of several seconds, will likely be larger than this tolerance. However at low frequencies, where the ground motion is largest, the motion is generally correlated over long distances which loosens the tolerance.

While much data exists on ground motion spectra, little is available on long-range correlations. To see how typical these measurements are, and to better understand the dynamics of ground motion, we did a series of seismic measurements in the SLAC linac tunnel. These are described in Appendix C together with the formalism needed to analyze the data and to compute the effect of ground motion on beam transport.

From this study, it was found that the vertical ground motion can be reasonably well described by a model in which the motion is due to horizontally-traveling waves that are isotropically distributed in direction. For two points separated by distance Δz , the model predicts that the correlation in the vertical motion equals $J_0(2\pi f\Delta z/v)$ where J_0 is the zero-order Bessel function, f is the frequency of the waves, and v is the wave phase velocity, which we find depends on f :

$$v(\text{km/s}) = 0.45 + 1.9 \exp(-f(\text{Hz})/2.0) \quad (7.6)$$

Using this correlation function, the tolerance on the rms vertical ground motion for a 1.5% reduction in the time-averaged luminosity was computed as a function of frequency. As a worst case, the tolerance was computed assuming that in addition to wave-like motion, there is an uncorrelated component of the motion that is equal to the seismometer electronic noise contribution to our measurements (see C.4 for details). The results for these two cases are shown in Figure 7-23. One sees that for frequencies above 4 Hz, the tolerance is roughly equal to the 6-nm value for uncorrelated ground motion. Below 4 Hz, the tolerance rises rapidly

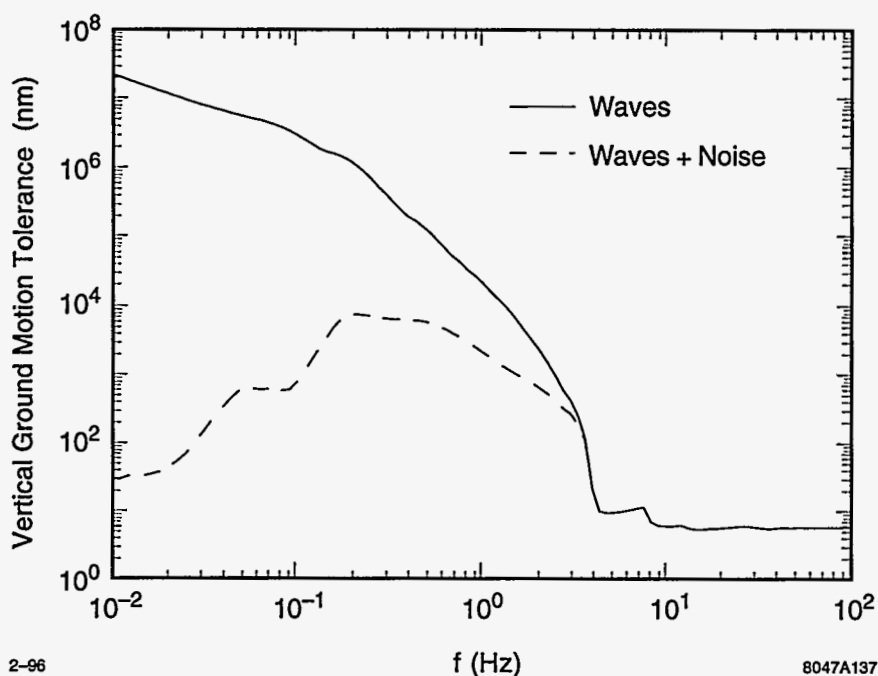


Figure 7-23. Linac rms vertical ground motion tolerance for a 1.5% luminosity reduction as a function of frequency for pure wave-like motion (solid) and for wave-like plus uncorrelated motion equal to the seismometer electronic noise (dashed).

due to the fact that the wavelengths of the ground motion, v/f , are longer than the betatron wavelengths, so that the sum of the quadrupole kicks average out. In fact, it is the 180-m betatron wavelength at the end of the linac that determines this transition point. With the inclusion of uncorrelated motion, the tolerances at low frequency reflect the fraction of the measured power that is due to seismometer noise (e.g., 1% noise power yields a $6/\sqrt{.01} = 60$ nm tolerance).

In Section 7.5.1, we compare these tolerances to measured ground motion spectra, and discuss ways to actively suppress the effects of quadrupole vibrations. We should note, however, that ground motion will not be the only source of quadrupole vibration. Vibrations caused by the water flow through the cooling circuits for the quadrupoles will have to be controlled, as will the motions of the structures if they couple through the supports and vacuum pipe to the quadrupoles (the structures themselves have a much looser vibration tolerance than the quadrupoles). Also, care will have to be taken in designing the support systems to avoid mechanical resonances.

Finally, we consider the beam trajectory jitter that results from random fluctuations in the quadrupole power supply currents. Since the beam will not travel exactly on-axis through the quadrupoles, pulse-to-pulse changes in the quadrupole magnetic fields will produce an effect similar to uncorrelated ground motion. We expect that the beam will be centered in the quadrupoles to better than $100\text{-}\mu\text{m}$ rms ($10\text{ }\mu\text{m}$ if no non-local steering is used), so the quadrupole power supplies must be regulated to 6×10^{-5} , assuming they are independent, to limit the luminosity reduction to less than 1.5%.

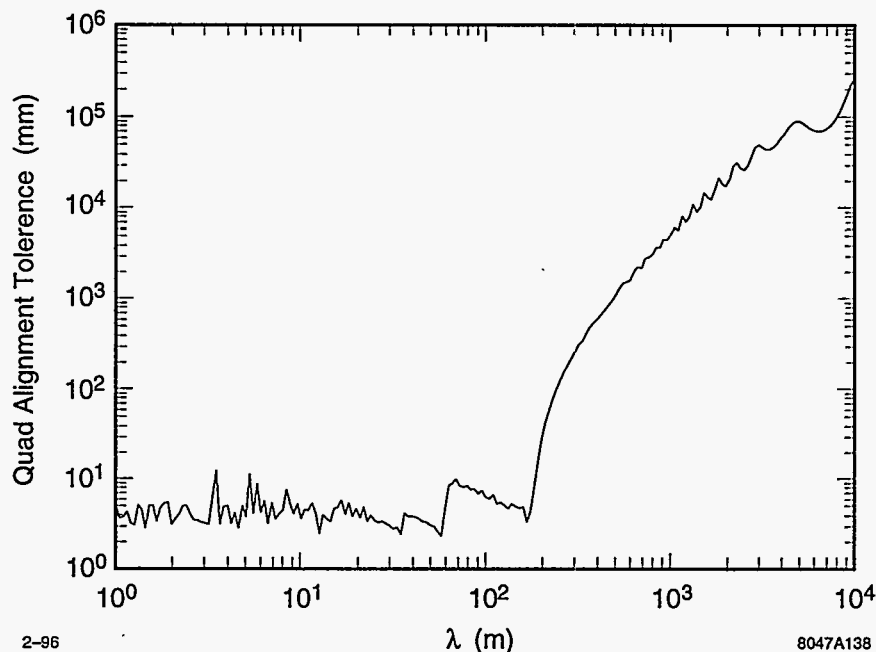


Figure 7-24. Quad alignment tolerance for a 25% vertical emittance growth as a function of the wavelength (λ) of the misalignment. A 0.6% bunch energy spread is assumed.

Quadrupole and BPM Offsets

If the quadrupoles are perfectly aligned along the linac axis and a bunch is injected on-axis, no dispersive emittance growth will occur. However, if the quadrupoles are offset from this axis, and the bunch is steered to the centers of the quadrupoles, then the differential kicks that the bunch receives due to its energy spread will generate emittance growth. This growth will be worse if the BPMs themselves are not centered within the quadrupoles since they will be used to steer the beam. The BPM offsets, which we define as the difference between the BPM centers (mechanical and electronic) and the quadrupole magnetic centers, will add in quadrature to the quadrupole offsets in their effect on dispersion if they are random. In this case, the tolerance on the sum is $3\ \mu\text{m}$ for a 25% emittance growth in the vertical plane assuming an effective bunch energy spread of 0.6%.

Since the quadrupole alignment accuracy will depend on the distance scale over which the alignment is done, a better way to characterize the tolerance is in terms of the wavelength of the misalignments. For this purpose, we assume that the quadrupole offsets are sinusoidal with wavelength λ , and that bunches are steered to zero in the BPMs, which themselves are centered in the quadrupoles. Figure 7-24 shows the tolerance on the offset amplitude for a 25% vertical emittance growth as a function of λ assuming that the beam is injected on-axis. One sees that for $\lambda < 180\ \text{m}$, the tolerances are nearly all less than $10\ \mu\text{m}$, and at larger λ , they rise rapidly. This rise occurs because λ becomes larger than the longest betatron wavelength in the linac, so the dispersion averages out (*i.e.*, for the same reason that the ground motion tolerances rise below 4 Hz in Figure 7-23). Using conventional survey methods, one would have a difficult time achieving a $3\text{-}\mu\text{m}$ alignment on a 1-m scale, let alone on a 180-m scale. The use of beam-based alignment will alleviate the need for such tight tolerances; this is discussed in Section 7.5.2.

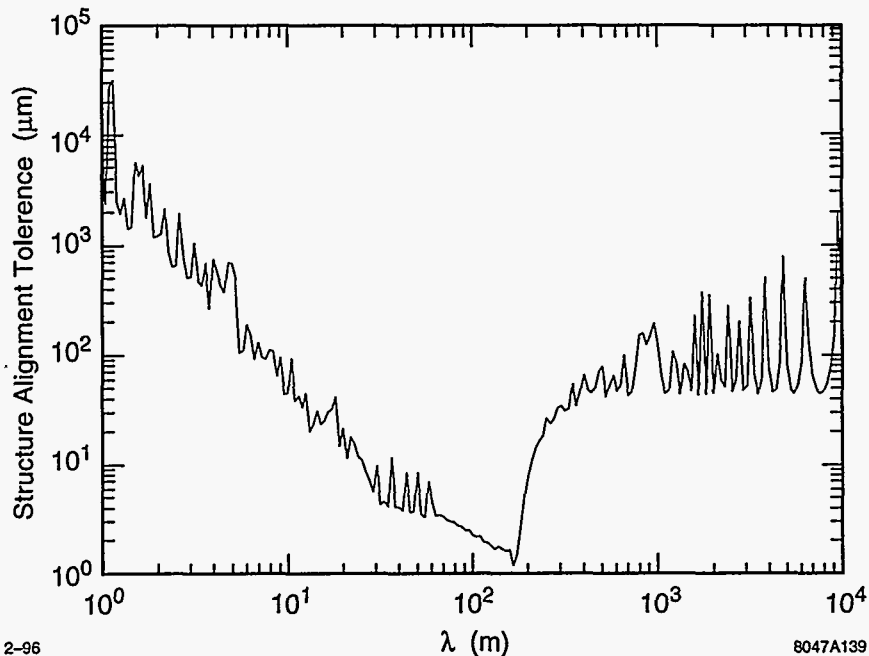


Figure 7-25. Structure alignment tolerance for a 25% vertical emittance growth as a function of the wavelength (λ) of the misalignment.

Structure Offsets

If a bunch travels off-axis through a structure, the transverse wakefield that is generated will produce a differential kick along the longitudinal profile of the bunch. Like the differential kicks due to the bunch energy spread, the wakefield kicks will generate an emittance growth. To a good approximation, the effect of the wakefield kicks can be treated to first order where one ignores the position variation along the bunch when computing the generated wakefields. In this approximation, the emittance growth depends on the rms variation of the wakefield kick along the longitudinal profile of the bunch, just as dispersive growth depends on energy spread. The rms wakefield kick used to obtain the results presented here is 6.2 V/pC/m/mm , which assumes a $150\text{-}\mu\text{m}$ bunch length.

To compute the structure alignment tolerances, we assume that the quadrupoles and BPMs are perfectly aligned, and that the net wakefield kick to the bunch is removed locally by steering the bunch centroid to zero in the BPMs. In this case, a $6\text{-}\mu\text{m}$ rms random misalignment of the structures parallel to the beam axis yields a 25% vertical emittance growth. Like the dispersion analysis, we also computed the tolerance for sinusoidal misalignments of the structures, where both intra-structure and inter-structure alignment varies. Figure 7-25 shows the results for a 25% vertical emittance growth as a function of the wavelength of the misalignment. One sees that the most sensitive wavelength is about 180 m. This wavelength is resonant with the betatron motion near the end of the linacs where the weaker focusing leads to a larger growth. Like the quadrupole alignment tolerances, achieving these values would be extremely difficult with conventional alignment techniques. Instead, we will rely on beam induced signals from the structures to keep them centered about the beam trajectory. This method is described in Section 7.5.2. Note that we revisit structure tolerances in Section 7.4.6, where we consider multibunch effects as well.

RF Deflections

Internal misalignments of the structures (*e.g.*, bookshelving) and dark currents within the structures can generate transverse rf fields that will deflect the beam. These fields, which can be static or vary pulse-to-pulse, will produce both a net and differential kick to the bunches. Using the wakefield tolerance result for uncorrelated structure offsets, one can readily compute the tolerance on the allowed integrated transverse rf field per structure assuming that the rf kicks are also uncorrelated structure-to-structure, as is likely to be the case.

To prevent an emittance growth of more than 3% as the result of the differential kicks produced along the longitudinal profile of a bunch, the tolerance on the integrated rf field amplitude is $1.2 \text{ keV}/\sin(\psi)$ where ψ is the phase offset of the bunch from the crest of the rf field. This tolerance holds whether the kicks are static, or vary pulse-to-pulse in amplitude but with a constant phase relative to the beam. Fields that are 90° out of phase with respect to the beam produce the largest slope and hence the tightest tolerance; for the transverse rf field effect on the net motion of the beam, the opposite is true. Here the tolerance is $0.04 \text{ keV}/\cos(\psi)$ for a 3% emittance growth if the transverse field jitters pulse-to-pulse, and $80 \text{ keV}/\cos(\psi)$ if the field is static but there is 10^{-3} pulse-to-pulse energy gain jitter in the groups of four structures that are powered in common.

For either emittance growth mechanism, it will be especially important that the tolerances be met if the rf transverse fields vary independently pulse-to-pulse since there will be no means to offset their effect. Currently we do not have much information on the size and temporal nature of the transverse rf fields in the X-band structures that have been built. (This is also true for the transverse field jitter in the SLC S-band structures, although there is a hint that it could be as high as 1-keV rms per 12-m section based on the observed white-noise-like beam jitter growth in the SLC linac.) From observing the power in the dipole modes that are excited in the DDS X-band structures without beam, we should be able to put limits on the transverse kicks. Also, from operating the NLCTA, we should learn enough to know whether the tolerances for most cases would be met in an NLC built with the same rf system.

The RF Phase Profile Along the Linac

To suppress betatron amplification due to short-range wakefields, we plan to vary the klystron rf phase profile along the linacs to best achieve autophasing while keeping the average phase such that the final-bunch energy width is 0.8%, as was discussed previously. To decide which particular rf phase profile to use, we studied the sensitivity of the final beam emittance to betatron oscillations in an error-free linac. As figures of merit, we define t_0 as the injection jitter tolerance, and t as the injection drift tolerance. Specifically, t_0 is the ratio of the initial vertical bunch jitter, y_0 , to the initial vertical bunch size, σ_{y0} , that results in a time-averaged emittance growth of 25% with respect to the beam line axis; t is defined similarly except that the emittance growth is with respect to the bunch centroid. Note that for the case of no wakefields and no energy spread, $t_0 = 0.75$ and $t = \infty$, and that for $t_0 > 0.75$, there is actual damping of the initial oscillation. The values of $t_0 = 0.75$ and $t = \infty$ are also the case for exact autophasing in the absence of an uncorrelated energy spread.

The oscillation studies were done using the parameters of the NLC-I, but with an active linac length of 7500 m, for which an energy width of 0.8% is obtained when $\langle\phi\rangle = -14.0^\circ$. The lattice used was a piecewise FODO array with 90° phase advance per cell. Between the quadrupoles there are an integer number of 1.8-m-long accelerating structures, beginning with two structures between the first two quadrupoles. Overall, β scales roughly as \sqrt{E} . Initially, $\langle\beta_0\rangle = 8 \text{ m}$.

First, let us consider the simple case where all rf phases are equal. Figure 7-26 shows the tolerances as a function of this phase, ϕ . We see that at $\phi = -14.0^\circ$, both the injection jitter and drift tolerances are 0.1.

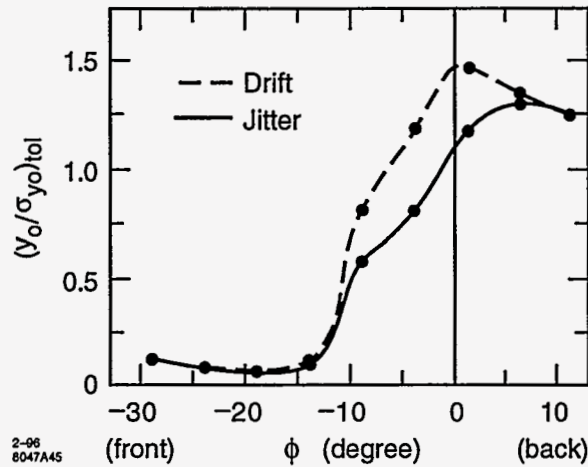


Figure 7-26. Tolerance to oscillations at injection, i.e., the ratio $(y_0/\sigma_{y0})_{tol}$ that gives 25% emittance growth at the end of the linac, when all klystrons are set to phase ϕ . For the jitter tolerance (solid curve) the emittance is calculated with respect to the beam line axis; for the drift tolerance, with respect to the bunch centroid.

To be near the autophasing condition ($t_0 \approx 0.75$) throughout the linacs, the klystron phases need to be shifted by about $+10^\circ$. Unfortunately, we cannot run this way since the final beam energy spread would be unacceptably large.

To constrain the final energy spread and still allow freedom to adjust the phase profile, we propose a method similar to that used in the SLC. We divide the klystrons into two families, with the first family containing the first n_a klystron units that are set to phase ϕ_a , and the second containing the rest of the units that are set to phase ϕ_b . In all cases the average phase is kept fixed at $\langle \phi \rangle = -14.0^\circ$. For the purposes of this calculation, the i^{th} klystron unit denotes all klystrons that feed into the i^{th} group of four lattice cells; in total there are 88 such units. Injection jitter tolerance curves were calculated for fixed amounts of energy overhead, ΔE_{BNS} , for the phase shifting; here $\Delta E_{BNS} = 2, 4, 6$ GeV. Plotted in Figure 7-27 are the injection jitter tolerance, the relative number of a -type klystron units n_a/n_{tot} , and ϕ_b , all as a function of ϕ_a . We see that if we are willing to give up 6 GeV, which is a 2.5% energy overhead, we can reach an injection jitter tolerance of $t_0 = 0.9$ with $\phi_a = 2^\circ$, $n_a/n_{tot} = 0.55$, and $\phi_b = -23.7^\circ$.

Next we studied the effect of jitter that begins at various locations along the linacs, not just at injection. In Figure 7-28 we plot the tolerances as functions of starting location of the jitter for the cases of no BNS damping, and with BNS damping, with $\Delta E_{BNS} = 6$ GeV and $\phi_a = 2^\circ$. Note that BNS damping helps primarily in the first half of the linac, which is precisely where we need it most.

In the tolerance studies described above, we were mainly concerned with the behavior of the core of the beam, which is the part that contributes most to luminosity. In the simulations that were done for these studies, the longitudinal distribution was truncated at $-2.5\sigma_z$ (in front of beam center) and $2.0\sigma_z$ (in back of it), so that a few particles far out in the tail of the distribution would not significantly affect the results. However, because of their potential for generating backgrounds, we would also like to know the behavior of particles in the tails. To show how a betatron oscillation affects such particles we have repeated the calculation for our BNS example, but now tracking longitudinal slices that cover $\pm 4\sigma_z$ of the bunch. In Figure 7-29, we show the phase space of a bunch that was injected with an initial vertical offset of σ_{y0} . Note that the largest amplitude slices are in the tail of the beam, at $z > 2.5\sigma_z$, followed by slices at the head, at $z < -2.5\sigma_z$. Therefore, it is desirable to truncate the longitudinal distribution of the bunches at $|z| \lesssim 2.5\sigma_z$.

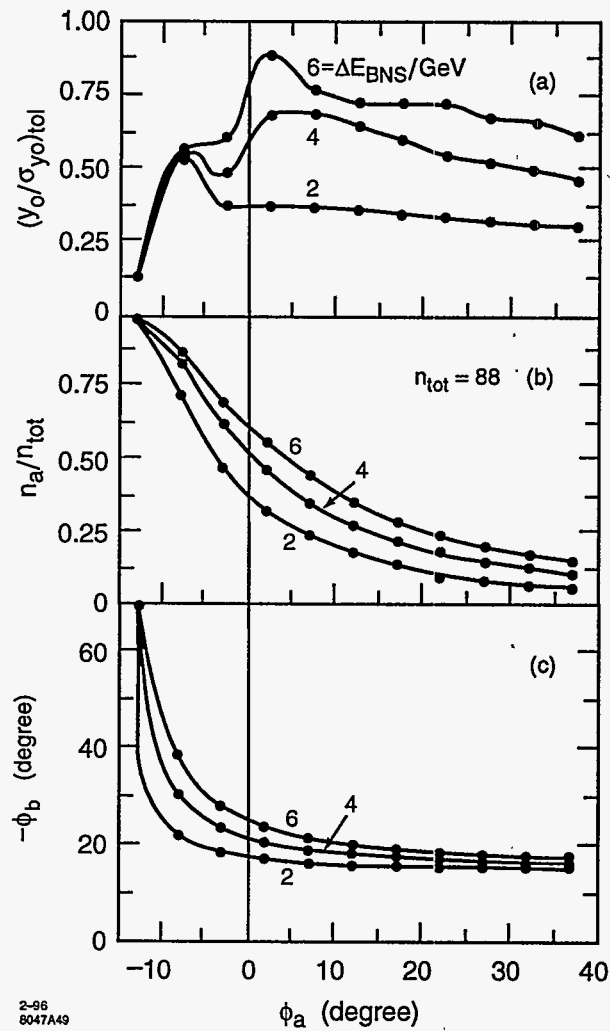


Figure 7-27. Injection jitter tolerance for 25% emittance growth for klystron configurations employing two families of phases, plotted as (a) function of the phase of the first family ϕ_a for $\Delta E_{bns} = 2, 4, 6$ GeV. In all cases the final energy distribution has a width of 0.8%. Also plotted are (b) the relative number of units in family a , and (c) the phase of the second family ϕ_b .

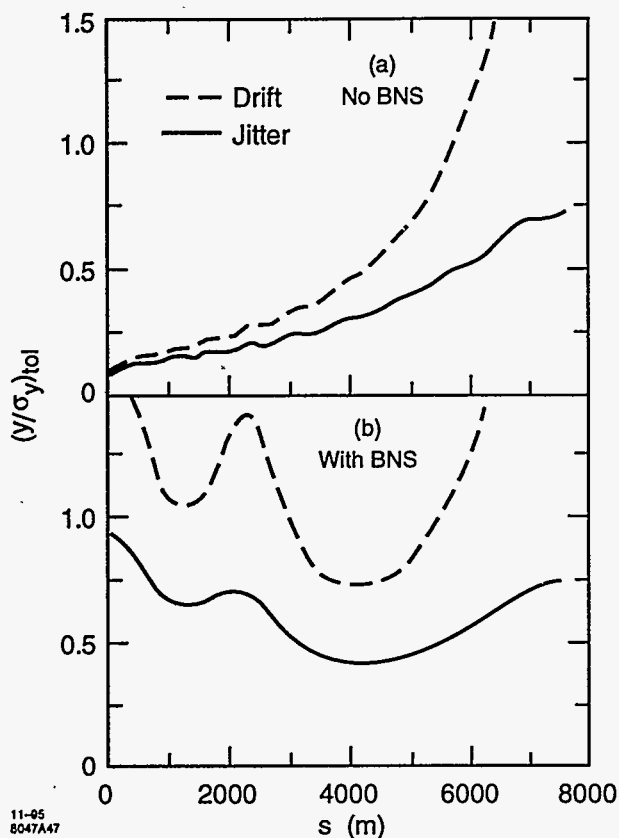


Figure 7-28. Tolerance to oscillations beginning in the linac as function of the starting location of the oscillation, for the case of (a) no BNS damping, and (b) with BNS damping, with $\Delta E_{BNS} = 6$ GeV and $\phi_a = 2^\circ$. Plotted is the ratio of the initial jitter to beam size at that location that yields a final emittance growth of 25%. For the jitter tolerance (solid curve), the emittance is calculated with respect to the beam linac axis; for the drift tolerance (dashed curve), the emittance is calculated with respect to the beam centroid.

The Option of Using RF Quadrupoles

In the CLIC project, rf quadrupoles have been proposed as a means to suppress wakefield-induced betatron growth as an alternate to the BNS method of using a correlated energy spread [Schnell 1987, Schnell 1991]. A small fraction of the accelerating structure cells ($\sim 10\%$) are built in a noncylindrically symmetric shape, resulting in a fundamental mode that focuses as well as accelerates. With this system, in principle, BNS-like damping can be effective throughout the linacs, with no additional cost in energy overhead. For cavities coupled by narrow slits, the focusing gradient (in T/m) is given by [Schnell 1987]:

$$G = \frac{k_{rf} E_z}{2c} \sin(k_{rf} z + \phi) \quad , \quad (7.7)$$

where k_{rf} is the rf wave number, E_z is the accelerating gradient, and ϕ is the rf phase. Near $\phi = 0$ there is a nearly linear variation of gradient along the bunch. Although the model used to compute G is very simplistic, it has been reported that in realistic accelerator structures, where either the normal irises have

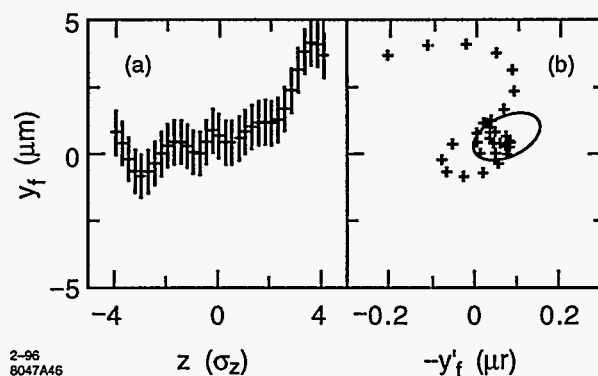


Figure 7-29. Vertical phase space of a bunch that was injected off axis by σ_{y0} in a linac with $\Delta E_{BNS} = 6 \text{ GeV}$ and $\phi_a = 2^\circ$. Shown are (a) the final centroid positions y_f (the error bars indicate $\pm\sigma_{yf}$) vs. longitudinal position within the bunch z , and (b) the final centroid positions vs. final centroid angles (the curve is the 1σ ellipse of the beam slice at $z = 0$).

been flattened, or where the cavity is elliptical with the ratio of the major to minor axis being about 2, the gradient can be 85% of that given by Equation 7.7 (though, in the latter case, with 25% reduction in fundamental mode R/Q) [Schnell 1991].

From Figure 7-26 we see that we would like an rf quadrupole focusing strength that is equivalent to about a $\Delta\phi = 10^\circ$ shift of average phase, or a focusing strength change at $z = \sigma_z$ of $k_{rf}\sigma_z \tan \Delta\phi \approx 0.5\%$. Assuming that the rf quadrupoles are 80% as effective as Equation 7.7, and using our machine parameters, we find that 4.5% of the structures need to be rf quadrupoles. Considering that we have a piecewise constant lattice, this number increases to 6.3%. Finally, assuming that only two versions of our accelerating structures will be built—one with an x -focusing rf quadrupole and one with an x -defocusing rf quadrupole—and that there will be on average many accelerating structures between neighboring quadrupoles, the fraction of each structure that would be used for rf focusing becomes 10%. This would require a major redesign of our accelerating structures.

Another approach is to build small, lossy rf quadrupole cells, one for each quadrupole (~ 350 in total), that are powered to an effective gradient of 100 MV/m. In this case, the total length of the rf quadrupole cells relative to the total accelerator structure length is 1.5%.

7.4.5 Multibunch Longitudinal Phase Space

This section discusses multibunch longitudinal dynamics, and the method of multibunch energy compensation planned for the NLC.

Without some method of compensation, there would be a drop in energy of about 25% from the head of a train to the tail due to beam loading in the accelerating mode. There is also potentially some bunch-to-bunch variation in energy due to HOMs—this must be controlled by detuning and/or damping those modes.

The tolerance on the multibunch energy spread and on the variation in the average energy of the beams have both been taken to be as little as $\Delta E/E \sim 10^{-3}$ in some of the simulations discussed or presented in this section. This may seem somewhat conservative since the energy bandwidth of the final focus is .8%. However, it needs to be kept small due to the residual dispersion in the linac.

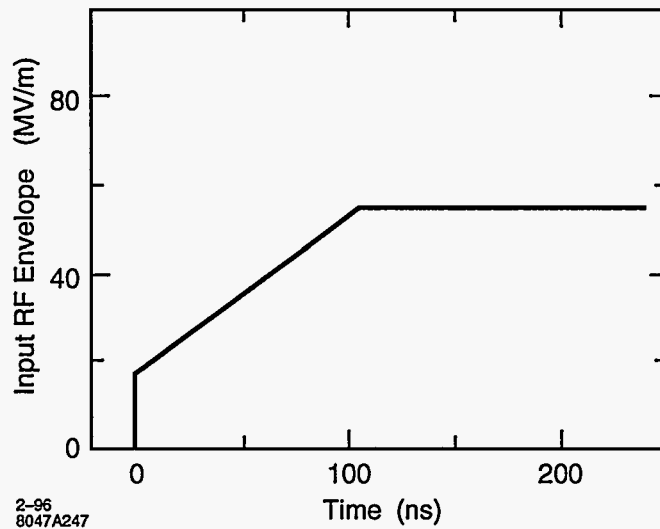


Figure 7-30. Envelope of input rf pulse, used in long-pulse pre-filling compensation scheme.

rf frequency, f_{rf}	11.424 GHz
Section length	1.8 m
Attenuation τ	0.505
Fundamental mode Q	7107
Fundamental mode loss factor, κ_1	203.75 V/pC
Filling time, T_f	100 ns
Bunch spacing	$16\lambda_{rf} \approx 42$ cm
Bunch charge	1×10^{10}

Table 7-7. Parameters used in energy compensation simulations.

The method of beam-loading compensation is to pre-fill the rf structure with a pulse shaped to simulate the steady-state beam-loaded rf profile in the structure. This profile is then automatically maintained if the incoming rf field amplitude is kept constant during the passage of the train. A simple linear ramp yields good compensation, but the rf pulse could be further corrected to increase the compensation (and maintain it via feedback as conditions vary).

The input rf pulse used in our example is shown in Figure 7-30. However, since dispersion creates large amplitude variations on the front of the rf pulse, it is desirable to wait an additional 10 ns before injecting the bunch train, to allow the worst of these dispersion “wiggles” to propagate out of the structure.

We model the linac structures as having a constant unloaded gradient, with $2\pi/3$ phase advance per cell. Parameters are shown in Table 7-7. In this subsection, the parameters of the ramp are chosen to give a loaded average energy gradient of 50 MV/m. Charge per bunch is 1×10^{10} and the bunch spacing is 16 rf buckets (~ 1.4 ns).

A detailed simulation program has been written [Thompson 1993] in which one may take into account input rf pulse shaping and timing, the dispersion of the rf pulse as it transits the structure, the longitudinal distribution of charge within the bunches, the long-range wake including both the fundamental (accelerating)

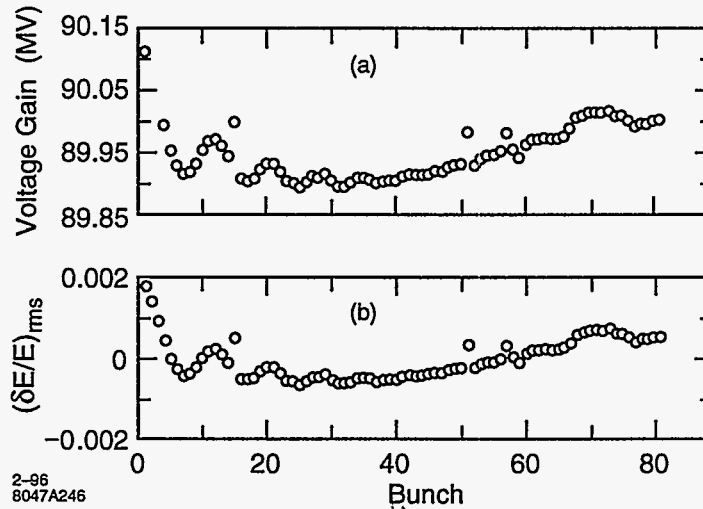


Figure 7-31. (a) Average energy gained by each bunch in a single 1.8-m accelerating section. (b) Fractional deviation of the energy centroid of each bunch from the average energy of the bunches.

mode and higher order modes, the short-range wake, and phasing of the bunches with respect to the crests of the rf.

Figure 7-31(a) shows the average energy gained by each bunch in a single 1.8-m accelerating section. Figure 7-31(b) shows the fractional deviation of the energy centroid of each bunch from the average energy of the bunches. Here we have included the effect of dispersion of different frequencies in the rf pulse as it travels through the structure; this is the cause of the ripples seen in the energy distribution of the bunches. The energy spread can be reduced further by shaping the rf pulse to be slightly different from the linear ramp used here.

We must also run the bunches off-crest to do intrabunch energy compensation of the short- and long-range wakefields. The short-range wakefield used here is an average of the short-range wakes for individual cells of the detuned structure (Figure 7-14).

We assume each bunch has an approximately Gaussian distribution and divide the charge into nine equally-spaced macroparticles with Gaussian weight, assuming $\sigma_z = 100 \mu\text{m}$. We seek the optimum phase for minimizing the energy spread by varying the rf phase, while also adjusting the height of the ramped rf pulse to keep the steady-state bunch centroid energy gain constant; the resulting energy spread as a function of rf phase at the bunch centroid is shown in Figure 7-32. There is some variation in the rms energy spread of individual bunches due to the effects of the long-range wakefields and the compensation scheme; thus optimization of BNS phase will be done for a bunch near the middle of the train which has an average energy spread.

Bunch Length Variations

Taking the bunch to be -13° off-crest (*i.e.*, 13° ahead of the crest, so that the tail receives more energy from the rf than the head, to make up for beam loading), we consider the effect of varying the bunch length, while keeping all other parameters constant. The effect on the rms fractional energy spread is shown in Figure 7-33.

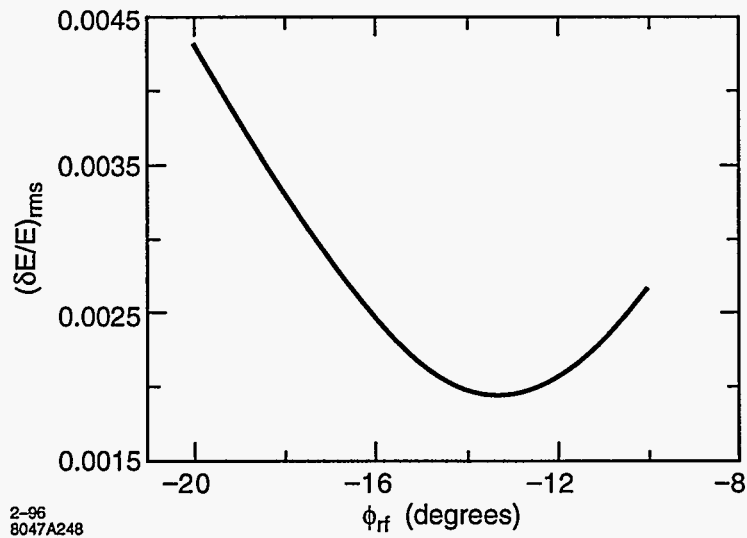


Figure 7-32. The rms energy spread as a function of rf phase at the bunch centroid.

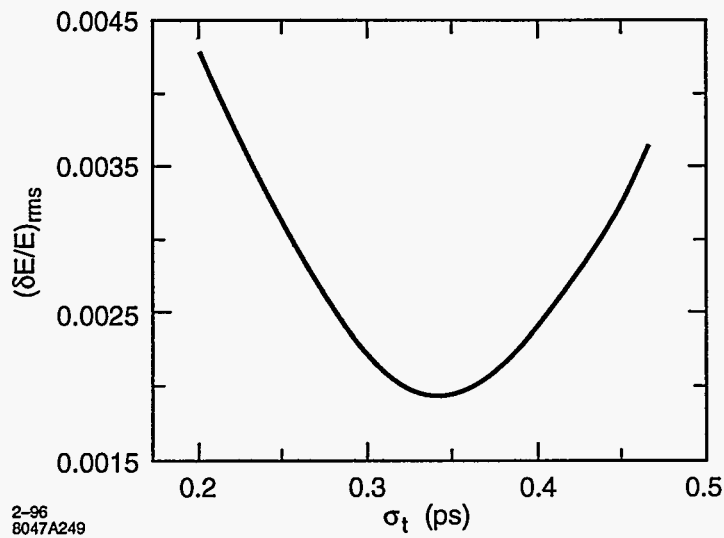


Figure 7-33. The rms fractional energy spread as a function of bunch length, for bunches -13° off-crest.

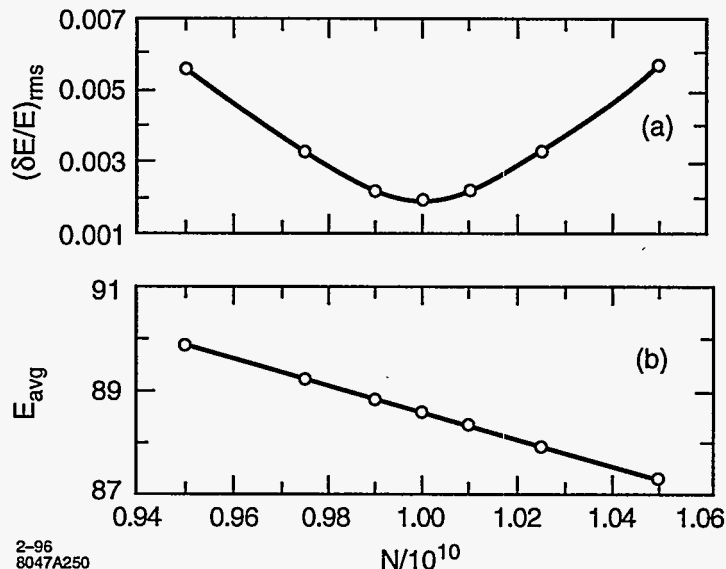


Figure 7-34. (a) The rms fractional energy spread, and (b) the average (over all slices in all bunches) energy as a function of bunch charge, taking the bunch to be -13° off-crest.

Bunch Charge Variations

Taking the bunch to be -13° off-crest, we consider the effect of varying the bunch charge, while keeping all other parameters constant. The effect on the rms fractional energy spread is shown in Figure 7-34(a). The effect on the average (over all slices in all bunches) energy is shown in Figure 7-34(b).

RF Phase Variations

We consider the effect of rf phase ripple superimposed on the incoming 11.424-GHz rf pulse. Suppose the ripple is a cosine with given period (in ns) and amplitude (in degrees at the rf frequency).

It is essential to include dispersion of the rf pulse as it transits the structure, in order to treat this problem correctly. (If dispersion is neglected, a given bunch sees the same phase throughout the structure, since the variation of phase velocity with frequency, away from its value c at the rf frequency, is neglected.) Since calculations with dispersion are quite time consuming, we have treated each bunch as a single macroparticle for the calculations of Figure 7-35. Thus the contribution of intrabunch energy spread to the overall beam energy spread is not included. Here the amplitude of the ripple was taken to be 2° . Figure 7-35(a) shows the rms fractional energy spread as a function of the period of the ripple. Figure 7-35(b) shows the average energy as a function of the period of the ripple.

The variation of the energy spread scales approximately linearly with the amplitude of the ripple.

Note that these are tolerances for variations that are the same from section to section. Thus they are pessimistic compared to tolerances for variations that are random from section to section.

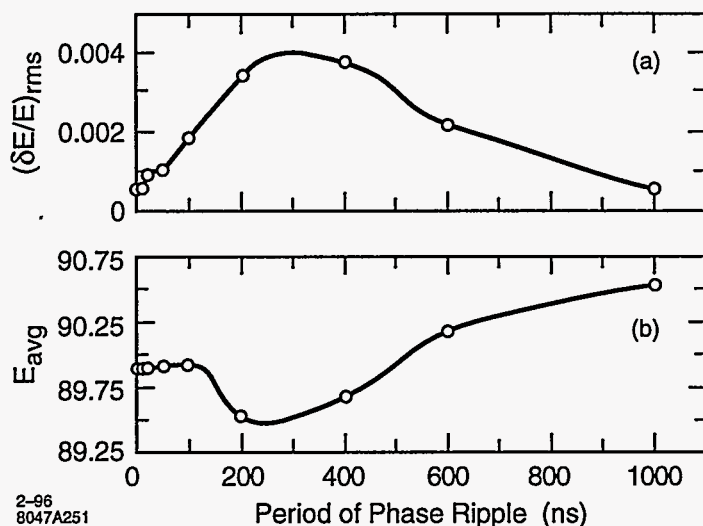


Figure 7-35. (a) The rms fractional energy spread, and (b) the average energy, as a function of the period of phase ripple with an amplitude of 2° .

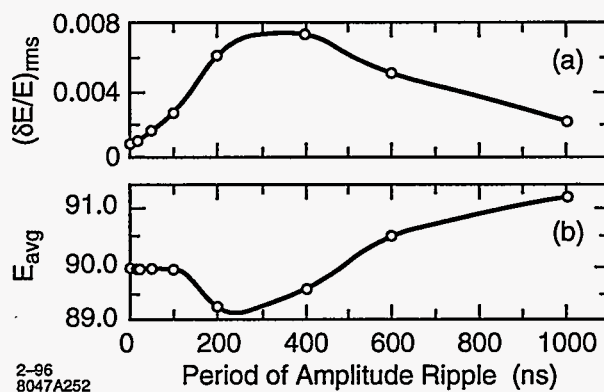


Figure 7-36. (a) The rms fractional energy spread, and (b) the average energy, as a function of the period of ripple on incoming field amplitude. Amplitude of the ripple is 1 MV/m.

RF Field-Amplitude Variations

We consider the effect of ripple in the amplitude of the incoming rf pulse. Suppose the ripple is a cosine with given period (in ns) and amplitude (in MV/m). We treat each bunch as a single macroparticle and include dispersion. Taking the amplitude of the ripple to be 1.0 MV/m, we obtain the result shown in Figure 7-36. Figure 7-36(a) shows the rms fractional energy spread (again ignoring the contribution from the intrabunch energy spread) as a function of the period of the ripple. Figure 7-36(b) shows the average energy as a function of the period of the ripple.

Again, note that for variations that are random from section to section, the tolerances should be looser than those computed here.

7.4.6 Multibunch Transverse Phase Space

In this subsection we discuss multibunch transverse phase space. Control of multibunch beam break-up has driven much of the work on accelerator structure design for the main linacs, since in the absence of a suitable cure (*e.g.*, detuning, damping of modes) it would be extremely severe. Some of the tolerances on the construction and alignment of these structures are very tight.

Structure Frequency Errors

The accelerating structures are designed to have a cell-to-cell variation in dimensions that detunes the dipole-mode frequencies and thus leads to a reduction in the amplitude of the long-range wakefield via decoherence of the modes. This frequency distribution is a truncated Gaussian (density in frequency space) and should be as smooth as possible to minimize partial recoherence of the wakefield over timescales less than or equal to the bunch train length. Small imperfections in the cell dimensions that lead to deviations in the mode frequencies by amounts comparable to or greater than the spacing between frequencies in the core of the Gaussian distribution produce a significant effect on the wakefield. The effect is worst if the frequency deviation is the same for a given mode in many or all of the structures. If, on the other hand, the frequency imperfections for the dipole modes are totally random from structure to structure, the effect is not as bad; in fact, randomizing the wakes at a given bunch spacing over a large number of sections can in some cases be beneficial.

Errors of $2.5 \mu\text{m}$ in the cavity diameter $2b$ produce fractional dipole frequency errors of about 1×10^{-4} . This is comparable to the fractional frequency spacing in the core of the Gaussian distribution used for detuning the structure.

The modification of the wakefield due to frequency errors has an effect on both the injection jitter tolerance and the misalignment tolerances. The effect can be quite significant for a detuned structure without any damping apart from the copper losses, and this was part of the motivation for going to the DDS.

Injection Jitter

There will be some offset of the injected trains with respect to the axis of the linac, and this offset will jitter from pulse to pulse. An off-axis bunch produces a transverse wake that drives bunches behind it. This wake must be kept small enough so that the projected multibunch emittance is not blown up significantly.

We have found that the emittance growth due to injection jitter is small if the envelope of the wake function is kept below about 0.8 V/pC/m/mm . For a structure with detuning alone, the wakefield envelope significantly exceeds this value even for a structure without fabrication errors (Figure 7-20).

As alluded to above, there are two extreme cases for the frequency errors: the case where the error in each frequency in the design distribution is the same in all sections (we denote this "systematic"), and the case where the error in each frequency is totally random from section to section. Note that our definition of "systematic" means that the errors are the same in corresponding cells of a given structure type, but they are still random from cell to cell in each structure type. In reality, the errors are not a simple superposition of these "systematic" and "totally random" errors, but for a first estimate, we shall treat them as such. Purely systematic errors of this sort would be a pessimistic extreme case. However, there will generally be some average error over all the cells of a given type, and this may be roughly approximated by the systematic

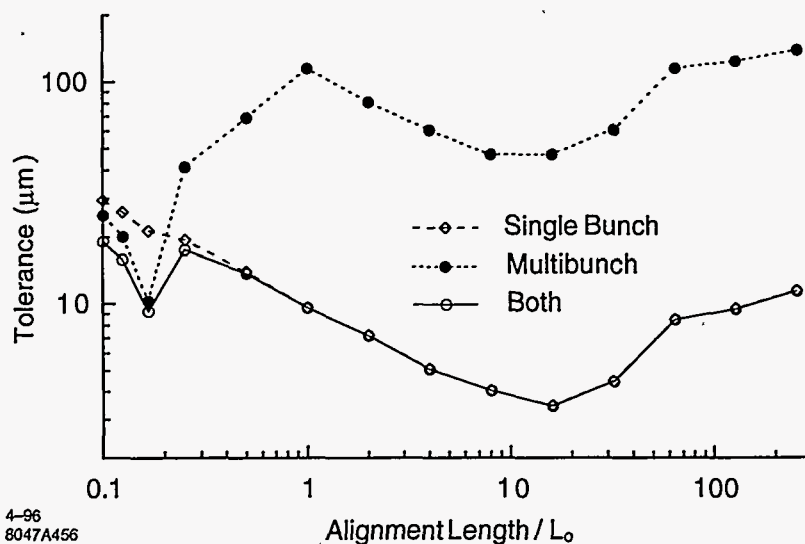


Figure 7-37. Tolerance on the structure alignment for a 50% emittance growth in the NLC-IIb linacs as a function of alignment length, when considering only single-bunch effects, only multi-bunch effects, and both effects together. L_0 is the 1.8-m structure length.

component as defined here. Superimposed on this systematic distribution is the “totally random” component of the errors.

For a detuned structure with no damping, one finds that the blow-up of the betatron amplitudes of the bunches and the resulting multibunch emittance growth are unacceptably large. For the DDS, the situation is much better—even with systematic frequency errors with rms $\delta f/f = 10^{-4}$, the transverse blow-up and projected multibunch emittance growth are acceptable. This is quantified in Section 7.6.5 where we present multibunch simulation results.

Structure Misalignments

One of the tightest sets of tolerances for the NLC is that for the alignment of the DDS accelerator structures. We computed these tolerances by simulating beam transport in the linac, with the accelerator structures randomly misaligned in a piecewise manner. We considered alignment lengths (*i.e.*, piece sizes) ranging from multiples to sub-multiples of the 1.8-m structure lengths. For the sub-multiple lengths, the long-range wakefield was recalculated to account for the relative offsets of the cells.

In computing the tolerance for a given alignment length, a “seed” of random offsets was first generated for the structure pieces. The simulation program then “launched” the beam on axis and “steered” it to the centers of the quadrupoles, which were assumed to be perfectly aligned. Using the resulting emittance growth at the end of the linac and the rms of the piece offsets, the tolerance was computed for a 50% emittance growth.

For the NLC-IIb parameters, the average tolerance obtained from 100 seeds is shown in Figure 7-37 as a function of the alignment length. Three cases are plotted: one where only single-bunch effects are included in the simulation, one where only multibunch effects are included, and one where both are included.

In the figure, a relative minimum occurs in both the single bunch and multibunch curves near the alignment length of $20L_0 \approx 40\text{ m}$, which is the average value of the beta function at the end of the linacs; this is

expected for a lattice for which $\beta \sim \sqrt{E}$. Also, for short lengths, the single bunch curve increases as the $-1/2$ power of the length: this is because the wake kicks average out over distances shorter than the betatron wavelength. However, the multibunch curve drops for alignment lengths less than L_0 because the detuning is less effective in the shorter pieces. Finally, note that the combined tolerance is dominated by the single bunch effects except for alignment lengths less than about $0.2L_0$.

As with the quad alignment, we do not expect to align the structures with conventional techniques. Instead we plan to use the signals from the structure manifolds to align them relative to the beam. In Section 7.5.2 we discuss this procedure and the emittance growth that is expected based on the tolerances in Figure 7-37.

Ion Effects

In the NLC linacs, ions are created by collisional ionization of the residual gas. Light ions, such as hydrogen, are over-focused and lost between bunches, while in the first part of the linacs, heavier ions are trapped within a bunch train. Trapped ions affect the beam dynamics in three different ways. First, the additional focusing of the trailing bunches due to the ions will lead to an increased filamentation which is insignificant only for a vacuum pressure below 10^{-8} Torr [Raubenheimer 1992]. Second, the ions cause a nonlinear octupole-like coupling of horizontal and vertical betatron motion, whose effect is greatly reduced when the horizontal and vertical phase advances are separated by about 5% [Raubenheimer 1992]. Third, the coupled motion of beam and ions may result in a fast transverse multi-bunch instability of the electron bunch train in the linacs. If the pressure is 10^{-8} Torr, the expected instability rise time at the start of the Linac is about 160 ns [Raubenheimer 1995], assuming 90 bunches of 6.6×10^9 particles each (NLC-I) and carbon monoxide (CO) ions. The beam-ion instability disappears when the ions are no longer trapped within the train. The distance at which this happens depends on the beam current and on the ion mass. As an example, for a bunch train of 90 bunches and 6.6×10^9 particles per bunch, CO ions are trapped up to a beam energy of about 38 GeV, which corresponds to a distance of about 800 m in the NLC linacs. For an average CO pressure of 2×10^{-8} Torr and an initial bunch-to-bunch offset of $0.01\sigma_y$, the expected total dilution of the vertical emittance due to the beam-ion instability is then about 4% (or $\Delta\epsilon_{yN} \approx 2 \times 10^{-9}$ m). At 5×10^{-8} Torr, the dilution would exceed 100%. For higher beam intensities, less ions are trapped over a shorter distance, and the pressure tolerance is looser.

7.5 Alignment, Stability, and Feedback

In this section, we review the methods that will be used to align and stabilize the quadrupoles, BPMs and structures, and to control the bunch orbits and energies. These methods will be essential for the successful operation of the linacs. Without them, many of the bare alignment and stability tolerances could not be met.

For control purposes it is useful to consider separately short-term (seconds or less) and long-term (hours) variations in the linacs. While feedback systems will certainly be needed to control short-term variations, they will stabilize long-term changes as well. However, it is expensive to employ them everywhere, so one generally uses more invasive beam-based techniques, such as the "autosteering" and "phase-golding" procedures in the SLC, when dealing with long-term variations of large portions of the linacs. Thus we begin in the next section with a review of the error sources and their timescales. In particular, we examine the effect of ground motion on luminosity via the quadrupole vibration it generates.

We then turn to a discussion of the alignment of the quadrupoles and accelerator structures. The quadrupoles will be initially aligned using conventional methods. Achieving the required accuracy for long length scales ($\lambda > 200\text{ m}$) will be particularly important since beam-based methods are likely to be limited by systematic errors in this regime. As a prerequisite to the beam-based quadrupole alignment, the offsets of the BPMs with respect to the quadrupoles will be determined by changing quadrupole strengths and measuring the resulting orbit changes. The BPM electronics will be designed to be stable over tens of hours to minimize the frequency of this procedure. Using the measured offsets, a beam-based quadrupole alignment algorithm will be run as a slow feedback loop ($\sim 30\text{-min}$ timescale) to limit dispersive emittance growth. As a fall-back position, beam-based correction schemes that are more invasive to machine operation will be used (*e.g.*, “dispersion-free” and “wake-free” steering).

For the accelerator structures, the alignment approach is to center them about the beam trajectory using as a guide the signals induced in their manifolds during the passage of the beam. This procedure, which we expect will be accurate to about $15\ \mu\text{m}$, will be iterated with the quadrupole alignment algorithm. Further discussion of the use of the DDS manifolds for measuring position of the structure relative to the beam is given in Section 7.10.3. In addition, or as a fall-back position, orbit bumps may be used to control the single-bunch emittance growth. Also, as discussed below, we will likely use multibunch feedback based on a fast kicker to control the projected emittance of the multibunch beam.

After the discussion of alignment procedures, we next consider how the beams will be stabilized using various feedback systems. We first discuss “fast transverse feedback” loops which will be used to stabilize the linac beam trajectory to ground motion and other disturbances that occur on timescales of a second and longer. These loops will measure the average properties of the bunch train with about a 100-nm resolution, and will reside in the five linac diagnostic stations. Information about corrections implemented at one station will be “cascaded” to subsequent stations, as is done in the SLC. As a fallback scheme to deal with ground motion, an expensive but realizable procedure is to implement feedback on each quadrupole based on information from a seismometer at the quadrupole.

Next we discuss bunch-by-bunch transverse feedback. Fast BPMs will be used to resolve transverse offsets at the sub-train level, and a fast kicker will be used to realign the bunches within a train. The main error source in this case is believed to be misalignments within and between accelerating structures, so the feedback loop will likely be operated at a relatively slow rate.

Some of the issues related to energy and energy spread have already been discussed, *e.g.*, manipulating the energy spread by the choice of rf phase profile along the linacs (Subsection 7.4.3) and the compensation of the heavy multibunch beam loading (Subsection 7.4.5). We conclude this section with a discussion of energy and energy spread feedback correction at the diagnostic stations. This last subsection also includes a discussion of linac energy management (LEM), which refers to the rescaling of the quadrupole magnet strengths when changes in the energy profile along the linacs are detected.

7.5.1 Error Sources and Timescales

For the NLC, it is important to know both the size and timescale of the sources of beam motion so that an efficient partition of feedback and alignment-type methods can be used. Data from the SLC linac operation gives us some measure of the quantities of interest. For example, attributing the Sector 18 position feedback corrections to the motions of quadrupoles between Sector 18 and Sector 11, where the next upstream feedback loop is located, yields a $0.3\text{-}\mu\text{m}$ to $0.6\text{-}\mu\text{m}$ -rms position variation per quadrupole on an hour timescale, and a $1.0\text{-}\mu\text{m}$ to $2.5\text{-}\mu\text{m}$ -rms position variation on a day timescale. These values are several times larger than can be tolerated in the NLC linacs if feedback is used only in the instrumentation regions. However, much of

the apparent quadrupole motion in the SLC is likely to be the result of dispersion. The measured variations in the betatron phase advance between Sectors 11 and 18 correspond roughly to a 0.2% (0.6%) rms energy variation on an hour (day) time scale. Given the size of the quadrupole misalignments and the orbit bumps, these energy changes could produce orbit variations of the sizes observed. Thus we would need to suppress the dispersion in the SLC to be able to observe the level of quadrupole motion of interest. Until we get a better handle on the temporal characteristics of such motion, we will design correction systems that are as fast as possible.

As for fast beam motion ($f > 1$ Hz), the vertical beam jitter at the end of the SLC linac is about 40 times larger than can be tolerated at the ends of the NLC linacs. Part of the SLC beam motion is due to injection jitter; however, if one subtracts the component of jitter that is correlated with incoming beam motion, generally more than 70% remains. In studies of the jitter, we have observed that both the incoming and additive components have a white-noise-like spectrum above 1 Hz, so neither ground motion nor magnet power supply fluctuations are likely to be the cause. Also, the jitter is not strongly correlated with bunch intensity or energy variations. Understanding the sources of this jitter remains an important goal, for if they are present in the NLC, trajectory feedback will be of little help in this frequency regime, as is the case in the SLC.

Vibration and Ground Motion

At a minimum, there will be a trajectory feedback system in each of the five instrumentation regions of the linacs (see Section 7.5.3 for more detail). In each region, BPMs with resolutions of about 100 nm will measure the average bunch position in the train, and the information will be used to control the beam trajectory on subsequent pulses via air-core dipole magnets. How well these loops will suppress betatron motion will depend on the feedback algorithms chosen. Figure 7-38 shows the response functions of two example algorithms that sample the beam orbit at 120 Hz. The "Exp(-i/6) Weighted" routine applies a correction to the next pulse based on an exponential weighting (6 pulse time constant) of the current and previously measured incident beam trajectories. The algorithm is similar to that used in the SLC except that the correction is not delayed by two pulses. (Figure 7-42 shows the SLC response curve including the effect of systematic errors). The "Next Pulse" algorithm applies a correction to the subsequent pulse to remove any orbit deviation measured on the current pulse. It provides more suppression at low frequencies at a cost of a larger amplification ($\times 2$) at high frequency. While the SLC loops sometimes oscillate, we believe that this problem will be solved to the degree that will allow us to achieve at least a factor of 10 suppression at 0.1 Hz in the NLC, even when including the complications associated with cascading the loops. We will also measure the stability of other algorithms to see if they would be practical to use as well.

If the ground motion in the NLC linac tunnel is comparable to that observed under "quiet" conditions in the SLAC linac tunnel, then its impact on the NLC luminosity should be small when the effect of trajectory feedback is included. To see this, we compare the measured ground motion spectrum with the tolerances. Figures 7-39 and 7-40 show the measurements of the differential and integrated ground motion spectra, respectively, that were made at SLAC as part of the ground motion study discussed in Appendix C. The power spectrum is actually the average of 10 spectra measured in Sector 4 of the SLAC linac on different days at 2 AM. The average power curve was used to compute the integrated spectrum which is the vertical rms ground motion that would be measured if only frequencies above the frequency plotted contributed to the motion (the plateau in the spectrum near 10 Hz results from the resonant vibration of the accelerator structure support system). Also shown in this figure are the ground-motion tolerances described in Section 7.4.4, "Single-Bunch Transverse Phase Space", for pure wave-like motion ("Waves"), and for wave-like plus uncorrelated motion ("Waves + Noise"), where as a worst case, an uncorrelated ground motion component equal to the seismometer electronic noise contribution to the measured power spectra is

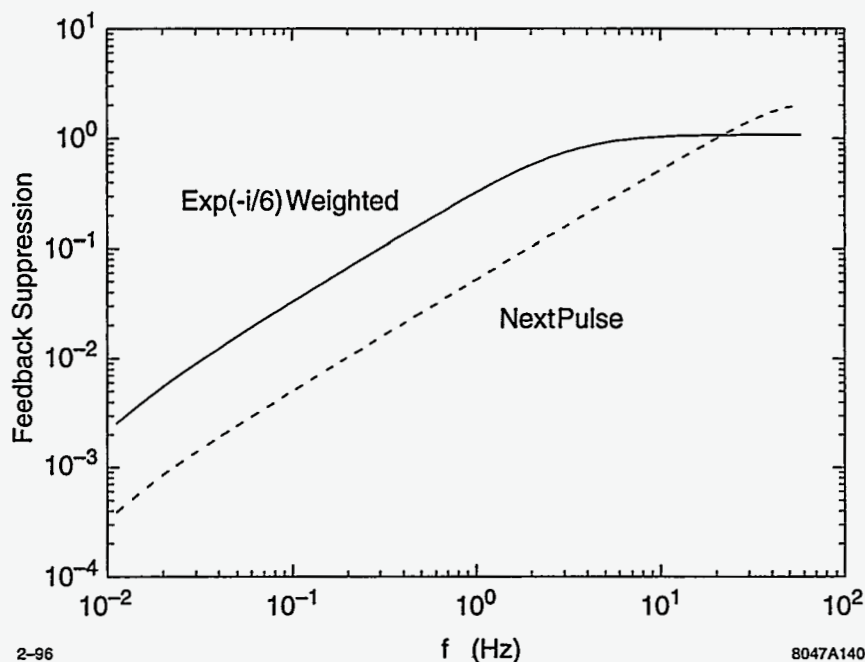


Figure 7-38. Feedback response curves for an algorithm that exponentially weights the previous pulses (solid) and for an algorithm that makes a 100% correction on the next pulse (dashed).

included. In addition, tolerances that include the effect of trajectory feedback, "Waves + Noise + FB", are plotted. They were generated by dividing the "Waves + Noise" result by the suppression obtained with the SLC-like "Exp(-i/6) Weighted" feedback algorithm. At frequencies where the integrated spectra are rapidly decreasing, one can compare the integrated spectra directly to the tolerance curves since most of the rms motion at any particular frequency is dominated the motion near that frequency.

The net effect on the luminosity is obtained by integrating the power spectrum weighted by the inverse square of the tolerance. For $f > 0.01$ Hz, this yields a luminosity reduction of 0.12% for the "Waves" case, 20% for the "Waves + Noise" case, and 0.13% for the "Waves + Noise + FB" case. Thus, the addition of feedback will still yield a small luminosity loss in the worst case scenario where uncorrelated ground motion is "hiding" just below our seismometer noise limits. Feedback will also be important for suppressing the non-wave-like components of ground motion that are significant at frequencies below 0.01 Hz.

The contribution to quadrupole vibration from "cultural" sources is hard to estimate since a site for the NLC has not been chosen. However, if the daytime activities at SLAC are typical of what will occur around the NLC, then the effect on quadrupole motion should not be large since the daytime tunnel measurements at SLAC generally do not exceed the tolerances in Figure 7-40. Also, vibration due to quadrupole cooling and support appear not to be a big problem. Seismometer measurements that were made on top of the quadrupoles and on the floor in the FFTB show that there is only a few nm of relative motion ($f > 0.1$ Hz) between them when the quadrupoles are powered.

As part of evaluating an NLC site, ground motion measurements will be made to obtain the power and correlation spectra. If the ground motion is much larger than that presented above, or if the motion is less correlated over long distances, active types of damping could be used to suppress the effect of the motion on the beam (passive damping would probably be difficult to implement below 10 Hz). For example, the vertical quadrupole vibrations could be measured with seismometers and fed back to fast corrector magnets that

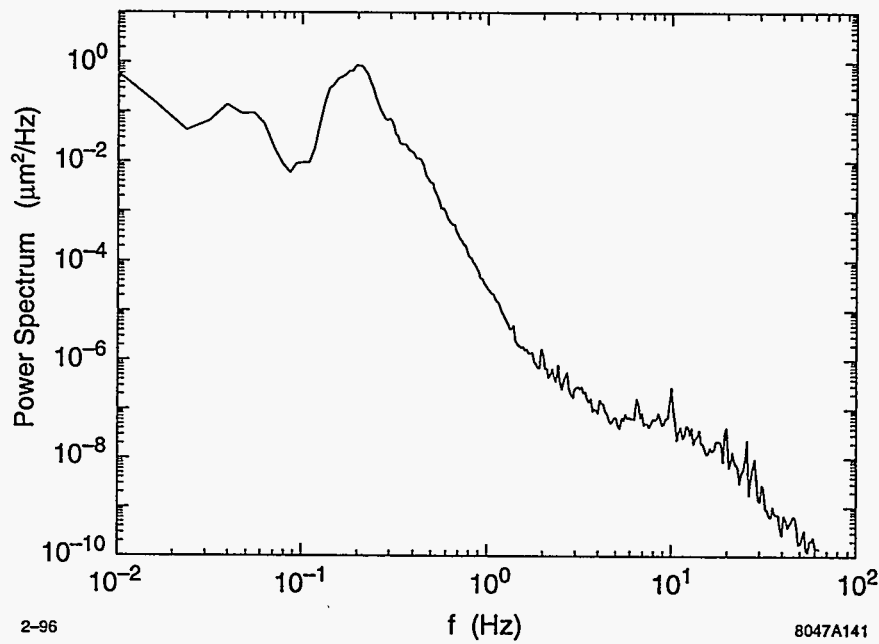


Figure 7-39. Average of 10 vertical ground motion power spectra that were measured on different days in Sector 4 of the SLC linac at 2 AM.

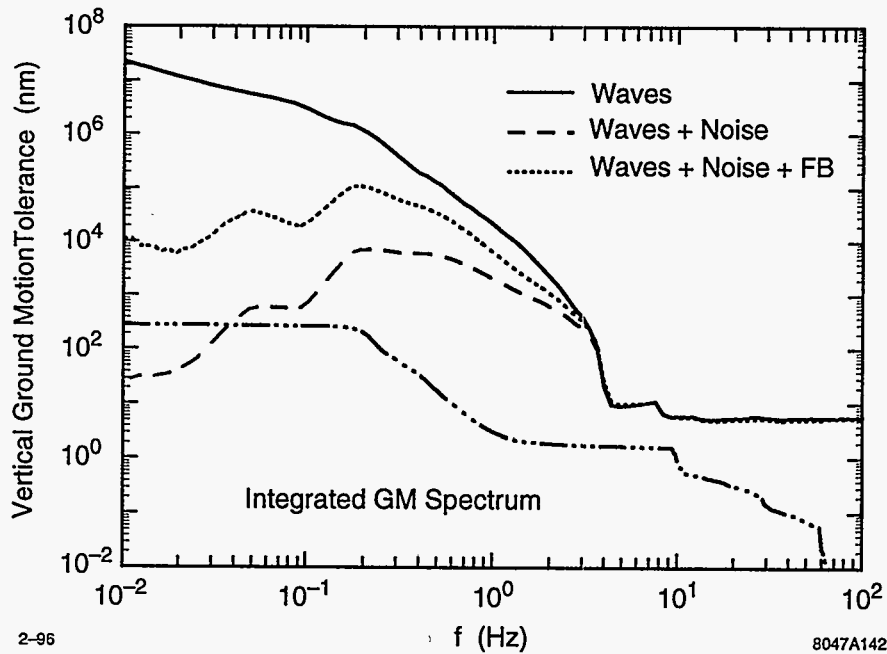


Figure 7-40. Integrated vertical ground motion spectrum (dot-dashed) and tolerances on the vertical rms ground motion for a 1.5% luminosity reduction for three cases: pure wave-like motion (solid), wave-like plus uncorrelated motion equal to the seismometer electronic noise (dashed), and feedback suppressed wave-like plus uncorrelated motion (dotted).

would offset the quadrupole kicks. A feed-forward scheme could also be used at the end of the linacs where the measured position of the first bunch in the train would be used to correct the motion of later bunches in the same train. However, limitations due to bunch filamentation would only loosen the quadrupole vibration tolerances by about a factor of three in this scheme.

7.5.2 Alignment Procedures

Quad and BPM Alignment

The initial placement of the quadrupoles and structures will be done with conventional surveying techniques. Most likely, triangulation and leveling methods will be used in combination with Global Positioning System (GPS) data from satellites. The long-range alignment accuracy will be within the dispersion related tolerances shown in Figure 7-24. However, at wavelengths less than a few hundred meters, the accuracy will level off to something that approaches $100\ \mu\text{m}$ on a 20-m scale. At these wavelength scales, a beam-based approach will be used to control the quadrupole alignment. Beam-based methods tend to be sensitive to systematic errors at longer length scales, which is why we will rely on the initial placement accuracy to achieve the long-wavelength tolerances. As noted earlier, if the displacements due to ground settling significantly exceed the long-wavelength tolerances, a global realignment of the beam line will be done. Hydrostatic monitors may be installed along the beam line to monitor these displacements.

The beam-based quadrupole alignment will use as input the measurements of the average bunch positions from the BPMs that will be located in the quadrupoles. Various beam-based algorithms have been shown to work in theory, although there are many subtleties involved because the derived quadrupole offsets have correlations which vary with length scale. Thus one does not speak of the level of alignment achieved, but instead judges the method in terms of the amount of dispersion remaining on average after alignment. Given that there is some uncertainty as to how often the dispersion correction will have to be made, the correction procedure should be designed to be as fast as possible. Also, the correction will be made by moving the quadrupoles with mechanical movers as opposed to using dipole corrector magnets to offset the quadrupole magnetic centers. This will be done in part because a large investment in mechanical movers will be made for the structures, so adding additional movers (about 14% more) for the quadrupoles will be straightforward. Also, having the beams nearly centered in the quadrupoles alleviates the need for a tight regulation of the quadrupole power supplies, and a tight limit on higher harmonics of the fields.

Given these considerations, we plan to use a quadrupole alignment algorithm that requires only beam trajectory data taken with the nominal linac lattice. Having readings from N BPMs in N quadrupoles will allow us to determine $N - 1$ quadrupole offsets, with the alignment end-points being the beam position in the first quadrupole and the BPM zero of the last quadrupole: the outgoing beam angle is unconstrained. Using this algorithm, we will align $N-1$ quadrupoles at a time, one group after the next, similar to the way that "autosteering" is done in the SLC linac. However, some global limitations in the quadrupole moves would have to be made to prevent the mechanical movers from "ranging-out."

This method will require BPMs with resolutions of about a micron. Such BPMs already exist, however they must also be aligned to the quadrupole magnetic centers to this same level (see reference [Adolphsen 1993] for more detail). This alignment can also be computed in a beam-based manner, but may be disruptive to normal operation. For example, the offsets could be derived from the BPM data taken in which the strengths of individual or strings of quadrupoles are changed. However, the changes in the quadrupole strength would have to be fairly large—turning off one quadrupole yields a betatron oscillation with an amplitude that is only a few times the size of the beam offset in the quadrupole. Thus we want to minimize how often we have

to perform this procedure. A calibration scheme that injects signals into the BPMs, and not just into the readout electronics, should help to stabilize the offsets. This is discussed in Section 7.10. Tests of the BPM stability in the SLC and FFTB will be done to study this problem.

Due to the effects of wakefields, it is hard to accurately estimate by analytical means the emittance growth that remains after applying the quadrupole alignment algorithm. Instead we simulate the application of this algorithm to the linac; the methodology and results are presented in Section 7.6.

Structure Alignment

As described in Section 7.3.3, the accelerator structures are supported in pairs on common strongbacks, which themselves are mounted on structure movers. The alignment of the structures will be based on measurements of the beam position relative to the structure axes that will be obtained by analyzing the dipole-mode signals from the structure damping manifolds. Although the original motivation for adding the structure manifolds was to damp the dipole modes, their capacity to be used as a BPM with micron-level resolution will be essential as well.

In the readout electronics, the signal from two modes near the ends of the structure will be selected with filters and measured so that both the position and orientation of the structure relative to the beam can be determined. The difference in the measurements from each structure pair will be used to check the relative structure alignment on the strongback, while the average of the measurements will be used to remotely adjust the mover positions at the micron level to better center the structure pair about the beam trajectory.

The accuracy of the structure alignment system will depend on the degree to which we can internally align the structures. Since we do not have much experience aligning single structures, let alone preserving the alignment of a pair of structures in an operating environment, we have tried to be conservative in our estimates. We believe that structure pairs can be made straight to better than 15 microns rms, and that this alignment can be maintained over long periods of time. Thus far, we have achieved straightnesses of a few microns for the 40-cell stacks that are built before being combined into 206-cell structures. As we assemble whole structures and monitor their straightness, we will be able to better characterize the misalignments.

For now, we assume 15-micron-rms misalignment. To estimate its effect on the beam emittance, we consider two cases whose contributions sum to the general case. In the first case, we assume that the beam travels along the mean axis of the structure pairs, which suppresses the short-range wakefield effects. This leaves the growth due to the long-range wakefields which depends on the spatial correlations of the misalignments. This dependence is shown in Figure 7-37 where the tolerances for piece-wise misalignments of the structures are plotted as a function of the length of the pieces. From these tolerances, a 20% vertical emittance growth is expected if the offsets are uniformly distributed in piece length. This growth will be larger if the offsets occur mainly on a length scale equal to 1/6 of the structure length. To be conservative, we have budgeted 40% emittance growth for these long-range wakefield effects.

In the second case, we assume that the structure pairs are perfectly aligned internally, and consider how well the beam can be aligned to the mean axis of the pair, which was assumed to be done exactly in the first case. Since we expect that the resolution on the beam position derived from the structure signals will be a few microns or better, the alignment accuracy will be dominated by the 15-micron-rms structure misalignments (note that we consider the internal misalignments for this purpose even though they are ignored in this case for the wakefields that they generate). Having four measures of the beam position relative to the axis of a structure pair yields a 7.5-micron-rms beam-to-structure alignment. The resulting vertical emittance growth, which is dominated by short-range wakefield effects, is about 50% based on the Figure 7-37 tolerance for an alignment length of two.

In this analysis, we have ignored systematic distortions of the structure pairs. However, they will likely occur on length scales where the internal alignment tolerances are large. For example, if the pairs bow with a 100-micron sagitta, the emittance growth due to long-range wakefield effects will only be a few percent. The short-range wakefield effects, which depend on the average bunch offset in the structures, would be suppressed in this case since the strongback would be aligned based on the beam offset measurements at the ends and middle, which would center it about the beam.

During the commissioning of the NLC, the structure alignment will be done with a low-intensity beam so as to minimize the wakefield steering effects (*i.e.*, one does not want large orbit changes after moving one pair of structures). During normal operation, it is likely that the structure alignment procedure will have to be iterated with the quadrupole alignment algorithm since moving the structures will kick the beam. If only the power in the wake signal is measured, a scan of the structure position versus signal would be needed to determine the direction to move the structure, which could significantly slow the alignment process. Prototype tests of a structure alignment system will be done in ASSET and the NLCTA to help resolve such issues.

7.5.3 Fast Transverse Feedback

In this section we discuss the feedback systems in the main linacs which operate on relatively fast timescales. The primary focus is on the transverse feedback loops which correct the average trajectory of the beam at the diagnostic stations along each linac, but the general principles are applicable to other loops as well.

A generalized feedback system has been developed and commissioned in the SLC, and has been essential to high-luminosity operation. Operational experience has provided valuable information on feedback-response characteristics, especially with regard to machine and feedback-system imperfections. The proposed NLC feedback is based on the SLC design, with some changes based on lessons learned from the SLC and performance requirements of the NLC. Appendix D provides more information on the design and characteristics of the feedback system. This chapter concentrates on design and performance issues for the NLC linacs.

Linac Feedbacks

In each linac, there are five diagnostic sections, each with a feedback loop. Each loop includes measurements of 10 BPMs for launch control, in addition to one or two BPMs which provide energy information. Each feedback loop calculates and controls five states: the X and Y positions and angles, and the beam energy. To provide feedback control of the launch parameters, two X correctors and two Y correctors are needed. For the energy control, klystron phase or amplitude controls may be used. The feedback design assumption is that the actuators can change to a new setting within one 180-Hz pulse, or 5.55 milliseconds. An additional beam pulse period is allowed for BPM digitization, feedback calculations, and communication. The result is that, after a beam perturbation is detected by the feedback system, the feedback begins to correct it two 180-Hz pulses later. For the initial NLC design, the correction begins two 120-Hz pulses after a perturbation.

Feedback System Design

The feedback design is based on the state space formalism of digital control theory. It uses a Linear Quadratic Gaussian (LQG) controller, which has a built-in model of the beam transport and the expected beam and BPM noise characteristics. Matrices are designed and calculated offline and downloaded for use by the real-

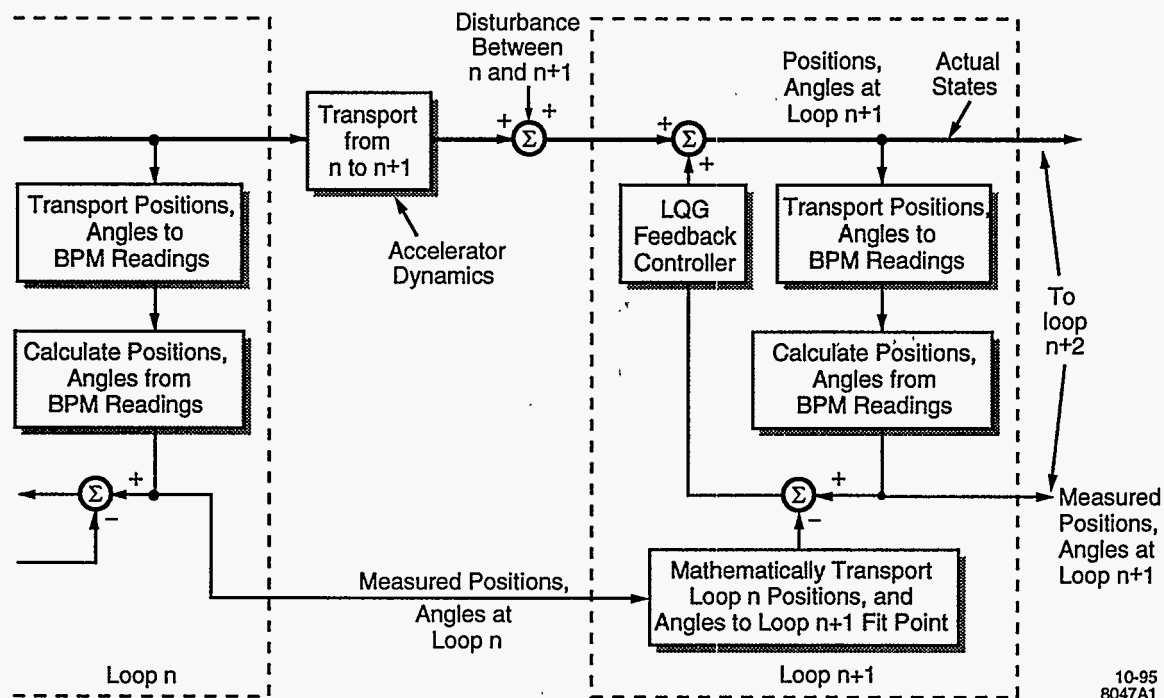


Figure 7-41. Schematic of cascaded feedback system.

time feedback system. The mathematical design goal for the feedback matrices is to minimize the rms of the beam states over time, given the noise inputs. By modifying the input beam noise design assumptions, it is possible to tune the feedback performance response characteristics. The initially proposed feedback algorithm does not adapt to modeling or noise spectrum changes, consistent with the current SLC design. It is hoped that in the future, adaptive methods may provide improved performance, but there is insufficient experience to make design assumptions with them at this point. The beam transport model within a single loop (*i.e.*, R12s which take beam position monitor readings and corrector settings to beam positions and angles) may either be derived from the accelerator model, or may be measured by an invasive online beam-based calibration method.

In the linacs, a series of feedback loops are controlling the same beam parameters (positions, angles, and energy) at different points along the beam line. If the loops do not communicate with each other, this would result in overshooting of the feedback corrections and excessive amplification of beam noise. To avoid this problem, a "cascade" system is developed. The goal of the cascade system is that each feedback loop responds only to perturbations which are generated immediately upstream of it. If the beam transport is approximately linear, this can be accomplished by having each loop send its calculated states to the next downstream loop. The downstream loop mathematically transports the upstream states to its own fit point, then subtracts them from the positions and angles calculated from its own BPMs. This scheme is depicted in Figure 7-41. With this design, each upstream feedback sends information only to the nearest downstream loop. The key is that each loop is sending the next loop information about what it measured in the beam, not what it is correcting. For example, if there is a perturbation upstream of Loop 1, this perturbation should be seen by all of the feedback loops. Loop 4, for example, will see it, and send this information to Loop 5, which will subtract the perturbation from what it has, so Loop 5 will correct nothing. Loop 5 doesn't know or care whether Loop 4 is correcting the perturbation, it just knows that someone upstream is

taking care of it, and actually Loop 1 will correct it. This scheme assumes that the beam transport is linear and independent of the source of a perturbation. (If the NLC transport is excessively nonlinear, it may be advisable to consider a more complicated communications algorithm, where downstream loops receive information from all upstream loops and have sufficient information about the source of a perturbation.)

An important issue in the cascade design is how to mathematically transport the beam from one feedback loop's fit point to the next loop. The distance between feedback loops is so great that the accelerator model is not good enough, and SLC experience has shown that the interloop beam transport changes with time. In the SLC, adaptive techniques are used for the mathematical transport calculations, but the adaptively calculated transport matrices have had some performance problems which degrade the feedback system performance. These problems are described fully later in this chapter and in the feedback appendix. As a result, the proposed method for interloop mathematical beam transport for the NLC is to steal a small number of beam pulses each hour to measure the beam transport by perturbing the beam. It should be possible to provide an adequate measurement by producing a single set of perturbations upstream of the series of feedback loops, and measuring the interloop transport elements for all downstream loops at once.

Operational Performance Issues

SLC feedback performance studies have included five main areas of interest: slow correctors, downsampled feedbacks, poor modeling of beam transport within a feedback loop, poor cascade modeling of interloop beam transport, and optimization of the feedback design response. Slow corrector response has had a detrimental effect on SLC feedback performance, but a new design now allows response within a single beam pulse. In the SLC, due to CPU and BPM constraints, many feedback loops operate at lower than the full 120-Hz beam rate. This degrades the feedback response, and increases aliasing of higher frequency noise to lower frequencies. For the NLC, sufficient CPU and BPMs will be available so that the feedback loops may run at the full machine rate. The remaining performance issues are more challenging, and are interrelated.

While it should be possible to develop a nearly perfect model of the accelerator beam transport within a single feedback loop, SLC experience has shown that the model has imperfections in some cases. Performing the calibration procedure for several SLC feedback loops has provided data to quantify the effects of typical imperfections (these involve errors in the R matrices between correctors and states of 10–20%). NLC design simulations include consideration of comparable imperfections.

If the long-range beam transport in the NLC linacs is reasonably linear and not changing quickly with time, then measuring the interloop transport elements every hour should provide perfect cascade correction, and each loop should perform corrections only on perturbations generated immediately upstream. If this were true, the global system feedback response would be identical to the response of a single feedback loop. But to be conservative and account for small nonlinearities and changing beam transport properties, NLC feedback simulations assume that part of a given beam perturbation leaks through to the downstream loop, so that each loop incorrectly compensates for a portion of an upstream perturbation. In the simulations, it is assumed that each loop compensates for 15% of perturbations which are not immediately upstream.

The SLC design's noise response results in correction of a beam perturbation exponentially with a time constant of about six pulses. In other words, after six pulses, most of an incoming perturbation is fixed by the feedback. This design provides a good response to a step function and provides a stable feedback which does not over-react to white noise. For the NLC, it is preferred to have a feedback response which is tuned to damp strongly at low frequencies. In the NLC, high-frequency noise is expected to be damped by passive systems and the expected input noise spectrum would be dominated by low-frequency ground motion. Note that while it is possible to tune the feedback response curve, any design will damp at some frequencies while amplifying at others. Several alternative noise designs have been simulated and evaluated.

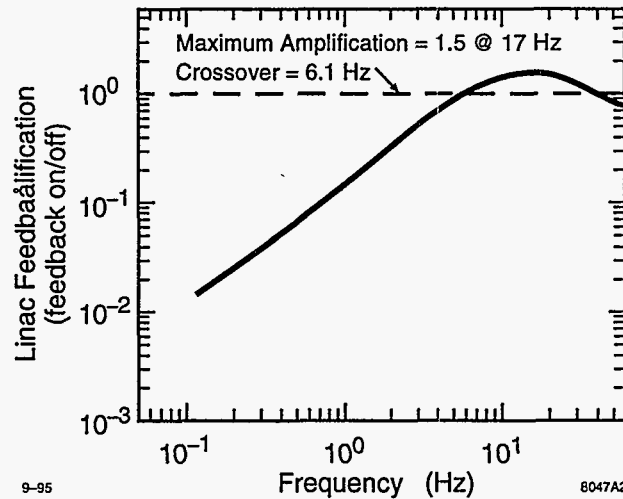


Figure 7-42. Feedback response curve for the SLC feedback design with a 120-Hz beam pulse and feedback rate, including the effects of imperfections.

While the more aggressive designs, which damp strongly at low frequencies, provide an excellent response curve under perfect conditions, these designs are more sensitive to imperfections in both intraloop modeling and interloop cascade transport. To provide a stable, robust feedback system with better response at lower frequencies, more work must be done. Figure 7-42 shows the feedback response curve for the SLC feedback design, which includes the effects of imperfections. Note that this curve is for a 120-Hz beam pulse and feedback rate. If the rate is 180 Hz, the response curve would be similar but shifted in frequency. At this point, the SLC design is proposed as a conservative initial approach, which provides adequate response and is not unduly sensitive to machine and modeling imperfections.

7.5.4 Bunch-by-bunch Transverse Feedback

The fast-feedback systems described in the preceding section operate on averages of the bunches in a train. The repetition rate of these loops is relatively fast. We turn next to loops which distinguish variations within a bunch train, but which perform corrections less frequently than the "fast" feedback loops previously described. It is probably not necessary to resolve all the bunches individually, but it is necessary to have some resolution within the train in order to control the multibunch emittance (and also bunch energies and energy spread, as is discussed later in this section).

These bunch-by-bunch feedbacks will also be implemented in the five diagnostic/control sections along each main linac. Measurement of the individual transverse bunch positions will be at these stations using special fast BPMs. Trajectory correction will be done using high-bandwidth kickers, able to tailor the kick delivered to individual bunches assuming the variation is fairly smooth along the train. Simulations yielding the requirements on BPM resolution, kicker strength, and kicker speed are given in the next subsection, and a design for a high-speed kicker suitable for use in such feedback loops is given in 7.9.4.

Multibunch Kicker Simulations

In the multibunch kicker simulations, bunch-by-bunch trajectories were assumed to be measured by two fast BPMs located at consecutive vertically-focusing quadrupole magnets (90° phase difference) at five locations in the NLC-I linacs: 30 GeV, 60 GeV, 100 GeV, 150 GeV, and 250 GeV; these positions closely correspond to the locations of the diagnostic stations. Two fast kickers were also located at consecutive vertically-focusing quadrupoles just upstream of the BPMs and the bunches were kicked to line all bunches to the trajectory of the first bunch. One-to-one trajectory correction was also performed to ensure that the beam centroid passes through the center of every focusing quadrupole magnet.

The tracking was performed with 90 bunches including both single- and multi-bunch effects. Each structure was divided into seven pieces and the pieces were aligned independently with rms errors of $25\ \mu\text{m}$. This misalignment was chosen so that the multi-bunch effects are much stronger than single-bunch effects because we are concentrating on multi-bunch correction. But, because it is possible that single-bunch effects become significant due to a large bunch offset caused by the multi-bunch effects, the single-bunch effects were also considered in this simulation. The expected emittance growth without corrections was simulated to be $\Delta\epsilon_y/\epsilon_y = 133\%$.

Figure 7-43(a), (b), and (c) show emittance growth as a function of the kicker strength, BPM resolution, and kicker speed, respectively. The kicker strength of 56 kV corresponds to a deflection of roughly six times the beam size. The residual emittance that remains after the correction is primarily due to the single bunch emittance dilution that arises from the misaligned structures and the large bunch offsets between correction stations. Finally, Figure 7-44 shows the effect of the kickers in one simulation with $25\text{-}\mu\text{m}$ -rms accelerator structure piece misalignments. The uncorrected emittance dilution was greater than 150% in this case. The residual dilution after correction is roughly 15%.

Given these results, we will design a kicker with a speed of 250 MHz and a strength of 56 kV, and a bunch-by-bunch BPM with a resolution better than $0.2\ \mu\text{m}$. This is discussed further in Section 7.9.4.

7.5.5 Linac Energy Management and Energy Feedbacks

The energy management of the main linacs includes the measurement of the energy, energy feedback and feedforward, the control of energy and magnet strength settings along the linacs, the handling of vetoes due to klystron faults, control of individual amplitudes and phases of the klystrons, and the confirmation of these parameters with beam-derived data. The energy spread within a bunch, which can be controlled by phase adjustments, is also discussed in this section.

Energy Measurement

The energy of the beam will be measured in high-dispersion regions that provide resolutions of about 0.1% or better. Five diagnostic stations are envisioned for this purpose, as discussed in Section 7.3.4. These stations will also be able to measure the energy variation along the bunch train.

Measurements of other quantities will also be important since they will influence the energy. Among these are the bunch train current and distribution, the beam phase, the state of the upcoming klystron pulses (*e.g.*, OK, veto, or in transition), cascaded information from upstream feedbacks, and any other information (such as history of slow ramps in current and energy) that is relevant to controlling the energy of the bunches.

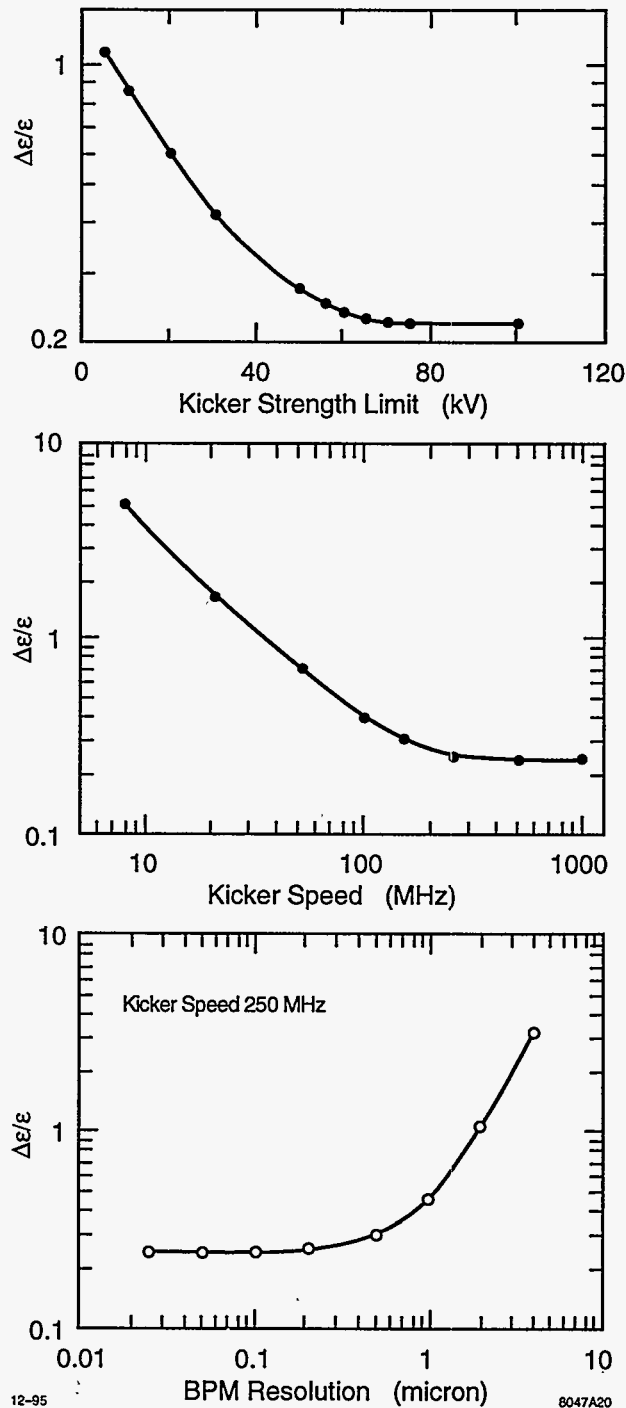


Figure 7-43. Emittance dilution versus: (a) kicker strength for a kicker speed of 250 MHz and a BPM resolution of $0.2\ \mu\text{m}$; (b) kicker speed for a kicker strength of 56 kV and a BPM resolution of $0.2\ \mu\text{m}$; (c) BPM resolution for a kicker strength of 56 kV and a speed of 250 MHz. Each structure was divided into seven pieces with a random misalignment of $25\ \mu\text{m}$ rms. Each symbol represents the average of tracking with 25 random seeds. The residual emittance dilution is due to the single-bunch dilutions arising from the trajectory and structure offsets.

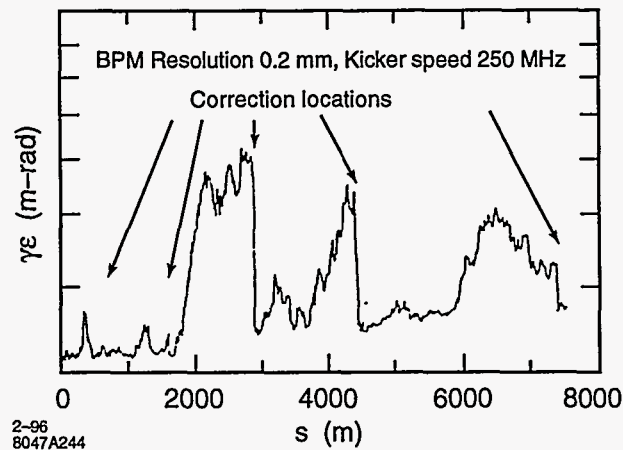


Figure 7-44. Example of a kicker simulation with 25- μm rms accelerator structure piece misalignments.

Energy Correction

The energy correction consists of a system of phase shifters, which will adjust the phase on a pulse-to-pulse basis like the SLC energy feedback loops. The slope and higher orders of the energy profile of the bunch train will also need to be controlled (this is discussed in Section 7.4.5 and at the end of this section).

Depending on the information source, the correction will be a feedback or feed-forward system. These systems should have a very general design with a self-calibrating mechanism. They should also allow auxiliary inputs and outputs (for instance, dumping the beam instead of correcting it).

A feed-forward system like that in the SLC will be necessary for different beam currents. By measuring the charge of each bunch in the damping ring and correcting the rf amplitude by opposite phase settings of two subboosters, good beam loading compensation can be achieved. Due to the high beam loading of about 25%, small current changes of 1% already cause a 0.25% energy change. The feed-forward information needs to be forwarded to the five energy stabilization stations (upstream from the chicanes) and combined with the local feedback.

Linac Energy Management

The management of the energy along the linacs is as important as controlling the energy at the ends, especially if a change in the energy profile might change a tail cancellation into an addition. Switching a klystron is probably the most important single event which requires a linac energy management (LEM) operation, that is, an adjustment of the magnets to reestablish the matching of the beam to the lattice. For this procedure we have to know the local beam energy and the energy gain (amplitude) and phase of the klystrons. The rf parameters should be checked with beam measurements. Also, the lattice should be checked with diagnostic pulses—special beam pulses which are transversely kicked and therefore oscillate down the linacs giving the required lattice information.

Another energy-related problem in the SLC that makes LEM necessary is changes in temperature which can generate energy variations of up to 2%. The linearized LEM adjustments help but are not sufficient so that the above mentioned additional tools will be helpful, especially in the front part of the main linacs. The NLC at 500 GeV is about 10 times less sensitive to energy changes of one klystron (230 MeV) than the

SLC. But it has also to maintain 100-times-smaller emittances. One klystron powers two structures (NLC-I) producing 100 MeV, which is 0.1% of the energy at 100 GeV, but 1% at injection where the energy is 10 GeV.

Bunch-by-bunch Energy and Energy Spread Feedback

It will be necessary to control the effects on the energy and energy spread of the multibunch train due to variations in the energy profile delivered by the rf system and to variations in the bunch charges. As discussed previously in Section 7.4.5, multibunch energy compensation can be done by shaping the rf pulse to simulate the steady-state beam loading profile before the beam is injected. Nearly ideal compensation of the beam loading will be obtained by a programmed series of phase shifts during the rf pulse (see Chapter 8 for details). However, there is no reason that the phase variations cannot be modified to obtain a slightly different shape to the rf pulse. A feedback system could thus be designed to fix small variations in energy along the bunch train, assuming the variation is smooth enough that the klystron variability has sufficient bandwidth.

Bunches belonging to a given train in the damping rings ride at different synchronous phases due to the differing amount of beam loading from bunch to bunch. The beam loading in turn depends on the bunch charges, which may vary on a pulse-to-pulse basis. We may have to compensate for such pulse-to-pulse variations by feedforward of bunch charge information from the damping rings to the main linacs.

7.6 Simulation Studies

The previous sections describe the basic design of the NLC main linacs. The results of analytical estimates and numerical simulations were used throughout the text, mainly to discuss and justify specific design choices. In this section, we describe numerical calculations that were performed to study the NLC main linacs in greater detail. By assuming realistic errors in all major accelerator components, we can study the complex interactions between different mechanisms of emittance growth and the proposed correction algorithms. Since stability problems are of major concern for the NLC, we also discuss simulation results for the alignment stability in the NLC main linacs.

In the following, we will briefly describe the simulation program LIAR ("Linear Accelerator Research code") which was recently developed [Assmann 1995]. Then, we discuss the overall objectives for the NLC linac simulations and present the simulation results. A final outlook will present the conclusions and will describe directions for future work.

The goal of the simulation studies done so far is to show the feasibility of the acceleration and emittance preservation in the NLC linacs. Several important problems still do not have their final solutions. However, we will show that we have working solutions to the major problems that already fulfill the requirements.

7.6.1 Simulation Program

The simulation and tracking program LIAR ("Linear Accelerator Research code") is designed as a general tool to study the beam dynamics of linacs. LIAR's major design goals are to provide a simulation platform that includes all the basic accelerator physics for linacs, that allows to add easily advanced features and that

is not bound to a specific linac design. Presently LIAR is used both for NLC and SLC simulations. We briefly describe its main features and observables.

All magnets are simulated using the thick lens representation. The beam line description includes "realistic" support points with a number of elements mounted on a common girder. Thus we can simulate the effects of ground motion and we can also study correction algorithms using movers at the support points. Rf structures can be divided into pieces and have an rf-BPM assigned at both ends.

The beam is described as a train of bunches. Each bunch is divided into slices along the longitudinal direction and each slice is described by a number of mono-energetic beam ellipses. The tracking part of the program performs a 6D coupled-beam transport including the beam-induced transverse and longitudinal wakefields in the rf structures.

The basic features of the simulation program are complemented by the ability to set random and systematic errors on most accelerator parameters:

1. Transverse misalignments and roll angles for most element types.
2. BPM misalignments with respect to the quadrupoles. Finite BPM resolution.
3. Strength errors for quadrupoles, bending magnets and correctors.
4. Phase and gradient errors of the rf structures.
5. Random or "ATL"-like misalignments of the accelerator support.
6. Misalignments of individual rf structure pieces ("bowing", etc.).

Given those capabilities we can simulate basic and advanced optimization schemes for the main linacs of NLC. So far the following correction methods have been implemented:

1. One-to-one steering using dipole correctors.
2. Trajectory feedbacks.
3. Beam-based quadrupole alignment.
4. Beam-based alignment of the rf structures.
5. SLC-type emittance bumps with deterministic optimization.

Other optimization schemes like dispersion-free steering or multibunch kickers will be added in the future. All those correction schemes can be applied and tested in the presence of multiple interacting error sources. Furthermore we can study the convergence of these techniques when they are iterated many times.

We use a number of different measures to describe the performance of the linacs. Many observables are available at each BPM so that they can easily be studied as a function of longitudinal position s :

1. Horizontal and vertical beam and bunch positions with respect to the design plane or the BPM centers (by beam we refer to the average of the bunches).
2. Horizontal and vertical emittances for all bunches.
3. Horizontal and vertical luminosity reduction for all bunches.

4. Energy spread of the beam.
5. Beam energy.
6. Horizontal and vertical B_{mag} (see Equation 7.3) for a selected bunch.

At every marker point the beam distribution in phase space is available for a selected bunch and the whole bunch train. Twiss parameters are available for every beam line element. All observables, together with other parameters like misalignments, can be saved into external files which then are further analyzed. LIAR also provides screen summary output about single and multibunch emittance growth, rms trajectory offsets and the other observables.

7.6.2 Objectives

The NLC main linac simulations are undertaken with the general objectives to study the complex interactions between different parameters and to get a complete and coherent picture of the relevant emittance growth and optimization processes. By studying multiple error sources we try to evaluate the main linac performance under “realistic” conditions. Here we give a list of relevant simulation studies.

- Static quadrupole and BPM misalignments and errors (compare Sections 7.4.4 and 7.4.6):
 - Dispersive emittance growth as a function of transverse quadrupole and BPM misalignments.
 - Sensitivity to lattice mismatch from quadrupole strength errors.
 - Sensitivity to betatron coupling from quadrupole rolls.
- Static structure misalignments and errors (compare Sections 7.4.4 and 7.4.6):
 - Emittance growth due to random structure misalignments. Sensitivity to different wavelengths of misalignments.
 - Emittance growth due to systematic structure misalignments (“bowing”, etc.).
 - Lattice mismatch from gradient and phase errors.
 - Sensitivity of dispersive emittance growth to changes in the BNS phases.
- Beam tails:
 - Determination of the average beam power that needs to be collimated.
- Beam line stability (compare Section 7.5):
 - Emittance growth from ATL-like drifts of the quadrupole and structure alignment.
 - Emittance growth from jitter and vibrations of the accelerator support.
 - Feedback requirements for effective trajectory stabilization.
 - Effects from bunch-to-bunch variations of charge or initial position and angle.
- Emittance control techniques (compare Section 7.5.2):

- Efficiency of interleaved quadrupole steering and rf structure alignment in the presence of errors (compare Section 7.5.2).
- Dispersion-free and wakefield-free steering.
- Emittance optimization with trajectory bumps.

Several of these studies are interdependent and some need to be done for both single-bunch and multibunch cases. We cannot yet present all the final results. However, most of the problems mentioned above are addressed in the simulations that we are going to present.

7.6.3 Simulation Parameters

The NLC tolerances are tighter for the higher bunch currents and the longer bunch lengths at the higher beam energies. Therefore we restrict the simulations to the 500-GeV version of NLC-II. This is the case "NLC-IIb" in Tables 7-1 and 7-2. The beam consists of 90 bunches, where each bunch contains 1.1×10^{10} particles, is 150- μm long and has an initial uncorrelated energy spread of 1.5%. We describe a single bunch at 10 longitudinal positions each with 3 mono-energetic beam slices. The initial bunch shape is Gaussian. The initial horizontal and vertical beam emittances are $\gamma\epsilon_x = 4.0 \times 10^{-6}$ m-rad and $\gamma\epsilon_y = 4.0 \times 10^{-8}$ m-rad. The beam is accelerated to a final beam energy of 500 GeV.

The full NLC-IIb lattice is used for the simulations and we assume that the chicanes in the diagnostics stations are switched off. Beyond that we assume that multibunch beam loading is perfectly compensated. Parametrizations for short-range and long-range wakefields were provided from detailed calculations as mentioned in Sections 7.4.1 and 7.4.2. The simulations that are presented here focus on the vertical plane where the small initial emittance makes it much harder to avoid dilutions.

7.6.4 BNS Configuration

As explained in Section 7.3.2, BNS damping significantly reduces the emittance growth in a linac. If the BNS autophasing condition is fulfilled then an incoming betatron oscillation will propagate downstream without perturbation. In this case, there will be minimal emittance growth. Figure 7-4 shows the autophasing energy spread for a simple two-particle model (compare Equation 7.2). The figure suggests an average autophasing energy spread of about 1.1%.

In order to identify an optimal BNS configuration we studied a number of energy spread profiles along the linac, each of which is generated by adjusting the rf phases in three groups. The BNS configurations number 1 to 9 are defined in Table 7-8. All BNS cases were calculated to give the required final beam energy spread of about 0.3% rms. In Figure 7-45 we show the beam energy spread along the linac for the different cases. Figure 7-46 characterizes the different BNS configurations in terms of average energy spread and the energy overhead required to generate them. The energy overhead is defined as the energy difference between operating with the nominal average rf phase and operating with the BNS phases. In the following we refer to the BNS cases by their BNS energy overhead.

To study the BNS configurations in terms of emittance preservation, we simulated the emittance growth for an initial 1σ vertical beam offset (2.2 μm). The initial uncorrelated beam energy spread was set to zero. As is shown in Figure 7-47 we find the smallest emittance growth for a BNS energy overhead of 1.3%. For lower energy overheads, wakefields cause large emittance growth while dispersive emittance growth dominates for

Config	ϕ_1 (°)	E_1 (GeV)	ϕ_2 (°)	E_2 (GeV)	ϕ_3 (°)
1	4	30	-7	485	-30
2	8	30	-5	455	-30
3	10	30	-3	425	-30
4	12	30	-1	400	-30
5	14	30	1	380	-30
6	16	30	3	360	-30
7	18	30	5	335	-30
8	20	30	7	320	-30
9	22	30	9	300	-30

Table 7-8. BNS configurations: ϕ_1 , ϕ_2 and ϕ_3 are the three rf phases in the linac and E_1 and E_2 are the switching points.

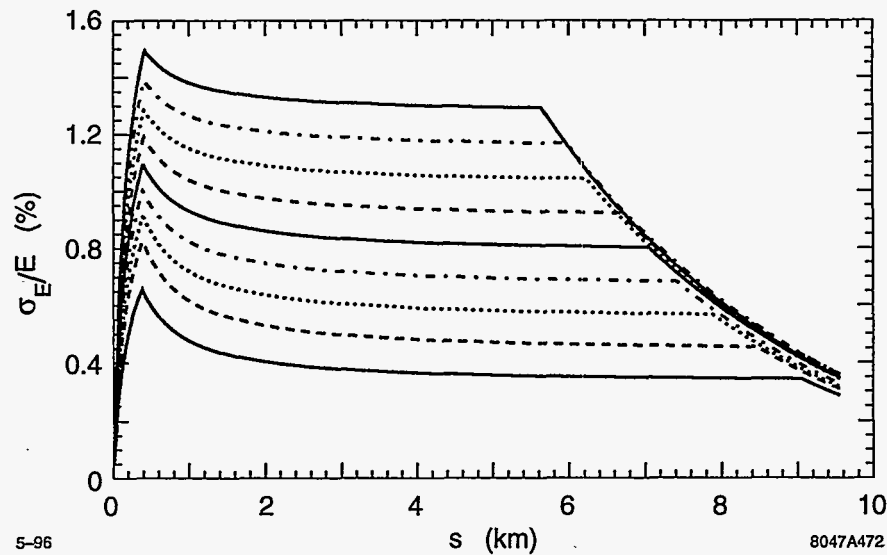


Figure 7-45. Beam rms energy spread along the linac for different BNS configurations. Note that the initial uncorrelated energy spread was set to zero. The final extracted rms energy spread is fixed to about 0.3% as required by the final focus energy bandwidth. The different BNS configurations are defined in Table 7-8 and are referred to as number 1 to 9, where 1 is the lowest curve.

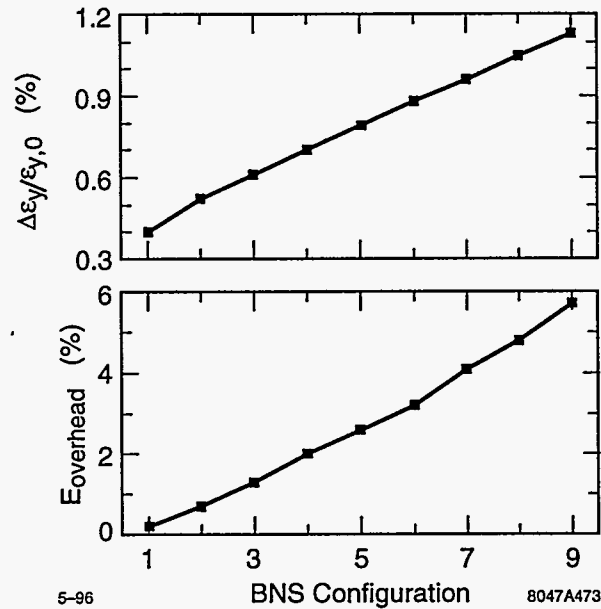


Figure 7-46. The different BNS configurations from Figure 7-45 are characterized by the average energy spread σ_E/E along the linac and the BNS energy overhead E_{overhead} .

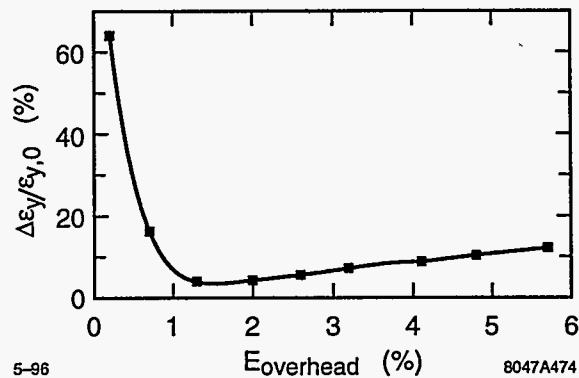


Figure 7-47. Average vertical emittance growth $\Delta\epsilon_y/\epsilon_{y,0}$ for the different BNS configurations from Figures 7-45 and 7-46 and a 1σ ($2.2 \mu\text{m}$) initial beam offset. The initial uncorrelated beam energy spread is set to zero.

higher BNS energy spreads. Since the BNS overhead of 1.3% is well inside the specifications (up to 3%), we chose the BNS configuration number 3 for all further studies. However, we always made sure that this BNS case is a good working point. Later we will discuss our choice of BNS energy spread for two other emittance growth problems and we will see that the BNS configuration number 3 is still the optimal working point within the cases that are considered. We note that the rms energy spread for this BNS configuration is about half of what is expected for autophasing from Figure 7-4.

If the autophasing condition is fulfilled, then we would expect that the betatron oscillations from the initial 1σ beam offset, normalized with the beta function and the beam energy, propagate downstream without perturbations. Figures 7-48 and 7-49 show the normalized betatron oscillations and the vertical single bunch emittance growth along the linac. The first figure does not include any initial uncorrelated energy spread,

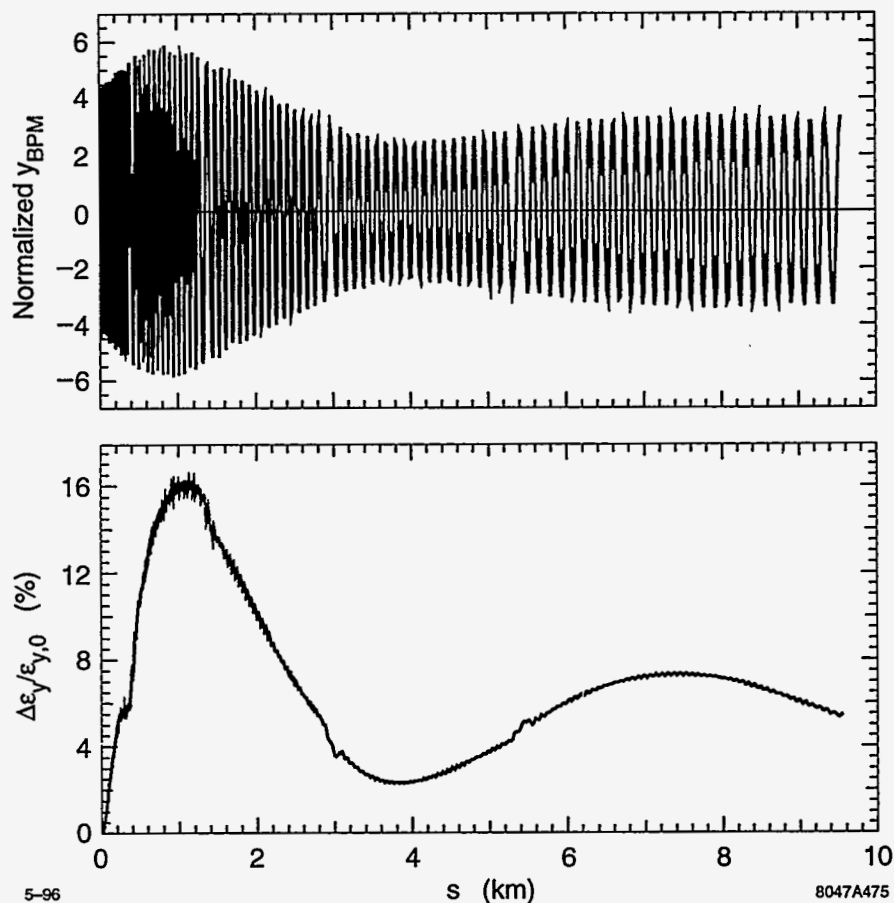


Figure 7-48. Beam offsets y_{BPM} , normalized with the beta function and the beam energy, and emittance growth $\Delta\epsilon_y/\epsilon_{y,0}$ for a 1σ ($2.2 \mu\text{m}$) initial beam offset and no initial uncorrelated beam energy spread. The BNS configuration number 3 with a BNS energy overhead of 1.3% is used.

while the second case includes the nominal 1.5% initial energy spread. It is easily seen that the amplitude of the normalized betatron oscillation is not maintained in either case. We note that the initial uncorrelated beam energy spread significantly changes the dynamics in the beginning of the linac. It causes strong filamentation and modifies tolerances for incoming jitter.

7.6.5 Static Imperfections and Their Correction

Imperfections are called static if they do not change during the typical timescale of beam-based alignment and correction procedures. Initially static imperfections in the NLC linacs are allowed to be large compared to the final tolerances. In order to achieve the required tolerances the “conventional” (not beam-based) alignment must be complemented by beam-based alignment techniques. In this section we explain the algorithm proposed for beam-based alignment and its implementation in the simulation program. We discuss detailed simulations that show that the required precision levels can indeed be achieved, even when many additional error sources are included.

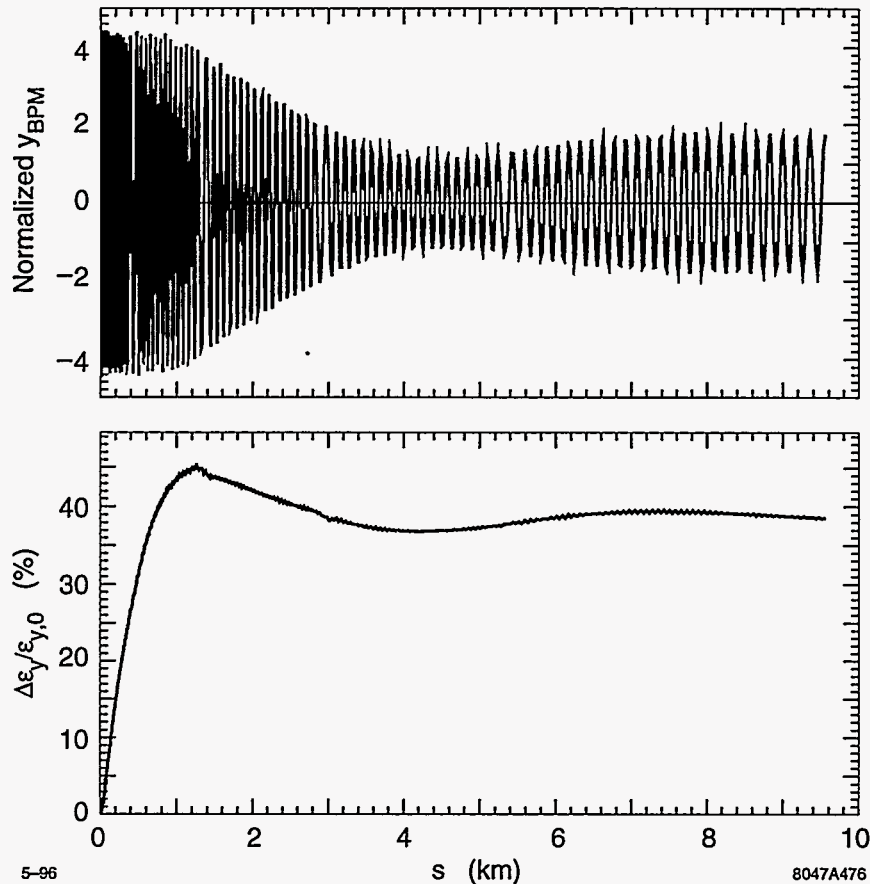
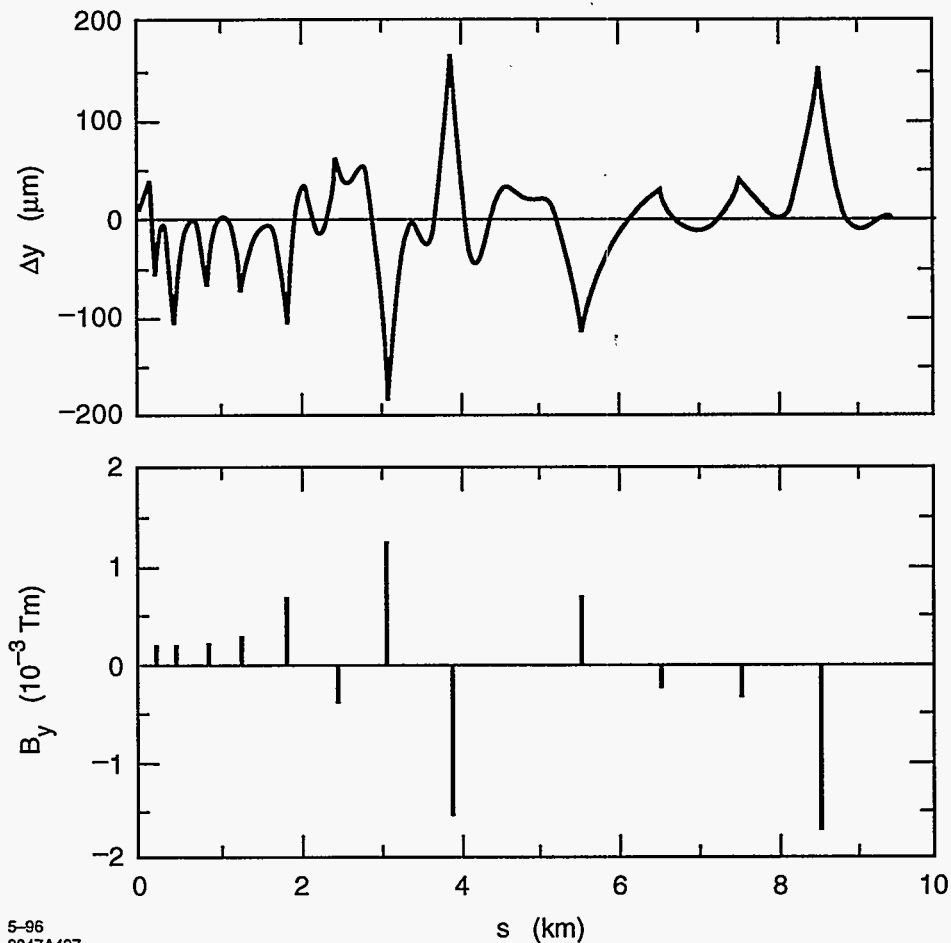


Figure 7-49. Beam offsets y_{BPM} , normalized with the beta function and the beam energy, and emittance growth $\Delta\epsilon_y/\epsilon_{y,0}$ for a 1σ ($2.2\mu\text{m}$) initial beam offset. Here the initial uncorrelated beam energy spread is set to 1.5%. Again we use the BNS configuration number 3 with a BNS energy overhead of 1.3%.

The Beam-based Alignment Algorithm for Quadrupoles and RF-structures

The emittance growth is driven by transverse offsets between the beam and the centers of quadrupoles and structures. Those offsets must be effectively minimized in order to maintain the normalized emittances.

The basic concept for the NLC beam-based quadrupole alignment is to use the available BPM information to solve for the beam-to-quadrupole offsets and the initial beam position and angle. Assuming that all beam deflections are caused by the quadrupoles, we can use N BPM measurements to solve for $N - 2$ quadrupole offsets and the initial y , y' of the beam. The positions of the first and last quadrupole in the corrected section are fixed. The endpoint BPMs define the reference line for the alignment. If the alignment is done in many sections then the beam is launched from one section into the other with a single dipole corrector at the border between the two. Therefore, for all but the first section we adjust only the initial y' . In the first section we adjust both y and y' of the incoming beam ("launch feedback"). The quadrupoles are aligned with magnet movers at each quadrupole support. Since the optics model is perturbed by wakefields and to account for other imperfections, the alignment is implemented as an iterative process. Furthermore, the quadrupole alignment is interleaved with the alignment of the rf-structures.



5-96
8047A497

Figure 7-50. Example of the beam-based alignment algorithm with perfect BPMs and rf-BPMs. The initial random quadrupole misalignment was $100\text{-}\mu\text{m}$ rms. The alignment is done in 14 sections and 15 iterations. At the end of each section a dipole corrector is used to launch the beam into the next section. The upper plot shows the misalignment Δy of quadrupoles, rf-structures and BPMs after alignment. The lower plot shows the integrated fields of the dipole correctors.

The rf accelerator structures have an rf-BPM at each end. Two rf-structures are always mounted on a single support structure. Every support structure can be moved by stepping motors at either end. Thus, for each support structure a total of four rf-BPMs measure the beam positions in the structures and two movers align the girder. The movers are adjusted such that the average rf-BPM reading on a girder is minimized. The rf-structure alignment is performed after each iteration of quadrupole beam-based alignment.

Here, we assume that the step resolution of the magnet and girder movers is infinitely small. The typical step size of $0.25\text{ }\mu\text{m}$ is indeed small compared to the resolution of the rf-BPMs of about $15\text{-}\mu\text{m}$ rms and can therefore be neglected for the rf-structures. However, for quadrupoles the step size of the movers is an important limitation. The problem is avoided by having dipole correctors at each quadrupole that shift its effective magnetic center. Small quadrupole misalignments are therefore “cured” with dipole correctors. If the dipole strengths get large enough they are “exchanged” for a step of the quadrupole mover.

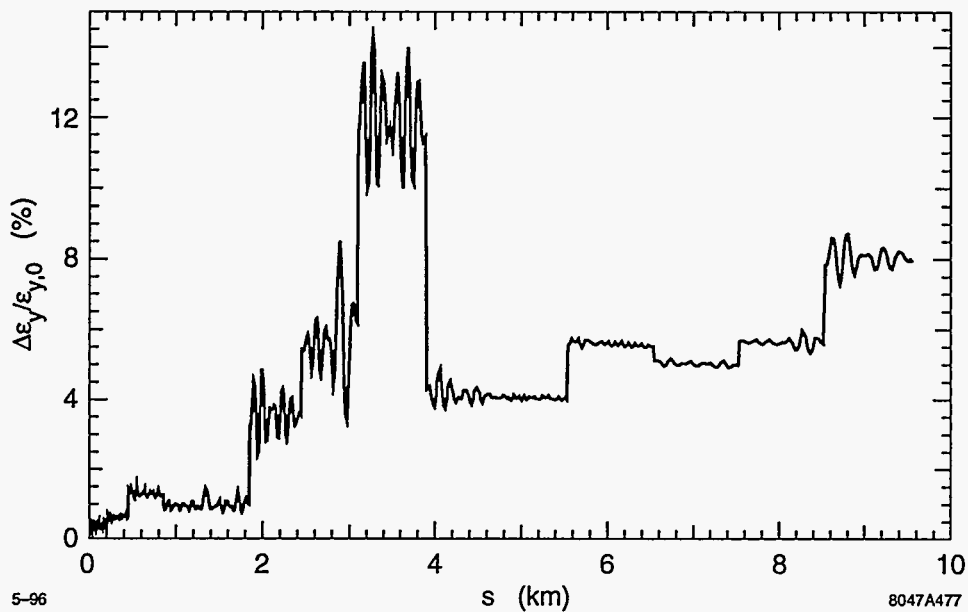


Figure 7-51. Emittance growth $\Delta\epsilon_y/\epsilon_{y,0}$ along the linac for the example from Figure 7-50. Note that the steps occur at the end of the alignment sections where dipole kicks launch the beam into the next section.

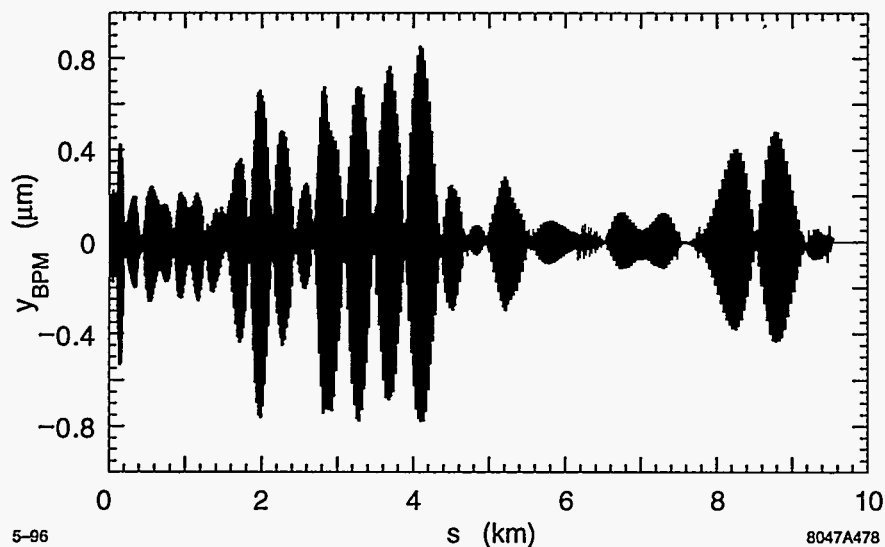


Figure 7-52. Vertical trajectory offsets at the quadrupole BPMs along the linac for the example from Figure 7-50. The residual beam offsets in the quadrupoles bend the beam along the “bowed” beam line after alignment. They are not betatron oscillations and cause only negligible emittance growth (compare to Figure 7-51).

The alignment algorithm that was sketched above was implemented into the simulation program LIAR. First, we consider a simple case where we start with a random quadrupole misalignment of $100\text{-}\mu\text{m}$ rms and assume perfect BPMs and rf-BPMs. Both kinds of BPMs have no offsets and zero resolution. The quadrupole alignment is done in 14 regions to allow for best convergence. Each region contains about 52 quadrupoles and is iterated 15 times. The number of iterations is chosen higher than necessary in order to explore the optimal solution.

The misalignment of quadrupoles, BPMs and rf structures, after the application of the interleaved alignment procedure, is shown in the upper part of Figure 7-50. The dipole kicks at the boundaries between correction regions are shown in the lower part of the same figure. A very smooth alignment between the endpoints of each section is indeed achieved. At the endpoints the beam is deflected into the next section, causing sharp kinks. The endpoints are not moved and reflect the initial random quadrupole misalignment of $100\text{-}\mu\text{m}$. Between the endpoints, the alignment is bowed towards zero. The absolute zero line is known to the system only because the initial misalignment was random about it. Constraints on the rms size of magnet movements bias the solution towards the initial average misalignment between endpoints.

The solution shown in Figure 7-50 is largely determined by the different weights on the "measured" BPM readings, the rms of the calculated magnet movements and the strength of the dipole kick that launches the beam into the alignment section. Changes in the relative weights will result in solutions that are not equivalent in terms of emittance growth. We have chosen to constrain the rms magnet movements and the rms of the "measured" BPM readings relatively strongly while allowing for large dipole kicks. This choice of weights results in a small final emittance growth.

The vertical single-bunch emittance growth and the trajectory along the linac are shown in Figures 7-51 and 7-52. The trajectory in Figures 7-52 shows residual sub-micron beam offsets in the quadrupoles that result from the "bowing" of the alignment trajectory. Figure 7-51 shows that these small beam offsets cause no significant emittance growth. The residual emittance growth occurs mainly at the transitions from one sector to the next. The large dispersive deflections cause a stepwise emittance growth behavior. One can imagine smoothing the transitions by distributing the beam deflection. A better method would be to also move the sector endpoint quadrupoles such that the deflection kicks are minimized.

We should stress that the present algorithm already works very well. The quadrupole and structure alignment is minimized over short wavelengths and beam offsets with respect to the BPMs are effectively reduced from many cm's to the sub-micron level. The smooth alignment of quadrupoles and structures minimizes the vertical emittance growth to about 20%. The convergence of the method is illustrated in Figure 7-53 where the vertical single-bunch emittance growth and the vertical rms beam offset in the BPMs are shown as a function of iteration number. It is seen that after about 5 iterations a very reasonable situation is achieved with almost no further improvements after about 15 iterations.

The emittance growth for the case of perfect BPMs is a function of the initial quadrupole misalignment which determines the magnitude of the dispersive deflections between sections. This is shown in Figure 7-54. The vertical single-bunch emittance growth and the rms trajectory offset at the BPMs are shown as a function of the initial rms quadrupole offset. As expected, the rms trajectory offset in Figure 7-54 increases linearly and the vertical emittance growth increases quadratically with the initial rms quadrupole misalignment.

Now we consider a more realistic case where the BPMs have a $2\text{-}\mu\text{m}$ -rms static offset with respect to the quadrupoles and a $1\text{-}\mu\text{m}$ -rms resolution. The initial quadrupole misalignment is $50\text{-}\mu\text{m}$ rms. We still assume perfect rf-BPMs. The alignment is done in 14 sections and 5 iterations. Figure 7-55 shows the average vertical single-bunch emittance growth for the different BNS cases and the imperfections defined above. The BNS configuration number 3 still yields the smallest emittance growth. However, due to the additional BPM

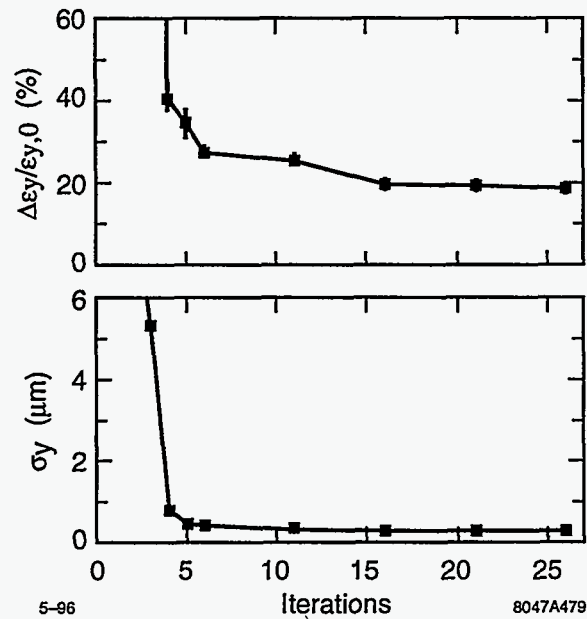


Figure 7-53. Convergence of the alignment algorithm for an initial random quadrupole misalignment of 100- μm rms and perfect BPMs. The upper plot shows the average emittance growth $\Delta\epsilon_y/\epsilon_{y,0}$ as a function of the iteration number. The lower plot shows the corresponding rms trajectory offset with respect to the BPMs.

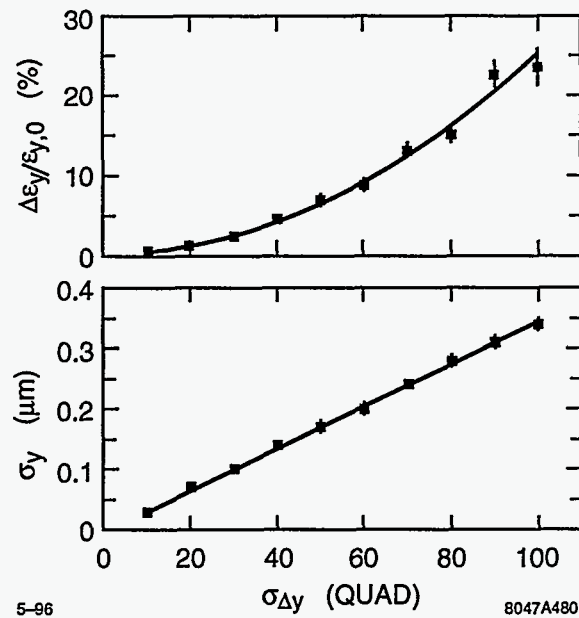


Figure 7-54. The average emittance growth $\Delta\epsilon_y/\epsilon_{y,0}$ and rms trajectory offset σ_y after alignment versus the initial rms quadrupole misalignment $\sigma_{\Delta y}$.

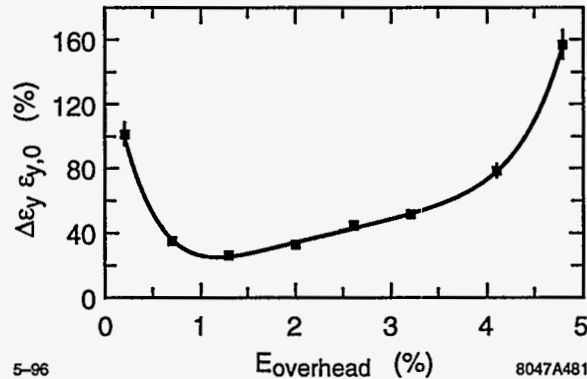


Figure 7-55. Average emittance growth $\Delta\epsilon_y/\epsilon_{y,0}$ after alignment for different BNS configurations. Here we assume an initial quadrupole alignment of $50\text{-}\mu\text{m}$ rms, a static BPM to quadrupole offset of $2\text{-}\mu\text{m}$ rms, a BPM-resolution of $1\text{-}\mu\text{m}$ rms and perfect rf-BPMs. The alignment is done in 14 sections and 5 iterations.

imperfections, the emittance growth for the nominal BNS increased from about 7% to about 28%. This is well below the emittance growth budget of 175% for NLC-IIb.

The Effects of Transverse Long-range Wakefields

Thus far, we have only considered single-bunch effects. However, for the bunch train of 90 bunches, transverse long-range wakefields become important. In order to set the scale of those effects, we show the multibunch emittance blowup due to a 1-sigma initial vertical beam offset. Figure 7-56 shows the special case where each bunch is described as a single beam ellipse (zero bunch length). Single-bunch wakefields do not apply and the phase space distribution of the bunch train only reflects long-range wakefields. The phase space distribution of the bunches is compared to the beam ellipse that is obtained from the average single-bunch emittance. The bunches spread all over the beam ellipse but do not reach far beyond that. Multibunch emittance growth is therefore small and is found to be 25.6%.

Figure 7-57 shows the same case for a more realistic beam distribution. The bunch has a finite length and single bunch wakefields apply. Filamentation and BNS damping cause the phase space distribution of the bunches to be smaller. In this case the emittance of the first bunch grows by 38.7%, the average single-bunch emittance growth is 49.0% and the total emittance growth is 54.4%. The difference between the last two numbers reflects the impact of the long-range transverse wakefields. Here emittance growth is dominated by single-bunch wakefield effects.

Betatron Coupling

In the NLC, the horizontal emittance is about 100 times larger than the vertical emittance. Betatron coupling can couple part of the large horizontal emittance into the vertical plane. This effect is illustrated in Figure 7-58. Since the horizontal trajectory was kept flat for this study, no vertical betatron oscillations are induced from the coupling. If there were any, they would be absorbed into the alignment and trajectory correction. The emittance growth shows a quadratic dependence on the rms quadrupole roll angle. Assuming the tolerance value of the roll angle of about $300\ \mu\text{rad}$ rms, the emittance growth is well below 10% and is not important.

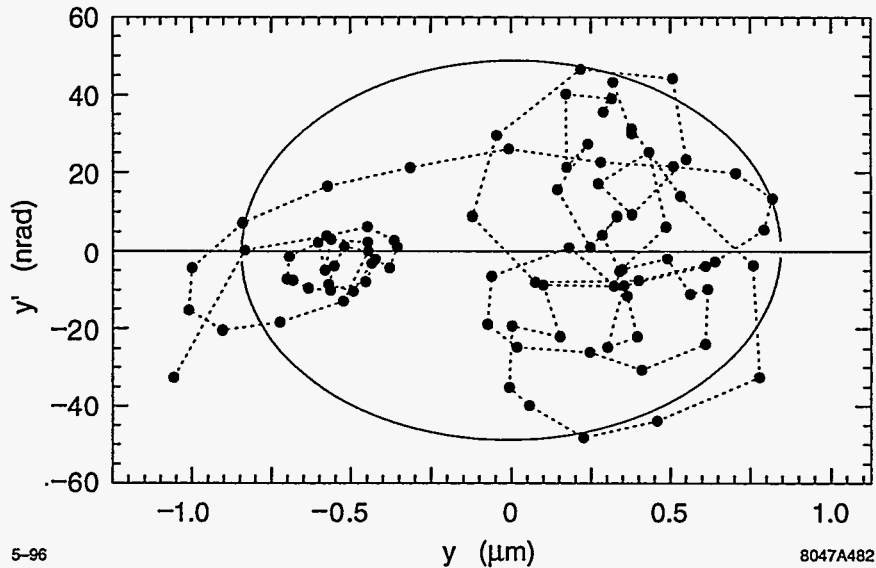


Figure 7-56. Phase space locations y and y' of the bunches at the end of the linac for a 1-sigma initial vertical beam offset. y and y' are referenced to their average values. The bunch positions are compared to the beam ellipse from the average single-bunch emittance. Every bunch is tracked as a single beam ellipse so that no single-bunch wakefield effects apply. For this case a multibunch emittance growth of 25.6% was calculated.

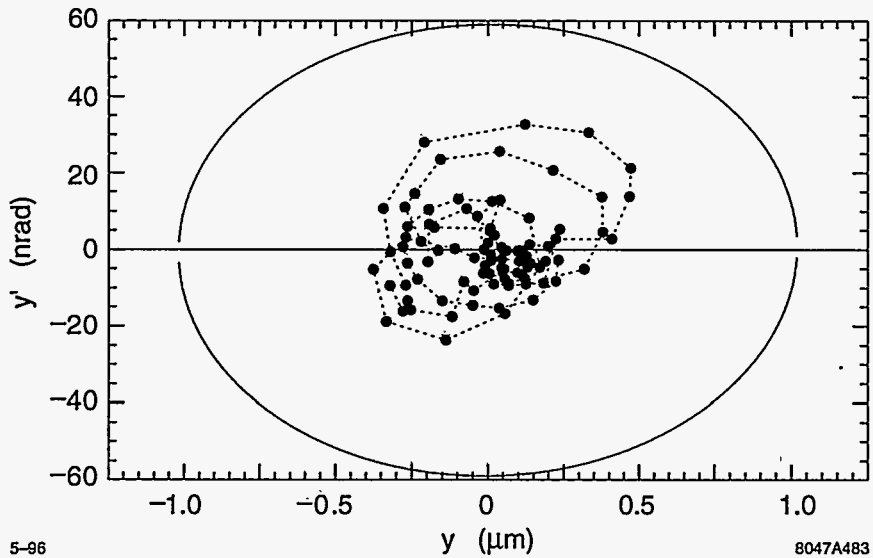


Figure 7-57. Phase space locations y and y' of the bunches at the end of the linac for a 1-sigma initial vertical beam offset. y and y' are referenced to their average values. Single-bunch wakefield effects are included. The amplitude of the incoming betatron oscillation and the resulting long-range wakefield effects are reduced by filamentation. The bunch positions are compared to the beam ellipse from the average single-bunch emittance. Here we obtain a total emittance growth of 54.4%. The emittance growth of the first bunch is 38.7% and the average single-bunch emittance growth is 49.0%.

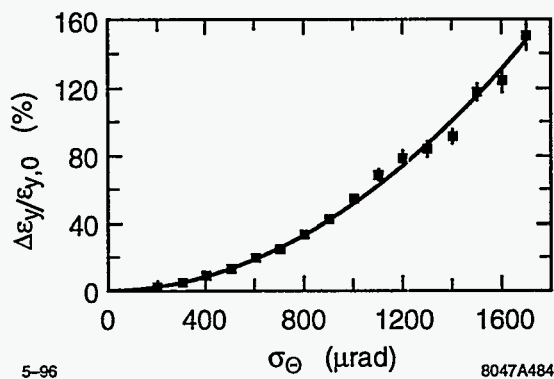


Figure 7-58. Average vertical emittance growth $\Delta\epsilon_y/\epsilon_{y,0}$ as a function of the rms quadrupole roll θ around the longitudinal direction. There are no horizontal beam offsets in the quadrupoles. The data only shows "emittance coupling".

7.6.6. Full Simulation

For a full simulation, we put the most important imperfections together, apply the correction algorithms and observe the emittance growth. In order to illustrate the importance of the several effects, we proceed in steps. For each case we quote the emittance growth $\Delta\epsilon_y/\epsilon_{y,0}$ at the end of the linac and the rms beam offset σ_y at the BPMs.

1. Initial random quadrupole misalignment of 100- μm rms. Rf structures are aligned to the beam.

$$\frac{\Delta\epsilon_y}{\epsilon_{y,0}} = (24.4 \pm 2.3)\% \quad (7.8)$$

$$\sigma_y = (0.35 \pm 0.01) \mu\text{m} \quad (7.9)$$

2. Add: BPM resolution of 1- μm rms. Static BPM-to-quadrupole offsets of 2- μm rms.

$$\frac{\Delta\epsilon_y}{\epsilon_{y,0}} = (41.1 \pm 2.4)\% \quad (7.10)$$

$$\sigma_y = (1.08 \pm 0.01) \mu\text{m} \quad (7.11)$$

3. Add: rf-BPM resolution of 15- μm rms.

$$\frac{\Delta\epsilon_y}{\epsilon_{y,0}} = (90.2 \pm 6.0)\% \quad (7.12)$$

$$\sigma_y = (1.21 \pm 0.01) \mu\text{m} \quad (7.13)$$

4. Add: Rf-phase errors of 1° rms. Rf amplitude errors of 0.2% rms. Quadrupole roll errors of 300- μr rms. Quadrupole gradient errors of 0.3% rms.

$$\frac{\Delta\epsilon_y}{\epsilon_{y,0}} = (97.8 \pm 3.6)\% \quad (7.14)$$

$$\sigma_y = (1.22 \pm 0.01) \mu\text{m} \quad (7.15)$$

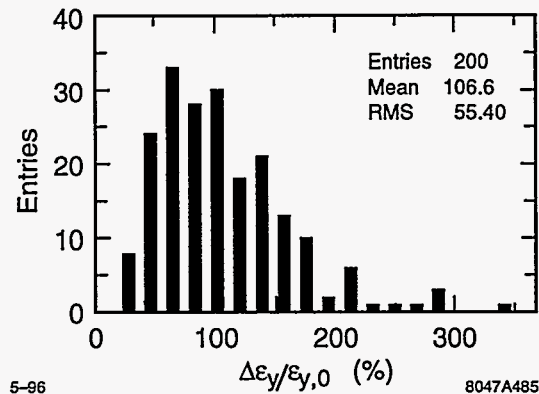


Figure 7-59. Histogram of vertical emittance growth $\Delta\epsilon_y/\epsilon_{y,0}$ for 200 different error distributions. The average emittance growth is $106.6\% \pm 3.9\%$. Note the exponential distribution for large emittance dilutions.

5. Add: Multibunch long-range wakefield effects.

$$\frac{\Delta\epsilon_y}{\epsilon_{y,0}} = (106.6 \pm 3.9)\% \quad (7.16)$$

$$\sigma_y = (1.23 \pm 0.01) \mu\text{m} \quad (7.17)$$

All emittance growth numbers, apart from the last one, refer to the single-bunch emittance growth. The total multibunch emittance growth of about 110% is well below the allowed emittance dilution of 175% for NLC-IIb (compare Table 7-2). Internal structure misalignments, special multibunch imperfections and the effects of missing BPMs will be added to the simulations in future studies.

The most important imperfections considered so far are BPM and rf-BPM errors. They determine the quality of the correction and the residual emittance growth. In all cases, the correction and alignment is done on the first bunch, assuming that all other bunches behave similarly. The small additional multibunch emittance growth shows that this is a valid assumption, although we have not yet included the effects of internal structure misalignments. The distribution of emittance growth for different error distributions is shown in Figure 7-59 for the full simulation (last case). The exponential tail for large emittance dilutions tends to bias the average emittance growth towards larger values. It results from error distributions that have a large component at the betatron frequency. Fortunately, these errors are easily corrected using bump (global) correction methods.

Figure 7-60 shows an alternate way to quantify the effect of imperfections. The so-called “luminosity reduction” (L_y) is calculated from a cross-correlation of the bunch distributions with themselves. Beam tails are naturally de-weighted in this process. The result is quoted as the fraction of the maximum luminosity that would be achieved for the particular case. The luminosity reduction comes out to be 71.1% for the full NLC simulation. That means that on average about 70% of the maximum luminosity would be obtained with the given errors.

Figure 7-61 shows the average emittance growth along the linac for 100 seeds of the full simulation. The growth shows a square-root dependence on the longitudinal position s . No particularly bad region can be identified and the emittance growth behaves rather smoothly. Small residual step increases of the emittance can be seen. They are caused by the transitions between alignment sections. However, they are of little importance to the overall emittance growth.

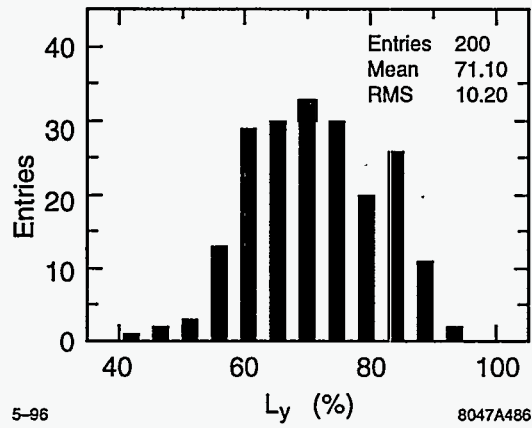


Figure 7-60. Histogram of the luminosity reduction L_y for 200 different error distributions. The average luminosity factor is $71.1\% \pm 0.7\%$.

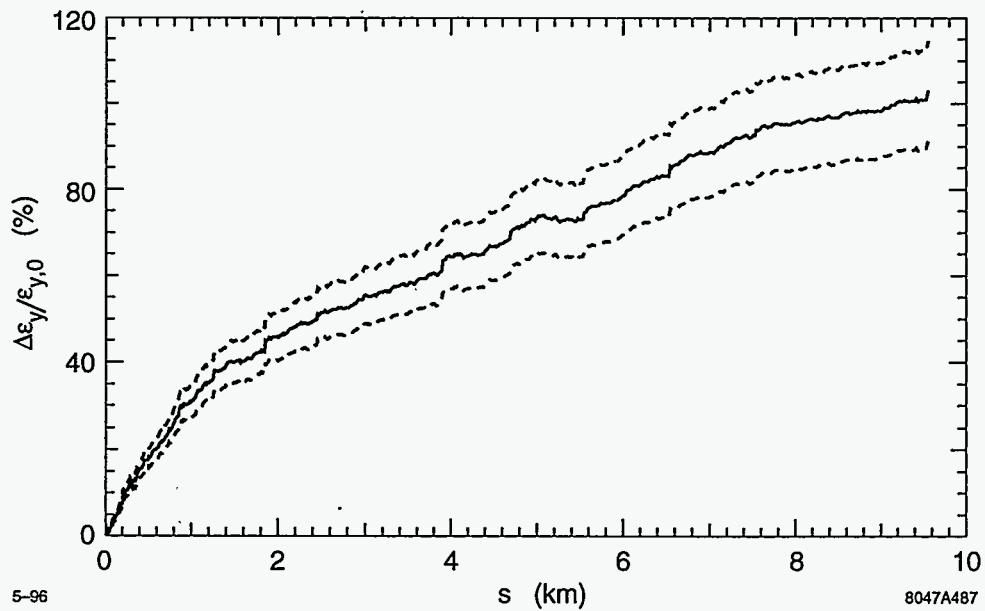


Figure 7-61. Average emittance growth $\Delta\epsilon_y/\epsilon_{y,0}$ along the linac for the full simulation. The dashed curves specify the error bars around the average (solid curve).

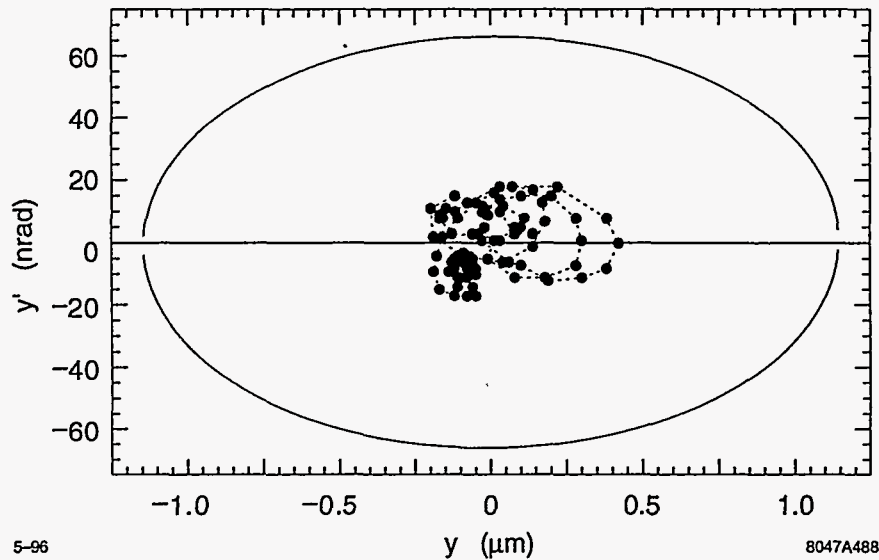


Figure 7-62. Example of the vertical phase space distribution of the bunch train at the end of the linac. The bunch locations are compared to the beam ellipse as obtained from the average single-bunch emittance. The total vertical emittance growth is 89.0% for this case. This is to be compared to an emittance growth of the first bunch of 83.0%, and an average single-bunch emittance growth of 85.2%.

Figures 7-62, 7-63 and 7-64 show an example of the long-range wakefield effects for the full set of imperfections. Figure 7-64 is of particular interest. The single-bunch emittance is shown as a function of the bunch number. It shows an oscillatory behavior and is even reduced below the value of the first bunch for some of the trailing bunches. Long-range wakefields induce bunch oscillations that can work as “emittance bumps” and reduce emittance. If one could measure the emittances and trajectories of all bunches one could pick the bunch with the smallest emittance and use multibunch kickers to correct the other bunches to this reference. The multibunch scheme can in principal be used to conveniently explore the phase space to find the smallest possible emittance dilution.

7.6.7 Stability

Stability questions determine how often the alignment and correction algorithms need to be applied. In the previous section we described a procedure that serves as both the alignment and trajectory correction algorithm. We have shown that static imperfections can be corrected down to the required levels. Now we consider the question of how stable the optimized linac is and how fast it deteriorates. From the beam dynamics point of view, linac stability problems are dominated by quadrupole drifts; the quadrupoles generally have the tightest alignment tolerances.

Here we do not discuss BPM stability questions in detail. However, the requirements are tight. For the alignment algorithm we require a 2- μm static rms offset between the BPM and quadrupole centers. This tolerance can be achieved with a time-consuming beam-based alignment procedure and it must be stable over significant periods of time (days). The question of BPM stability is discussed elsewhere. Since quadrupoles and BPMs are mechanically mounted together, the BPM stability that can be achieved is mainly determined by the BPM electronics, cable lengths and similar factors.

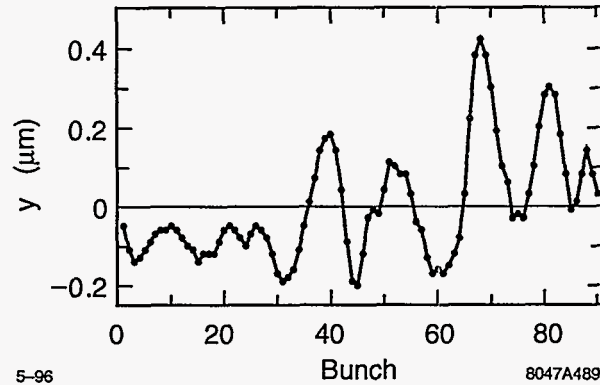


Figure 7-63. Vertical bunch positions y as a function of bunch number at the end of the linac (same example as in Figure 7-62).

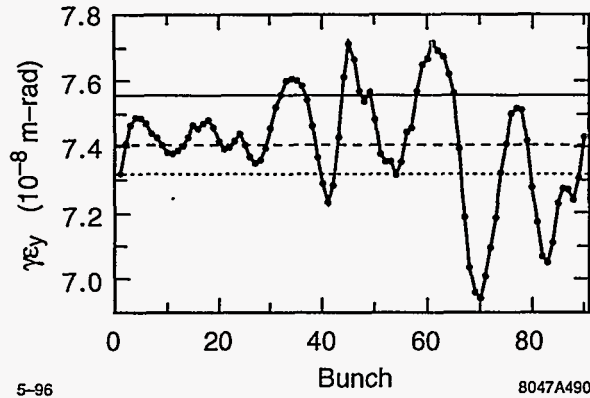


Figure 7-64. Vertical normalized single-bunch emittance ϵ_y as a function of bunch number at the end of the linac (same example as in Figures 7-62 and 7-63). The three lines indicate the emittance growth of the first bunch (dotted), the average single-bunch emittance growth (dashed) and the total beam emittance growth (solid).

Quadrupole Vibrations

Vibrations are fast random motions of the quadrupole alignment around its average position. Here we assume that the vibrations are white noise and that they are not damped by trajectory feedbacks. In reality the quadrupole vibrations due to ground motion, cooling water turbulence, etc will depend on frequency and will be partly suppressed by the trajectory feedbacks.

The average vertical emittance growth is shown in Figure 7-65 as a function of the vertical rms quadrupole offset $\sigma_{\Delta y}$. Here we only consider single-bunch emittance growth with respect to the beam centroid. Offsets that make the beams miss at the IP are assumed to be suppressed by fast feedbacks. Those effects are discussed in more detail in Section 7.4 and in the final focus chapter. From Figure 7-65 we see that the quadrupole white noise jitter should be kept below 20 nm in order to avoid single-bunch emittance growth

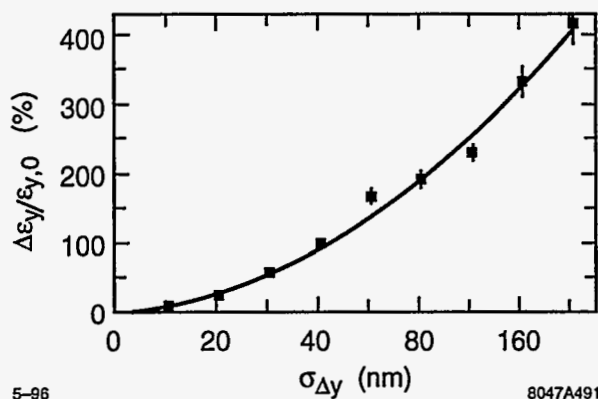


Figure 7-65. Average single-bunch emittance growth $\Delta\epsilon_y/\epsilon_{y,0}$ as a function of the rms quadrupole offset Δy .

in excess of 10%; this tolerance is well above the measured quadrupole jitter. Note that a tighter tolerance results if one considers the emittance growth with respect to the beam axis.

The emittance growth for quadrupole jitter is mainly caused by the uncorrected betatron oscillation that builds up along the linac. This will be discussed in the next section.

ATL-like Alignment Drifts

Next, we consider the question of how often the alignment and correction algorithm needs to be applied. Assuming a perfect starting point (flat trajectory, no emittance growth) we let the alignment drift and observe the deterioration of the trajectory and the emittance. In order to model alignment drifts we use the ATL-model. The ATL-model predicts that the rms vertical misalignment $\sigma_{\Delta y}$ (in μm) deteriorates with time T (in seconds) and over the length L (in m) as follows:

$$\sigma_{\Delta y}^2 = A \cdot T \cdot L \quad (7.18)$$

We use an A coefficient of $5 \times 10^{-7} \mu\text{m}^2/\text{s}/\text{m}$. This value was inferred from data taken on the SLAC site for times T over 30 hours. We should caution that the validity of the ATL-model (diffusive drifts) is not well established. Recent observations indicate a linear increase of the rms misalignment with time for longer periods (systematic drifts). Assuming diffusive alignment drifts from the ATL-model for time periods of the order of hours might well be overly pessimistic.

Figure 7-66 illustrates ATL-like alignment drifts. It shows the displacements and corresponding trajectory offsets at the BPMs after 30 minutes of deterioration. The offsets of quadrupoles, BPMs and rf-structures are overlaid in the plot and are essentially indistinguishable. The trajectory offsets at the BPMs show the coherent betatron oscillations that build up. The dotted lines indicate the locations of seven trajectory feedbacks that constrain y and y' to zero. The coherent betatron oscillations are thus broken up into eight smaller oscillations. The oscillation amplitude is a few μm and is large enough to be detected with a BPM resolution of $1 \mu\text{m}$.

A histogram of the vertical single-bunch emittance growth from alignment drifts after 30 minutes and an A of $5 \times 10^{-7} \mu\text{m}^2/\text{s}/\text{m}$ is shown in Figure 7-67. The average emittance growth is found to be $29.0\% \pm 0.8\%$. This size of emittance growth will prompt a beam-based alignment of the quadrupoles, that serves as an effective trajectory correction at the same time. Note, however, the exponential distribution for large emittance

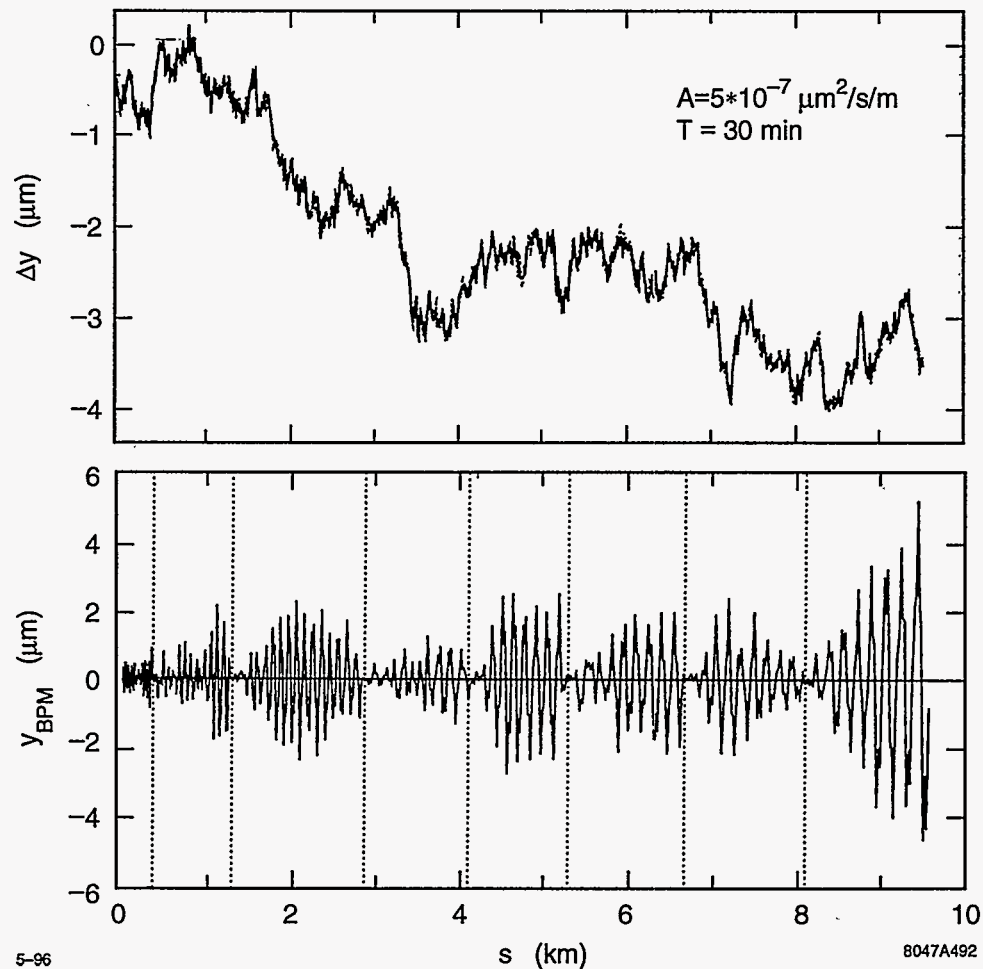


Figure 7-66. Example of ATL-like alignment drifts. The upper plot shows the displacements of quadrupoles, rf-structures and BPMs after 30 minutes with an A -coefficient of $5 \times 10^{-7} \mu\text{m}^2/\text{s}/\text{m}$. The alignment was flat initially. The lower plot shows the corresponding trajectory offsets y_{BPM} at the BPMs. The dotted lines indicate the locations of trajectory feedbacks where y and y' are corrected back to zero. Thus the size of coherent betatron oscillations is constrained.

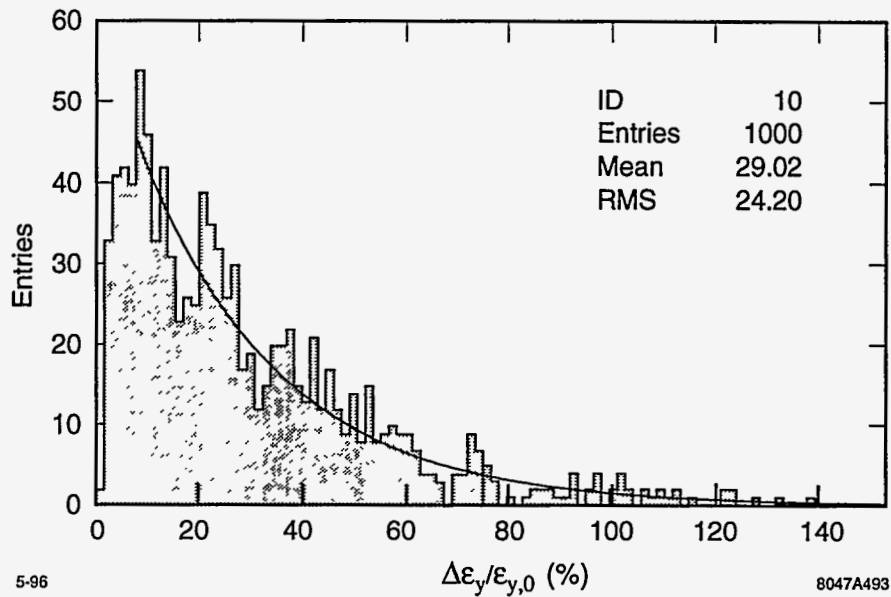


Figure 7-67. Histogram of vertical emittance growth $\Delta\epsilon_y/\epsilon_{y,0}$ for 1000 different error distributions. The average emittance growth is $29.0\% \pm 0.8\%$. The solid curve shows an exponential fit for large emittance dilutions.

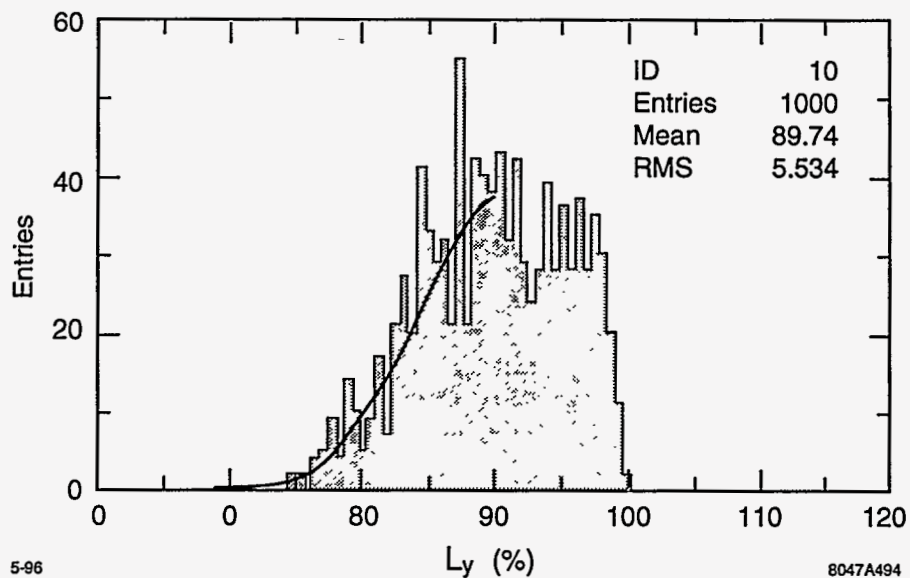


Figure 7-68. Histogram of the luminosity factor L_y for 1000 different error distributions. The average luminosity is $89.7\% \pm 0.2\%$. The solid curve shows a Gaussian fit to the lower half of the distribution.

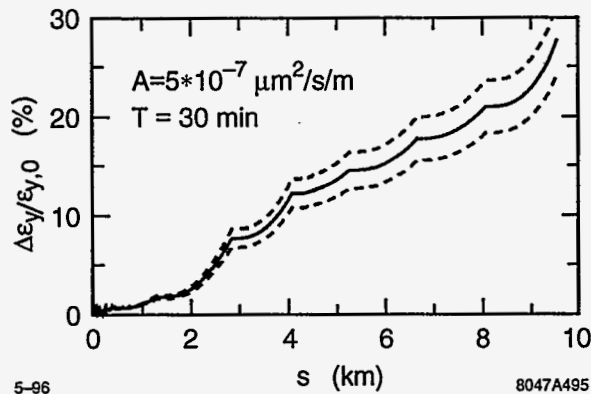


Figure 7-69. Average vertical emittance growth $\Delta\epsilon_y/\epsilon_{y,0}$ along the linac for ATL-like drifts after 30 minutes. We assume an A-coefficient of $5 \times 10^{-7} \mu\text{m}^2/\text{s}/\text{m}$. The dashed curves specify the error bars around the average (solid curve).

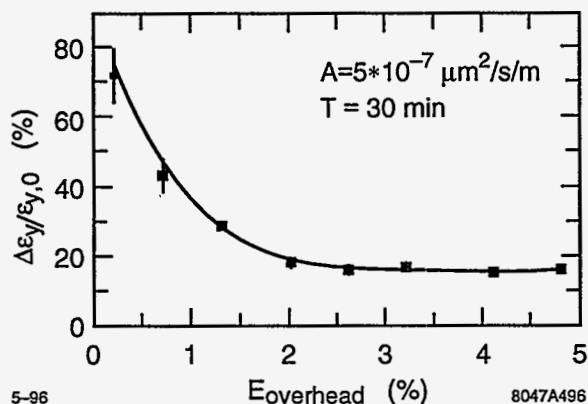


Figure 7-70. Average vertical emittance growth $\Delta\epsilon_y/\epsilon_{y,0}$ from ATL-like alignment drifts for different BNS configurations.

dilutions. The most probable emittance growth is only about 10%. Figure 7-68 shows a histogram for the luminosity reduction in the same case. The distribution shows an approximately Gaussian distribution for smaller luminosity, with an average luminosity of about 90% of its ideal value.

The average emittance growth along the linac is shown in Figure 7-69. The locations of the trajectory feedbacks are clearly seen. As a coherent betatron oscillation builds up the emittance starts to grow exponentially. The feedbacks stop this exponential growth. More effective feedbacks can be imagined if the average y and y' is minimized up to the next feedback instead of correcting y and y' locally.

Figure 7-70 shows the average vertical single-bunch emittance growth for different BNS configurations. We consider the same case as above. All previous results were obtained using the standard BNS configuration with an energy overhead of 1.3%. Figure 7-70 shows that BNS configurations with higher energy overheads reduce the emittance growth from 29% to about 16%. This result is in better agreement with the simple two-particle model autophasing condition than the other results that were discussed before. One can therefore imagine to trade alignment performance against better stability. However, this is not necessary.

Let us relate the ATL-like alignment drifts to the other results. Since the emittance growth is linear in time we would get an additional average emittance growth of about 15% when we assume a beam-based alignment every 30 minutes. This is about a factor of six smaller than the emittance growth expected after beam-based alignment of quadrupoles and rf-structures. It is small enough not to be an important limitation of the NLC linac performance as long as the linacs are corrected regularly every 30 minutes. Since the alignment and correction algorithm does not interfere with the standard operation, its frequent application should be no major obstacle.

7.6.8 Summary and Outlook

A beam-based alignment algorithm for quadrupoles and rf-structures was simulated with a realistic BNS configuration. It was shown that the large initial misalignments from conventional alignment procedures can be corrected to acceptable levels. The emittance growth that finally can be achieved depends on the initial misalignment and most importantly on the performance of the BPMs and rf-BPMs. Assuming an initial misalignment of 100- μm rms, static BPM to quadrupole offsets of 2- μm rms, a BPM resolution of 1- μm rms and an rf-BPM resolution of 15- μm rms, we find an average emittance growth of $90.2\% \pm 6.0\%$ for a single bunch. Adding errors of the rf-phases, rf-amplitudes, quadrupole roll angles and quadrupole gradient errors increases the emittance growth to $97.8\% \pm 3.6\%$. Adding the effects of transverse long-range wakefields on the bunch train yields the final multibunch emittance growth of $106.6\% \pm 3.9\%$. This emittance growth is smaller than the allowed total emittance growth of 175%. As the emittances roughly add in quadrature the impact of additional imperfections gets smaller with larger emittances. It is anticipated that the alignment algorithm can be further optimized by smoothing the transitions between alignment sections. Further details can be found in the text.

The dominant stability problem is caused by drifts of the quadrupole alignment. We simulated this effect by using the ATL-model with a coefficient $A = 5 \times 10^{-7} \mu\text{m}^2/\text{s}/\text{m}$ as measured at SLAC. The use of this model for times of about 1 hour might be overly pessimistic. We showed that the alignment drifts drive coherent betatron oscillations that lead to exponential emittance growth. The addition of seven trajectory feedbacks breaks the coherent betatron oscillation down into eight smaller oscillations. Assuming a beam-based quadrupole alignment every 30 minutes, we get an additional average emittance growth contribution of 15%. Since the emittances roughly add up in quadrature, this is small compared to the 107% average emittance growth after alignment. The alignment algorithm does not interfere with the normal linac operations, so that it can be applied very frequently. We conclude that we can handle alignment drifts safely.

Future simulation studies will include internal structure misalignments, multibunch imperfections (bunch-to-bunch charge, energy, etc. variations) and the effects of missing BPMs. In addition, we further want to apply emittance bumps in order to compensate the emittance growth below what has already been achieved. Finally, we need to study the impact of different bunch shapes on the linac emittance transport and we need to simulate the collimation requirements at the end of the linacs.

7.7 Tolerances

In this section we give a brief summary of the tolerances needed to control emittance growth in the main linacs. Simulation studies leading to these tolerance numbers have been discussed in previous sections, especially Section 7.6.

Source	$\Delta\epsilon_y/\epsilon_y$	Dynamics
Quad alignment: BPM resolution 1 μm BPM-to-quad alignment 2 μm	40%	Incoherent dispersion
Quad drift between alignment: Steering period 30 min	10%	Coherent dispersion and wakes
Structure alignment: Internal alignment 15 μm Beam measurement accuracy 15 μm	25% 50%	Long-range wakes Short-range wakes
Other (<i>e.g.</i> , quad roll, ion effects, and rf deflections):	50%	
Total:	175%	

Table 7-9. NLC-IIb linac emittance growth budget.

Unless otherwise noted, we assume the NLC-IIb parameters, *i.e.*, a charge per bunch of 1.10×10^{10} with a 150- μm bunch length and an injected normalized vertical emittance $\gamma\epsilon_y = 4 \times 10^{-8}$ m-rad. The tolerances are specified to deliver a beam with a vertical emittance of $\gamma\epsilon_y = 11 \times 10^{-8}$ m-rad. As noted earlier, the primary source of emittance dilution arises from the accelerator structure misalignments with respect to the beam. In the NLC design, the other sources are relatively insignificant, primarily because established beam-based alignment techniques can be used to attain accurate alignment of the BPMs and quadrupoles.

The total emittance budget is given in Table 7-9 for the NLC-IIb linac design. At the present time, we have budgeted roughly half of the allowed 175% total emittance growth to the misaligned accelerator structures. As stated, this partitioning arose because we have more confidence in the quadrupole alignment techniques. Regardless, in the future, we will probably redistribute the tolerances to allow a greater margin for the other effects; this work is awaiting more simulations that incorporate the interactions of these many disparate sources and account for stability errors.

Finally, we should note two points: First, we are calculating the *expected* average emittance growth. In any given case, the growth can be larger or smaller. The larger growths occur when there is a significant correlation of the errors at the betatron frequency, thereby driving the dilution resonantly. Fortunately, these cases are usually very straightforward to correct with simple global correction schemes and thus we are not very concerned about getting a bad "seed" in the collider.

Second, when considering large emittance dilutions, the rms emittance growth is not a very accurate measure of the luminosity degradation. This occurs because the emittance growth mechanisms, such as wakefields, are nonlinear. Thus, they populate the beam tails without degrading the core emittance as greatly as suggested by the rms emittance growth. A more representative quantity is the luminosity reduction which describes the decrease in the overlap of the beams at the IP; we will adopt this measure in the future.

dispersion ($\delta_{\text{eff}} = .2\%$)

7.8 Operations and Machine Protection System

The operation of the linacs is constrained by the requirements of the Machine Protection System (MPS); the MPS is described in greater detail in Chapter 16. Because the beams have extremely high charge densities, a single bunch train, or even a single bunch, incident on an accelerator structure could cause damage. The philosophy of the MPS is that all preliminary beam-based alignment, tuning, and diagnostics be performed with a full current high emittance single-bunch beam which cannot cause damage in the linac; these operations can be performed at low repetition rates.

As described, the accelerator structures are protected from this diagnostic single-bunch beam with spoilers which are located after every accelerator structure. The spoilers have an aperture that is 2mm in radius, this is roughly half that of the accelerator structure irises, and they are 0.2 radiation lengths in length. If the beam is steered sufficiently far off-axis to intercept an accelerator structure, it must first pass through one of more spoilers. These will increase the beam angular divergence so that, by the time the single bunch beam strikes a structure, it will not cause any damage. To prevent damage to the spoilers themselves, the emittance of the diagnostic beam must be increased by a factor of ten.

Once the initial beam-based alignment, the basic beam trajectory, and the energy profile are established, a high repetition rate of 120–180 Hz can be established. At this point, the beam emittance can be decreased and additional bunches can be added to the bunch trains. All subsequent tuning must be performed at the high repetition rate.

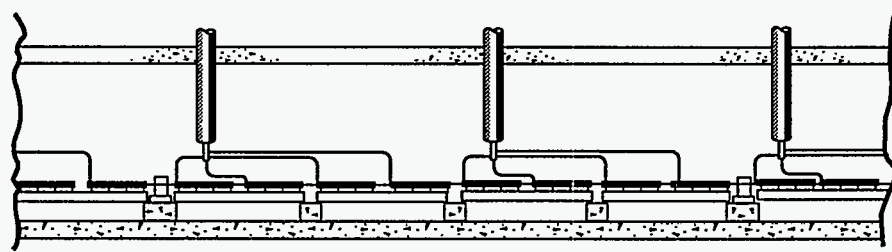
To verify the beam loading compensation when going to the longer bunch trains, the train length will be increased in steps. Presently, we believe that the loading could be checked using only one intermediate train length, namely, going from one bunch per train to 10 bunches per train and then to a full 90 bunches per train; this needs further verification and increasing the steps has minimal implications for the rest of the systems. In addition, to prevent thermal changes of the accelerator structures when changing from low repetition rate to high rate and from the single- to the multibunch modes, the klystron phases are varied so that the addition power which normally would accelerate the missing bunches is dumped into loads rather than into the accelerator structures; this is discussed further in Chapter 8.

To prevent the high rate beams from striking accelerator components, a $\pm 200 \mu\text{m}$ trajectory window and 10% energy window are established about the nominal values. If the beam deviates beyond these limits in any single pulse, the collider is returned to the high-emittance single-bunch diagnostic mode while the source of the problem is diagnosed from data that was taken during the errant pulse. Extensive logic will be used to prevent erroneous MPS faults due to bad BPMs readings.

This system relies on the fact that there are no transverse deflecting fields that can change sufficiently, within a single interpulse period (roughly 8 ms), to deflect the beams from the operational trajectory window into the accelerator structures. This is attained by limiting the strength of all fast correctors and limiting the decay time of the quadrupole and bending magnet fields by using solid core magnets and thick conducting vacuum chambers.

In addition, the MPS must verify that the rf systems are operational before the beams are launched into the linacs. However, fairly large energy deviations can be tolerated. For example, a 20% energy deviation in combination with 100- μm random quadrupole misalignments, which are well in excess of what we expect, would only cause 1-mm orbit offsets.

Thus, the MPS system must only verify that 85% of the rf systems are operational. To this end, all modulators will be polled roughly 100- μs before beam time. At the same time, the klystron timing and



2-96

8047A356

Figure 7-71. Tunnel cross section and accelerator supports.

phase information will be checked. If there are a sufficient number of failures, the beams will be aborted downstream of the damping rings; this verification procedure is described in greater detail in Chapter 8. Finally, there will be sacrificial spoilers and dumps located in the diagnostic station chicanes to prevent energy errors larger than 25% from propagating further down the linac.

7.9 Linac Components

In this section we give more detailed information on various components of the linacs. In the case of supports and movers, we present our most recent design ideas, and discuss the issues that impact the design.

7.9.1 Supports and Movers

Support Layout

The beam line components will be supported 0.5-m above the tunnel floor at roughly four-m intervals (Figure 7-71). This low height minimizes amplification of ground vibrations but still leaves access below the accelerator. Between supports, accelerator modules will consist of two 1.8-m-long sections of disc loaded wave guide which will be assembled and aligned on a common support girder. Focusing quadrupole magnets will be mounted to the supports at intervals along the accelerator. The spacing between quadrupoles will increase in five discrete steps, scaling roughly as the square root of the beam energy along the accelerator. Figure 7-71 shows the support layout at approximately the 200-GeV point.

Support Design

Both the quadrupole and accelerator structure positions will be remotely controllable. All accelerator and magnet supports will have stepper motor positioning mechanisms with a ± 1.5 -mm range and a $0.3\text{-}\mu\text{m}$ resolution. Both the accelerator structures and quadrupoles will be kinematically supported in cradles formed by motor-driven roller cams as illustrated for a quadrupole in Figure 7-72.

These mover systems will be similar to the Final Focus Test Beam (FFTB) magnet movers which provide a ± 1.5 -mm range with $0.3\text{-}\mu\text{m}$ position resolution. The type of kinematic support which will be used, where

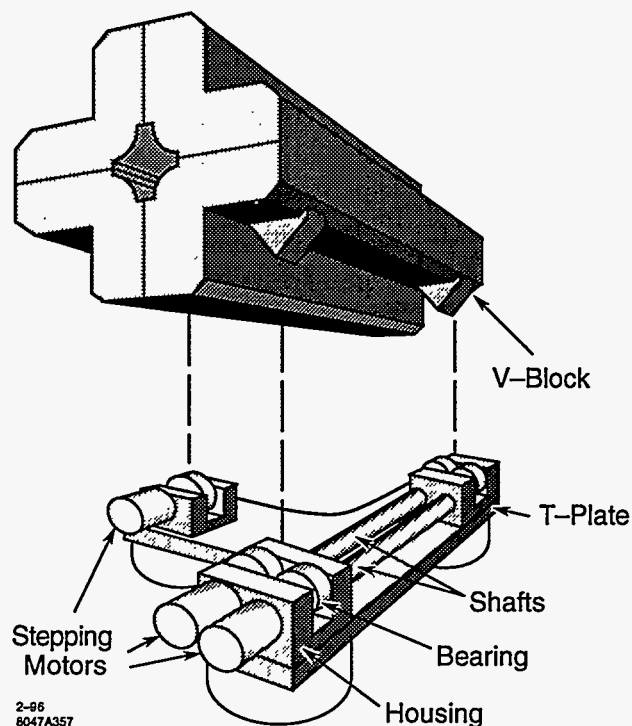


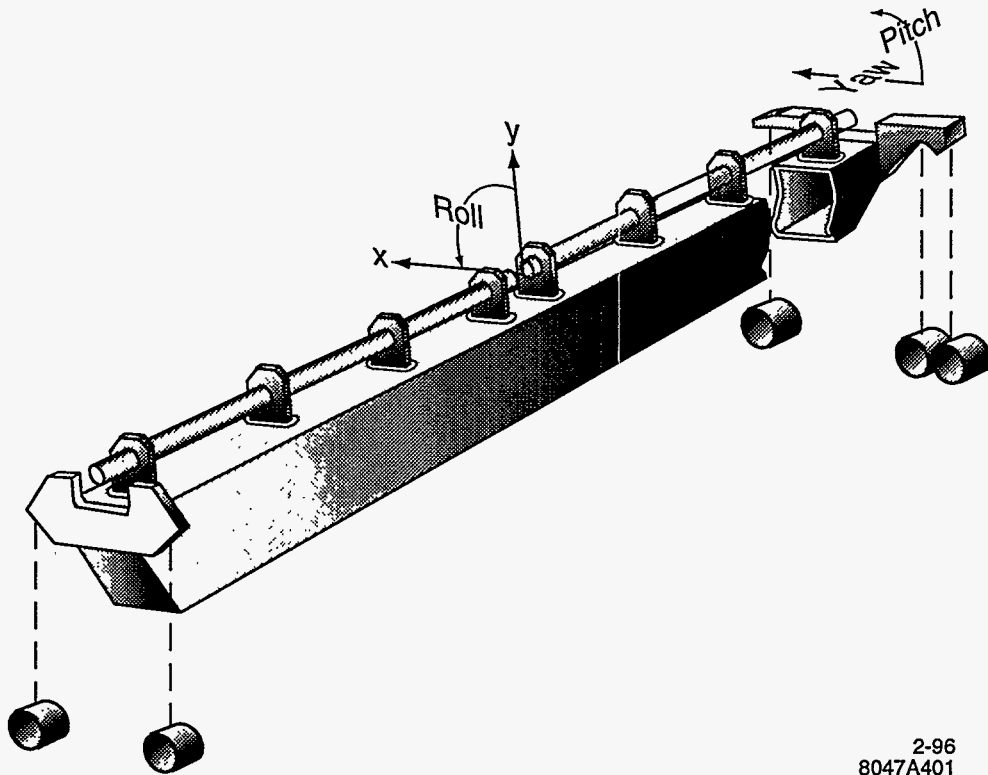
Figure 7-72. Quadrupole roller cam support.

the number of contact support points equals the number of spatial degrees of freedom, is similar to the kinematic support designs for laboratory optics. It insures reproducible zero-play fixturing of components and will be free of all bending moments which might distort magnets or accelerator modules when they are remotely repositioned. The accelerator modules will rest on 5 cams: cams (1,2,3) on one support will fix roll and the x, y coordinates of that end. Cams (4,5) on the next support will fix the x, y position of the module's other end. Thus each module will be adjustable in x, y , roll, pitch and yaw as illustrated in Figure 7-73.

During operation only the inner eccentric shaft of a support cam will rotate under motor control. The outer bearing race remains fixed in contact with the magnet or module contact foot as shaft rotation lifts the module. Motion is strictly bounded by the design geometry. Limit switches and electronic override protection are not needed. Control system failures can only cause a cam to continue rotating. This is an important advantage for any system with as many as 30 thousand channels of motion. All support cams are arranged so that gravity applies a load torque to each cam shaft drive removing all backlash. All parts move by pure rolling motion and are free of hysteresis from intermittent and reversing sliding friction. These features make sub-micron positioning of heavy objects practical using inexpensive mass produced ball or roller bearings. Details of this mechanism are fully covered in [Bowden, 1996].

Initial Alignment

All supports will incorporate standard screw and shim manual adjustments which will be used during initial installation to align each support. After the support is manually aligned, accelerator modules and quadrupole magnets will be lowered into their cam cradles as illustrated in Figure 7-74. No further manual alignment is possible or needed. Each module or magnet has had its cam contact feet aligned to their nominal position



2-96
8047A401

Figure 7-73. Accelerator girder module support geometry.

during assembly. This guarantees the relative alignment between module and quadrupole on installation, reducing, by a factor of two, the number of objects to be manually aligned during installation in the tunnel.

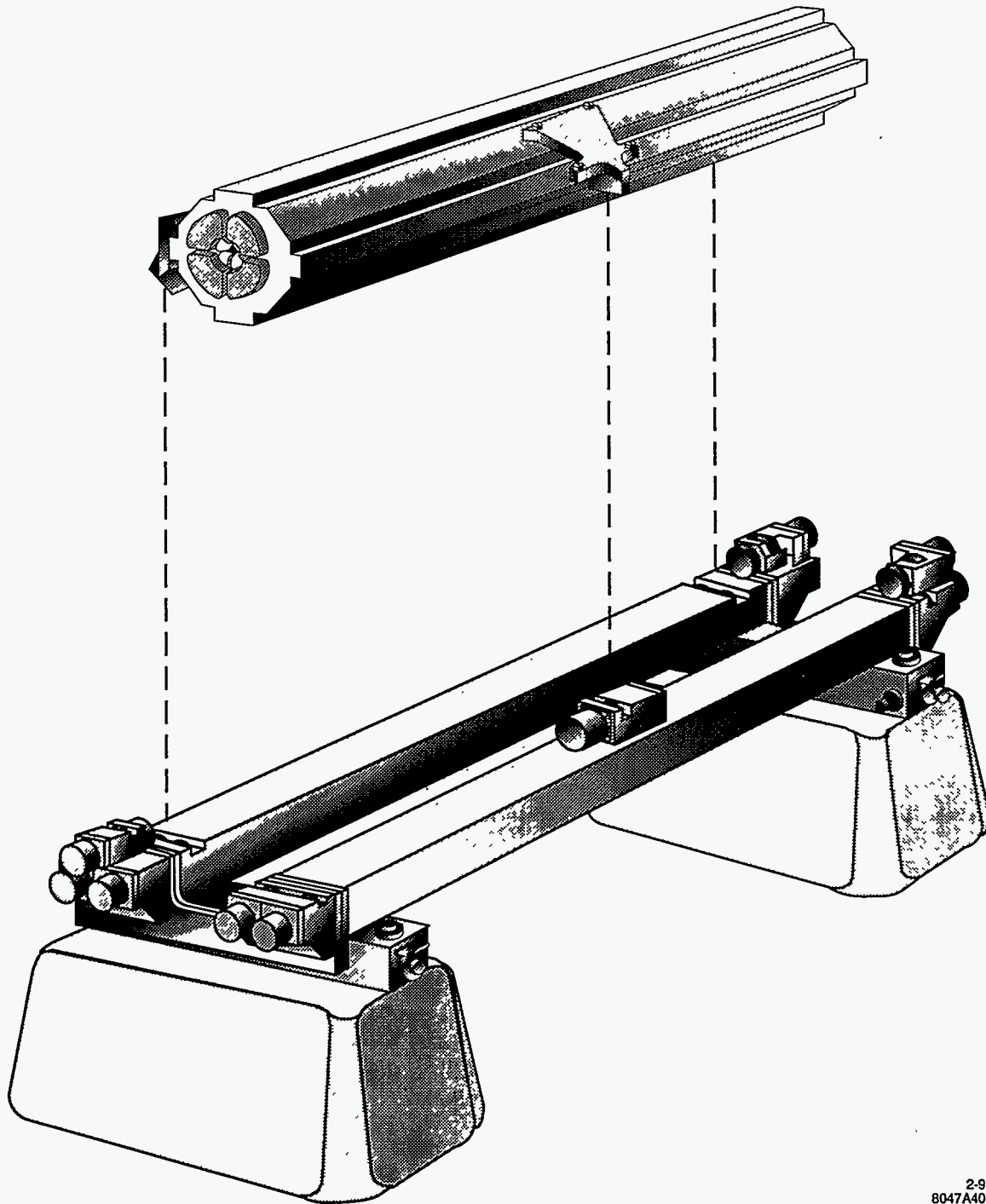
Tunnel Heat Transfer

During operation, thermal distortion can cause serious misalignment of the accelerator. Any successful support system design must avoid or accommodate temperature gradients which could alter alignment. Thermal distortion is the result of thermal gradients which develop when heat is lost by the accelerator to its immediate surroundings. The accelerator cooling system temperature must be set at a temperature sufficiently above the outside air temperature that heat can be expelled even on the warmest days. For example, the existing SLAC accelerator runs with 45°C cooling water because summertime temperatures sometimes reach 40°C in that part of California. This cooling system heats the buried accelerator tunnel to about 40° which is 20° warmer than the surrounding earth. The temperature field for heat flow up from the warm tunnel to the cooler surface is illustrated in Figure 7-75.

The thermal conductance between a circular tunnel and the surface is;

$$\kappa = 2\pi\lambda \left(\cosh^{-1} \left(\frac{d}{R} \right) \right)^{-1} \quad (\text{W/m}^\circ\text{C}) \quad (7.19)$$

Heat loss depends on thermal conductivity of the earth λ and the ratio of tunnel depth to radius d/R . For the SLAC accelerator ($\lambda_{\text{sandstone}} = 1.85 \text{ W/m}^\circ\text{C}$, $d = 10 \text{ m}$, $R = 1.5 \text{ m}$), approximately 100 W is lost by



2-96
8047A402

Figure 7-74. Floor-mounted accelerator remote positioning support assembly.

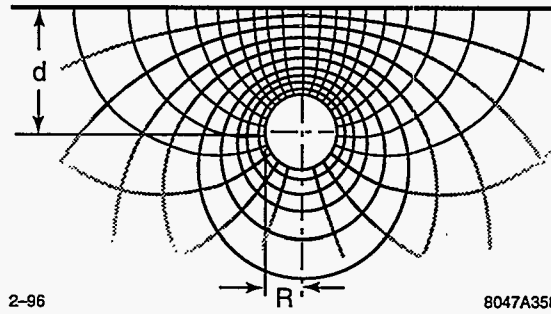


Figure 7-75. Thermal field of a buried heat source

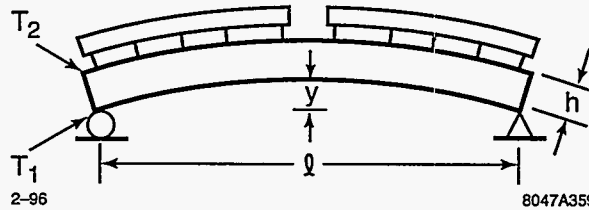


Figure 7-76. Thermal distortion of a girder

the tunnel every meter of its length. Although this heat is small compared to the several kW/m carried away from the accelerator structure by cooling water, it is the source of thermal distortions which disturb accelerator alignment.

Girder Distortion

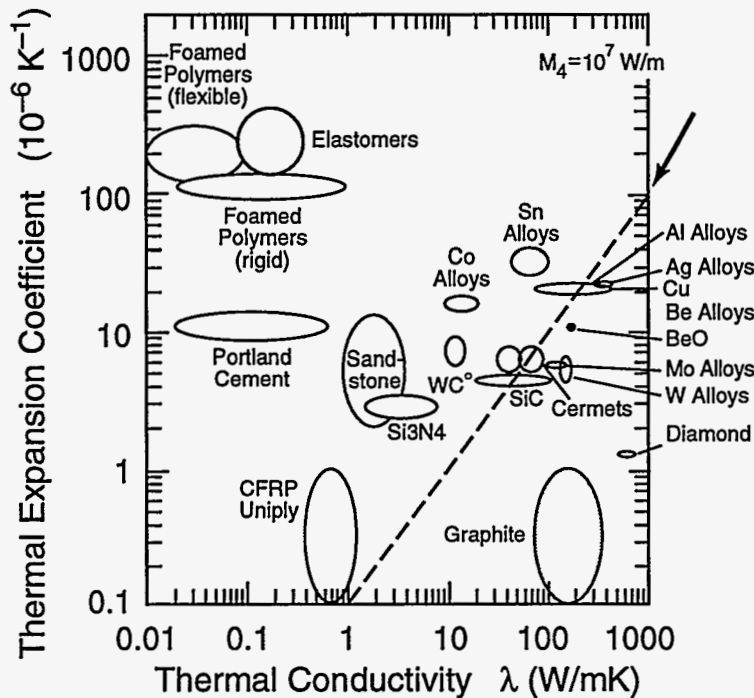
Accelerator modules consist of two 1.8-m-long accelerator structures mounted to a support girder. If the accelerator is mounted on top of its support girder, heat flow will create a thermal gradient across the girder section. The top surface of the girder will be warmer than the bottom which is further away from the source and cooled by natural convection. Differential expansion will cause the girder to arch up toward the warm accelerator, misaligning it. If the girder temperature gradient is linear across its depth, then the distortion is a circular arc of sagitta:

$$y = \frac{\alpha l^2}{8} \left(\frac{T}{h} \right) \quad \alpha = \text{expansion coefficient } \frac{\Delta l}{l} / ^\circ\text{C} \quad (7.20)$$

This is illustrated in Figure 7-76. To limit the sagitta to 100 μm, for example, for a 4-m-long, 150-mm-tall, aluminum girder, the thermal gradient can not exceed $\Delta T = 8(100 \times 10^{-6} \text{ m})(.150 \text{ m}) / [(4 \text{ m})^2 (23 \times 10^{-6} \text{ } ^\circ\text{C}^{-1})] = 0.33^\circ\text{C}$. For comparison, measurements across a similar support girder on the SLAC accelerator during operation show a ΔT of .25°C.

Material Choice

Aluminum has a moderately high expansion coefficient which might appear to make it a poor choice for girder construction. Since thermal gradients are inversely proportional to thermal conductivity, thermal distortion



2-96

8047A360

Figure 7-77. Thermal properties of materials.

depends on the ratio of conductivity to expansion coefficient λ/α . Judged by this criterion, aluminum is a good choice because of its high thermal conductivity. In a plot of conductivity versus expansion coefficient (Figure 7-77) aluminum proves superior to such low expansion coefficient materials as carbon fiber reinforced plastic (CFRP). Furthermore aluminum has an expansion coefficient ($23 \times 10^{-6} \text{ C}^{-1}$) similar to copper ($17 \times 10^{-6} \text{ C}^{-1}$) which is used for the accelerator structure and wave guides.

Low Distortion Girders

One method of removing the thermal gradient which distorts girder alignment is to heat the cooler side of the girder, perhaps with a cooling water tube. It may also be possible to enclose the girder in a common insulation jacket together with the temperature stabilized accelerator. From the standpoint of thermal distortion, the girder, ideally, should be an insulated shell enclosing the accelerator.

7.9.2 Quadrupole Magnets

Based on the optics requirements, a design study for these quadrupoles was done by scaling the "QE" quadrupole design that is used in the SLC linac. As a starting point, the transverse quadrupole size was halved so the resulting gap width of 13.8mm will comfortably accommodate a stripline BPM and still not be a limiting aperture compared to the structure irises. To allow the use of standard-sized conductor (0.1875" square with a 0.100" diameter cooling hole), and to reduce the magnet power consumption, the coil pocket

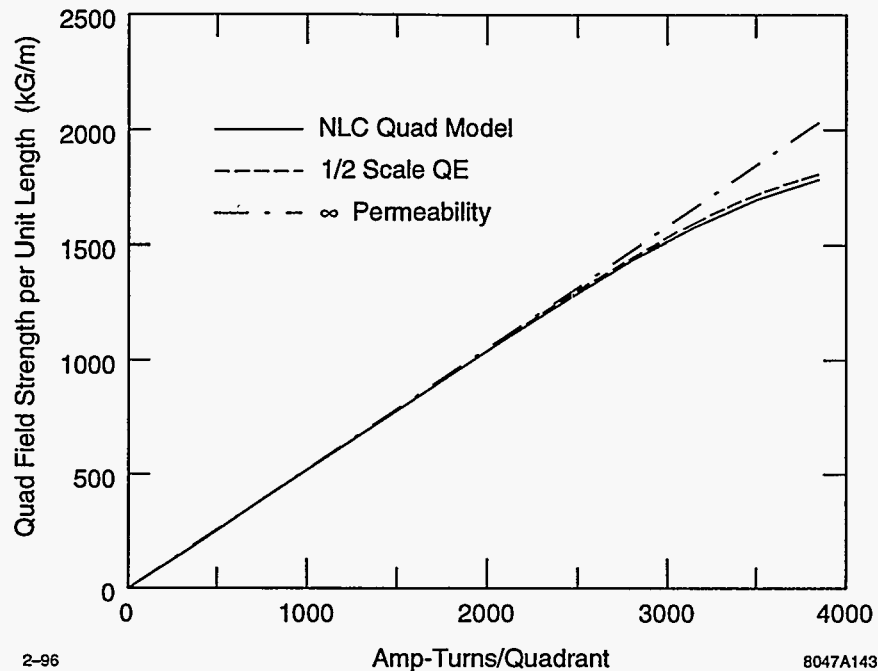


Figure 7-78. Excitation curve for the NLC model quadrupole magnet and the half scale SLC linac QE magnet. Also shown is the ∞ permeability result, which is essentially the same for both magnets.

size was increased while taking care not to significantly reduce the field strength to amp-turn ratio near saturation. A reasonable solution was found even after roughly doubling the coil pocket size. Figure 7-78 shows the resulting excitation curve together with the QE result with a 50% scaling, and the result if the magnet material had infinite permeability (1010 steel was assumed nominally). The NLC quadrupole model magnet would accommodate 17 turns of the standard sized conductor per quadrant compared to 35 turns in the nominal size QE design. This yields a conductor current density of 8.3 kA/in^2 at the maximum current setting (226 A) in Figure 7-78. The field harmonics of this design are also reasonable: 2.6% 12 pole and 2.9% 20 pole at the pole-tip radius, which easily meet the NLC field-quality requirements.

Based on this quadrupole design, quadrupole lengths were chosen to match the linac optics requirements plus allow some overhead (generally more than 30%) at the highest energy operation. Five lengths were chosen which range from 0.2 m to 0.8 m. The operating properties of these magnets can be estimated from Table 7-10 which lists the properties of a somewhat shorter (0.1 m) and longer (1.0 m) magnet that is operated at high current.

7.9.3 Quadrupole Power Supplies

Since the maximum power dissipation levels in the quadrupoles will be under 10 kW, the quadrupoles can be powered individually at a cost that is competitive with powering them in strings and using shunts. This is because much of the cost is in the control electronics, and because the individual power supplies can be of the simple rack-mounted variety. Having individual control of the quadrupoles is very desirable for beam-based alignment measurements, so we will likely power them individually. This also eases the supply stability tolerance—a regulation of 6×10^{-5} will be required, which should not be difficult to meet.

Property at $I = 225$ A	0.1-m magnet	1.0-m magnet
Power Dissipation	1.1 kW	6.9 kW
Water Flow	0.5 gpm	1.5 gpm
Water ΔT	8.7°C	17°C
# of Water Circuits	2	8
Total Coil Resistance	26 m Ω	160 m Ω
Magnet Inductance	0.96 mH	9.6 mH
Time Constant	37 ms	59 ms

Table 7-10. NLC linac quadrupole magnet properties for two magnet lengths.

7.9.4 Multibunch Kicker

The kicker for the bunch-by-bunch trajectory correction is assumed to be a terminated TEM-mode parallel plate vacuum transmission line. The electric and magnetic kicks are equal in magnitude, but cancel unless the TEM wave is traveling in the direction opposite to the beam, so it is not possible to synchronize the wave with the beam. If the stripline length is shorter than half the bunch spacing, different bunches are deflected by entirely independent parts of the driving waveform.

The Fourier spectrum of the kicker was assumed to cut off abruptly at some frequency for the beam dynamics studies. There was no improvement for cutoffs above 250 MHz, which is lower than the bunch frequency of 714 MHz. This indicates that it is not necessary to have independent control of each bunch. A stripline of length 60 cm would have a zero-crossing in its response at 250 MHz, but the response is not flat. A 30-cm stripline length would have a flatter response out to 250 MHz, and would have its first zero-crossing at 500 MHz.

The kicker strength available was assumed to be 56 keV/c for the beam dynamics studies. For $E = 100$ GeV, $\epsilon = 3 \times 10^{-8}$ mr, and $\beta = 10$ m, we have $\sigma_\theta \approx 0.1 \mu\text{r}$. This is equivalent to $\sigma_{p_\perp} \approx 10$ keV/c. Thus the kicker strength is about 6σ in the beam dynamics simulation.

A deflection of $10 \text{ keV/c} \approx 1\sigma$ requires about 30 Gauss-cm. For a deflection of 10σ , the magnetic field integral is $BL \approx 300$ Gauss-cm = 3×10^{-4} Tm. Generating a magnetic field B between strips of width w separated by gap g requires a current $I = Bwf/\mu_0$, where f is a geometrical form factor that depends on g/w and is of order 2. In terms of BL , this can be written $I = (BL)(w/L)f/\mu_0$. For $L = 30$ cm for independent bunch control, and $w = 1$ cm, a $10\text{-}\sigma$ deflection requires 16 A of current. The impedance of the stripline structure is $Z \approx (g/w) \times 377\Omega$. Assuming $Z = 200\Omega$, 3.2 kV are required for 16 A. These parameters are within the range of solid-state components. The instantaneous power is 50 kW, but with a very low duty factor.

There are several conservative assumptions in the above estimates. The kicker strength is 100 keV/c, where 56 keV/c was adequate. The electric kick was neglected, though it is equal to the magnetic kick. Doubling the strip length would allow the same kick strength at half the voltage and current, although it would cost some strength near the 250-MHz cutoff.

The striplines would see the full beam image current, which would be coupled into the input and output ports. The coupling should be very strong, to avoid trapped modes on the strips. The drivers and terminations would be exposed to the coupled image currents. Since the bunches are very short compared to the drive bandwidth, low-pass filters would protect the equipment. Reflections of the image currents would disturb

Chicane	Max. Energy (GeV)	Num. Bends	Max. B (kG)	L_{eff} (m)
1st	32	4	5.25	1.60
2nd	80	4	2.26	3.50
3rd	165	8	1.63	2.65
4th	290	8	1.27	3.50

Table 7-11. Dipole magnets for the linac diagnostic chicanes.

subsequent bunches. A simple way to avoid this problem is to use cables or waveguides with delays longer than half the bunch-train length between the striplines and the filters, drivers, and terminators.

7.9.5 Chicanes

The chicanes are constructed from relatively low field rectangular bending magnets. They have 2-cm vertical gaps and a horizontal good field region $\Delta B/B \leq 10^{-3}$ of 4 cm; the magnet lengths and fields are listed in Table 7-11. All magnets in each chicane, *i.e.*, the four or eight magnets, are powered in series with a 20-kW power supply that is rated at 100 V and 200 A and has a stability of $\Delta I/I \leq 1 \times 10^{-4}$ over the period of one hour.

7.9.6 Beam Dumps

The present design does not have any beam dumps located along the linacs. There is a high power dump after the final diagnostic station at the end of each linac. These dumps will be able to absorb the full 16-MW beam power so that the linacs can be commissioned and studied without sending beams downstream. The design is the same as final beam dumps located after the IPs which is described in Chapter 11.

The beams will be deflected to the dumps using pulsed kickers that operate at the full 180-Hz repetition rate. This allows tuning of the linacs before sending full-rate beam downstream as required for the MPS. At this time we do not have designs for the dump line kickers, but they are straightforward magnets, similar to pulsed dumper magnets in the SLC.

7.10 Instrumentation

The NLC Beam Position Monitor System (BPM) must measure the average beam position of a single pulse containing from 1 to 90 bunches, and must provide bunch-by-bunch position information to the feedback system. Different systems are used to accomplish these tasks: quadrupole BPMs ("Q"), feedback BPMs ("FB"), and structure BPMs ("S"). There are about 3000 "Q" BPMs, 200 "FB" BPMs, and 9700 "S" BPMs. The "Q" and "FB" BPM mechanical detectors are realized with four buttons or short striplines, two in each plane. The "S" BPMs are realized with rf couplers within the cavities. The BPM layout is not included in this study, and therefore no cable plan or signal attenuation is considered in the analysis.

Resolution (minimum variation meas.) at 10^{10} ppb	1- μ m rms
Position stability during 24 hours timescale	1- μ m rms
Position absolute accuracy	0.2 mm
Position dynamic range	0-2 mm
Number of bunches	1-90
Bunches separation	1.4 ns
Beam current dynamic range	$5 \times 10^8 - 1.4 \times 10^{10}$ ppb
Maximum cycle frequency	180 Hz
Maximum time for data processing	1 ms
Total number of monitors	3000

Table 7-12. Requirements for "Q" BPMs.

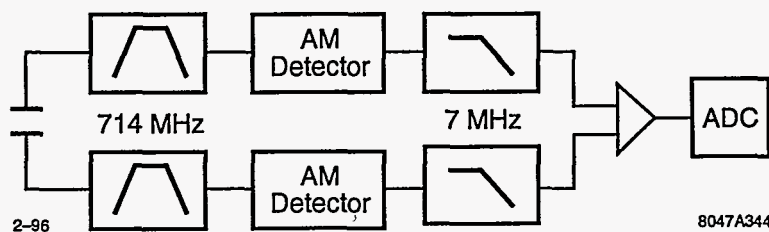


Figure 7-79. "Q" BPMs signal processing block diagram.

General design considerations should be applied: keep as much electronics as possible out of the tunnel for low radiation and easy maintenance, keep as much preprocessing as possible at the BPMs electronics rack location to reduce the communication bandwidth and expedite the feedback system.

7.10.1 Quadrupole and Feedback Beam Position Monitors

The quadrupole BPMs ("Q" BPMs) must be able to detect the average position of the train of bunches, that can contain from 1 to 90 bunches in the single pass. The system's requirements are shown in Table 7-12.

The toughest requirement is the position stability, which asks for better than 1- μ m systematic error. This means 0.005-dB stability for a 6-mm-radius circular beam pipe. In order to achieve such a good performance, a special calibration scheme is necessary.

A synchronous detection technique is used to process the signals from the striplines, which amplitude demodulates the signal and provides either linear or logarithmic functions, as shown in Figure 7-79.

The expressions to calculate the position are respectively:

$$x = \frac{b}{2} \frac{A - B}{A + B} \quad (7.21)$$

for linear demodulation, where b is the beam pipe half aperture, and:

$$x = \frac{1}{S_x} \log \left(\frac{A}{B} \right) \quad (7.22)$$

for logarithmic demodulation, where S_x is the sensitivity (in dB/mm), dependent on the electromagnetic sensor geometry.

The expected signal level for a gaussian beam with a bunch length much shorter than the bunch spacing, is given by:

$$V(\omega) = \sqrt{2} \frac{Ne}{T} gZ \sin\left(\frac{\omega l}{c}\right) \quad (7.23)$$

where N ($=10^{10}$) is the number of particles per bunch, T ($=1.4$ ns) is the bunch spacing, g ($=0.2$) is the electrode coverage, Z ($=50$) is the impedance, l ($=20$ mm) is the stripline length, and ω is the processing frequency ($=2\pi \times 714$ MHz). Under these assumption the rms voltage at the stripline is:

$$V = 1.3V \quad (7.24)$$

The system's resolution is given by the following formula:

$$x[mm] = \frac{b}{4} \left(\frac{N}{S} \right) \quad (7.25)$$

where b is the beam pipe radius (in mm) and N/S is the voltage signal-to-noise ratio. One of the resolution limits is the thermal noise, which is:

$$P_n[dBm] = -174 + 10 \log(BW) + NF \quad (7.26)$$

where BW is the electronics bandwidth and NF is the electronics noise, while the signal strength must be computed for the different type of electromagnetic pickup and electronic processing.

The rms noise voltage, using 7-MHz bandwidth and 15-dB noise, is:

$$V = 7 \mu m V \quad (7.27)$$

and the expected resolution due to the thermal noise is:

$$x = 8 \text{ nm} \quad (7.28)$$

Another resolution limit is given by the amplifier's Common Mode Rejection Ratio (CMRR) which is defined as the ratio of response for a differential change signal when both signals have the same amplitude. A hard but achievable value is 80 dB, which corresponds to:

$$x = 150 \text{ nm} \quad (7.29)$$

according to the expression in Eq. 7.21. If ADCs are used to digitize the values and the difference is digitally calculated, 14 bits are required for a comparable resolution. Things get worse when additional dynamic range must be used for beam current fluctuation, because part of the CMRR must be used to take care of it. When the signal generated by the single bunch pass through the bandpass filter that has 714-MHz center frequency and $Q = 50$, to give 7-MHz bandwidth to the electronics, it produces a ringing whose amplitude is attenuated by 24 dB with respect to the 90 bunches case, as shown in Figure 7-80. This number was derived assuming the demodulation process bandwidth to be limited by the single-pole low-pass filter.

The expected resolution due to thermal noise in single-bunch s therefore:

$$x = 127 \text{ nm} \quad (7.30)$$

to which the CMRR contribution should be added as well.

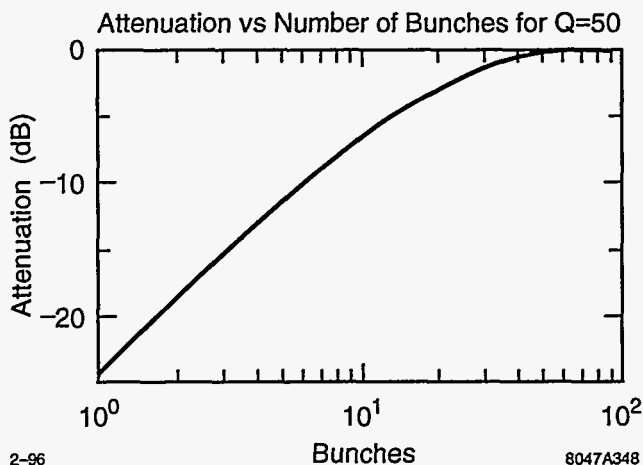


Figure 7-80. Attenuation vs. number of bunches.

Number of channels	4
Analog bandwidth	1 GHz
Sampling rate	$10^9/s$
Number of bits	10
Triggering	int/ext

Table 7-13. Single-bunch BPM characteristics.

7.10.2 Feedback BPMs

The "FB" BPMs must be able to detect the position of individual bunches within the pulse, for feedback correction. The same "Q" BPMs system requirements in Table 7-12 apply, the only difference being the resolution:

$$x = 0.25 \text{ nm} \quad (7.31)$$

The electronics processing is realized with four channels digitizers that sample the signal peaks from the striplines. An example of such a module is the Tektronix TVS545, a \$20k VXIbus based module whose pertinent characteristics are shown in Table 7-13.

The trigger is either generated on the signal's peak, or generated by the timing system. It is very important to minimize the trigger jitter, because it produces $1\text{-}\mu\text{m}$ position error each 5 ps jitter, given the 12-mm beam pipe full aperture. A possible solution to this problem is to oversample the signals and to reconstruct the waveform, but higher sampling rate than currently possible will be required. This technique will reduce the jitter performance requirements and will not require the clock to be beam synchronous. The expected signal level peak for a gaussian beam with a bunch length much shorter than the stripline length, is given by:

$$V = \frac{gZ}{2} \frac{Ne}{\sqrt{2\pi\sigma}} \left(1 - \exp\left(-\frac{\tau^2}{2\sigma^2}\right) \right) \approx \frac{gZ}{2} \frac{Ne}{\sqrt{2\pi\sigma}} \quad (7.32)$$

Where N ($=10^{10}$) is the number of particles per bunch, g ($= 0.2$) is the electrode coverage, Z ($= 50$) is the impedance, $\tau = 2l/c$ (0.7 ns), l ($=20 \text{ mm}$) is the stripline length, $\sigma = 1/(2\pi BW)$, and BW is the filter -3

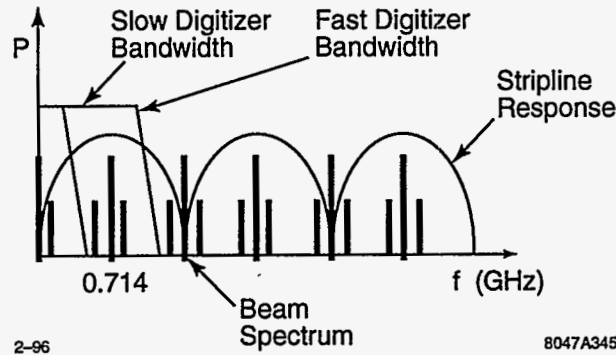


Figure 7-81. Principle of "FB" BPMs

dB point. Under these assumption the rms voltage at the stripline is:

$$V = 14V \quad (7.33)$$

and the rms noise voltage, using 1-GHz bandwidth and 15-dB noise, is:

$$V = 80 \mu\text{m} V \quad (7.34)$$

The expected resolution is:

$$x = 9 \text{ nm} \quad (7.35)$$

Another resolution limit is given by the ADC number of bits. The TVS545 module, with its 10 bits, guarantees:

$$x = 1.5 \mu\text{m} \quad (7.36)$$

In order to achieve the required resolution performance, the ADC must provide at least 13 bits or the use of hybrids must be included to reduce the system's required CMRR.

If the technology becomes available and the cost is affordable it might be possible to include the "FB" BPMs in the "Q" BPMs using a wideband AM detector, working, for example, with 11.4-GHz carrier and 350-MHz bandwidth. An interesting possibility is to reduce the system bandwidth to 350 MHz and maintain the oversampling process. The equivalence of the two processes is shown in Figure 7-81 where the beam spectrum is relative to a 714-MHz pulses repetition, with sidebands indicating amplitude modulation due to current and position fluctuation, and the length of the stripline is adequate to peak the pulse repetition rate. The fast digitizer samples synchronized with the bunch spacing, and in this way amplitude demodulates the signal, providing the equivalent power of the first three sidebands. When the slow digitizer is used, there is still signal available, but the power is only given by the first sideband.

The best condition for the slow digitizer option is when the length of the stripline is approximately 15 cm: in this case its response notch corresponds to the bunch repetition frequency.

This slow digitizer principle is different from the amplitude demodulation in the sense that there is no DC signal available because of the stripline transfer function. A way of defining this type of signal processing would be: AC coupled amplitude demodulation, where the modulation signal is the position variation versus time. It is important to notice that when the beam doesn't move there is no modulation, and therefore no signal. In a sense this type of signal processing provides the modes of the position variation: if the beam presents a bunch-by-bunch displacement, the output of the BPM will show a 357-MHz line in the frequency

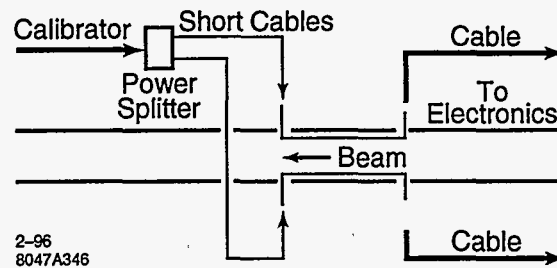


Figure 7-82. Calibration scheme.

plot, if it presents a sinusoidal displacement with period 10 bunches, the output will be a 71.4-MHz line in the frequency plot, and so on.

It is possible to deduce from the picture in Figure 7-81 that the amplitude of the signal increases with the frequency of the modulation signal, that is the position variation. It is possible, in principle, to recover the signal information using the transient at the beginning of the pulse. The idea is to calibrate the system with a single bunch, measuring the impulse response. The position is then available by deconvolving the measured signal with the impulse response.

Calibration

In order to achieve $1\text{-}\mu\text{m}$ stability from the "Q" and "FB" BPMs, which corresponds to 0.005 dB for a 6-mm-radius circular beam pipe, it is necessary to include an efficient calibration scheme.

The calibration scheme in Figure 7-82 includes a signal to be injected at the other end of the striplines. The power splitter divides the signal between the two striplines simulating the beam on center. In this way both electronics and cables will be calibrated. This calibration scheme is more expensive than the conventional one, where the signal is injected at the electronics through a combination of three power splitter/combiner, because each stripline needs two feedthroughs instead than one and each BPM needs one more long cable for the calibration signal. The possible sources of instability are the power splitter unbalance and the power splitter insertion loss. Off-the-shelf stripline power splitters have 0.2-dB typical amplitude unbalance, which corresponds to $40\ \mu\text{m}$ in our case, and 0.005-dB drift over 10°C temperature change.

The short cables insertion loss variation can be kept under control by using good cables as short as possible. A typical temperature change for 12-ft coaxial cable is 0.05 dB/ 10°C : that means that the cables must track to better than 10% in order to maintain within the required tolerance.

7.10.3 Structure Beam Position Monitors

Overview

In this section, we outline the physical scalings and technique for use of accelerating structures as monitors of beam position and beam phase. We also discuss briefly their employment as monitors of higher-order moments.

The "S" or structure BPMs are the damped detuned accelerating structures, operated parasitically as beam position monitors. In this structure, as described in Chapter 8, four nearly rectangular vacuum manifolds are situated parallel to and mated in the structure in such a way as to couple out deleterious "dipole" modes which otherwise would disturb the beam. These manifolds effectively lower the Q of the dipole modes of the structure, reducing the multibunch wakefield and aiding in the control of emittance growth. At the same time these manifolds provide a conduit for microwave signals that can provide information about the beam. Our use of this structure as a BPM is entirely parasitic to this manifold-damping.

The S-BPM allows one to monitor the transverse position of the bunch train with respect to the *electrical center* of the front, rear, or other specific portions of the structure. This is distinguished from other BPMs that measure the transverse position of the bunch train (Q-BPMs) or a single bunch (F-BPMs) with respect to a locus (the BPM structure centroid) with no *a priori* dynamical significance, except that established by accurate alignment with respect to other beam line elements (*e.g.*, quadrupole centroids). Misalignments revealed by an S-BPM could (on a time-scale to be determined) be subject to feedback to zero them out, as such offsets give rise to deflecting wakefields that tend to produce emittance growth. The feedback might take the form of a pair of movers (X and Y) at the front and rear of each structure.

Physical Principles

Structure "dipole" modes are rather similar to the TM_{11} modes of cylindrical guide, insofar as they couple linearly (for sub-mm displacements) to the beam offset from the electrical center of the structure. However, each structure consists of some $N_{\text{cell}} = 206$ coupled cavities or "cells," and thus there are some 206 different dipole modes, each of which tends to be synchronous with the beam over only a limited region of a few cells. For the DDS as presently designed, the mode frequency is correlated with position along the structure, such that the lower frequency range (14 GHz) modes tend to couple well to the beam near the entrance of the structure, while the higher frequency range modes (16 GHz) tend to couple well near the exit. Thus the filtered microwave signal emanating from the manifold ports provides information on the misalignment of the beam relative to different portions of the structure. The raw phase and amplitude of a dipole mode can only be interpreted as a signed displacement if we have knowledge of beam phase and amplitude. The phase information will come from the timing system and the amplitude will come from "Q" BPMs located in the nearest quadrupole. We expect to be able to measure the position of trains of 90 bunches of 5×10^9 particles per bunch to a resolution of better than 1 micron rms for at least several modes corresponding to both ends of each structure.

Some simple scalings can be employed to describe the rf structure as a pick-up. In one 1.8-m structure the N_{cell} modes will be distributed in frequency from 14–16 GHz (roughly a mode-spacing of 10 MHz) and a mode $Q_e \sim 1000$, corresponding to a decay time $2Q_e/\omega \sim 20$ ns. Modes will overlap since the typical FWHM $= \omega/4\pi Q_e \sim 15$ MHz. The energy deposited in one mode by a single bunch of charge Q_b is $U = k_l Q_b^2 (x/a)^2$, with x the beam offset, $a \sim 0.3$ – 0.7 cm the iris radius, and $k_l \sim 1$ – 4 V/pC/cell the loss factor for the mode in question. For a bunch train, the figure for stored energy is U multiplied by a train form factor F , which is a function of mode frequency and the number of bunches in a decay-time, $N_{bf} \sim 14$. This form factor can be computed by convolving a periodic sequence of delta-functions with a damped sinusoid. For modes with frequencies that are integer multiples of the bunch train frequency (714 MHz), $F = N_{bf}^2 \sim 200$. These frequencies are 14.280 GHz (0.714×20), 14.994 GHz ($\times 21$), 15.708 GHz ($\times 22$), 16.422 GHz ($\times 23$). For modes that are half-integer multiples of the bunch train frequency, $F = 1/4$. These frequencies are 14.637 GHz ($\times 20.5$), 15.531 GHz ($\times 21.5$), 16.065 GHz ($\times 22.5$). For other modes, $F \sim N_{bf} \sim 14$. A rough estimate of peak power flowing through one manifold arm from a given mode is just $P \sim \omega U/2Q_e$. For the time being, we adopt this as an estimate for power coupled out of the manifold port, recognizing that the actual figure will depend on attenuation and propagation characteristics in the manifold.

To appreciate these scalings, consider the extreme cases. Maximum peak power from one mode, resonantly excited by a bunch train steered into an iris would be 1×10^3 W, assuming $k_1 \sim 4$ V/pC/cell, and 5×10^9 particles per bunch (0.8 nC). Peak power in the full bandwidth (14.5–16.5 GHz) would be about 1×10^4 W. Average power deposited in this case would be less than 1 W. Minimum power would correspond to the case of a single bunch of 3×10^9 particles (0.5 nC) offset by $5 \mu\text{m}$, $P \sim 6 \mu\text{W} (-22 \text{ dB})$, assuming $k_1 \sim 1$ V/pC/cell and $a \sim 0.7$ cm. For comparison note that thermal noise in any 15-MHz interval is $N \sim -102$ dB, roughly the power level corresponding to a 0.5-nm beam offset. In addition one wants to compare this figure with that for the $m \neq 1$ terms in the impedance (both broadband and resonant terms if there is any coincidental overlap) over the bandwidth of interest, a figure not yet calculated.

Technique

Each structure has four damping manifolds. The manifolds must be terminated on each end to dissipate the higher-order mode power. Two of the terminations, one on a horizontal manifold and one on a vertical manifold, will be provided by waveguide to coaxial vacuum feedthroughs which bring the higher-order mode power out onto external cable to provide the position signals. The other six terminations are probably internal to the manifold to minimize costs. Coaxial cable can be used since a run of no more than 80 ft will extend out of the accelerator housing proper to a front-end electronics rack. Cable losses are high in this frequency range, *e.g.*, ~ 30 dB/100', but signal power is plentiful if we're only trying to achieve micron resolution. No special requirements for temperature-stability of the cable are envisioned.

Rf pre-processing modules are located at the top of the nearest tunnel penetrations. These integrated microwave modules bandpass filter, attenuate (through fixed and programmable attenuators), and selectively mix down any frequency in the dipole band to a fixed intermediate frequency (IF). Mode selection is accomplished by tuning the local oscillator provided at each crate of rf processing modules. The down-conversion mixers can be protected from burnout by a combination of fixed attenuation and PIN diode limiters even if programmable attenuators are inappropriately set. The IF signals are pre-amplified and sent to the nearest instrumentation alcove for further processing.

In the instrumentation alcove is a VME crate containing IF processors for the structure BPMs. Each IF processor measures the phase and amplitude of the X and Y IF signals from each of four structure BPMs. The input signals are quadrature demodulated, sampled at a time specified by the timing system, and digitized. Phase rotation and amplitude normalization is provided by an onboard signal processor. The processor will provide simultaneous X and Y position measurements for all four structure BPMs on the same beam pulse. Since the local oscillator is shared across BPMs, they all measure the same mode (frequency) on any one machine pulse.

Other Issues

We intend to study two additional signals as possible candidates for the list of raw signals to be processed. These are a second-moment coupled signal (TM₂₁-like, at f_2) and a third-moment signal (TM₃₁-like, f_3). Such signals derived from several structures can provide single-shot measurements of beam emittance and beam profile asymmetry, at least, in the horizontal. A rough estimate of energy deposited in such modes would be $U = k_1 Q_e^2 (x/a)^{2m}$ where $m = 2$ or 3 . Assuming $Q_e \sim 5000$, $k_1 \sim 1$ V/pC/cell and $a \sim 0.7$ cm, and a single bunch of 3×10^9 particles (0.5 nC), this corresponds to $P_2 \sim -40$ dB for a 100- μm beam feature and $P_3 \sim -77$ dB. These numbers indicate that pursuit of still-higher moments is probably not practical. The third moment is looking a bit problematic for a single bunch.

The contribution of the $m \neq 1$ terms in the impedance to the 14.5-16.5-GHz-band signal offset will be studied at ASSET.

Conclusion

The electronics alluded to here and the structure itself are still being designed and will be tested with beam during the next ASSET experiment and at the NLCTA. It is expected that modifications and improvements will derive from practical operating experience.

Primary issues will be cost, reliability, dynamic range, and circuit protection. For a simple nonsigned S-BPM, the primary cost is the GADC unit. For a signed S-BPM, the primary cost is likely to be in the microwave electronics (LOs, mixers, etc.). An assessment of reliability awaits experimental studies at ASSET. The need to protect the processing electronics in the worst case (bunch train steered into an iris) will probably limit the useful dynamic range.

To summarize, S-BPM resolution is favored by minimum insertion loss for microwave signals emerging from the manifold. The S-BPM will be capable of resolving 5- μm beam offsets shot-to-shot relative to specific portions of the structure, *e.g.*, near the entrance and the exit. The limits of S-BPM resolution and functionality, as well as tests of the electronics await experimental studies at ASSET.

7.10.4 Laser Wire Scanners

Laser-based beam profile monitors, to be used with damped beam, will be described in this section. The laser-based profile monitors will be similar to the one under construction for the SLC/SLD IP. This device uses a diffraction limited, 350-nm wavelength, laser. The laser beam will be scanned across the particle beam on a consecutive sequence of pulses. The system will have four components, a single synchronized laser, a transport line to deliver photons to several interaction chambers, the interaction chambers themselves and scattered radiation detectors that detect boosted photons and/or degraded e^+ or e^- from the interaction of the laser light with the particle beam. The amplitude of the light can be varied in order to accommodate a very wide dynamic range of beam size and intensity.

Laser

A laser will be used to provide a 10-mW peak power pulse to six interaction chambers. In these chambers the particle beam will be brought into collision with the focused laser beam. The light pulse will be 0.1-ns-long, short enough to interact with only one of the 90 bunches. The synchronization of the light pulse with the particle beam will be done using a mode locked seed laser. The seed laser output can be amplified using a regenerative YAG 20-pass amplifier. Expected synchronization accuracy is at worst 10 ps. The laser phase space is defined by a high-power pinhole spatial filter. The laser will be located in an accessible area.

The laser can be operated in the lowest transverse spatial harmonic mode or in a higher mode. In the first mode, a null is generated where the center of the gaussian beam would ordinarily be. Two side lobes are arranged around the null and this structure can be scanned across the beam as an alternative to scanning the gaussian zero mode spot. The spacing between the lobes provides an estimate of the performance of the laser focusing and transport optics.

Transport

The transport is used to bring the laser light to up to one of six interaction chambers. It can be of roughly any length provided the surface figure of its optics is good enough. Typical surfaces must be $1/40$ or better. Starting from the spatial filter and progressing through the transport and the interaction chambers, the accumulated optical errors must be kept below a modest surface figure budget of about a half wave. The transport must be evacuated and free from significant contaminants. Steering elements are required for trajectory stabilization and optimization. Diagnostic imagers are needed to maintain transport alignment and monitor optical quality.

Interaction Chambers

The function of the interaction chambers is to focus the light to a spot small compared to the expected beam size. This can be done using an F2 focusing system with a 95% transmission aperture. In this system demagnification is traded off against diffraction-related tails and distortion. Absorbing materials are needed to keep the optics free from the contamination caused when metal material is removed by stray laser light.

The locations of the interaction chambers will be dictated by the local optics. For the measurement of an uncoupled beam matrix a minimum of three scanners, separated by 45 degrees of optical phase advance, are required. For the determination of a fully-coupled beam matrix, six scanners are needed. The placement of the scanners in the diagnostic stations is described in Section 7.3.4.

The laser beam will be scanned across the particle beam using piezo-electrically-driven mirror actuators. The laser beam can either be scanned slowly, so that it advances a fraction of a bunch size on each successive machine pulse, or scanned rapidly, so that it crosses the entire bunch train during a single passage. In the latter case, an estimate of the projected full train emittance can be derived from the response of a single high-bandwidth detector or group of detectors. The focused laser spot must move <4 sigma during the 100-ns passage time. Fine synchronization is required to time the collision between the light and the particles.

Detectors

Scattered radiation detectors are needed to detect the degraded particles and the boosted photons. In the latter case, the beam line geometry requires a bend to remove the electron beam from the path of the photons. A very large signal of about 1000 photons is expected for the single-bunch parameters and laser power listed above. In some cases the Compton scattered signal may be used as an indication of the degree of polarization of the beam.

7.11 Discussion

In this chapter, we have presented the design of the NLC main linacs and have described how the linacs will be operated so as to prevent large dilutions of the beam emittances. We have presented the emittance dilution budgets for the different operating modes of the linacs: NLC-Ia—NLC-IIc. The budgets are generous and have been chosen to allow for reasonable fabrication and construction tolerances.

As discussed, the approach to preserving the small beam emittances is two-fold. First, many problems have been explicitly 'designed-out'. In particular, the damping and detuning of the accelerator structures

will make the wakefield effects associated with multibunch operation manageable. Similarly, the thermal regulation in the tunnel and gallery will prevent significant fluctuations in alignment and instrumentation response. Second, we will utilize beam measurements to suppress unavoidable imperfections that are not readily solvable by design. These include the alignment of the quadrupole magnets and accelerator structures and the stabilization of the beam orbits and energies.

To perform the alignment, each quadrupole and pair of accelerator structures will have remotely adjustable supports. With this control, the only tight alignment tolerance that will have to be achieved prior to operation is that for the straightness of the accelerator structure pairs. The beam-based alignment algorithms that will be used are fairly straightforward. The quadrupole alignment method is a variation of one that has been successfully applied in the SLC and FFTB, although it places higher demands on the BPM stability and the performance of the control system. The structure alignment technique is more novel in that it uses the signals from the structure damping manifolds to infer the beam offset in the structure. With this information, each pair will be aligned to the beam after a suitable orbit has been established.

It is important to note that these beam-based alignment techniques do not need to interrupt standard operation and we have shown that the emittance growth due to slow alignment drifts (ATL-model) can be controlled by re-aligning every 30 minutes. To further stabilize the beams, there are trajectory and energy feedback loops, like those used in the SLC, implemented throughout the linacs. These feedbacks will heavily suppress the effect of low-frequency (<0.1 Hz) sources of beam jitter and drifts. At higher frequencies where the feedbacks are not effective, we do not foresee any significant sources of jitter. The primary source of high frequency jitter is due to ground motion which, as discussed in Appendix C, we have measured and found to be well below tolerance.

The estimates of the emittance growth in both NLC-I and NLC-II are based in part on detailed simulations of beam transport in the linacs that include the significant deleterious effects and have been calibrated against SLC experience. Smaller effects have been estimated analytically with guidance from SLC observations. Furthermore, we have a number of fallback methods available to control the emittance growth, such as orbit bumps, which we are confident will provide additional suppression.

In the future, we plan to continue to optimize the linac design. Additional simulations and experience from operating the NLCTA and the SLC will guide the work. In particular, the NLCTA will give us a measure of the energy gain stability and beam-loading compensation in an NLC-like multibunch environment. In addition, there are number of dedicated studies planned for the next year that will develop or verify other key design concepts. These include tests of the structure alignment technique, development of stable stripline BPMs, and monitoring of the long-term straightness of the accelerator structures. From this work, we will be able to transform the linac design to a full CDR in the near future.

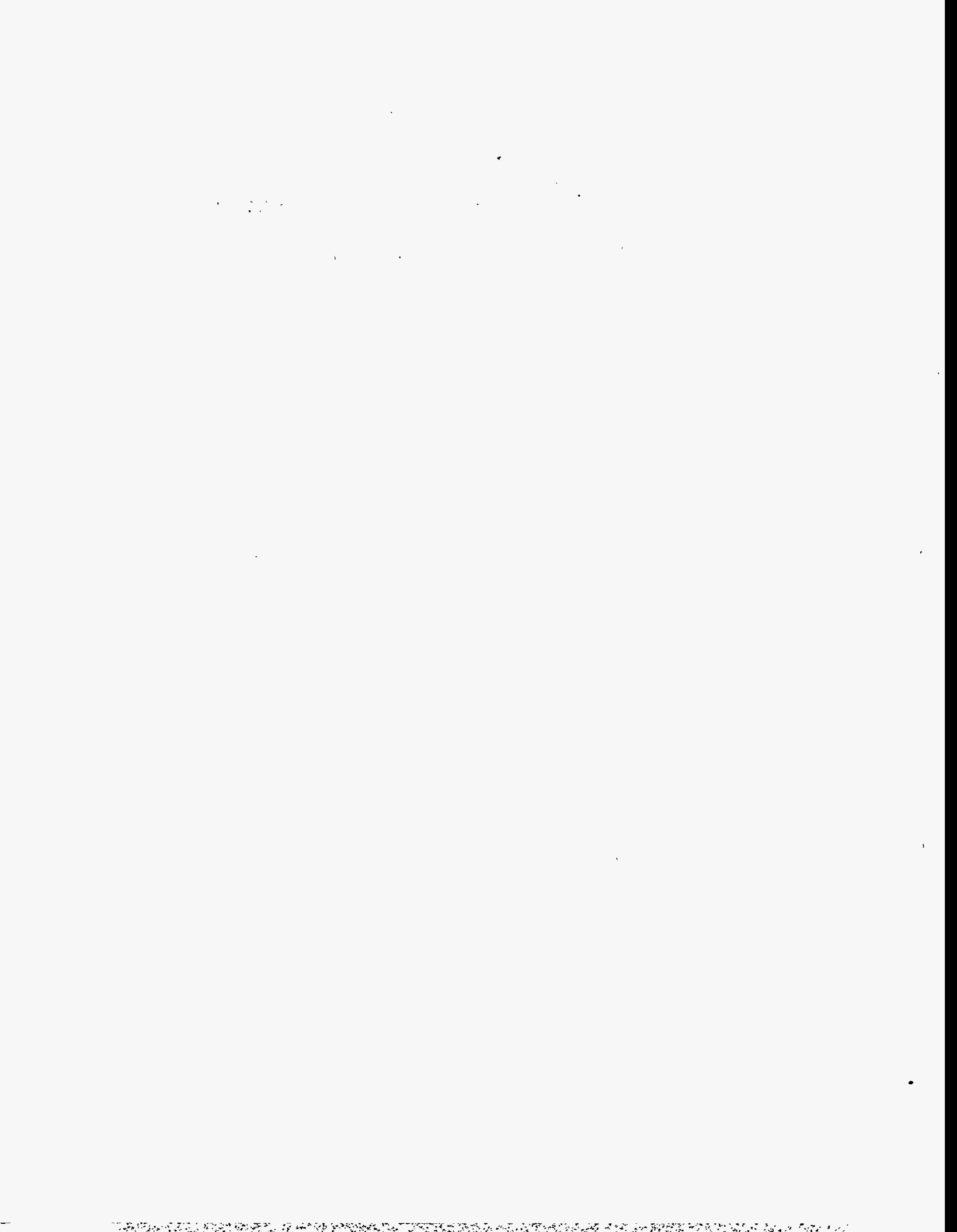
References

- [Adolphsen 1993] C. Adolphsen and T.O. Raubenheimer, "Method to Evaluate Steering and Alignment Algorithms for Controlling Emittance Growth", Presented at the 1993 IEEE Part. Acc. Conf., Washington D.C. (1993).
- [Assmann 1995] R. Assmann, C. Adolphsen, K. Bane, T.O. Raubenheimer, R. Siemann, K. Thompson, "LIAR: A Computer Program for Linear Collider Simulations", SLAC-AP-NOTE-103 (1996); to be published as a SLAC-REPORT.
- [Balakin 1983] V. Balakin, A. Novokhatsky, V. Smirnov, "VLEPP: Transverse Beam Dynamics", Proceedings of the 12th Int. Conf. on High Energy Accelerators, Fermilab, 119 (1983).
- [Bane 1980a] K. Bane and P. Wilson, "Longitudinal and Transverse Wake Potentials in SLAC", Proceedings of the 11th Int. Conf. on High Energy Accelerators, CERN, Birkhäuser Verlag, Basel, 592 (1980).
- [Bane 1980b] K. Bane and B. Zotter, "Transverse Modes in Periodic Cylindrical Cavities", Proceedings of the 11th Int. Conf. on High Energy Accelerators, CERN, Birkhäuser Verlag, Basel, 581 (1980).
- [Bane 1993] K.L.F. Bane and R.L. Gluckstern, "The Transverse Wakefield of a Detuned X-Band Accelerating Structure", *Particle Accelerators* **42**, 123 (1993).
- [Bane 1994] K.L.F. Bane, C. Adolphsen, K. Kubo, and K.A. Thompson, "Issues in Multibunch Emittance Preservation in the NLC", Fourth European Particle Accelerator Conference, London, England, (June 27-July 1, 1994).
- [Bane 1995] K. Bane, "The Short-range NLC Wakefields", NLC-Note 9, (February 1995).
- [Bowden, 1996] G. Bowden, P. Holik, S.R. Wagner, G. Heimlinger, R. Settles, "Precision magnet movers for the Final Focus Test Beam", *Nucl. Instr. and Methods* **368A**, 579-592, (1996).
- [Brandt 1982] D. Brandt and B. Zotter, "Calculation of the Wakefield with the Optical Resonator Model", CERN-ISR/TH/82-13 and LEP Note 388 (1982).
- [Brandt 1984] D. Brandt, "Optical Resonator Model for the Wakefields of the Deflecting mode $m = 1$ ", CERN-LEP Note 484 (1984).
- [Gluckstern 1989] R. Gluckstern, "Longitudinal Impedance of a Periodic Structure at High Frequency", *Phys. Rev. D* **39**, 2780 (1989).
- [Heifets 1989] S.A. Heifets and S. Kheifets, "High-frequency Limit of the Longitudinal Impedance of an Array of Cavities", *Phys. Rev. D* **39**, 960 (1989).
- [Keil 1972] E. Keil, "Diffraction Radiation of Charged Rings Moving in a Corrugated Cylindrical Pipe", *Nucl. Instr. and Methods* **100**, 419 (1972).
- [Kroll 1994] N. Kroll *et al.*, "Manifold damping of the NLC detuned accelerating structure", 6th Workshop on Advanced Accelerator Concepts, Lake Geneva, WI, June 12-18, (1994).
- [Palmer 1990] R. Palmer, "A Qualitative Study of Wakefields for Very Short Bunches", *Particle Accelerators* **25**, 97 (1990).

- [Panofsky 1956] W. Panofsky and W. Wenzel, "Some Considerations Concerning the Transverse Deflection of Charged Particles in Radio-frequency Fields", *Rev. Sci. Instr.* **27**, 967 (1956).
- [Raubenheimer 1992] T.O. Raubenheimer and P. Chen, "Ions in the Linacs of Future Linear Colliders", presented at LINAC 92, Ottawa, (1992).
- [Raubenheimer 1995] T.O. Raubenheimer and F. Zimmermann, "A Fast Beam-Ion Instability in Linear Accelerators and Storage Rings", *Phys. Rev. E* **52**, 5487 (1995).
- [Schnell 1987] W. Schnell, "Microwave Quadrupoles for Linear Colliders", CERN-LEP-RF/87-24, (1987).
- [Schnell 1991] W. Schnell and I. Wilson, "Microwave Quadrupole Structures for the CERN Linear Collider", Proc. of the 1991 IEEE Particle Acc. Conf., San Francisco, 3237, (1991).
- [Thompson 1990] K.A. Thompson and R.D. Ruth, "Controlling transverse multibunch instabilities in linacs of high energy linear colliders", *Phys. Rev. D* **41**, 964 (1990).
- [Thompson 1993] K.A. Thompson and R.D. Ruth, "Simulation and Compensation of Multibunch Energy Variation in NLC", in Proceedings of 1993 Particle Accelerator Conference, Washington, D.C. (17-20 May 1993).
- [Thompson 1994] K.A. Thompson *et al.*, "Design and Simulation of Accelerating Structures for Future Linear Colliders", *Particle Accelerators* **47**, 65 (1994).
- [Weiland 1983] T. Weiland, "On the Computation of Resonant Modes in Cylindrically Symmetric Cavities", *Nucl. Instr. and Methods* **216**, 329 (1983).

Contributors

- Chris Adolphsen
- Roberto Aiello
- Ralph Assmann
- Karl Bane
- Gordon Bowden
- Franz Josef Decker
- Linda Hendrickson
- Tom Mattison
- Kiyoshi Kubo
- Yuri Nosochkov
- Tor Raubenheimer
- Kathy Thompson
- Dave Whittum
- Frank Zimmermann



RF System for the Main Linacs

Contents

8.1	Introduction	457
8.1.1	Overview	457
8.1.2	Upgrade to 1 TeV	459
8.1.3	The NLC Test Accelerator (NLCTA)	463
8.1.4	Outlook	466
8.2	Accelerator Structure	466
8.2.1	Calculation of Structure Dimensions	467
8.2.2	Tolerances on Dimensions and Alignment	469
8.2.3	Calculation of Steady-State Gradients	470
8.2.4	Mechanical Design of the Accelerator Structure	473
8.2.5	Thermal Calculations	483
8.2.6	High-power Tests and Dark Current Studies	484
8.2.7	Material Handling and Processing Techniques	485
8.2.8	Multibunch Energy Spread and Compensation	486
8.2.9	NLC Test Accelerator Experiments	488
8.2.10	ASSET Measurements	492
8.2.11	Use of Beam-Excited Modes to Monitor Alignment of Structures	493
8.3	RF Pulse Compression and Power Transmission	493
8.3.1	Performance	494
8.3.2	Physical Layout	497
8.3.3	Power Losses	500
8.4	High-Power Klystrons	502
8.4.1	Design Features	502
8.4.2	Results To Date	508
8.4.3	Ongoing R&D	511
8.4.4	Manufacturing	516
8.5	Klystron Pulse Modulator	517
8.5.1	Modulator Requirements	518
8.5.2	Pulse Modulator Design Outline	520
8.5.3	Charging Power Supply Design Outline	523
8.5.4	Station Cooling System and Oil Circulation	526
8.5.5	Simulations and Efficiency Projections	526
8.5.6	Prototype Modulator Development and Performance	528
8.6	RF Drive and Phasing Systems	530
8.6.1	Functional Overview	530
8.6.2	System Functional Requirements and Specifications	533

8.6.3	Systems Overview	537
8.6.4	Spectrometers	545
8.7	RF Protection and Monitoring Systems	546
8.7.1	Waveguide Protection and Monitoring	546
8.7.2	Klystron Protection and Monitoring	547
8.7.3	Modulator and Support Electronics Protection and Monitoring	548
8.7.4	Klystron and Modulator Logic Controller	548
8.7.5	Modulator Interactions with the Machine Protection System	548

8.1 Introduction

The basic design of the NLC main linacs rests on global experience gained from the design, construction, and 30 years of operation of the 3-km-long SLAC linac, which is powered at a frequency of 2.856 GHz [Seeman 1991, Seeman 1993]. Since its initial operation in 1966, the SLAC linac has been continuously upgraded for higher energy, higher intensity, and lower emittance.

The radio frequency (rf) system for the NLC main linacs is similar in character to the SLAC linac. The SLAC linac is currently energized by 240 high-power S-band klystrons. The klystron peak power and pulse duration are, respectively, 65 MW and 3.5 μ s. The power from each klystron is compressed by a SLED pulse compressor, and then split to feed four, 3-m-long, constant-gradient S-band accelerator structures operating in the $2\pi/3$ mode.

When the SLAC linac was built, the accelerating gradient was 7 MV/m. The original design included a future upgrade path in which the number of klystrons would be quadrupled. The upgrades that were eventually implemented involved replacing each of the initial 24-MW klystrons with a single higher-power klystron (first with 35-MW, XK-5 tubes and, later on, with 65-MW, 5045 tubes), and adding a SLED pulse compressor downstream of each klystron. For present-day SLC operations, fully upgraded with 240 SLEDed, 65-MW klystrons, the accelerating gradient has been tripled, to 21 MV/m, and the maximum beam energy is 60 GeV (for unloaded, on-crest operation).

8.1.1 Overview

The rf power system for the NLC's two high-gradient linacs that accelerate the electron and positron beams separately from 10 GeV to 250 GeV (in the initial design), and to 500 GeV or more (after the upgrade), operates at 11.424 GHz. This system includes all the hardware through which energy flows, from the AC line to the accelerator structures. Figure 8-1 shows one module of the rf system schematically, with emphasis on the flow of energy. Electrical energy is transformed at each stage shown in the diagram: the modulator converts AC power into high-voltage pulsed DC, the klystron transforms pulsed DC into high peak power rf, the SLED-II pulse-compression system increases the peak power by about a factor of four (at the expense of a reduced pulse width), and the accelerator sections convert rf power into beam power. Because of the high average rf power required to drive the accelerator structures, it is important that the highest possible efficiency be maintained for the processing and transmission of energy at every stage of the rf system.

The primary technical choice for the rf system is the use of the 11.424-GHz frequency. This frequency, high in the X-band (8.2–12.4 GHz), is exactly four times the operating frequency of the existing SLAC 60-GeV linac. The choice of such a high frequency, relative to existing high-energy linacs, allows higher accelerating gradient, shorter linac length, and lower AC power consumption for a given beam energy. Considering the size, weight, cost, and availability of standard microwave components, we have chosen a frequency in the X-band for a design that is upgradeable from an initial 250-GeV beam energy to 500 GeV or more. This choice requires the development of klystrons capable of delivering peak power significantly greater than previously achieved by commercially available X-band sources. As described in Section 8.4, klystrons which meet the 50-MW peak-power goal necessary for the initial 250-GeV beam energy in the NLC design have been developed, and are now operating in the Klystron Test Laboratory at SLAC.

The general parameters of the high-power rf system and its major subsystems (klystrons, modulators, rf pulse compressors, and the accelerator structure itself) are specified in Table 8-1. The set of parameters has

been optimized to provide high acceleration gradient (35–64 MV/m) for trains of bunches with moderate charge per bunch (1.2–1.8 nC). This optimization keeps single-bunch wakefields under control and reduces the beamstrahlung at the collision point to tolerable levels. The upgrade to 500-GeV beam energy (1-TeV center-of-mass energy) is accomplished by doubling the number of modulators (as shown by dashed lines in Figure 8-1), and by replacing each 50-MW klystron with a pair of 75-MW klystrons. The total active length of linac must also be increased from 16,300 m to 17,700 m. The upgrade also includes improvements in the modulator and pulse compression systems to increase the rf system efficiency. The upgrade to 1-TeV center-of-mass energy is described in more detail in Section 8.1.2.

The rf accelerator structure (discussed in Section 8.2) is designed to be very nearly a constant-gradient traveling-wave structure. The design of the structure has been optimized to reduce the wakefield seen by trailing bunches. This has been accomplished by tailoring the cell-to-cell frequency distribution of the dominant deflecting mode to yield an initial Gaussian-like decay of the wakefield amplitude. On a longer timescale, the higher-order beam-induced modes of the structure will be damped by vacuum manifolds to which each cell of the structure is coupled. This structure is designated by the acronym DDS (damped detuned structure). The damping manifolds run parallel to the beam channel and are terminated into matched loads. (The slots that couple the cells to the manifolds are cut off to the fundamental accelerating mode.) This damping scheme will reduce the typical quality (Q) factors of the deflecting modes to about 1000. The first prototype 1.8-m-long accelerator section, which was detuned but not damped, was high-power tested up to a gradient of 67 MV/m. The effect of the detuning in that first prototype section was demonstrated experimentally by using positron and electron bunches from the SLC damping rings as probe and witness beams, respectively. Another prototype 1.8-m section that is both damped and detuned is being manufactured and will be used for a similar test before it is installed in the NLCTA.

Obtaining the X-band peak power for the NLC has required the development of klystrons (Section 8.4) capable of delivering peak power significantly greater than previously achieved by commercially available X-band sources. Both the peak power and the pulse length have already been achieved by four solenoid-focused X-band klystrons at SLAC. These klystrons will be used to power the NLC Test Accelerator (Section 8.1.3). The most recent refinement of the klystron has achieved the peak power and exceeded the pulse length required for the NLC design and upgrade, at an efficiency of 48%. The solenoid which focuses the electron beam in the prototype klystrons has a weight of 750 kg and a power consumption of 20 kW. Currently nearing completion is the first prototype of a 50-MW klystron which is focused instead by a periodic permanent magnet (PPM) array of samarium cobalt ring magnets weighing about 9 kg. It is this klystron, which operates at a higher voltage and lower beam current for compatibility with PPM focusing, which is slated as the prototype for the NLC. Based on computer projections, the tube, designated X5011, is expected to operate at about 57% efficiency with 50 MW of peak output power.

Each high-power rf station consists of a pair of PPM-focused klystrons (50 or 75 MW) and a pulsed-DC energy delivery system (modulator) that is tightly integrated in design with the electron guns of the klystrons. The modulator system (discussed in Sections 8.5 and 8.7) includes a single-thyratron switch, a Blumlein pulse-forming network (PFN), a high-efficiency power supply for charging the PFN's capacitance, and a pulse transformer. Using a Blumlein PFN allows for a relatively low transformer turns ratio (7:1), which yields a reasonably fast rise time (0.3 μ s), and hence, an improved efficiency.

The rf pulse-compression system (discussed in Section 8.3) is based on the SLED-II technique which is a modification of the SLED system currently in use on the existing 60-GeV SLAC linac. For SLED-II, the energy storage cavities of SLED are replaced by resonant delay lines in order to produce flat output pulses. A prototype SLED-II system has been tested up to compressed-pulse power levels of 200 MW. Transmission of high power with low loss is accomplished by using oversized waveguide components. Three SLED-II systems are being manufactured for the NLC Test Accelerator.

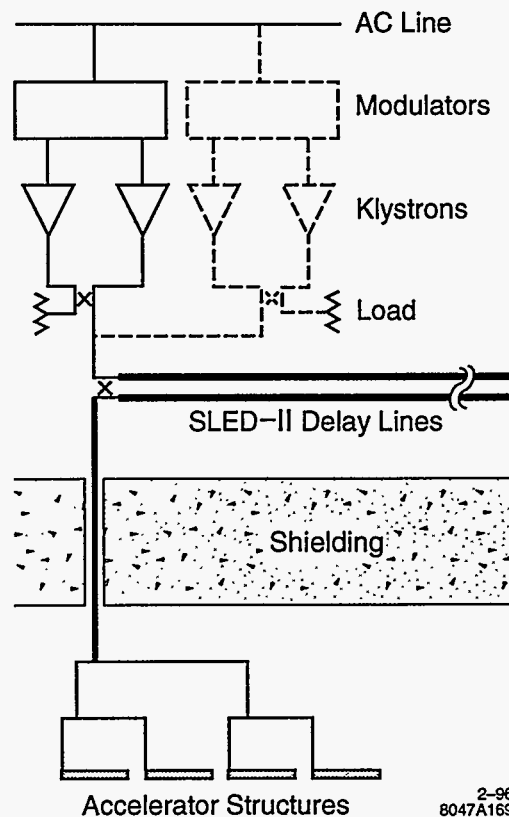


Figure 8-1. One module of the high-power rf system for the main linacs. Dashes indicate additions for the beam-energy upgrade from 250 GeV to 500 GeV. Energy flows from the AC line to the accelerator structures.

To achieve a highly mono-energetic multibunch beam pulse for the final focus, the beam loading induced by the bunch train must be compensated. The initial transient can be eliminated by pre-loading the sections by shaping the input rf pulse using an approximately linear rise of the field amplitude for one filling time of the structure. In this way, the first electron bunch will see a filled rf structure that appears to be in the steady state. As will be seen, this requires phase-agile control of the rf before it is amplified by the klystron.

The design of the rf control system proposed for the NLC main linacs is based on experience derived from operating the SLAC linac. In particular, the methods of beam-loading compensation have been inspired, in part, by experience gained with beam-loading compensation while operating the SLAC linac in its long-pulse, high-average-current mode (for fixed-target experiments).

8.1.2 Upgrade to 1 TeV

As mentioned previously, the upgrade to 1-TeV center-of-mass energy is accomplished primarily by doubling the number of klystrons and modulators, and by increasing the peak power per klystron from 50 MW to 75 MW. Taking into account a small reduction in the power gain of the rf pulse compression system (which has been upgraded for higher efficiency at a lower compression ratio), this increase in rf power provides for an increase in the unloaded accelerating gradient from 50 MV/m to 85 MV/m. To obtain a center-of-mass

	NLCTA Achieved	500-GeV Design Goal	1-TeV Upgrade
<u>General Parameters</u>			
Frequency (GHz)	11.4	11.4	11.4
Accel. Gradient (MV/m), Unloaded/Loaded	67/--	50/35.3	85/63.5
Overhead Factor, ^a F_{OH}		1.20	1.15
Active Linac Length ^b (m)	1.8	16,300	17,700
Total Linac Length (m) (1.08 × Active Length)		17,600	19,100
# 7.2-m RF Units and Pulse-Compression Systems		2264	2454
# Modulators		2264	4908
# Klystrons		4528	9816
Peak Power per Meter of Structure (MW/m)		50	145
RF Pulse Length at Structure (ns)	150	240	240
Repetition Rate (Hz)	60	180	120
Particles per Bunch (10^{10})		0.75	1.10
Number of Bunches per Pulse		90	90
Peak Beam Current (A)		0.86	1.26
RF Energy/Pulse at Structure Input (J/m)		12.0	34.7
Total Average RF Power at Structure ^c (MW)		34.1	71.3
<u>Klystron</u>			
Output Power (MW)	50, 75	50	75
Pulse Length (μ s)	2.0, 1.1	1.2	0.96
Microperveance (μ A/V ^{3/2})	1.2	0.6	0.75
Electronic Efficiency ^d (%)	48	57	60
Beam Voltage (kV)	440	465	487
Beam Energy per Pulse ^e (J)	310, 130	105	119
Focusing	Electromagnet	PPM	PPM
Cathode Loading (A/cm ²)	7.4	7.4	7.6
Overall Length (m)	1.3	1.3	1.3
Cathode Heater Power ^f (kW)		0.33	0.41
<u>Modulator (Blumlein PFN, transformer ratio 7:1)</u>			
PFN Voltage (kV)	48	68	71
Pulse Rise Time (ns)	500	275	175
Rise/Fall Energy Efficiency (%)		80	83
I^2R /Thyratron/Core Loss Efficiency (%)		97	97
Net Energy Transfer Efficiency (%)		77.4	80.6
$\frac{1}{2}CV^2$, two klystrons (J)		272	295
Power Supply Efficiency (%)		93	93
Net Modulator Efficiency (%)	58	72	75
Thyratron Heater + Reservoir Power ^f (kW)		1.5	1.5
Average AC Input Power (kW), Excl. Aux.	45	53	38

Table 8-1. NLC main linac rf system parameters. (Continued on next page.)

	NLCTA Achieved	500-GeV Design Goal	1-TeV Upgrade
<u>RF Pulse Compression</u>			
System Type	SLED-II	SLED-II	BPC/DLDS
Compression Ratio	5-7	5	4
Intrinsic Efficiency (%)	80.4-69.2	80.4	100
Loss Efficiency of Delay Lines, 3-db Coupler and Mode Converters (%)	92-90	95	93
Pulse Compression Efficiency (%)	73-64	76.5	93
Pulse Compression Power Gain	3.7-4.5	3.8	3.7
Power Transmission Efficiency (%)	90	94	94
Net Pulse-Compression Efficiency (%), Including Power Transmission Loss	66-58	72	87.5
Net Power Gain	3.3-4.1	3.6	3.5
<u>Net RF System Parameters</u>			
Total AC Power (MW), Excl. Aux.		116	181
RF System Efficiency (%), Excl. Aux.	19	29.6	39.4
Total Auxiliary Power ^g (MW)		5.4	12
Total AC Power, Including Auxiliary (MW)		121	193
RF System Efficiency (%), Including Auxiliary		28.2	37.0
Average Beam Power ^h (MW)		9.3	18.6
AC-to-Beam Efficiency (%)		7.7	9.4

^a Includes overhead for BNS, feedback, and stations off for repair (see Table 7-1).

^b Active length = $F_{OH} (E_0 - 20 \text{ GeV}) / (\text{Loaded Gradient})$.

^c Assumes 3% of klystrons and modulators are off (repair margin) or running off beam time (on standby).

^d Given by simulated efficiency less 5 percentage points for 500-GeV design; equal to simulated efficiency for 1-TeV design.

^e Useful energy in flat-top portion of pulse.

^f Included in auxiliary power.

^g Also includes power for modulators on standby (0.5%).

^h Excludes injected beam power.

Table 8-1. (continued): NLC main linac rf system parameters.

energy of 1 TeV, the active linac length must also be increased slightly, from 16,300 m to 17,700 m. (If this additional length is not provided, the upgraded energy will be about 925 GeV).

A major part of the upgrade to 1 TeV will be to increase the efficiency of the rf system so that the AC wall-plug power is kept below 200 MW. After the 500-GeV design has been finalized, and before the 1-TeV upgrade is carried out, several years of additional R&D will be possible in order to realize these potential gains in efficiency. The parameters listed in Table 8-1 for the 1-TeV upgrade are therefore somewhat less conservative than for the 500-GeV design.

In order to realize a substantial gain in the net rf system efficiency, each of the subsystems—klystrons, modulators, and pulse compression—must be examined for potential efficiency improvements. A slight gain is assumed in klystron efficiency (from 57% to 60%) by pushing closer to efficiency values given by simulations which are, in turn, expected to increase as experience is gained in klystron design. A modest improvement is assumed in modulator efficiency (from 72% to 75%), due mainly to a reduction in pulse transformer rise time. Several design approaches are being studied to reduce rise time. The greatest gain in rf system efficiency

will result from an upgrade in the rf pulse compression system. The SLED-II system used in the 500-GeV design has a maximum intrinsic efficiency of 80.4%, even for lossless components, due mainly to reflected power during the period when the resonant delay lines are being charged with energy.

The SLED-II efficiency may be improved by using an active microwave switch to rapidly change the coupling (or Q) of the resonant delay lines [Tantawi 1995b]. Such a switch might be implemented as an optically-triggered silicon device operating in a low-field region of the microwave network. Experimental studies of optically-triggered silicon devices for this purpose are underway at SLAC [Tantawi 1995c]. For a compression ratio of 4, the efficiency of the Q -switched SLED-II would be about 91%. Including the 94% power transmission efficiency, the net efficiency would be about 85% (a power gain of 3.4). Assuming the improvement in SLED-II efficiency can be realized, it remains to be determined that the power handling capability of the SLED-II configuration is adequate for the combined power of four 75-MW klystrons. (SLED-II has demonstrated its ability to handle a single 50-MW klystron. Tests with two 50-MW klystrons are expected to be performed in Summer 1996. Tests with four 75-MW klystrons will be performed when the 75-MW klystrons become available.)

An alternate upgrade path is to replace the SLED-II with a different type of rf pulse compression. By replacing this system with a Binary Pulse Compression (BPC) system [Farkas 1986, Lavine 1991], which has an intrinsic efficiency of 100%, the net pulse compression efficiency (including power transmission losses) can be increased from 75% to 87.5%. At the same time, the compression ratio is reduced from 5 to 4, and the klystron pulse length is reduced from 1.2 μ s to 0.96 μ s. The higher compression efficiency together with the lower compression ratio results in a slight reduction in power gain from 3.6 to 3.5. The power-handling capability required of the BPC configuration is only half that of SLED-II because the BPC system has two outputs, each of which feeds only two structures, in contrast to SLED-II where a single output feeds four structures. The chief disadvantage of the BPC scheme is the longer length of delay-line pipe which is required (three times that for SLED-II). When upgrading from SLED-II, the components of the existing SLED-II delay lines can be reconfigured as the shorter of the two required BPC delay lines. However, an additional delay, twice as long, must be added to each system.

Variations of BPC can be utilized. Half of the BPC delay can be eliminated by the use of the Delay Line Distribution System (DLDS), as proposed at KEK. In the DLDS, rf energy is propagated upstream (toward the gun) by a distance equal to one half the required delay; the beam propagation time provides the other half of the delay. Loaded delay lines can also be used in principle to reduce the length of the added delay line.

Both of the above upgrade paths (adding Q switches to SLED-II, or replacing SLED-II with BPC or a variation of BPC) can be performed gradually, taking only one station offline at a time.

Since the BPC concept has been experimentally demonstrated [Lavine 1991], and the Q -switched SLED-II capable of handling four 75-MW klystrons has not, the upgrade path in Table 8-1 is based on the more conservative option of replacing the SLED-II systems with BPC systems. Additional R&D during the years after the 500-GeV design has been finalized, and before the 1-TeV upgrade, may make the Q -switched SLED-II (or other developments) possible, and more attractive.

Taken together, the above improvements lead to an increase in net rf system efficiency from about 30% for the 500-GeV design to almost 40% for the 1-TeV upgrade. Some of these potential design improvements may, in fact, be ready in time to be included in the final design of a 500-GeV machine. The 500-GeV parameters listed in Table 8-1 are, however, conservatively based on experience with, and measurements on, prototypes which exist at the present time.

8.1.3 The NLC Test Accelerator (NLCTA)

The design of the high-power X-band rf system for the NLC is based on specific experience gained from building X-band prototypes and operating them at high power, and on an rf systems-integration test—the Next Linear Collider Test Accelerator (NLCTA)—which is currently under construction at SLAC. The goals of the NLCTA project [SLAC 1993, Ruth 1993] are to integrate the technologies of X-band accelerator structures and high-power rf systems, to demonstrate multibunch beam-loading energy compensation and suppression of higher-order beam-deflecting modes, to measure any transverse components of the accelerating field, and to measure the growth of the dark current generated by rf field emission in the accelerator. The NLCTA design parameters and a possible upgrade path are summarized in Table 8-2.

The peak power and rf-system efficiency needed for the NLCTA have been demonstrated in a prototype system (discussed in Section 8.3.1). Upgrades to the NLCTA rf system will test the SLED-II design at the higher power levels and efficiencies needed for the NLC (Table 8-7). The NLCTA high-power rf system is depicted schematically in Figure 8-2. The system is comprised of four modules. Each module consists of a DC pulse modulator, up to two X-band klystrons (50 or 75 MW), a SLED-II pulse compressor, and two X-band accelerator sections. One module serves the injector. Three modules serve the linac. Power from the third and fourth modules will be combined in the pulse compressor of the third module, and then re-divided to energize the last four accelerator sections in order to test the topology that is proposed for the NLC.

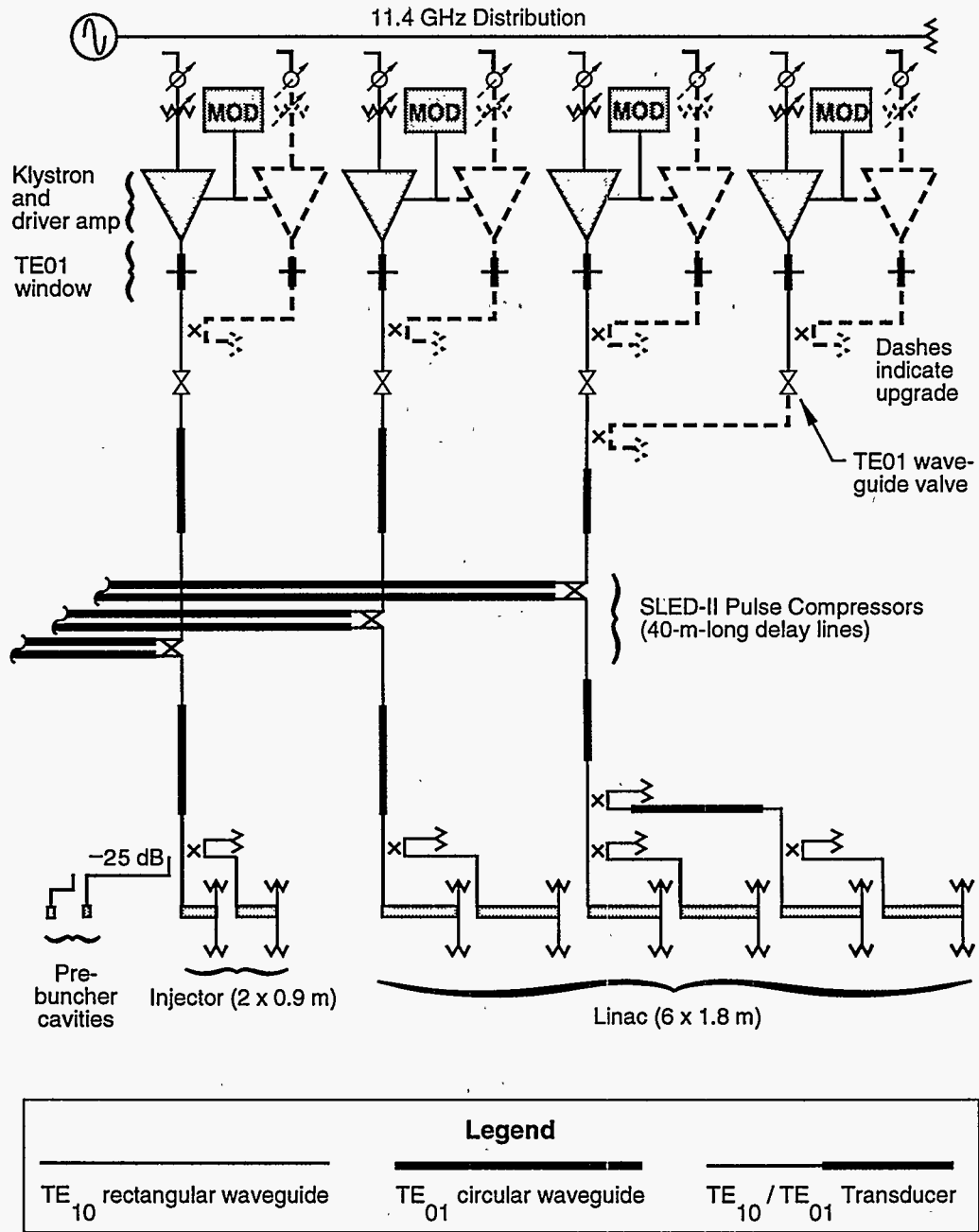
The six accelerator sections in the NLCTA linac are each 1.8-m long. The two accelerator sections in the injector are similar to the linac sections, except that each is 0.9-m long to maintain beam loading comparable to the linac in the presence of approximately twice the current. All the X-band sections in the NLCTA will suppress transverse wakefields, either by cell-to-cell detuning [Thompson 1993], or by a combination of detuning and damping [Kroll 1994], as discussed in Section 7.4.2. The effect of detuning has been demonstrated experimentally with the prototype 1.8-m detuned X-band section by using positron and electron bunches from the SLC damping rings as probe and witness beams, respectively [Adolphsen 1994], as discussed in Section 8.2.10.

The high-power rf source for the NLCTA is the 50-MW, X-band klystron [Wright 1994] discussed in Section 8.4.2. Thus far, four prototype tubes (XL1, XL2, XL3, and XL4) have been manufactured and operated at 50-MW peak power for the required 1.5- μ s pulse duration at 60 pulses per second.

Rf pulse compression in the NLCTA will be performed by the SLED-II technique. A prototype SLED-II system has been tested with an X-band klystron at compressed-pulse power levels up to 200 MW, to validate the design of the NLCTA pulse-compression system and its components [Nantista 1993], as discussed in Section 8.3. Power from the SLED-II prototype has been used to achieve a 67-MV/m accelerating gradient in the prototype 1.8-m-long accelerator section in the Accelerator Structure Test Area (ASTA) of the Klystron Test Laboratory at SLAC [Vlieks 1993, Wang 1994].

To achieve low rf losses, oversized circular waveguide will be used for the SLED-II delay lines and for the transmission lines that carry the rf from the klystron to SLED-II, and from SLED-II to the accelerator. The TE_{01} mode will be propagated in the circular waveguide. Matching to the TE_{10} mode in rectangular waveguide will be performed by compact, low-loss-mode transducers [Tantawi 1993], as discussed in Section 8.3.

The NLCTA rf system has been designed to accommodate the possibility of a future upgrade which would increase the accelerating gradient from 50 MV/m to 85 MV/m by replacing each 50-MW klystron with a pair of 75-MW klystrons. Each NLCTA pulse modulator is capable of accommodating a pair of either 50-MW or 75-MW tubes.



2-96

8047A273

Figure 8-2. Schematic layout of the NLC Test Accelerator's high-power rf system.

Parameter	Design	Possible Upgrade
Beam:		
Electrons per bunch	0.4×10^9	6.5×10^9
Bunch frequency	11.424 GHz	0.714 GHz
Bunches per pulse	1440	90
Pulse length	0.125 μ s	
Beam pulse repetition rate	10 Hz	
Accelerator:		
Accelerating gradient, unloaded	50 MV/m	85 MV/m
Accelerating gradient, full current	37 MV/m	64 MV/m
Filling time	0.1 μ s	
Section length	1.8 m	
Sections per module	2	
Modules in linac (excluding injector)	3	
RF Pulse Compression:		
Compressed rf pulse length	0.25 μ s	
Compression ratio	6	
Efficiency (intrinsic \times components)	$0.75 \times 0.90 = 0.67$	
Peak power gain	4.0	
RF Power Transmission:		
Transmission Efficiency	0.86	
Klystrons:		
Klystrons per module	1	2
Peak rf power per klystron	50 MW	75 MW
Klystron pulse length	1.5 μ s	1.1 μ s
Voltage	440 kV	500 kV
Perveance	$1.2 \mu\text{A}/\text{V}^{3/2}$	$0.75 \mu\text{A}/\text{V}^{3/2}$
Electronic efficiency	0.43	0.60
Rf pulse repetition rate	180 Hz	120 Hz

Table 8-2. NLCTA design parameters and a possible upgrade path.

The 70-MeV, X-band injector module and two of the three 130 MeV, X-band linac modules of the NLCTA are expected to become operational in 1996, with each module powered by a single 50-MW klystron. The first accelerator physics experiments are planned for 1996–1997. The last linac rf module (including the fifth and sixth 1.8-m-long X-band sections) is planned to be installed in 1997. It is expected that the upgrade from 50-MW klystrons to 75-MW klystrons will occur gradually as the new higher-power tubes become available through the klystron development program. The initial complement of 50-MW klystrons, and the first of the 75-MW klystrons, will be solenoid-focused. Later versions of both 50-MW and 75-MW klystrons are expected to be focused by cylindrical arrays of PPMs, as discussed in Section 8.4.

8.1.4 Outlook

The design of the rf system for the main linacs of the NLC is supported by existing and planned developmental prototypes, and by the NLCTA. Key NLC parameters such as the klystron power, acceleration gradient, and pulse-compression power gain have been exceeded in prototype systems. The next steps in the development program are completion of the NLCTA, the first damped and detuned structure, and the first PPM klystron prototype. The design of the NLC high-power rf system is mature and is progressing toward detailed engineering considerations. Because of the magnitude of the project, special emphasis is now being placed on designing for manufacturability and for overall system reliability.

8.2 Accelerator Structure

The design of the X-band accelerator structures for the NLC is based on theoretical and experimental experience gained by numerically modeling and building accelerator structures for the NLCTA, and operating them at high gradients. One of the main challenges is to suppress the deflecting modes that will otherwise cause severe multibunch emittance growth in the NLC linacs. Suppression of the transverse wakefield will be achieved through a combination of precision alignment and by detuning and damping higher-order modes. Another challenge in the design of the accelerator structures for the NLC is suppressing field emission at the high-surface field gradients encountered in these structures. This suppression, so far, has been achieved through machining, processing, and handling techniques that minimize surface roughness and eliminate contamination of the high-gradient surfaces. Other, additional methods may be adopted later.

There is a significant amount of overlap in the discussions of the previous chapter and this present one, since both deal with the design and performance of the main linacs. The previous chapter focused on beam dynamics issues, most importantly preservation of the beam emittance and stability. This chapter is concerned with the systems needed to accelerate the beams. This section outlines an engineering design of the accelerator structures that will meet the beam dynamics requirements.

As part of the process of developing the structure design for the NLC, several 1.8-m NLC-type accelerating structures are being built for use in the NLCTA. These are of two types: some with detuning alone, and others with both detuning and damping. In both cases, the accelerator structure is a disk-loaded waveguide driven at 11.424 GHz, the phase advance per cell for the accelerating mode is chosen to be $2\pi/3$, and the detuned distribution of the synchronous lowest dipole-mode frequencies has a density in frequency space that is Gaussian with truncation at $\pm 2\sigma$ and a total detuning range of 10%. (Only damped, detuned structures will be used in the NLC main linacs.)

The frequency spread in this detuned-mode distribution results in an interference between modes that strongly attenuates the corresponding component of the wakefield that drives multibunch beam break-up. The desired Gaussian distribution of detuned modes is obtained (while also keeping the accelerating mode frequency fixed) by varying the dimensions along the structure, the main influence coming from the cell radii (b) and the iris radii (a). To reduce the smaller but non-negligible effect of the higher dipole modes, we also vary the disk thickness (t) ranging from 1 mm in the first cell to 2 mm in the last cell, in a truncated Gaussian pattern having standard deviation $\sigma_t = 0.25$ mm. (See discussion in Section 7.4.2.) Because the number of cells used to implement the Gaussian detuning pattern is finite, the wakefield resurges on a distance scale of about $c/2\Delta f \approx 30$ m, where Δf is the cell-to-cell frequency separation in the center of the distribution. To suppress this resurgence of the long-range wakefield, the damped and detuned structure (DDS) incorporates dipole-mode damping in addition to the detuning discussed above. This damping is

accomplished by coupling each accelerator cell to four evacuated waveguide manifolds running parallel to the structure, symmetrically located around its circumference. The manifolds are terminated at each end by matched loads. No manifold modes propagate at the frequency of the accelerating mode, so there can be large coupling to the dipole modes without significant damping of the accelerating mode. (We have set a limit of a few percent degradation of the shunt impedance of the accelerating mode.) Because the higher-order modes are tuned to different frequencies, one finds (Section 7.4.2) that they have a broad spectrum of phase velocities of both signs. They are therefore capable of coupling effectively to all propagating modes in the damping manifolds.

In this section, we discuss the calculation of the dimensions of the individual cells, which vary along the structure. Next, tolerances on the dimensions and alignment of the cells in the structure are discussed. Following this, the steady-state unloaded and beam-loaded gradients are calculated. In the absence of beam-loading compensation, there would be a large sag (on the order of 25%) in the beam energy during the first 100 ns (equal to the structure filling time) following beam turn-on. There are several possibilities for compensating this transient energy variation. The method chosen here is to tailor the amplitude of the rf power during the structure filling time so that the exact steady-state beam-loaded gradient (at every position along the length of the structure) is present at the moment the beam passes through. This method of multibunch energy compensation has already been introduced in Section 7.4.5, where for simplicity the approximation of a constant-gradient structure was assumed. In this chapter the scheme is extended to calculate the exact final amplitude function needed for the NLC quasi-constant-gradient structure described here.

We then discuss in some detail the mechanical design of the structure, including vacuum and thermal calculations, high-power tests, and material handling and processing techniques.

Next, we summarize the tolerances on ripple of the phase and amplitude of the incoming rf pulse that are needed to meet given requirements on the energy and energy spread of the multibunch beam. The experimental program planned for the NLC Test Accelerator, which is designed to achieve these tolerances, is discussed.

Finally, we discuss some of the tests and diagnostics related to the detuning and damping of the accelerator structures. The Accelerator Structure SETup (ASSET) Facility at SLAC uses the SLC positron and electron bunches to probe and witness, respectively, the wakefields in accelerator structures. Excitations of the dipole modes in a structure may be used as a diagnostic to measure the alignment of the structure with respect to the beam.

8.2.1 Calculation of Structure Dimensions

The task of designing the accelerator structure includes calculating the physical dimensions of a set of cells with a common rf feed (a section) that results in a truncated Gaussian distribution for the lowest dipole-mode frequencies, while maintaining the desired frequency and phase advance per cell for the accelerating mode. The truncated Gaussian distribution has a given standard deviation σ_f and a density of frequency components near the central frequency \bar{f}_1 proportional to $\exp[-(f - \bar{f}_1)^2 / 2\sigma_f^2]$. This means that the spacing between adjacent modes near the i th mode is given implicitly by

$$\operatorname{erf}\left(\frac{f_{1,i} - \bar{f}_1}{\sqrt{2}\sigma_f}\right) = \operatorname{erf}\left(\frac{f_{1,i-1} - \bar{f}_1}{\sqrt{2}\sigma_f}\right) + A \quad , \quad (8.1)$$

where A is a constant, given by

$$A \equiv \frac{2 \operatorname{erf}(n_\sigma/2\sqrt{2})}{N-1} \quad (8.2)$$

Here, N is the number of cells in the accelerator structure,

$$n_\sigma \equiv \Delta f_{\text{tot}}/\sigma_f \quad (8.3)$$

is the full width of the truncated distribution in units of σ_f , and $\operatorname{erf}(x)$ is the error function:

$$\operatorname{erf}(x) \equiv \frac{2}{\sqrt{\pi}} \int_0^x e^{-u^2} du \quad (8.4)$$

In the central core of the distribution, the fractional spacing between adjacent frequency components is approximately

$$\frac{\delta f}{\bar{f}_1} \approx \frac{\sqrt{2\pi}}{N-1} \frac{\sigma_f}{\bar{f}_1} \operatorname{erf}\left(\frac{n_\sigma}{2\sqrt{2}}\right) \quad (8.5)$$

We discuss next how we arrive at structure dimensions that satisfy these requirements on the accelerating mode and higher-order modes. Increasing the cavity radius b causes both the accelerating mode frequency and the first dipole-mode frequency f_1 to decrease, while increasing the iris radius a leads to an increased accelerating mode frequency and a decreased first dipole-mode frequency. As noted earlier, we also choose to vary the disk thickness t in a specified pattern. Keeping the frequency of the accelerating mode constant (11.424 GHz) yields a unique relation between iris radius a , cell radius b , and disk thickness t . Each of these triplets (a, b, t) corresponds to a different dipole-mode frequency. If a certain detuning range of the dipole modes is given, and t is varied in the specified truncated Gaussian pattern from 1 mm to 2 mm, the triplets (a, b, t) for the two end-cells of the accelerator section can be found. It is always possible to find a unique triplet (a, b, t) to set the dipole-mode frequency to any value between the frequencies of the first and last cells and also to keep the frequency of the accelerating mode constant; we choose to vary the lowest dipole-mode frequency in a truncated Gaussian pattern, with total frequency spread of about 10% and truncation at $\pm 2\sigma_f$.

We first discuss the calculation of dimensions for the detuned structure. The overall design procedure, which uses polynomial three-parameter fits, is as follows:

1. Using the computer code YAP [Nelson 1992a], the relationship among a , b , and t , given the fixed accelerating frequency and phase advance per cell ($2\pi/3$), may be found for the structure (taking into account the effect of the rounded corners on the irises).
2. Again using YAP, the relationship among the synchronous dipole-mode frequency f_1 , a , b , and t may be found (where b is fixed by step 1).
3. The desired spacings of the dipole-mode frequencies, $\{f_{1,i} - f_{1,i-1}\}$, and the distribution of disk thicknesses, $\{t_i\}$, are specified. As already noted, both of these are chosen to be truncated Gaussian distributions.
4. Given a value a_1 for the iris radius of the first cell, the central frequency \bar{f}_1 and all of the a_i and b_i are uniquely determined by the above constraints. We adjust a_1 to obtain the desired filling time T_f for the structure.

The resulting structure parameters are summarized in Table 8-3. When a parameter varies along the structure, the range of values from the first to the last cell is given.

Accelerating mode frequency	11.424 GHz
Phase advance per cell	$2\pi/3$
Structure length	1.8 m
# of cells	205 + 1 couplers
Iris radius, a	0.572 to 0.390 cm
Cell radius, b	1.084 to 0.998 cm
Disk thickness, t	1 to 2 mm
Frequency range of dipole modes	14.312 to 15.834 GHz
Mean dipole-mode frequency, \bar{f}_1	15.073 GHz
σ_f/\bar{f}_1	2.5%
Total fractional spread, $\Delta f_{\text{tot}}/\bar{f}_1$	10.1%
Group velocity, v_g/c	0.12 to 0.03
Filling time, T_f	100 ns
Attenuation parameter, τ	0.533
Elastance, $s \equiv \omega r/Q$	652 to 946 V/pC/m
Peak power per feed (for 50 MV/m unloaded)	89.8 MW
Q of lowest dipole mode	≈ 6500

Table 8-3. Parameters for an NLC structure.

This procedure must be further modified to calculate the dimensions for the DDS. The reduction of each cell diameter required to compensate for the presence of the damping manifolds is calculated using the 3-D MAFIA code. Starting from the (a, b) pairs obtained for the purely detuned structure, we calculate the increment in b that is needed to tune the fundamental mode back to the desired rf frequency of 11.424 GHz. These calculations are to be verified by microwave measurements on a series of uniform cavity stacks corresponding to different cavities in the section.

For an accelerator structure consisting of N cells, the above procedure gives the frequencies of the synchronous dipole modes for each of N periodic structures, where each such structure is constructed from cells like one of those in the actual structure. The relationship between the dipole mode frequencies in these equivalent periodic structures and the coupled-mode frequencies (and mode field distribution patterns) in the 206-cell accelerator structures is calculated using equivalent circuit models, both for the undamped detuned structure [Bane 1993a] and for the DDS [Kroll 1994]. In the case of the DDS, the damping of the structure modes due to their coupling to the manifolds is also obtained from the model. Detailed discussion of these equivalent circuit models and the resulting calculations of long-range wakefields were given in Section 7.4.2.

8.2.2 Tolerances on Dimensions and Alignment

The tolerance on the structure dimensions, particularly on cell radius b , comes from the effect on the distribution of dipole mode frequencies, which is designed to be a truncated Gaussian. The tolerance on the frequency is roughly the core spacing of the truncated Gaussian distribution of frequencies. The tolerance on misalignments of the structures comes from the effect on the transverse emittance of the multibunch beam. This tolerance is dependent on the longitudinal correlation length of the misalignments, but it is fairly tight on all scales. (See Section 7.4.6: "Structure Misalignments".) Both these tolerances are looser for the DDS than for the undamped Gaussian detuned structure.

Tolerances on Frequency Errors

There are two extreme cases for the frequency errors: the case where the error in each frequency in the design distribution is the same in all sections (we denote this as "systematic"), and the case where the error in each frequency is totally random from section to section. Note that our definition of systematic means that the errors are the same in corresponding cells of a given structure type, but they are still random from cell to cell in each structure type. Systematic errors can lead to considerable worsening of the long-range wakefield behavior; the totally random errors are much less harmful. If care is taken to randomize the production of various cell types, it should be possible to keep the systematic components of the errors significantly smaller than the random component, perhaps by nearly an order of magnitude.

As one might expect, the transverse multibunch beam emittance growth is not much affected by the frequency errors, provided that the fractional errors in the frequency distribution are kept small compared to the core spacing.

For a single detuned accelerator section, the fractional core spacing $\delta f/\bar{f}_1$ for the fundamental dipole-mode frequencies is about 3×10^{-4} . Machining precisions for conventional machining and diamond-point machining (obtained at KEK), and alignment tolerances of stacks of cells, are given in Table 8-4. Since the cell radius is about a centimeter, diamond point machining should produce a random $\delta f/f$ error somewhat less than the core spacing. The systematic error, as noted above, should be significantly less than this.

Misalignment Tolerances

Misalignment tolerances, on scales ranging from a few cells within a structure to several structures, were discussed in the preceding chapter. It was found that the tightest tolerances occurred for the alignment of groups of about 20–40 cells. Thus, great care must be taken in brazing together the subsections of structures after their initial assembly from individual cups.

8.2.3 Calculation of Steady-State Gradients

In this section, we discuss the calculation of the unloaded and loaded accelerating gradients. We also discuss the proposed compensation of the transient beam loading that occurs during the first filling time after the beam is injected.

Unloaded Gradient

The power flow in the accelerator structure can be expressed as

$$P(z) = P_{in} e^{-2\tau(z)} \quad , \quad (8.6)$$

where P_{in} is the input power and $\tau(z)$ is the attenuation along the structure, given by:

$$\tau(z) = \omega_{rf} \int_0^z \frac{dz'}{2Q(z')v_g(z')} \quad . \quad (8.7)$$

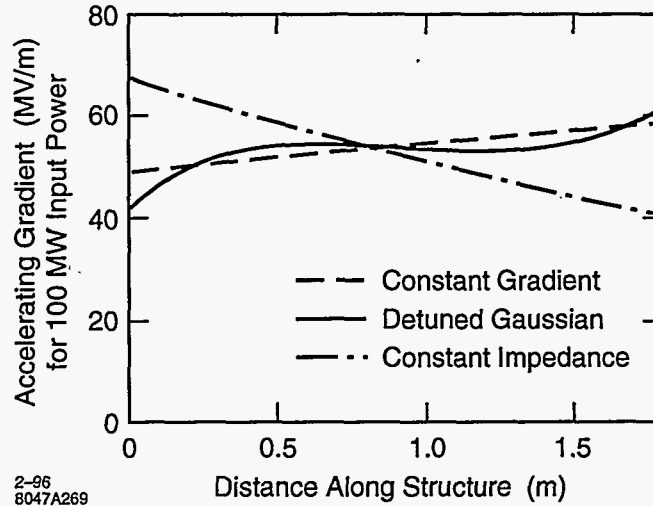


Figure 8-3. Accelerating electric field gradient along the axis of detuned structure. Electric field gradients for conventional constant-impedance and "constant-gradient" structures with the same input power and attenuation are also shown for comparison.

The shunt impedance $r(z)$ can be calculated using the code SUPERFISH. Then the accelerating electric field $E_z(z)$ can be calculated as

$$E_z(z) = \sqrt{r(z) \frac{dP(z)}{dx}} \quad , \quad (8.8)$$

where $r(z)$ is the shunt impedance per unit length. In Figure 8-3, $E_z(z)$ is shown for an input power of 100 MW. For comparison, $E_z(z)$ for a conventional constant-gradient structure and for a constant-impedance structure, with the same input power and attenuation as the detuned structure, are also plotted.

Beam-loaded Gradient

In this section, we generalize Equation 8.8 so that the discrete nature of the structure is explicitly taken into account. The analysis is then extended to include beam loading. The underlying assumption is that the structure parameters vary slowly and smoothly with length, and that the structure can be treated as locally periodic. In this case, the unloaded steady-state gradient in the n th cell is given by

$$G_0(n) = [2\alpha(n)r(n)P(n)]^{1/2} \quad , \quad (8.9)$$

where α is the attenuation parameter per unit length. It is related to the other structure parameters by

$$\alpha = \frac{\omega}{2v_g Q} = \frac{s}{2v_g r} \quad , \quad (8.10)$$

where $s = \omega(r/Q)$ is the local elastance per unit length. Using Floquet's theorem with Equation 8.9, we get

$$G_0(n+1) = \left[\frac{\alpha(n+1)r(n+1)}{\alpha(n)r(n)} \right]^{1/2} e^{-\alpha(n)d} G_0(n) \quad (8.11)$$

Here $d = L_s/N$ is the cell length, where N is the total number of cells in a structure of length L_s . The gradient in the first cell is $G_0(1) = [2\alpha(1)r(1)P_0]^{1/2}$, where P_0 is the steady-state input power. The distance,

attenuation, filling time and voltage from the input to the end of the n th cell are

$$z(n) = nd \quad (8.12)$$

$$\tau(n) = d \sum_{i=1}^n \alpha_i \quad (8.13)$$

$$T_f(n) = d \sum_{i=1}^n 1/v_{gi} \quad (8.14)$$

$$V(n) = d \sum_{i=1}^n G_i \quad (8.15)$$

We assume that the structure is operated synchronously (no cell-to-cell phase error for a velocity-of-light electron), although the analysis can easily be extended to the nonsynchronous case.

The gradient induced by a charge Δq passing through the n th cell is $\Delta G_b(n) = s(n)\Delta q/2$. Using $\Delta q = I_0 d/v_g(n)$ and Equation 8.10, the gradient induced during the time it takes for the accelerating wave to pass through the cell is

$$\Delta G_b(n) = \alpha(n)r(n)I_0 d \quad (8.16)$$

where I_0 is the steady-state beam current. The beam-induced gradient in the first cell is $G_b(1) = \alpha(1)r(1)I_0 d$. The net beam-loading gradient in the n th cell is the sum of $\Delta G_b(n)$ and a term due to power flow from the gradient induced in upstream cells. In analogy with Equation 8.11, the gradient in cell $n+1$ in terms of the gradient in cell n is then

$$G_b(n+1) = \left[\frac{\alpha(n+1)r(n+1)}{\alpha(n)r(n)} \right]^{1/2} e^{-\alpha(n)L_c} G(n) + \alpha(n)r(n)I_0 d \quad (8.17)$$

The net beam-loaded gradient in the n th cell is

$$G_L(n) = G_0(n) - G_b(n) \quad (8.18)$$

The functions G_0 , G_b and G_L are plotted in Figure 8-4 for an average unloaded gradient $\bar{G}_0 = V_0(N)/L_s = 50$ MV/m. It is assumed that the presence of a damping manifold results in a 3% reduction in Q . The required input power is 89.2 MW per structure (50 MW/m). The average beam-loading gradient is 14.7 MV/m for a charge per bunch of 7.5×10^9 electrons, giving a net loaded gradient of 35.3 MV/m. The beam-loading derivative is 17.13 MV/A. Further details are given in NLC Technical Notes [Farkas 1994, Farkas 1995].

Transient Beam-Loading Compensation

To compensate for transient beam loading, it is necessary to produce the steady-state beam loaded gradient profile, $G_L(n)$, by varying the generator power flow during one filling time prior to beam turn-on at time $t = 0$. This compensation is tantamount to "pre-loading" the structure. Taking into account the attenuation and propagation time from the input cell to cell n , and the relation between power flow and gradient as given by Eq. 8.9, the required ramping profile is

$$P[-T_f(n)] = \frac{G_L^2(n)e^{2\tau(n)}}{2\alpha(n)r(n)} \quad (8.19)$$

where $T_f(n)$ and $\tau(n)$ are given by Eqs. 8.13 and 8.14.

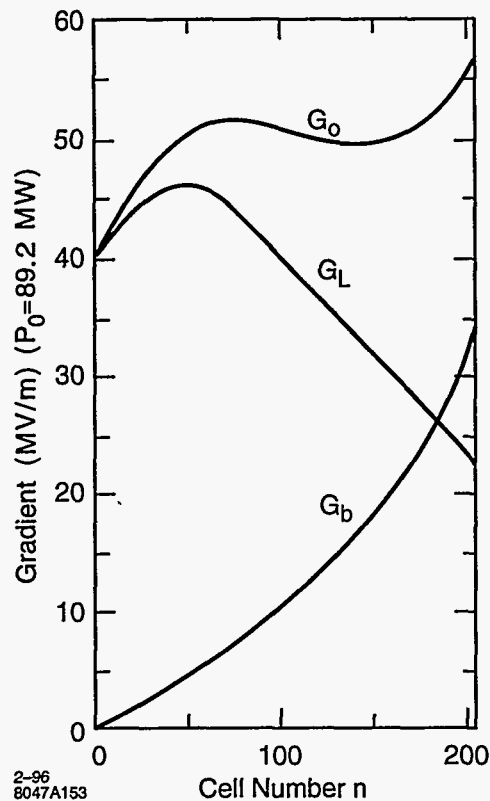


Figure 8-4. Generator (G_0), beam (G_b), and loaded (G_L) gradients as a function of cell number n .

The normalized field ramp $[P(t)/P_0]^{1/2}$ is plotted in Figure 8-5. For a true constant-gradient structure, this field ramp would be exactly linear. A linear ramp is also plotted in Figure 8-5 for comparison, along with the relative field difference on an expanded scale. The relative deviation from a linear ramp reaches about 1.5% (3% in power) at $t \approx -0.5T_f$. Use of a linear ramp instead of the exact compensation profile would result in an energy variation of about 1% along the bunch train.

8.2.4 Mechanical Design of the Accelerator Structure

This section gives a general description of the mechanical design of the damped and detuned structure (DDS). The discussion covers the design and tolerances of the cells, vacuum pumping and water cooling systems, the input coupler, and the supporting strongback. Stack assembly for diffusion bonding is described. Starting with the unavoidable geometrical complexity which is mandated by the theoretical specifications, an attempt has been made to keep the rest of the design as simple as possible to minimize costs and to facilitate automation of the production of the very large quantities of components required.

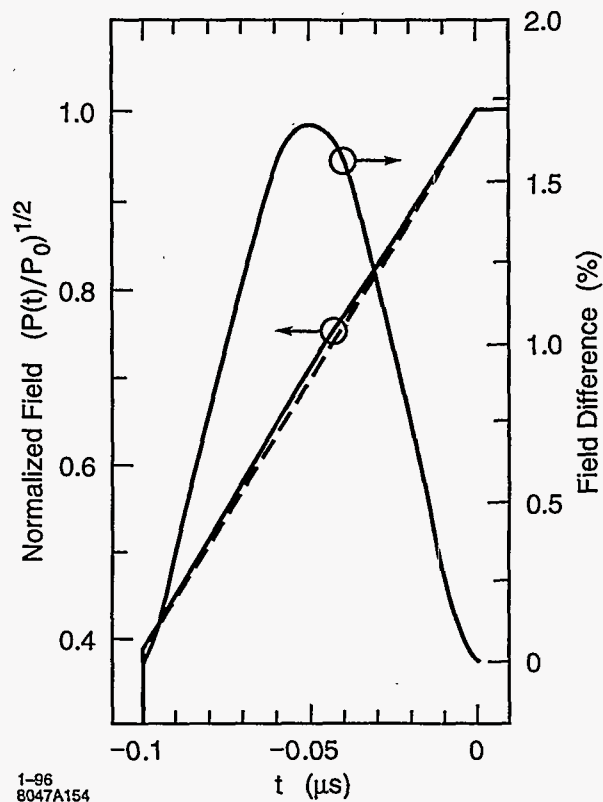


Figure 8-5. Normalized input field $[P(t)/P_0]^{1/2}$ and the difference between it and a linearly-ramped field (dashes), vs. time. (The initial normalized input field is 0.385.)

Cell Design

The basic features of the cell are shown in Figure 8-6. The central portion is the conventional "cup" consisting of a cylindrical cavity wall and an apertured iris which, when stacked in a row with other cells, forms the disk-loaded waveguide accelerator structure. The diameter of the cavity wall, the thickness of the iris, and the diameter of its aperture vary progressively from cell to cell to "detune" the beam-deflecting dipole modes and suppress short-range cumulative build-up of wakefields, while maintaining the quasi-constant-gradient characteristics of the fundamental accelerating mode. The central cavity is slot-coupled to four outer rectangular holes. When the cells are stacked, the holes form four waveguides which run parallel to the axis of the structure. When terminated in matched loads, the four waveguides become "damping manifolds." The slots (which are cut off for the fundamental accelerating mode) couple power from beam-excited dipole modes into these damping manifolds, lowering the Q and suppressing long-range wakefield build-up. Microwave signals from the damping manifolds can be used to monitor the alignment of the structure with respect to the beam.

The waveguide height and its distance from the structure axis vary progressively from cell to cell, as described in Section 8.2.1. Thus, for example, cells 10, 70, 122 and 196 appear as shown in Figure 8-7. All cells have the same thickness.

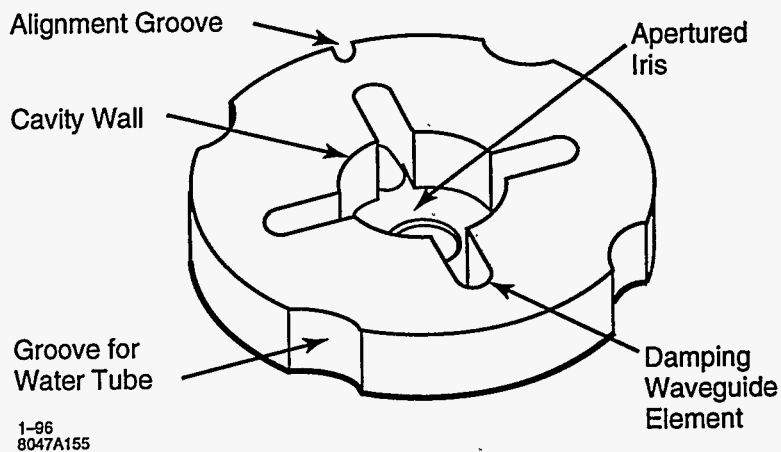


Figure 8-6. Basic cell design.

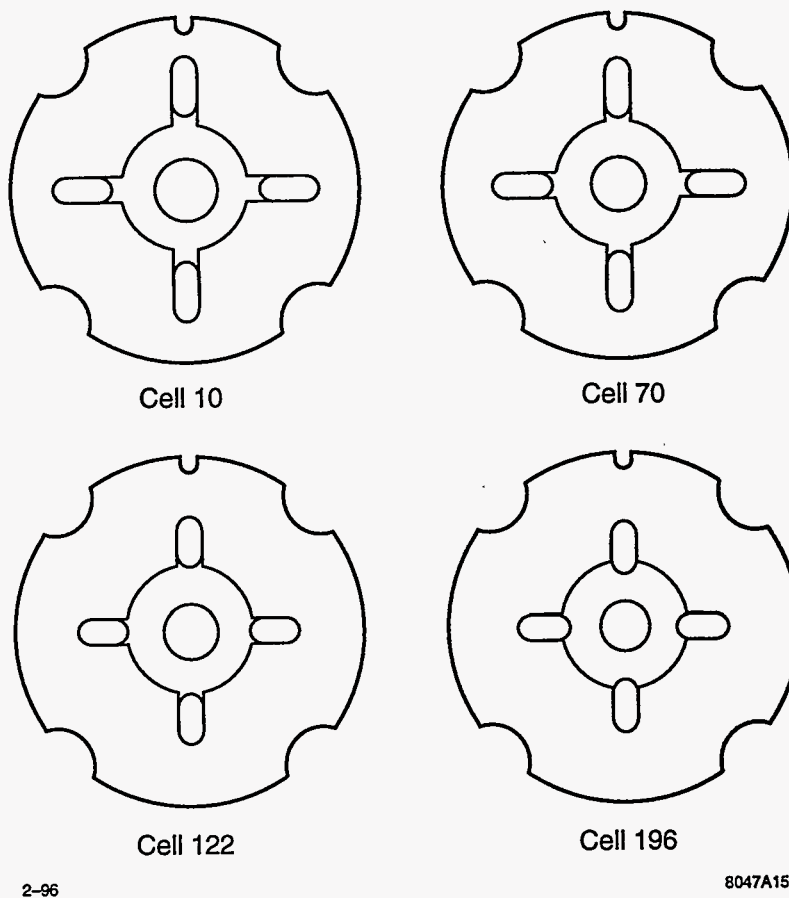


Figure 8-7. Front view of typical cells.

The cells have four circular-sector grooves equispaced around their periphery to accommodate four water-cooling tubes which are attached in a final brazing operation. The partially inset tubes provide adequate thermal conductance while avoiding direct water-to-vacuum diffusion bond interfaces. Since there are 205 cells in each accelerator section, forming the water channels by lining up four holes drilled through each cell would have resulted in over 800 such bonds in each section, greatly increasing the probability of failure due to leakage.

Each cell has an additional groove which is used to determine rotational alignment during assembly.

Cell Tolerances

The goal is an accelerator section 205 cells long (plus the input coupler) in which the axes of the individual cavities lie on a straight line to within $15\ \mu\text{m}$ (rms).

To avoid a cumulative tolerance build-up which exceeds this goal, many other cell dimensions have to be held to tolerances in the 2 to $3\ \mu\text{m}$ range. This applies particularly to the diameter and coaxiality of the outer surface of the cell, since this has to be the reference surface used in stacking the cells prior to bonding. It also applies to the perpendicularity, flatness and parallelism of the cell faces. Errors here will cause "bookshelving" [Seeman 1985] in the cell stack. Equally important is the coaxiality of the iris aperture with respect to the cavity outer wall.

These tight tolerances on cavity dimensions (including the thickness of the iris and the radius of its edge) are also necessary to achieve the design fundamental and dipole-mode frequency characteristics, because provision for tuning after assembly has been eliminated.

Flatness of cell faces is also essential to achieve diffusion bonding (discussed below) over relatively large surface areas with a very low expected failure rate.

Single-crystal diamond-point machining is to be used on all surfaces of each cavity, the cell faces and outer periphery. The hardness, high thermal conductivity, and low thermal expansion of diamond result in a superior tool which, when used in a vibration-free lathe, yield mirror-like surfaces on copper which have a roughness of $0.1\ \mu\text{m}$ or less. This finish is necessary to obtain good diffusion bonding, high Q factors, low dark current and high power-handling capability. The sharpness, mechanical stability, and minimal wear of the tool allow the dimensional tolerances to be met.

Surface finish and dimensional tolerances are less stringent for the side-coupled holes which form the damping waveguides. Respectively, $0.5\ \mu\text{m}$ and $\pm 20\ \mu\text{m}$ are sufficient. The surface finish in the grooves for the water tubes can be $1\ \mu\text{m}$.

Table 8-4 illustrates what tolerances on dimensions and alignment have been achieved to date at SLAC, and what can reasonably be expected with the best technology available today. It can be seen that the most significant advances have been made by resorting to diamond-point machining and by using precision granite vee-blocks to align the stacks of cells prior to brazing or diffusion bonding. Cells designed to nest into each other have to fit loosely enough to permit assembly without galling, and this can result in unacceptable misalignment.

Our present experience is that stacks of 38 cells can have a bow of a few tens of microns after diffusion bonding. This can be reduced to a few microns by setting the stack horizontally in cradles on a granite block and applying bending forces while monitoring movement with a precision coordinate measuring machine.

	Detuned 1.8-m Section #1	Detuned 0.9-m Sections #1 & 2	Detuned 1.8-m Section #2 and DDS #1
Machining Technique	Conventional	Conventional	Diamond-point
Alignment Technique	Nesting	Vee-Block	Vee-Block
Diameters	±7	±7	±2
Concentricity	10	10	1
Thickness	±7	±7	±2
Parallelism	10	10	0.5
Flatness	10	10	0.5
Surface Finish	0.4	0.4	0.05
Cell-to-cell Alignment of Outer Cylindrical Surfaces:			
(a) Expected	22	10	3
(b) Measured after diffusion bonding or brazing	10	6	4

Table 8-4. Cell machining and assembly tolerances achieved (in microns).

Vacuum Pumping

In addition to direct pumping along the beam-interaction region, the structure is pumped in parallel by the four damping waveguides. Assuming a residual outgassing rate of 10^{-12} Torr-ℓ/cm²/s for the copper surfaces, the combined conductance of this system is high enough to reduce the pressure to approximately 10^{-8} Torr in the middle of the structure when pumps are connected only at each end. Since lower pressure may be required, two groups of four special pumping cells will be inserted into the structure, at points one-fourth of the section length from each end. Each pumping cell has high-conductance slots cut in the middle of the broad walls of the damping waveguides. These slots, which are cut off to the fundamental accelerating mode, connect to four ducts and two pumping manifolds and pumps, as shown in Figure 8-8. By pumping only at the two quarter-points, the maximum pressure will be four times less than when pumping only at the end points (and 20 times less than when pumping from the ends of the beam-interaction region in the absence of any manifolds).

A longitudinal cross section of the accelerator section is shown in Figure 8-9. Each pumping cell group is connected to two pumps via short transverse manifolds. Each of these contains two short bellows sections to allow for a small range of accelerator movement in the vertical plane with the two pumps rigidly attached to the strongback (accelerator support beam). The horizontally opposed system ensures that there is no net transverse force on the accelerator due to atmospheric pressure.

The Input Coupler

Some details of the input coupler are shown in Figure 8-10. The coupler is a compact version of the symmetrical coupler used on the first 1.8-m sections for the NLCTA. The input cavity has double symmetrical matching irises in the horizontal plane which couple into the *sides* of two WR-90 low-impedance waveguides (instead of the ends, as used in the NLCTA design).

The waveguides are matched into standard WR-90 by step transformers, after which they combine into a common feed guide by means of a symmetrical post-matched "Y" power divider. This compact design can be

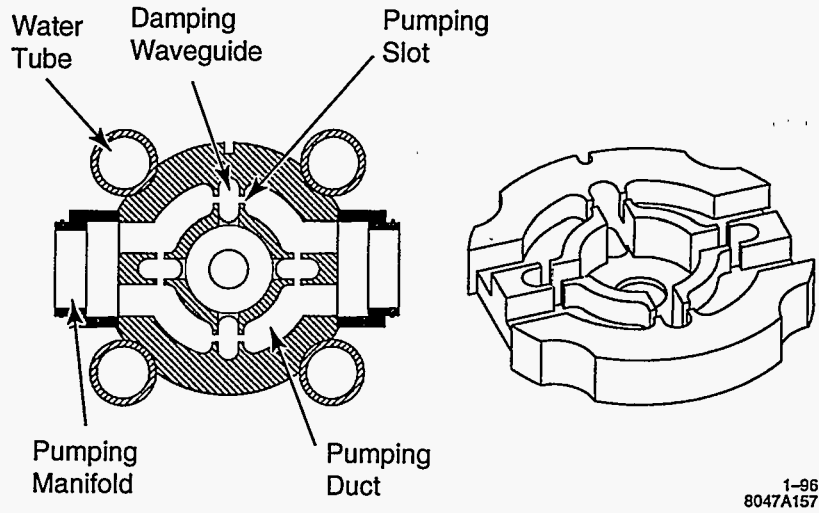


Figure 8-8. Cross section and isometric view of pumping cell.

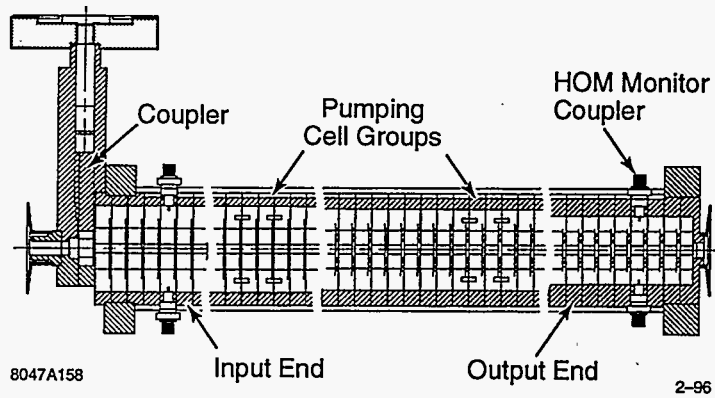


Figure 8-9. Longitudinal cross section of accelerator section.

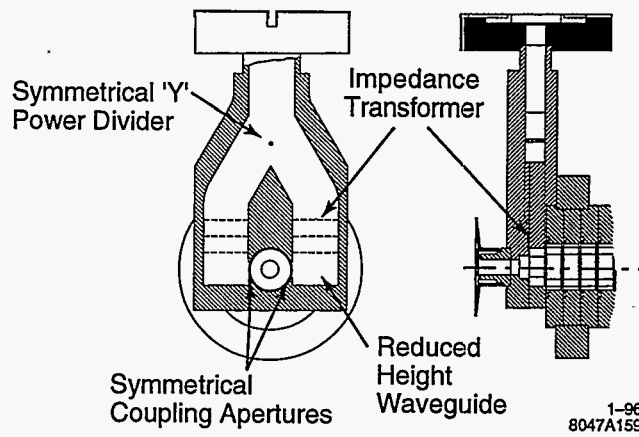


Figure 8-10. Symmetrical input coupler.

machined in two blocks of copper and brazed together, ensuring electrical symmetry and minimum insertion loss.

Figure 8-9 shows no output coupler. The intention is to provide internal matched terminations for both the fundamental accelerating mode and the wakefield modes by depositing lossy coatings on the walls of the cavities and the damping manifolds in the last four cells. A coaxial loop loosely coupled to the last cavity will be used to monitor the fundamental-mode power. This signal will pass through a coaxial rf window in the cell wall, and will be used by the klystron phasing system. However, if satisfactory internal terminations cannot be developed, external loads and couplers will have to be used.

Water Cooling

After the stack of cells has been assembled by diffusion bonding, four water-cooling tubes are brazed into the grooves which are shown in Figures 8-6, 8-7, and 8-8. At each end of the section, the tubes connect to circular manifolds which provide additional conduction cooling of the input coupler and the lossy termination cavities at the output end. The direction of flow alternates from tube to tube.

Strongback Design

The standard strongback supports two 1.8-m accelerator sections. It is a 15-cm \times 10-cm, aluminum box beam with a 6-mm wall. The input coupler of the first accelerator section is rigidly attached to the strongback. All other supports are flexible. Four supports are situated under the pumping cell regions of the two sections. In addition, there are supports under the middle of each section and under the input coupler and the output end of the second section. The latter is fixed in height, but all other flexible supports have adjustment mechanisms which can set the height to a few microns. These are intended only to compensate for residual elastic bowing of the accelerator-and-strongback assembly due to gravity. Any straightening of the sections which requires bending them beyond their elastic limit must be done before attaching them to the strongback.

The flexible supports are, of course, necessary to allow for differential expansion between accelerator and strongback. As presently designed, the bending radius of the flexible arm is approximately 48 mm. Thus, if the temperature of the two accelerator sections is allowed to rise 20°C above the strongback temperature, the free end will expand about 1.5 mm, which results in the accelerator axis drooping by 23 μ m. An adequate solution to this problem is to maintain the strongbacks at close to the same temperature as the accelerator sections by using the same water supply in series to control their temperatures. The temperature match between accelerator and strongback does not need to be very close. Even a 5°C average difference results in a drop at the free-end of only 1 μ m.

For a discussion of distortions due to transverse thermal gradients across the strongback (girder) itself, see Section 7.9.1.

Assembly: Diffusion Bonding and Brazing

The cells are presently aligned in stacks by placing them in a precision granite vee-block, as shown schematically in Figure 8-11. Actually, the cells rest on a table (Figure 8-12) which is held against the end of the block. A tension frame presses the cells against the table, so that they retain their precise alignment as the stack and table are moved away from the vee-block and transferred to the furnace.

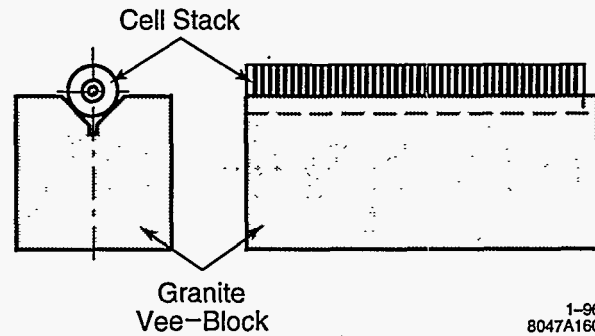


Figure 8-11. Schematic of cell assembly on vee-block.

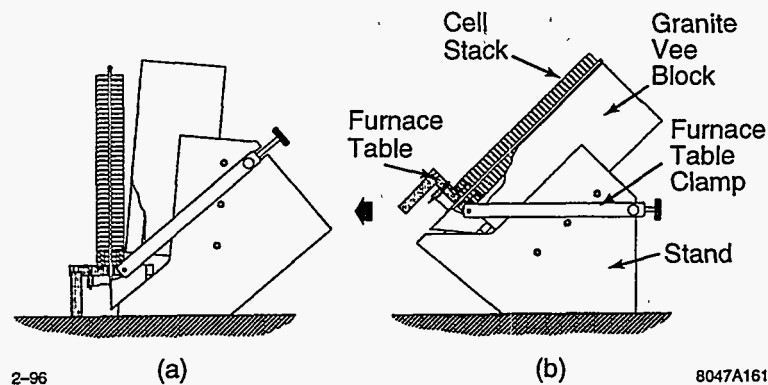


Figure 8-12. Cells stacked on table in vee-block.

The cells, pressed together by the tension frame as shown in Figure 8-13, are diffusion-bonded together by heating to 1000°C in hydrogen. The number of cells bonded into a stack at one time is to be determined. Long stacks reduce the number of assembly steps but increase the difficulty of handling.

The coupler, drift tubes, and vacuum and water manifolds are added in a final furnace cycle, using a copper/gold braze. Coupling tubes are also added in two special manifold cells (one near each end of the section), into which coaxial feedthroughs (Figure 8-14) can be welded for monitoring dipole mode-induced fields in the lossy waveguides.

Leak Checking and Straightening

After the final braze, the coaxial feedthroughs are welded in. The completed section is leak-checked and then attached to a special straightening strongback. Each assembly, at present, is then transferred to a coordinate measuring machine, where the alignment of every cell is checked (with the section still hanging vertically to eliminate bending due to gravity). Corrective bending is done at intervals along the section by applying transverse forces from adjustable micrometer jacks built into the special strongback. Two sets of jacks allow bending corrections to be made in two orthogonal planes through the axis of the section.

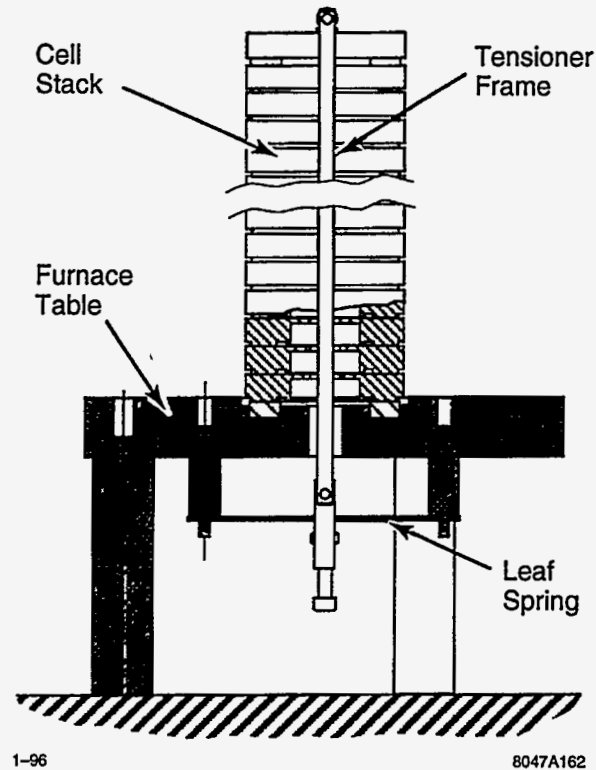


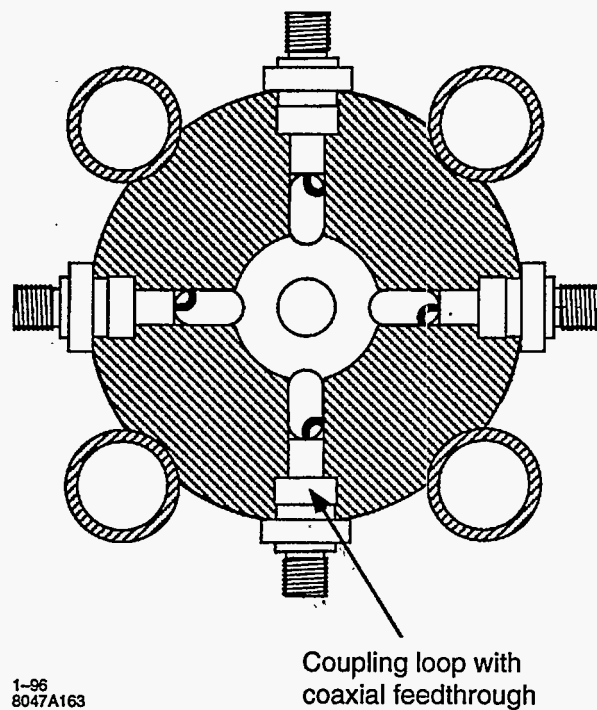
Figure 8-13. Cells stacked for diffusion bonding.

Cold Testing

After straightening, the section is moved to a cold-testing station where network analyzer measurements are made to determine the input match and the phase advance per cell of the fundamental mode. The measurements are made and recorded rapidly and largely automatically (possibly by dropping a reflecting bead along the beam axis from output to input). A second set of measurements is made in the frequency band of the dipole modes, using the coaxial feeds to check the transmission characteristics from one damping waveguide across the cavities to the opposite damping waveguide. All these tests result in a simple "accept" or "reject" decision for the section, as no provision for tuning or other adjustment is made.

Bakeout

Still hanging vertically, the section is removed from the special strongback and transferred to a bake station. The section is evacuated and baked at about 500°C (in a vacuum oven) until the internal vacuum stabilizes in the low 10^{-8} -Torr region. After cooling, the section is back-filled with filtered, purified, nitrogen gas, and attached, with a second section, to a standard double-length strongback on which it will be installed in the NLC machine. The double-section assembly is shown in Figure 8-15.



1-96
8047A163

Figure 8-14. Wakefield monitoring cell.

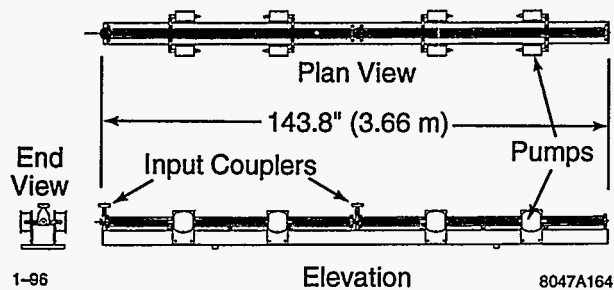


Figure 8-15. Two NLC accelerator sections mounted on a strongback.

Large Quantity Production of Accelerator Cells

The two main linacs will contain about 1.5 million cells, which have to be produced in about three years. Assuming that a specialized plant set up to fabricate the cells operates 50 weeks per year at two shifts per day, then, at 80% efficiency, a production rate of about 2.6 cells per minute is required. A close estimate of the time taken to machine a single cell cannot be made without reference to specific machines and machining techniques. (See, for example, the study reports prepared for the CERN CLIC cells [Read 1993] [OWGR 1993].) However, very rough estimates may be drawn from those reports, noting that the surface area of the X-band DDS cell is about three times that of the CLIC cell. All the features of the DDS cell shown in Figure 8-6 could be machined to conventional tolerances on the end of bar stock (leaving excess material on the critical surfaces to be diamond-point machined in subsequent operations), using a multipurpose CNC turning and milling machine. The cell could thus be cut from the bar using a parting-off tool, stress-relieved and delivered to a diamond-point lathe for finishing in two steps. In the first step, the cell could be gripped on the outside by a precision chuck while the back face is diamond turned. In the second step, the back face could be held in a vacuum chuck while the front face and cavity surfaces are diamond finished. Estimated operation times are: 1.5 min for conventional turning, 7 min for milling, 1 min for first-cut diamond-point turning, and 2 min for second-cut diamond-point turning. These machining times indicate that the plant will need a minimum of 22 conventional CNC turning and milling machines and 8 diamond-point lathes, with appropriate numbers of all supporting equipment (automatic handling and transfer machines, stress-relieving ovens, cleaning, QC, and packing stations) to maintain the required throughput.

8.2.5 Thermal Calculations

The thermal expansion of accelerator sections under high gradient with or without beam loading must be considered. A finite element analysis code is used to calculate the structure distortions. To maintain stabilized beam phase, a control loop is needed for adjustment of cooling water temperature.

Thermal expansion of accelerator sections under high gradient induces phase shifts with respect to the beam, and therefore detracts from beam energy stability. The heat dissipation in accelerator sections varies with the degree of beam loading and must be automatically compensated by controlling the inlet low conductivity water (LCW) temperature.

The thermal effects for the NLC accelerator sections have been calculated under the following conditions. Onto each 1.8-m-long accelerator section are brazed four cooling pipes of 0.325" inner radius, which are made of oxygen-free high-conductivity (OFHC) copper, aligned along the length of the structure, and spaced azimuthally 90° apart. The pipes are connected in a counterflow pattern such that one pair of 180°-separated pipes carries water from one end of the structure and the other pair carries water from the other end of the structure. The total flow rate is 16 gallons per minute. The average copper temperature is 45°.

The cooling water for the accelerator structure is provided from a manifold which supplies water to a large number of accelerator sections. The manifold will be supplied with water regulated to better than 0.1°C using a three-way mixing valve. Water flow to individual sections will be controlled using either manually adjustable control valves with optical flow meters, or flow-limiting orifices. This level of thermal control has been maintained, in the absence of varying rf power levels, for the S-band accelerator sections of the SLC at SLAC. For the NLC, the average rf power dissipated by the accelerator structure will be kept constant by combining, in phase quadrature, the power from pairs of klystrons.

	0.5 TeV		1.0 TeV	
	Peak power/section 90 MW Total pulse length 240 ns Repetition rate 180 Hz		Peak power/section 261 MW Total pulse length 240 ns Repetition rate 120 Hz	
	No Beam	Peak Beam Curr. 0.86 A	No Beam	Peak Beam Curr. 1.26 A
Avg. dissipated power/section (kW)	2.88	2.17	5.56	4.39
Avg. temp. rise of structure (°C)	2.03	1.55	3.93	3.10
Integrated phase shift per section (°)	14.2	10.9	27.5	21.7

Table 8-5. Thermal effects in 1.8-m-long X-band accelerator sections.

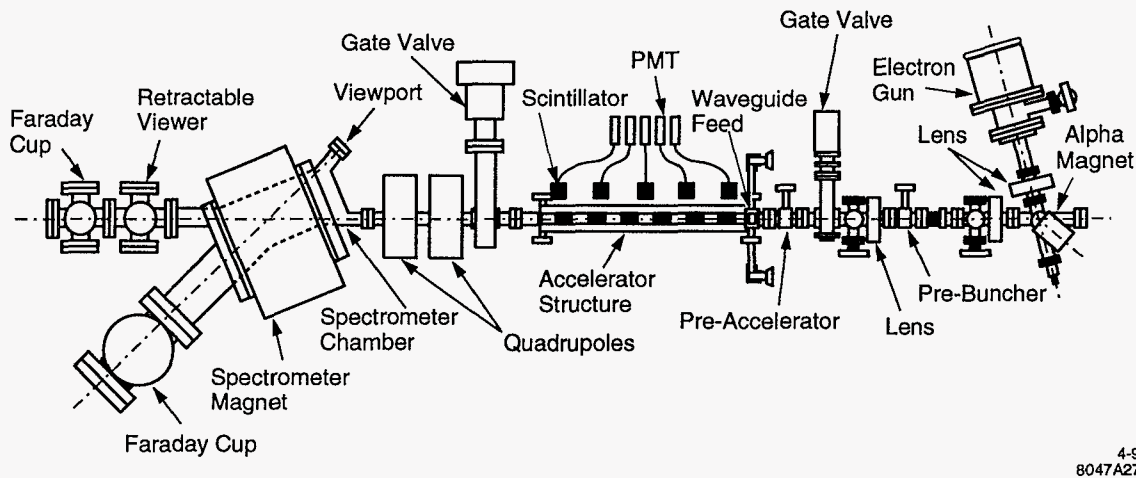
In the calculation of rf power dissipation, the rf pulse in the first 100 ns is modulated to create a quasi-linearly ramped accelerating field profile at the input end of the accelerator section. The heating contribution of rf power due to the intrinsic efficiency of the SLED-II is also included. The average temperature increase of the copper structure is considered to be the average bulk water temperature change plus average film temperature drop. Table 8-5 shows the average temperature increase and corresponding integrated phase change per section for the 0.5-TeV and 1-TeV center-of-mass cases, with and without beam loading.

A finite element analysis code was used to calculate the structure distortions. The maximum asymmetry in distortion at the ends of an accelerator section is negligible (less than $0.4 \mu\text{m}$ in cavity diameter). This will not introduce excitation of higher-order dipole modes.

8.2.6 High-power Tests and Dark Current Studies

The theoretical and experimental studies on the behavior of copper accelerator structures under extremely high-rf fields have been carried out at SLAC for several years [Loew 1988a, Wang 1994a]. We have studied in considerable detail the problems of rf breakdown and dark current generated by field emission at high gradient. The dark current may absorb rf energy, get captured, and produce undesirable steering effects and detrimental x-ray radiation. Many experiments have been done to measure the amplitude and energy spectrum of the dark current and to study phenomena related to rf breakdown such as outgassing, radiation, heating, etc. We have concluded that the dark current can be minimized by improving surface finish and cleanliness, and by rf processing.

The structures which have been examined at X-band are a 6-cm standing-wave (SW) section and a 26-cm constant-impedance traveling-wave (TW) section, a 75-cm constant-impedance TW section, and a 1.8-m TW section. All of the structures were tested in the Accelerator Structure Test Area (ASTA) facility located in a shielded area. As shown in Figure 8-16, ASTA consists of a gun and beam focusing system, a prebuncher,



4-96
8047A272

Figure 8-16. Schematic of Accelerator Structure Test Area (ASTA).

a preaccelerator, a precision rail for mounting the accelerator sections to be tested, and a 45° spectrometer capable of analyzing electron beam energies up to 200 MeV with a resolution of $\pm 0.5\%$. Four directional couplers at input and output ports of the accelerator sections are used to pick up forward and reflected rf signals. Five collimated scintillators alongside the accelerator sections monitor localized radiation and breakdown. The accelerator structures are powered by a SLAC X-band klystron followed by a SLED-II pulse compression system.

The characteristics, main rf parameters of those structures, and high-power test results are listed in Table 8-6. The high-power tests with an electron beam have demonstrated that the 1.8-m section is properly tuned to 11.424 GHz and can accelerate a beam at a gradient of more than 67 MV/m.

Figure 8-17 shows the dark current measured in a Faraday cup as a function of average accelerating field for the 75-m constant-impedance structure and the 1.8-m detuned structure. The dark current for an accelerating gradient of 50 MV/m was found to be negligible. At 85 MV/m, it was estimated to be tolerable. The energy spectrum of the dark current was measured and found to be sufficiently low that the quadrupoles will overfocus and sweep the field-emission beam away from the primary, high-energy beam.

8.2.7 Material Handling and Processing Techniques

Experiments performed with S-band accelerators at KEK [Takeda 1991, Matsumoto 1991] have shown that the dark current produced by field emission from the accelerator disks is reduced by an order of magnitude when stringent precautions are taken to exclude dust during fabrication, assembly, processing and testing. These experiments indicate that the NLC accelerator cells should be cleaned in ultra-pure, dust-free chemical solutions and rinses, assembled and bonded under clean-room conditions, and perhaps given a final rinse in ultra-pure water before vacuum bakeout and installation.

Parameter	6 cm (SW)	26 cm (TW)	75 cm (TW)	1.8 m (TW)
Frequency, f (MHz)	11424	11424	11424	11424
Structure type	C.I.	C.I.	C.I.	Detuned
Iris diameter, $2a$ (cm)	0.75	0.75	0.856	1.134–0.786
Cavity diameter, $2b$ (cm)	2.12	2.12	2.158	2.284–2.139
Disk thickness, t (cm)	0.146	0.146	0.146	0.1–0.2
Total # of cavities	7	30	86	206
Shunt impedance ($M\Omega/m$)	98/2	98	88	67–88
Figure of merit, Q	6960	6960	7005	7020
Coupler type	Single	Double	Double	Double
Group velocity, v_g/c	–	0.033	0.048	0.118–0.03
Filling time, T_f (ns)	80	26.5	52	100
Attenuation, τ	–	0.136	0.267	0.505
Rf pulse length (ns)	770	60	75	150
Peak input power (MW)	13.8	116	130	160
Maximum E_{acc} (MV/m)	–	108 ^b	90 ^b	70 ^b
Average E_{acc} (MV/m)	110 ^a	101 ^b	79 ^b	67 ^b
Maximum surface field, E_s (MV/m)	500 ^a	235 ^b	206 ^b	180 ^b
Ratio E_s/E_{acc}	4.55	2.275	2.292	2.37 ^c

^a Limited by rf breakdown

^b Limited by klystron output power

^c Ratio E_s/\bar{E}_{acc}

Table 8-6. Characteristics of tested structures

8.2.8 Multibunch Energy Spread and Compensation

Multibunch energy spread and the scheme for multibunch energy compensation were discussed in Section 7.4.5 and in Section 8.2.3: "Transient Beam-Loading Compensation". As noted in those sections, transient beam loading for both regular accelerator sections (quasi-constant gradient structures) and injector sections (over-compensated quasi-constant gradient structures) can be compensated by using a specially-modulated rf pulse, so that the rf electrical field envelope at the input end is ramped quasi-linearly during one filling time before the injection of a bunch train.

Here we summarize the tolerances (on rf phase and amplitude ripple) that come from the effect of the ripple on multibunch energy and energy spread. As noted in Chapter 7, the effect of dispersion of different frequency components in the rf pulse needs to be taken into account, and we have treated each bunch as a single macroparticle (*i.e.*, intrabunch energy spread is ignored in these calculations). Also, the calculations presented here do not take into account the averaging of the ripple over different rf sections, which loosens the tolerances by approximately \sqrt{N} where N is the number of sections over which we average. (We expect N to be approximately the number of rf sections between linac diagnostic stations, unless there are effects that cause the ripple to be correlated over different stations.)

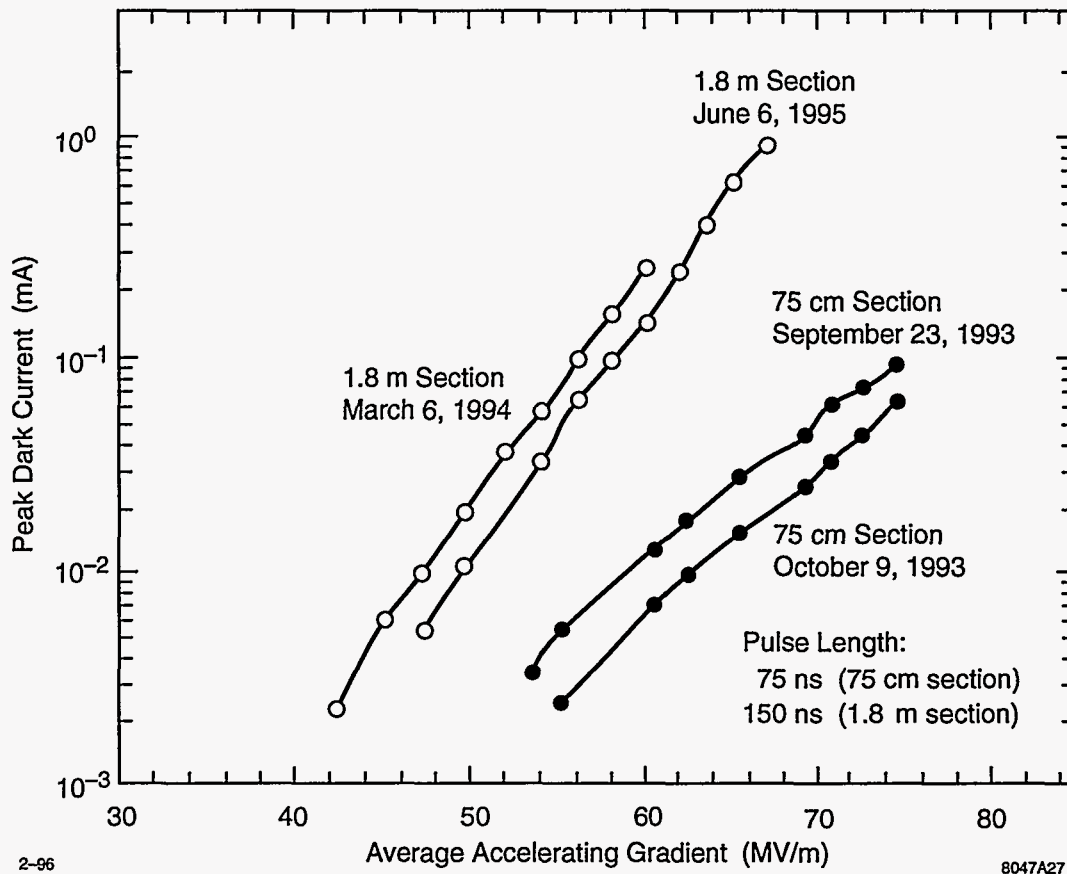


Figure 8-17. Dark current as a function of average accelerating field for the 75-cm constant-impedance structure and 1.8-m detuned structure.

RF Phase Variations

We considered the effect of rf phase ripple superimposed on the incoming 11.424-GHz rf pulse in the preceding chapter, where we assumed that the ripple is a cosine wave with a given period (in nanoseconds) and amplitude (in degrees at the rf frequency). For convenience, we summarize here the resulting tolerance on phase ripple as a function of ripple time scale, in order to meet given energy and energy spread tolerances on the beam pulse, consisting of a train of 90 point-like bunches. Here the tolerances on the multibunch energy spread and on the variation in the average energy of the beam have both been taken to be about $\Delta E/E \sim 10^{-3}$.

We take the tolerance on the rms fractional bunch-to-bunch energy spread to be 0.1%. As noted above, we ignore the contribution from the intrabunch spread, which would add about another 0.1% to the spread. We also take the tolerance on the energy centroid shift to be $\pm 0.1\%$. Figure 8-18 (a) shows the approximate tolerance on the rf phase ripple as a function of the period of the ripple, to meet the tolerance on the rms energy spread. Figure 8-18 (b) shows the approximate tolerance on the rf phase ripple as a function of the period of the ripple, to meet the tolerance on the centroid energy shift. The tolerances in the middle of the range of ripple timescales are approximate since they are somewhat dependent on the phase of the ripple with respect to the beam; we have recorded the most conservative values obtained in simulations.

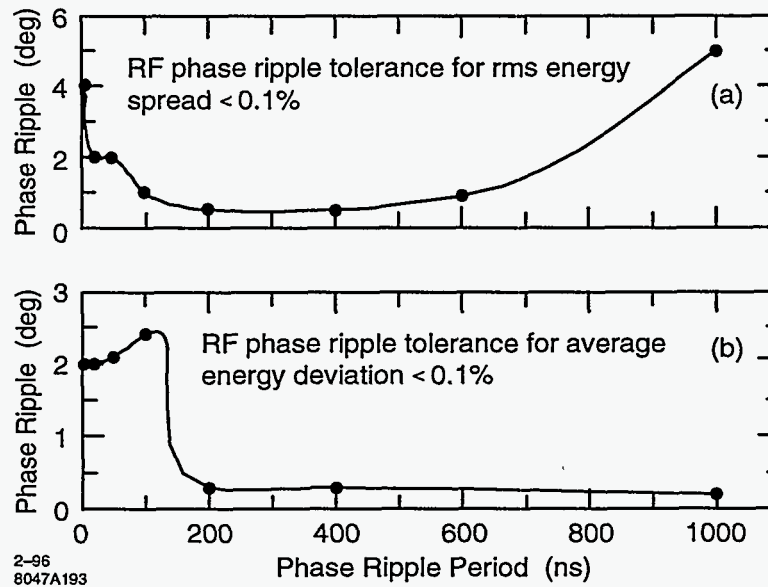


Figure 8-18. (a) Tolerance on the rf phase ripple as a function of the period of the ripple, to meet a tolerance of 0.1% on the rms energy spread. (b) Tolerance on the rf phase ripple as a function of the period of the ripple, to meet a tolerance of 0.1% on the centroid energy shift.

RF Field-Amplitude Variations

In Chapter 7 we also considered the effect of ripple in the amplitude of the incoming rf pulse, supposing that the ripple is a cosine wave with given period (in nanoseconds) and amplitude (in megavolts).

Figure 8-19 (a) shows the approximate tolerance on the rf field-amplitude ripple as a function of the period of the ripple, to meet the 0.1% tolerance on the rms energy spread. Figure 8-19 (b) shows the approximate tolerance on the rf field-amplitude ripple as a function of the period of the ripple, to meet the $\pm 0.1\%$ tolerance on the centroid energy shift. Again these are rough estimates, especially in the middle of the range of ripple time scales, since they are somewhat dependent on the phase of the ripple with respect to the beam.

8.2.9 NLC Test Accelerator Experiments

The goal of the NLCTA experimental program is to measure the performance characteristics of the multi-section X-band linac and high-power rf systems. The experiments will go beyond the work with single power sources and structures at the Accelerator Structure Test Area (ASTA) in the Klystron Test Laboratory; the NLCTA beam will be much more intense, will be much better defined, and will be more precisely analyzed, both before and after acceleration. In addition to system operations tests, beam-dynamics studies will be done using three types of bunch trains: a short bunch train of a few nanoseconds will be used to measure the unloaded energy-gain characteristics of the linac, a variable-length bunch train will be used to measure field-emission currents in the linac with and without injected beam, and the nominal 125-ns-long bunch train will be used to test multibunch beam-loading compensation. The specifics of these experiments are discussed in the following sections, concluded by a discussion of other types of wakefield studies that will be

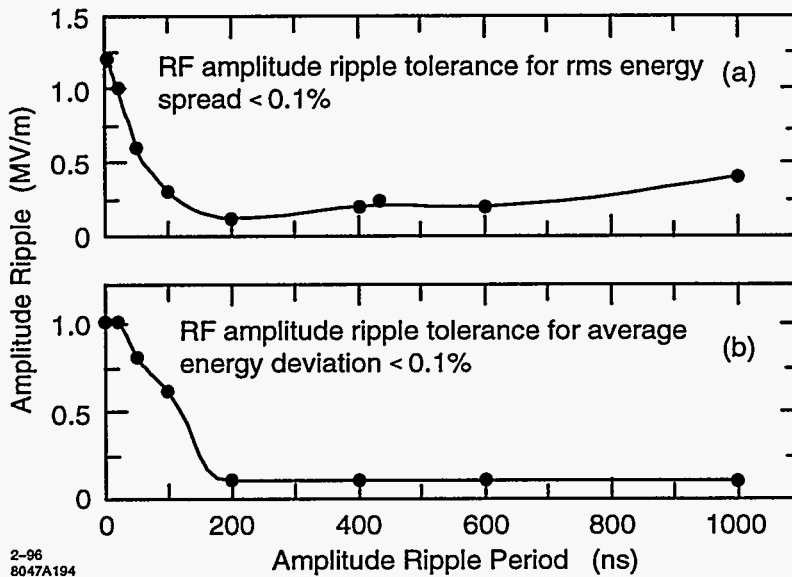


Figure 8-19. (a) Tolerance on the rf field-amplitude ripple as a function of the period of the ripple, to meet tolerance of 0.1% on the rms energy spread. (b) Tolerance on the rf field-amplitude ripple as a function of the period of the ripple, to meet tolerance of 0.1% on the centroid energy shift.

made possible by upgrading the NLCTA injector. An important part of the NLCTA experimental program, of great relevance for the NLC, is the commissioning of the multibunch beam instrumentation.

System Studies

The NLCTA rf system was designed to be large enough in scale, with four klystrons powering eight structures through SLED-II rf pulse compressors, that it will serve to test system control and monitoring methods applicable to NLC-scale linacs. A key component of the monitoring system will be instrumentation that can detect and digitize the phase and amplitude envelopes of the 250-ns-long rf pulses. This waveform system, which will be based on commercially available high-speed waveform digitizers, is intended to resolve 0.1% amplitude and 0.1° phase variations on time-scales longer than a few nanoseconds. The data acquisition will be controlled by local microprocessors, one of which will be assigned to each rf station, in order to permit parallel, high-level processing of the data.

We plan to monitor the transmitted and reflected rf pulses at many points along the route between each klystron and its associated accelerator structures. There will be two waveform digitizers per rf station, into which the rf phase and amplitude signals from the monitor points can be multiplexed. In this way, correlations between any two signals can be examined. An important function of the monitoring system will be to characterize the stability of the rf pulses. For this purpose, the signals will be analyzed in two basic ways. To characterize the short-term stability of some aspect of the waveform, a few hundred consecutive pulses will be sampled and analyzed. To monitor long-term stability, a sample will be taken every few minutes and stored in history buffers.

Unloaded Energy Gain

To measure the unloaded energy gain characteristics of the linac, only one klystron will be run at a time. A short bunch train, which makes the beam loading negligible, will be used to simplify the measurement. The energy gain of the bunch train depends on the rf waveform entering the two energized structures, on the rf transmission properties of the structures, and on any field emission (or breakdown) that occurs in the structures. The rf transmission properties of the structures have been computed so that, from a measurement of the input rf waveform, one can predict how the ideal energy gain should vary as a function of the transit time of the bunch train relative to the rf pulse. By comparing this calculation to measurements done at low rf-power levels, we will test our theoretical understanding of the rf transmission properties of the accelerator sections. By comparing low- and high-power measurements, we will look for effects from possible field emission within the structures. Checks for field emission will also be made by observing the energy-gain stability at a fixed transit time for different rf power levels.

Linac Field-Emission Current

In addition to over-loading individual structures, there is a concern that field emission currents will be accelerated sufficiently to be captured by the accelerating wave and transported in an NLC-like linac. To investigate this possibility, and to provide more data on field-emission activity in the structures, the NLCTA linac will be instrumented with two types of detectors. An extended scintillation counter will be placed alongside each of the structures to provide a measure of the expelled (uncaptured) field-emission current, and toroids will be installed in the beam line at the beginning, middle, and end of the linac to measure the transported current. The time-resolution of the scintillation counters will be approximately 20 ns. The time-resolution of the toroids will be approximately 1 ns.

With the beam off, we will measure the expelled and transported current signals as functions of the rf power and of the strengths of the intervening quadrupole and dipole magnetic fields. With a strong dipole field, any wall monitor currents should be due only to field emission in the structure immediately upstream. By observing the change in the currents with no dipole field, but with different-strength quadrupole configurations, we will characterize the transport of field-emission current in the linac. Although the quadrupole field strengths available in the NLCTA will not be as great as the strengths that will be used in an NLC main linac, we believe that they will be sufficient to fully suppress the transport of the field-emission current. Studies will also be done to measure how much of the field-emission activity is associated with the presence of the beam by varying the length of the bunch train and observing the change in the time-structure of the monitor signals.

Multibunch Beam-Loading Compensation

One of the goals of the NLCTA is to demonstrate that multibunch beam-loading compensation can be readily maintained at the 0.1% level for a beam current yielding a steady-state loading of 25%. To achieve the compensation, the shape and/or timing of the rf pulses will be adjusted so that the resulting change in unloaded energy gain along the bunch train offsets the energy loss from the loading. Demonstrating compensation at the 0.1% level will require careful preparation of the bunch train so as not to generate other sources of bunch-to-bunch energy differences. The bunch train injected into the linac will be checked for tolerances on the uniformity of bunch energy, intensity, and spacing. To measure the degree of compensation, the bunch train will be analyzed in the spectrometer using a vertical kicker magnet, which will spread the bunches on a screen. From the measurements of the rf waveform entering the structures, and from our

theoretical understanding of the rf transmission through the structures we should be able to predict the gross features of the bunch-to-bunch energy differences that are observed.

The method for shaping the rf waveforms will be to modulate the phase of the rf drive to the klystrons, prior to SLED-II pulse compression. Maintaining the stability of the rf pulses may require feedback which should be relatively straightforward to implement in the rf control system of the NLCTA.

Transverse Components of the Accelerating Field

The tolerances on the allowable transverse components of the accelerating field in the structures of an NLC linac are fairly tight compared to SLC standards. These tolerances differ depending on whether the transverse electric field is in-phase or 90° out of phase with the bunches, and on whether the field jitters from pulse to pulse or is static. In the NLCTA, we will be able to measure transverse electric-field components with resolution on the order of, or smaller, than the NLC tolerances.

The basic approach in these measurements is to vary the phase of one klystron at a time and to record the change in the bunch trajectories using the BPMs downstream from the associated pair of structures. Fitting the amplitudes of the observed betatron oscillations to a sinusoidal function of the klystron phase will yield the in-phase and out-of-phase static components of the accelerating field. To measure the jitter in these components, the pulse-to-pulse rms variation of the induced betatron motion will be computed with the klystron on and off, and at the in-phase and out-of-phase settings.

To obtain accurate results will require special attention to how the data are taken. A short bunch train will be used, only one linac klystron will be powered at a time, and the quadrupoles will be turned off downstream of the associated structures so that bunch energy changes do not produce trajectory changes. The measured outgoing trajectory will be corrected pulse-to-pulse to account for any changes in the incoming trajectory. This correction will be based on the trajectory fit to the BPM data in the region between the center of the chicane and the structures being powered. With this procedure, a resolution of about 0.2keV in the transverse accelerating field should be achieved.

The out-of-phase component of the transverse field, which will degrade the bunch emittance in the NLC due to the differential kick it produces along the length of the bunch, should be less than 1 keV to keep the emittance growth below 10%. Therefore both static and jitter components of this magnitude should be discernible in the NLCTA. Jitter in the in-phase component of the transverse field will also lead to emittance growth in the NLC, as a result of the dispersion it generates. The tolerance for a 10% growth is much smaller, about 0.2keV, so we will not be able to put tight limits on the NLC emittance growth from this mechanism if indeed no jitter is observed.

A static in-phase component of the transverse field is fairly benign since its effect can be offset with a dipole magnet. Coupled with jitter in the energy gain, however, it also contributes to the emittance growth in the same manner as in-phase jitter. A 1% jitter in energy gain, which is reasonable for the klystrons being developed, yields a tolerance 100 times larger, or 20 keV, on the static in-phase component. Our resolution for measuring this component is also much larger since an absolute measure of the bunch angular trajectories relative to the structure axes is needed to correct the measurement for the transverse field component due to off-angle trajectories. For this correction, we will rely on the absolute BPM calibration and on the BPM alignment to the structure axes, each of which will be known to about $100 \mu\text{m}$. These errors translate into a 10-keV uncertainty in the static field strength so, again, the measurement resolution is near the tolerance.

Transverse Multibunch Beam Breakup

The NLCTA (like the NLC) would not operate stably if conventional constant-impedance accelerator structures were used. In both cases the offset of the bunches would be amplified by many orders of magnitude by the end of the linac. The detuned structures for the NLCTA will eliminate this blowup. This will be tested experimentally using the straight-ahead line of the spectrometer and the vertical kicker magnet.

Using corrector magnets in the chicane, the bunch train will be launched into the linac with a horizontal position or angle offset. The resulting positions of the bunches exiting the linac will be measured using a profile monitor in the straight-ahead line of the spectrometer in conjunction with the vertical kicker. This will allow us to distinguish the bunches along the train by their vertical offset while observing the amplification of the initial horizontal betatron amplitude.

Studies with an Upgraded NLCTA Injector

There are a number of NLC linac beam-dynamics issues which cannot be readily addressed with the NLCTA as designed. The small bunch intensity produced by the X-band injector makes single-bunch longitudinal- and transverse-wakefield effects too small to be measured easily. Also, the small bunch spacing makes it extremely difficult to accurately measure the strength of the long-range transverse wakefield from its effect on betatron motion. We plan to upgrade the NLCTA injector in the future to produce NLC-like bunch trains with 0.75×10^{10} electrons per bunch and 1.4-ns bunch spacing. If a photocathode rf gun is used, we may be able to produce an adjustable-length bunch train (from 1 to 100 bunches) with a fairly small normalized (invariant) emittance ($\epsilon_n < 10^{-5}$ m-rad) and NLC-like bunch lengths (100 μm after compression).

With such an injector operating in a single-bunch mode, the mean energy of the bunch in the spectrometer would be measured as a function of bunch intensity to infer the short-range longitudinal wakefield strength. The size of this quantity is of particular interest since it has some theoretical uncertainty for such short bunches. Similarly, the strength of the short-range transverse wakefield would be inferred by measuring the change in the transverse bunch profile, using the wire scanner before the spectrometer bend, as a function of bunch intensity and betatron amplitude in the linac. To study the long-range transverse wakefields, a long bunch train would be used and the effects of the wakefields on the betatron motion of the bunches in the linac would be measured.

Until a new injector is built, some of these issues will be addressed with the Accelerator Structure SET-up (ASSET) facility at the SLC. (See Section 8.2.10.)

8.2.10 ASSET Measurements

To test the suppression of the transverse wakefields in the proposed NLC accelerator structures, a new facility has been incorporated into the SLC. This facility, the Accelerator Structure SETup (ASSET) [Adolphsen 1992] [Adolphsen 1995a], takes advantage of the low-emittance e^+ and e^- bunches that can be produced in the SLC, with individual control of the two bunch intensities and relative timing. Using the e^+ bunch as a probe, and the e^- bunch as a witness, the wakefields can be measured over an interbunch separation from zero to several hundred nanoseconds, with the sensitivity that is needed to verify the wakefield suppression required in the NLC.

The layout of ASSET is shown in Figure 8-20. One of the 3-m-long S-band accelerating sections has been removed from the SLC, and the X-band structure to be tested is inserted in its place, followed by

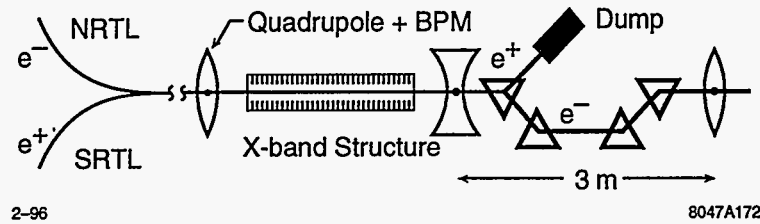


Figure 8-20. Layout of the ASSET facility in the SLC.

a combination of a beam dump (for the e^+ probe bunch) and chicane (for the e^- witness bunch). The wakefield kick from the probe bunch is determined from the betatron oscillations it induces on the witness bunch.

Measurements of the wakefield amplitude in a 1.8-m-long detuned X-band structure are shown (points) in Figure 8-21, along with theoretical predictions of the amplitude (solid curves), with and without cell frequency errors included. The fractional frequency errors have an rms of 1.5×10^{-4} . The agreement, when frequency errors are included, is reasonably good, although the wake is somewhat more suppressed at long distances than was predicted by the equivalent circuit model, assuming Q values of 6500 for the lowest-dipole deflecting mode.

Measurements of the wakefield in the DDS will be made using ASSET when the first prototype DDS becomes available.

8.2.11 Use of Beam-Excited Modes to Monitor Alignment of Structures

Each dipole mode in the DDS (as well as the structure with detuning alone) is localized in a particular region of the structure, depending on the mode's frequency and where that frequency is cut off in the structure. Thus it is proposed to pick up the frequency of two modes, one localized near each end of the structure, and use them to measure the alignment of the structure with respect to the beam.

The desired dynamic range for the detection of position offsets in such a system is large—from about a millimeter down to a micron. Details on the design of such structure beam position monitors are given in Section 7.10.3.

8.3 RF Pulse Compression and Power Transmission

This section describes the use of rf pulse compression to multiply peak power in the NLC linac high-power rf system. The 1.2- μ s-long X-band klystron pulses will be compressed by a factor of five—to 0.24 μ s—using the SLED-II rf pulse compression technique [Wilson 1990]. SLED-II is a modification of SLED [Farkas 1974]. SLED is used to increase the rf power into the 60-GeV SLAC linac by a factor of about 3. In this section, we discuss the performance required, present a physical layout, and analyze its efficiency.

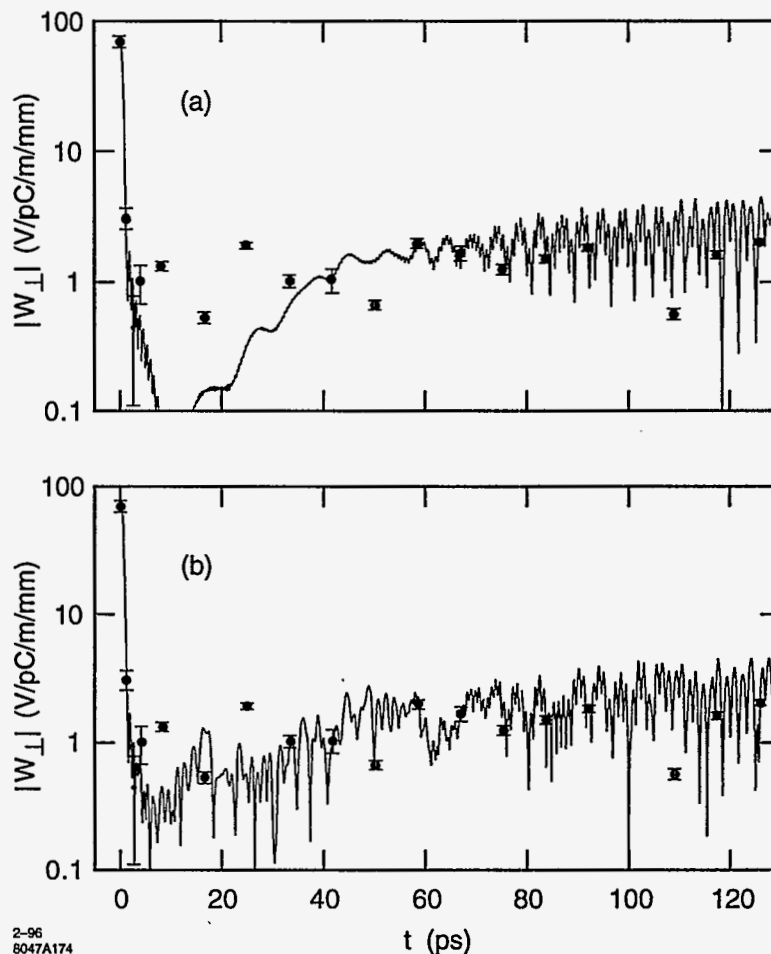


Figure 8-21. Dipole wakefield amplitude measurements and prediction from equivalent circuit model (a) without cell frequency errors and (b) with 1.5×10^{-4} rms fractional frequency errors.

8.3.1 Performance

A SLED-II pulse compressor works by storing microwave energy in a pair of high- Q resonant delay lines for most of the duration of the klystron pulse. The round-trip transit time of the rf in the delay lines determines the duration of the compressed pulse. The SLED-II microwave network is shown schematically in Figure 8-22. The delay lines are coupled to input and output waveguides by a four-port 3-dB coupler (such as a "Magic T"). In normal operation with a pulse-compression ratio of five, the delay lines are filled with microwave energy for four round-trip-delay times. The microwave energy stored in the delay lines is discharged by reversing the phase of the drive power to the klystron. The stored energy then is discharged through the fourth port of the 3-dB coupler, where it combines constructively with power still coming from the klystron, forming the compressed, high-power pulse.

To achieve low losses, oversized circular waveguide, propagating the TE_{01} mode, has been used for delay lines in SLED-II prototypes. Delay-line quality (Q) factors between 4.3×10^5 and 1.0×10^6 have been achieved [Tantawi 1995a, Tantawi 1996]. Converting between the TE_{01} circular-waveguide mode and

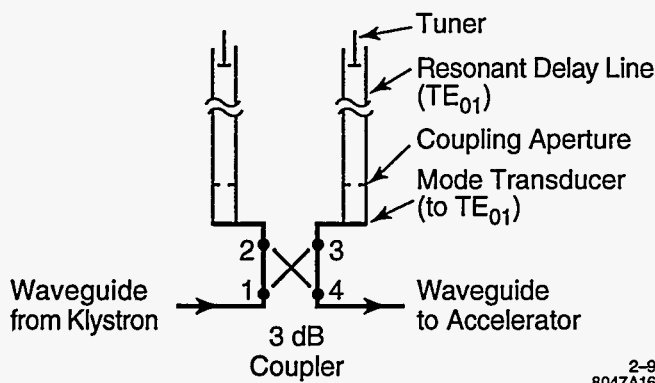


Figure 8-22. Microwave network of a SLED-II pulse compressor.

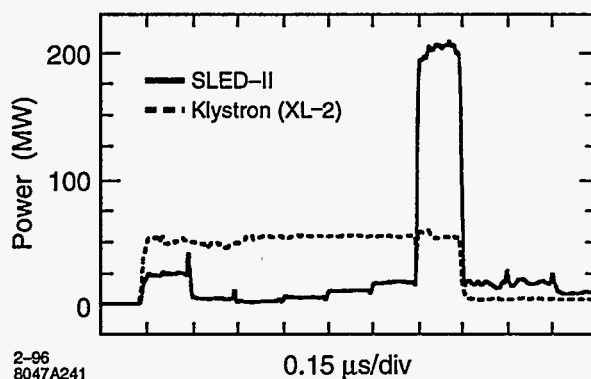


Figure 8-23. Demonstrated performance of a prototype high-power SLED-II pulse compressor.

the TE_{10} rectangular-waveguide mode has been performed by compact, flower-petal type, low-loss mode transducers (see below) [Lanciani 1953, Hoag 1993, Tantawi 1993]. Figure 8-23 shows the demonstrated performance of a prototype high-power SLED-II pulse compressor at SLAC. The small variations on top of the compressed pulse are not a property of the SLED-II pulse compressor, as demonstrated by low-power testing that produced a flat pulse [Tantawi 1995a], but are due to mode impurities in the transmission line from the klystron to the pulse compressor. The design of the mode transducer has been modified, to better suppress mode impurities in the oversized TE_{01} waveguide, by adding a choke for TE_{41} and a pair of interacting chokes for TE_{11} and TM_{11} [Tantawi 1995b]. The effectiveness of this modification has already been demonstrated in a low-power “cold test” of the new mode-transducer design.

In general, there is a trade-off between the peak-power gain achieved by pulse compression, and the efficiency of the pulse compressor. For SLED and SLED-II pulse-compression systems, the trade-off is shown in Figure 8-24 [Wilson 1992]. The intrinsic inefficiency of SLED-type pulse compressors results from the inability of a SLED energy storage cavity, or a SLED-II resonant delay line, to charge or discharge completely, in a finite amount of time, through the coupling aperture that is shown schematically in Figure 8-22. A SLED-II pulse compressor with a compression ratio of five has a maximum (intrinsic) efficiency of 80.4%, which is achieved when the voltage-reflection coefficient of the coupling aperture is 0.651. (Hence, 0.651^2 , or 42% of the power incident on SLED-II is reflected at the beginning of the klystron pulse.)

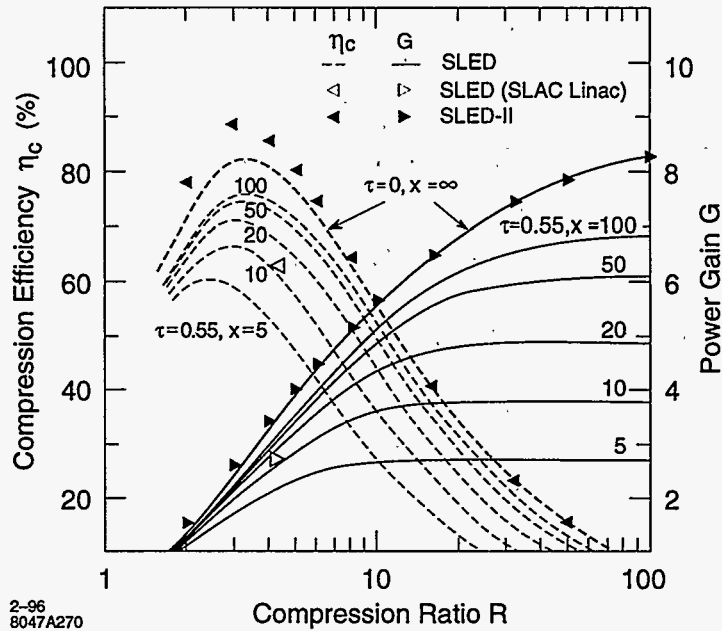


Figure 8-24. Power gain (solid curves) and compression efficiency (dashed curves) for a SLED-II rf pulse compressor driving an accelerator structure with τ and x as indicated. τ is the voltage attenuation parameter (nepers) for the structure. x is the unloaded time constant of the pulse-compression energy-storage cavities ($2Q/\omega$) normalized to the structure filling time. The top curves show gain and efficiency for SLED as implemented for the SLAC linac. The solid triangular points are for a SLED-II system with lossless components.

The net peak-power gain is the product of the pulse-compression ratio (5), the intrinsic efficiency of the pulse compressor (0.804), and the cumulative efficiency of all of the waveguides and other microwave components in the pulse compressor and transmission lines. The minimum peak power gain required to achieve the NLC-design accelerating gradient is 3.6. Therefore, the cumulative losses that occur due to finite conductivity and mode conversion in the entire system must be limited to 10% to achieve the desired power gain product:

$$5(0.804)(1 - 0.10) = 3.6 \quad (8.20)$$

Developmental SLED-II systems have been tested at SLAC with high-power X-band klystrons to validate the design and its components [Nantista 1993, Vliks 1993, Wang 1994]. The peak power and efficiency needed for the NLCTA have been demonstrated in a prototype system. Further validation of the SLED-II design at the higher power levels and efficiencies needed for the NLC will be performed in upgrades to the NLCTA. Table 8-7 summarizes the performance of the SLED-II prototype and the plans for using SLED-II in the NLCTA and in the NLC. The rf pulse compression systems in the NLC and NLCTA are designed to accommodate future upgrades in which the peak rf power is nearly tripled, by replacing each 50-MW klystron with a pair of 75-MW klystrons, as indicated in Table 8-7.

	Prototype 3/95 ^a	NLCTA Design	NLCTA Upgrade	NLC Design	NLC Upgrade
Klystron pulse width	1.05 μ s	1.5 μ s	1.5 μ s	1.2 μ s	1.1 μ s
Compressed pulse width	0.15 μ s	0.25 μ s	0.25 μ s	0.24 μ s	0.22 μ s
Compression ratio	7	6	6	5	5
Klystron peak power	55 MW	50 MW	4×(50–75) MW	2 × 50 MW	4 × 75 MW
Intrinsic efficiency of SLED-II without losses ^b	0.692	0.746	0.746	0.804	0.804
Efficiency of SLED-II components	0.92	0.90	0.90	0.95	0.95
SLED-II gain (Max. possible)	4.42 (4.82) ^c	4.0 (4.48)	4.0 (4.48)	3.8 (4.02)	3.8 (4.02)
Efficiency of transmission lines	0.84	0.90	0.90	0.95	0.95
Transmitted power	205 MW	180 MW	720–1080 MW	360 MW	1080 MW
Net power gain	3.7	3.6	3.6	3.6	3.6

^a Achieved.

^b Assumes the delay-line reflection coefficient is optimized for the stated compression ratio.

^c The delay-line reflection coefficient was optimized for a compression ratio of 8 in the prototype test.

Table 8-7. Performance of SLED-II rf pulse compressors.

8.3.2 Physical Layout

Figure 8-25 illustrates the physical layout of the waveguide network for rf pulse compression and power transmission to four 1.8-m-long linac sections for the two-tunnel (“SLAC-type”) configuration shown in Figure 7-11.

To achieve low rf power losses, oversized circular waveguides will be used for the SLED-II delay lines, and for the high-power transmission lines. The TE₀₁ mode will be propagated in the circular waveguides that comprise the delay lines, in the transmission lines from the klystrons to the power combiners, and in the transmission lines from the klystron gallery to the linac tunnel. The waveguide diameters that have been chosen to avoid spurious-mode cut-offs near the operating frequency are 4.75 in (WC475) for the delay lines and 2.93 in (WC293) for the transmission lines from the klystrons. The HE₁₁ “hybrid” mode will be propagated in flexible corrugated circular waveguides of approximately two-inch inner diameter that distribute power to the four accelerator sections powered by each SLED-II pulse compressor.

Rectangular waveguides, propagating the TE₁₀ mode, also will be used in parts of the transmission system. The rectangular waveguide sizes that have been chosen are WR100 (1.0 in × 0.5 in) and oversize WR100 (1.0 in × 0.9 in).

Conversion between the TE₀₁ circular-waveguide mode and the TE₁₀ rectangular-waveguide mode will be performed by compact, flower-petal type, low-loss mode transducers [Lanciani 1953, Hoag 1993, Tantawi 1993]. Transducers of this type, shown in Figure 8-26 have been analyzed, measured, and used extensively at SLAC.

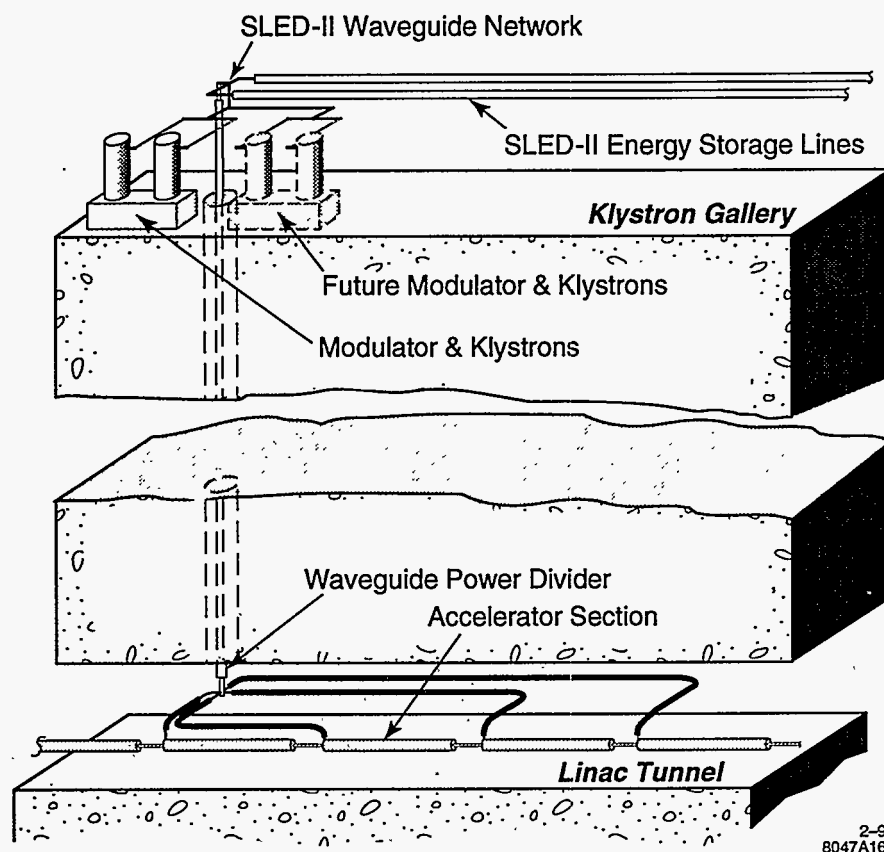
2-96
8047A166

Figure 8-25. Physical layout of the waveguide network for rf pulse compression and power transmission.

The four-way power splitter that will divide the compressed rf pulses into four equal parts has been designed by computer simulation [Kroll 1995], but the design has not yet been manufactured and tested. The four-way splitter is shown in Figure 8-25; an enlarged view is shown in Figure 8-27. The device accepts the TE_{01} circular-waveguide mode, and divides the power equally into four TE_{10} -mode rectangular waveguides.

Matching the HE_{11} "hybrid" mode in corrugated circular waveguide to the TE_{10} mode in rectangular waveguide may be performed by relatively simple tapers, since the two modes have essentially the same character.

The waveguide layout is sufficiently flexible to absorb the absolute motion of the accelerator sections due to their mechanical movers (± 1 mm) and the relative motion between the klystron gallery and the accelerator tunnel due to settling (± 10 mm).

The SLED-II waveguide networks are located in the low-radiation environment of the klystron gallery so that the rf pulse-compression system may be modified, station by station, if necessary for upgrade to higher beam energies, simultaneously with colliding beam operations.

Since the round-trip delay time in the 4.75-in-diameter waveguide (at the group velocity, $0.964c$) must equal the rf pulse duration ($0.24 \mu s$), the physical length of the SLED-II delay lines is 34.7 m. The physical layout can accommodate this delay-line length by spatially overlapping the delay lines from adjacent rf stations.

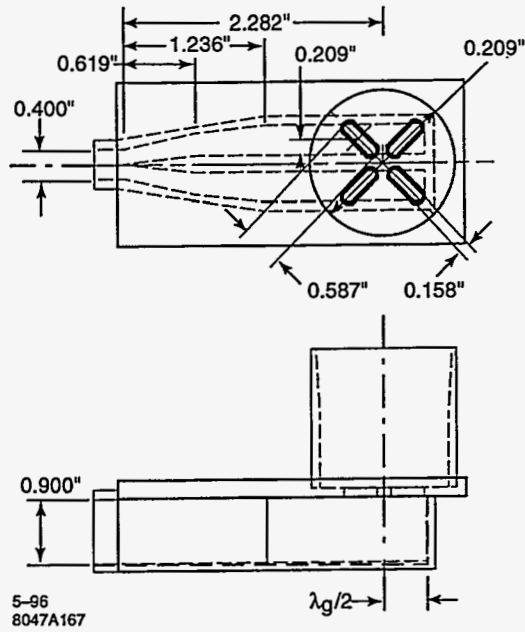


Figure 8-26. Mechanical drawing of the "flower-petal" mode transducer.

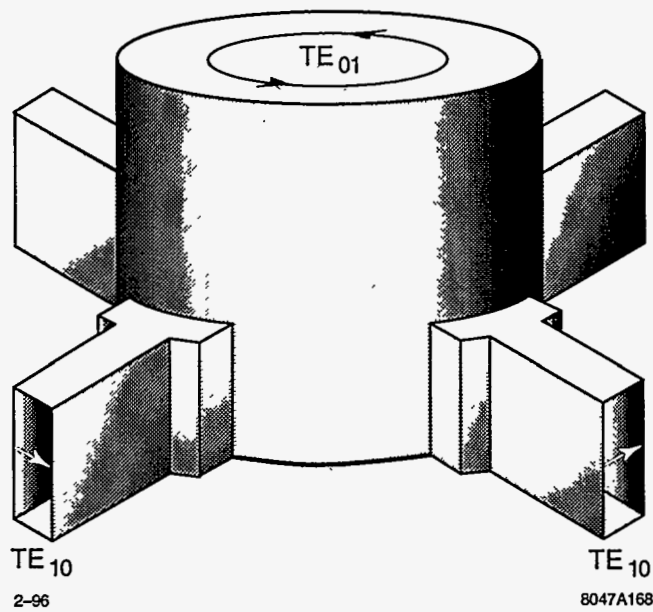


Figure 8-27. Sketch of the four-way power splitter designed by computer simulation.

Since the total length of linac fed by each rf station is approximately eight meters, each pair of delay lines will overlap parts of five other pairs of delay lines.

The alternate tunnel configuration, the semi-elliptical highway-style tunnel shown in Figure 7-12 is topologically similar to the physical layout presented above. The waveguide configurations differ only in the lengths of very low-loss oversized circular waveguides. The circular waveguide from each klystron to the power combiner is longer (3 m *vs.* 1 m) since it must pass through the shielding wall. The waveguide from the pulse compressor to the accelerator is much shorter (1 m *vs.* 10 m) since, in this configuration, the pulse compressors are in close proximity to the linac.

8.3.3 Power Losses

To realistically estimate the peak power gain of the physical layout illustrated in Figure 8-25 we have constructed a "loss budget" for the rf system based on the separate components from which the above physical layout might be assembled. The losses assumed for the individual components are based on a combination of actual experience with identical or similar devices, and theoretical estimates derated for imperfect conductivity and manufacturing tolerances.

Ohmic losses in all waveguides are assumed to exceed standard theory [Ramo 1984] by 20% to allow for imperfect conductivity and surface roughness. This has been confirmed empirically for the NLCTA's WC293 transmission lines.

The 3-dB power combiner/divider is assumed to be a WR100 "Magic T" with one-way power loss of 1%. Our experience with WR90 Magic Ts consistently has yielded losses of about 1.2%, due to a combination of ohmic loss, energy trapped in the junction, and finite reflection. Using a WR100 is expected to reduce the ohmic contribution by the ratio of ohmic losses in WR100 compared to WR90, which is 3/4.

The power loss assumed for the flower-petal-type mode transducer, 0.7%, is consistent with the measured loss of the NLCTA mode transducers.

Power losses in the four-way power splitter are assumed (in the absence of a measured prototype) to be the same as for the flower-petal-type transducer, 0.7%. Less loss is expected due to the symmetry of the device, which guarantees mode purity (in the absence of mechanical imperfections).

The loss budget for the physical layout shown in Figure 8-25 is summarized in Table 8-8. In the table, power losses and transmission fractions are tabulated for individual components and for groups of components, including the SLED-II pulse compressor, the transmission lines from the klystrons, and the transmission lines to each accelerator section. The net power gain is tabulated separately for each of the four accelerator sections. The table presents a detailed accounting of the power losses for each of the four accelerator sections. The average power transmission is 89.6%, resulting in a net power gain (averaged over the four accelerator sections) of 3.60.

For the semi-elliptical highway-style tunnel configuration shown in Figure 7-12, the waveguide configuration differs only in the lengths of very low-loss oversized circular waveguides. The loss budget and the resulting net power gain are nearly identical to those in the two-tunnel (SLAC-type) configuration.

Component	Unit	Loss (Linear)	Transmission Subtotals				Net Gain ^a	
			(Linear)	(dB)	(dB)	(Linear)	(dB)	(Linear)
Definitions of Components								
TE ₀₁ -TE ₁₀ Transducer	(each)	0.0070	0.993	-0.031				
WR100 "Magic T"	(each)	0.0100	0.990	-0.044				
WR100 (1.0" × 0.5")	(m)	0.0205	0.979	-0.090				
Oversize WR100 (1.0" × 0.9")	(m)	0.0133	0.987	-0.058				
Corrugated WC220 (HE ₁₁)	(m)	0.0011	0.9989	-0.0048				
WC293 (TE ₀₁)	(m)	0.0010	0.9990	-0.0042				
WC475 (TE ₀₁)	(m)	0.00022	0.99978	-0.00093				
Trans. Line from Klystron								
WC293 (TE ₀₁)	1.0	0.0010	0.999	-0.004	-0.137	0.969		
Mode Transducer	1	0.0070	0.993	-0.031				
Oversize WR100	0.5	0.0067	0.993	-0.029				
WR100 "Magic T" Combiner	1	0.0100	0.990	-0.044				
Oversize WR100	0.5	0.0067	0.993	-0.029				
SLED-II Pulse Compressor								
WR100 "Magic T"	2	0.0199	0.980	-0.087	-0.233	0.948		
Mode Transducer	2	0.0140	0.986	-0.061				
WC475 Delay Lines (TE ₀₁)	34.7	0.0193	0.981	-0.084				
Trans. Line to Linac Tunnel								
Mode Transducer	1	0.0070	0.993	-0.031	-0.070	0.984		
WC475 (TE ₀₁)	10	0.0021	0.998	-0.009				
Mode Transducer (4-way split)	1	0.0070	0.993	-0.031				
Trans. Line to Section #1								
WR100 Taper	0.1	0.0021	0.998	-0.009	-0.023	0.995	5.580	3.614
Corrugated WC220 (HE ₁₁)	1.0	0.0011	0.999	-0.005				
WR100 Taper	0.1	0.0021	0.998	-0.009				
Trans. Line to Section #2								
WR100 Taper	0.1	0.0021	0.998	-0.009	-0.030	0.993	5.572	3.608
Corrugated WC220 (HE ₁₁)	2.5	0.0028	0.997	-0.012				
WR100 Taper	0.1	0.0021	0.998	-0.009				
Trans. Line to Section #3								
WR100 Taper	0.1	0.0021	0.998	-0.009	-0.040	0.991	5.563	3.600
Corrugated WC220 (HE ₁₁)	4.5	0.0050	0.995	-0.022				
WR100 Taper	0.1	0.0021	0.998	-0.009				
Trans. Line to Section #4								
WR100 Taper	0.1	0.0021	0.998	-0.009	-0.049	0.989	5.553	3.592
Corrugated WC220 (HE ₁₁)	6.5	0.0072	0.993	-0.031				
WR100 Taper	0.1	0.0021	0.998	-0.009				
Average over all four sections					-0.475	0.896	5.567	3.603

^a Net gain includes SLED-II compression ratio (5) and intrinsic efficiency (0.804).

Table 8-8. Summary of the microwave power losses, power-transmission fractions, and power gains. The losses assumed for the separate components are defined in the topmost section.

8.4 High-Power Klystrons

The design of the 50-MW (X5011) klystron is the product of an ongoing development program which began at SLAC in 1988. At that time, the peak power, frequency, and pulse duration required in combination were well beyond the state of the art. As a result, rf circuit breakdown and output window failures plagued early development efforts at SLAC. Through a steady stream of improvements, the failure modes are largely under control. SLAC presently has four 50-MW solenoid-focused klystrons in operation. Three of these are suitable for use in the NLC Test Accelerator. The PPM-focused X5011 klystron, in which a periodic permanent magnet (PPM) array replaces the solenoid, is in the final stages of computer simulation, mechanical design and fabrication. Those parameters which have not yet been demonstrated have been shown to be achievable through computer simulation.

The upgrade of the NLC to 1 TeV center-of-mass energy requires a 75-MW peak power klystron. The preliminary electrical and mechanical design of this klystron, designated X7511, has been carried out. The criteria applied in the design of the 75-MW klystron were not to exceed the design limits imposed on the 50-MW klystron and, to the greatest extent possible, to stay within the gradients and stress levels demonstrated in the X5011. The upgrade is discussed in Section 8.4.3, "Upgrading Performance".

Design and performance parameters for the X5011, 50-MW X-band klystron are given in Table 8-9. Key features of the tube are identified in Figure 8-28.

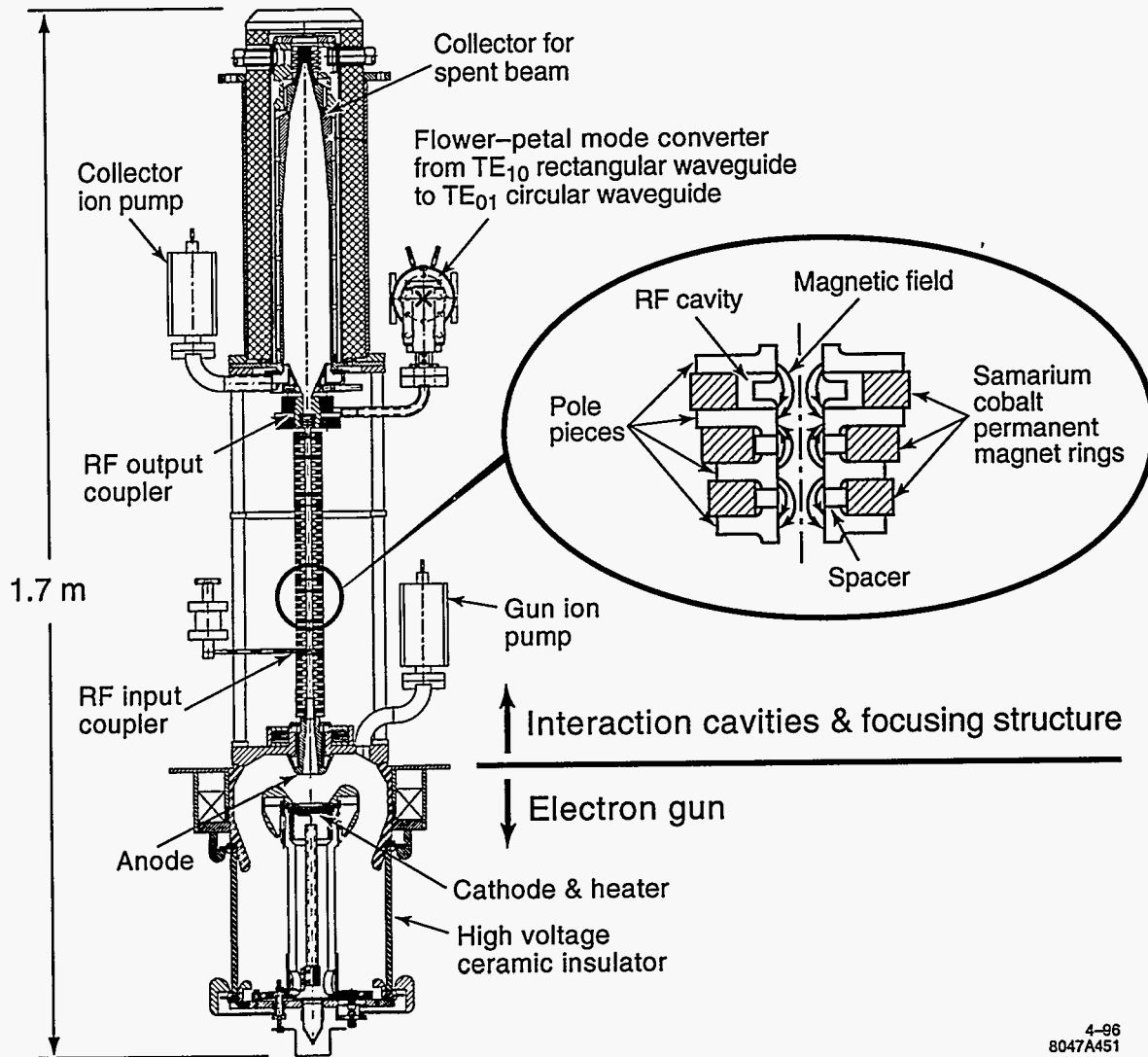
8.4.1 Design Features

Table 8-9 lists the design and performance parameters which make up the preliminary specification for the X5011 klystron. The design features and innovations which make the specification achievable are described below.

Electron Gun

Figure 8-29 shows the electrode configuration of the electron gun and the electron beam which is produced, based on the computer code EGUN. The cathode diameter (5.72 cm) is a compromise. A larger cathode would reduce the maximum voltage gradient (230 kV per cm, which is high, but acceptable), but would increase the beam area convergence (currently 144/1, also high, but achievable). The resulting cathode current density, which averages 7.4 A/cm^2 , with a peak value of 10 A/cm^2 at the cathode edge, is consistent with long cathode life. The 7.4 A/cm^2 compares with 6 A/cm^2 in the 5045 SLC klystron, which has a mean time between failures (MTBF) in excess of 40,000 hours.

Elimination of the solenoid made possible by the PPM beam focusing removes any constraint on the size of the high-voltage ceramic, which allows for conservative high voltage-seal gradients. The absence of the solenoid also makes room for an ion pump which will be used to pump the gun directly through the anode, further reducing the risk of high-voltage gun breakdown.



4-96
8047A451

Figure 8-28. Preliminary layout of the X5011 klystron, with water jacket removed. The insert shows one representative buncher cavity, to illustrate the use of oversize permanent magnets.

Parameter	Units	Value
Electrical:		
Frequency	(GHz)	11.424
Peak Power	(MW)	50
Beam Voltage	(kV)	465
Beam Current	(A)	190
Beam Microperveance	($\mu\text{A}/\text{V}^{3/2}$)	0.6
Gain	(dB)	57
Bandwidth	(MHz)	100
Beam Modulation		Cathode Pulsed
Pulse Duration	(μs)	1.20
Rep Rate	(Hz)	180
RF Efficiency	(%)	57
Cathode Current Density	(A/cm^2)	7.4
Heater Voltage	(V)	15
Heater Current	(A)	21.5
Mechanical and Magnetic:		
Beam Focusing		Periodic Permanent Magnet (PPM)
Tube Weight	(kG)	32 (without lead)
Tube Length	(m)	1.3
Cathode Diameter	(cm)	5.72
Cathode Half Angle	($^\circ$)	25
Beam Area Convergence		144

Table 8-9. Design and performance parameters for the X5011 klystron.

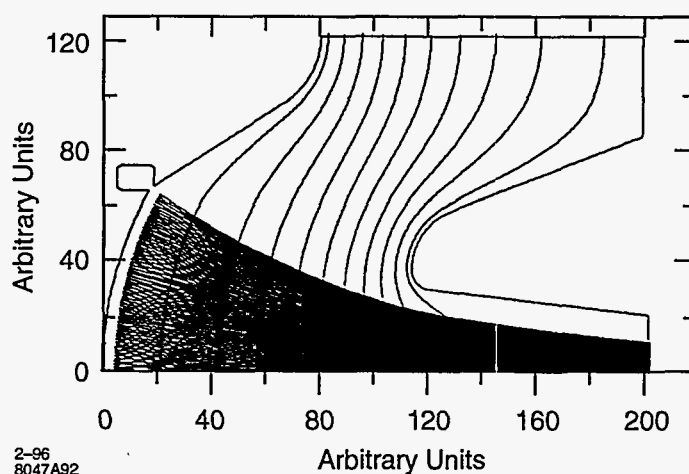


Figure 8-29. Computer printout of gun electrodes and electron beam for the X5011.

Beam Focusing

Figure 8-28 shows details of the periodic magnetic structure and magnets which supply the beam focusing magnetic field. The magnetic circuit is designed to minimize the volume of the relatively high-cost samarium cobalt ring magnets. Oversized magnets are required at the location of the gain and buncher cavities as shown. A segmented magnet is used to supply the unidirectional field for the extended interaction output circuit (not shown).

Two key features of the magnetic circuit design make it possible for the periodic magnetic field to provide focusing, with and without rf drive, which is comparable with that provided by a high field solenoid.

- **Short Magnet Period:** The periodic length of the PPM focusing structure used here is about one-half that customarily used in traveling-wave tubes, most of which are PPM focused. As a result, the stop-band voltage, the voltage below which all focusing ceases, a feature of all axially symmetric PPM focusing, occurs at about 6% of operating voltage where it does not materially worsen intercepted beam current during the pulse. By contrast, traveling-wave tubes with their longer magnet periods are forced to operate with stop-band voltage ratios of 25–50% of operating voltage.

An even more important benefit of the short magnet period is that it produces a contoured field, having an rms value at the beam tunnel wall as much as twice that on the axis, which results in a high degree of beam stiffness. The higher field at the wall is capable of focusing a beam having a current density almost four times that which can be focused on the axis.

- **Tailored Field Amplitude:** Another advantage of PPM focusing over solenoid focusing is that the field amplitude can be tailored to a much greater degree to match the known beam conditions. As the beam is bunched and charge density increases in passing through the buncher cavities, the on-axis magnetic field required to maintain optimum focusing increases. The required tailoring of the magnetic field amplitude is easily carried out by simply using either larger diameter or higher-energy product magnets in the region where a higher field is required.

Figure 8-30 is a plot of the on-axis magnetic field which has been found in computer simulation to produce the best rf performance while avoiding beam interception. Figure 8-31 is a computer simulation of the focused beam with no rf drive.

RF Circuit

Figure 8-32 shows the layout of the rf circuit cavities approximately to scale and in their correct relative positions. The circuit consists of an input plus two gain cavities, three buncher cavities, and a five-cell, disk-loaded, extended-interaction, traveling-wave output circuit. These are described in more detail below:

Gain Cavities: The input and gain cavities are tuned near synchronism for maximum gain but with enough stagger to provide the bandwidth needed to ensure proper operation of the pulse compression system.

Buncher Cavities: The three buncher cavities replace the single penultimate cavity found in most klystrons. The buncher function was split into three parts to maintain an acceptable rf surface gradient. It was discovered that this approach has the further advantage that it provides a more adiabatic bunching of the beam with a higher rf current (I_1/I_0) which enhances efficiency.

Output Circuit: For the same reason that three buncher cavities are used, it was found necessary to employ an extended interaction type of output circuit to control rf breakdown. For high efficiency, rf voltage across

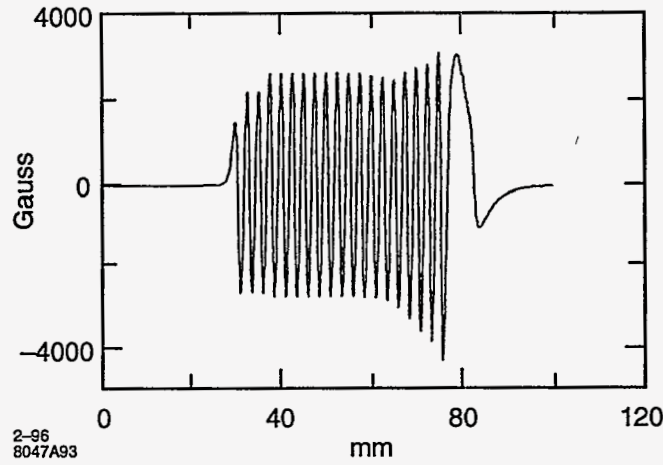


Figure 8-30. Magnetic field profile for best efficiency without beam interception.

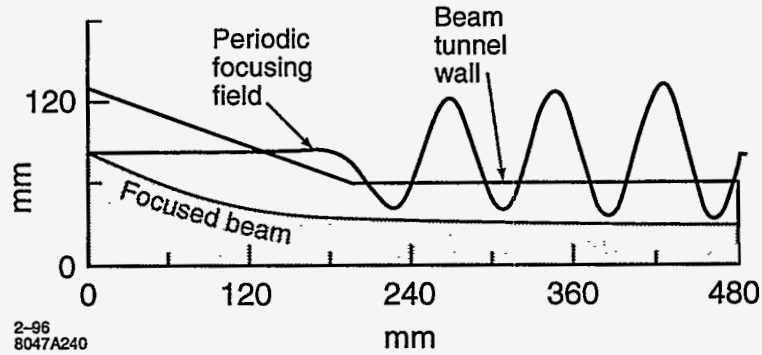


Figure 8-31. Computer simulations of X5011 PPM-focused beam in the launch region. The periodic focusing field is also shown.

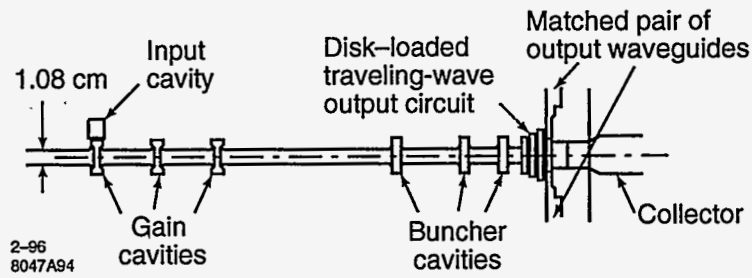


Figure 8-32. Rf circuit cavity layout, drawn approximately to scale.



Figure 8-33. Computer simulation of bunched beam passing through the X5011 disk-loaded output circuit. The vertical scale is magnified by 3 to emphasize the growth of bunch amplitude in the output circuit.

the total length of the output circuit must be comparable with the 465-kV beam voltage. The maximum surface gradient is necessarily much higher than the on-axis gradient.

The output circuit is tapered in both impedance and velocity. Tapering the impedance from cavity to cavity by a factor of about five, from highest in the first cavity to lowest in the fifth cavity, produces a nearly constant rf voltage per gap. The velocity taper ensures that the wave remains in synchronism with the slowing beam for maximum energy extraction. It is fortuitous that the impedance taper is achieved with a physical taper of the circuit, with each successive cavity disk having an increased inner diameter, as efficiency is enhanced by allowing the highly bunched beam to expand as it traverses the output circuit. The circuit taper accommodates the beam expansion, free of beam interception. The computer simulation "snapshot" of the bunched beam traversing the output circuit under saturation conditions of Figure 8-33 clearly illustrates this phenomenon. The computed efficiency in the simulation was 63%. We have derated the specification efficiency to 57%, pending hot tests. A 10% reduction in measured versus simulated performance is not uncommon.

Output Coupler and RF Window

Rf power exits the klystron and passes through a pair of symmetrically-disposed, rectangular waveguides. It is then combined in a single rectangular waveguide before being converted to the TE_{01} circular waveguide mode, using a flower-petal mode converter. The power exits the klystron through a TE_{01} disk window. Figure 8-34(a) is a sketch of the circular disk window and matching irises which complete the rf output coupling from the tube. The matching irises and quarter wavelength ceramic disk window in combination are designed to produce a traveling-wave through the ceramic disk, as opposed to the standing wave which is used in the more conventional half-wave resonant window. The advantage of the traveling wave is that the rf gradient on the window surface is half as great for a given power flow as that for the standing-wave window. The lower gradient reduces the chance of window breakdown. The advantage of coupling the power through the window in the TE_{01} mode is the total absence of rf electric field terminating on the metal wall of the waveguide, again enhancing power handling capability.

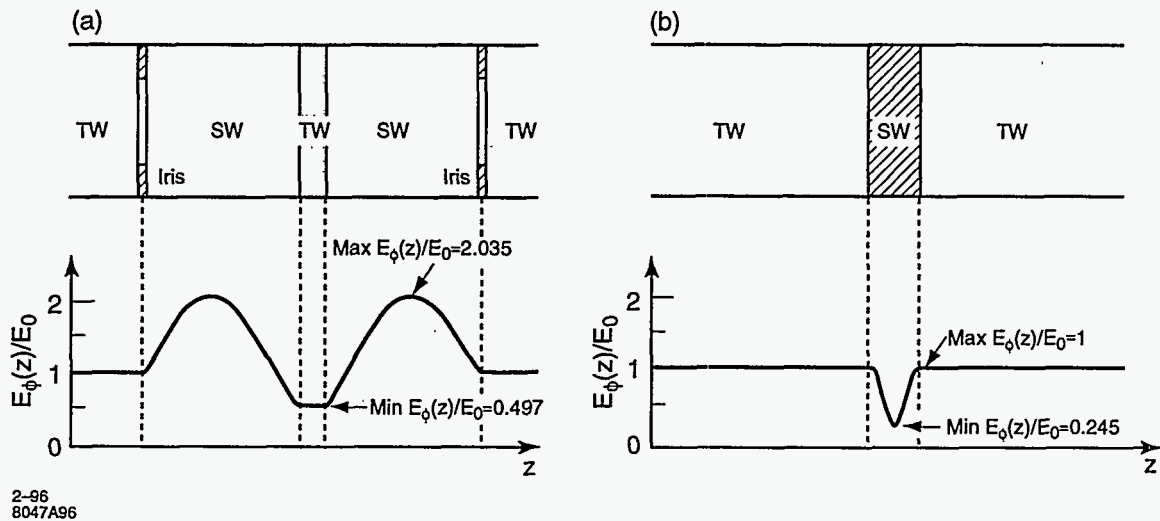


Figure 8-34. Comparison of the reduced-field TW window (a) with a half-wave resonant SW window (b), both operating in the TE_{01} circular mode. In addition to the TW version having substantially lower rf electric field at the window surface, the integrated dielectric power losses are only 23% those of the half-wave resonant window. The horizontal scale is expanded for clarity.

8.4.2 Results To Date

Status

SLAC currently has four operating 50-MW, X-band klystrons. Three of these will serve as klystrons for the NLCTA. The first of the series, XL-1, is not suitable for the NLCTA because of insufficient bandwidth. XL-2 and XL-3 operate at 50-MW peak power, at approximately 440-kV beam voltage, and at 36%–40% rf efficiency, depending upon operating settings. Preliminary testing of XL-4 has demonstrated up to 48% rf efficiency. These solenoid-focused klystrons use a micropervance 1.2 electron gun, with an input cavity, two gain cavities, and three buncher cavities. Both XL-1 and XL-2 have three-cell, disk-loaded, standing-wave, extended-interaction output circuits while the disk-loaded circuits in XL-3 and XL-4 are traveling wave. The 2.5D CONDOR computer simulation for XL-1 and XL-2 predicts a maximum efficiency of approximately 43% which yields about 10% more power than obtained experimentally. The maximum efficiency measured with XL-3 was 43% with a simulated value of 50%. XL-4 incorporates rf cavity design refinements and spurious mode suppression techniques which result in a simulated efficiency of 52% compared with the preliminary measured value of 48%.

Figure 8-35 is a pictorial overview of XL-1, including a drawing of the tube and solenoid, a table of design and performance parameters, and an oscillographic recording of beam current and rf input and output pulses.

XL-4, the most recent refinement of the solenoid-focused 50-MW klystron designs, has produced clean, stable rf pulses of 50-MW peak power for pulse durations up to $2 \mu\text{s}$, and 75-MW peak power for pulse durations up to $1.1 \mu\text{s}$. This performance exceeds the pulse durations required for the NLC design and upgrade. The 75-MW, $1.1 \mu\text{s}$ pulse is shown in Figure 8-36.

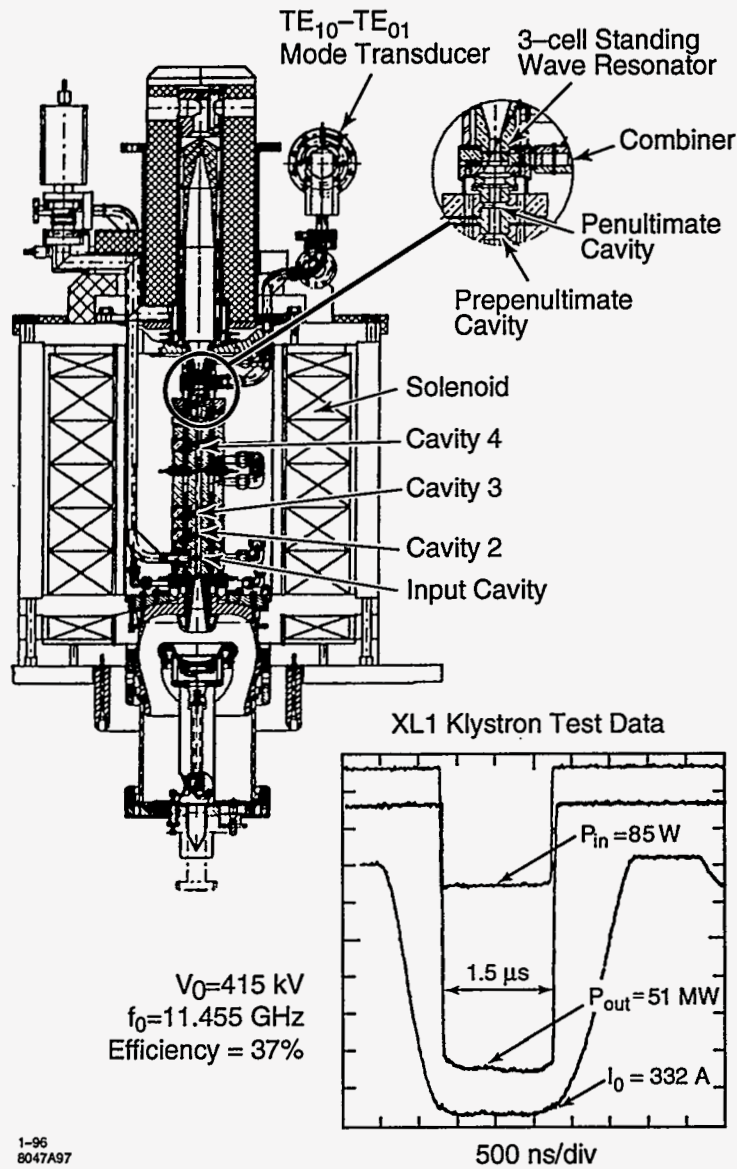


Figure 8-35. Overview of XL-1, 50-MW klystron, and high-power test results.

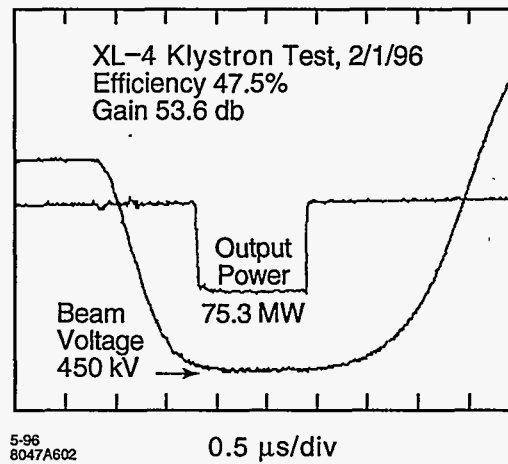


Figure 8-36. High-powered test of XL-4 klystron. Output power, 75.3-MW. Pulse duration, 1.1 μ s.

Development History

All experimental results to date are based on solenoid-focused tubes. The XL series of klystrons is the most recent. These were preceded by the XC series of eight higher current tubes (microperveance 1.8). It was the experience gained from this earlier series of tubes that narrowed the choice of rf circuits suitable for the required peak power and pulse length, and that led to gun and rf window improvements which resulted in functional, long-pulse, 50-MW klystrons. Highlights of the development history follow.

Choice of Voltage and Current. The initial objective was to achieve 100 MW of peak power at 1 μ s pulse length. It was necessary that these initial tubes match the capability of the modulators on hand at SLAC, which were limited to 440 kV. This, in turn, required high beam currents (1.8 microperveance) to obtain sufficient beam power to have a chance of producing 100 MW of peak power. The plan was to convert to higher voltage, lower current designs (for higher rf efficiency) when an appropriate modulator came online.

The choice, four years into the program, to develop 50-MW tubes for the NLCTA, made it possible to reduce the beam microperveance to 1.2 at the same 440-kV voltage with a consequent improvement in efficiency. This led to the XL tubes described earlier. In order to obtain equivalent power from PPM-focused tubes, the beam perveance needed to be reduced still further. This adjustment was imposed by the limit on the rms magnetic field obtainable from permanent magnets. The available range varies from microperveance 0.47 on the low side, dictated by the 500-kV maximum desirable beam voltage, to 0.9 on the high side, dictated by magnetic field considerations. The first PPM klystron, the X5011, described in Table 8-9, is currently in the design stage and will be tested in mid-year 1996. Computer simulations, showing up to 63% rf efficiency, have been carried out. The tube is designed to produce 50 MW of peak power at 465 kV at a microperveance of 0.6.

Rf Circuits. Figure 8-37 shows all of the rf circuit types that were tested in the XC phase of the development program. They include a conventional, single-reentrant cavity; two reentrant cavities; both inductively coupled and uncoupled; and three versions of disk-loaded (capacitively coupled) extended-interaction circuits; four- and five-cell traveling-wave and four-cell standing-wave. The single and double inductively coupled reentrant cavities were limited by rf breakdown to a pulse length of less than 200 ns.

The uncoupled reentrant cavities performed well, producing 86-MW peak power at 36% efficiency at 600 ns of pulse length. This design approach was not pursued further because of the necessity of combining the power from four output waveguides, with an uncertain impact on rf stability.

The disk-loaded, traveling-wave circuit showed the best pulse length capability at $1\ \mu\text{s}$ with 51-MW peak output power. The low measured efficiency, about 24%, also demonstrated the need for a more sophisticated design approach. This was achieved using 2.5D computer simulations which incorporated circuit tapers in both impedance and velocity. The first disk-loaded, standing-wave circuit, the four-cell XC8, exhibited a destructive zero mode oscillation which was eliminated in the subsequent XL-1 and XL-2 klystrons. The XL-1 and XL-2 use three-cell, standing-wave circuits.

One important design criterion to emerge from the XC series of the development was the need for good axial symmetry in the output circuit, including output and cavity-to-cavity coupling. All of the circuits with single-coupling slots or single (one-sided) output waveguides broke down at pulse lengths below 200 ns, in general with asymmetrical cavity damage. Symmetrical, disk-loaded cavities with two balanced output ports, and uncoupled reentrant cavity pairs with four balanced output ports performed best. It appears that field asymmetries cause beam steering which becomes destructive in much less than the required $1.5\ \mu\text{s}$.

Rf Windows. The rf window development and refinement is the most nearly complete of the major development efforts associated with the X-band klystron. The use of the traveling-wave, TE_{01} mode window as contrasted with the TE_{10} standing-wave, modified pill box window of our early X-band klystrons has had a remarkable effect on power handling capability. In the resonant ring, the traveling-wave TE_{01} windows have demonstrated the capability of transmitting 100 MW of rf power at $1.5\ \mu\text{s}$ pulse length. By contrast, breakdown in the TE_{10} mode windows has been observed at as little as 25-MW peak power at a pulse length less than half of that achieved with the TE_{01} window.

The development progression was from TE_{10} modified pill box to the TE_{01} standing-wave window, followed by the TE_{01} traveling-wave window and finally the latter window using a high-purity, isostatically-pressed window disk. Isostatically-pressed windows have yet to fail in the resonant ring, even at a peak power above 100 MW. One traveling-wave window of standard grade alumina was punctured at 100 MW. At the present time, the high-purity, isostatically-pressed window is limited by vacuum leaks through the brazed joint. This has been of sufficient concern that no isostatically-pressed window has been used in a tube. The development effort to obtain better metalizing is continuing. Meanwhile, the 100-MW maximum capability demonstrated by the standard grade alumina disk provides an adequate margin.

8.4.3 Ongoing R&D

The remaining R&D is of three types:

- Validating basic design concepts.
- Strengthening those areas where more performance margin could lead to longer life and higher reliability.
- Upgrading performance.

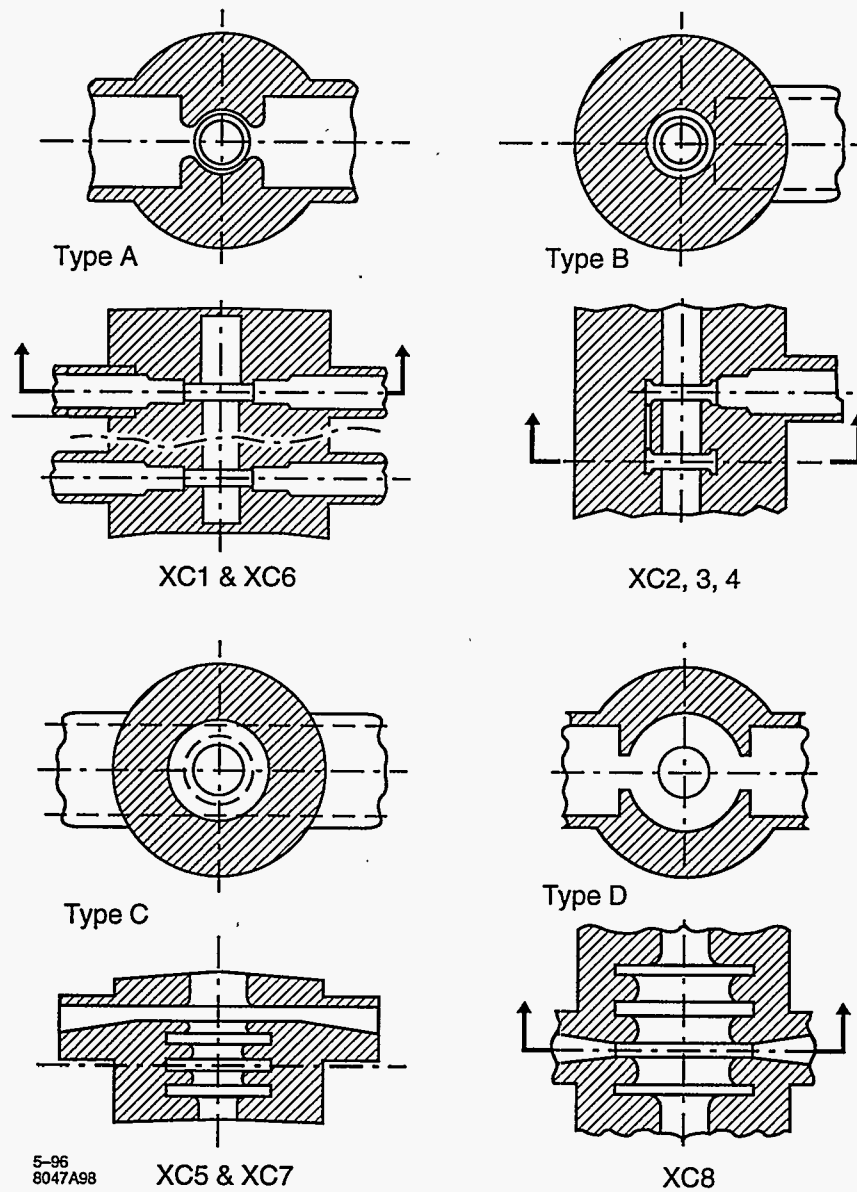


Figure 8-37. Comparison of the rf output circuit types tested on the high-current XC series of NLC klystrons.

Validating Basic Design Concepts

Disk-Loaded, Traveling-Wave Output Circuit (XL-3). At this writing (February 1996), the solenoid-focused XL-4 with the four-cell, disk-loaded output circuit, has undergone preliminary testing. In computer simulation, this circuit showed the highest rf efficiency (52%) of the XL solenoid-focused series. This compares with a measured value of 48%.

PPM Focusing. Two PPM-focused test vehicles are currently under development. The first is the beam stick pictured in Figure 8-38. It is essentially a klystron without cavities. The beam stick is being used to test DC transmission (no rf) in two modes of operation:

- Brillouin Focusing (No flux threading the cathode)
- Partially Immersed Flow (50% flux threading the cathode)

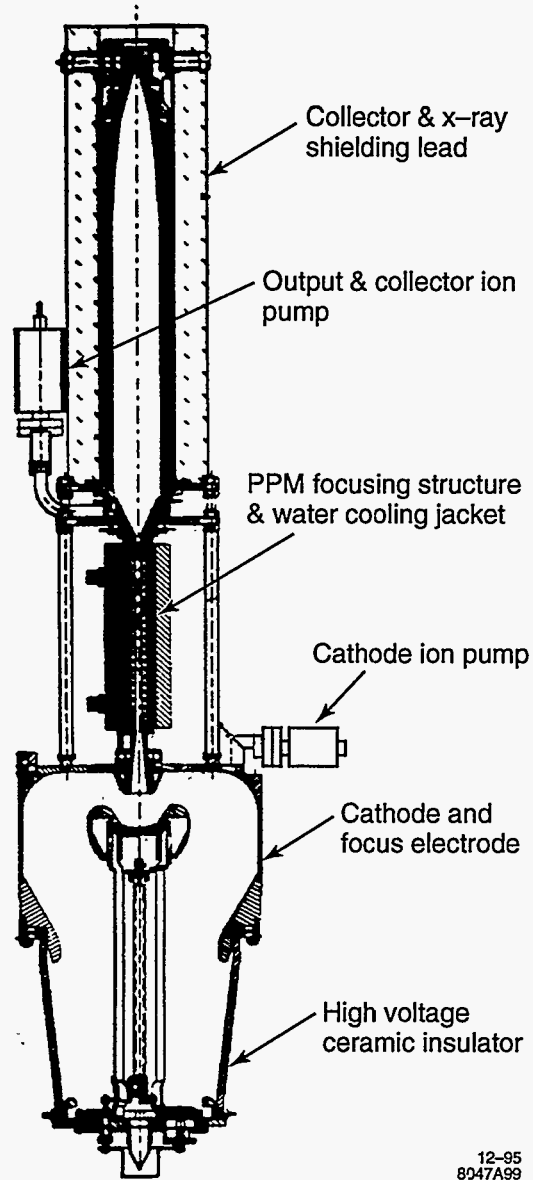
All solenoid-focused, high-power klystrons use extensive cathode immersion (up to 95%) to achieve a high degree of beam stiffness to prevent rf driven beam interception. PPM simulations to date indicate that the combination of short magnet period which produces a contoured field, and the use of a profiled field (increase in amplitude with increased bunching) make it unnecessary to use partially immersed flow to further enhance beam stiffness. Because the simulations do not take into account a possible current halo around a real beam, we have also carried out PPM-focusing simulations, and the required design modifications to achieve beam flow with 50% cathode immersion.

The second test vehicle will be the X5011 klystron, which is designed to produce 50-MW output power at 465 kV with a beam microperveance of 0.6. Computer simulations of this tube predict an efficiency of 63% and no beam interception.

Performance Margin

Output Circuit RF Voltage Hold-off. An experimental program has been launched to identify the source of rf breakdown at relatively low-surface gradient which has been observed in all X-band klystron output circuits at SLAC. The output circuit breakdown occurs at about 20% of the rf surface gradient to which SLAC accelerator structures have been successfully subjected. At the present time, it is believed that the degradation in hold-off gradient is the result of the presence of the high-current electron beam, perhaps in conjunction with the solenoidal field which is used to confine the beam. The presence of the confining magnetic field alone has been ruled out as the cause, by initial tests of a cavity in the X-band resonant ring with and without magnetic field. A series of additional cavities is being tested in the resonant ring, to determine the effect on breakdown voltage of diamond-turned surfaces and more exotic surface cleaning procedures as well as the use of both sputter coatings and alternative cavity materials such as Elkonite (tungsten-copper) and perhaps Glidcop.

Use of Internal Loss. Most high-voltage klystrons display high-frequency anomalies in the form of observable oscillations at frequencies that are capable of propagating in the beam tunnel. The degree to which these occur appears to increase with increasing beam voltage. At SLAC, they became most pronounced in the first of two recently completed 535-kV, 150-MW, S-band klystrons developed for DESY in Germany. The problem was largely eliminated by substituting lossy stainless steel for copper in the beam drift tunnel in the second klystron. Similar oscillations, which limit the range of usable operating parameters, such as beam



12-95
8047A99

Figure 8-38. PPM-focused "beam stick" which simulates the X5011 without rf drive. Transmission will be tested with and without flux through the cathode by means of separately tunable electromagnets (not shown).

voltage and focusing field were encountered in the testing of XL-3. The objective of this R&D effort is to incorporate loss in the beam tunnel for the purpose of preventing, or at least damping out, such oscillations. The simple expedient of using stainless steel has been added to XL-4 in a manner similar to that of the second DESY klystron. It is too early in the test cycle to be sure that the modification has been completely successful.

The testing of a more invasive, but potentially more effective approach is planned. The initial test-bed for these experiments is the 65-MW, 5045, S-band klystron used in the SLC at SLAC. Lossy sleeves are to be inserted in a modified 5045 klystron to determine whether there are any deleterious effects, and whether any improvement can be detected. A pair of sleeves ground from single-crystal doped silicon having a resistivity between 1 and 4 Ω -cm have been procured. Should there be no deleterious effects, the experimental tube will be placed in a nonsensitive area in the accelerator gallery where many thousands of hours of testing can be observed. In the meantime, we will proceed with testing this increased oscillation damping loss in one or more future experimental X-band tubes.

Diffusion Bonding. Diffusion bonding of the individual cavities which make up the klystrons may result in a significant reduction of manufacturing cost. Diffusion bonding is somewhat complicated in the case of the klystron because of the need to bond spacers and pole pieces which are of different materials (monel or copper for the spacers and iron for the pole pieces). These materials also have different thermal coefficients of expansion. An experimental program, intended to develop the process technology (varying temperature, pressure and time) to obtain strong, reliable, vacuum-tight bonds has been launched. Diffusion bonding of a short stack of copper spacers and copper-plated, iron pole pieces of the type to be used on the PPM test diode has been carried out. This work has already demonstrated that vacuum-tight bonds can be made using this bonding technique.

Upgrading Performance

The upgrade to 1-TeV center-of-mass energy requires a 75-MW peak power klystron. The preliminary electrical and mechanical design of the 75-MW klystron, designated X7511, has been carried out. This includes rf simulations which show 60% operating efficiency. The criteria applied in the design were not to exceed the design limits imposed on the 50-MW klystron and, to the greatest extent possible, stay within the gradients and stress levels demonstrated in the X5011.

These restrictions ruled out simply increasing the beam voltage, which would exceed the self-imposed 500-kV limit while also increasing cathode current density and electron gun gradients to unacceptable levels. To stay within the 500-kV beam voltage limit, it was necessary to increase the beam micropervance from 0.6 to 0.75. To maintain cathode current density, the cathode diameter was increased from 5.72 cm to 6.75 cm. Finally, in order to maintain a realizable cathode area convergence and stay within the capability of existing permanent magnets, it was necessary to increase the diameter of the beam tunnel from 0.95 cm to 1.08 cm.

With these changes, cathode current density and gun gradients are approximately the same for the two tubes. Also, a common set of magnets will focus both beams. Based on 2.5D computer simulations, the rf efficiency drops by only 2 percentage points from 63% to 61%. Because of the reduction in repetition rate from 180 Hz to 120 Hz and a small decrease in pulse length, the average power required of the two klystrons is the same. The margin provided by the rf output window, which has demonstrated 100-MW peak power capability, remains adequate. Table 8-10 summarizes the design and performance parameters for the X7511 PPM-focused klystron.

Parameter	Units	Value
Electrical:		
Frequency	(GHz)	11.424
Peak Power	(MW)	75
Beam Voltage	(kV)	490
Beam Current	(A)	255
Beam Microperveance	($\mu\text{A}/\text{V}^{3/2}$)	0.75
Gain	(dB)	57
Bandwidth	(MHz)	100
Beam Modulation		Cathode Pulsed
Pulse Duration	(μs)	1.0
Rep Rate	(Hz)	120 (180 for NLCTA)
RF Efficiency	(%)	60
Cathode Current Density	(A/cm ²)	7.4
Heater Voltage	(V)	15
Heater Current	(A)	27
Mechanical and Magnetic:		
Beam Focusing		Periodic Permanent Magnet (PPM)
Tube Weight	(kg)	32 (without lead)
Tube Length	(m)	1.3
Cathode Diameter	(cm)	6.75
Cathode Half Angle	($^{\circ}$)	29
Beam Area Convergence		124

Table 8-10. Design and performance parameters for the X7511 klystron.

8.4.4 Manufacturing

Because of the large numbers of klystrons required during the NLC construction phase, the cost of manufacturing and testing each tube is significant to the feasibility of the NLC project. Diffusion bonding is one example of possible cost reduction. The substitution of a low-cost oxide cathode for the present dispenser cathode is another possible cost reduction. After completion of the NLC, monthly tube replacement during operation is estimated to be at least 15 times that of the SLC. On-site production and test capability must be considered in detail. Automation of klystron construction and testing, as well as the accelerator structure construction and testing, is key to the economics of the overall project.

An "Alliance for the Advancement of Robotics Technology" (AART) has been set up among several DOE National Laboratories which seeks to foster collaborative research ties between these organizations. The AART has agreed that its first project is to study the concept of building an NLC klystron factory relying on robotic machining, cleaning, inspection, assembly, brazing, processing and testing of klystrons. With funding of the study provided by both the DOE and DOD, the work will include a complete design and cost analysis.

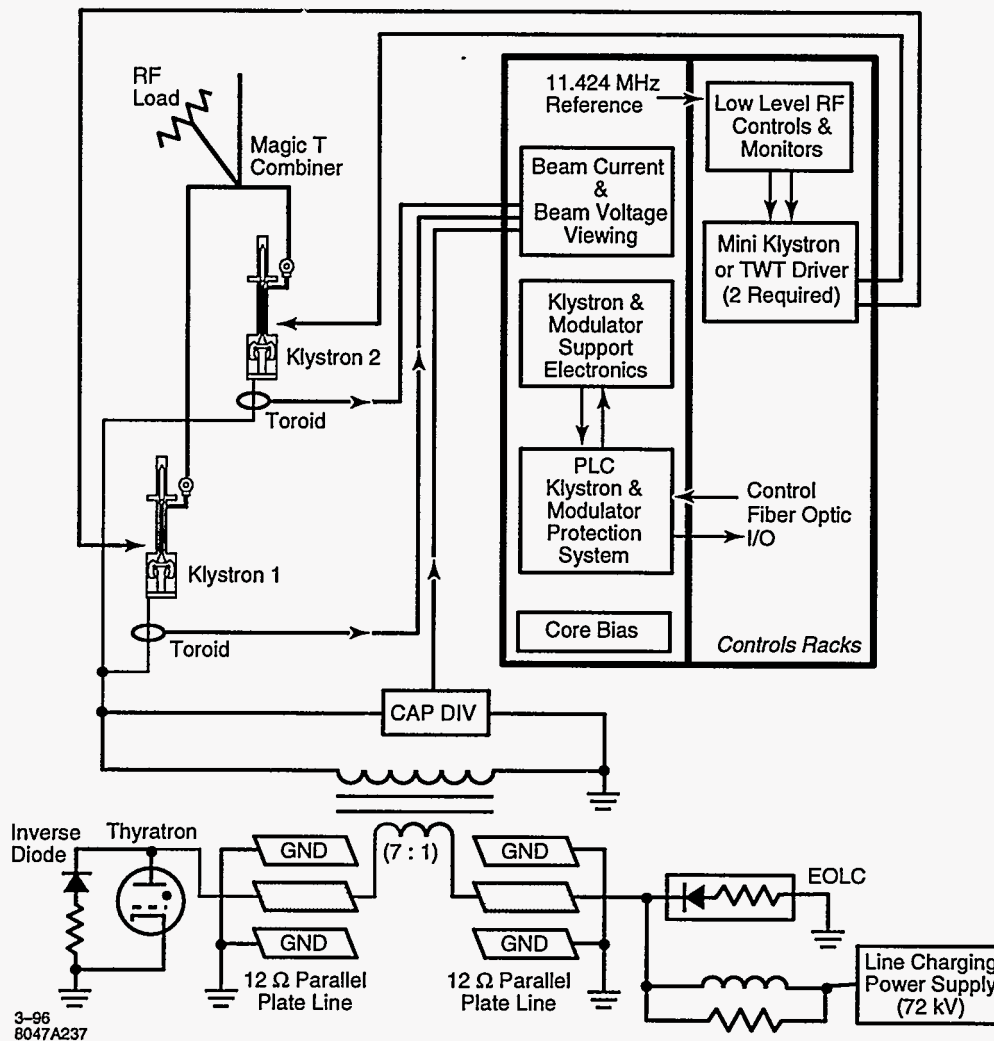


Figure 8-39. NLC RF Station Block Diagram

8.5 Klystron Pulse Modulator

Each high-power rf station includes a pulsed energy delivery system that is tightly integrated in design with the beam generation section of the klystron, and a high-efficiency power supply for charging the PFN (pulse forming network) capacitance. A preliminary design is shown in the diagram in Figure 8-39.

The subsystems of each rf station, discussed in this section, include a single-thyratron Blumlein modulator (Section 8.5.2) driving two PPM-focused klystrons, the modulator power supply (Section 8.5.3), and the station-cooling and oil-circulation systems (Section 8.5.4). The protection systems will be discussed in Section 8.7. All of these subsystems are closely interlinked.

There is much basic research and development that must be accomplished to characterize a final system that will maximize efficiency at minimal cost, and will be reliable and serviceable. Some elements of a program for developing prototype modulator components are outlined in Section 8.5.6. In the meantime, modulator performance can be estimated through simulations. These simulations are based on the best knowledge available for modulator components, in particular the pulse transformer. Simulation examples are given in Section 8.5.5; these are used to obtain the efficiency estimate for the NLC modulator design goals as shown in Table 8-11.

8.5.1 Modulator Requirements

Specifications for the NLC modulator are given in Table 8-11. These specifications are driven by the requirements of the NLC klystron, as listed in the first part of the table. Although the initial design goal for this klystron is an output power of 50 MW, as required by the 500-GeV NLC design, an improvement program is in progress which will eventually increase the power output to the 75 MW required for the 1-TeV upgrade. The modulator must therefore be capable of driving two klystrons at this higher power level. The repetition rate for the initial 500-GeV NLC design is 180 Hz. To save AC power, this drops to 120 Hz for the later 1-TeV machine. However, during the transition to the higher energy, there may be a mix of 50-MW and 75-MW klystrons on the linac, operating at 180 Hz. In fact, the higher power tube may be available even at the time construction begins on the 500-GeV collider. In either case, the modulator must be capable of driving the higher-power tube at the 180-Hz repetition rate.

The first two columns in Table 8-11 list the design goals for the 50-MW and 75-MW klystrons, and a corresponding set of parameters for a modulator capable of driving two such klystrons. However, as mentioned above, the 75-MW klystron and the modulator must also be capable of operating at a 180-Hz repetition rate, as reflected in the third column of Table 8-11. The efficiency of the 75-MW klystron may also fall short of the 60% efficiency goal, at least initially. To be conservative, the modulator parameters have therefore been chosen so that the modulator can drive a klystron with an efficiency as low as 55% to the required 75-MW output power.

A key consideration for a modulator in a linear-collider application is the efficiency with which power is transferred from the AC line to the klystron beam power in the flat-top portion of the high-voltage output pulse. A 1% decrease in efficiency at any point in this efficiency chain results in an increase by between one and two megawatts in the AC line power required for the NLC rf system. An important component in this efficiency is the ratio of the useful energy in the flat-top portion of the pulse to the total pulse energy, including the energy in the rise and falltime portions of the pulse. This rise- and fall-time energy efficiency is given (very roughly) by the ratio $T_K/(T_K + 1.1T_R)$, where T_K is the flat-top pulse width and T_R is the rise time (the constant 1.1 depends on the precise definition of rise time). In turn, the rise time is determined in large part by the physical design of the pulse transformer, and in particular by the leakage inductance (due to imperfect coupling between the primary and secondary windings). In practical pulse transformer designs, it is observed that the leakage inductance tends to decrease as the transformer turns ratio is decreased. However, a lower transformer turns ratio implies a higher value for the charging voltage for the pulse-forming network (PFN), and a correspondingly high hold-off voltage for the thyatron and other high-voltage components. For a modulator using a standard PFN design which can deliver a 500-kV output pulse, this charging voltage would be about 145 kV for the 7:1 pulse-transformer turns ratio listed in Table 8-11. However, by using a Blumlein-type of PFN, the charging voltage can be reduced by a factor of two to about 72 kV. Although a Blumlein PFN design is somewhat more complex, it makes possible both a low pulse-transformer turns ratio and a reasonable value for the charging voltage.

Description: Blumlein PFL configuration with individual line-charging power supply and 7:1 pulse transformer turns ratio.			
	50-MW Klystrons	75-MW Klystrons	Design Min/Max
Klystron Parameters:			
Klystron Peak Output Power (MW)	50	72	
Klystron Microperveance (μperv)	0.60	0.75	
Klystron Beam Voltage (kV)	465	490	
Klystron Efficiency (%)	57	60	55 Min
RF Pulse Width (μs)	1.2	1.0	
Repetition Rate (Hz)	180	120	180 Max
Modulator Parameters:			
Output Pulse Voltage (kV)	465	490	510 Max
Output Pulse Current, for two klystrons (A)	380	510	550 Max
Flat Top Pulse Width (μs)	1.2	1.0	
Repetition Rate (Hz)	180	120	180 Max
Pulse Flatness (%)	1	1	
PFL Voltage (kV)	68	71	75 Max
Est. Energy Transfer Efficiency ^a (%)	77.5	80.5	76 Min
PFL Stored Energy (J)	274	310	370 Max
Pulse Energy Width (μs)	1.5	1.2	
Pulse Rise Time (ns)	275	175	
Thyratron Current (kA)	5.3	7.15	7.7 Max
PFL Impedance ^b (Ω)	12.4	9.9	9.7 Min
Auxiliary AC Power ^c (kW)	2.2	2.3	2.5 Max
Est. Power Supply Efficiency (%)	93	93	92 Min
Net Modulator Efficiency (%) (excluding auxiliary power)	72	75	70 Min
AC Input Power (kW) (excluding auxiliary power)	53	40	72 Max

^aSee Section 8.5.5. The energy-transfer efficiency is given by the rise- and fall-time energy efficiency times a series loss efficiency (97% is assumed here).

^bAdjusted to match impedance of production klystrons.

^cIncludes thyratron heater, thyratron reservoir, and klystron cathode heater supply.

Table 8-11. Klystron-modulator specifications (two klystrons per modulator).

In a standard modulator design with output pulse lengths longer than a microsecond or so, lumped elements (capacitors and inductors) are used for the PFN. Such a lumped network has the advantage that it can be readily tuned to adjust the pulse shape, although it is still difficult to eliminate all of the ripples to attain a truly flat pulse unless a very large number of elements are used. Also, it is difficult and expensive to manufacture pulse capacitors with a very low series inductance and long life, especially when the polarity must reverse during the pulse, as required by the Blumlein configuration. For these reasons, the use of lengths of smooth transmission line (termed here a pulse-forming line, or PFL) is being proposed for the NLC modulator. The major disadvantage of such lines (long length) can be ameliorated by choosing an appropriate packing geometry and good mechanical design (Section 8.5.2).

The rise- and fall-time efficiency is the major component which determines the overall modulator efficiency. In addition, a voltage drop across the thyatron, eddy currents and hysteresis losses in the transformer core, and resistive losses in the transformer windings and connecting leads contribute an additional loss of several percent. The charging voltage on the PFL must be slightly higher (about 1.5%) to compensate for these losses. The corresponding loss in efficiency (97%), multiplied by the rise- and fall-time efficiency, gives the net efficiency with which energy stored in the capacitance of the PFL is transferred through the pulse transformer into the useful flat-top portion of the output pulse. A discussion of the projected efficiency for the NLC modulator design, based on simulations of the output pulse shape is given in Section 8.5.5.

8.5.2 Pulse Modulator Design Outline

The pulse modulator described in the section below is presented as an example of a design that is physically realizable with present design technology or modest extensions to that technology. In Section 8.5.6, an R&D program is outlined whose results will undoubtedly change this design.

The station klystron modulator drives two PPM-focused klystrons. The modulator is of the Blumlein type, and uses as its energy storage elements distributed-type transmission lines rather than lumped element artificial lines. The design is driven by the need to synthesize the klystron cathode pulse with the highest efficiency consistent with reasonable cost. In a modulator, the major areas where energy is lost are in the rise and fall times of the cathode pulse where energy is dissipated, but no useful rf energy is produced, and in the IR drops and capacitive and inductive stored energy that is dumped after each pulse ends. There is also the power lost in the thyatron voltage drop, and the energy necessary to operate the thyatron heater and reservoir.

In a thyatron-PFN modulator, the element determining the rise time is usually the pulse transformer. Because of the voltage hold-off necessary between the primary and secondary of the transformer, there is always leakage flux generated by the primary that does not couple to the secondary. This shows up as leakage inductance in series with the primary which limits the voltage rise time of the secondary. There is a minimum stray capacity associated with the klystron cathode, and the high-voltage secondary of the pulse transformer. This capacity must be charged on each pulse, and the charging energy is lost during each pulse fall time. The transformer core does not have infinite magnetic permeability, and so a real inductance which is not infinite appears in parallel with the primary of the transformer. This has the effect of lowering the load impedance as a function of pulse length, leading to droop at the tail end of the pulse. The transformer leakage inductance can be minimized by keeping the pulse transformer turns ratio as low as possible. A low ratio dictates a high-primary pulse voltage, and the primary voltage is limited by the switching capability of the thyatron and the voltage holdoff of the pulse forming line.

In the standard-design modulator, a single PFN switched by a single thyatron drives a high-ratio (typically 23:1) pulse transformer. A modulator using this conventional design was optimized for efficiency and

minimum rise time in the Test Stand 13 position in the Klystron Test Lab at SLAC. The rise time was less than 600 ns. This is typical of conventional design technology. A modulator design in which two PFNs are used, charged in parallel, and discharged in series (called the Blumlein design) allows the use of a low ratio (7:1) pulse transformer and a thyatron with reasonable voltage hold-off capability. In a lumped element PFN, internal inductance in the capacitors limits the shortness of the rise time that can be obtained. If a distributed transmission line is used instead of the LC lumped line, this limit can be circumvented. Figure 8-40 shows the simple Blumlein modulator concept using two 10- Ω distributed lines, a 75-kV thyatron, and pulse transformer with a 7:1 turns ratio and a primary impedance of 20 Ω . This circuit can provide a pulse rise time of less than 300 ns, delivering a 490-kV pulse of about 500 A to drive two 75-MW klystrons.

The Blumlein pulser circuit as shown in Figure 8-40 operates as follows:

1. A capacitor-charging power supply charges both inner plates of the two lines to a DC potential of +72 kV. The two inner plates and the primary of the pulse transformer are now at a +72-kV potential.
2. The thyatron is triggered and presents a short circuit to the left end of the left transmission line. The 10- Ω transmission line presents to the thyatron a voltage source of 72 kV in series with an internal impedance (line characteristic impedance) of 10 Ω . The current in the thyatron is thus 7.2 kA. In order to match the current and voltage conditions at the thyatron after switching, a -72-kV, 7.2-kA wave must be launched traveling to the right on the transmission line. After a time T (where T is the electrical length of the line), this wavefront reaches the end of the line at the connection to the pulse transformer. There it sees a load impedance of 30 Ω (the pulse transformer primary in series with the 10- Ω impedance of the second line). From transmission line theory, this mismatch launches a reflected wave of -36 kV, which travels back toward thyatron carrying a current of 3.6 kA.
3. The remaining current in the initial wave (7.2 kA - 3.6 kA = 3.6 kA) will start to flow through the primary of the pulse transformer at time $t = T$. It will also launch a wave with an amplitude of -36 kV traveling to the right in the second transmission line. The net voltage at the right side of the transformer primary is 72 kV - 36 kV = +36 kV. The net voltage drop across the primary is therefore 72 kV (also given by 3.6 kA \times 20 Ω). The transformer output voltage is this voltage drop times the 7:1 turns ratio, or about 500 kV.
4. The two -36-kV waves, traveling to the left on the first line and to the right on the second line, leave behind them voltages of -36 kV and +36 kV, respectively. Note that the polarity has reversed on the first line; this reversal imposes an additional burden on the design of pulse capacitors for Blumlein networks.
5. After a second period T , the two waves reach the left and right ends of their respective transmission lines. At that time a reflected wave of +36 kV (short circuit termination) is launched in the first line, and a -36-kV wave (open circuit termination) is launched in the second line. These waves travel back toward the pulse transformer during a third period T , and wipe out all the remaining energy stored in the two lines. At time $t = 3T$, the waves reach the pulse transformer and cancel the current flowing in the primary.

Distributed energy storage lines are most familiar as coaxial cables. There are many low-power applications where coaxial cables are used for smooth-pulse energy discharge. At high power, there is a good technology development in water-filled pulse lines for very short pulses at low impedance. These water-filled energy storage lines make use of the very high dielectric constant of pure water, $\epsilon_r > 80$, but they must be charged very rapidly because water as a dielectric cannot withstand high electric fields for more than tens of

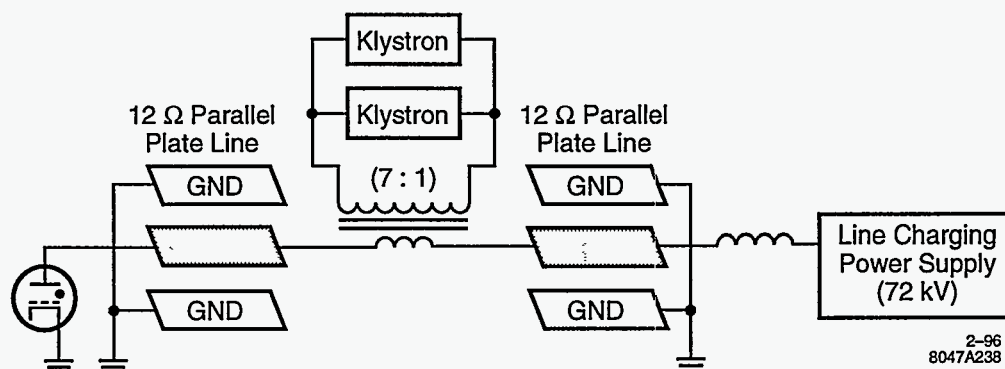


Figure 8-40. NLC modulator Blumlein schematic.

microseconds before it becomes lossy. An oil-filled line with high dielectric oil ($\epsilon_r = 7$) can in principle hold off a high voltage, but the support structure of the inner coaxial element is subject to creepage breakdown. For the NLC application, physically realizing a 10- Ω distributed line as a coaxial cable requires a very large diameter cable, since high-voltage creepage across the inner support insulator would otherwise limit the charging voltage. Any breakdown across the inner support insulator would be difficult to repair or replace.

An oil-filled five-layer parallel plate transmission line as shown in Figure 8-41, is physically realizable and relatively easy to manufacture and repair. The structure as shown contains two lines of 10- Ω impedance each. The dielectric constant of the oil is just that of normal transformer oil, 2.6. The oil containment for the transmission line is shown as separated from the klystron and pulse transformer oil so that high-dielectric ($\epsilon_r = 7$) oil can be considered in the design development or upgrade. Note that with normal transformer oil, $\epsilon_r = 2.6$, the transmission lines shown match klystrons of 0.6 μ perv. By increasing just the dielectric constant of the oil, lower impedance lines result that can match higher perveance klystrons. These lines would also be electrically longer by the square root of the dielectric constant ratio.

A proposed modulator tank supporting two klystrons is shown in Figure 8-41. The parallel plate transmission lines are shown mounted in the space between the inner oil tank and the outer containment tank. The total length of this double transmission line assembly is about 460 ft. The oil is contained in an aluminum racetrack-shaped inner tank that also serves as the support for the transmission line assembly. The transmission line assembly consists of continuous aluminum strips supported by molded nylon support insulators approximately one-inch-thick spaced at 12-in intervals. This construction allows easy servicing and repair of the pulse line if an arc destroys one of the support insulators. By supporting the parallel plates from the end of the aluminum strips, the creepage path between the plates can be made long enough to prevent discharge while still keeping the plate-to-plate gap small enough to take advantage of the greater breakdown properties of the oil.

There are a number of secondary elements also housed in the modulator tank: the end-of-line clipper diode stack, the charging diode (if one is used), the current viewing transformers and voltage viewing capacity divider, the core reset inductor, and the thyatron inverse clipper diode. All of these elements are contained in the inner tank adjacent to the thyatron and pulse transformer.

A double-rack enclosure adjacent to the modulator tank contains all the support electronics for the modulator, and the rf-drive electronics. The support electronics includes the klystron cathode heater supply, the thyatron cathode supply, the thyatron reservoir supply, the control power distribution, the rf low-level driver and interlock system, and a custom designed programmable logic controller (PLC) that provides the control and monitor functions for both the pulse modulator and the klystron rf drive and protection

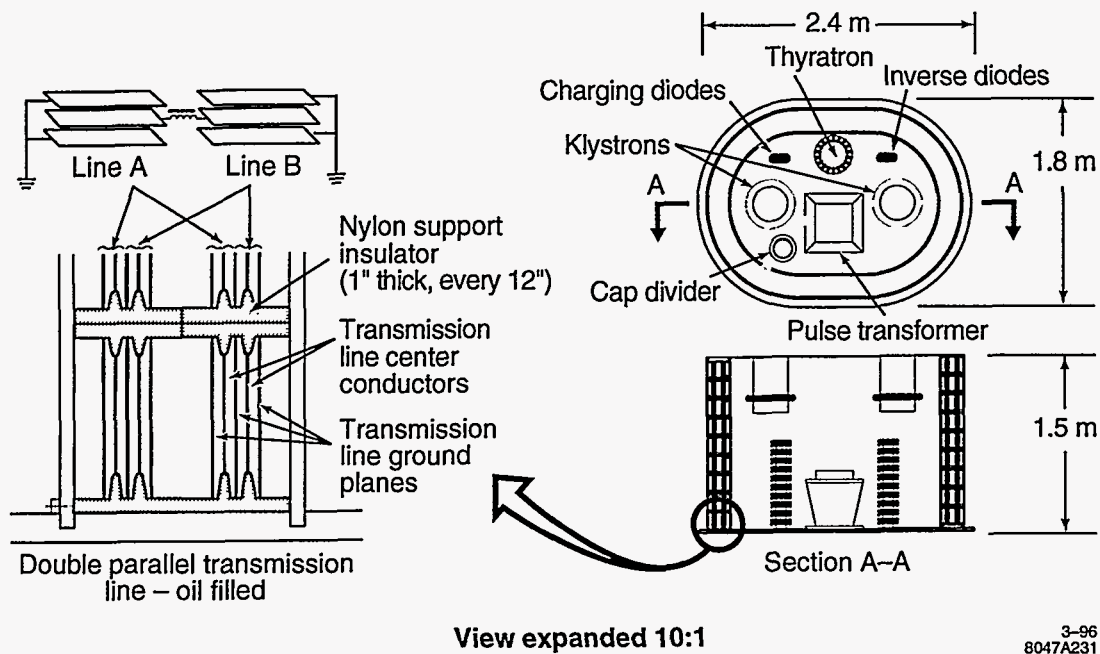


Figure 8-41. NLC modulator tank assembly showing two klystrons, thyatron, pulse transformer, and two multilayer plate transmission lines.

Charging Voltage	72 kV
Pulse Forming Line Capacitance	0.12 μ F
Joules/pulse, 2 klystrons	310
Repetition Rate	180 pps at 500 GeV; 120 pps at 1 TeV
Charging Voltage Regulation	0.1%
AC Line	480 V, 3-phase, 60 Hz
AC Line Stability	3%
Power Supply Efficiency	93%

Table 8-12. Charging power supply specifications.

systems. Depending on the construction design, this set of racks may also contain the primary capacitor charging power supply.

8.5.3 Charging Power Supply Design Outline

Specifications for 500-GeV Operation

The power supply that charges the PFL must fulfill the requirements shown in Table 8-12.

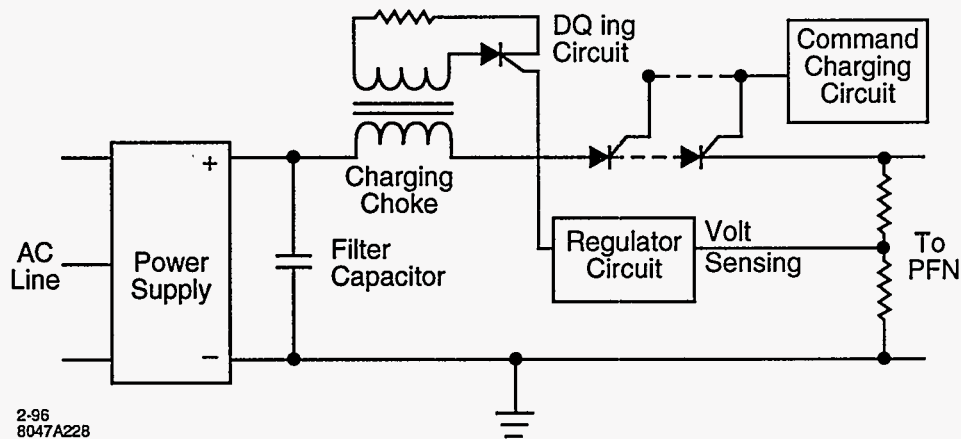


Figure 8-42. Conventional PFN charging power supply.

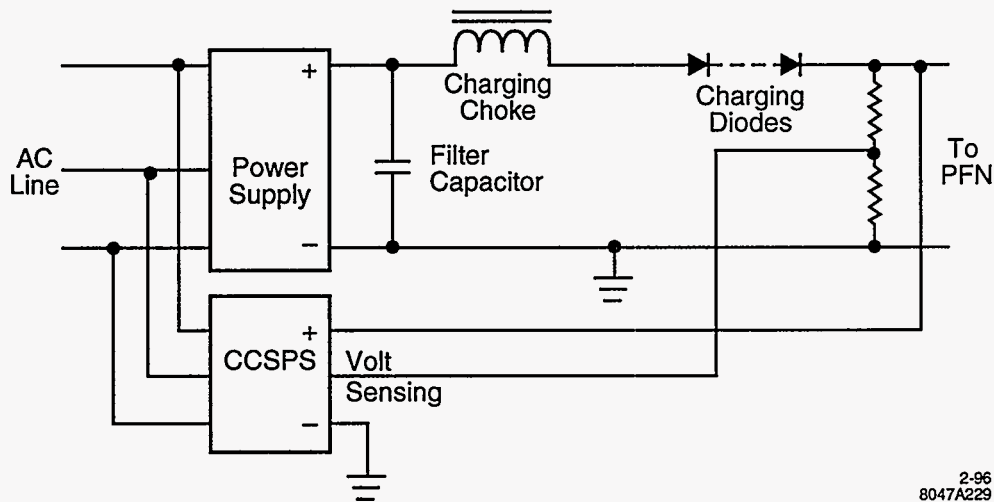


Figure 8-43. Hybrid circuit consisting of a conventional power supply and a small capacitor charging switching power supply (CCSPS) in parallel.

Conventional Charging System

Traditionally, the power supply that charges the PFL capacitance consists of an AC to DC power supply, a filter capacitor bank, a charging choke, a charging diode or a command-charging SCR circuit, and deQing circuit that regulates the PFN charging voltage (Figure 8-42).

If we assume an AC line stability of 3%, then we must deQ at least 6% to meet the regulation requirements. If the deQing power is dissipated, the efficiency of the power supply charging system is diminished. An energy recovery scheme could be developed to recover the energy and feed it back to the power lines, but it would be expensive and would only recover a portion of the energy. With energy recovery, we could only achieve a total power supply efficiency of about 90%. The output voltage could also be regulated by using a primary SCR line regulator instead of the deQing circuit.

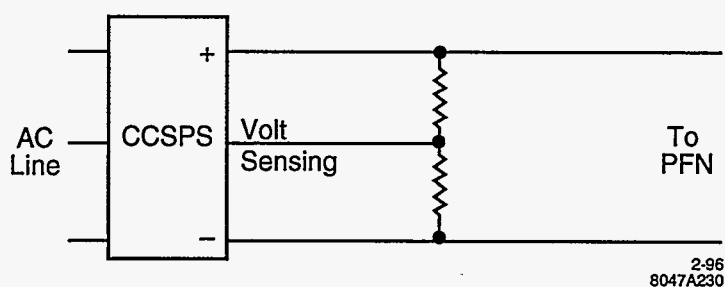


Figure 8-44. Capacitor charging switching power supply (CCSPS) scheme.

Hybrid Charging System

A better scheme would be to use a small capacitor charging switching power supply (CCSPS) in parallel with the charging choke output (Figure 8-43). At the lowest line voltage, the PFN would then be charged to 94% of its peak voltage by the charging choke, and the switching power supply would be used to charge the final 6% of the voltage. What we have done is substitute an additive process for a subtractive one with a resulting increase in efficiency. With this additive scheme, power supply efficiency could be as high as 93%.

Capacitor Charging Switching Power Supply System

An even more attractive idea is to use a CCSPS to charge the PFN directly (Figure 8-44). The charging cycle starts with the PFL capacitor at zero volts. The CCSPS starts charging the PFL at constant current until the desired voltage is reached. At that time, the supply becomes a constant-voltage power supply and keeps the PFL charged at the desired value. The charging waveform looks like a linear ramp which flattens out at the desired voltage.

The CCSPS supplies are becoming commercially available now and will be common in the near future. A single 50-kV power supply is presently available which will charge the PFL to 50 kV at 120 pps, will tolerate a voltage reversal of 20%, and has an efficiency of approximately 93%. Research is required to increase the charging voltage to a minimum value of 72 kV. To be able to charge at 180 pps, two CCSPSs, operated in parallel using master/slave connections, are required.

This solution will greatly simplify the charging circuit topology since there is no need for a filter capacitor bank, charging choke, command charging circuit, and high-voltage blocking SCR strings. The elimination of the filter capacitor bank reduces the amount of energy storage and the possibility of thyatron damage in a latch-up condition (when the thyatron fails to turn off, or breaks down during PFL charging). With a filter capacitor bank, a false trigger or a thyatron breakdown will cause the filter bank to discharge completely through the thyatron, and the power supply will then short circuit itself through the thyatron. With the CCSPS, a thyatron breakdown would only result in a maximum current equal to the nominal charging current since the CCSPS reverts to constant current operation when it is short circuited. As an additional advantage, the CCSPS is much more compact than a conventional power supply. For example, the 50-kV supply cited is rack mountable, 19" wide, 22" deep, and only 12.25" high.

Other manufacturers have built power supplies of this power level, housed in a single chassis and having an efficiency of approximately 85%. Additional development is needed to increase the efficiency and to develop a reliable 75-kV supply.

8.5.4 Station Cooling System and Oil Circulation

There are several cooling circuits that remove heat from the klystron and modulator. The klystron has just one water cooling circuit that is a combination of all the passages in the klystron. Temperature monitor points on parts of the klystron (body, anode, collector, etc.) provide interlocking for over-temperature conditions. The modulator contains two oil systems, one for the transmission lines oil which may have a higher dielectric than the main tank, and the other for the low-dielectric oil for the klystron guns, the thyratron, the end-of-line clipper (EOLC) and charging diodes, and the pulse transformer. Each of these systems will have a small oil-circulation pump and an oil-to-water heat exchanger appropriately interlocked.

There is no cooling required in the rf system support racks unless the charging power supply is mounted in these racks and it needs water cooling. There may be a need for water temperature stabilization if the rf components cannot be made to be phase-stable with temperature changes.

8.5.5 Simulations and Efficiency Projections

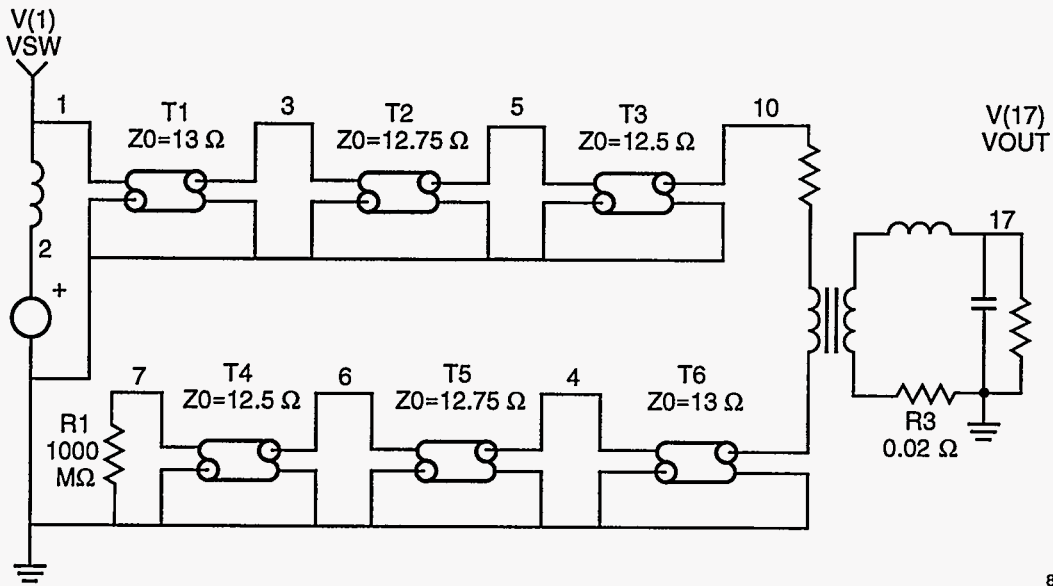
At the time of this writing, the efficiencies of the various components and subsystems are being analyzed, and the numbers will become clearer as R&D progresses. Pulse response simulations based on projected parameters of various lines, discrete capacitors, and pulse transformers are shown in this section.

Distributed Blumlein

There have been several preliminary network simulations run, using the program ISPICE, which show the general waveshapes on a Blumlein circuit using one or several segments of transmission line, as shown in Figure 8-45. By using several segments of varying impedance, the voltage at the tail of the pulse can be boosted to compensate for transformer droop. A simulated pulse shape is shown in Figure 8-46 for the case of a modulator driving a 50-MW klystron at 465 kV. The flat-top pulse length is about $1.4 \mu\text{s}$, the rise time is about 250 ns, the energy efficiency is about 83% and the peak-to-peak ripple about 2%.

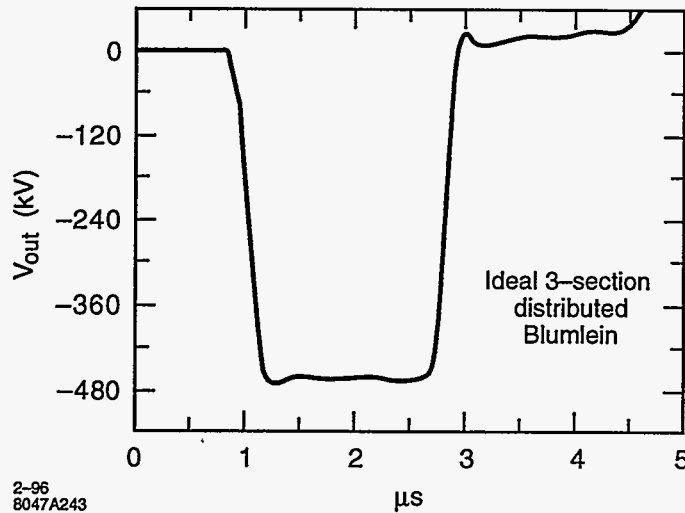
More detailed simulations are planned to look at waveshapes using more complex equivalent circuits that approximate real lines and pulse transformers. All the secondary parameters such as klystron stray capacity, the real characteristics of the various diode stacks and monitor elements, and the actual characteristic of a switched thyratron will be added to the model to get a better picture of what the real pulse response will be.

The dielectric constant of the various normal and high-dielectric oils must be characterized as a function of frequency, including dielectric losses, since the propagation of the wavefront on the lines will be limited by these parameters. High frequency losses limit the wavefront rise time, and dielectric constant variations with frequency can smear out the rise time, and cause pulse overshoot if all frequency components of the wavefront do not arrive at the end of the line at the proper times. It will take more development work with a simulation program to allow the dielectric constant to have a real and imaginary part corresponding to loss and propagation velocity.



2-96
8047A242

Figure 8-45. Example of a three-section Blumlein circuit.



2-96
8047A243

Figure 8-46. Voltage pulse obtained from simulation of an ideal three-section distributed Blumlein.

Discrete Element Blumlein

While smooth distributed transmission lines are attractive substitutes for lumped element lines with discrete capacitors, there are some advantages to using lumped elements, especially if the capacitors can have high-energy storage density, low inductance, and easy manufacturability leading to low cost. Strontium Titanate (ceramic type) capacitors have high-energy storage density, and because they can be automatically manufactured, can have very low per-unit cost. A lumped element line using as many as two hundred elements can approximate the characteristics of a smooth oil-filled line, but can be packaged into a much smaller volume because of the high energy storage density in the Strontium Titanate dielectric. Much R&D will be necessary to physically realize such a line and to produce low-inductance capacitors.

8.5.6 Prototype Modulator Development and Performance

In the Klystron Test Lab at SLAC, there are two modulators which can give some experimental check points to compare with simulations. Test Stand 13 is a high-power conventional modulator which contains close-coupled PFNs and a direct connection to a 23:1 pulse transformer. It produces 550-kV pulses driving a 1.8 microperveance klystron for a 3- μ s flat-top pulse.

Test Stand 3 contains a three-section Darlington line modulator driving a 6:1 pulse transformer with all primary pulse-forming elements in one large oil tank. It also is designed to produce 600-kV pulses, but it has not run at full voltage in oil as yet. The capacitors that make up the three PFNs have too much series internal inductance to allow a very fast rise time, flat-top pulse. Additional testing will be done on this modulator to get better data. This test stand will be used as the location for new R&D work on distributed and lumped element pulse line modulators.

As the paper design of a possible NLC modulator evolves, the R&D areas where the new ideas must be tested start to surface. At the present time, we can divide the R&D effort into two categories: System concept development, and component and subsystem design and testing.

System Concept Development

Conventional klystron beam-delivery pulse-modulator systems proceed in design with microwave-oriented klystron engineers developing the klystrons, and electronics-oriented modulator engineers designing modulators to meet klystron specifications. While this cooperative effort can sometimes produce well-coordinated results, more often performance, cost, and efficiency savings are lost in the interface process. By considering the klystron beam formation design as an integrated system with the pulse transformer and primary pulsed energy storage system, trade-offs can be made at an early stage in the design development resulting in a better optimized system.

New concepts can be considered when the system is an integrated whole. As an example, the klystron interface with the pulsed high voltage is traditionally a large, cylindrical ceramic interfacing the high vacuum of the klystron to the oil insulation of the pulse transformer tank. Consider the advantages of a pulse tank under high vacuum instead of being filled with oil. With vacuum on both sides of the klystron cathode seal, the seal can be redesigned to be smaller, radial rather than cylindrical, and much easier to manufacture. The capacity of the gun structure decreases because of the smaller cathode system, and the absence of high dielectric oil. Inside the tank, the pulse transformer size might be reduced because of the better insulating properties of high vacuum. This smaller size, together with the lower dielectric constant, would reduce the

distributed capacitance between windings and other stray capacitances, and possibly also the leak inductance. All these reductions in stray energy storage work to decrease the rise and fall times of the cathode pulse, the whole system becomes more efficient.

To physically realize such a system, new R&D on a variety of components and subsystems must be conducted. These efforts are included in the proposed R&D program outlined below.

Component and Subsystem Design and Testing

In the component and subsystem area, R&D programs are needed to develop both oil-immersed and high-vacuum systems. Efficient charging supplies are a separate area of R&D where cooperation with industry should produce reliable, high-efficiency units that can be adapted for large-scale production. Some of the pulsed energy storage and delivery development efforts are as follows:

Thyratrons: The present design of two- and three-gap thyratrons is well advanced and with minor modifications can meet the needs of the NLC pulsed power switch. Long cathode life, on the order of 50,000 hours, has been achieved with a large dispenser cathode and increased-size hydrogen reservoirs. The R&D effort for thyratrons includes mechanical packaging for low-cost fabrication and quick changing in the field, and the reduction of power needed to heat the cathode and hydrogen reservoirs. This can be done as a joint effort with industry. We are fortunate in having at least three interested thyratron manufacturers with the skills and facilities to enter this development and optimization process.

Distributed Energy Storage Lines: Several different energy storage lines have been suggested, including oil-filled Andrews cable, either coaxial or triaxial, and the parallel plate open network described earlier. The oil dielectric-medium used in these lines requires further study to understand the breakdown properties and the dispersive characteristics of the various oils and other possible dielectric liquids.

The lines themselves need further detailed mechanical and electrical design analysis, including building some full-voltage test models to see how these lines perform. The manufacturability, fabrication cost, and maintainability of such lines must also be studied.

Lumped Element Quasi-distributed Storage Lines: Strontium Titanate (ceramic) high-voltage capacitors have very large energy storage density and in quantity are simple to manufacture. The temperature coefficient is rather large, but in a temperature stabilized oil environment, this drawback is not severe. A quasi-distributed energy storage line can be physically realized with as many as 100 elements which looks much like a distributed line, but is much smaller. R&D would be conducted on examples of this type of line to establish the feasibility of using it for the NLC pulsed power storage.

Pulse Transformers: Since all the pulsed energy storage systems envisioned for the NLC operate below 100 kV, a pulse transformer is required to transform the low-impedance line pulse to the higher impedance 500-kV level needed by the beam-forming elements of the klystron. Traditionally, this pulse transformer has operated in oil for insulation. The core material has been 2-mil tape-wound iron. Improvements can be made in pulse transformers both in the winding of the primary and secondary of the transformer, the use of oil versus vacuum insulation in the windings, and in the properties of the core material. This area is central to the R&D effort to produce a more efficient pulsed energy delivery system.

An oil-immersed transformer is fairly well understood. A transformer using high vacuum as the insulation medium is a challenge in that the materials used in the transformer and core are not usually good vacuum elements. However, with some innovative design both for the core and the windings, and for a bare ion pump contained within the pulse tank vacuum enclosure, a significantly improved pulse transformer and klystron cathode high-voltage seal can be physically realized. The resulting klystron and pulse transformer

tank package would be much smaller and lighter than the present 5045 klystron assembly, and would look more like the early-generation, SLAC XK-5 klystron, without the barrel permanent magnet.

Primary Materials Developments: Improvements in the understanding of performance and limitations of basic materials such as insulators, oil and general dielectric fluids, and core materials such as iron, nickel alloys, Metglas, etc. are necessary to develop the pulsed-energy storage elements envisioned above. With better understanding of basic material properties, more compact and reliable devices will be developed. The appropriate materials science research will be part of the modulator and klystron development program.

8.6 RF Drive and Phasing Systems

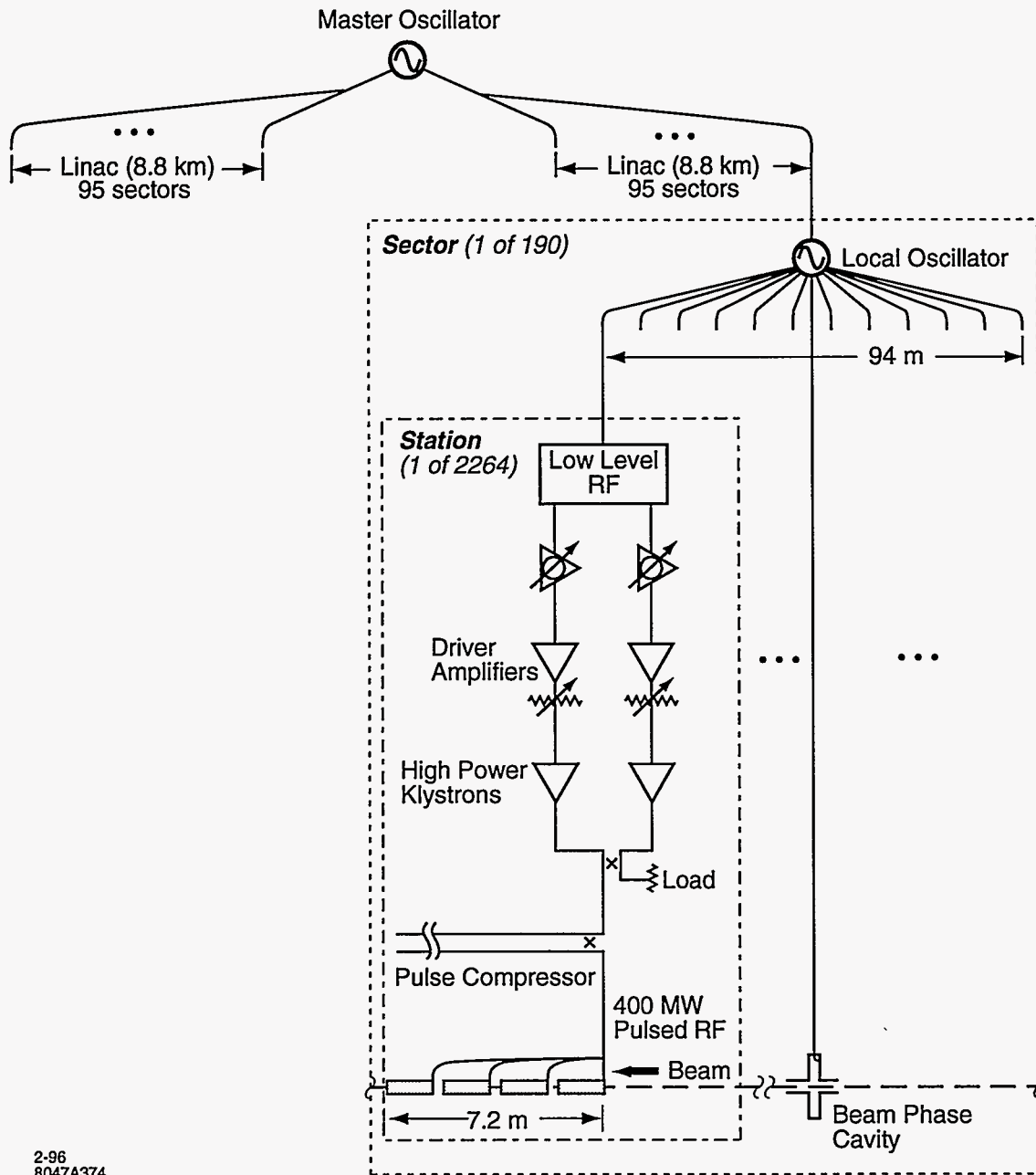
The design of the rf drive and phasing systems for the NLC will be based heavily on experience gained from existing systems developed for the SLAC linac and its 60-GeV upgrade for the SLC, with further extensions based on the design of the NLCTA. The challenges to be met for the NLC arise from its greater length, number of components that must be controlled, required tolerances, maintainability, and reliability. The requirements imposed on the rf drive and phasing systems are summarized below:

- The drive system must provide stable, adjustable, and reliable input power to 4528 klystrons (approximately 1-kW pulsed peak power per tube). The layout of the system must be such that individual subsystem failures do not cause the beam energy to decrease to less than 85% of its operating level. This requirement is dictated by potential collimator and other damage caused by off-energy beams.
- The amplitude of the drive power must be adjustable so as to individually saturate the high-power klystrons.
- The phase of the drive power must be adjustable in several ways:
 - Slowly, to take care of phase drifts and drifts caused by length changes in equipment and terrain. Included here are the couplers, coax lines, intermediate amplifiers, high-power klystrons, SLED-II, waveguide components, and the changes in time at which the bunch trains are injected into the X-band linacs by the S-band bunch compressors.
 - Quickly (within each 1.2- μ s klystron rf pulse), to create the proper resultant amplitude and phase profiles necessary to produce the desired fields in the accelerator structures and to place the bunches at the desired phase positions with respect to the X-band waves. These positions are dependent on bunch number and charge, which can change from pulse to pulse, and are dictated by BNS phasing, single bunch and multibunch beam loading, and other considerations.
 - The phasing system design must also include initial adjustments (upon installation) of the waveguide runs which feed the four accelerator sections driven by one pair of klystrons.

The phases of high-power rf fields which act on bunch trains should be adjusted to about 0.5° at 11.424 GHz. A schematic layout of the rf drive and phasing system for the NLC is shown in Figure 8-47.

8.6.1 Functional Overview

For NLC, the rf system must meet the challenges listed above, while giving the collider control system the tools required to model the machine performance accurately, and to change the operating parameters as



2-96
8047A374

Figure 8-47. Schematic of rf drive system. The master oscillator provides phase-stable rf to local oscillators in each sector over a fiber distribution system. Local sources in each sector provide 11.424 GHz to each rf station in the sector using coaxial lines. A beam-phase cavity uses the beam to determine the rf phase for optimum operation. Power levels are low (several milliwatts) until the final drive for the high-power klystrons.

Master Oscillator Quantity: 1	Logical Sectors Quantity: 190	RF Stations Quantity: 2264
<ul style="list-style-type: none"> • 11.424-GHz reference signal • Fiber optic distribution 	<ul style="list-style-type: none"> • Local oscillator • Beam phase correction • Coaxial rf distribution within sector • 12 rf stations per sector • 94 meters sector length 	<ul style="list-style-type: none"> • One modulator • Two klystrons • SLED-II rf pulse compression (5:1) • Four accelerator sections • Phase coupler for klystron and beam-induced rf • Rf phase detectors

Table 8-13. Contents and granularity of rf sub-systems.

conditions mandate. The machine rf requirements and the proposed solutions which follow constitute a proposal to meet these goals.

The sub-systems of the NLC rf drive and phasing systems are shown in Table 8-13 and outlined below. The individual subsystems are fully described in later sections.

The master oscillator for the accelerator generates the accelerator's primary 11.424-GHz reference and uses a fiber-optic based transport system to provide the frequency reference to each sector's local rf source. This signal is used as a diagnostic reference and serves to maintain system stability in the absence of a transported beam.

Each accelerator is divided into 95 sectors of up to 12 rf stations each. The sector size is determined primarily by two operational factors: the practical length of coaxial distribution systems for rf systems, and the requirement of the machine protection system that no single failure of a subsystem result in a destructive, non-transportable beam. For comparison, SLAC has 30 sectors consisting of eight high-power klystron/modulator stations.

Each sector has a local oscillator to generate a harmonically-clean rf signal which is phase locked to the beam for additional stability. This signal is distributed to each station for rf drive and monitoring purposes.

The smallest unit in the accelerator rf systems is the station. Each station consists of a pair of high power klystrons powered by a single modulator. The klystrons are differentially phase modulated to achieve the phase and amplitude control required for SLED-II pulse shape control and to address thermal considerations associated with beam loading (see below). The high power klystron outputs are combined using a four-port power combiner with a high power load on the "unused" quadrature-phase output. The "used" output of the combiner drives a single pair of SLED-II energy compressor delay lines and four accelerator sections.

The amplitude output of the SLED-II compressor is shaped by phase modulation of the two klystrons in order that the power extracted by each electron bunch is exactly matched by the input rf power. In this way all bunches in the bunch train experience equal accelerating gradients. Indeed, the operational goal is to provide an accelerator gradient that will accelerate all bunches equally, allowing for changes in pulse length, shape and total charge.

- The beam energy gain must be stable and understood.
- The rf entering the accelerator must be modulated in amplitude and phase as a function of time to produce the design acceleration of the entire pulse-train. (Transient beam loading compensation was discussed in Section 8.2.3).
- The phase of the rf at the accelerator must be adjustable. Machine operation requires that sectors operate slightly off phase.
- The overall rf amplitude and phase of a sector must be controlled, even in the presence of large changes in beam loading.

Table 8-14. Basic rf control functions for NLC operation.

8.6.2 System Functional Requirements and Specifications

The acceleration of long trains of electron bunches places heavy demands on the control and monitoring of each sector's rf sources. The general monitoring and control functions for basic machine operation are listed in Table 8-14. Additional diagnostics and monitoring are required, with some specific items detailed in the sections that follow.

Performance specifications for rf devices, monitoring, and control functions depend on the nature of potential disturbances of the accelerating phase and amplitude, and general beam dynamics considerations. Disturbances with uncorrelated noise spectra ("gaussian processes") act weakly on the beam while disturbances which are strictly correlated across larger sections of the machine have a stronger effect on the beam.

Disturbances which have high frequency components (greater than $1/2\pi T_{\text{fill}}$ where T_{fill} is the rf filling time) lead to further relaxation of the tolerances which depends on the power spectrum of the disturbance (see Section 8.2.8) and the characteristics of the SLED-II and accelerator structures. Disturbances with very low frequency components (less than the feedback bandwidth) which are corrected by feedback systems also have relaxed tolerances.

Examples of several rf noise sources for consideration are:

- Errors in SLED-II shaping due to klystron bandwidth limits. These errors have both high and low frequency components, and are correlated and stable.
- Modulator thyatron induced phase and amplitude noise. Thyratrons are the primary source of modulator-induced errors, and are uncorrelated with an intermediate frequency spectrum.
- Local oscillator phase noise. These are broadband and are correlated within a sector.
- Thermally induced phase errors due to changes in average beam current. These have an intermediate frequency spectrum and are strongly correlated among all accelerating devices in the accelerator.
- Thermally induced phase errors due to tunnel temperature changes. These are typically very slow changes and are strongly correlated.

As seen by the above examples, no single set of tolerance values can apply. An interesting metric for gauging a disturbance's effect is obtained by comparing the coherence length of the effect (correlation length of a station, a sector, a linac) to the "interaction length" of the process. The device tolerances may generally be reduced statistically by the square root of the ratio of the interaction length to the coherence length of

Parameter	Accuracy	Stability & Resolution	Units
Energy profile	± 0.5	± 0.1	% voltage
Energy gain knowledge	± 5	± 0.1	% voltage
Phase readback	± 1	± 0.1	degree
Phase stability	N/A	± 0.1	degree

Table 8-15. Summary of rf control specifications for each station.

the disturbance. (For the SLC at SLAC, the effective interaction length is on the order of several betatron wavelengths or, near the injector, the length to achieve an energy gain of several 10's of percent.) Because of this scaling, specifications for station and sector performance are looser than the accelerator performance goals. Since different errors have different interaction lengths, different relaxations of tolerances apply.

An example is found in the tolerance on the energy gain of each station, where the modeling code must know the beam's energy to scale the magnetic lattice. Errors in the energy result in the phase of the betatron oscillation "slipping" from the modeled values, generating errors in correction by steering and cascaded feedback systems.

Phase and Amplitude Specifications

As noted above, an additional complication (and relaxation of tolerance) comes from optimizing tuning procedures and feedback systems. Sensitivity to accuracy errors in phase and amplitude are quite low, while slow changes and fast jitters may range from annoying to debilitating for machine operation, depending on the power spectrum and the beam energy. Table 8-15 summarizes these goals.

Energy Profile Control

Knowing the expected beam current and pulse profile, a shaped rf voltage output is computed and programmed into the SLED-II energy compression system. Ramping allows a pre-loading of the accelerator with rf energy prior to the passage of the first bunch, with a reduced energy gain for the first bunch. The accelerator rf power immediately following the start of the passing beam would be near the full available power. This is done to allow the wakefields (which diminish the energy gains) of the leading bunches to be compensated before the subsequent bunches arrive.

The ramping of the power from the saturated klystrons can be done by either of two methods: identical phase modulation or complementary (opposite) phase modulation of the two klystrons in a pair. Identical phase modulation is achieved by applying identical time-dependent phase modulation to each of the two klystrons and thus to the SLED-II compressor input, such that four delay cycles of stored power leaving the delay line ports, plus the incoming klystron power, results in the desired rf voltage and phase modulation at the input to the accelerator during the beam's passage. Alternatively, the complementary phase modulation method takes advantage of the symmetry of the power combiner joining a pair of klystrons. Pulse shaping is achieved by phase modulation of the paired klystrons by equal amounts in opposite directions, resulting in a pure amplitude modulation at the SLED-II compressor input, with unused power being dissipated as heat in the combiner load. Complementary phase modulation need not apply any time-dependent phase

modulation at the SLED-II input. In the absence of system bandwidth considerations, both methods can generate the same waveforms for the duration of the rf filling time and beam passage.

For the NLC, we plan to use the method of complementary phasing (in opposite directions) of the accelerator klystrons to program the desired time-dependent SLED-II output. This method has several advantages over the identical phase-modulation method from the perspectives of improving performance and simplifying rf control design. These advantages are:

- Reduction of power dissipated in the accelerator. The unused power is dissipated in the power combiner load and not in the accelerator.
- A simpler correction for average power effects when the bunch count or the beam current is temporarily reduced.
- The bandwidth and finite rise time of the klystrons and drive systems do not result in complicated waveforms which may decrease performance and increase diagnosis and maintenance costs.
- A simpler monitoring system. Since the phase input and output of SLED-II are approximately flat (modulo a 180° phase jump), lower cost phase detectors may be used: either simple mixer-type phase detectors or quadrature-type phase detectors operating at a fraction of their potential capability. Phase modulated waveforms require detectors with a large phase dynamic range, and thus careful calibration to insure that changes in the overall phase do not affect the diagnostic reliability.

Sample modulation waveforms for the complementary phase modulation method are shown in Figure 8-48. For this study, the desired SLED-II output pulse shape is a ramped increase in gradient from 40% to 100% over the 100-ns fill time, followed by a 150-ns flattop. (See Section 8.2.3 on Transient Beam Loading.) In this study, the klystron's output bandwidth is modeled by the convolution of a 10-ns gaussian with an ideal klystron's output in the time domain. While there are an infinite number of equivalent solutions satisfying the output requirements, the following simple model with five-fold repeated symmetry for each of the compressed sub-sections is proposed to reduce the diagnostic problems presented to the rf systems maintenance personnel. Amplitude is shown as a solid line, phase as dotted, and the fill/acceleration interval is delineated with vertical dashed lines.

The desired resultant SLED-II envelope and the mathematical basis for the waveform are introduced in Section 8.2.3, "Transient Beam Loading". The operational goal for the NLC rf control system is to minimize beam energy errors; thus the controls must allow the development of models and algorithms for near real-time modification of the input waveforms to achieve the necessary energy-gain profile needed for the real current pulse shape and charge.

Knowledge of the Energy Gain

Control of the machine lattice (the magnetic optics which guide the beam) requires knowledge of the energy of the beam at all points in the accelerator, and of changes in the energy profile incidental to any significant bunch phasing, klystron phasing, or klystron population changes. Absolute calibration of the results is not as important as the consistency of the derived energy gain readings, since the total machine energy is ultimately determined by direct spectrometer measurements.

Modeling inputs use the nominal energy gain of the individual stations, beam current information, and other factors to compute the energy profile. Rf controls must be able to accurately report the approximate energy gain expected from the station as well as the current operational status of the station.

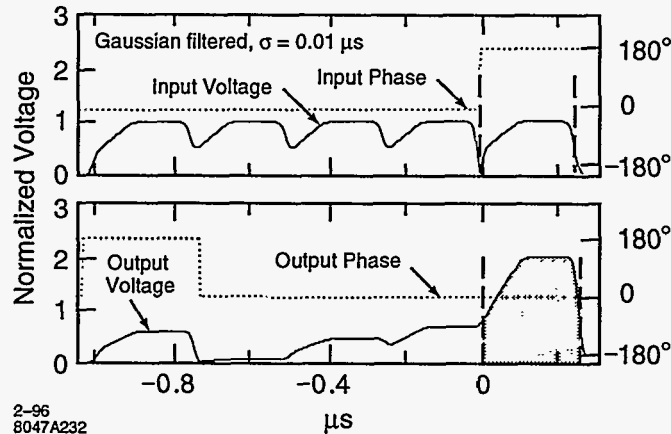


Figure 8-48. Illustration of SLED-II compression with pulse shaping achieved by complementary modulation of the phases of paired klystrons (equally, but in opposite directions) to achieve the input power modulation. Note that the phase of the SLED-II input is zero (modulo 180°), allowing use of simple nulling phase detectors. Klystron impulse response modeled as a gaussian with $\sigma = 0.01 \mu\text{s}$.

Experience with the SLC at SLAC has shown that the models for machine operation must be updated whenever the klystron population is varied, and that consistency in the predicted energy contribution of any individual station is more important than the absolute accuracy. Even so, each station's energy contribution has been individually calibrated using bolometric power meters and known coupling ratios, and the results have been compared with direct beam-based energy contribution measurements. Discrepancies in beam energy of greater than 5% have been observed in the two methods, and correction factors are generally placed in the database to insure that the instrumentation accurately reports each station's energy gain.

Phase Control

The DC phase of the output from each SLED-II compressor will be monitored and set to the nominal value using low-level phase shifters upstream of each klystron. Desired phase values will be derived by using a coaxial loop loosely coupled to the last cavity of an accelerator section and comparing a beam-induced rf signal in the accelerator section with the SLED-II rf signal.

Phase Stability

Stable beam operation is required over a range of 1 to 90 bunches and bunch charges varying between 10^9 and 10^{10} electrons per bunch. Uncorrected changes in either parameter vary the power deposited in the accelerator sections, with resultant changes in accelerator temperature of a degree Fahrenheit and average phase changes of 3° to 5° . Thermal characteristics of the accelerator structure are discussed in Section 8.2.5.

Corrections for changes in microbunch configuration will be done iteratively, allowing local controllers to modify energy profile appropriately.

Machine protection system (MPS) algorithms immediately reduce the bunch count to zero in the presence of beam loss. Operation resumes with a single-bunch, high-emittance probe beam at a low rate (1-10 pulse per second), followed by single bunch operation at full machine rate, with a ramped bunch count increase

as machine losses permit. Multibunch operation is always initiated with a single bunch probe beam on the previous machine cycle. Bunches are always deleted from the tail of the pulse, and thus will not require real-time modifications to the rf shaping. (Machine protection issues are discussed in Chapter 16.)

Machine repetition rate will be stepped up from the lower to full bunch count, with stable machine operation demanded without any allowance for thermal corrections. Corrections for this effect must be incorporated into the design, reducing the related phase error to less than 0.1° maximum net phase excursion averaged over all klystrons. (See Section 8.6.2.)

Two control paradigms are being considered, both of which may be required to meet the phase-stability imposed by the above MPS requirement for the main linacs. They are:

- Complementary phase modulation of pairs of klystrons to reduce the excess power entering the accelerator by dissipating power in the fourth port of the primary power combiner. In the same manner as the power is ramped up for the fill time prior to injection of the beam, rf amplitude will be stepped down following the passage of the leading bunches to reduce average power to the beam-loaded level. (This requires that klystrons be separately driven by pairs of klystron drivers to allow fast control of power.)
- Feed-forward control of the thermal regulation system for the accelerator cooling water to directly compensate for anticipated thermal changes related to beam current changes. Control using such regulation could practically reduce the thermal excursion by factors of 10 to 30, bringing the net effect to within operational tolerances. Such a feedback system is an NLC-specific development project since the requirements are more stringent than those generally met by industrial control specialists. Experience at SLC also indicates that use of thermal controls of accelerator related water systems has very high installation and maintenance costs, and thus is not being considered as the preferred option.

Phasing of the Accelerator

Phasing of the accelerator will use the beam to establish the optimal phase for each rf station. Fields left in the accelerator following the passage of a short pulse (containing 1 to 10 bunches of 3 to 7×10^9 electrons per bunch) will be used to determine the phase of the beam via a coaxial loop loosely coupled to the last cavity of an accelerator section. Phase measurement equipment monitoring the phase of the rf exiting an accelerator section will measure: a) the rf in the absence of beam loading, b) the beam-induced rf in the absence of klystron rf, or c) a vector combination of klystron and beam-induced rf during normal operation. The optimal accelerating rf phase will be determined from the difference (modulo 180°) of the klystron-driven phase and the beam induced phase, with knowledge of the current beam offset phase (the "phase closure" value). The difference in the readings will be used to phase the klystron station during routine setting of the nominal station phase offset. The phase signal during normal operation (case c) is of limited interest, and is not used for station operation.

8.6.3 Systems Overview

Low-level Accelerator-wide RF Distribution

Phase-stable distribution of X-band rf over the entire length of the NLC by coax is infeasible with current technologies. The NLC rf distribution will be based on:

- A master X-band oscillator.
- Fiber-optic distribution of primary rf to satellite rf oscillators using temperature-stable fiber distribution line.
- Phase-locked ultra-stable satellite oscillators at each sector locked to a phase-shifted reference derived from fiber optic distribution.
- Local beam-induced rf reference cavity near each satellite oscillator.
- Phase feedback controlling phase offset between fiber reference and local oscillator to null phase detector monitoring beam reference cavity.

Sector RF Source

Each sector will receive an amplitude modulated fiber frequency source, which will serve as the basis for the local oscillator's phase lock to master clock. The local oscillator serves as an extremely narrow-band filter, reducing the quantum (shot) noise and thermal noise power that would otherwise dominate the short term stability of an optical based distribution system. Distribution within each sector is achieved using low temperature coefficient copper coaxial lines [Andrew], which deliver a low power signal to each station. An additional cable will transmit the signal to the next sector, allowing a cross-check of each system's stability.

The local beam phase reference will consist of a tuned cavity, or of a few cells similar to the accelerator, that will provide a temperature-invariant reference signal or a high-bandwidth beam pickup followed by an appropriate bandpass circuit. The resultant phase information will be used to remove the local source's residual phase errors prior to distribution to the rf devices in the sector, as shown in Figure 8-49. The use of a beam pickup is considered a technical option which can eliminate an additional tuned cavity in each sector but will require the development of an specialized phase monitoring circuit. (Beam-phase pickups are used successfully at the SLC at SLAC for damping ring phase control at somewhat looser requirements.) Knowledge of the present beam parameters is required for this feedback loop, since the induced phase depends on the so-called "Phase closure" setting.

Long-haul distribution using fiber optic transmission lines has shown promise at SLAC and abroad. Special time of flight stabilized single mode fiber is manufactured with a proprietary coating system [Kakuta 1987, Kotseroglou, Sumitomo, Urakawa 1991], which substantially reduces the thermal drift inherent in glass-based transmission systems. Communication starts at a source laser using either direct intensity modulation or a narrow-band laser followed by an intensity modulator. Parallel fibers distribute signals to local sources in key sectors, where secondary fiber optic lines carry frequency information to each sector's rf source. Instrumentation at distribution points will consist of a local oscillator followed by a laser and modulator system as described above, and may share the oscillator with phase feedback of the standard local source oscillator. An additional fiber will transmit rf information to the next distribution point, allowing a cross-check of each system's stability. The long-haul fibers will be equipped with an interferometric length correction to remove the majority of the fiber's residual phase error. Similar fiber systems are used at SLAC to synchronize a laser for the E-144 experiment to the electron beam [Kotseroglou], with a residual fiber sourced phase error believed to be better than a fraction of a degree at X-band. The use of interferometric length correction has been used successfully for the primary rf distribution system for the two-mile-long SLC linac at SLAC, with distribution-based errors believed to be better than several degrees at X-band diurnally.

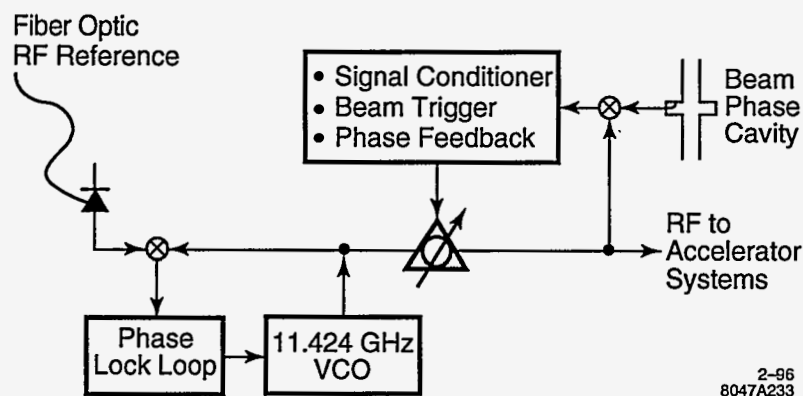


Figure 8-49. Schematic of a local rf source for each sector. Sector rf is derived from a low-noise oscillator with phase locking to detected beam-induced phase reference. Fiber-optic reference using liquid-crystal polymer (LCP) time-stabilized fiber provides stable reference in absence of beam.

Sector RF Distribution

Conventional coaxial distribution systems are proposed to transport rf drive and reference signals from the sector's rf source to each station. The choice of coaxial lines is based partially on the quantity of such connections and demonstrated reliability of the medium. Fiber-optic based transmission has been considered, but fails to meet the phase noise requirements of the klystron rf instrumentation without the use of an additional local oscillator at each station.

The cable plant consists of two identical rf cables from the sector rf source to each station: one cable is used for the amplification of the high-power rf by the linac klystrons, while the second cable is used solely for the rf instrumentation for a local phase reference (Figure 8-50). The use of a second reference helps for identifying distribution-related phase problems as anomalous station phase errors which can (with care) be identified and corrected. Experience at the SLC at SLAC has shown such redundancy is critical in identifying problems in the rf distribution system and has been specifically cited as a major factor in achieving the SLC's availability and reliability.

Station RF Components

The smallest unit for control of rf-related devices is the station. Each station consists of a pair of klystrons driven by a common modulator. Rf power is combined using a hybrid "T" with a load on the fourth port, and is compressed in time with a SLED-II compressor. Each station supplies power to four accelerator sections, as shown in Figures 8-47 and 8-51. Rf drive and rf reference signals come directly from the sector's low level rf distribution system on separate cables to allow diagnosing of rf distribution-related failures. The phase modulation generators will deliver different phase modulation when a klystron station is at standby (off-beam) time to maintain correct thermal equilibrium.

Monitor and control points are summarized in Table 8-16.

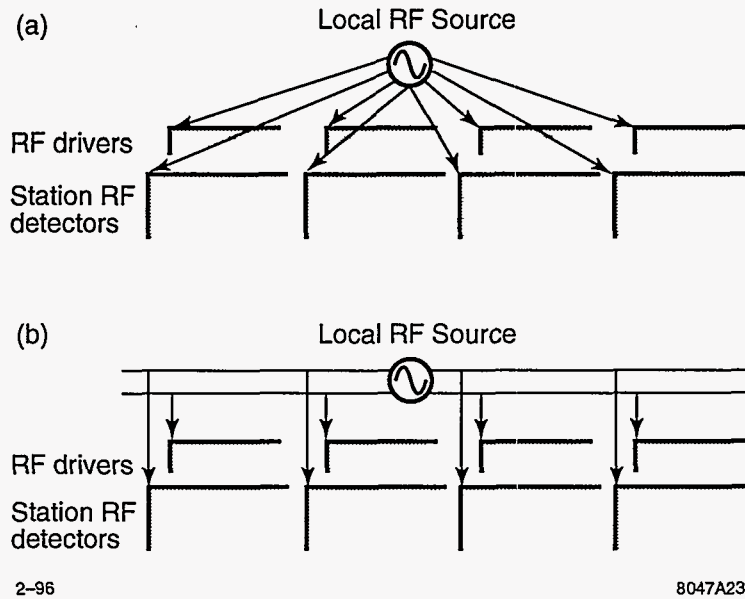


Figure 8-50. Two methods of rf distribution within any given sector. The use of redundant distribution lines allows identification of distribution-related phase errors. The first schematic (a) uses sets of dedicated lines to each klystron/modulator and instrumentation station, while the second (b) uses common lines for each function, with signal extraction through the use of a directional coupler.

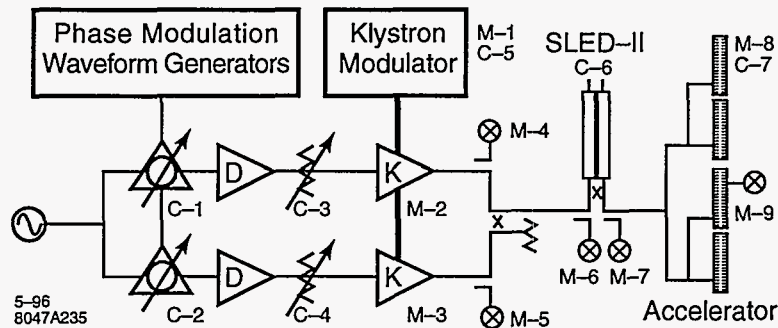


Figure 8-51. Schematic of rf components and controls for each station. Klystron drive is derived from the sector's rf source, with an adjustable phase and drive control for each klystron. Major control and monitor points are shown.

C-1 C-2	Klystron Phase Controls	Correction for slow and thermal drifts.
C-3 C-4	Klystron attenuator	Set for saturated operation. Part of klystron protection system.
M-1 C-5	Modulator monitor and controls	Triggering of klystron in response to control systems needs, readback of modulator status plus modulator (beam) voltage and current waveforms.
M-2 M-3	Monitor of klystron parameters	Signals such as klystron vacuum, body beam interception, etc.
M-4 M-5	Monitor of klystron rf forward and reflected signals	Klystron phase and amplitude waveforms. Primary monitor point for klystron performance. Reflected power for klystron protection systems.
M-6	Monitor of SLED-II input	SLED-II input phase and amplitude.
C-6	SLED-II cavity length tuning control	Motors or heaters as chosen to achieve modeled compression factor.
M-7	Monitor of SLED-II output and accelerator input	Phase monitor point for "trimming" phase of klystrons. Phase and amplitude waveforms of forward rf.
M-8 C-7	Accelerator cooling monitors and controls	Adjustment of water cooling set points and readback of temperatures.
M-9	Accelerator output monitor	Phase monitor allows independent measurement of phase of beam and phase of klystron system.

Table 8-16. Monitor and control points in the rf system.

Klystron RF Driver (TWT or Low-power Klystron)

There are various schemes for providing the approximately 1 kW of pulsed rf needed to drive each high-power klystron. It is useful to have individual drivers because the various phase manipulations involved in the operation of the rf compressors are best done at the milliwatt-level. Power-combining of the two klystrons on the single modulator is done by phase modulation of the two klystron inputs by equal amounts in opposite directions. This has the effect of sending the desired vectorial sum into the rf pulse compressor and dumping the vectorial difference into a load.

There exists extensive traveling-wave tube (TWT) technology at this frequency and power level as a product of military applications. The available TWTs are reliable, but fairly complex to manufacture and operate. They have already been extensively cost-optimized, and are still very expensive.

A small X-band driver klystron of fairly narrow bandwidth and modest gain could be designed. In construction, it would be relatively simple compared to a TWT. It is possible that after the initial engineering models are tested, a modest program of redesign for automatic manufacturing could reduce the unit cost significantly.

Low-level RF Station Controls

The rf for each klystron is appropriately phase modulated, at milliwatt power levels. Downstream from the kilowatt-driver amplifier, klystron attenuator controls are used to maintain saturation levels of individual

klystrons. The attenuators will also facilitate soft run-up of stations as might be required following venting of vacuum systems. Interlocks are discussed in Section 8.7.3.

Klystron and Modulator RF-Related Control and Monitor Points

Each station has a single modulator station powering two klystrons. The modulator instrumentation and protection system receives triggers from the rf support system, as well as indications of excessive reflected power requiring a modulator trip.

When the station is not used for the current beam pulse, it is fired in a standby mode, where the trigger time is offset from the normal beam time by at least several microseconds, and the modulation phase patterns are altered to maintain thermal equilibrium in the absence of beam loading. Appropriate triggers and phase controls are supplied by the rf support systems. For the accelerator at SLAC, standby time offsets are used as part of the beam containment system to insure that even a dark-current beam is not generated coherently through the linac. These delays are set on a sector-based pattern and implemented in hardware. The NLC may require similar logic to ensure that the radiation safety considerations have been met, without burdening the operation with unreasonable thermal settling delays.

The modulator system will provide the rf controls status information as well as a few high quality video-bandwidth monitoring signals of klystron beam voltage and beam current for monitoring by the rf digitization system (three channels per station).

High-Power RF Monitor Points

Between the output of the klystrons and the input of the accelerator is a high-power combiner and a SLED-II pulse-compressor system. Forward and reflected rf phase and amplitude are monitored at each point as identified in Figure 8-51.

Klystron forward output couplers are used to diagnose the performance and stability of individual klystrons, while reflected output peak values are provided to the modulator protection system. Phase and amplitude waveforms for the forward rf signal are required.

Combiner output signals are used to identify the performance of the SLED-II system, while reflection signals measure SLED-II tuning accuracy. Phase and amplitude waveforms are required in the forward direction (combiner output), while amplitude is required for the reverse output (SLED-II reflection).

The SLED-II output coupler is used to routinely trim the phase of the two klystrons to meet accelerator phase requirements. Outputs at this point are expected to exactly reflect the modeled rf power profile, and differences in this waveform will be corrected by cautious modifications to the klystron input waveform. The phase stability of this monitor point must exceed the station's phase stability requirements. Phase and amplitude waveforms for the forward rf signal are required.

Peak values of each monitor for each pulse will be sampled and digitized. Waveform recording of each channel will occur periodically and as requested by the control program. Periodic analysis allows a historical monitor (jitter and values) to be stored over days and months, while on request waveform acquisition allows the control room and maintenance personnel to diagnose suspect devices.

Sample size and resolution must allow device bandwidth limited signal acquisition with sufficient granularity. Minimum sampling speeds of 100 MSample/second and buffer depths of 256 allow the entire pulse to be represented with 10-ns sample sizes. 0.1% amplitude and 0.1° phase stability requirements can be met with

digitizers with resolution limits of 12 bits per sample (± 2048). The actual instrumentation sampling speed and resolution will be determined to take best advantage of commercially available instrumentation.

There are several cost-containment decisions which must still be made regarding station instrumentation. Current costs for VXI-bus (computer interfaced) digital oscilloscopes of the required bandwidth are quite high, and suggest that dedicated signal acquisition hardware for each channel will be prohibitively expensive. Cost control may dictate multiplexing of the signal inputs into a common digitizer. If the reliability of multiplexers can be improved, their use can reduce instrumentation investments at the operational cost of limiting simultaneous monitoring of multiple channels within a station. Alternately, instrument development efforts combined with waiting for the growth of the related industries may allow cost effective solutions not currently available.

Instrumentation may be shared between adjacent klystron stations or between clusters of stations, resulting in further reductions in cost. The locations and granularity of instrumental and computational support in the NLC must be based on an evaluation of the cost and power of available instrumentation. Serious attention must be paid to the relative costs of shipping rf signals in phase stable cables *vs.* the local conversion of phase data to video and shipping video to the analysis points. The most probable configurations are to have instrumentation centrally located between pairs of stations, or individual instrumentation for each rf station.

SLED-II Delay-line Tuning

The SLED-II delay lines must be tuned to maintain both differential and common errors to a small fraction of a wavelength. This tolerance can only be met through the use of an active temperature or electrical length control.

Differential length errors will result in rf power reflections into the klystrons and reduced energy gain for the station. Differential length adjustment must be done by minimizing the rf power reflections back into the klystron power combiner (by tuning). Common and differential length errors result in a reduction of the station's energy gain. These errors can be removed mechanically by controlling the delay line length. The common length errors can be removed electronically by step-modulation of the input phase to compensate for the common phase-length error in the SLED-II delay lines. Common length errors can be directly measured from the SLED-II forward power coupler as follows: (1) measure the phase of the earliest delay-line fill (this is from the reflections off the coupling irises), and (2) measure the phase of a subsequent fill (reflections off the irises plus the emitted field from the cavity). The second measurement should be at a phase angle of 180° shifted from the first.

The SLED-II delay lines in the NLC will be tuned either by sliding choked shorts at the end of each line (as used in the NLC Test Accelerator), or by thermal control of delay lines. Either solution will work.

Accelerator Control and Monitor Points

The pickup loops at the downstream end of each accelerator structure will extract the beam-induced signal for phasing the accelerator, as discussed in Section 8.6.2. Temperature monitoring of the copper of the accelerator combined with measurements of the average rf power and beam current will be used to set the water system to the optimal control temperature. The pickup loops at the downstream end of the each accelerator structure will be used to optimize this control. The time-dependent phase angle of the output of the accelerator following the passage of a short (single or few bunch) beam will be used as a cross-check of the temperature settings for the accelerator structures.

Accelerator RF Beam Position Monitor

Signals from the damping manifold monitor couplers will be used to optimize the transverse positions of the accelerator structures to minimize steering due to dipole wakefields.

Trigger Timing

The timing system must deliver to each klystron station the appropriate triggers and machine-configuration information to allow the triggering of the modulator and the rf and protection sampling systems. Configuration information will include information identifying if the trigger should result in a beam acceleration, or if the station is on standby timing for the next pulse. Due to the Machine Protection System constraints, the triggers and configuration information must be delivered and sampled at least 100 μ s prior to beamtime. The modulator trigger and rf shaping electronics will require timing that is adjustable in steps of about 5 ns, with short- and long term-stability a factor of two smaller.

Feedback and Related Systems

Active feedback systems, similar to those used in the SLC, are required to meet the NLC beam quality and machine performance requirements. Feedback systems, as defined below, which will directly interact with the rf systems are:

- Machine Energy Feedback
- Machine Energy Spread Feedback
- Bunch Energy Spread Feedback
- Pulse Energy Error Feedback
- Intensity Energy Feedforward
- Downstream Feedback Systems

Figure 8-52 illustrates the parameterization of energy and energy spread space for the NLC.

“Machine energy error” is the error in the energy of the bunch centroid. Errors are measured by the feedback system using beam position monitors in a dispersive region and computing the beam parameters (ΔE , X , X' , Y , and Y') using the modeled machine lattice. Changes in desired accelerator energy gain are computed and transmitted to the effected sector controllers. The energy gain is controlled by deliberately misphasing sector pairs of klystrons with complimentary phase offsets, producing changes in the net energy gain without affecting the beam energy spread. Experience in the SLC suggests that at least $\pm 2\%$ of the total gradient be available for total energy correction, which will be used to correct for gradient errors in the accelerator, and for changes in centroid energy from energy spread and pulse energy corrections [Sheppard 1987]. Experience also suggests that the feedback correction rate for this system will require at least 20 energy corrections per second at 180-Hz machine repetition rate.

Machine energy spread is measured by a dedicated spectrometer which measures the composite energy spread of the entire bunch train. Energy spread errors are fixed by changing the injection phase of the bunch from

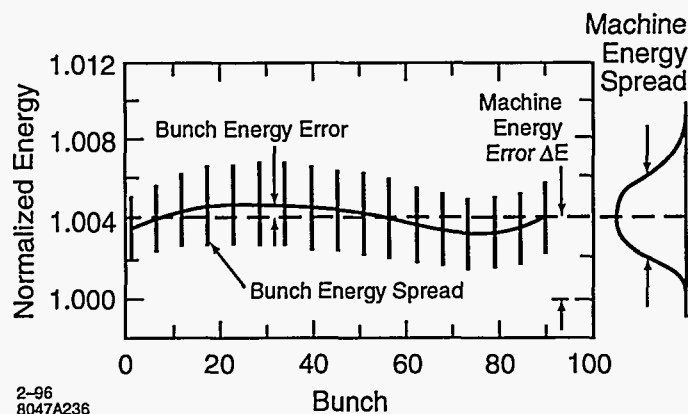


Figure 8-52. Plot of selected bunches within a NLC pulse. Parameters Energy Error, Pulse Energy Error, and Bunch Energy Spread are shown in the central graph. The projection at right depicts total machine energy spread, with the Machine Energy Error as its mean, and the width representing both the Pulse Energy Error and the Bunch Energy Spread.

the damping ring (the “phase closure”). Communication channels for this loop are similar to those for the ΔE correction with a system speed of several corrections per second.

Average beam energy errors and individual bunch energy spread are continuously measured by a dedicated spectrometer which can separately resolve the energy differences and the rms energy spread of the bunches. Energy errors are corrected by designing a modified SLED-II compressed rf profile, while energy spread errors in the individual bunches are corrected by controls in the damping ring extraction system and by the imposition of a phase modulation in the shaped SLED-II output. Communication channels for this loop are similar to those for the ΔE correction with a system speed of order a correction per hour with results available for history buffer logging every several minutes.

Intensity feedforward systems require the energy of the accelerator to be changed within a damping-ring store time. The measured stored beam current is used to predict an expected centroid energy shift ΔE due to off-normal beam loading effects. Communication channel speeds for this loop must be quite high, A dedicated channel to each sector may be necessary to maintain a rate of 180 corrections per second [Jobe 1991, Seeman 1991b].

Specific downstream feedback systems (such as steering systems, energy feedback systems, and detector noise minimization systems) may require knowledge of klystron errors or modulator protection cycles. Detector noise minimization systems, for example, will need to know if an rf station in the early section of the machine has faulted prior to computing orbit corrections to minimize beam scraper spray into the detector. Additionally, in the presence of extended error conditions (such as a vacuum fault), the machine protection system might abort beams to minimize detector backgrounds. In the SLC, each rf station announces its faults to the control system using a dedicated communication channel [Jobe].

8.6.4 Spectrometers

Primary machine optimization for the rf phase settings for the individual stations will use beam-induced phasing; all other optimizations will require a beam line spectrometer. Resolution requirements are summa-

Parameter	Resolution
Average Energy Measurement	<0.5%
Machine Energy Spread	<0.05%
Bunch Energy Spread	<0.1%
Bunch Energy Error	<0.05%

Table 8-17. Spectrometer resolution.

rized in Table 8-17 and such measurements should be available at the machine end, and at several points along the accelerator.

In order to meet target resolutions for machine and bunch energy spread, the spectrometers must be located at points of high dispersion ($\eta \gg 2000\sigma$). For a horizontal beam size (σ) of 0.1 mm at the spectrometer, the horizontal dispersion (η) should be greater than 0.2 m. Backgrounds for the spectrometer detectors must be sufficiently low for the spectrometers to operate in the machine environment.

The spectrometer detectors could utilize a pulsed laser beam probing the density of the bunch at the high dispersion point. Compton scattered electrons and a scanned laser probe beam, would provide all the information required. Individual bunch analysis might not be necessary, if the detector is capable of reporting separate values for early, middle, and later bunches in the train with sufficient resolution.

8.7 RF Protection and Monitoring Systems

All protection systems are serviced by dedicated local computers or programmable logic controllers (PLCs) plus some additional faster protection circuitry. This protection system combines the logical protection and operating functions of the modulator, the klystron, and the waveguide and structure systems. It includes the water-cooling system, the temperature-monitoring system, the various electronic monitors of the klystron support power supplies and the modulator electronics, the related vacuum systems, and the high-power rf protection. While these various protection and interlock systems are serviced by one PLC, the functions will be discussed separately in the sections below. The PLC communicates with the central computer to allow remote data logging, error reporting, and configuration control.

8.7.1 Waveguide Protection and Monitoring

Protection includes the high-power X-band waveguide, the SLED-II energy compressors, and the disk-loaded waveguide. Other than accelerated electron beam interception damage over which this interlock system has no control, the primary causes of potential component damage are arcing brought on by poor vacuum and loss of cooling. Because of the limited pumping speed of small waveguide, the high-power rf distribution system contains many individual ion pumps. It is expected that these ion pumps will be powered by a small number of multiple-output ion-pump power supplies that will be interlocked with the rf system module.

There will be a limited number of reflected energy pickup points, especially in the output arms of the klystrons, that will detect reflected energy due to arcs or SLED-II mistuning, and will operate through the PLC to inhibit either the drive rf to the klystron, or the klystron pulse modulator.

8.7.2 Klystron Protection and Monitoring

Klystron protection is accomplished by providing monitoring and interlocks on the systems which provide power and cooling water to the klystron, the klystron vacuum and the rf systems including the system vacuum. These monitoring and interlock signals are both analog and digital.

Most of the interlocking is done with a PLC which provides the interlocking and sequencing logic for the klystron system. Critical interlocks such as Klystron Output Reflected Power, which require faster response time, may be hard-wired for speed, and redundant to the PLC interlock.

The water system is designed for two klystrons per station with separate water circuits for each klystron. Each klystron will have a water circuit for its anode, its body and window and its collector. This water manifold will provide the cooling water for the klystron and modulator oil tank. Water flows will be monitored by the PLC for interlock and general monitoring functions.

Each klystron is instrumented separately for window temperature and body temperature. Increases in the body temperature, which increases if beam interception increases, is fed to the PLC and compared against a predetermined level; exceeding this level will cause the PLC to turn off the klystron beam. Window temperature will cause the rf drive to be removed if a maximum temperature is exceeded.

The klystron ion pumps will be connected in parallel into one controller for each klystron. The controller will have an internal vacuum pressure limit interlock which will be manually set. An excessive vacuum pressure interlock will turn off the klystron beam.

The klystron heater circuit, separate for each klystron, is equipped with an interlock for minimum heater current, and a warm-up time delay is provided by the PLC once the minimum current is exceeded. The klystron beam is inhibited until these interlocks are cleared. Analog signals for heater voltage and current are read by the PLC.

Klystron peak-cathode voltage and peak-cathode current are digitized in the support electronics and read into the PLC for over-current and over-voltage interlocking and into the main computer system for data-taking and storage. Klystron heater and high voltage operating hours will be totaled in the PLC.

The rf output waveguide transport system, which is under vacuum, is connected to ion pump supplies with manually set high-vacuum pressure interlocks. These feed into the klystron and modulator PLC to remove the rf drive when there is an excess pressure condition.

The rf output waveguide transport system also has various forward and reflected monitor points. An example of one of these monitor points is at the output of the klystron. These signals are each transmitted through a four-port coupler. One of these ports feeds a crystal detector into a video amplifier interlock system which provides buffered video outputs, a peak and hold-detected output, and a comparator circuit. The comparator circuits with manual adjustment can be used to interlock any of these detected signals. The output of the interlock is sent to the PLC for action. Klystron-reflected power is one of the critical interlocks which will also be hard-wired from the video amplifier interlock to directly remove the rf drive.

8.7.3 Modulator and Support Electronics Protection and Monitoring

The modulator control, interlocking, and protection is also accomplished through the PLC. The main protection interlocks are excessive EOLC current (for a klystron arc) and high-voltage-power-supply-overcurrent (HVOC).

The modulator protection system contains discharge solenoids, barriers, and door interlocks for protection of both personnel and equipment. It may be connected to the overall accelerator Personnel Protection System.

Thyratron warm-up time delay will be provided in the PLC after the thyratron electrodes are energized. Thyratron heater hours will also be totaled in the PLC.

8.7.4 Klystron and Modulator Logic Controller

At the present time, PLCs are being used for monitor and interlock functions in the Klystron Test Lab. On the NLCTA, two PLCs are used at each klystron station to provide modulator interlocking and control, and to monitor the operation of the klystron rf system and the various interlocks that protect the rf station. It is expected to use this same technology for each NLC rf station, but the general PLC will be replaced by a dedicated logic controller that is designed and optimized for NLC rf station operation.

8.7.5 Modulator Interactions with the Machine Protection System

The Machine Protection System (MPS) requires that the beam quality be maintained at an energy of at least 85% the expected energy. This requirement is determined by the limited ability of the collimators and beam line transport systems to handle a wildly off-energy beam. Under certain failure modes, catastrophic system failures can result from a single errant pulse.

Because of the large number of klystron/modulator stations, the interactions between MPS and klystron controls are fairly weak. The MPS is expecting each station to deliver a readiness confirmation which will be summed using a majority logic system to insure that the energy profile of the machine will follow the modeled values within a small tolerance ($\pm 15\%$ nominal). The implications and rules for the modulator and klystron systems are as follows:

1. The triggers for the klystron operation will be delivered at least $100 \mu\text{s}$ prior to beam time.
2. Following the receipt of the trigger, the modulator should be fully charged, and ready to fire.
3. The modulator system will promptly return a status indicator to the MPS controller indicating the readiness of an rf station and ability to fire its modulator.
4. Once confirmed, the modulator must fire at the designated time. Normal interlock conditions can not be allowed to disable modulator operation following the transmission of an MPS confirmation.

These MPS rules will insure that vacuum failure, AC power loss, trigger systems failure, and other larger system failures will not result in accelerator damage. Failures which are statistical in nature (such as thyratron triggering failure) are not expected to violate the MPS guidelines. (Special consideration also must be given to the readiness of kickers, dumpers, and perhaps certain critical klystron-driven systems.)

References

- [SLAC 1993] SLAC, "Next Linear Collider Test Accelerator Conceptual Design Report", SLAC Report 411 (Stanford University 1993).
- [Andrew] Andrew Corporation (Orland Park, Illinois), *Phase Stabilized Cables*, General Catalog No. 34, pp. 454-455.
- [Adolphsen] C. Adolphsen, K. Bane, H. Higo, K. Kubo, R. Miller, R. Ruth, K. Thompson, and J. Wang, "Measurement of Wakefield Suppression in a Detuned X-Band Accelerator Structure", SLAC-PUB-6629, submitted to *Phys. Rev. Lett.*
- [Adolphsen 1992] C. Adolphsen, K. Bane, G. Loew, R. Ruth, K. Thompson, J. Wang, "Measurement of Wakefields Generated in Accelerator Test Structures Using the SLC", SLAC-PUB-5941, 15th International Conference on High Energy Accelerators, Hamburg, Germany (1992).
- [Adolphsen 1994] C. Adolphsen *et al.*, "Measurement of Wakefield Suppression in a Detuned X-Band Accelerator Structure", *Proc. 17th Int. Linear Acc. Conf.*, Tsukuba, Japan, submitted to *Phys. Rev. Lett.* (1994).
- [Bane 1993a] K.L.F. Bane and R.L. Gluckstern, "The Transverse Wakefield of a Detuned X-Band Accelerating Structure", SLAC-PUB-5783, *Particle Accelerators* 42, 123 (1993).
- [Farkas 1974] Z.D. Farkas *et al.*, "SLED: A Method of Doubling SLAC's Energy", SLAC-PUB-1453, *Proc. 9th Int. Conf. on High Energy Accelerators*, Stanford, CA, 576-583 (1974).
- [Farkas 1986] Z.D. Farkas, "Binary Peak Power Multiplier and Its Application to Linear Accelerator Design", *IEEE Trans. MTT-34*, 1036-1043 (1986).
- [Farkas 1994] Z.D. Farkas and P.B. Wilson, "Ramping Profile for Exact Beam Loading Energy Compensation in the NLC Detuned Structure", NLC-Note 4 (Rev. 1), SLAC (December 1994).
- [Farkas 1995] Z.D. Farkas and P.B. Wilson, "RF and Beam Loading Parameters for the NLC Detuned Structure with Damping Manifold", NLC-Note 15, SLAC (June 1995).
- [Hoag 1993] H.A. Hoag *et al.*, "Flower-Petal Mode Converter for NLC", SLAC-PUB-6182, *Proc. 1993 Part. Acc. Conf.*, Washington, DC, 1121-1123 (1993).
- [Jobe 1991] R. Keith Jobe *et al.*, "Energy Feed Forward at the SLC", SLAC-PUB-5541, May 1991, in *Proc. 1991 Part. Acc. Conf.*, San Francisco CA, 1464-1466 (1991),
- [Jobe] R.K. Jobe, SLC Veto System, unpublished.
- [Kakuta 1987] T. Kakuta and S. Tanaka, "LCP Coated Optical Fiber with Zero Thermal Coefficient of Transmission Delay Time", *Proceedings of the 36th International Wire and Cable Symposium*, Arlington, VA 234-240 (US Army Communications Electronics Command, Fort Monmouth, New Jersey, 1987).
- [Kotseroglou] T. Kotseroglou, "Picosecond Timing of Terawatt Laser Pulses with the SLAC 46-GeV Electron Beam", SLAC-PUB-7130 (March 1996), submitted to *Nucl. Instr. and Methods*

- [Kroll 1994] N.M. Kroll *et al.*, "Manifold Damping of the NLC Detuned Accelerating Structure", SLAC-PUB-6660, in *Proc. 6th Workshop on Advanced Accel. Concepts*, Lake Geneva, WI (1994).
- [Kroll 1995] N. Kroll and K. Ko, private communication about work in progress (1995).
- [Lanciani 1953] D.A. Lanciani, "H₀₁ Mode Circular Waveguide Components", Conference on Millimeter Wave Research and Applications, Washington, DC (1953).
- [Lavine 1991] T.L. Lavine *et al.*, "High-Power Radio-Frequency Binary Pulse Compression Experiment at SLAC", SLAC-PUB-5451, *Proc. 1991 Part. Acc. Conf.*, San Francisco, CA (IEEE 91CH3038-7), 652-655 (1991).
- [Loew 1988a] G.A. Loew and J.W. Wang, "RF Breakdown Studies in Room Temperature Electron Linac Structures", SLAC-PUB-4647, presented at 13th Int. Symp. on Discharges and Electrical Insulation in Vacuum, Paris, France (1988).
- [Matsumoto 1991] H. Matsumoto *et al.*, "Applications of Hot Isostatic Pressing (HIP) for High Gradient Accelerator Structure", *Proc. 1991 Part. Acc. Conf.*, 1008-1010, San Francisco, CA (1991).
- [Matsumoto 1994] H. Matsumoto *et al.*, "High Power Test of a High Gradient S-Band Accelerator Unit for the Accelerator Test Facility", 17th Int'l Linac Conf., Tsukuba, Japan (1994).
- [Nantista 1993] C. Nantista *et al.*, "High Power RF Pulse Compression with SLED-II at SLAC", SLAC-PUB-6145, in *Proc. 1993 Part. Acc. Conf.*, Washington, DC, 1196-1198 (1993).
- [Nelson 1992a] E.M. Nelson, "A Finite Element Field Solver for Dipole Modes", SLAC-PUB-5881, in *Proc. 1992 Linear Accel. Conf.*, Ottawa, Canada (1992).
- [OWGR 1993] "Technology and Costs for 2 Million Copper Discs of the CLIC Accelerator at CERN", Optische Werke G. Rodenstock (1993).
- [Ramo 1984] S. Ramo, J.R. Whinnery, and T. Van Duzer, *Fields and Waves in Communications Electronics*, Second Edition (John Wiley & Sons, 1984). See Sections 7.8 and 7.10 for theoretical ohmic losses in waveguides.
- [Read 1993] R.F.J. Read and W.J. Wills-Moren, Cranfield Precision Engineering, Ltd., Bedford, England. "Study Report for the Estimation of Unit Cost of Mass Producing Discs for the CLIC Accelerating Sections" (1993).
- [Ruth 1993] R.D. Ruth *et al.*, "The Next Linear Collider Test Accelerator", SLAC-PUB-6252, in *Proc. 1993 Part. Accel. Conf.*, *loc. cit.*, 543-545 (1993).
- [Ruth 1993a] R. Ruth *et al.*, "A Test Accelerator for the Next Linear Collider", SLAC-PUB-6293, in ECFA Workshop on e^+e^- Linear Colliders (LC92), Garmisch-Partenkirchen, Germany (1992).
- [Seeman 1985] J. Seeman *et al.*, "RF Beam Deflection Measurements and Corrections in the SLC Linac", *IEEE NS32*, No. 5, in *Proc. 1985 US Part. Accel. Conf.*, Vancouver, Canada, 2629-2631 (1985).
- [Seeman 1991] J. Seeman, "The Stanford Linear Collider", *Ann. Rev. Nucl. Part. Sci.* 41, 389-428 (Annual Review, Inc., Palo Alto, CA, 1991).

- [Seeman 1991b] J. Seeman *et al.*, "Multibunch Energy and Spectrum Control in the SLC High-Energy Linac", SLAC-PUB-5438, in *Proceedings of the 1991 IEEE Particle Accelerator Conference*, San Francisco, CA, 3210-3212 (1991).
- [Seeman 1993] J. Seeman, "Accelerator Physics of the Stanford Linear Collider and SLC Accelerator Experiments Towards the Next Linear Collider", *Advances of Accelerator Physics and Technologies* (Vol. 12 of *The Advanced Series on Directions in High Energy Physics*), edited by Herwig Schopper, 219-248, (World Scientific, 1993).
- [Sheppard 1987] J.C. Sheppard *et al.*, "Three Bunch Energy Stabilization for the SLC Injector", SLAC-PUB-4100, in *Proc. 1987 Part. Acc. Conf.*, Washington, DC (1987).
- [Sumitomo] Sumitomo Electric Corporation (Yokohama, Japan), Liquid-Crystal Polymer (LCP) Fiber data.
- [Takeda 1991] S. Takeda *et al.*, "High Gradient Experiments by the ATF", *Proc. 1991 Part. Acc. Conf.*, San Francisco, CA, 2061-2063 (1991).
- [Tantawi 1993] S.G. Tantawi, K. Ko, and N. Kroll, "Numerical Design and Analysis of a Compact TE₁₀ to TE₀₁ Mode Transducer", SLAC-PUB-6085, *Proc. of the Computational Accel. Conf.*, Pleasanton, CA (1993).
- [Tantawi 1995] S.G. Tantawi, private communication about work in progress (1995).
- [Tantawi 1995a] S.G. Tantawi, A.E. Vlieks, and R.J. Loewen, "Performance Measurements of SLAC's X-band High-Power Pulse Compression System (SLED-II)", SLAC-PUB-95-6775, submitted for publication to *IEEE Microwave and Guided Wave Letters* (1995).
- [Tantawi 1995b] S.G. Tantawi, R.D. Ruth, and A.E. Vlieks, "Active radio frequency pulse compression using switched resonant delay lines", SLAC-PUB-95-6748, in *Nucl. Instr. and Methods A370*, 297-302 (1996).
- [Tantawi 1995c] S.G. Tantawi, T.G. Lee, R.D. Ruth, A.E. Vlieks, and M. Zolotarev, "Design of a multimegawatt X-band solid state microwave switch", SLAC-PUB-95-6827, in *Proc. 1995 Part. Acc. Conf.*, Dallas, TX (1995).
- [Tantawi 1996] S.G. Tantawi, NLCTA test results, unpublished (1996).
- [Thompson 1990a] K.A. Thompson and R.D. Ruth, "Controlling transverse multibunch instabilities in linacs of high energy linear colliders", SLAC-PUB-4801, in *Phys. Rev. D* 41, 964 (1990);
- [Thompson 1993] K.A. Thompson *et al.*, "Design and Simulation of Accelerating Structures for Future Linear Colliders", SLAC-PUB-6032, in *Particle Accelerators* 47, 65-109 (1994).
- [Thompson 1993a] K.A. Thompson and R.D. Ruth, "Simulation and Compensation of Multibunch Energy Variation in NLC", SLAC-PUB-6154, in *Proc. 1993 Part. Acc. Conf.*, Washington, DC (1993).
- [Thompson 1994a] K.A. Thompson *et al.*, "Design and Simulation of Accelerating Structures for Future Linear Colliders", SLAC-PUB-6032, in *Particle Accelerators* 47, 65 (1994).
- [Urakawa 1991] J. Urakawa and T. Kawamoto, "The Improvement of TRISTAN Timing System", *Proc. 1991 Part. Acc. Conf.* (IEEE Catalog No. 91CH3038-7) 1555-1557 (1991).
- [Vlieks 1993] A. E. Vlieks *et al.*, "Accelerator and RF System Development for NLC", SLAC-PUB-6148, in *Proc. 1993 Part. Accel. Conf.*, *loc. cit.*, 620-622 (1993).

- [Wang 1994] J.W. Wang *et al.*, "High Gradient Tests of SLAC Linear Collider Accelerator Structures", SLAC-PUB-6617, in *Proc. 17th Int'l Linac Conf., loc. cit.* (1994).
- [Wang 1994a] J.W. Wang *et al.*, "High Gradient Tests of SLAC Linear Collider Accelerator Structures", SLAC-PUB-6617, presented at 17th International Linear Accelerator Conference (LINAC 94), Tsukuba, Japan, (1994).
- [Wilson 1990] P. B. Wilson, Z.D. Farkas, and R.D. Ruth, "SLED-II: A New Method of RF Pulse Compression", SLAC-PUB-5330, in *Proc. 1990 Linear Accel. Conf.*, Albuquerque, NM (1990).
- [Wilson 1992] P. B. Wilson *et al.*, "Progress at SLAC on High-Power RF Pulse Compression", SLAC-PUB-5866, in *Proc. of the 15th Int'l. Conf. on High Energy Accel.*, Hamburg, Germany (1992).
- [Wright 1994] E. L. Wright *et al.*, "Design of a 50-MW Klystron at X-Band", Pulsed RF Sources for Linear Colliders: SLAC-PUB-6676, in *AIP Conference Proceedings 337*, Montauk, NY 1994, edited by Richard C. Fernow, 58-66 (AIP, New York, 1995).

Contributors

- George Caryotakis
- Dick Cassel
- Len Genova
- Saul Gold
- Harry Hoag
- Keith Jobe
- Ron Koontz
- Ted Lavine
- Greg Loew
- Bob Phillips
- Ron Ruth
- Sami Tantawi
- Kathy Thompson
- Juwen Wang
- Perry Wilson